

Springer Proceedings in Physics 125

Kaoru Yamanouchi
Katsumi Midorikawa *Editors*

Multiphoton Processes and Attosecond Physics

 Springer

SPRINGER PROCEEDINGS IN PHYSICS

Please view available titles in *Springer Proceedings in Physics* on series homepage
<http://www.springer.com/series/361/>

Kaoru Yamanouchi
Katsumi Midorikawa

Editors

Multiphoton Processes and Attosecond Physics

Proceedings
of the 12th International Conference
on Multiphoton Processes (ICOMP12)
and the 3rd International Conference
on Attosecond Physics (ATTO3)

With 178 Figures

 Springer

Editors

Professor Kaoru Yamanouchi

The University of Tokyo, Department of Chemistry
7-3-1 Hongo, Bunkyo-ku, Tokyo 113-0033, Japan
kaoru@chem.s.u-tokyo.ac.jp

Dr. Katsumi Midorikawa

RIKEN, Extreme Photonics Research Group
2-1 Hirosawa, Wako-shi, Saitama 351-0198, Japan
kmidori@riken.jp

Springer Proceedings in Physics

ISSN 0930-8989

ISBN 978-3-642-28947-7

ISBN 978-3-642-28948-4 (eBook)

DOI 10.1007/978-3-642-28948-4

Springer Heidelberg New York Dordrecht London

Library of Congress Control Number: 2012944400

© Springer-Verlag Berlin Heidelberg 2012

This work is subject to copyright. All rights are reserved by the Publisher, whether the whole or part of the material is concerned, specifically the rights of translation, reprinting, reuse of illustrations, recitation, broadcasting, reproduction on microfilms or in any other physical way, and transmission or information storage and retrieval, electronic adaptation, computer software, or by similar or dissimilar methodology now known or hereafter developed. Exempted from this legal reservation are brief excerpts in connection with reviews or scholarly analysis or material supplied specifically for the purpose of being entered and executed on a computer system, for exclusive use by the purchaser of the work. Duplication of this publication or parts thereof is permitted only under the provisions of the Copyright Law of the Publisher's location, in its current version, and permission for use must always be obtained from Springer. Permissions for use may be obtained through RightsLink at the Copyright Clearance Center. Violations are liable to prosecution under the respective Copyright Law.

The use of general descriptive names, registered names, trademarks, service marks, etc. in this publication does not imply, even in the absence of a specific statement, that such names are exempt from the relevant protective laws and regulations and therefore free for general use.

While the advice and information in this book are believed to be true and accurate at the date of publication, neither the authors nor the editors nor the publisher can accept any legal responsibility for any errors or omissions that may be made. The publisher makes no warranty, express or implied, with respect to the material contained herein.

Printed on acid-free paper

Springer is part of Springer Science+Business Media (www.springer.com)

Preface

This volume compiles research papers presented at the 12th International Conference on Multiphoton Processes (ICOMP12) and the 3rd International Conference on Attosecond Physics (ATTO3), held consecutively during July 3–8, 2011, at the same venue in Sapporo, Hokkaido, Japan.

The ICOMP conference series has a long history of 34 years. The first meeting was held in 1977 in Rochester, USA, and it has since been held every 3 years in various parts of the world: Budapest, Hungary (1980), Crete, Greece (1984), Boulder, USA (1987), Paris, France (1990), Quebec, Canada (1993), Garmisch-Partenkirchen, Germany (1996), Monterey, USA (1999), Crete, Greece (2002), Orford, Canada (2005), and Heidelberg, Germany (2008). This conference series has been essential in deepening our understanding of multiphoton phenomena. Indeed, it is no exaggeration to say that the scientific basis of intense laser science in the recent years has been established through the exchanges of ideas fostered by the ICOMP conferences.

The ATTO conference series, established in 2007 in Dresden, Germany, is designed to promote the newly emerging research field of attosecond science. The second conference was held 2 years ago in Kansas, USA. Special emphasis has been placed on attosecond pulse generation and its application as well as on the theoretical understanding of attosecond phenomena.

As both ICOMP12 and ATTO3 were scheduled to be held in Japan in 2011, and as they could share a variety of common topics in the rapidly developing research fields of ultrafast laser science, we decided to hold these two conferences together as a joint event, with a one-day overlap in their programs.

More than 180 oral and poster papers were presented in total, with participants arriving from more than 20 countries and regions. It is a tremendous honor for us that these two conferences attracted such a large number of attendees, particularly in light of the chain of disasters that have struck Japan, starting with the historic earthquakes of March 11, 2011. Indeed, as many as 67 of the presentations given have been turned into proceedings papers and contributed to this volume, reflecting the keen interest and excitement that were shared among all at the joint conference.

During their time in Hokkaido, the attendees enjoyed oral and poster presentations at the forefront of the rapidly developing research fields, and engaged in fruitful discussions, surrounded by the heritage of the centuries-old campus of Hokkaido University. Animated discussions continued as the participants enjoyed dinner at the Sapporo Biergarten, and made a trip to Otaru. We believe both ICOMP12 and ATTO3 have served to stimulate international research cooperation and exchanges.

Further information on the conference, including the lists of invited papers and contributed oral and poster papers, can be found on our website at: <http://www.icomp-atto.org/>.

We would like to thank Professor See Leang Chin, Honorary Chair of ICOMP12, for his invaluable presence and contribution to the discussions. We also thank all of the invited speakers of ICOMP12 and ATTO3 for their wonderful presentations.

The programs were organized by the international organizing committees of ICOMP12 and ATTO3, listed below. We would like to thank all of our fellow committee members for their commitment and generous contribution of their time.

Members of the ICOMP International Organizing Committee: Pierre Agostini (Ohio State University, USA); André D. Bandrauk (University of Sherbrooke, Canada); Wilhelm Becker (MBI, Germany); Joachim Burgdörfer (Vienna University of Technology, Austria); See Leang Chin (Laval University, Canada); Eric Constant (University of Bordeaux, France); Paul Corkum (University of Ottawa/NRC, Canada); Mikhail Federov (Moscow State University, Russia); Misha Ivanov (Imperial College, UK); Henry Kapteyn (JILA, University of Colorado, USA); Ferenc Krausz (MPI of Quantum Optics, Germany); M. Krishnamurthy (TIFR, India); Panagiotis Lambropoulos (IESL-FORTH, Greece); Anne L’Huillier (Lund University, Sweden); Ruxin Li (SIOM, China); Chii-Dong Lin (Kansas State University, USA); Katsumi Midorikawa (RIKEN, Japan); Mauro Nisoli (CNR-INFN/Politecnico of Milan, Italy); Jan M. Rost (MPI for the Physics of Complex Systems, Germany); Pascal Salieres (CEA-Saclay, France); Henrik Stapelfeldt (Aarhus University, Denmark); Kiyoshi Ueda (Tohoku University, Japan); Joachim Ullrich (MPI for Nuclear Physics, Germany); Marc Vrakking (MBI, Germany); Barry Walker (University of Delaware, USA); Ian Williams (Queen’s University Belfast, UK); Kaoru Yamanouchi (The University of Tokyo, Japan).

Members of the ATTO International Organizing Committee: Zenghu Chang (Kansas State University, USA); Dimitrios Charalambidis (FORTH-IESL, Greece); Paul Corkum (University of Ottawa/NRC, Canada); Louis DiMauro (Ohio State University, USA); Pedro Echenique (Univeristy of the Basque Country, Spain); Henry Kapteyn (JILA, University of Colorado, USA); Ursula Keller (ETH Zurich, Switzerland); Ferenc Krausz (MPI of Quantum Optics, Germany); Andy Kung (IAMS, Taiwan); Stephen Leone (LBNL/University of California Berkeley, USA); Anne L’Huillier (Lund University, Sweden); Chii-Dong Lin (Kansas State University, USA); Lars Madsen (Aarhus University, Denmark); Jonathan P. Marangos (Imperial College, UK); Deepak Mathur (ITFR, India); Katsumi

Midorikawa (RIKEN, Japan); Chang Hee Nam (KAIST, Korea); Mauro Nisoli (CNR-INFN/Politecnico of Milan, Italy); Gerhard G. Paulus (Friedrich Schiller University of Jena, Germany); Hrvoje Petek (University of Pittsburgh, USA); Alexander Pukhov (Heinrich Heine University of Dusseldorf, Germany); Jan M. Rost (MPI for the Physics of Complex Systems, Germany); Pascal Salieres (CEA-Saclay, France); Armin Scrinzi (Ludwig Maximilians University Munich, Germany); Joachim Ullrich (MPI for Nuclear Physics, Germany); Don Umstadter (The University of Nebraska-Lincoln, USA); David Villeneuve (NRC, Canada); Marc Vrakking (MBI, Germany); Zhiyi Wei (IOP-CAS, China); Martin Wolf (Free University of Berlin, Germany); Kaoru Yamanouchi (The University of Tokyo, Japan).

Also essential to the success of this joint conference were the efforts of the local organizing committee members, listed below. Our gratitude goes to each of them, as well as Yusuke Furukawa, Tsuneto Kanai, Yosuke Kojima, Pengfei Lan, Amani Abdolreza, Reika Kanya, Katsunori Nakai, Erik Lötstedt, and our three secretaries, Takiko Wakabayashi, Mihoshi Abe, and Chie Sakuta, who have helped organize the event and worked hard to make everything run as smoothly as possible.

Members of the ICOMP Local Organizing Committee: Yuji Fukuda (Japan Atomic Energy Agency); Koji Hatanaka (The University of Tokyo); Akiyoshi Hishikawa (Nagoya University); Tetsuya Ishikawa (RIKEN); Atsushi Iwasaki (The University of Tokyo); Tsuyoshi Kato (The University of Tokyo); Hirohiko Kono (Tohoku University); Takashi Nakajima (Kyoto University); Nobuhiro Ohta (Hokkaido University); Taro Sekikawa (Hokkaido University); Eiji Takahashi (RIKEN); Kiyoshi Ueda (Tohoku University).

Members of the ATTO Local Organizing Committee: Koji Hatanaka (The University of Tokyo); Kenichi Ishikawa (The University of Tokyo); Jiro Itatani (The University of Tokyo); Atsushi Iwasaki (The University of Tokyo); Toru Morishita (The University of Electro-Communications); Yasuo Nabekawa (RIKEN); Kazutaka Nakamura (Tokyo Institute of Technology); Kenji Ohmori (Institute for Molecular Science); Nobuhiro Ohta (Hokkaido University); Tomoya Okino (The University of Tokyo); Taro Sekikawa (Hokkaido University).

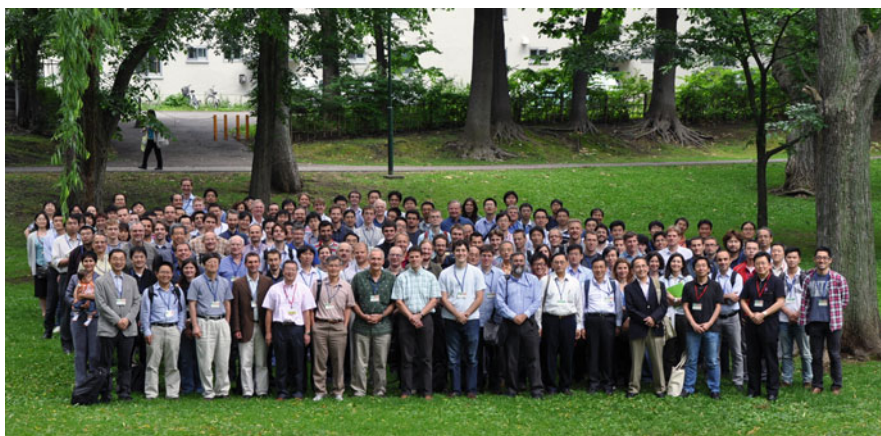
Last but not least, we would like to thank the following organizations for their generous sponsorship, which has made such a memorable occasion possible.

Japan Intense Light Field Science Society; CORAL, School of Science, the University of Tokyo; Extreme Photonics, RIKEN; Springer; IOP Publishing; Andor Technology plc.; Broadband, Inc.; Coherent Japan, Inc.; Excel Technology Japan K.K.; Femtolasers; Hamamatsu Photonics K.K.; Horiba, Ltd.; Japan Laser Corp.; Kantum Electronics; MegaOpto Co., Ltd.; Nippon Roper, K.K.; NTT Advanced Technology Corp.; Optima Corporation; Phototechnica Corp.; Sigma Koki Co., Ltd.; Spectra-Physics K.K.; Suruga Seiki Ltd.; Thales Japan K.K.; Thorlabs; Tokai Optical Co., Ltd.; Tokyo Instruments, Inc.; Visual Technology, Inc.

We feel that the ever-expanding frontiers of multiphoton processes and of attosecond physics have been exhibited well at the lively ICOMP12–ATTO3 conference. We hope that this conference and the current volume of the proceedings series contribute to further new developments in this interdisciplinary field of research.

Tokyo, Japan
Saitama, Japan

Kaoru Yamanouchi
Katsumi Midorikawa



Group photos of the participants at ICOMP12 (top) and ATTO3 (bottom).



Scenes from the ICOMP12-ATTO3 joint conference.

Contents

Part I Laser Light Sources

1 Self-Referenced Scheme for Direct Synthesis of Carrier-Envelope Phase Stable Pulses with Jitter below the Atomic Time Unit	3
Günter Steinmeyer, Christian Grebing, Bastian Borchers, and Sebastian Koke	
2 Single Shot Carrier Envelope Phase Stabilization of a 10 kHz, 10 W Regenerative Amplifier	9
Chengquan Li, Alex Schill, Florian Emaury, Jack Chu, Philippe Féru, Jean-Marc Héritier, and William Tulloch	
3 Intense Few-Cycle Mid-Infrared Laser Pulse Generation and Applications	15
Ruxin Li, Chuang Li, Liwei Song, Ding Wang, Canhua Xu, Cheng Gong, Yuxin Leng, Peng Liu, Zhinan Zeng, and Zhizhan Xu	
4 Few-Cycle, Phase-Locked, Octave IR OPA Using BIBO and 800-nm Pump	27
N. Ishii, K. Kitano, T. Kanai, S. Watanabe, and J. Itatani	
5 CEP-Stable, Few-Cycle, kHz OPCPAs for Attosecond Science: Energy Scaling and Coherent Sub-Cycle Pulse Synthesis	33
Kyung-Han Hong, Shu-Wei Huang, Jeffrey Moses, Xing Fu, Giovanni Cirmi, Chien-Jen Lai, Siddharth Bhardwaj, and Franz X. Kärtner	

6	Dual-Chirped Optical Parametric Amplification for Generating High-Power Infrared Pulses	41
	Q. Zhang, E.J. Takahashi, O.D. Mücke, P. Lu, and K. Midorikawa	
7	Development of High Power Infrared Optical Parametric Amplification Laser System Seeded by Self-difference Frequency Generation Pulses	45
	Tsuneto Kanai, Sébastien Weber, Amelle Zaïr, Christopher Hutchinson, Thomas Siegel, Malte Oppermann, Simon Hutchinson, Tobias Witting, Leonardo Brugnera, Rashid A. Ganeev, Toshiyuki Azuma, Katsumi Midorikawa, and Jonathan P. Marangos	
8	Spatially Resolved Characterization of Sub-4-fs Laser Pulses Using Spectral Shearing Interferometry	49
	T. Witting, F. Frank, C.A. Arrell, W. Okell, J.P. Marangos, and J.W.G. Tisch	
9	Enhancement of the Photon Flux of a Time-Compensated Monochromator by Phase Matching in a Hollow Fiber	53
	H. Igarashi, A. Makida, and T. Sekikawa	
10	Temporal Optimization of the Time-Delay-Compensated Monochromator	57
	A. Makida, H. Igarashi, and T. Sekikawa	
11	Characterization of Extreme Ultra-Violet Free-Electron Laser Pulses by Autocorrelation	61
	A. Senftleben, T. Pfeifer, K. Schnorr, K. Meyer, Y.H. Jiang, A. Rudenko, O. Herrwerth, L. Foucar, M. Kurka, K.U. Kühnel, M. Kübel, M.F. Kling, A. Yamada, K. Motomura, K. Ueda, R. Treusch, C.D. Schröter, R. Moshhammer, and J. Ullrich	
Part II High-Order Harmonics and Attosecond Pulse Generation		
12	Formation of Attosecond XUV Pulses via Resonance with Hydrogen-Like Atoms Irradiated by Intense Laser Field	71
	V.A. Polovinkin, Y.V. Radeonychev, M.Yu. Ryabikin, and Olga Kocharovskaya	
13	Exploration of Below-Threshold Harmonic Generation Mechanisms of Cesium Atoms in Intense Mid-Infrared Laser Pulses	79
	Y.-J. Chen, C. Laughlin, and S.-I. Chu	

14	XUV Supercontinuum Generated by Incommensurate Two-Color Mid-IR Optical Parametric Amplifier	85
	M. Negro, C. Vozzi, K. Kovacs, C. Altucci, R. Velotta, F. Frassetto, L. Poletto, P. Villoresi, S. De Silvestri, V. Tosa, and S. Stagira	
15	Ionization Gating for the Generation of Tunable XUV Radiation and Isolated Attosecond Pulses	91
	F. Calegari, M. Lucchini, K.S. Kim, C. Vozzi, S. Stagira, G. Sansone, and M. Nisoli	
16	Efficient Generation of Isolated Attosecond Pulse with CEP-Unstabilized Multicycle Infrared Double Optical Gating	97
	Pengfei Lan, Eiji J. Takahashi, and Kastumi Midorikawa	
17	Frequency-Controlled Isolated Attosecond Pulses Characterized by Both 750 and 400 nm Wavelength Streak Fields ...	101
	H. Mashiko, M.J. Bell, A.R. Beck, M.J. Abel, K.R. Siefermann, P.M. Nagel, J. Robinson, D.M. Neumark, and S.R. Leone	
18	Generation of Highly Phase-Matched Isolated Attosecond Pulses Using Multi-mJ, Carrier-Envelope Phase Stabilized, Few-Cycle Laser Pulses	105
	Tsuneto Kanai, Yuxi Fu, Yasuhiro Kamba, Samuel Bohman, Hiroshi Yoshida, Takuya Kanai, Shigeru Yamaguchi, Eiji J. Takahashi, Yasuo Nabekawa, Akira Suda, and Katsumi Midorikawa	
19	Route to One Atomic Unit of Time: Development of a Broadband Attosecond Streak Camera	109
	Kun Zhao, Qi Zhang, Michael Chini, and Zenghu Chang	
20	Quantum Path Interference in HHG: Impact on Harmonic Polarization and Molecular Imaging	121
	M. Yu. Ryabikin, A.A. Gonoskov, I.A. Gonoskov, and V.V. Strelkov	
21	XUV Interferometry of Attosecond Pulses	127
	Yasuo Nabekawa, Eiji J. Takahashi, Yusuke Furukawa, Tomoya Okino, Kaoru Yamanouchi, and Katsumi Midorikawa	
22	Exploiting Energetic XUV Super-Continua	137
	P. Tzallas, E. Skantzakis, L.A.A. Nikolopoulos, and D. Charalambidis	
23	The Influence of Plasma Defocusing in High Harmonic Generation	145
	Chien-Jen Lai, Kyung-Han Hong, and Franz X. Kärtner	

24	Beam Splitters for High-Order Harmonics Using Transparent Materials to Visible Light	151
	Yosuke Kojima, Yuske Furukawa, Yasuo Nabekawa, Eiji J. Takahashi, Fumihiko Kannari, and Katsumi Midorikawa	
25	Enormous Amplification of Full-Coherent Radiation in the Extreme Ultraviolet Region with a Free-Electron Laser	155
	Eiji J. Takahashi, Tadashi Togashi, Makoto Aoyama, Koichi Yamakawa, Takahiro Sato, Atsushi Iwasaki, Shigeki Owada, Kaoru Yamanouchi, Toru Hara, Shinichi Matsubara, Takashi Ohshima, Yuji Otake, Hitoshi Tanaka, Takashi Tanaka, Hiromitsu Tomizawa, Takahiro Watanabe, Makina Yabashi, Katsumi Midorikawa, and Tetsuya Ishikawa	
Part III Ionization of Atoms		
26	Breakdown of the Independent Electron Approximation in Sequential Double Ionization	165
	C. Cirelli, A.N. Pfeiffer, M. Smolarski, X. Wang, J.H. Eberly, R. Dörner, and U. Keller	
27	Sequential Double Ionization: The Timing of Release	169
	A.N. Pfeiffer, C. Cirelli, M. Smolarski, R. Dörner, and U. Keller	
28	Study of Asymmetric Electron Emission in Two-Color Ionization of Helium (XUV-IR)	173
	G. Laurent, W. Cao, I. Ben-Itzhak, and C.L. Cocke	
29	Control the Electron Dynamics in Nonsequential Double Ionization with the Orthogonal Two-Color Field	179
	Yueming Zhou and Peixiang Lu	
30	Sideband and Angular Distribution Oscillation of Photoelectrons Observed with XUV/IR 3D Momentum Imaging Spectroscopy	183
	A. Sperl, H. Rietz, M. Schoenwald, A. Fischer, K. Simeonidis, and J. Ullrich	
31	Attosecond Pump-Probe of Doubly Excited States of Helium through Two-Photon Interferometry	187
	Johannes Feist, Stefan Nagele, Christopher Ticknor, Barry I. Schneider, Lee A. Collins, and Joachim Burgdörfer	
32	Controlling and Reading Interference Structures Created by Strong Field Ionizing Attosecond Electron Wave Packets	193
	X. Xie, S. Roither, D. Kartashov, L. Zhang, E. Persson, S. Gräfe, M. Schöffler, J. Burgdörfer, A. Baltuška, and M. Kitzler	

33	Electron Wavepacket Interference Observed by Attosecond Transient Absorption Spectroscopy	199
	L. Gallmann, M. Holler, F. Schapper, and U. Keller	
34	Observing the Real-Time Evolution of Helium Atoms in a Strong Laser Field	203
	Niranjan Shivaram, Henry Timmers, Xiao-Min Tong, and Arvinder Sandhu	
35	Electron Correlation and Interference Effects in Strong-Field Processes	209
	Markus C. Kohler, Carsten Müller, Christian Buth, Alexander B. Voitkiv, Karen Z. Hatsagortsyan, Joachim Ullrich, Thomas Pfeifer, and Christoph H. Keitel	
36	Adiabatic Theory of Ionization of Atoms by Intense Laser Pulses	219
	Toru Morishita and Oleg I. Tolstikhin	
37	Trajectory-Based Coulomb-Corrected Strong Field Approximation	221
	T.-M. Yan, S.V. Popruzhenko, M.J.J. Vrakking, and D. Bauer	
Part IV Molecules in Intense Laser Fields		
38	Classical Models of H_3^+ Interacting with Intense Laser Fields	233
	E. Lötstedt, T. Kato, and K. Yamanouchi	
39	Electron-Scattering and Photoionization of H_2^+ and HeH^{2+}	239
	H. Miyagi, T. Morishita, and S. Watanabe	
40	Molecular Orientation by Intense Visible and THz Optical Pulses ...	243
	K. Kitano, N. Ishii, and J. Itatani	
41	Below-Threshold High-Harmonic Spectroscopy with Aligned Hydrogen Molecular Ions	247
	Fu-Yuan Jeng, Dmitry A. Telnov, and Shih-I Chu	
42	Two-Center Interference of Heteronuclear Diatomic Molecules in High-Order Harmonic Generation	253
	Xiaosong Zhu and Peixiang Lu	
43	Toward the Extension of High Order Harmonic Spectroscopy to Complex Molecules: Investigation of Aligned Hydrocarbons	259
	C. Vozzi, R. Torres, M. Negro, L. Brugnera, T. Siegel, C. Altucci, R. Velotta, F. Frassetto, P. Villoresi, L. Poletto, S. De Silvestri, J.P. Marangos, and S. Stagira	

44	Nonlinear Fourier-Transform Spectroscopy of D₂ Using High-Order Harmonic Radiation	263
	Yusuke Furukawa, Yasuo Nabekawa, Tomoya Okino, Kaoru Yamanouchi, and Katsumi Midorikawa	
45	Steering of Molecular Multiple Dissociative Ionization with Strong Few-Cycle Laser Fields	269
	Yunquan Liu, Xianrong Liu, Yongkai Deng, Chengyin Wu, and Qihuang Gong	
46	A Generalized Approach to Molecular Orbital Tomography	277
	C. Vozzi, M. Negro, F. Calegari, G. Sansone, M. Nisoli, S. De Silvestri, and S. Stagira	
47	Tracing Attosecond Electron Motion Inside a Molecule	283
	Liang-You Peng, Ming-Hui Xu, Zheng Zhang, and Qihuang Gong	
48	Natural Orbital Analysis of Ultrafast Multielectron Dynamics of Molecules	289
	Hirohiko Kono, Takayuki Oyamada, Tsuyoshi Kato, and Shiro Koseki	
49	Protonic Configuration of CH₃OH within a Diatomic-Like Molecular Picture	299
	Tsuyoshi Kato and Kaoru Yamanouchi	
50	Siegert-State Method for Strong Field Ionization of Molecules	305
	L. Hamonou, T. Morishita, O.I. Tolstikhin, and S. Watanabe	
51	Ionisation and Fragmentation of Small Biomolecules with Femtosecond Laser Pulses	309
	L. Belshaw, O. Kelly, M.J. Duffy, R.B. King, T.J. Kelly, J.T. Costello, I.D. Williams, C.R. Calvert, and J.B. Greenwood	
52	Initial Process of Proton Transfer in Salicylideneaniline Studied by Time-Resolved Photoelectron Spectroscopy	313
	T. Sekikawa, O. Schalk, G. Wu, A.E. Boguslavskiy, and A. Stolow	
53	Visualizing Correlated Dynamics of Hydrogen Atoms in Acetylene Dication by Time-Resolved Four-Body Coulomb Explosion Imaging	317
	Akitaka Matsuda, Mizuho Fushitani, Eiji J. Takahashi, and Akiyoshi Hishikawa	
54	Ultrafast Delocalization of Protons in Methanol and Allene in Intense Laser Fields	323
	Huailiang Xu, Tomoya Okino, Katsunori Nakai, and Kaoru Yamanouchi	

55	Double Proton Migration and Proton/Deuteron Exchange in Methylacetylene in Intense Laser Fields	335
	T. Okino, A. Watanabe, H. Xu, and K. Yamanouchi	
56	High Energy Proton Ejection from Hydrocarbon Molecules Driven by Highly Efficient Field Ionization	341
	S. Roither, X. Xie, D. Kartashov, L. Zhang, M. Schöffler, H. Xu, A. Iwasaki, T. Okino, K. Yamanouchi, A. Baltuška, and M. Kitzler	
57	Efficient Ionization of Acetylene in Intense Laser Fields	347
	E. Lötstedt, T. Kato, and K. Yamanouchi	
58	Laser-Assisted Electron Scattering and Its Application to Laser-Assisted Electron Diffraction of Molecules in Femtosecond Intense Laser Fields	351
	Reika Kanya, Yuya Morimoto, and Kaoru Yamanouchi	
Part V Laser-Induced Surface and Nanoscale Dynamics		
59	A System for Conducting Surface Science with Attosecond Pulses ...	359
	C.A. Arrell, E. Skopalova, D.Y. Lei, T. Uphues, Y. Sonnefraud, W.A. Okell, F. Frank, T. Witting, S.A. Maier, J.P. Marangos, and J.W.G. Tisch	
60	Attosecond Transversal Streaking to Probe Electron Dynamics at Surfaces	365
	Luca Castiglioni, D. Leuenberger, M. Greif, and M. Hengsberger	
61	Dynamics of Coherent Optical Phonons in PbTiO₃ Excited by Impulsive Stimulated Raman Scattering	369
	K.G. Nakamura, H. Koguchi, J. Hu, H. Takahashi, M. Nakajima, S. Utsugi, and H. Funakubo	
62	High-Order Harmonic Photoelectron Spectroscopy System towards Measuring Attosecond Electron Dynamics on Solid Surfaces	373
	Katsuya Oguri, Hidetoshi Nakano, Keiko Kato, Tadashi Nishikawa, Atsushi Ishizawa, Hideki Gotoh, Kouta Tateno, and Tetsuomi Sogawa	
63	Effect of Light Polarization on Plasma Distribution and Filament Formation	379
	L. Arissian, D. Mirell, J. Yeak, S. Rostami, and J.-C. Diels	

64 Ignition of Doped Helium Nanodroplets in Intense Few-Cycle Laser Pulses	385
S.R. Krishnan, L. Fechner, M. Kremer, V. Sharma, B. Fischer, N. Camus, J. Jha, M. Krishnamurthy, T. Pfeifer, R. Moshhammer, J. Ullrich, F. Stienkemeier, and M. Mudrich	
65 Ultrafast Nanoscale Imaging Using High Order Harmonic Generation	391
Willem Boutu, David Gauthier, Xunyou Ge, Fan Wang, Aura Ines Gonzalez, Benjamin Barbrel, Ana Borta, Mathieu Ducouso, Bertrand Carré, and Hamed Merdji	
66 Strong-Field Effects and Attosecond Control of Electrons in Photoemission from a Nanoscale Metal Tip	401
M. Krüger, M. Schenk, and P. Hommelhoff	
67 Femtosecond Laser-Induced X-Ray Emission from Gold Nano-Colloidal Solutions	407
K. Hatanaka, K. Yoshida, A. Iwasaki, and K. Yamanouchi	
Index	411

Part I
Laser Light Sources

Chapter 1

Self-Referenced Scheme for Direct Synthesis of Carrier-Envelope Phase Stable Pulses with Jitter below the Atomic Time Unit

Günter Steinmeyer, Christian Grebing, Bastian Borchers,
and Sebastian Koke

Abstract A method for stabilizing the carrier-envelope phase of mode-locked oscillators is introduced. Other than previous concepts that exerted feedback action directly on the oscillator, our novel feed-forward concept employs an acousto-optic frequency shifter after the oscillator to correct the phase drift. This novel method is shown to simultaneously provide superior residual phase jitters and long-term performance, enabling previously considered impossible experiments in attosecond physics.

G. Steinmeyer (✉)

Max-Born-Institut für Nichtlineare Optik und Kurzzeitspektroskopie, 12489 Berlin, Germany

Optoelectronics Research Centre, 33101 Tampere, Finland

e-mail: steinmey@mbi-berlin.de

C. Grebing

Max-Born-Institut für Nichtlineare Optik und Kurzzeitspektroskopie, 12489 Berlin, Germany

Physikalisch-Technische Bundesanstalt (PTB), 38116 Braunschweig, Germany

e-mail: christian.grebing@ptb.de

B. Borchers

Max-Born-Institut für Nichtlineare Optik und Kurzzeitspektroskopie, 12489 Berlin, Germany

e-mail: borchers@mbi-berlin.de

S. Koke

Max-Born-Institut für Nichtlineare Optik und Kurzzeitspektroskopie, 12489 Berlin, Germany

InnoLight GmbH, 30419 Hannover, Germany

e-mail: koke@innolight.de

1.1 Introduction

The ability to measure and control the relative phase between carrier and envelope of a light pulse is one of the key inventions that made attosecond pulse generation possible [1–5]. Inside a laser oscillator, the envelope of the pulses propagates at the group velocity whereas the underlying carrier propagates at the phase velocity. In all intracavity dispersive media, in particular inside the laser gain crystal, both propagation velocities differ, which gives rise to a slippage of the envelope relative to the carrier. Given a per-roundtrip phase slippage $\Delta\phi_{\text{CE}}$, one computes a slippage rate

$$f_{\text{CE}} = \frac{\Delta\phi_{\text{CE}}}{2\pi} f_{\text{rep}}, \quad (1.1)$$

with f_{rep} being the repetition rate of the laser oscillator. Computing phase and group velocities for a typical Ti:sapphire few-cycle laser with about 2.5 mm crystal length, one computes a $\Delta\phi_{\text{CE}}$ on the order of 1,000 rad. It is important to understand that integer multiple phase shifts of 2π exactly reproduce the initial electric field transient. Therefore only the fractional sub-cycle part of $\Delta\phi_{\text{CE}}$ enters into the carrier-envelope phase dynamics. However, it also becomes clear that even the tiniest variation in crystal temperature or atmospheric conditions inside the laser cavity will have a measurable effect on f_{CE} . Assuming that the total phase shift between carrier and envelope changes by only one part in 10^6 , (1.1) indicates a 15 kHz change of f_{CE} , i.e., dephasing between carrier and envelope occurring on the microsecond scale. These considerations make it immediately clear that a stabilization of f_{CE} needs to be extremely agile, capable of reacting to perturbations within a few microseconds.

1.2 Traditional Stabilization Scheme

All approaches towards stabilizing the carrier-envelope frequency rely on the heterodyne measurement scheme originally proposed in [1]. In its most common implementation, this scheme heterodynes fundamental frequency components $f_i = f_{\text{CE}} + i f_{\text{rep}}$ from the blue edge of an octave-spanning spectrum with frequency-doubled components $2f_j = 2f_{\text{CE}} + 2j f_{\text{rep}}$ from the infrared edge. Measuring the difference frequency between f_i and $2f_j$ with $2j = i$ gives access to f_{CE} , with the rf beat note signal being measurable directly by a photo diode. This scheme is referred to as f - $2f$ scheme. Another commonly used variant of the heterodyne scheme is the 0 - f scheme that employs beating of fundamental frequency components from the red edge of the comb with difference frequency components generated within the frequency comb itself [6]. The latter method has the advantage of being less demanding in terms of bandwidth, often obviating the need for additional external broadening of the laser spectrum in a photonic crystal fiber.

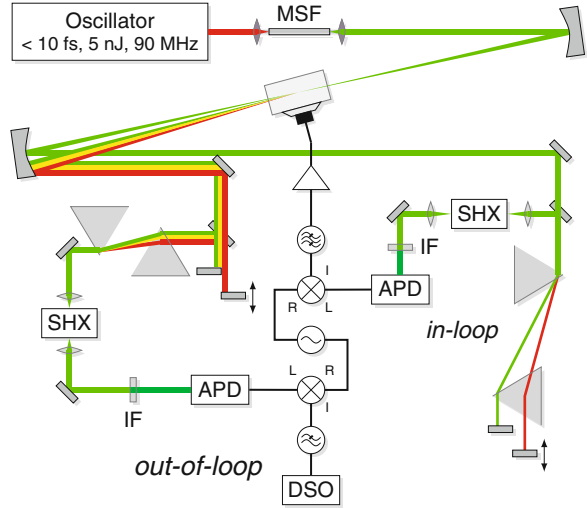
Either of the above measurement schemes delivers a radio frequency signal with frequency f_{CE} . All methods for stabilizing this frequency so far enforced a phase lock between f_{CE} and a reference signal that was typically derived from the laser repetition rate f_{rep} . Using a phase-locked loop for stabilizing f_{CE} comes with two fundamental issues. First, it is difficult to stabilize f_{CE} to zero, i.e., the case of exactly identical electric field transients of subsequent pulses. At exactly zero frequency, the heterodyne scheme fails to provide unambiguous information on the sign of an intracavity phase distortion. Several more elaborate schemes have been proposed to overcome this difficulty [7, 8]. Second and probably more importantly, a feedback scheme requires some means for controlling the carrier-envelope frequency of the oscillator. At first sight, this requirement does not appear to be overly restrictive, as f_{CE} varies virtually with all mechanical and environmental parameters of the laser. However, as discussed above, the feedback mechanism needs to be very fast with at least several kilohertz bandwidth to be able to compensate the rapid fluctuations of f_{CE} . Even though many different feedback mechanisms have been explored, the bandwidth requirements strongly favor electro-optic or acousto-optic modulation of the pump power, which allow for modulation bandwidths of hundreds of kilohertz or more. Nevertheless, there is still a caveat with this fast feedback mechanism: pump power modulation will not only change the carrier-envelope frequency via nonlinear index changes inside the laser crystal, but it will also affect pulse duration, peak power, and the repetition rate of the laser. To date, there is no known side-effect-free feedback mechanism for the carrier-envelope frequency.

In conclusion, the proven traditional feedback method for stabilizing f_{CE} comes with a series of drawbacks that render long-term stabilization difficult. In particular, there is always a trade-off between the precision of a servo loop and the phase capture range, i.e., the largest phase distortion that the servo loop can handle without dropping out of lock or suffering a cycle slip. Many highly stabilized pump lasers exhibit rare needle-like fast transients in their output power, which make it necessary to extend the capture range of the phase detector well beyond 2π . Nevertheless, mapping a large phase range on to, e.g., a 10 V range also increases the susceptibility of the electronics towards voltage noise. In the following, we will discuss a scheme that overcomes all these limitations and allows for long-term stabilization without sacrificing phase stability on short time scales.

1.3 Feed-Forward Scheme

The setup of the feed-forward scheme is depicted in Fig. 1.1. Rather than acting back upon the laser oscillator, we directly employ the measured offset of the frequency comb f_{CE} and shift each and every line within it by this amount [9, 10]. For this purpose, we employ an acousto-optic frequency-shifter (AOFS) that we drive directly with the amplified f_{CE} signal. In the first diffraction order of the AOFS, we therefore generate a zero-offset comb with all individual frequencies being integer

Fig. 1.1 Set-up employed for the out-of-loop characterization of residual CEP jitter. *SHX*: periodically poled lithium niobate crystal phase matched for frequency doubling 1,064 nm; *IF*: interference filter at 532 nm; *APD*: avalanche photodiodes; *MSF*: microstructured fiber; *DSO*: digital storage oscilloscope



multiples of the repetition rate, i.e., $f_i = i f_{\text{rep}}$. Consequently, all pulses in the pulse train exhibit identical electric field transients. Apart from automatically providing an offset-free comb, the servo bandwidth of our system is only limited by the travel time of the acoustic wave from the actuator to the interaction zone with the laser beam. Given the high speed of sound in silica, we computed a microsecond lag in the AOFS, allowing a bandwidth well in excess of 200 kHz. Compared to the best reported bandwidths of feedback schemes [11] of about 50 kHz, this about fivefold increased bandwidth encompasses typical parasitic laser power modulations stemming from the primary switching power supplies of the pump lasers.

We tested the stabilization with the scheme depicted in Fig. 1.1. In these experiments, the laser was deliberately stabilized not to zero offset. This avoids the phase ambiguity at exactly zero offset frequency as well as $1/f$ noise issues. Measured phase noise spectra are shown in Fig. 1.2. Integrating over the entire frequency range we measure a total rms phase noise of 45 mrad. Subtracting internal noise contributions generated in our electronics, we deduce a residual timing jitter between carrier and envelope of 12 as ($5\text{ s} - 0.2\text{ }\mu\text{s}$). This number is a factor 2 smaller than the atomic unit of time, which is normally considered a limit for the fastest transient events in atomic and molecular physics. Using a more elaborate scheme than depicted in Fig. 1.1, we have recently been able to further push residual timing jitter down to 8 as, i.e., a phase jitter of 20 mrad [13].

The residual carrier-envelope phase jitters of the feed-forward schemes have to be compared with the best obtained values of the feedback scheme, which lie in the range of about 100 mrad [12]. Therefore, the feed-forward scheme improves the obtainable precision of carrier-envelope phase stabilization by about a factor five. Moreover, the feed-forward scheme cannot fall out of lock, at least as long as there is a detectable beat signal. Even after brief interruption of the input signal, the stabilization immediately restores itself. We ran overnight tests and

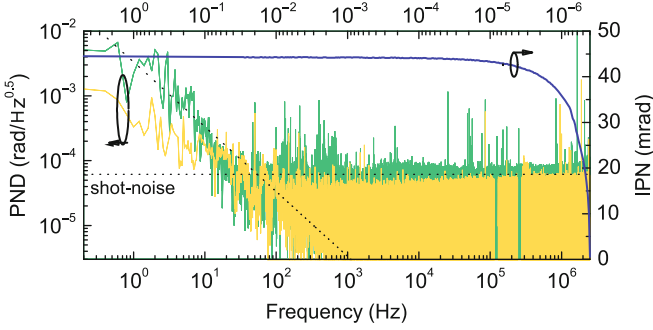


Fig. 1.2 Residual phase noise of the feed-forward stabilized Ti:sapphire oscillator. *Black curve*: integrated phase noise of the stabilized oscillator, amounting to a total of 45 mrad over the entire frequency range. *Dark gray curve*: spectral phase noise density of the stabilized oscillator. *Light gray curve*: background measurement

observed more than 12 h of phase-stable operation of the laser without any need for readjustment or the appearance of dropouts. Therefore the feed-forward scheme enables unprecedented precision without compromising the phase capture range.

Despite the obvious advantages of using an AOFS for phase stabilization, this scheme also appears to exhibit some disadvantages over the traditional scheme. One possible issue is angular dispersion inside the diffracted beam. We found, however, that this potential problem is readily compensated for by introducing a BK7 prism with 18° apex angle inside the stabilized beam path [6]. A second possible issue is caused by a slow drift of f_{CE} , translating into beam pointing variations and changing the period of the acousto-optic index grating, which will also cause a slow drift of the phase of the stabilized pulses. In our experiments we found stabilization of the carrier-envelope frequency to within 100 kHz around the center frequency completely sufficient to suppress all these undesired drift effects [13]. Compared to stabilization within a phase-locked loop, such a stabilization is much less demanding and removes all long-term drift effects that may otherwise appear on a time scale of some ten minutes and above.

1.4 Conclusion

The feed-forward scheme offers a row of advantages over traditional carrier-envelope phase stabilization schemes. Most importantly, it combines locking precision and long-term stability in an unprecedented way. Moreover, the scheme comes without complicated servo controllers that may fall out of lock, which is particularly cumbersome for the heavy statistics often required in attosecond physics. We therefore believe that feed-forward stabilization will widely replace feedback schemes in stabilized chirped-pulse amplifier chains. A precision beyond the atomic unit of time together with added statistical capabilities appear to enable previously impossible experiments in attosecond physics.

References

1. H.R. Telle, G. Steinmeyer, A.E. Dunlop, J. Stenger, D.H. Sutter, U. Keller, *Appl. Phys. B* **69**, 327 (1999)
2. D.J. Jones, S.A. Diddams, J.K. Ranka, A. Stentz, R.S. Windeler, J.L. Hall, S.T. Cundiff, *Science* **288**, 635 (2000)
3. T. Udem, R. Holzwarth, T.W. Hänsch, *Nature* **416**, 233 (2002)
4. T.W. Hänsch, *Rev. Mod. Phys.* **78**, 1297 (2006)
5. A. Baltuška, T. Udem, M. Uiberacker, M. Hentschel, E. Goulielmakis, C. Gohle, R. Holzwarth, V.S. Yakovlev, A. Scrinzi, T.W. Hänsch, F. Krausz, *Nature* **421**, 611 (2003)
6. F. Lücking, A. Assion, A. Apolonski, F. Krausz, G. Steinmeyer, *Opt. Lett.* **37**, 2076 (2012)
7. E.B. Kim, J.-H. Lee, L.T. Trung, W.-K. Lee, D.-H. Yu, H.Y. Ryu, C.H. Nam, C.Y. Park, *Opt. Express* **17**, 20920 (2009)
8. S. Rausch, T. Binhammer, A. Harth, E. Schulz, M. Siegel, U. Morgner, *Opt. Express* **17**, 20282 (2009)
9. S. Koke, C. Grebing, H. Frei, A. Anderson, A. Assion, G. Steinmeyer, *Nat. Photon.* **4**, 462 (2010)
10. S. Koke, A. Anderson, H. Frei, A. Assion, G. Steinmeyer, *Appl. Phys. B* **104**, 799 (2011)
11. M.Y. Sander, E.P. Ippen, F.X. Kärtner, *Opt. Express* **18**, 4948 (2010)
12. T. Fujii, J. Rauschenberger, C. Gohle, A. Apolonski, T. Udem, V.S. Yakovlev, G. Tempea, T.W. Hänsch, F. Krausz, *New J. Phys.* **7**, 116 (2005)
13. B. Borchers, S. Koke, A. Husakou, J. Herrmann, G. Steinmeyer, *Opt. Lett.* **36**, 4146 (2011)

Chapter 2

Single Shot Carrier Envelope Phase Stabilization of a 10 kHz, 10 W Regenerative Amplifier

Chengquan Li, Alex Schill, Florian Emaury, Jack Chu, Philippe F  ru, Jean-Marc H  ritier, and William Tulloch

Abstract In this paper, we introduced an every-single-shot carrier envelope (CE) phase locking setup, which was applied to measure and stabilize the CE phase drift in a 10 kHz, 10 W regenerative amplifier system. Using independent slow and fast control loops, the residual root mean square (RMS) CE phase noise was stabilized at the level of 200 mrad as measured by spectrometer based f -to- $2f$ interferometer.

2.1 Introduction

In recent decades, the carrier-envelope (CE) phase plays a very important role in the research of strong field processes with the rapid development of ultrashort laser pulse generation. The electric field of this ultrashort laser pulse can be described by $E(t) = E_0(t) \cos(\omega_c t + \beta(t)t + \varphi_{CE})$, where the CE phase, φ_{CE} , specifies the offset between the peak of the envelope amplitude $E_0(t)$, and the oscillation peak of the carrier wave with frequency ω_c , $\beta(t)$ represents possible chirp in pulse. It is important to approach accurate measurement and precision control of the CE phase in the field of attosecond pulse generation and other atomic physics studies [1–7].

In the past few years, CE phase stabilization was mainly studied on multi-pass chirped pulse amplifier (CPA) systems [8, 9]. As a widely used amplification system, regenerative amplification has been shown to preserve a great extent of the CE phase stability of the seed laser pulse after the amplification [10]. CE phase stabilized regenerative-based laser systems have been reported [11, 12]. Most of the above mentioned CE phase stabilization was done with spectrometer based f -to- $2f$ interferometer technique. Due to the slow sampling rate of spectrometer, the bandwidth of phase measurement and feed back control was limited in the range of several tens Hertz.

C. Li (✉) · A. Schill · F. Emaury · J. Chu · P. F  ru · J.-M. H  ritier · W. Tulloch
Coherent Inc., Santa Clara, CA 95054, USA
e-mail: Chengquan.li@coherent.com

Previously, two techniques were used to measure real time every-single-shot CE phase measurement: Balanced detection method [13] and above threshold ionization (ATI) phase meter [14]. However ATI phase meter only works with very short pulse (~ 6 fs) and can not be used for longer pulses of 30 fs. In this work, we introduce an every-single-shot CE phase locking setup, which was applied to stabilize the CE phase drift in a 10 kHz, 10 W regenerative amplifier system. Compared to the balanced detection method, single photodiode was used to measure the CE phase drift. Using our newly developed locking electronics, the CE phase of this regenerative amplifier system has been actively stabilized over several hours. The out of loop overall single shot noise was 200 mrad measured by the conventional spectrometer based f -to- $2f$ method.

2.2 Experiment and Results

The laser system consists of a CE phase stabilized oscillator (Coherent Micra-CEPS) and a regenerative based amplifier (Coherent Legend Elite Duo), as shown in Fig. 2.1a. Half of the oscillator beam was sent to a Mach-Zehnder (M-Z) f -to- $2f$ interferometer (not shown in the figure) to lock the oscillator CE phase using locking electronics (Menlo System XPS800-E). This MZ f -to- $2f$ interferometer was integrated together with the oscillator and thermally-controlled through a water cooled base-plate. The oscillator beam generated a beat note more than 40 dB signal-to-noise inside the f -to- $2f$ interferometer. By actively locking the beat note to a quarter of the repetition rate, in-loop RMS phase noise levels of 50 mrad were achieved for several hours without interruption or adjustment.

The CE phase stabilized output of the oscillator beam was stretched in grating based stretcher and used to seed a regenerative amplifier (RGA) operating at 10 kHz. A single pass amplifier (SPA) is used to further amplify the laser pulse after the regenerative amplifier. Both the RGA stage and the SPA were thermo-electrically cooled and were pumped by a single Nd:YLF DPSS pump laser (Coherent Evolution HE). Finally a pair of gratings was used to compress the amplified pulse to deliver 10 kHz, 10 W laser pulses with duration less than 30 fs.

In order to investigate the CE phase stability of the high power laser system, 2% of the full beam was sent to a collinear f -to- $2f$ interferometer (Coherent Elite CEP) [8]. Figure 2.1b shows the detail of CE phase measurement. Half of the f -to- $2f$ beam was split to monitor the interference pattern using a spectrometer and fast Fourier transform (FFT) software as an out of loop measurement. Furthermore, the other half of the beam was diffracted by a grating (G) and focused by a cylindrical lens (L) to get f -to- $2f$ interference pattern. A slit was used to select single interference fringe and a photodiode was used to measure the intensity of fringe. The measured voltage change on the photodiode was corresponding to the every-single-shot CE phase drift. Finally, the measured analog signal was sent to the amplifier phase locking electronics (Coherent CPS Elite). Most critically, the locking electronics processed the analog signal in the frequency domain and

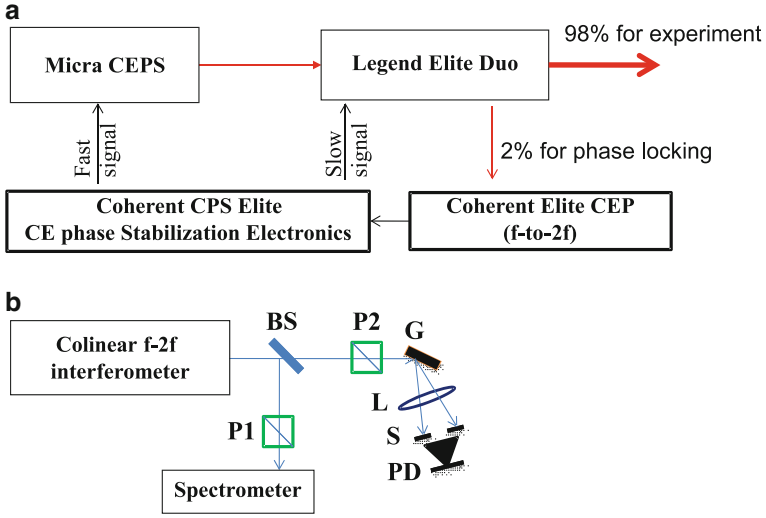


Fig. 2.1 (a) Schematic of CE phase stabilized laser system. Micra-CEPS: the f -to- $2f$ integrated oscillator; Legend Elite Duo: amplifier including regenerative stage and single pass amplifier; Elite CEP: collinear f -to- $2f$ interferometer for amplifier CE phase measurement; CPS Elite: electronic controller for amplifier CE phase locking; (b) Diagram of Elite CEP setup; BS: 50% beam splitter; P: polarizer; G: grating; L: cylindrical lens; S: slit; PD: photodiode

generated a low frequency and high frequency phase error signals. Using two independent PID controllers, the high and low frequency signals were used to lock the CE phase of the amplifier. This control circuits generated two control signals: a slow feedback signal was sent to horizontally tilt the stretcher grating [15], while the fast signal was sent to the oscillator CE phase controller. By careful selection of the frequency domain filtering and independent optimization of the gain and bandwidth characteristics of the PID controllers, the CE phase of the amplified laser beam was stabilized at 10 kHz rate [16].

Figure 2.2 shows the out of loop single shot CE phase data recorded by the spectrometer and calculated from FFT software. The black line represents the stabilized CE phase result when only the slow controller was acting, while the gray plots, which is offset by 2 radian in Y axis, is the stabilized CE phase result when both the slow and fast control loops were turned on. The RMS noise was reduced from 285 down to 186 mrad when the fast loop was on.

To understand the frequency characteristic of the stabilized analog signal, the photodiode signal was recorded using DAC acquisition card. Figure 2.3 shows the FFT spectra of the analog signal measured by the photodiode. The black plot represents the spectrum when only slow controller was acting, while the gray plot shows the spectrum when both slow control loop and fast control loop were turned on. Compared with the slow loop locking only spectrum, the fast control loop suppresses the noise up to 400 Hz. The power spectrum density was decreased almost by 20 dB in the range from 10 upto 300 Hz, where the spectrometer based feedback method was limited by its slower sampling rate.

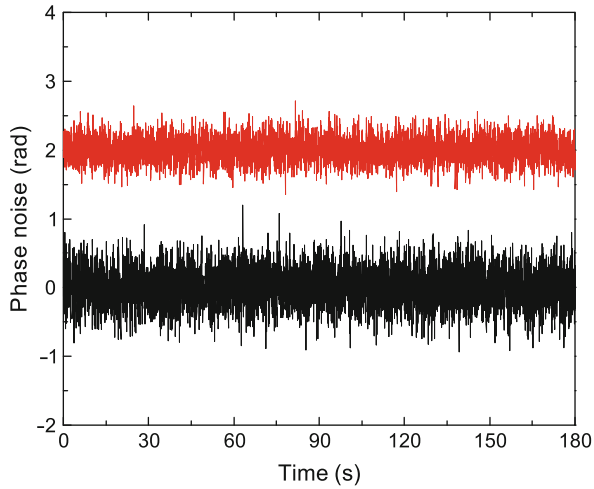


Fig. 2.2 Out of loop measurement of the stabilized amplifier CE phase. *Black*: only the slow control loop was on, the RMS noise is 285 mrad; *gray*: both the slow and fast control loops were on and offset by 2 radian in Y axis, the RMS noise is 186 mrad

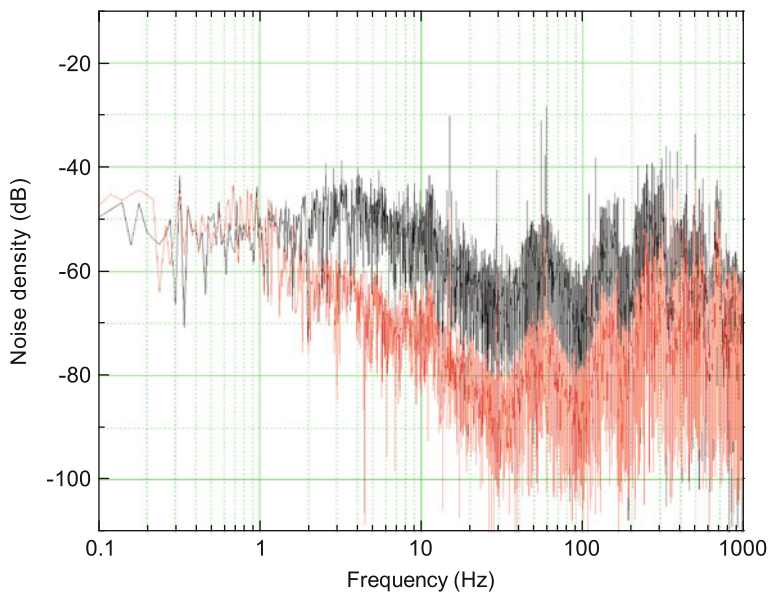


Fig. 2.3 FFT spectrum of the stabilized analog signal. *Black*: only the slow control loop was on, *gray*: both the slow and fast control loops were on, the integrated noise was 48.3 mV and 30 mV, respectively

2.3 Conclusion

In conclusion, a new analog CE phase detector was employed to measure the every-single-shot CE phase drift in a 10 kHz, 10 W laser system. Using independent PID controllers and separated slow and fast control signals, the single shot CE phase was stabilized below 200 mrad.

References

1. F. Krausz, M. Ivanov, *Rev. Mod. Phys.* **81**, 163 (2009)
2. E. Goulielmakis, M. Schultze, M. Hofstetter et al., *Science* **320**, 1614 (2008)
3. M.F. Kling, M.J.J. Vrakking, *Annu. Rev. Phys. Chem.* **59**, 463 (2008)
4. H. Mashiko, S. Gilbertson, C. Li et al., *Phys Rev. Lett.* **100**, 103906 (2008)
5. G. Sansone, E. Benedetti, F. Calegari et al., *Science* **314**, 443 (2006)
6. A. Baltuška, T. Udem, M. Uiberacker et al., *Nature* **421**, 611 (2003)
7. G.G. Paulus, F. Grasbon, H. Walther et al., *Nature (London)* **414**, 182 (2001)
8. C. Li, E. Moon, Z. Chang, *Opt. Lett.* **31**, 3113 (2006)
9. A. Baltuška, M. Uiberacker, E. Goulielmakis et al., *IEEE J. Sel. Top. Quantum Electron.* **9**, 972 (2003)
10. M. Kakehata, H. Takada, Y. Kobayashi et al., *Opt. Express* **12**, 2070 (2004)
11. T. Fordell, M. Miranda, A. Persson et al., *Opt. Express* **17**, 21091 (2009)
12. S. Chen, M. Chini, H. Wang et al., *Appl. Opt.* **48**, 5692 (2009)
13. S. Koke, C. Grebing, B. Manschwetus et al., *Opt. Lett.* **33**, 2545 (2008)
14. A.M. Sayler, T. Rathje, W. Müller et al., *Opt. Lett.* **36**, 1 (2011)
15. C. Li, U.S. Patent US 12/689845
16. A. Schill, C. Li, P. Féréu, U.S. Patent (pending)

Chapter 3

Intense Few-Cycle Mid-Infrared Laser Pulse Generation and Applications

Ruxin Li, Chuang Li, Liwei Song, Ding Wang, Canhua Xu, Cheng Gong, Yuxin Leng, Peng Liu, Zhinan Zeng, and Zhizhan Xu

Abstract The recent progress in the development of few-cycle laser pulses with passively stabilized carrier-envelope phase (CEP) at SIOM is reported. A three-stage high conversion efficiency optical parametric amplifier (OPA) with passively stabilized carrier-envelope phase is shown. After passing through an argon-filled hollow fiber and the dispersion compensator for pulse compression, CEP stabilized 0.7 mJ, 1.5 cycle laser pulses at 1.75 μ m center wavelength are obtained. Applications of the laser system in high order harmonic generation leading to the short wavelength supercontinuum emission and the terahertz (THz) generation with a pronounced CEP dependence will be discussed. THz emission spectroscopy is adopted also to determine the value of CEP, indicating an excellent long-term CEP stability.

3.1 Introduction

Ultrashort laser pulses are powerful tools for the investigation of the ultrafast dynamics process in various fields including physics, chemistry, biology, and material science research [1]. To investigate these processes, the laser pulses are required to have shorter pulse duration than the time range of phenomena of interest. The advances in ultrashort pulse laser technology make it possible to observe ultrafast dynamics process in femtosecond resolution [2]. Isolated bursts of attosecond extreme ultraviolet (XUV) radiation make it possible to probe ultrafast dynamics on a previously unexplored timescale (~ 100 as) [3, 4].

R. Li (✉) · C. Li · L. Song · D. Wang · C. Xu · C. Gong · Y. Leng · P. Liu · Z. Zeng · Z. Xu
State Key Laboratory of High Field Laser Physics, Shanghai Institute of Optics and Fine
Mechanics, Chinese Academy of Sciences, Shanghai 201800, China
e-mail: ruxinli@mail.shnc.ac.cn; chuang_li@siom.ac.cn; slw@siom.ac.cn;
wangding@siom.ac.cn; canhua_xu@siom.ac.cn; gongcheng@mail.siom.ac.cn;
lengyuxin@mail.siom.ac.cn; peng@mail.siom.ac.cn; zhinan_zeng@mail.siom.ac.cn;
zzxu@mail.shnc.ac.cn

Such attosecond pulses are produced via high harmonic generation (HHG) in noble gases, driven by intense carrier-envelope phase (CEP) stabilized few-cycle laser pulses [5]. Usually, the driving sources for HHG are the compressed few-cycle laser pulses from a CEP stabilized Ti:sapphire laser at wavelength of 800 nm. To obtain higher photon energy harmonic supercontinuum for the shorter attosecond pulses, the driving laser pulses at longer wavelength is suggested [6]. In addition, the longer wavelength laser also has an advantage to improve the isolated attosecond pulse contrast due to higher nonlinearity. Especially the laser pulses with center wavelength lies in the range of 1.5–3 μm , as a balance between high cut-off energy and acceptable conversion efficiency of HHG, is regarded as a suitable driver for attosecond pulse generation [7, 8]. Using 2 μm laser pulses, fully phase-matched HHG spanning the water window spectral region has been realized recently [9]. Isolated attosecond pulses with wavelength lies in the water window spectral region may be obtained in the near future.

In order to obtain the CEP stabilized pulses in longer wavelength region, the difference-frequency generation (DFG) technique has been developed [10]. Compared with the active CEP stabilization technique, the passive stabilization technique is relatively insensitive to the environmental disturbance. Moreover, as the phase drift is naturally eliminated in the DFG process, excellent long-term CEP stability can be expected. There are two methods for CEP stabilized pulse generation by the DFG technique: (a) the CEP stabilized seed is generated in the DFG process within a single pulse, then amplified in the following optical parametric amplifier (OPA) or optical parametric chirped-pulse amplifier (OPCPA) stages. 1.2 mJ, 17 fs at 1.5 μm [8] and 740 μJ , 15.6 fs at 2.1 μm [11] CEP stabilized pulses were generated by using this method; (b) the CEP stabilized idler pulse is generated in a OPA process directly, if the pump and the signal pulses are from the same laser source with the same carrier phase offset. 1.5 mJ, 19.8 fs at 1.5 μm [12] and 0.4 mJ, 11.5 fs at 1.8 μm [13, 14] CEP stabilized pulses were obtained in this way.

We report the generation of CEP stabilized 8.4 fs, 0.7 mJ pulses at 1.75 μm center wavelength by an OPA system followed by a hollow fiber compressor. Firstly, we obtained CEP stabilized 1.6 mJ, 57 fs pulses at 1.8 μm from a three-stage MIR OPA pumped by a commercial 8 mJ, 40 fs Ti:sapphire laser amplifier at 1 kHz repetition rate. The obtained 1.8 μm pulses are then spectrally broadened by the nonlinear propagation in an argon-filled hollow fiber and subsequently compressed to 8.4 fs (less than 1.5 cycles) with energy of 0.7 mJ simply using a pair of thin fused silica wedges. The compressed pulses are CEP stabilized with ~ 547 mrad root-mean-squared (rms) CEP fluctuations, making this source a suitable driver for attosecond pulse generation. Nonlinear spectral interferometry and terahertz (THz) emission spectroscopy are employed to test the short-term and long-term CEP stability. Applications of the laser system in high order harmonic generation leading to the short wavelength supercontinuum emission with a pronounced CEP dependence will be discussed.

3.2 Few-Cycle Mid-Infrared Laser Pulse Generation

3.2.1 Optical Parametric Amplifier

The configuration of the three-stage OPA is shown in Fig. 3.1. The pump laser pulses are from a commercial Ti:sapphire laser amplifier (Coherent LEGEND-HE-Cryo) which provides 40 fs pulses with pulse energy up to 8 mJ at 1 kHz repetition rate. The pump pulses are divided into four parts using three beam splitters. The smallest part of the laser pulses ($<30 \mu\text{J}$) is focused into a 2-mm-thick sapphire plate to generate a single-filament white light continuum (WLC), which is used as the seed pulses for the following OPA stages.

A fraction of the pump laser pulses with $\sim 120 \mu\text{J}$ pulse energy is used to pump the first near-collinear OPA stage (OPA1) consisting of a 2.5-mm-thick BBO crystal cut for type II phase matching ($\theta = 27.2^\circ$, $\varphi = 30^\circ$). The intersection angle between the pump and seed beams is $\sim 1^\circ$. The WLC is amplified to $\sim 4 \mu\text{J}$ in OPA1 with the center wavelength at $1.44 \mu\text{m}$. Although OPA with type I BBO crystal in this spectral region has broader phase matching bandwidth [15], in the experiment, we found a lower efficiency and strong parasitic self-diffraction.

The amplified pulses at $1.44 \mu\text{m}$ from OPA1 are collimated and injected into the second collinear OPA stage (OPA2) consisting of a 2-mm-thick BBO crystal cut for type II phase matching ($\theta = 27.2^\circ$, $\varphi = 30^\circ$). About 1.2 mJ laser pulse with a diameter of $\sim 4 \text{ mm}$ is used to pump OPA2, corresponding to a pump intensity of about $250 \text{ GW}/\text{cm}^2$. In order to get high efficiency and prevent wave front tilt [16], both the signal and the pump beams are well collimated and the two beams are

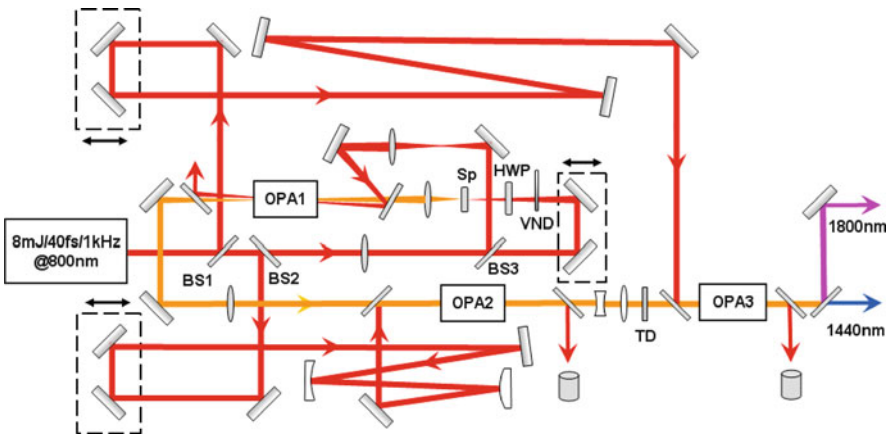


Fig. 3.1 Experimental setup for the generation of high energy self-phase-stabilized pulses: VND variable neutral density filter; HWP half-wavelength waveplate; Sp sapphire plate; TD time delay crystal

collinearly injected into the BBO crystal. The seed pulses are amplified to $\sim 90 \mu\text{J}$ in this stage.

The amplified signal pulses from OPA2 are enlarged and collimated to $\sim 9 \text{ mm}$ in diameter with a Galilean telescope. A 1.5-mm-thick a-cut YVO_4 crystal is employed as a time delay crystal to separate the signal and the idler pulses in time. Then the laser beam is injected into the third collinear OPA stage (OPA3) consisting of a 2-mm-thick BBO crystal cut for type II phase matching ($\theta = 27.2^\circ$, $\varphi = 30^\circ$). The remaining $\sim 6.4 \text{ mJ}$ pump laser with diameter of $\sim 9 \text{ mm}$ is used to pump OPA3 corresponding to pump intensity of about 250 GW/cm^2 . The same as OPA2, the pump and the signal beams are firstly collimated and then collinearly injected into the BBO crystal. This collinear setup is quite necessary to avoid angular dispersion in the generated idler beam. The signal pulses are further amplified to $\sim 2 \text{ mJ}$ at $1.44 \mu\text{m}$, corresponding to the idler pulses with energy of $\sim 1.6 \text{ mJ}$ at $1.8 \mu\text{m}$. The energy conversion efficiency is approximately 55% in OPA3. Usually, it is necessary to optimize the grating-based compressor (both the angle of incidence and the separation distance) in the Ti:sapphire laser system to optimize the chirp of the pump laser to obtain this high conversion efficiency. The pulse duration of the output signal pulses and the idler pulses are measured when the highest conversion efficiency is obtained by a home-built single-shot autocorrelator. The signal pulse duration is $\sim 40 \text{ fs}$ at $1.44 \mu\text{m}$ and the idler pulse duration is $\sim 57 \text{ fs}$ at $1.8 \mu\text{m}$ without any further pulse compression.

In fact, both the signal and the idler pulses from OPA2 can be used to seed OPA3 and the energy conversion efficiency is almost the same. The near-field beam profiles are measured in these two conditions using an IR beam profiler (Spiricon, PY-III-C-A). The results are shown in Fig. 3.2. Although the near-field beam profiles show significant difference, they are all about two times diffraction limited according to our measurement. In the experiment, the signal pulse from OPA2 is chosen to seed OPA3 to get a relatively better near-field beam profile.

3.2.2 Pulse Compression

The $1.8 \mu\text{m}$ idler beam from above OPA system is coupled into a 1-m long hollow fiber filled with argon ($400 \mu\text{m}$ inner diameter, 0.5-mm-thick fused silica window) using a $f = 0.75 \text{ m}$ plano-convex lens. The output beam is collimated with an $R = 2 \text{ m}$ silver-coated concave mirror. We measured the pulse duration when the hollow fiber is evacuated, it is reduced from $\sim 57 \text{ fs}$ before the hollow fiber to $\sim 45 \text{ fs}$.

Significant spectral broadening appears when argon gas is filled in the hollow fiber, as shown in Fig. 3.3. Normally, the pressure of argon is set to be $\sim 400 \text{ mbar}$, as a balance between broad spectrum and single mode purity of the output beam. In this case, the supercontinuum in the range of $1,200\text{--}2,100 \text{ nm}$ is obtained which support the Fourier transform-limited pulse duration of about 8 fs . Only a pair of fused silica wedge is used to compensate the pulse dispersion due to its negative group delay dispersion (GDD) in this spectral range [13].

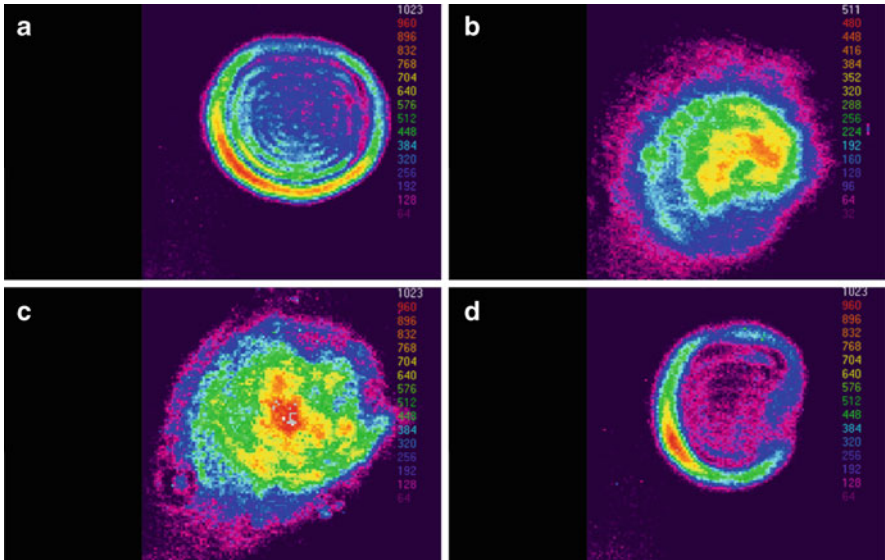


Fig. 3.2 Near-field beam profile of 1.44 μm (a) and 1.8 μm (b) laser when the signal pulses of OPA2 are used to seed OPA3; near-field beam profile of 1.44 μm (c) and 1.8 μm (d) laser when the idler pulses of OPA2 are used to seed OPA3

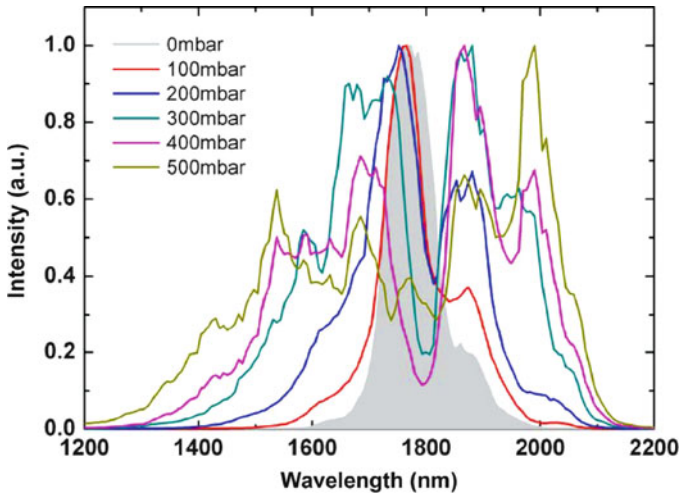


Fig. 3.3 The spectra of the input (*shaded*) and the output pulses from the hollow fiber

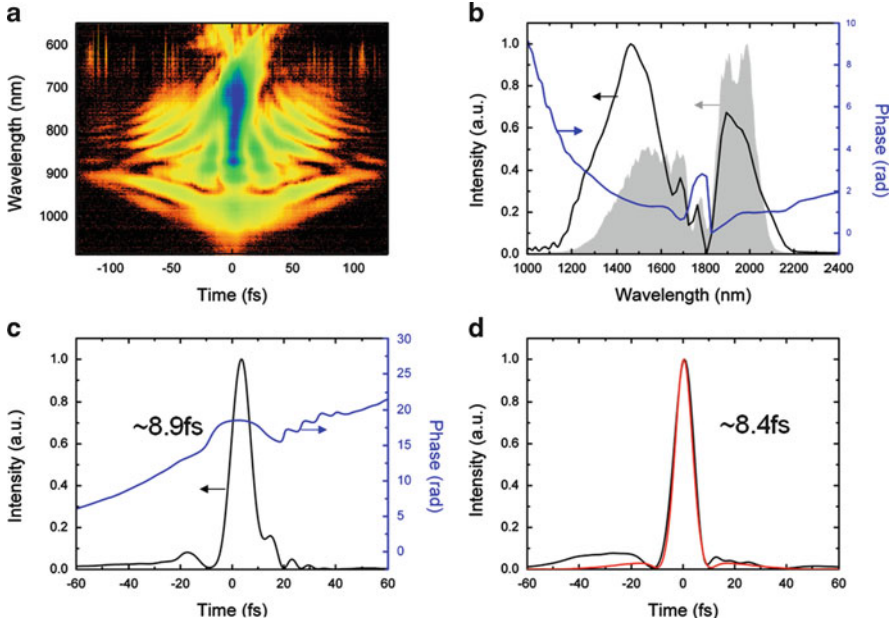


Fig. 3.4 (a) Measured SHG-FROG trace of the compressed pulses. (b) Measured (*shaded*) and retrieved (*black*) spectral intensity and retrieved phase (*blue*). (c) Retrieved temporal intensity (*black*) and phase (*blue*). (d) The *black* curve is the temporal intensity profile corresponding to the measured spectrum and retrieved spectral phase, the *red* curve is the ideal Fourier-limit intensity profile corresponding to the measured spectrum

Pulse duration characterization is carried out with a home-built second harmonic generation frequency resolved optical grating (SHG-FROG). No transmissive optics elements are used in the SHG-FROG which makes it suitable to measure the pulse duration of few-cycle laser pulses. A 20- μm -thick type I BBO crystal ($\theta = 20.2^\circ$) is used in the SHG-FROG which ensures broad enough SHG bandwidth. The best pulse compression is achieved when the total thickness of fused silica after hollow fiber is ~ 2 mm, the corresponding SHG-FROG trace and the reconstructed electric field are as shown in Fig. 3.4, with a retrieval error of 0.009.

It can be seen from Fig. 3.4b that the reconstructed spectrum (*black*) is not well in agreement with the spectrum measured directly using spectrometer (Ocean Optics, NIR 256), which could be caused by frequency filtering effect [17] and different spectral sensitivity of the instruments we used, because all these factors tend to decrease the intensity in the longer wavelength region. According to consistency of the fine structure of the retrieved spectrum and directly measured spectrum around 1,600–1,800 nm, we believe the reconstructed spectral phase (*blue* line in Fig. 3.4b) is reasonable. The temporal intensity is calculated based on the directly measured spectrum and the retrieved spectral phase, as shown in Fig. 3.4d, the pulse duration is 8.4 fs, which is ~ 1.5 optical cycles considering the 1.75 μm center wavelength.

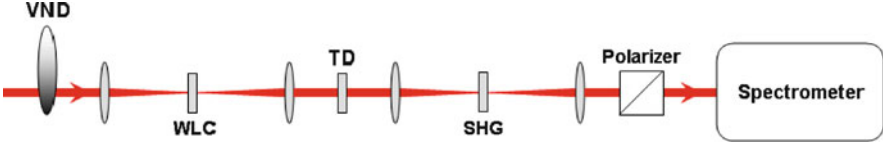


Fig. 3.5 Setup for CEP characterization by nonlinear spectral interferometry: VND variable neutral density filter, WLC white light continuum, SHG second harmonic generation, TD time delay crystal

3.2.3 Carrier Envelope Phase

The CEP stability is characterized with a home-built collinear f–2f interferometer. A schematic diagram is shown in Fig. 3.5. A fraction of the output energy of the OPA system is focused on a 2 mm thick sapphire plate to generate a WLC by self-phase-modulation. After passing through the time delay crystal and a 3 mm thick BBO crystal for second harmonic generation (SHG). The interference spectrum between the fundamental frequency (FF) and the second harmonic frequency (SH) is recorded by the computer-controlled spectrometer. The interference between the FF and SH components can be written as [18]:

$$S(\omega) = I_{WL}(\omega) + I_{SHG}(\omega) + 2[I_{WL}(\omega)I_{SHG}(\omega)]^{1/2} \cos[\varphi_{SHG}(\omega) - \varphi_{WL}(\omega) + \omega\tau + \varphi] \quad (3.1)$$

Here, $\varphi_{WL}(\omega)$ and $\varphi_{SHG}(\omega)$ are phases brought in by white-light generation and second-harmonic generation; τ is the time delay between FF and SH. Generally, $\varphi_{WL}(\omega)$ and $\varphi_{SHG}(\omega)$ are set to be constants during the measurement. From the interference fringes, the CEP stability can be worked out using the standard algorithm of Fourier transform spectral interferometer [19].

In the experiment, a 5-mm-thick c-cut LiNbO₃ crystal is introduced between the WLC and SHG crystal. Because the group delay is almost the same for 900 nm and 1,800 nm laser in glass, the fringe period can not be observed if the time delay crystal is not introduced. Frequency overlap between the spectral broadened FF and SH is achieved in the 800–900 nm spectral range. Figure 3.6 shows the CEP fringes and phase stability for the 1.8 μm idler pulses before the hollow fiber and the 8.4 fs pulses after compression over a 30 min observation time (the exposure time and the delay time of the spectrometer are 2 ms and 0.2 s respectively). The rms CEP drift before and after the hollow fiber is ~ 401 and ~ 547 mrad, respectively.

Similar to [20], terahertz (THz) emission spectroscopy is also adopted in the experiment to determine the value of CEP. Using the cross polarizer electro-optic sampling scheme [21], the THz waveforms from air filamentation of our few-cycle IR pulses are recorded at different CEP in a step of 0.2π radian, as seen in Fig. 3.7. It can be seen that the measured THz field reverse its polarity as the CEP change from 0 to π , and from π to 2π as well. The cosinoidal dependence of THz intensity on CEP lasts over two periods of 2π in 4 h data acquisition time, which indicates an excellent long-term CEP stability.

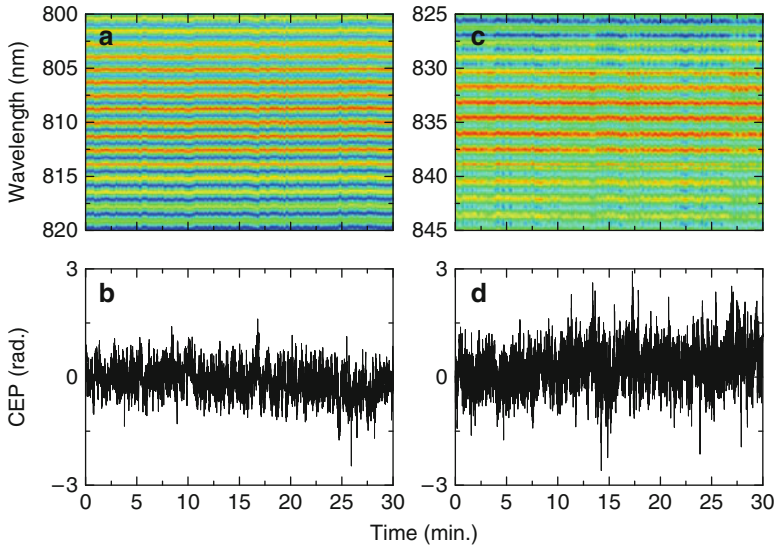


Fig. 3.6 CEP fringes (a) and phase drift (b) of the 1.8 μm pulses before the hollow fiber. CEP fringes (c) and phase drift (d) of the compressed pulses

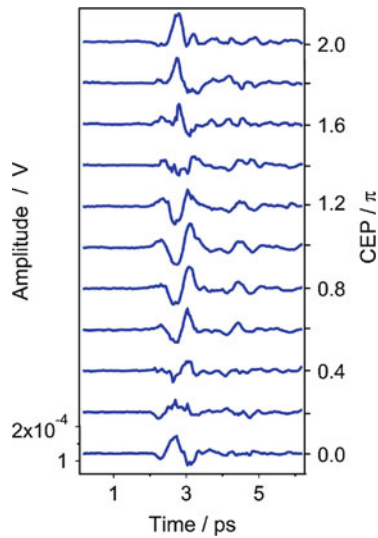


Fig. 3.7 Temporal THz waveforms measured by adjusting the CEP of few-cycle IR pulses in a step of 0.2π using thin fused silica wedges

3.3 High Order Harmonic Generation Experiments

The schematic of the experimental setup is shown in Fig. 3.8. The CEP stabilized 0.7 mJ, 12 fs laser pulses at $1.75 \mu\text{m}$ center wavelength were used to drive the harmonic generation in neon. In order to create a sufficiently high focal intensity, we used a two times telescope to expand the laser beam size, which is composed of a concave mirror ($f = 600 \text{ mm}$) and a convex mirror ($f = 300 \text{ mm}$). Then the driving laser pulse was focused by a concave mirror with a focal length of 500 mm . A steel tube with an inside diameter of 1 mm was used as a gas cell, which is filled with neon gas. The tube was mounted inside a vacuum chamber and can be translated along the beam propagation direction by a high-precision translation stage. The generated lower-order harmonics and the residual IR driving laser were blocked by a 150-nm -thick aluminum foil. A flat-field grating spectrometer equipped with a soft-X-ray CCD was used for the harmonic spectrum measurement. The spectrometer consists of a spherical concave gold mirror (SM), a cylindrical concave gold mirror (CM) and a flat-field grating (Hitachi, 001-0266, $1,200 \text{ lines/mm}$, 87.2° grazing angle).

In the experiment, the driving laser pulse energy was 0.68 mJ and the neon gas pressure was 400 Torr . The laser focus was set at 4 mm before the center of gas tube. The CEP of the driving laser pulse was changed by translating the wedge, which leading to a variation of CEP from 0 to 2π with a step of $1/8\pi$ radian. The high order harmonic spectra ranging from 68 to 160 eV at different CEP values (from 0 to π) are shown in Fig. 3.9. The spectral resolution of the flat field grating

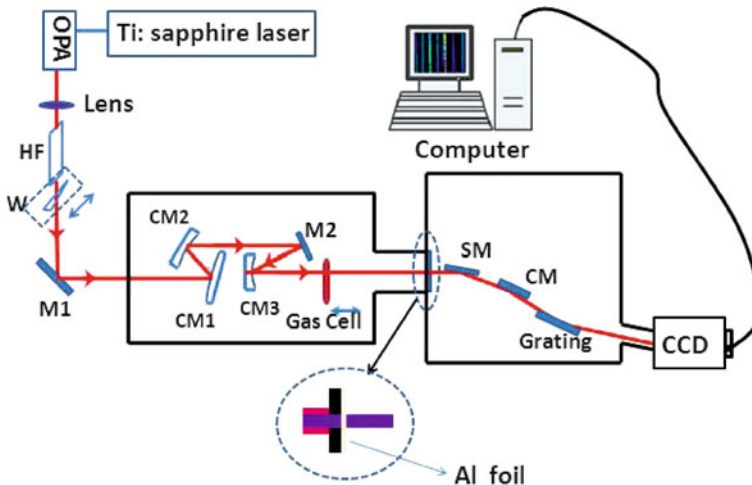


Fig. 3.8 Schematic of experimental setup for high order harmonic generation: *HF* hollow fiber, *M1*, *M2* silver mirror, *CM1* convex mirror ($f = 300 \text{ mm}$), *CM2* concave mirror ($f = 600 \text{ mm}$), *CM3* concave mirror ($f = 500 \text{ mm}$), *SM* a spherical concave gold mirror, *CM* cylindrical concave gold mirror

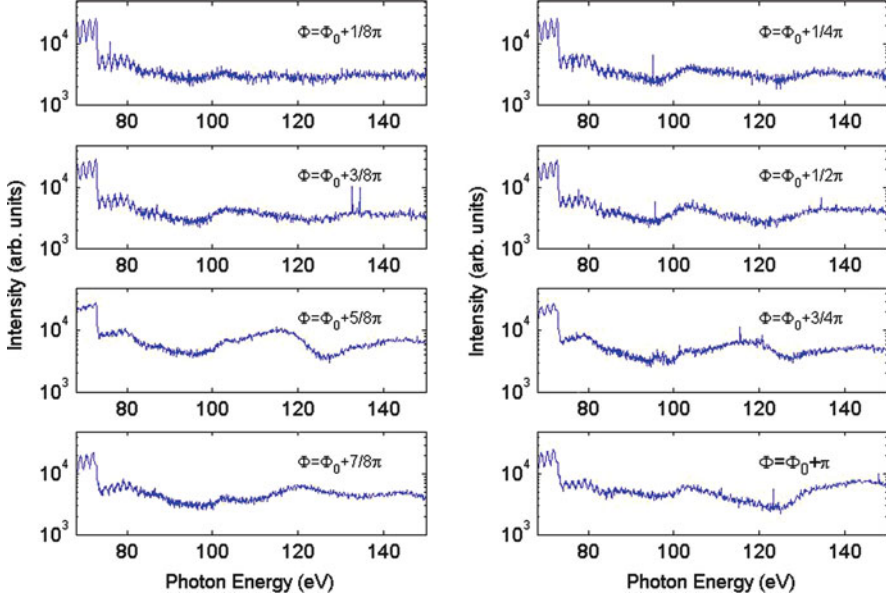


Fig. 3.9 The harmonic spectra obtained with different CEP values

spectrometer was good enough to resolve the harmonic peaks at the low photon energy region. As shown in Fig. 3.9, the harmonic spectra near the aluminum absorption edge were discrete for most of the CEP values. But when the CEP is changed $5/8\pi$, the spectrum near the aluminum absorption edge is continuous and a broad supercontinuum is obtained.

3.4 Summary

We have developed a CEP stabilized 1.5 cycle, sub-millijoule level laser system at $1.75\ \mu\text{m}$ center wavelength at 1 kHz repetition rate. Benefit from the character of passive CEP stabilization of the idler pulse during the OPA process, 1.6 mJ, 57 fs pulses at $1.8\ \mu\text{m}$ with rms CEP fluctuation of ~ 401 mrad are obtained by three-stage OPA system. After passing through a hollow fiber and block material for dispersion compensation, the pulses are finally compressed to 8.4 fs and 0.7 mJ, with rms CEP fluctuation of ~ 547 mrad. The system provides an excellent laser source for isolated attosecond pulse generation and other HHG experiments. The preliminary experimental results of short wavelength high order harmonic generation and terahertz (THz) generation with a pronounced CEP dependence were shown.

Acknowledgements We acknowledge the support from Chinese Academy of Science, National Natural Science Foundation (Grant Nos. 10734080, 60921004, 60908008, 61078037), National 973 Program (Grant No. 2011CB808100), National Basic Research Program of China (Grant No. 2011CB808101), and Shanghai Commission of Science and Technology (Grant No. 09QA1406500).

References

1. A.H. Zewail, *Science* **242**, 1645 (1988)
2. A.H. Zewail, *J. Phys. Chem. A* **104**, 5660 (2000)
3. E. Goulielmakis, M. Schultze et al., *Science* **320**, 1614 (2008)
4. E. Goulielmakis, Z.H. Loh et al., *Nature* **466**, 739 (2010)
5. E. Goulielmakis, V.S. Yakovlev et al., *Science* **317**, 769 (2007)
6. P. Colosimo, G. Doumy et al., *Nat. Phys.* **4**, 386 (2008)
7. V.S. Yakovlev, M. Ivanov et al., *Opt. Express* **15**, 15351 (2007)
8. C. Vozzi, C. Manzoni et al., *J. Opt. Soc. Am. B* **25**, B112 (2008)
9. M.C. Chen, P. Arpin et al., *Phy. Rev. Lett.* **105**, 173901 (2010)
10. A. Baltuška, T. Fuji et al., *Phys. Rev. Lett.* **88**, 133901 (2002)
11. X. Gu, G. Marcus et al., *Opt. Express* **17**, 62 (2009)
12. O.D. Mücke, S. Ališauskas et al., *Opt. Lett.* **34**, 2498 (2009)
13. B.E. Schmidt, P. BÉjot et al., *Appl. Phys. Lett.* **96**, 121109 (2010)
14. P. BÉjot, B.E. Schmidt et al., *Phy. Rev. A* **81**, 063828 (2010)
15. C. Vozzi, F. Calegari et al., *Opt. Lett.* **32**, 2957 (2007)
16. T. Kobayashi, A. Baltuška, *Meas. Sci. Technol.* **13**, 1671 (2002)
17. A. Baltuška, M.S. Pshenichnikov et al., *IEEE J. Quantum Electron.* **35**, 459 (1999)
18. A. Baltuška, M. Uiberacker et al., *IEEE J. Sel. Top. Quant. Electron.* **9**, 972 (2003)
19. M. Takeda, H. Ina et al., *J. Opt. Soc. Am.* **72**, 156 (1982)
20. M. Kreß, T. Löffler et al., *Nat. Phys.* **2**, 327 (2006)
21. Z. Jiang, F.G. Sun et al., *Appl. Phys. Lett.* **74**, 1191 (1999)

Chapter 4

Few-Cycle, Phase-Locked, Octave IR OPA Using BIBO and 800-nm Pump

N. Ishii, K. Kitano, T. Kanai, S. Watanabe, and J. Itatani

4.1 Infrared Laser for Attosecond Pulse Generation in the Soft X-Ray

Few-cycle, high-energy, infrared (IR) lasers have been recognized as promising drivers to generate coherent radiation and attosecond pulses beyond the soft X-ray, reaching the water window. Based on a high harmonic generation (HHG) process driven by IR pulses, preliminary researches have demonstrated the drastic extension of a cutoff energy to a soft X-ray regime compared to Ti:sapphire-based lasers at 800 nm [1–3]. Although few IR drivers aiming at soft X-ray attosecond pulse generation have been constructed [4–7], these prototypes still require further improvement for potential applications in strong field physics and ultrafast spectroscopy. In this work, we describe a proof-of-principle experiment on a few-cycle, high-energy, carrier-envelope-phase (CEP)-stabilized, IR laser system

N. Ishii (✉) · K. Kitano · T. Kanai

Institute for Solid State Physics, University of Tokyo, Kashiwanoha 5-1-5, Kashiwa,
Chiba 277-8581, Japan

CREST, Japan Science and Technology Agency, Sanbancho 5, Chiyoda-ku,
Tokyo 102-0075, Japan
e-mail: ishii@issp.u-tokyo.ac.jp

S. Watanabe

CREST, Japan Science and Technology Agency, Sanbancho 5, Chiyoda-ku,
Tokyo 102-0075, Japan

Tokyo University of Science, Yamasaki 2641, Noda, Chiba 278-8510, Japan

J. Itatani

Institute for Solid State Physics, University of Tokyo, Kashiwanoha 5-1-5, Kashiwa,
Chiba 277-8581, Japan

PRESTO, Japan Science and Technology Agency, Sanbancho 5, Chiyoda-ku,
Tokyo 102-0075, Japan

based on octave-spanning optical parametric amplification (OPA) using BiB_3O_6 (BIBO) and 800-nm pump. This demonstration relied on widely-used Ti:sapphire lasers and related technologies and can be easily extended to the construction of a novel laser driver that can meet all requirements for the generation of coherent light radiation as well as attosecond pulses in the soft X-ray.

4.2 Octave-Spanning OPA Using BIBO and 800-nm Pump

We used a combination of difference frequency generation (DFG) to obtain CEP-locked seed pulses and degenerate OPA using BIBO pumped by a Ti:sapphire laser at 800 nm. The detailed explanation of these experimental results as well as the unique characteristics of BIBO OPA are described elsewhere [8, 9]. A part (about 0.3 mJ) of a 40-fs output beam from a Ti:sapphire amplifier was loosely focused into a gas cell filled with 3.2-bar krypton to generate a broadband continuum through optical filamentation. The blue and red components of the continuum are frequency-mixed in a BBO crystal to generate IR seed pulses via DFG. The generated seed spectrum is depicted by the dotted line of Fig. 4.1. The seed pulses with an energy of 100 nJ are successively amplified to 10 μJ in a 4-mm-thick BIBO crystal pumped by another part (0.1 mJ) of the Ti:sapphire output. The BIBO crystal is cut at $\theta = 11.4$ degrees for type I interaction in the xz plane. The OPA output spectrum, plotted by

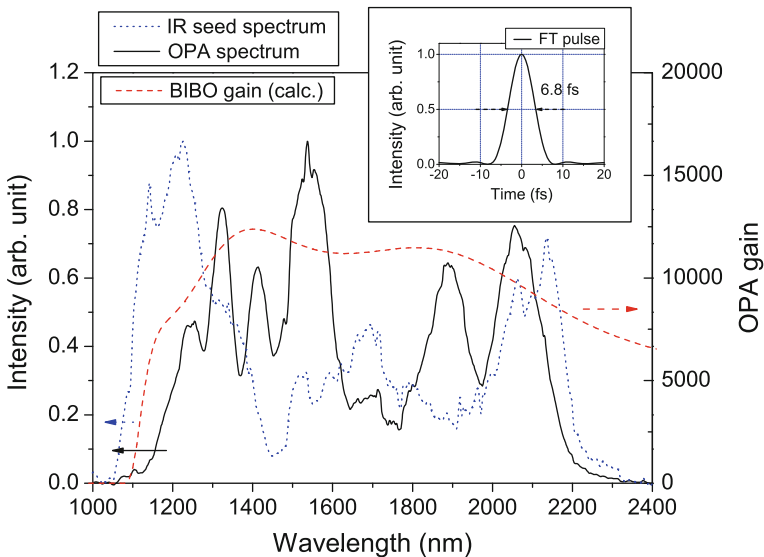


Fig. 4.1 Spectra of seed pulses produced via DFG (*dotted line*), OPA output (*solid line*), and calculated OPA gain (*dashed line*). Inset: transform-limited pulse with a duration of 6.8 fs (FWHM) calculated from the OPA spectrum

the solid line in Fig. 4.1, corresponds well to the overlap between the seed and the calculated BIBO gain spectra (dashed line in Fig. 4.1). The inset of Fig. 4.1 shows a calculated transform-limited pulse from the OPA spectrum, which has a duration of 6.8 fs and contains a 1.4-cycle carrier at the central wavelength of 1,470 nm.

4.3 CEP Measurement of the Octave OPA Output Without External Spectral Broadening

Advantages of seed generation via DFG are the ultrabroad bandwidth of generated difference frequency as well as the self-CEP-stabilization mechanism of produced pulses [10–12]. In order to check the stabilization and preservation of CEP during DFG and OPA, we measured the CEP of amplified pulses with an f -to- $2f$ interferometer without external spectral broadening. Because the OPA spectrum spans more than one octave, we are able to measure the CEP without additional spectral broadening, eliminating a potential noise source. The spectral components around 2,100 nm were frequency-doubled in a 3-mm-thick BBO crystal and combined with the blue components around 1,050 nm. We observed stable CEP fringe patterns as shown in Fig. 4.2a. The peaks of this spectral interference stay constant even

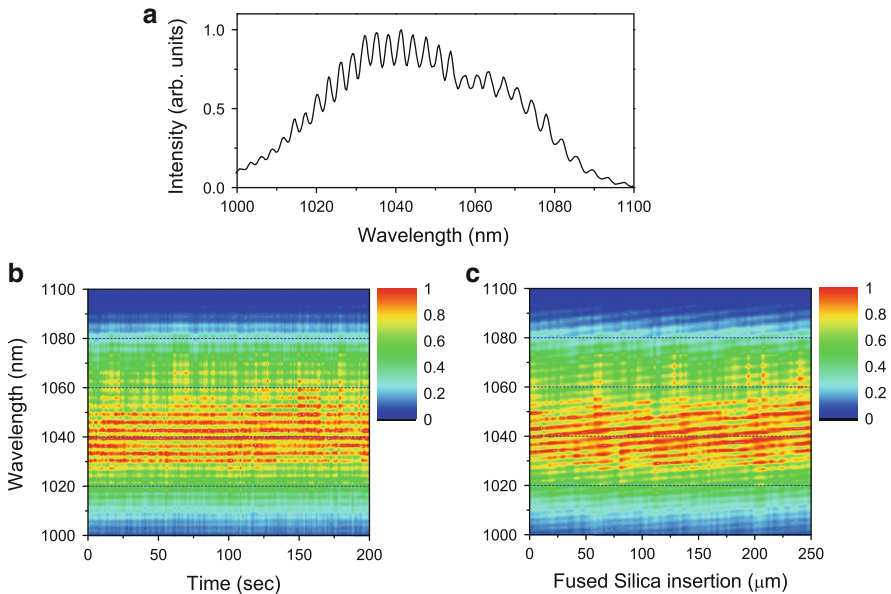


Fig. 4.2 Spectral interferograms acquired with an f -to- $2f$ interferometer. (a) Observed fringe pattern around 1,050 nm. Collection of spectral interferogram (b) without any external feedback, and (c) with the change of the CEP by a fused silica wedge pair

without any external feedback over 200 s as in Fig. 4.2b. Figure 4.2c demonstrates the fringe patterns moving as we change the dispersion in the beam path by a fused silica wedge pair. The slope of the fringe corresponds to that calculated from the dispersion relationship of fused silica.

4.4 Conclusion

In this report, we presented a proof-of-principle experiment applicable to the generation of few-cycle, high-energy, CEP-stable laser pulses in IR. In our setup, octave-spanning seed pulses are produced by DFG between spectral components of an ultrabroadband continuum generated through optical filamentation. The produced seed pulses are parametrically amplified to 10 μJ in a BIBO crystal pumped by 800-nm pulses, sustaining its one-octave spectrum. We succeeded in measuring the CEP of the OPA output pulses without additional spectral broadening with an f -to- $2f$ interferometer. Although pulse compression has not been conducted in this experiment, the compression is feasible because (1) the CEP measurements indicate the stable phase relationship between both edges of the whole spectrum and (2) the dispersion control of an octave-spanning spectrum can be handled with an acousto-optic programmable dispersive filter (AOPDF) (P. Tournois, 2010, private communication). Assuming perfect pulse compression, we expect to produce the shortest pulse with a duration of 6.8 fs (1.4 cycles) in the IR range. Our proposed amplification scheme is easily scaled up to a multi-millijoule level using 1-kHz Ti:sapphire chirped pulse amplifiers as pump sources.

Acknowledgements This research was partially supported by the Photon Frontier Network Program of the Ministry of Education, Culture, Sports, Science and Technology, Japan.

References

1. A. Gordon, F.X. Kärtner, *Opt. Express* **13**, 2941–2947 (2005)
2. B. Shan, Z. Chang, *Phys. Rev. A* **65**, 011804(R) (2001)
3. E.J. Takahashi, T. Kanai, K.L. Ishikawa, Y. Nabekawa, K. Midorikawa, *Phys. Rev. Lett.* **101**, 253901 (2008)
4. T. Fuji, N. Ishii, C.Y. Teisset, X. Gu, Th. Metzger, A. Baltuška, N. Forget, D. Kaplan, A. Galvanauskas, F. Krausz, *Opt. Lett.* **31**, 1103–1105 (2006)
5. D. Brida, G. Cirmi, C. Manzoni, S. Bonora, P. Villorosi, S. De Silvestri, G. Cerullo, Sub-two-cycle light pulses at 1.6 μm from an optical parametric amplifier. *Opt. Lett.* **33**, 741–743 (2008)
6. O.D. Mücke, S. Ališauskas, A.J. Verhoef, A. Pugžlys, A. Baltuška, V. Smilgevičius, J. Pocius, L. Giniūnas, R. Danielius, N. Forget, *Opt. Lett.* **34**, 2498–2500 (2009)
7. B.E. Schmidt, P.Béjot, M. Giguère, A.D. Shiner, C. Trallero-Herrero, É. Bisson, J. Kasparian, J.P. Wolf, D.M. Villeneuve, J.C. Kieffer, P.B. Corkum, F. Légaré, *Appl. Phys. Lett.* **96**, 121109 (2010)

8. N. Ishii, K. Kitano, T. Kanai, S. Watanabe, J. Itatani, *Appl. Phys. Exp.* **4**, 022701 (2011)
9. A. Gaydardzhiev, I. Nikolov, I. Buchvarov, V. Petrov, F. Noack, *Opt. Express* **16**, 2363–2373 (2008)
10. T. Fuji, A. Apolonski, F. Krausz, *Opt. Lett.* **29**, 632–634 (2004)
11. M. Zimmermann, Ch. Gohle, R. Holzwarth, Th. Udem, T.W. Hänsch, *Opt. Lett.* **29**, 310–312 (2004)
12. C. Manzoni, G. Cerullo, S. De Silvestri, *Opt. Lett.* **29**, 2668–2670 (2004)

Chapter 5

CEP-Stable, Few-Cycle, kHz OPCPAs for Attosecond Science: Energy Scaling and Coherent Sub-Cycle Pulse Synthesis

**Kyung-Han Hong, Shu-Wei Huang, Jeffrey Moses, Xing Fu, Giovanni Cirmi,
Chien-Jen Lai, Siddharth Bhardwaj, and Franz X. Kärtner**

Abstract We report on the energy scaling and coherent waveform synthesis of a carrier-envelope phase (CEP)-stable, few-cycle, kHz-repetition-rate optical parametric chirped-pulse amplifiers (OPCPAs) for high-field physics applications. First, amplification of ultrabroadband 2.1- μm pulses to 0.85 mJ is demonstrated using a novel high-energy, *ps*, cryogenic Yb:YAG pump laser. Pulse compression to 4.5 optical cycles has been achieved. Initial high-harmonic generation (HHG) experiments with Xe have shown a significant cutoff extension to >85 eV. Second, we have coherently synthesized the 2.1- μm pulse with a CEP-stable, few-cycle near-infrared OPCPA pulse seeded by the same laser oscillator and generated a 15- μJ sub-cycle waveform. Simulations confirm that this waveform is suitable for isolated attosecond pulse generation. The pulse synthesis method can be extended to a novel energy-scalable wavelength multiplexing scheme based on multi-color OPCPAs.

K.-H. Hong (✉)

Department of Electrical Engineering and Computer Science (EECS) and Research Laboratory of Electronics (RLE), Massachusetts Institute of Technology (MIT), 77 Massachusetts Avenue, Cambridge, MA 02139, USA

e-mail: kyunghan@mit.edu

S.-W. Huang · J. Moses · X. Fu · G. Cirmi · C.-J. Lai · S. Bhardwaj

EECS and RLE, MIT, 77 Massachusetts Avenue, Cambridge, MA 02139, USA

F.X. Kärtner

EECS and RLE, MIT, 77 Massachusetts Avenue, Cambridge, MA 02139, USA

Center for Free-Electron Laser Science, DESY, and Department of Physics, University of Hamburg, Notkestraße 85, 22607 Hamburg, Germany

e-mail: kaertner@mit.edu

5.1 Introduction

High-energy, CEP-stable, few-cycle optical pulses have been a major driving source for producing isolated attosecond pulses via HHG. Besides the Ti:sapphire chirped-pulse amplification (CPA) technology with external pulse compression technique, recently, ultrabroadband OPCPA has provided a promising way for next-generation attosecond science because of several unique features, such as wavelength coverage from the visible to the mid-infrared, energy scalability while maintaining few-cycle pulse durations, and low CEP drift during the amplification. Especially, mid-IR few-cycle OPCPA [1] can greatly extend the cut-off energy of HHG, enabling attosecond science at high photon energy [2]. Recently, phase-matched HHG results reaching the water window and even keV ranges have been demonstrated using a 10Hz, multi-mJ, 2- μm optical parametric amplifier [3] and a 20-Hz, multi-mJ, 3.9- μm OPCPA [4], respectively. The number of the generated XUV photons per second, however, is still as low as 10^6 – 10^7 (1% bandwidth), limiting potential applications. Increasing the repetition rate to the kHz-range is a clear path for increasing XUV photon flux by two orders of magnitude. Energy scaling of kHz OPCPAs has been limited by the *ps* Nd:YLF pump laser technology. In Sect 5.2, we present a kHz, 2.1- μm ultrabroadband OPCPA using a high-energy highpower cryogenic Yb:YAG pump laser [5], and the HHG experiments using this source. OPCPA-based coherent pulse synthesis is an interesting approach for energy scaling while increasing the spectral bandwidth. In Sect. 5.3, we address the challenge of high-energy sub-cycle optical waveform synthesis based on two few-cycle OPCPA systems as a further step towards the generation of sub-cycle pulses and show that these pulses can be useful for attosecond science.

5.2 High-Energy, kHz, Ultrabroadband OPCPA at 2.1- μm Wavelength

In our early research [6] we demonstrated a 0.2-mJ, kHz OPCPA at 2.2- μm wavelength using a Nd:YLF pump laser. This pump laser was still used for the first two OPCPA stages in the upgraded system as pre-amplifiers to minimize the modification of the OPCPA operating stably and already optimized for superfluorescence (SF) suppression. The Nd:YLF laser is a 4-mJ, 12-ps CPA system at 1047 nm, composed of a chirped fiber Bragg grating (CFBG) stretcher, ytterbium-doped fiber amplifier (YDFA), a regenerative amplifier (RGA) followed by two multi-pass slab amplifiers, and a diffraction grating compressor [6]. The required pump energy for the first two stages of the OPCPA was only ~ 1.9 mJ. The final (third) OPCPA stage was pumped by the newly developed cryogenic Yb:YAG CPA, which was slightly modified from the original setup [5]. The output energy of the RGA was set to ~ 5 mJ and the pulses were further amplified in a double-pass cryogenic Yb:YAG amplifier with two crystals in an evacuated chamber.

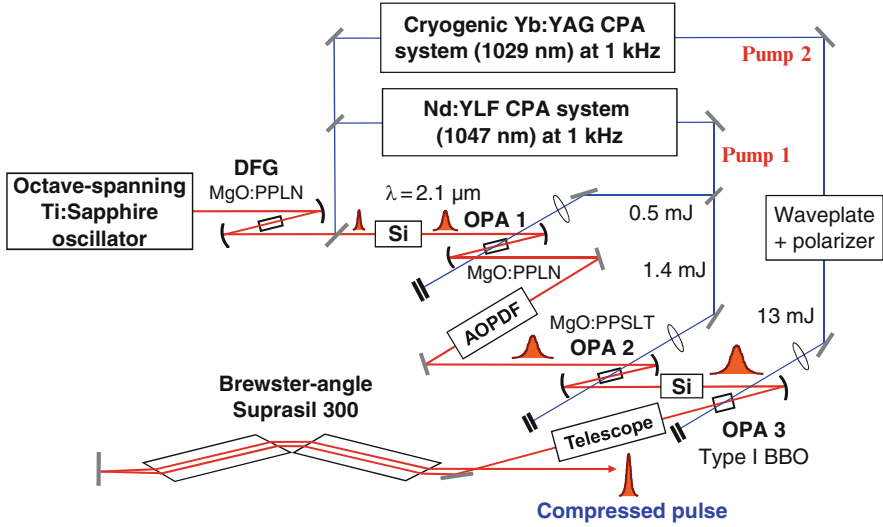


Fig. 5.1 Optical layout of the ultrabroadband kHz, CEP-stable, 2.1- μm three-stage OPCPA system

We maintained the maximum energy of 20 mJ with a relatively large pump beam size (~ 3.6 mm diameter) to ensure damage-free long-term operation. The pulse is compressed to 14.2 ps using a multi-layer dielectric grating pair with a throughput efficiency of 75%. The available pump energy at the third OPCPA stage was 13 mJ after the optics for energy and optical delay control. Both pump lasers are seeded by one Ti:sapphire laser for achieving optical synchronization.

Figure 5.1 illustrates the schematic of the 2.1- μm OPCPA [7]. The CEP-stable 2.1- μm seed pulses, produced by intra-pulse difference frequency generation (DFG) in MgO:PPLN, are stretched and amplified to 25 μJ in the two OPCPA stages based on MgO:PPLN and MgO:PPLSLT, respectively. The pulses are stretched to ~ 14 ps in full width at half-maximum (FWHM) for the third OPCPA stage with a 5-mm-thick type I BBO crystal. The pump intensity was ~ 40 GW/cm² at 13 mJ of energy. After optimization of temporal and spatial overlaps and incidence angle of the pump beam into the BBO crystal, we obtained a maximum energy of 0.85 mJ with a conversion efficiency of 7.5% including the reflection loss of the pump beam on the uncoated BBO crystal. The amplified spectrum from the third OPCPA stage (the solid line in Fig. 5.2a) shows spectral bandwidth of 474 nm (FWHM) centered at 2.1- μm , which supports a transform-limited pulse duration of 24.5 fs or 3.5 optical cycles (Fig. 5.2b). An output bandwidth broader than the second-stage output (405 nm) indicates gain saturation at the third stage.

The compression was achieved using Brewster-angle Suprasil 300 glass. We finely adjusted the AOPDF to minimize the pulse duration and suppress the pedestal while monitoring interferometric autocorrelation (IAC) traces. Figure 5.2b shows the compressed pulse with a duration of 31.7 fs or 4.5 optical cycles.

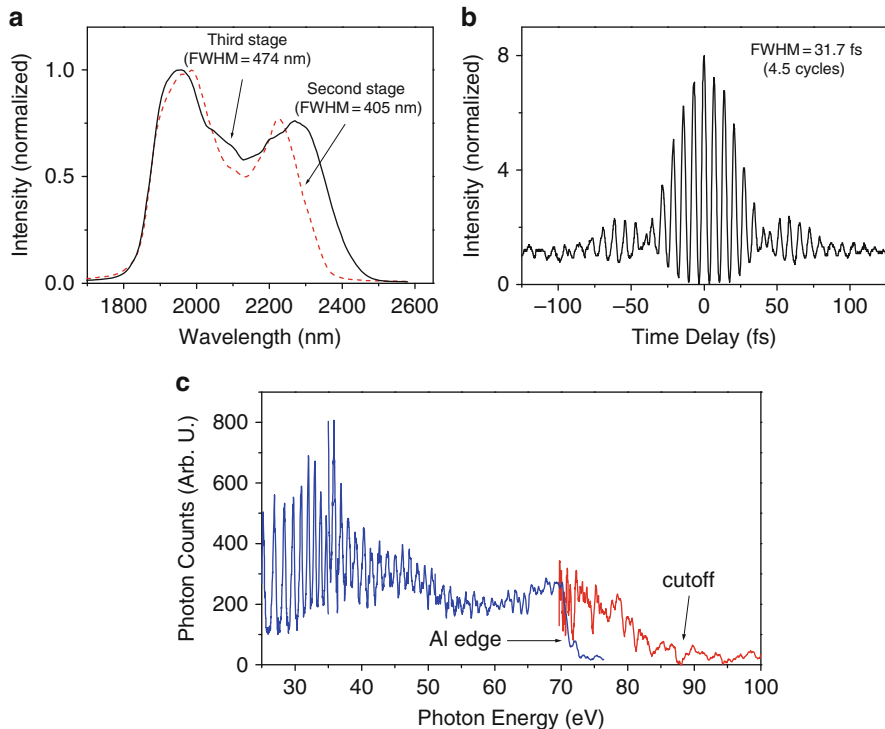


Fig. 5.2 Amplified spectra from the second and third stages of kHz, 2.1- μm OPCPA (a), the measured IAC trace after compression to 4.5 optical cycles (b), and HHG spectrum using a Xe gas jet (c). The *blue line* is measured with an Al filter while the *red line* is measured with a Zr filter in (c)

The compressed beam had a near Gaussian spatial profile. The shot-to-shot energy stability was $\sim 4\%$ (rms) and the SF noise was estimated as $\sim 9\%$ (rms). The CEP stability was measured to be 194 mrad in ~ 30 s.

As a first step to show the feasibility of approaching water-window XUV region at kHz repetition rates, we performed HHG experiments in Xe, a heavy noble gas with low saturation intensity. The 2.1- μm OPCPA output was focused onto a gas jet using an $f = 200$ mm CaF₂ lens in a vacuum chamber. The HHG signal was first detected with an Al-coated XUV photodiode after a 500-nm-thick Al filter and then magnified using a low-noise electronic amplifier that significantly improves the detection sensitivity. A strong HHG signal was observed at the peak intensity of $(0.5\text{--}1) \times 10^{14}$ W/cm² at ~ 50 mbar of Xe. The HHG efficiency was limited by the gas pressure loadable (maximum backing pressure of ~ 2 bar). The spectra measured using our XUV spectrometer with Al and Zr filters are shown in Fig. 5.2c, clearly showing high-order harmonics up to > 85 eV, where the Al edge at 70 eV is well identified. The cutoff extension to ~ 85 eV in Xe is already significant, compared to ~ 35 eV obtained using our 35-fs, 800-nm driver. The phase

matching cutoff, which scales with $\lambda^{1.5-1.7}$ [8], is calculated to be ~ 94 eV for our experimental conditions, indicating near phase-matched HHG. The HHG efficiency per harmonic is estimated to be $\sim 10^{-10}$, which can be improved with increased pressure. Experimental demonstration of cutoff extension to water-window radiation at kHz repetition rate using Ne and He is in progress.

5.3 High-Energy Waveform Synthesis Based on Few-Cycle OPCPAs

As a new approach of energy scaling of optical pulses in the single-cycle regime, we demonstrate a novel method, based on coherent wavelength multiplexing of ultra-broadband OPCPAs with a spectrum spanning close to two octaves [9]. As illustrated in Fig. 5.3, the system coherently combines two CEP-controlled, few-cycle pulses obtained from an 870-nm OPCPA, producing 25- μ J, 9-fs pulses and 2.1- μ m OPCPA, producing 25- μ J, 24-fs pulses. In this section we utilized only the Nd:YLF pump laser and two OPCPA stages, all seeded by a single Ti:sapphire laser oscillator. Using a single front-end for the entire system ensures the coherence of the two OPCPA pulses to within environmental fluctuations and drifts on subsequent beam paths. The inclusion of an acousto-optic programmable dispersive filter (AOPDF) in each OPCPA allows independent spectral phase and amplitude adjustment of each pulse, enabling control and optimization of the synthesized waveform.

Outputs from the two OPCPAs are combined in a broadband neutral beamsplitter. The overall spectrum spans over 1.8 octaves and the energy of the synthesized pulse is 15 μ J. Besides the spectral phases (controlled by the AOPDFs), three other independent parameters determine the synthesized electric-field waveform: the CEP of the 870-nm OPCPA pulse (ϕ_1), the CEP of the 2.1- μ m OPCPA pulse (ϕ_2), and

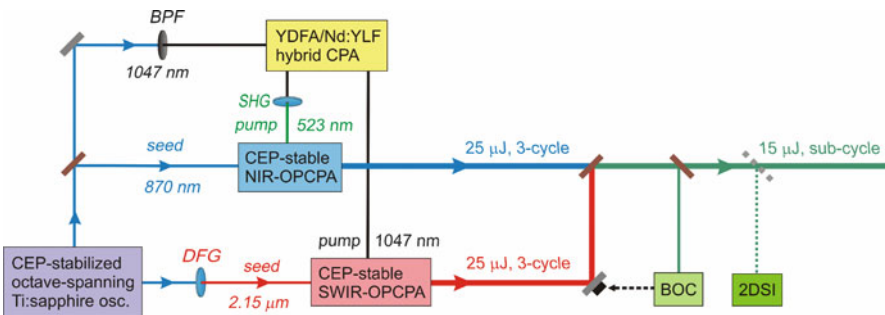


Fig. 5.3 Scheme of the high-energy optical waveform synthesizer. Two CEP-stabilized, few-cycle OPCPAs centered at different wavelengths (NIR at 870 nm and SWIR at 2.1- μ m) are combined by coherent wavelength multiplexing. *YDFA* Yb-doped fiber amplifier, *BPF* bandpass filter

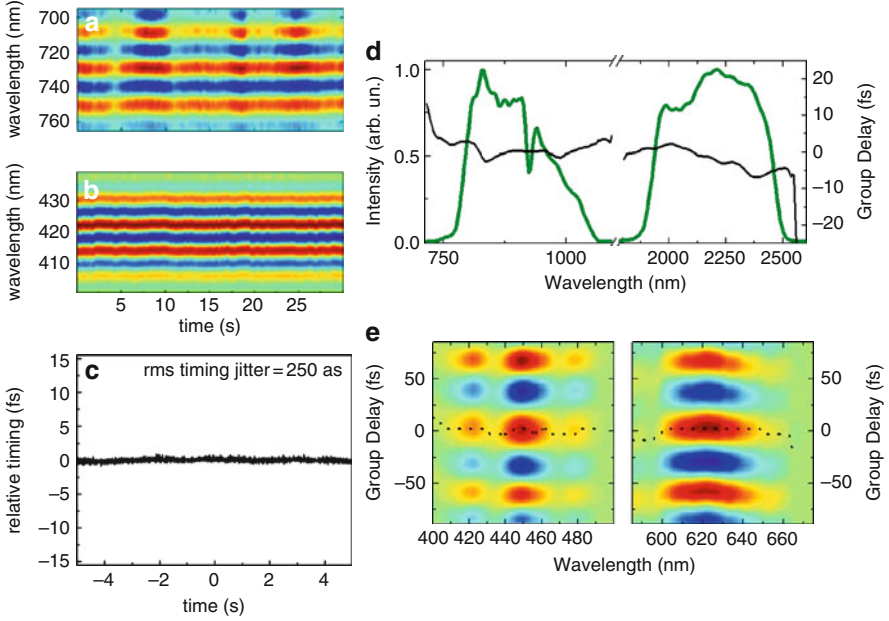


Fig. 5.4 Characterization of the synthesized pulses. Measured f – $2f$ interferogram showing 135 mrad rms CEP fluctuations over 30 s for the 870-nm OPCPA (a) and f – $3f$ interferogram showing 127 mrad rms CEP fluctuations for the 2.1- μm OPCPA (b), the measurement of relative timing drift of 250 as with feedback control (c), the optical spectrum and the frequency-dependent group-delay of the synthesized pulses measured by 2DSI (d), and the raw data of 2DSI (e)

the relative timing between the two OPCPA pulses (Δt). Precise stabilization and subsequent control of these three parameters are required for coherent synthesis and precise waveform shaping. While ϕ_2 is passively stabilized due to the intrapulse DFG process of its seed, an active feedback loop on the oscillator is implemented to ensure the stability of ϕ_1 . The CEP fluctuations of the two individual pulses are as low as 135 mrad (ϕ_1 , Fig. 5.4a) and 127 mrad (ϕ_2 , Fig. 5.4b), respectively. Figure 5.4c characterizes the relative timing stability, where a feedback loop based on a balanced optical cross-correlator (BOC) is implemented to synchronize the two pulses, allowing attosecond-precision relative timing stability. With the feedback control of the 2.1- μm OPCPA's path length over a bandwidth of 30 Hz, we have demonstrated a timing jitter of 250 as, less than 5% of the oscillation period of the 2.1- μm OPCPA (7.2 fs).

Once the BOC-assisted feedback loop stabilizes the relative timing between the two pulses, a two-dimensional spectral-shearing interferometer (2DSI) is used to simultaneously measure the spectral phase of each pulse and the relative timing. Figure 5.4e shows the raw data of a 2DSI measurement while Fig. 5.4d plots the extracted frequency-dependent group-delay, which is the derivative of the spectral phase with respect to frequency. The 2DSI measurement shows that the two pulses are temporally overlapped and well compressed to within 10% of the transform-limited pulse duration.

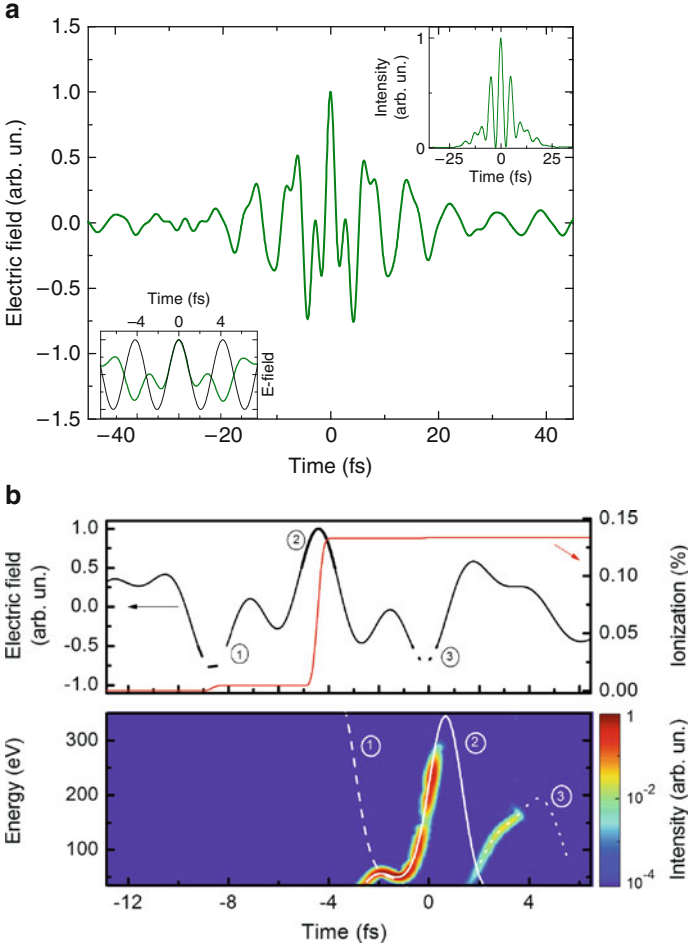


Fig. 5.5 Synthesized electric field (a) and extreme nonlinear optics with sub-cycle manipulated waveforms (b). Ionization dynamics (red) induced in He by the given electric-field waveform (black) assuming a peak intensity of $6 \times 10^{14} \text{ W/cm}^2$, $\phi_1 = 960 \text{ mrad}$, and $\phi_2 = -440 \text{ mrad}$. Spectrogram of the HHG superimposed with the calculated classical trajectories. Returning trajectories from three ionization events (2: the main pulse; 1 and 3: the satellite pulses) are shown for clear interpretation of the spectrogram. The synthesized pulse isolates the ionization process to a half cycle and a continuum spectrum spanning $>250 \text{ eV}$ can be achieved

The CEPs can be varied by slight tuning of any dispersive element and can be determined *in situ* when strong-field experiments are conducted. Therefore the CEP tunability is sufficient from an experimental point of view. Our system is capable of stabilizing and controlling all independent parameters that define the synthesized electric-field waveform. Figure 5.5a plots a synthesized pulse electric-field waveform and intensity profile assuming the CEPs ($\phi_1 = 650 \text{ mrad}$, $\phi_2 = -750 \text{ mrad}$)

optimal for achieving the shortest high-field transient, which lasts only 0.8 cycles (amplitude FWHM) of the carrier frequency of $1.26\ \mu\text{m}$. Due to the large gap in the synthesized pulse spectrum, there are wings 4.8 fs from the main pulse, which can be suppressed by extension of the coherent wavelength multiplexing scheme to include a third OPCPA covering the spectral gap. The synthesized waveform is important for optimizing isolated attosecond pulse generation via HHG. As an example, we numerically solve the time-dependent Schrödinger equation (TDSE) for He in a strong laser field to illustrate a possible use of our source for driving direct isolated soft-X-ray pulse generation. The achievable peak intensity ($6 \times 10^{14}\ \text{W}/\text{cm}^2$) is chosen such that the total ionization is below the critical ionization level in He. With optimal choice of CEPs and timing, substantial ionization can be limited to a half cycle and an isolated soft-X-ray pulse spanning over 250 eV is directly generated (Fig. 5.5b). Using an additional Sn filter, which blocks the strong IR driving field and the nonlinearly chirped low-photon-energy spectral content below 70 eV, leads to an isolated 150-as pulse centered at 200 eV. Of note, the non-sinusoidal electric-field waveform leads to drastically changed electron trajectories resulting in changes in quantum diffusion and atto-chirp, which can be controlled by means of the pulse synthesis parameters (ϕ_1 , ϕ_2 , and Δt). This gives an example of the capability of our sub-cycle pulse to simultaneously isolate the ionization process and manipulate electron trajectories within an optical cycle, allowing unprecedented control of the HHG process. It should be also noted that this pulse synthesis system can be further scaled to higher energy with our pump laser technology based on cryogenic Yb:YAG amplifiers.

References

1. B. Shan, Z. Chang, Dramatic extension of the high-order harmonic cutoff by using a long-wavelength driving field. *Phys. Rev. A* **65**, 011804(R) (2001)
2. A. Gordon, F.X. Kärtner, Scaling of keV HHG photon yield with drive wavelength. *Opt. Express* **13**, 2941–2947 (2005)
3. M.C. Chen et al., Ultrafast soft x-ray harmonics spanning the water window from a tabletop light source. *Phys. Rev. Lett.* **105**, 173901 (2010)
4. T. Popmintchev et al, CLEO/QELS 2011 (Baltimore, MD, May 1–6, 2011) PDPC12
5. K.-H. Hong et al., High-energy, kHz-repetition-rate, ps cryogenic Yb:YAG chirped-pulse amplifier. *Opt. Lett.* **35**, 1752–1754 (2010)
6. J. Moses et al, Highly stable ultrabroadband mid-IR optical parametric chirped-pulse amplifier optimized for superfluorescence suppression. *Opt. Lett.* **34**, 1639–1641 (2009)
7. K.-H. Hong et al., High-energy, phase-stable, ultrabroadband kHz OPCPA at $2.1\ \mu\text{m}$ pumped by a picosecond cryogenic Yb:YAG laser. *Opt. Express* **19**, 15538–15548 (2011)
8. T. Popmintchev et al, Phase matching of high harmonic generation in the soft and hard X-ray regions of the spectrum. *Proc. Nat. Acad. Sci. USA* **106**, 10516 (2009)
9. S.-W. Huang et al., High-energy pulse synthesis with sub-cycle waveform control for strong-field physics. *Nat. Photon.* **5**, 475–479 (2011)

Chapter 6

Dual-Chirped Optical Parametric Amplification for Generating High-Power Infrared Pulses

Q. Zhang, E.J. Takahashi, O.D. Mücke, P. Lu, and K. Midorikawa

Abstract We propose and calculate a novel OPA method for obtaining an ultrafast high-power infrared pulse source, called dual-chirped OPA (DC-OPA), based on a Ti:sapphire laser system in a collinear configuration. By chirping both pump and seed pulses in an optimized way, high-energy pump pulses can be utilized for a DC-OPA process without exceeding the damage threshold of BBO crystals, and broadband signal and idler pulses can be generated with a total conversion efficiency approaching 40%. Furthermore, the few-cycle idler pulses with a passively stabilized carrier-envelope phase (CEP) can be generated by the difference frequency generation (DFG) process.

6.1 Introduction

To further develop the applications of high-order harmonic generation (HHG), one of the most important issues is the extension of the wavelength range into the soft-

Q. Zhang (✉)

RIKEN Advanced Science Institute, 2-1 Hirosawa, Wako, Saitama 351-0198, Japan

School of Physics, Huazhong university of Science and Technology, Wuhan 430074, China

e-mail: zhangqb0807@gmail.com

E.J. Takahashi · K. Midorikawa

RIKEN Advanced Science Institute, 2-1 Hirosawa, Wako, Saitama 351-0198, Japan

e-mail: ejtak@riken.jp, kmidori@riken.jp

O.D. Mücke

Photonics Institute, Vienna University of Technology, Gusshausstrasse 27-387, A-1040 Vienna, Austria

e-mail: oliver.muecke@tuwien.ac.at

P. Lu

School of Physics, Huazhong university of Science and Technology, Wuhan 430074, China

e-mail: lupeixiang@mail.hust.edu.cn

and hard-X-ray region. According to the cutoff law of HHG [1], harmonics of higher photon energy can be produced by a driving laser with longer wavelength. This has motivated HHG experiments with near-IR to mid-IR pulse sources. For IR sources, although pulse durations in the few-cycle regime can be achieved, the output energy of the IR pulses barely reaches the mJ level [2–5]. To generate a harmonic beam of not only higher photon energy but also higher photon flux, IR pulses having a sufficient output energy and ultrashort pulse duration are required. Generally, the power-scaling potential of OPA/OPCPA is limited by the pump laser energy and the size of the nonlinear crystals. Therefore, we propose and investigate in detail a novel OPA method, DC-OPA, which permits to simultaneously obtain high peak power and ultrashort pulse duration in the IR region [6]. In this scheme, the damage of the BBO crystal with commercially available size can be avoided by chirping both pump and seed pulses in an optimal way. DC-OPA allows us to not only apply the powerful scalability of the IR energy while maintaining ultrashort pulse duration (<50 fs), but also employ high pump energy in the OPA. Moreover, DC-OPA can also produce a self-CEP-stabilized IR idler pulse.

6.2 The DC-OPA Scheme

The DC-OPA is seeded with a chirped, broadband seed pulse and pumped by a stretched, broadband pump pulse. In our envisaged DC-OPA system, automatically synchronized pump and seed pulses are obtained because they come from a common Ti:sapphire laser source. The pump pulse can be spatially separated into two pulses on a beam splitter, one strong and the other one weaker. The strong one will be used as pump pulse, and the weaker one will be used to generate the seed pulse via white-light generation, e.g., in a sapphire plate. Moreover, the seed pulse (and consequently the signal pulse) inherits the phase of the pump pulse. Since the idler pulse arises from DFG between the pump and signal pulses, the phase for a non-CEP-stabilized pump laser fluctuates from shot to shot in the pump and signal pulses, automatically cancelling out in the idler pulse.

During the OPA process, several undesirable effects, e.g., the Kerr nonlinearity and superfluorescence background may limit the choice of parameters such as pump intensity and the length of a nonlinear crystal, therefore the parameters must be chosen carefully. To produce a high-power IR laser source with pulse duration of a few tens of femtoseconds, it is necessary to investigate into the simultaneous optimization of the conversion efficiency and bandwidth for signal and idler pulses. We utilize pump and seed pulses at center wavelengths of 800 and 1,400 nm, producing idler pulse at 1,867 nm. The 35-fs pump is stretched to 792 fs by adding group delay dispersion (GDD) of $-10,000 \text{ fs}^2$, while the seed pulse duration varies from 35 to 792 fs by increasing the seed GDD from 0 to $10,000 \text{ fs}^2$. At an intensity of 100 GW/cm^2 and designed energy gain of 10^3 , it is found that the optimized GDD of the seed pulses range from 3,000 to $5,000 \text{ fs}^2$ for producing the signal pulse (Fig. 6.1a) and 3,500 to $5,500 \text{ fs}^2$ for the idler pulse (Fig. 6.1b). The

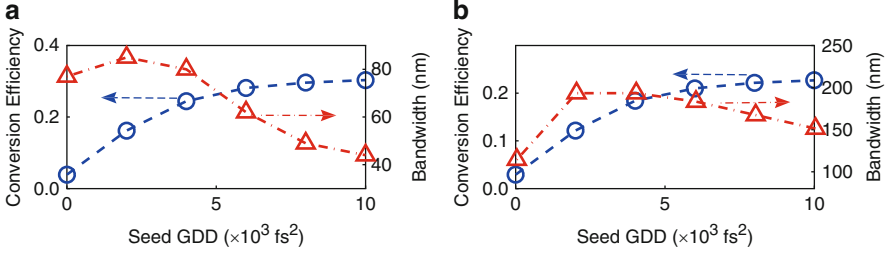


Fig. 6.1 Conversion efficiency (blue, open circle) and bandwidth (red, triangle) obtainable from the DC-OPA as function of the seed GDD (0–10,000 fs^2) in BBO Type-I phase matching for the (a) signal and (b) idler pulses, respectively

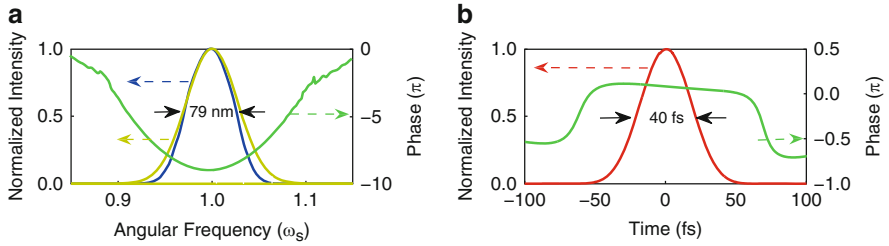


Fig. 6.2 (a) Spectrum of the injected seed pulse (yellow solid line), and spectral intensity of the amplified signal pulse (blue solid line) together with its phase (green solid line) before phase compensation. (b) Temporal intensity (red solid line) and phase (green solid line) profiles of the amplified signal pulse after phase compensation

upper and lower limit for the optimized GDD range are determined by the gain narrowing effect and conversion efficiency, respectively. Actually, the combination of GDD signs between pump (p) and seed (s) pulses is not important for generating broadband signal pulse. On the other hand, we have to choose an opposite sign GDD combination (“+p, -s” or “-p, +s”) to generate a broadband idler pulse.

We then discuss in detail the situation in which the pump and signal pulses are chirped by GDD values of $-10,000$ and $4,000 \text{ fs}^2$. For Type-I phase matching as shown in Fig. 6.2a, the amplified signal pulse at 1,400 nm exhibits a smooth distribution with a bandwidth of 79 nm, which is just slightly narrower than the injected spectra of the seed pulse. The spectral phase shows a parabolic profile originating from the added GDD and accumulated phase in the BBO crystal. Figure 6.2b shows the temporal profile of the amplified signal pulse after phase compensation. The compensation is realized by adding the inverse GDD of the seed pulse to that of the amplified signal pulse. A signal pulse with a pulse duration of 40 fs is obtained, which approaches the transform limit (TL) of 36 fs supported by the 79 nm bandwidth. We also show the temporal phase that was compensated for without considering the rapidly changing phase induced by the carrier frequency. The temporal phase profile of the signal pulse is very flat, which provides evidence for the good compensation of the second-order spectral phase.

6.3 Conclusion

We proposed a novel OPA scheme called DC-OPA for producing high-power IR pulses with a few-cycle pulse duration. In this scheme, a pump pulse at 800 nm and an IR seed pulse are generated employing a common Ti:sapphire laser system; thus, low-timing-jitter all-optical synchronization between the pump and seed pulses can easily be realized without the need of costly synchronization electronics. By introducing chirps to both pump and seed pulses, a sufficiently high-energy pump pulse can be applied in an OPA. For an optimized GDD combination between the pump and seed pulses, a total conversion efficiency approaching 40% and broadband signal and idler pulses can be obtained.

We believe that DC-OPA has great potential to markedly increase the IR pulse energy, which will pave the way for the generation and application of not only intense ultrafast coherent water window X-rays [7] but also high-intensity laser physics. Especially, an intense water window X-ray source can open the door to demonstrate direct seeding [8] of an FEL in the water window [9].

References

1. F. Krausz, M. Ivanov, *Rev. Mod. Phys.* **81**, 163–234 (2009)
2. D. Brida, G. Cirimi, C. Manzoni, S. Bonora, P. Villoresi, S. De Silvestri, G. Cerullo, *Opt. Lett.* **33**, 741–743 (2008)
3. T. Fuji, N. Ishii, C.Y. Teisset, X. Gu, T. Metzger et al., *Opt. Lett.* **31**, 1103–1105 (2006)
4. X. Gu, G. Marcus, Y. Deng, T. Metzger, C. Teisset et al., *Opt. Express* **17**, 62–69 (2009)
5. E.J. Takahashi, T. Kanai, Y. Nabekawa, K. Midorikawa, *Appl. Phys. Lett.* **93**, 041111 (2008)
6. Q. Zhang, E.J. Takahashi, O.D. Mücke, P. Lu, K. Midorikawa, *Opt. Express* **19**, 7190–7212 (2011)
7. E.J. Takahashi, T. Kanai, K.L. Ishikawa, Y. Nabekawa, K. Midorikawa, *Phys. Rev. Lett.* **101**, 253901 (2008)
8. T. Togashi, E.J. Takahashi, K. Midorikawa, M. Aoyama, K. Yamakawa et al., *Opt. Express* **19**, 317–324 (2011)
9. W. Ackermann, G. Asova, V. Ayvazyan, A. Azima, N. Baboi et al., *Nat. Photon.* **1**, 336–342 (2007)

Chapter 7

Development of High Power Infrared Optical Parametric Amplification Laser System Seeded by Self-difference Frequency Generation Pulses

Tsuneto Kanai, Sébastien Weber, Amelle Zaïr, Christopher Hutchison, Thomas Siegel, Malte Oppermann, Simon Hutchinson, Tobias Witting, Leonardo Brugnera, Rashid A. Ganeev, Toshiyuki Azuma, Katsumi Midorikawa, and Jonathan P. Marangos

Abstract We report on our recent development of a femtosecond infrared laser system based on self-phase-stabilized seed by difference-frequency generation of supercontinuum obtained with so-called hollow fiber compression technique and two-stage optical parametric amplification. After the final amplifier, we obtained pulses with duration of <40 fs, tunable center wavelength from 1.2 to 1.8 μm , maximum pulse energy of >500 μJ and as a first demonstration of this new laser system, we generated high-harmonics up to 47th order in a tube target filled with Xe gas.

T. Kanai (✉)

Atomic, Molecular, and Optical Physics Laboratory, RIKEN ASI, 2-1 Hirosawa, Wako-shi, Saitama 351-0198, Japan

Department of Physics, Blackett laboratory, Imperial College London, London SW7 2BW, United Kingdom

Extreme Photonics Research Group, RIKEN ASI, 2-1 Hirosawa, Wako-shi, Saitama 351-0198, Japan

e-mail: tkanai@riken.jp

T. Azuma

Atomic, Molecular, and Optical Physics Laboratory, RIKEN ASI, 2-1 Hirosawa, Wako-shi, Saitama 351-0198, Japan

S. Weber · A. Zaïr · C. Hutchison · T. Siegel · M. Oppermann · S. Hutchinson · T. Witting · L. Brugnera · R.A. Ganeev · J.P. Marangos

Department of Physics, Blackett laboratory, Imperial College London, London SW7 2BW, United Kingdom

K. Midorikawa

Extreme Photonics Research Group, RIKEN ASI, 2-1 Hirosawa, Wako-shi, Saitama 351-0198, Japan

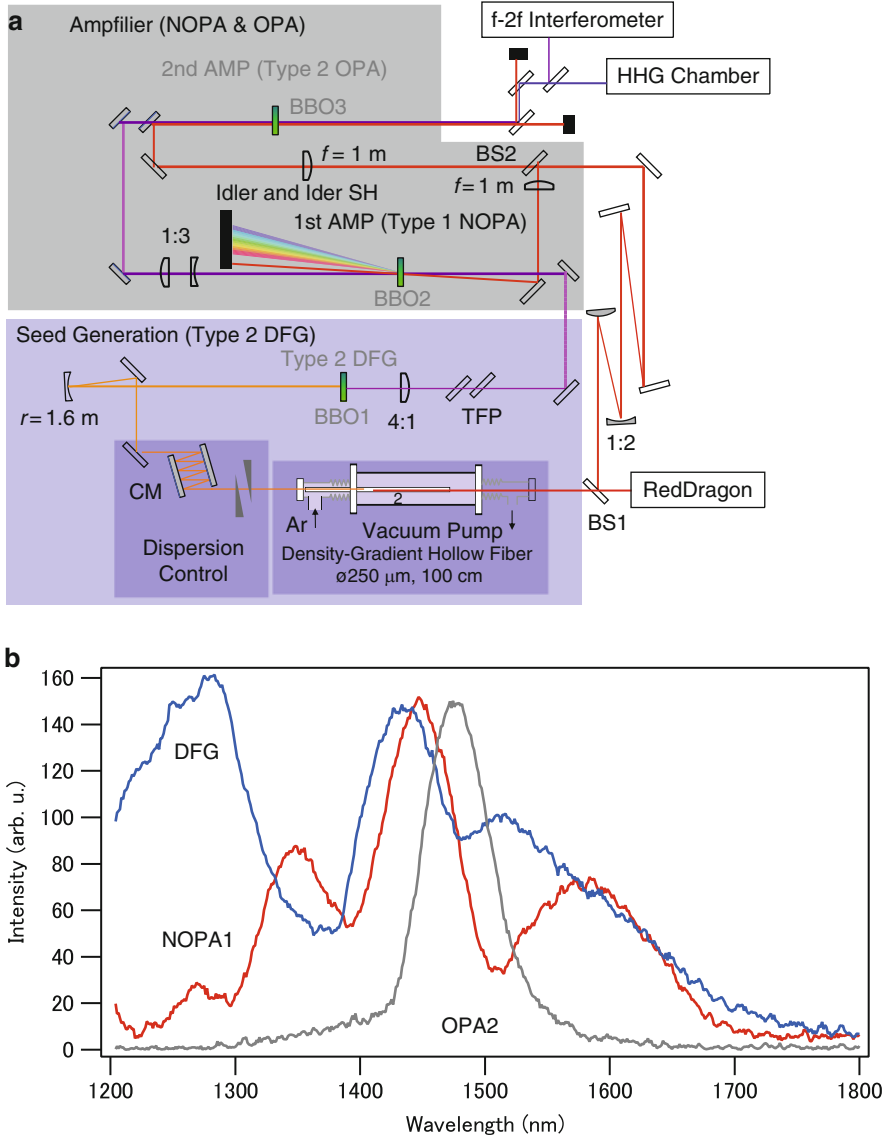


Fig. 7.1 (a) Schematic of our OPG laser system. (b) Normalized spectra of the pulses of the seed (blue line), the first OPA stage (red line), and the second (gray line) OPA stage

For attosecond physics [1,2], it is important to develop carrier-envelope phase (CEP) stabilized, high power, few cycle lasers. For this, it is required (1) to generate CEP-stabilized seed and (2) to suppress the noise to the CEP from its amplification process. In the gain region of Ti:Sa, (1) can be realized by adding active feedback loop(s) on CEP for a standard Ti:Sa oscillator and to show (2) and use it have

been a present issue [3]. In the IR, mid-IR, and THz regions, on the other hand, it is possible to generate CEP-stabilized seed by using self-difference frequency generation (DFG) [4], and it is now important to investigate the method to amplify this seed. In this paper, we report on our recent development of a laser that uses this seed and two-stage optical parametric amplifiers (OPAs) for it.

Figure 7.1 shows the schematic of the laser system (a) and the spectra of each stages (b). To realize optical synchronization during the OPA stages, the pump and the seed were generated by the same outputs from a Ti:Sa multi-pass amplification system (Red Dragon, KMLab, 40 fs (detuned), 5 mJ, 790 nm, 1 kHz). The seeds were generated by type II DFG of supercontinuum spectra (550–1,000 nm) obtained by using the so-called hollow fiber compression technique. For their amplification, we adopted simple two-stage ultrafast OPA method pumped by the residual 800-nm light. The first stage was pumped by 200 μ J and used a 2 mm thick BBO crystal cut for type I phase matching ($\theta = 21^\circ$); it produced pulse energies up to 13 μ J with a spectrum (Fig. 7.1b). The second OPA stage was pumped by 2.5 mJ and used a 3 mm thick BBO cut for type II phase matching ($\theta = 28.5^\circ$) to control the amplified pulse spectrum and generate pulses with TL duration. In the first OPA stage we used a non-collinear geometry with a small angle ($\approx 2^\circ$) but to achieve pulse front matching, we used a collinear geometry for the second OPA stage. After this final amplifier, we could get pulses with duration of <40 fs, tunable center wavelength from 1.2 to 1.8 μ m, maximum pulse energy of >500 μ J and as a first demonstration of this new laser system, we could generate high-harmonics in a tube target filled with Xe gas up to 47th order.

References

1. E. Goulielmakis et al., *Science* **320**, 1614 (2008)
2. T. Kanai, S. Minemoto, H. Sakai, *Nature (London)* **435**, 470 (2005)
3. T. Kanai et al., in *Proceedings of CLEO/Europe-EQEC, CG5.5*, Munich, 2011
4. C. Vozzi et al., *Opt. Lett.* **32**, 2957 (2007)

Chapter 8

Spatially Resolved Characterization of Sub-4-fs Laser Pulses Using Spectral Shearing Interferometry

T. Witting, F. Frank, C.A. Arrell, W. Okell, J.P. Marangos, and J.W.G. Tisch

Abstract We report on the spatially resolved full amplitude and phase characterization of high intensity few-cycle laser pulses. The sub-4-fs pulses are generated in a single stage hollow core fiber system with subsequent compression by ultrabroadband chirped mirrors. We use a spatially-encoded arrangement (SEA-)SPIDER with spectral filters for ancilla generation to fully characterize the sub-4-fs pulses with spatial resolution in a single shot.

8.1 Introduction

In the few-cycle regime, the light-matter interaction becomes extremely sensitive to the pulse shape and it is highly advantageous to use techniques such as frequency resolved optical gating (FROG) [1] and spectral phase interferometry for direct electric field reconstruction (SPIDER) [2] to obtain a full amplitude and phase characterization of the laser pulse. A unique advantage of SPIDER is the direct algebraic field reconstruction that facilitates online monitoring and optimization of the pulse [3]. High intensity few-cycle pulses are typically generated by nonlinear spectral broadening in a gas-filled hollow core fiber (HCF) [4] or a filament [5] followed by compression using chirped mirrors. Using HCFs, pulse energies up to 5 mJ [6] and pulse durations below 4 fs [7] have been previously demonstrated. Both these methods can lead to pulses with spatially-dependent temporal properties, but to-date, only a few spatially resolved pulse characterization measurements have been made [8–10].

In this letter we report the spatially resolved characterization of up to 0.2 mJ, sub-4-fs pulses generated in a single stage differentially pumped hollow core fiber

T. Witting (✉) · F. Frank · C.A. Arrell · W. Okell · J.P. Marangos · J.W.G. Tisch
Blackett Laboratory, Imperial College, London, SW7 2AZ, UK
e-mail: t.witting@imperial.ac.uk

followed by compression with chirped mirrors. We characterize the compressed pulses with a spatially encoded arrangement for direct electric field reconstruction by spectral shearing interferometry (SEA-SPIDER) [9]. SEA-SPIDER offers significant advantages over the traditional SPIDER device and is especially suited for few-cycle pulse characterization. It is a zero-additional phase measurement and benefits from less demanding spectrometer resolution requirements. For a pulse with field $E(y, t) = \int_{-\infty}^{+\infty} A(y, \omega) \exp[i\phi(y, \omega) - i\omega t] dt$, where $A(y, \omega)$ and $\phi(y, \omega)$ are the spectral amplitude and phase, respectively, and y is the transverse spatial coordinate (here the vertical direction), the SEA-SPIDER trace is given by

$$S(y, \omega) = |E(y, \omega')|^2 + |E(y, \omega' - \Omega)|^2 + 2|E(y, \omega')| |E(y, \omega' - \Omega)| \times \cos[\phi(y, \omega') - \phi(y, \omega' - \Omega) + \Delta ky], \quad (8.1)$$

where $\omega' = \omega - \omega_{up}$, Ω is the spectral shear, ω_{up} the upconversion frequency, and Δk is the wavevector difference arising from the angle between the two signal beams. From $S(y, \omega)$ the temporal field $E(y, t)$ can be reconstructed at every individual spatial position y_i enabling single-shot spatially resolved pulse characterization. The absolute phase between spatial slices remains unknown. A separate measurement is necessary to determine it [10]. A relative error in the spectral shear translates into a relative error in the retrieved pulse duration. For higher order phase the FWHM pulse duration error is around 1/5th of the shear error. For large GVD the mapping converges to 1:1. Thus the calibration of the spectral shear and also upconversion frequency, is crucial, but becomes increasingly difficult with increasing bandwidth. We employ the SEA-SPIDER with direct spectral filtering for ancilla preparation (SEA-F-SPIDER) [11] to increase the accuracy in determination of these parameters.

The experimental setup for this study is shown in Fig. 8.1. The laser system provides carrier-envelope phase stabilized pulses of 25 fs duration and energies of up to 0.8 mJ at a repetition rate of 1 kHz. The amplified pulses are focused into a 1 m long differentially pumped hollow core fiber (250 μm inner core diameter) [12]. The spectrally broadened pulses at the output of the fiber system are compressed by 10 bounces from double-angle technology chirped mirrors CMs (Ultrafast Innovations GmbH).

For spatially resolved full amplitude and phase characterization the compressed pulses are sent into the SEA-F-SPIDER device, shown in Fig. 8.1. A fraction (6%) of the pulse is split off by beamsplitter BS1 and is guided to the upconversion crystal using only reflective optics. The transmitted beam is again split into two equal energy parts by beamsplitter BS2. These two beams are spectrally filtered by narrow transmission window filters (Semrock) to prepare the ancillae beams. A detailed description of the setup can be found in [13].

In Fig. 8.2 we demonstrate the pulse reconstruction at different positions y_i in the beam. Figure 8.2a shows one reconstruction near the center of the beam. Figure 8.2a shows the temporal intensity and phase. The FWHM pulse duration is evaluated to

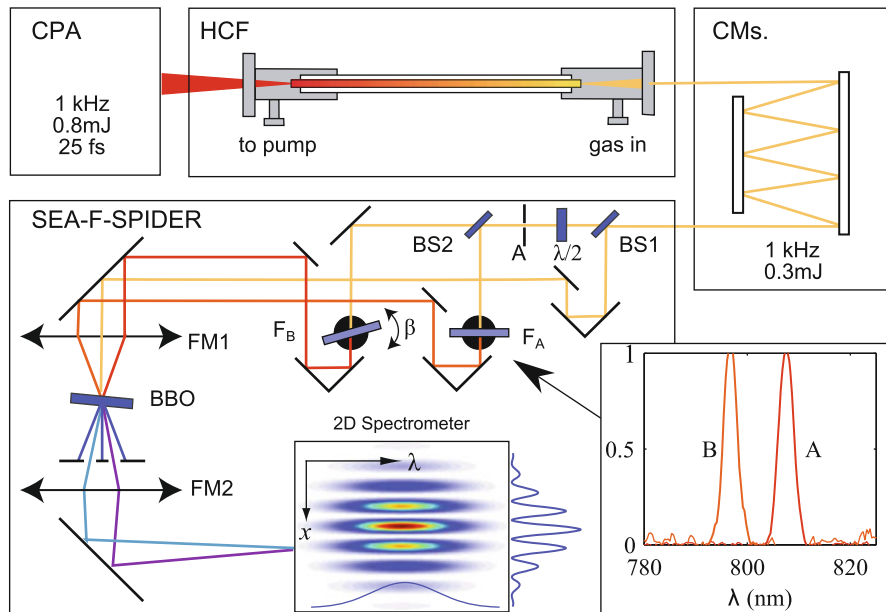


Fig. 8.1 (Color online) Experimental setup. For detailed explanation, see text

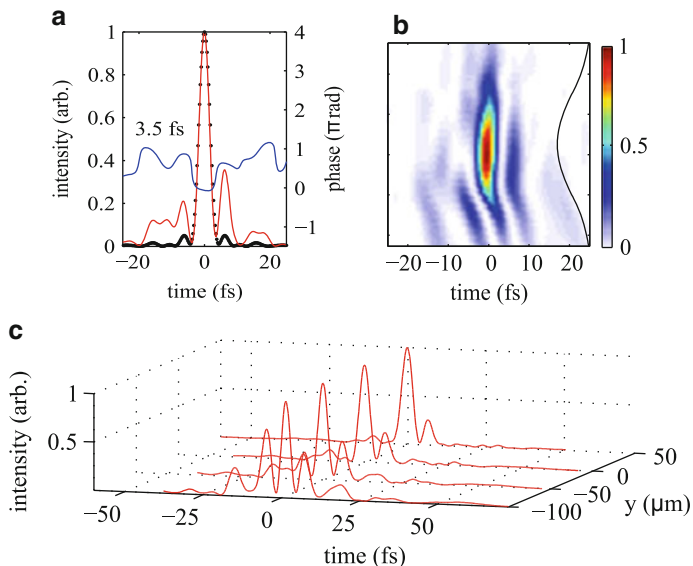


Fig. 8.2 (Color online) Spatially resolved pulse reconstruction. 1D reconstruction and Fourier-transform limit in beam center (a), spatially reconstructed temporal intensity (b), 1D lineouts at various positions (c)

be 3.5 fs. The spatially dependent reconstructed temporal intensities are displayed in Fig. 8.2b and lineouts at $y = -100, -50, 0, +50 \mu\text{m}$ are shown in (c). As SPIDER is inherently incapable of determining the pulse arrival time (linear phase term) we centered every spatial slice $E(y_i, t)$ on its first order moment. Apart from deviations in the low energy wings of the beam the pulse appears spatially homogeneous; the standard deviation of the pulse duration is 0.6% over the FWHM of the spatial profile. 52% of the total pulse energy spread over space and time is contained within a sub-4-fs window. For a reconstruction of the combined spatio-temporal field including the identification of non-trivial space-time couplings a separate spatial shearing measurement is necessary. Though somewhat cumbersome, this is, in principle, straightforward to implement.

In conclusion we have demonstrated the characterization of sub-4-fs pulses with the possibility to extract spatial information from a single-shot data trace for the first time. We envisage our characterization method to be useful in identifying spatial dependencies in few-cycle pulses generated in nonlinear pulse compressors and optimizing their performance.

Acknowledgements This research was supported in part by EPSRC grants EP/F034601/1, and EP/E028063/1. The authors gratefully acknowledge useful discussions with Dane R. Austin, Adam S. Wyatt, and Ian A. Walmsley. T. Witting's email address is twitting@imperial.ac.uk.

References

1. D.J. Kane, R. Trebino, *IEEE J. Quant. Electron.* **29**, 571 (1993)
2. C. Iaconis, I.A. Walmsley, *Opt. Lett.* **23**, 792 (1998)
3. W. Kornelis, J. Biegert, J.W.G. Tisch, M. Nisoli, G. Sansone, C. Vozzi, S.D. Silvestri, U. Keller, *Opt. Lett.* **28**, 281 (2003)
4. M. Nisoli, S.D. Silvestri, O. Svelto, *Appl. Phys. Lett.* **68**, 2793 (1996)
5. C. Hauri, W. Kornelis, F. Helbing, A. Heinrich, A. Couairon, A. Mysyrowicz, J. Biegert, U. Keller, *Appl. Phys. B* **79**, 673 (2004)
6. S. Bohman, A. Suda, T. Kanai, S. Yamaguchi, K. Midorikawa, *Opt. Lett.* **35**, 1887 (2010)
7. A.L. Cavalieri, E. Goulielmakis, B. Horvath, W. Helml, M. Schultze, M. Fieß, V. Pervak, L. Veisz, V.S. Yakovlev, M. Uiberacker, A. Apolonski, F. Krausz, R. Kienberger, *New. J. Phys.* **9**, 242 (2007)
8. L. Gallmann, G. Steinmeyer, D.H. Sutter, T. Rupp, C. Iaconis, I.A. Walmsley, U. Keller, *Opt. Lett.* **26**, 96 (2001)
9. E. Kosik, A. Radunsky, I. Walmsley, C. Dorrer, *Opt. Lett.* **30**, 326 (2005)
10. C. Dorrer, E.M. Kosik, I.A. Walmsley, *Opt. Lett.* **27**, 280 (2002)
11. T. Witting, D.R. Austin, I.A. Walmsley, *Opt. Lett.* **34**, 881 (2009)
12. J.S. Robinson, C.A. Haworth, H. Teng, R.A. Smith, J.P. Marangos, J.W.G. Tisch, *Appl. Phys. B Laser. Opt.* **85**, 525 (2006)
13. T. Witting, F. Frank, C.A. Arrell, W.A. Okell, J.P. Marangos, J.W.G. Tisch, *Opt. Lett.* **36**, 1680 (2011)

Chapter 9

Enhancement of the Photon Flux of a Time-Compensated Monochromator by Phase Matching in a Hollow Fiber

H. Igarashi, A. Makida, and T. Sekikawa

Abstract The output photon number from a time-compensated monochromator was increased up to 7.1×10^9 photons/sec by employing phase-matching technique: Ti:sapphire laser pulses (30 fs, 1.0 mJ, 800 nm pulse at a 1 kHz repetition rate) were focused into a 1-cm-long, 500- μ m-bore-diameter, hollow fiber filled with krypton gas. The harmonic photon energy was tunable between 23 and 39 eV. The output photon number on target was comparable to a small synchrotron radiation at the same wavelength region.

9.1 Introduction

In recent years, high harmonic generation has been actively researched to generate high power ultrashort extreme ultraviolet (XUV) pulses for the application to time-resolved and nonlinear spectroscopy. However, all harmonics are generated collinearly with the strong fundamental pulses. Thus, to detect only the target signals in spectroscopy, it is necessary to separate the single order high harmonic pulses from the others. For that purpose, a time-compensated monochromator selecting and compressing single order high harmonic pulses by a pair of toroidal gratings was proposed [1]. We constructed and evaluated the pulse energies, spot sizes, and pulse durations of the output high harmonic pulses from the system [2]. In this work, to develop a more effective light source for spectroscopy, the output power of a selected high harmonic was increased by fulfilling the phase-matching condition for high harmonic generation in a hollow fiber. The interaction between the laser field and gas medium in a hollow fiber makes it possible to improve the conversion efficiency owing to the longer coherent length.

H. Igarashi (✉) · A. Makida · T. Sekikawa
Department of Applied Physics, Hokkaido University, Sapporo 060-8628, Japan
e-mail: h.igarashi@eng.hokudai.ac.jp

9.2 Results and Discussion

High harmonics were generated by focusing Ti:sapphire laser pulses (30 fs, 1.0 mJ, 800 nm pulse at a 1 kHz repetition rate) into a 1-cm-long, 500- μ m-bore-diameter, hollow fiber filled with krypton. The optimum phase matching condition was explored by changing the gas pressure inside the hollow fiber. Figure 9.1 shows the pressure dependence of the intensity of the 19th harmonic. While the photon number increased with pressure, the intensity saturation was observed at more than 90 Torr. We also calculated the pressure dependence of the phase-matching factor by taking account of the phase mismatch from the neutral gas dispersion, the absorption, the refractive index variation by ionizing, the dispersion of waveguide, and the dispersion of nonlinear refractive index. The calculated phase-matching factor is shown by the dotted line in Fig. 9.1. Which is almost consistent with the experimental result. This pressure dependence indicates that the optimum condition of the phase matching was almost realized under the balance between the negative dispersion of the ionizing gas and the positive dispersion of the gas. Then, the conversion efficiency of high harmonic generation is well described by phase matching.

Based on the pressure dependence, we set the pressure at 100 Torr to satisfy the phase-matching condition in a gas-filled hollow-core fiber. Then, a single order harmonic was intensified up to seven times higher than in the gas jet. Figure 9.2 shows the spectra of high harmonics between the 17th and the 23rd. Under the optimum condition, the photon number of the 19th harmonic reached to a maximum value of 7.1×10^9 photons/s on target. The output photon numbers on target are comparable to a small synchrotron radiation in the same wavelength region. The single-order high harmonics selected by the time-compensated monochromator is a promising light source for XUV spectroscopy.

This work was supported by KAKENHI(23654140).

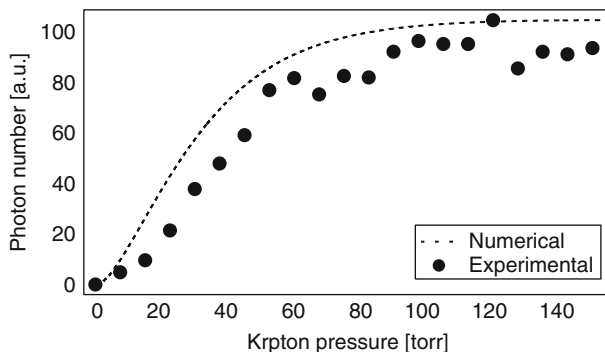


Fig. 9.1 Pressure dependence of the intensity of the 19th harmonic. The *circles* and the *dotted line* indicate the experimental and numerical results, respectively

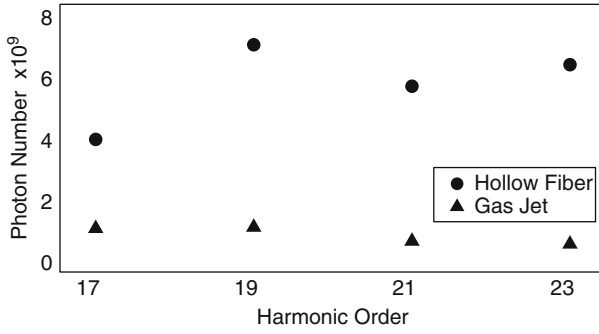


Fig. 9.2 Photon numbers per second of odd harmonics from 17th to 23rd using the gas jet (*triangle*) and the hollow fiber (*circle*) from krypton

References

1. P. Villorosi, Appl. Opt. **38**, 6040 (1999)
2. M. Ito, Y. Kataoka, T. Okamoto, M. Yamashita, T. Sekikawa, Opt. Express **18**, 6071 (2010)

Chapter 10

Temporal Optimization of the Time-Delay-Compensated Monochromator

A. Makida, H. Igarashi, and T. Sekikawa

Abstract We experimentally explored the optimum condition of a time-delay-compensated monochromator to compress the single high harmonics pulses. The pulse-front tilt coming from the diffraction on the grating was compensated by adjusting the slit position of the monochromator and the pulse duration was compressed down to 11 fs. The dependence of the pulse duration on the slit position was well explained by a theoretical model taking account of the pulse front tilt.

10.1 Introduction

The recent development of high harmonics, X-ray lasers, and free-electron lasers is providing us with unique opportunities to investigate nonlinear optics and ultrafast phenomena in the extreme ultraviolet (XUV) and soft X-ray regions. Among these opportunities, high harmonics, generated by the interaction between ultrashort laser pulses and rare gases, appear to be promising for spectroscopy because of the compactness of their experimental apparatus and their ultrashort temporal durations that break into the attosecond regime.

However, it is necessary to separate a single harmonic from the others for spectroscopic applications, since all high-order harmonics are generated collinearly. Thus, we developed a time-delay-compensated monochromator, consisting of two toroidal gratings, shown in Fig. 10.1 [1]. In the past study, using this monochromator, the pulse duration was compressed down to 47 fs [2], there still remains a question that what limits the compressed pulse duration. The pulse front tilt arises from the 2π phase shift per one groove on the grating. Therefore the pulse broadening in the monochromator comes from the difference in the irradiation areas of two gratings by

A. Makida (✉) · H. Igarashi · T. Sekikawa
Department of Applied Physics, Hokkaido University, Sapporo 060-8628, Japan
e-mail: ayumu_makida@eng.hokudai.ac.jp

Fig. 10.1 Time-delay compensated monochromator, consisting of two toroidal gratings and a slit

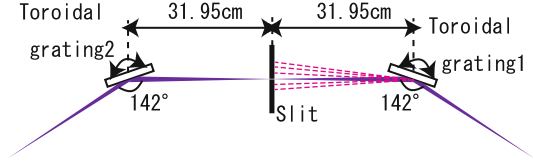
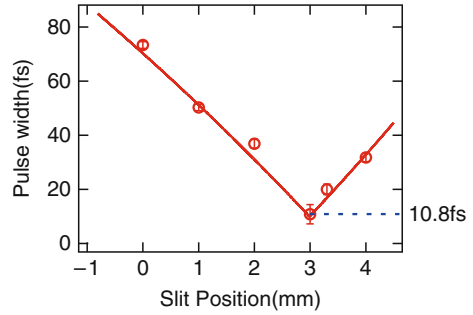


Fig. 10.2 Pulse width from the time-delay-compensated monochromator as a function of the slit position: the *solid line* shows the theoretical calculation and the *open circles* are the experimental results



high harmonics. This difference is caused by the misalignment of the incident angles of the beam to the gratings. In this paper, for the optimization of the monochromator, we noted the slit position selecting a single harmonic, because the irradiation areas are sensitive to the slit position. Thus, we experimentally explored the optimum condition for pulse compression as a function of the slit position in the dispersion direction.

10.2 Results and Discussion

The pulse duration of the 21st harmonic (32.6 eV) was measured as a function of the slit position by the cross correlation method. The open circles in Fig. 10.2 show the measured pulse duration as a function of the slit position in the dispersion direction. The pulse duration had a V-shaped dependence on the slit position and the shortest pulse duration was 11 fs, when the slit was moved 3 mm from the initial position.

To understand the dependence of the pulse duration, we calculated the pulse broadening coming from the incomplete compensation of the pulse front tilt and the result is shown by the solid line in Fig. 10.2. The experimental results were well explained by this model. Therefore, the pulse broadening is mainly due to the incomplete compensation of the pulse front tilt. The complete pulse recompression was achieved by equalizing the irradiated area of two gratings. We also calculated the pulse shape using the Lewenstein model under our experimental conditions [3]. Then, a pulse duration of 13 fs was obtained, which is consistent with the experimental result.

10.3 Conclusion

The output pulses from the time-delay-compensated monochromator was almost completely compressed by adjusting the slit position, corresponding to equalizing the irradiated area of the grating by high harmonics. To keep the broadening of the pulse duration less than 10% from the optimum, the slit position should be determined within 0.10-mm accuracy.

Acknowledgements This work was supported by a Grant-in-Aid for Scientific Research (B)(23340116) from Japan Society for the Promotion of Science.

References

1. P. Villorosi, *Appl. Opt.* **38**, 6040 (1999)
2. M. Ito, Y. Kataoka, T. Okamoto, M. Yamashita, T. Sekikawa, *Opt. Express* **18**, 6071 (2010)
3. M. Lewenstein, Ph. Balcou, M.Yu. Ivanov, A. L'Hukkie, P.B. Corkum, *Phys. Rev. A* **49**, 2117 (1994)

Chapter 11

Characterization of Extreme Ultra-Violet Free-Electron Laser Pulses by Autocorrelation

A. Senftleben, T. Pfeifer, K. Schnorr, K. Meyer, Y.H. Jiang, A. Rudenko, O. Herrwerth, L. Foucar, M. Kurka, K.U. Kühnel, M. Kübel, M.F. Kling, A. Yamada, K. Motomura, K. Ueda, R. Treusch, C.D. Schröter, R. Moshhammer, and J. Ullrich

Abstract We present EUV autocorrelation measurements of free-electron laser (FEL) pulses at 28 eV photon energy exploiting multiple ionization of argon as a non-linear process. In this way, the average pulse duration is measured while in parallel insight is gained into the temporal structure of the pulses. We compare the obtained results with FEL pulse simulations using our partial-coherence method (T. Pfeifer et al., *Opt. Lett.* **35**:3441 (2010)).

11.1 Introduction

Free-electron lasers have recently become available in the extreme ultra-violet (EUV) and X-ray spectral regions [1,2]. With their small beam divergence and short pulse durations they achieve unprecedented intensities, thus enabling to study non-linear processes with high-energy photons e.g. non-sequential two-photon double ionization of helium [3] or multiple ionization of other rare gas atoms [5–8].

A. Senftleben (✉) · T. Pfeifer · K. Schnorr · K. Meyer · Y.H. Jiang · M. Kurka · K.U. Kühnel · C.D. Schröter · R. Moshhammer · J. Ullrich
Max-Planck-Institut für Kernphysik, Saupfercheckweg 1, 69117 Heidelberg, Germany
e-mail: arne.senftleben@mpi-hd.mpg.de

A. Rudenko · L. Foucar
Max-Planck Advanced Study Group, 22607 Hamburg, Germany

O. Herrwerth · M. Kübel · M.F. Kling
Max-Planck-Institut für Quantenoptik, 85748 Garching, Germany

A. Yamada · K. Motomura · K. Ueda
IMRAM, Tohoku University, Sendai, Japan

R. Treusch
DESY, 22607 Hamburg, Germany

On the other hand, EUV FELs open new possibilities in the studies of molecular dynamics. This area comprises processes such as progression of vibrational wave packets [9, 10], different kinds of isomerization [11–16] or electron density oscillations. A tool to visualize molecular dynamics is ultra-fast Coulomb explosion imaging (CEI) [17], where a multiply charged molecule is formed that undergoes fast dissociation. Usually employing a pump–probe scheme where a first pulse starts a molecular reaction and the second pulse realizes CEI, it can be used to study the photon induced molecular dynamics on very short time scales. This requires the duration of the pulses to be shorter than the time scale of the studied reaction. Before the advent of EUV FEL sources this was only possible with very intense laser pulses in the near-infrared (NIR) region or NIR pulses in combination with high-harmonic radiation. Intense NIR pulses are especially unsuitable as probe pulses, because their strong electric field itself alters the structure of the molecule. In the EUV spectral region a single photon can induce Coulomb explosion while only being a marginal perturbation. However, knowledge of the actual temporal and spectral structure of the FEL pulse is inevitable for successful conducting and interpretation of such studies.

11.2 Generation of Coherent Extreme Ultra-Violet Radiation

In free-electron lasers, radiation is coherently amplified by a relativistic electron beam co-propagating with an electromagnetic wave inside an alternating magnetic field, produced by an undulator. For long wavelengths, FELs have been applied like a conventional laser medium, i.e. inside a cavity to allow multiple passes of the light pulse through the medium. This is not possible in the EUV spectral region where high-reflectivity normal-incidence mirrors do not exist. Additionally, the machines currently open for user research do not utilize seeding lasers to trigger the amplification due to the undulating electron beam. Therefore, FELs in this spectral region have to rely on synchrotron radiation emitted spontaneously in the first part of the undulator and amplified in the following. This principle is called self-amplified spontaneous emission (SASE) [18].

A consequence of the SASE method is that the pulses are different from shot to shot, exhibiting noise-like features in their temporal and spectral intensity profile. Measured single-pulse spectra [19] show distinct spikes at shifting spectral positions instead of the broad distribution obtained when averaging over a couple of shots [18]. Here we want to provide physical insight into the temporal structure of the pulses.

11.3 Intensity Autocorrelation

The autocorrelation technique allows to monitor the structure of an optical signal by convoluting it with itself. Therefore, the incoming pulse is split in halves and sent through different optical paths with a controllable path difference. As a consequence

the two half-pulses have a time delay τ at the point where they are merged again. After they have been superimposed, an n -th order non-linear process is employed to obtain the autocorrelation signal $\mathcal{A}^{(n)}$ as a function of τ :

$$\mathcal{A}^{(n)}(\tau) = \int_{-\infty}^{\infty} dt |(E(t) + E(t - \tau))^n|^2 \quad (11.1)$$

Here, $E(t - \tau)$ and $E(t)$ are the time-dependent electric fields of the delayed and undelayed half-pulses, respectively. $\mathcal{A}^{(n)}(\tau)$ is also called interferometric autocorrelation, because it resolves the optical-cycle interference between the fields of the half-pulses. In the case of short wavelengths, the uncertainty in τ is usually larger than the optical period T . Therefore, field oscillations and interferences are washed out and we obtain a cycle-averaged or intensity autocorrelation signal:

$$\bar{\mathcal{A}}^{(n)}(\tau) = \int_{\tau-T}^{\tau} d\tau' \mathcal{A}(\tau') = \sum_{i=1}^{n-1} \binom{n}{i} \int_{-\infty}^{\infty} dt I(t)^i I(t - \tau)^{n-i} + C \quad (11.2)$$

where C is a constant independent of τ and I is the intensity of the respective light field.

In the current experiment, multiple ionization of argon is the non-linear process employed to visualize the autocorrelation signal. Therefore, the FEL beam is focussed by a multilayer mirror onto a dilute argon gas sample. Ionized atoms are extracted using an electric field inside a reaction microscope [20]. Their charge state can be identified by the time-of-flight towards the detector where they are counted. The focussing mirror is split in halves which can be moved individually. By shifting their relative position in the beam propagation direction, a time delay between the half-pulses is introduced (Fig. 11.1).

11.4 Partial-Coherence Method for FEL Pulse Modeling

In order to model FEL pulses generated in the SASE mechanism we have developed a simple partial coherence method (PCM) which has been introduced recently [21]. It is a top-down approach that generates arbitrary pulses which obey the same statistics as real pulses. We start with the (average) measured intensity spectrum $\bar{I}(\omega_i)$ for the discrete frequency intervals ω_i . Each interval is assigned a completely random phase. After Fourier transformation, this will result in an infinitely long pulse (Nyquist-limited). Therefore, we then multiply the electric field in the time domain with the (average) temporal profile of the FEL pulses. This results in a final phase that is no longer random but constant over certain parts of the spectral distribution. In addition, spikes are visible in the simulated single pulse temporal structures as displayed in Fig. 11.2a. We call the average duration of these spikes the coherence time of our pulses.

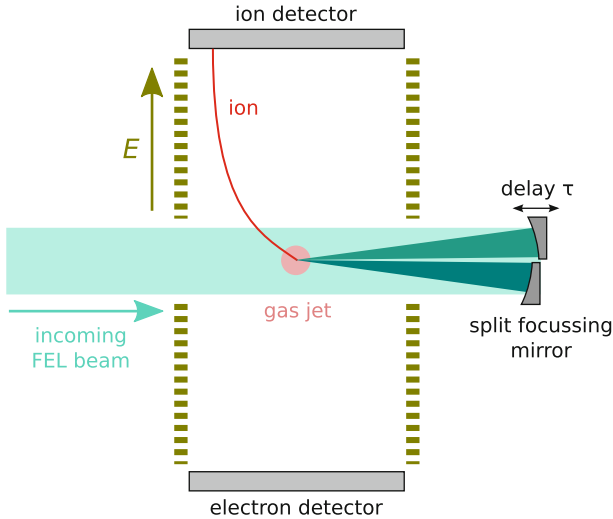


Fig. 11.1 Experimental scheme: The time delay τ to perform the autocorrelation measurement is introduced by the movable part of the split focussing mirror on the right. The mass-to-charge ratio of an detected ion is obtained from its time-of-flight

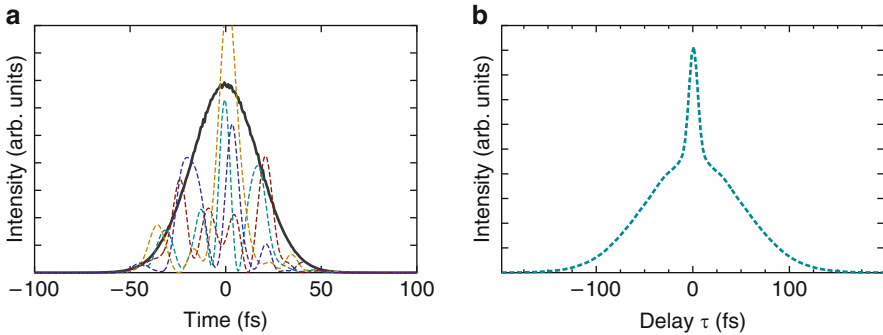


Fig. 11.2 (a) *Dashed lines*: temporal intensity profiles of individual FEL pulses generated with the partial-coherence method. *Broad line*: Corresponding average spectrum. (b) Example for an (averaged) 2nd order intensity autocorrelation trace of the simulated pulses

The resulting arbitrary pulses can now be used to simulate a real experiment such as an intensity autocorrelation measurement. An example is given in Fig. 11.2b where the second order autocorrelation trace is calculated and averaged over some hundred individual pulses. One can see two features: A broad hump and a sharp spike. The width of the hump is proportional to the average pulse duration with a factor depending on the order of the non-linear process. In our simulations the extension of the narrow feature is inversely proportional to the width of the average spectrum.

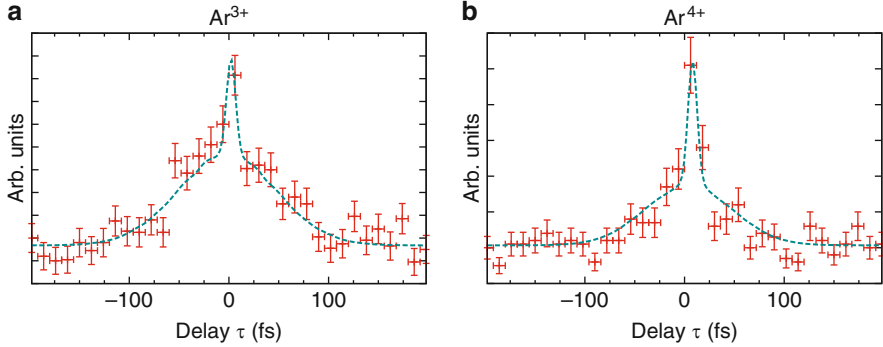


Fig. 11.3 Autocorrelation traces obtained at low charge (0.1 nC) of the FEL electron bunches: (a) Ar^{3+} and (b) Ar^{4+} signal as a function of the pulse delay τ . Experimental data are displayed as crosshairs representing the error margins. *dashed line*: PCM simulation with Gaussian spectrum of 0.24 eV FWHM and Gaussian time profile of 80 fs FWHM. The experimental points and the simulated trace are normalised to each other at the baseline and the crest of the broad peak. For this purpose, two Gaussians have been fitted to the experimental results

11.5 Results for Multiple Ionization of Argon

At a photon energy of 28 eV neutral argon can be singly ionized by one photon. The second ionization step can proceed with another photon. These two processes are very efficient in the present experiment, as Ar^{2+} is the most abundant ion measured on the detector. To further ionize doubly charged argon, at least two photons are necessary. Ionization from Ar^{3+} to Ar^{4+} requires even three photons. Consequently, the latter two species are candidates for the observation of autocorrelation traces. The following experiments have been performed at the free-electron laser in Hamburg (FLASH).

Figure 11.3 shows ionization yields for triply and quadruply charged argon ions as function of the pulse delay τ . For comparison we have performed PCM simulations to match the experimental data. For these calculations, Gaussian profiles with adjustable widths are employed for either the average spectrum ($\Delta\omega$) and the mean duration (Δt) of the FEL pulses. While the same parameters are incorporated for both charge states, second order autocorrelation is used to simulate the Ar^{3+} results, while third order is employed for the Ar^{4+} ions. The best agreement is achieved for $\Delta\omega = (0.24 \pm 0.05)$ eV (corresponding to a coherence time of (10 ± 2) fs) and $\Delta t = (80 \pm 10)$ fs. For this experiment, the FEL was optimized to generate as short pulses as possible. Therefore the bunch charge of the electrons in the undulators was set to a rather small value of 0.1 nC.

One can clearly see the differences between the second and third order autocorrelation traces: For triply charged argon, the broad structure is $\sqrt{2}$ times longer than the average pulse duration, while the factor is $\sqrt{3/2}$ for the Ar^{4+} signal. Additionally, the amplitude ratio between the sharp spike and the broad peak

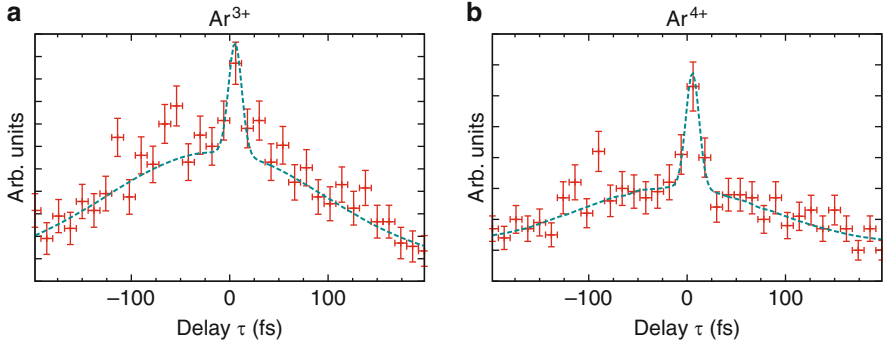


Fig. 11.4 Same as Fig. 11.3, but with higher charge (0.4 nC) of the FEL electron bunches. PCM parameters are: Gaussian spectrum of 0.16 eV FWHM and Gaussian time profile of 180 fs FWHM with a half-pulse asymmetry of 20 fs

changes from 2:1 for second order autocorrelation to 3:1 for the third order. That the experimental results are in good agreement with the simulation also shows that the first two ionization steps are virtually saturated.

In Fig. 11.4 we show yields of multiply charged argon ions obtained at a higher electron bunch charge of 0.4 nC. Here we observe that the average pulse duration spreads out to (180 ± 15) fs. As a consequence, the maximum field intensity at the focus changes little as compared to the 0.1 nC bunches. The coherence time has also increased to (14 ± 3) fs, corresponding to a spectral width $\Delta\omega = (0.16 \pm 0.2)$ eV. Furthermore, the experimental traces exhibit a distinct temporal shift between the centers of the broad and the sharp peak. This can be explained by a “tilted” FEL pulse, i.e. a temporally varying spatial intensity distribution. If such a pulse hits the split mirror, non-identical halves are created that cause the asymmetries. To account for this in our PCM simulation we introduce a time offset d between the center of the Gaussian time profiles multiplied onto the pump and the probe pulse copies of the infinitely long, noisy pulse. $d = 20$ fs was found to fit best with the experimental results.

11.6 Conclusion

We have examined multiple ionization of argon in order to study extreme ultraviolet (EUV) pulses delivered by FLASH using the autocorrelation technique. Thereby, the average pulse duration could be extracted as well as the coherence time that is a consequence of the FEL pulses’ noisy nature. Using our partial-coherence model such pulses could be simulated and employed to reproduce the measured autocorrelation traces. Furthermore, asymmetric autocorrelation signals are obtained if the temporal structure of the pulse changes over the FEL beam

diameter. It was also found that the FEL pulses grow longer as the electron bunch charge increases.

Finally, we would like to point out that the short coherence time can actually be used to study molecular dynamics in a pump–probe scheme, where the time scale of nuclear motion is shorter than the average duration of the FEL pulses. Such dynamics have been recently measured [10] and interpreted in terms of noisy pulses with partial coherence [4]. This would be a significant boost for further pump–probe studies, as many molecular processes are faster than the average pulse duration achievable at the FLASH facility in the spectral region studied here.

Acknowledgements The authors are greatly indebted to the scientific and technical team at FLASH, in particular, the machine operators and run coordinators. Support from the Max-Planck Advanced Study Group at CFEL is gratefully acknowledged. Y.H.J. acknowledges support from DFG Project No. JI 110/2, T.P. from the MPRG program of the Max-Planck-Gesellschaft, M.F.K. from the DFG via the Emmy-Noether program and the Cluster of Excellence: Munich Center for Advanced Photonics. K.U. acknowledges the support from by the Budget for “Promotion of X-ray Free Electron Laser Research” from MEXT, by the Management Expenses Grants for National Universities Corporations from MEXT, by Grants-in-Aid for Scientific Research from JSPS, and IMRAM research program.

References

1. W. Ackermann, G. Asova, V. Ayvazyan, A. Azima, N. Baboi, J. Baehr, V. Balandin, B. Beutner, A. Brandt, A. Bolzmann, R. Brinkmann, O.I. Brovko, M. Castellano, P. Castro, L. Catani, E. Chiodroni, S. Choroba, A. Cianchi, J.T. Costello, D. Cubaynes, J. Dardis, W. Decking, H. Delsim-Hashemi, A. Delserieys, G. Di Pirro, M. Dohlus, S. Duesterer, A. Eckhardt, H.T. Edwards, B. Faatz, J. Feldhaus, K. Floettmann, J. Frisch, L. Froehlich, T. Garvey, U. Gensch, C. Gerth, M. Goerler, N. Golubeva, H.J. Grabosch, M. Grecki, O. Grimm, K. Hacker, U. Hahn, J.H. Han, K. Honkavaara, T. Hott, M. Huening, Y. Ivanisenko, E. Jaeschke, W. Jalmuzna, T. Jezynski, R. Kammering, V. Katalev, K. Kavanagh, E.T. Kennedy, S. Khodyachykh, K. Klose, V. Kocharyan, M. Koerfer, M. Kolleye, W. Koprek, S. Korepanov, D. Kostin, M. Krassilnikov, G. Kube, M. Kuhlmann, C.L.S. Lewis, L. Lilje, T. Limberg, D. Lipka, F. Loehl, H. Luna, M. Luong, M. Martins, M. Meyer, P. Michelato, V. Miltchev, W.D. Moeller, L. Monaco, W.F.O. Mueller, O. Napieralski, O. Napolly, P. Nicolosi, D. Noelle, T. Nunez, A. Oppelt, C. Pagani, R. Paparella, N. Pchalek, J. Pedregosa-Gutierrez, B. Petersen, B. Petrosyan, G. Petrosyan, L. Petrosyan, J. Pflueger, E. Ploenjes, L. Poletto, K. Pozniak, E. Prat, D. Proch, P. Pucyk, P. Radcliffe, H. Redlin, K. Rehlich, M. Richter, M. Roehrs, J. Roensch, R. Romaniuk, M. Ross, J. Rossbach, V. Rybnikov, M. Sachwitz, E.L. Saldin, W. Sandner, H. Schlarb, B. Schmidt, M. Schmitz, P. Schmueser, J.R. Schneider, E.A. Schneidmiller, S. Schnepf, S. Schreiber, M. Seidel, D. Sertore, A.V. Shabunov, C. Simon, S. Simrock, E. Sombrowski, A.A. Sorokin, P. Spanknebel, R. Spesyvtsev, L. Staykov, B. Steffen, F. Stephan, F. Stulle, H. Thom, K. Tiedtke, M. Tischer, S. Toleikis, R. Treusch, D. Trines, I. Tsakov, E. Vogel, T. Weiland, H. Weise, M. Wellhoeffler, M. Wendt, I. Will, A. Winter, K. Wittenburg, W. Wurth, P. Yeates, M.V. Yurkov, I. Zagorodnov, K. Zapfe, *Nat. Photon.* **1**(6), 336 (2007)
2. P. Emma, R. Akre, J. Arthur, R. Bionta, C. Bostedt, J. Bozek, A. Brachmann, P. Bucksbaum, R. Coffee, F.J. Decker, Y. Ding, D. Dowell, S. Edstrom, A. Fisher, J. Frisch, S. Gilevich, J. Hastings, G. Hays, P. Hering, Z. Huang, R. Iverson, H. Loos, M. Messerschmidt, A. Miahnahri, S. Moeller, H.D. Nuhn, G. Pile, D. Ratner, J. Rzepiela, D. Schultz, T. Smith,

- P. Stefan, H. Tompkins, J. Turner, J. Welch, W. White, J. Wu, G. Yocky, J. Galayda, *Nat. Photon.* **4**(9), 641 (2010)
3. M. Kurka, J. Feist, D.A. Horner, A. Rudenko, Y.H. Jiang, K.U. Kühnel, L. Foucar, T.N. Rescigno, C.W. McCurdy, R. Pazourek, S. Nagele, M. Schulz, O. Herrwerth, M. Lezius, M.F. Kling, M. Schöffler, A. Belkacem, S. Düsterer, R. Treusch, B.I. Schneider, L.A. Collins, J. Burgdörfer, C.D. Schröter, R. Moshhammer, J. Ullrich, *New J. Phys.* **12**(7), 073035 (2010)
 4. K. Meyer, C. Ott, P. Raith, A. Kaldun, Y. Jiang, M. Kurka, R. Moshhammer, J. Ullrich, T. Pfeifer, *Phys. Rev. Lett.* **108**, 098302 (2012)
 5. R. Moshhammer, Y.H. Jiang, L. Foucar, A. Rudenko, T. Ergler, C.D. Schröter, S. Lüdemann, K. Zrost, D. Fischer, J. Titze, T. Jahnke, M. Schöffler, T. Weber, R. Dörner, T.J.M. Zouros, A. Dorn, T. Ferger, K.U. Kühnel, S. Düsterer, R. Treusch, P. Radcliffe, E. Plönjes, J. Ullrich, *Phys. Rev. Lett.* **98**, 203001 (2007)
 6. A.A. Sorokin, S.V. Bobashev, T. Feigl, K. Tiedtke, H. Wabnitz, M. Richter, *Phys. Rev. Lett.* **99**, 213002 (2007)
 7. K. Motomura, H. Fukuzawa, L. Foucar, X.J. Liu, G. Prümper, K. Ueda, N. Saito, H. Iwayama, K. Nagaya, H. Murakami, M. Yao, A. Belkacem, M. Nagasono, A. Higashiya, M. Yabashi, T. Ishikawa, H. Ohashi, H. Kimura, *J. Phys. B Atom. Mol. Opt. Phys.* **42**(22), 221003 (2009)
 8. M. Richter, S.V. Bobashev, A.A. Sorokin, K. Tiedtke, *J. Phys. B Atom. Mol. Opt. Phys.* **43**, 194005 (2010)
 9. T. Ergler, B. Feuerstein, A. Rudenko, K. Zrost, C.D. Schröter, R. Moshhammer, J. Ullrich, *Phys. Rev. Lett.* **97**, 103004 (2006)
 10. Y.H. Jiang, A. Rudenko, J.F. Pérez-Torres, O. Herrwerth, L. Foucar, M. Kurka, K.U. Kühnel, M. Toppin, E. Plésiat, F. Morales, F. Martín, M. Lezius, M.F. Kling, T. Jahnke, R. Dörner, J.L. Sanz-Vicario, J. van Tilborg, A. Belkacem, M. Schulz, K. Ueda, T.J.M. Zouros, S. Düsterer, R. Treusch, C.D. Schröter, R. Moshhammer, J. Ullrich, *Phys. Rev. A* **81**(5), 051402 (2010)
 11. Y.H. Jiang, A. Rudenko, O. Herrwerth, L. Foucar, M. Kurka, K.U. Kühnel, M. Lezius, M.F. Kling, J. van Tilborg, A. Belkacem, K. Ueda, S. Düsterer, R. Treusch, C.D. Schröter, R. Moshhammer, J. Ullrich, *Phys. Rev. Lett.* **105**(26), 263002 (2010)
 12. A. Hishikawa, A. Matsuda, E.J. Takahashi, F. Mizuho, *J. Chem. Phys.* **128**, 084302 (2008)
 13. H. Xu, T. Okino, K. Nakai, K. Yamanouchi, S. Roither, X. Xie, D. Kartashov, L. Zhang, A. Baltuska, M. Kitzler, *Phys. Chem. Chem. Phys.* **12**, 12939 (2010)
 14. H. Xu, T. Okino, K. Yamanouchi, *J. Chem. Phys.* **131**, 151102 (2009)
 15. S. Takeuchi, S. Ruhman, T. Tsuneda, M. Chiba, T. Taketsugu, T. Tahara, *Science* **322**(5904), 1073 (2008)
 16. S. Deb, P.M. Weber, *Annu. Rev. Phys. Chem.* **62**(1), 19 (2011)
 17. S. Chelkowski, P.B. Corkum, A.D. Bandrauk, *Phys. Rev. Lett.* **82**, 3416 (1999)
 18. V. Ayvazyan, N. Baboi, I. Bohnet, R. Brinkmann, M. Castellano, P. Castro, L. Catani, S. Choroba, A. Cianchi, M. Dohlus, H. Edwards, B. Faatz, A. Fateev, J. Feldhaus, K. Flöttmann, A. Gamp, T. Garvey, H. Genz, C. Gerth, V. Gretchko, B. Grigoryan, U. Hahn, C. Hessler, K. Honkavaara, M. Hüning, R. Ischebeck, M. Jablonka, T. Kamps, M. Körfer, M. Krassilnikov, J. Krzywinski, M. Liepe, A. Liero, T. Limberg, H. Loos, M. Luong, C. Magne, J. Menzel, P. Michelato, M. Minty, U.C. Müller, D. Nölle, A. Novokhatski, C. Pagani, F. Peters, J. Pflüger, P. Piot, L. Plucinski, K. Rehlich, I. Reyzl, A. Richter, J. Rossbach, E. Saldin, W. Sandner, H. Schlarb, G. Schmidt, P. Schmüser, J. Schneider, E. Schneidmiller, H.J. Schreiber, S. Schreiber, D. Sertore, S. Setzer, S. Simrock, R. Sobierajski, B. Sonntag, B. Steeg, F. Stephan, K. Sytchev, K. Tiedtke, M. Tonutti, R. Treusch, D. Trines, D. Türke, V. Verzilov, R. Wanzenberg, T. Weiland, H. Weise, M. Wendt, T. Wilhein, I. Will, K. Wittenburg, S. Wolff, M. Yurkov, K. Zapfe, *Eur. Phys. J. D Atom. Mol. Opt. Plasma Phys.* **20**, 149 (2002)
 19. R. Mitzner, B. Siemer, M. Neeb, T. Noll, F. Siewert, S. Røling, M. Rotkowsky, A.A. Sorokin, M. Richter, P. Juranic, K. Tiedtke, J. Feldhaus, W. Eberhardt, H. Zacharias, *Opt. Express* **16**(24), 19909 (2008)
 20. J. Ullrich, R. Moshhammer, A. Dorn, R. Dörner, L.P.H. Schmidt, H. Schmidt-Böcking, *Rep. Prog. Phys.* **66**, 1463 (2003)
 21. T. Pfeifer, Y.H. Jiang, S. Düsterer, R. Moshhammer, J. Ullrich, *Opt. Lett.* **35**, 3441 (2010)

Part II
High-Order Harmonics and Attosecond
Pulse Generation

Chapter 12

Formation of Attosecond XUV Pulses via Resonance with Hydrogen-Like Atoms Irradiated by Intense Laser Field

V.A. Polovinkin, Y.V. Radeonychev, M.Yu. Ryabikin, and Olga Kocharovskaya

Abstract We show the possibility to produce a short bunch of few nearly bandwidth-limited few-cycle attosecond pulses via the time-dependent resonant interaction of an incident radiation pulse with the bound states of hydrogenlike atoms. Time-dependence of the resonant interaction is based on time-dependent tunnel ionization from the excited states and temporal adiabatic Stark splitting of the excited energy levels, provided by far-off-resonant laser pulse whose intensity is much below the atomic ionization threshold. Without external synchronization of the spectral components it is possible to produce pulses of XUV radiation with duration up to 80 as at the carrier wavelength 13.5 nm in Li^{2+} -plasma.

The fast development of attosecond physics is stimulated by fundamental challenge and important applications ([1] and references therein). At present high-order harmonic generation from atoms and molecules ionized by high-power laser systems is the basic source of attosecond pulses suitable for spectroscopy. The pulses of durations below 200 as require the selection of harmonics and their external synchronization [2]. Small pulse energy and low conversion efficiency are typical for this method.

Recently a novel approach to production of extremely short pulses in various spectral ranges from far-infrared domain up to gamma-rays and in different media (gases, liquids or solids) was proposed [3–8]. It uses radiation intensities much

V.A. Polovinkin (✉) · Y.V. Radeonychev · Olga Kocharovskaya
Institute of Applied Physics of the Russian Academy of Science, 46 Ulyanov Street, Nizhny
Novgorod 603950, Russia

Department of Physics of Texas A&M University, College Station, 77843-4242 TX, USA
e-mail: vpolo@appl.sci-nnov.ru

M.Yu. Ryabikin
Institute of Applied Physics of the Russian Academy of Science, 46 Ulyanov Street, Nizhny
Novgorod 603950, Russia

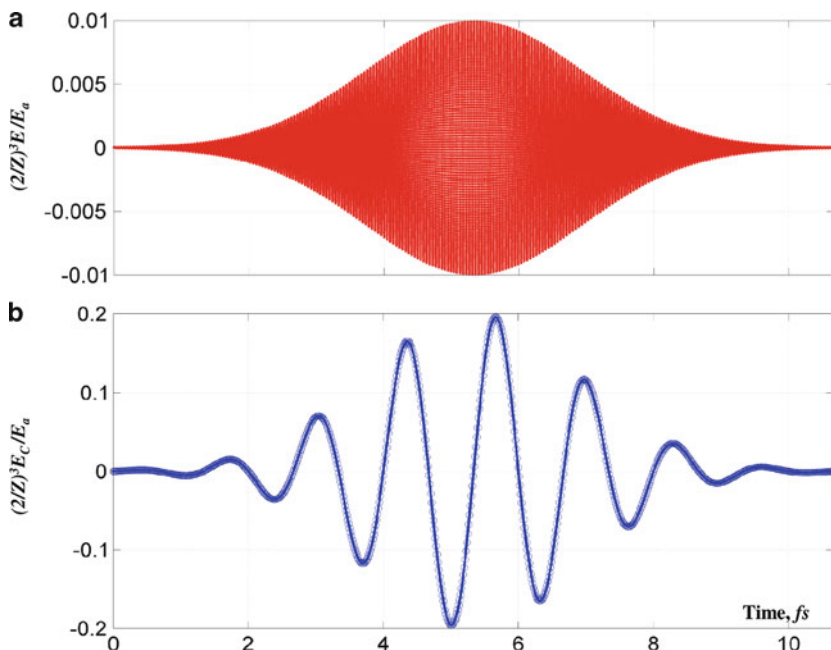


Fig. 12.1 The HF incident field (a) and LF control field (b) in the case of Li^{2+} ($Z = 3$). Both fields have Gaussian envelope and the same pulse duration 2.7 fs. The maximum in (a) corresponds to the HF field intensity $4 \times 10^{13} \text{ W/cm}^2$, the maximum in (b) corresponds to the LF field intensity $1.6 \times 10^{16} \text{ W/cm}^2$

below atomic ionization threshold, does not require external phase synchronization of the spectral components, and promises high efficiency of conversion of the incident radiation into ultrashort pulses. The approach utilizes highly efficient resonant interaction of radiation with a medium. It was shown that making the resonance periodic in space and time allows one to produce a train of extremely short output pulses from quasi-monochromatic input radiation under the action of sufficiently strong quasi-monochromatic control laser field [3–7].

In this paper we consider experimental situation where hydrogenlike atomic system interacts with pulsed radiation produced by currently available sources. Incident pulse of a high-frequency (HF) incident radiation with carrier frequency ω has envelope of arbitrary form,

$$\vec{E}(z \leq 0, t) = \vec{E}_{in} = \vec{x}_0 A_{in}(t - z/c) \cos\{\omega(t - z/c)\}, \quad (12.1)$$

where c is the light velocity in free space. We assume in numerical simulation that the envelope has the Gaussian form (Fig. 12.1a). The HF radiation propagates through an optically dense medium $0 < z \leq h$ (h is the length of the medium) of hydrogen-like atoms with frequency ω_{21}^0 of the transition $|n = 1\rangle \leftrightarrow |n = 2\rangle$ (n is

the principal quantum number) under the condition of resonance, $|\omega - \omega_{21}^0| \ll \omega_{21}^0$. The medium is simultaneously irradiated by a very-far-off-resonance low-frequency (LF) control field,

$$\vec{E}_C(z, t) = \vec{x}_0 A_C(t - z/c) \cos\{\Omega(t - z/c)\}. \quad (12.2)$$

We assume in numerical simulation the control field pulse of the Gaussian shape depicted in Fig. 12.1b. We suppose that $\Omega \ll \omega_{21}^0$, and the intensity of the LF field is far below the atomic ionization threshold. This means that the perturbation of atoms by the LF field is quasistatic while the multiphoton transitions from the ground state to the excited atomic states as well as the direct ionization from the ground state to the continuum are negligible. Hence, the LF field does not interact with atoms in the ground state. Meanwhile, the LF field does interact with atoms in the excited energy states. The excited states are selected and populated by the HF field, which is resonant to the transition from the ground to the first excited four-fold degenerate energy level $|2lm\rangle$ [numerals nlm ($n = 2$) label principal, orbital, and magnetic quantum numbers, respectively]. The LF control field aligns the dipole moments, $\vec{d}_{ij} \parallel \vec{E}_C$, produces a quasistatic space–time-dependent energy shifts of the excited states via the Stark effect, and causes space- and time-dependent tunnel ionization from the excited states. Both the Stark shift value and the rate of tunnel ionization for each state are determined by the instantaneous strength of the LF field and oscillate together with the LF field. Taking into account the selection rules, one can consider a three-level system of the ground state, $|1\rangle = |100\rangle$, and two excited bound states,

$$|2\rangle = (|200\rangle + |210\rangle)/\sqrt{2} \text{ and } |3\rangle = (|200\rangle - |210\rangle)/\sqrt{2}, \quad (12.3)$$

prepared by the LF field [9] and resonantly coupled to the HF field (Fig. 12.2). In such a way, resonant selection of atomic states by the HF field allows one to take into consideration only three bound states instead of the full wave function of electron.

The instantaneous energies of the excited states, $|2\rangle$; $|3\rangle$, calculated within the perturbation theory [10] up to the third order, have the form (Fig. 12.2a)

$$E_{2;3}(z, t) = -\frac{m_e e^4 Z^2}{8\hbar^2} \left(1 \pm 3F_C + \frac{21}{2}F_C^2 \pm \frac{195}{8}F_C^3 \right), \quad (12.4)$$

where m_e and e are mass and charge of the electron, Z is the atomic number, and $F_C = (2/Z)^3 E_C/E_a$ is the normalized LF-field strength (12.2) ($E_a = m_e^2 e^5 / \hbar^4$ is the atomic unit of the electric field strength). Along with $E_1 = -m_e e^4 Z^2 / (2\hbar^2)$ equation (12.4) (valid for $A_C/E_a < 0.1Z^3$ [10]) determines spatio-temporal dependence of the atomic transition frequencies, $\omega_{ij}(z, t) = (E_i - E_j)/\hbar$. The instantaneous ionization rates from the states $|2\rangle$; $|3\rangle$ calculated perturbatively [10] have the form (Fig. 12.2c)

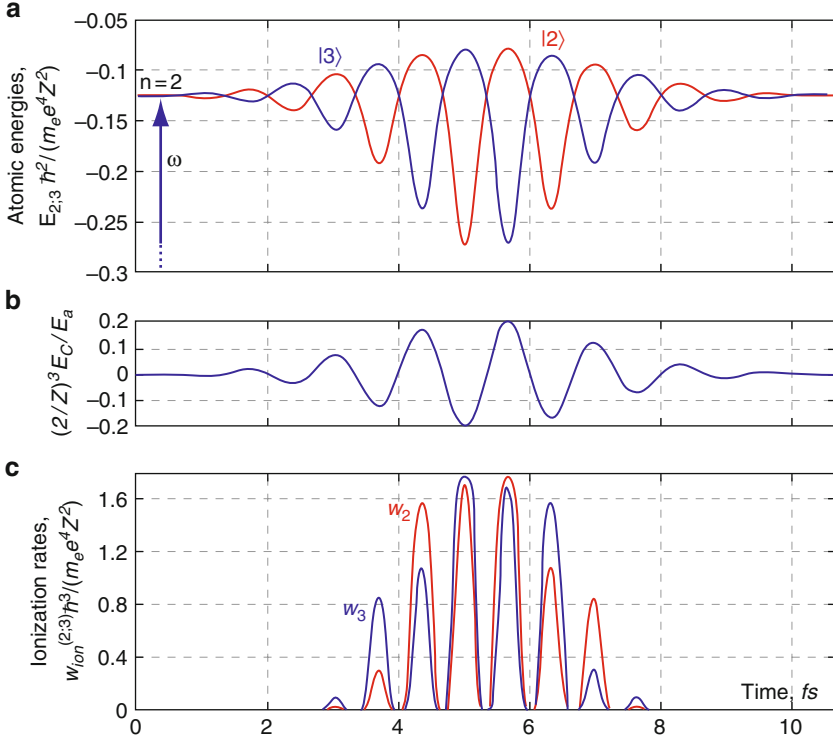


Fig. 12.2 The Stark shifts of the first excited states (a) and ionization rates from them (c) as the functions of instantaneous strength of the LF electric field (b) (the same as in Fig. 12.1b) for the case of Li^{2+} ($Z = 3$) calculated according to (12.4) and (12.5), respectively

$$w_{ion}^{(2;3)}(z, t) = \frac{m_e e^4 Z^2}{8\hbar^3} \left(\frac{4}{|F_C|} \right)^{2\pm s} \exp \left\{ -\frac{2}{3|F_C|} \mp 3s \right\}, \quad (12.5)$$

where $s = \text{sgn}(F_C)$.

As follows from (12.4) and (12.5) and shown in Fig. 12.2, the Stark shifts and particularly ionization rates are essentially nonlinear functions of instantaneous strength of the LF field. It can be seen from Fig. 12.2 that at the beginning and at the end of the LF pulse as well as in the time intervals around the field zero-crossings, relatively weak control field, $E_C/E_a < 0.01Z^3$, causes mainly linear Stark splitting of the excited atomic energy level resulting in variation of the resonant transition frequencies while ionization is small. Electric field of the middle part of the LF pulse causes sharp nonlinear oscillations of ionization rates from the excited states, which follow oscillation of the instantaneous field strength. There are time intervals (corresponding to $E_C/E_a > 0.01Z^3$) where strong ionization completely blurs out the discrete atomic energy level structure via increased transition linewidth $2\gamma_{ij}(\tau)$, see (12.8). During these time intervals the medium becomes transparent for the HF radiation. In other words, sufficiently strong LF control field induces time

windows of transparency for the HF radiation alternating with resonant opacity of the medium. Hence, such a system can be considered as a kind of optical shutter/switcher having the switching period of about one femtosecond.

Propagation of the HF field (12.1) is described by the wave equation

$$\frac{\partial^2 E}{\partial z^2} - \frac{1}{c^2} \frac{\partial^2 E}{\partial t^2} = \frac{4\pi}{c^2} \frac{\partial^2 P}{\partial t^2}, \quad (12.6)$$

where the atomic polarization P ,

$$P = N(d_{tr}(\rho_{21} - \rho_{31}) + d_{ex}(\rho_{22} - \rho_{33}) + c.c.) \quad (12.7)$$

is expressed via the elements of atomic density matrix, $\rho_{ij} \equiv \langle i|\rho|j\rangle$, $i, j = 1, 2, 3$, the density of atoms, N , and the projections of the dipole moments on the polarization of the incident radiation, $d_{ij} \equiv \langle i|d|j\rangle$, here $d_{tr} = d_{21} = -d_{31} = 2^7 e a_0 / (3^5 Z)$ and $d_{ex} = d_{22} = -d_{33} = 3 e a_0 / Z$, a_0 is the Bohr radius.

The equations for the elements of density matrix complete the self-consistent system describing formation of extremely short pulses at the output edge $z = h$ of the medium resulted from propagation of the incident near-resonant HF radiation:

$$\left\{ \begin{array}{l} \frac{\partial \rho_{21}}{\partial t} + \left(i \left(\omega_{21}(\tau) - \frac{d_{ex} E}{\hbar} \right) + \gamma_{21}(\tau) \right) \rho_{21} = i \frac{d_{tr} E}{\hbar} (\rho_{11} - \rho_{22}) + i \frac{d_{tr} E}{\hbar} \rho_{32}^* \\ \frac{\partial \rho_{31}}{\partial t} + \left(i \left(\omega_{31}(\tau) + \frac{d_{ex} E}{\hbar} \right) + \gamma_{31}(\tau) \right) \rho_{31} = -i \frac{d_{tr} E}{\hbar} \rho_{32} - i \frac{d_{tr} E}{\hbar} (\rho_{11} - \rho_{33}) \\ \frac{\partial \rho_{32}}{\partial t} + \left(i \left(\omega_{32}(\tau) + 2 \frac{d_{ex} E}{\hbar} \right) + \gamma_{32}(\tau) \right) \rho_{32} = -i \frac{d_{tr} E}{\hbar} \rho_{31} - i \frac{d_{tr} E}{\hbar} \rho_{21}^* \\ \frac{\partial \rho_{11}}{\partial t} = A (\rho_{22} + \rho_{33}) - 2 \frac{d_{tr} E}{\hbar} \text{Im} \{ \rho_{21} \} + 2 \frac{d_{tr} E}{\hbar} \text{Im} \{ \rho_{31} \} \\ \frac{\partial \rho_{22}}{\partial t} = - \left(A + w_{ion}^{(2)}(\tau) \right) \rho_{22} + 2 \frac{d_{tr} E}{\hbar} \text{Im} \{ \rho_{21} \} \\ \frac{\partial \rho_{33}}{\partial t} = - \left(A + w_{ion}^{(3)}(\tau) \right) \rho_{33} - 2 \frac{d_{tr} E}{\hbar} \text{Im} \{ \rho_{31} \} \end{array} \right. , \quad (12.8)$$

where E is the HF radiation strength, $\tau = t - z/c$ is the local time, associated with a constant phase of the LF control field, $\omega_{ij}(\tau) = (E_i - E_j)/\hbar$ are the instantaneous frequencies, while $\gamma_{ij}(\tau) = (A + w_{ion}^{(i)} + w_{ion}^{(j)})/2 + \gamma_c$ are the instantaneous decoherence rates of the atomic transitions, γ_c is the collisional broadening, and A is the radiative decay rate.

From (12.6)–(12.8) a first-order propagation equation directly for the electric field was deduced beyond the approximation of slowly-varying amplitudes [11] via the change of variables $(z, t) \rightarrow (z, \tau = t - z/c)$:

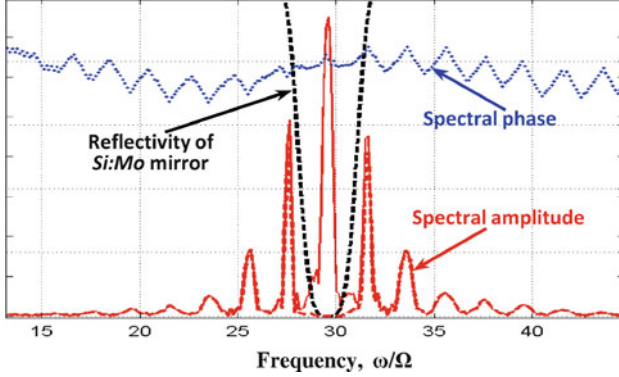


Fig. 12.3 Output HF radiation spectrum

$$\begin{aligned} \frac{\partial E(z, \tau)}{\partial z} = & \frac{4\pi N d_{tr}}{c} \left[(\gamma_{21}(\tau) \operatorname{Re}\{\rho_{21}\} - \gamma_{31}(\tau) \operatorname{Re}\{\rho_{31}\}) - (\omega_{21}(\tau) \operatorname{Im}\{\rho_{21}\} \right. \\ & \left. - \omega_{31}(\tau) \operatorname{Im}\{\rho_{31}\}) + (d_{ex}/d_{tr}) \right. \\ & \left. \cdot \left((A + w_{ion}^{(2)}(\tau)) \rho_{22} - (A + w_{ion}^{(3)}(\tau)) \rho_{33} \right) \right]. \end{aligned} \quad (12.9)$$

The resultant system (12.8)–(12.9) was solved numerically for the initial conditions $E(z > 0, \tau = 0) = 0$, $\rho_{11}(z, \tau = 0) = 1$, $\rho_{ij \neq 11}(z, \tau = 0) = 0$, and the boundary conditions $E(z = 0, \tau) = E_{in}(\tau)$, and $E_{out}(\tau) = E(z = h, \tau)$. Various cases were studied and several sets of parameter values, optimal for production of (a) shorter pulses at the cost of lower peak intensity (lower conversion efficiency), (b) more intensive but longer pulses (higher conversion efficiency), (c) pulses with intermediate between (a) and (b) parameters, were found. Below we discuss an experimental case related to the (c)-category. Let us consider Li^{2+} ions irradiated by the control pulse of second harmonic of the Ti:Sa laser (12.2) of duration 2.7 fs at the wavelength $\lambda_C = 400$ nm with peak intensity $I_C = 1.6 \times 10^{16}$ W/cm² (corresponding to $A_C/E_a \cong 0.025 \times 3^3$). The length of interaction volume is $h = 100$ μm , the density of Li^{2+} ions is $N = 10^{20}$ cm⁻³. Emission at $\lambda = 13.51$ nm from the Li^{2+} -plasma source (produced from metal lithium and commonly utilized for XUV lithography [12, 13]) is used as the HF incident radiation (12.1). Duration of the incident HF pulse is 2.7 fs and maximum intensity is $I_{in} = 4 \times 10^{13}$ W/cm² (Fig. 12.1).

The output spectrum in Fig. 12.3 consists of a number of parametrically generated spectral components. Removal of the dominant central component at the carrier frequency (Fig. 12.3, black dashed curve) by means of reflection from the Si:Mo mirror commonly used in XUV lithography [14] results in a short bunch comprising five nearly bandwidth-limited two-cycle XUV radiation pulses (Fig. 12.4), separated by half-cycle of the LF control field. The pulse duration is 90 as and the maximum peak pulse intensity is $I_{max} \cong 3.4 \times 10^{13}$ W/cm² that is 85% of the maximum

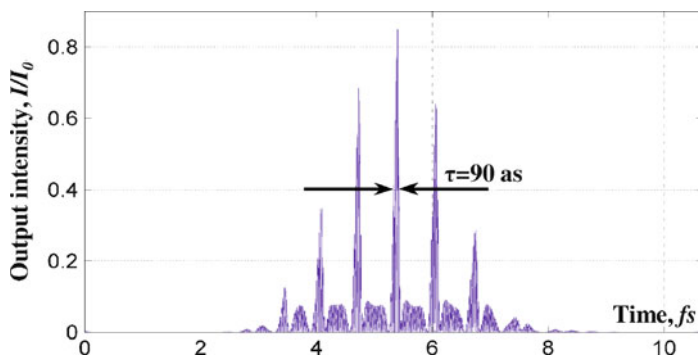


Fig. 12.4 A bunch of five attosecond nearly bandwidth-limited two-cycle XUV pulses, formed during propagation of the incident XUV radiation pulse of intensity $4 \times 10^{13} \text{ W/cm}^2$, duration 2.7 fs, and carrier wavelength 13.51 nm, through $100 \mu\text{m}$ of Li^{2+} ions at the density 10^{20} cm^{-3} , under the action of 2.7 fs pulse of 01 frequency doubled Ti:Sa laser (carrier wavelength 400 nm) with the peak intensity $1.6 \times 10^{16} \text{ W/cm}^2$ after removing of the central spectral component

intensity of the incident XUV radiation. The conversion efficiency determined as the ratio of the output peak pulse intensity to the intensity of the total (HF plus LF) input field is $\sim 0.2\%$.

It should be noted that according to our calculations in the case of stronger incident XUV radiation, up to intensities $I_{\text{in}} = 10^{15} \text{ W/cm}^2$, the output pulses with duration up to 80 as, and the total conversion efficiency up to 10%, can be produced. The number of pulses in the output bunch depends on the form, duration, time-delay, and intensities of the incident HF and LF radiation pulses. Currently available sources of the LF control field with carrier wavelength $0.4\text{--}10.65 \mu\text{m}$ and intensity up to 10^{16} W/cm^2 (Nd:YAG-laser, Ti:Sa-laser, CO-laser, CO_2 -laser, optical parametric systems) can be used. There exists a possibility to produce a single high energy attosecond pulse that will be considered elsewhere.

Acknowledgements This research was supported by RFBR (Grants #09-02-01158, #10-02-01250) and NSF grant #0855688. V.A. Polovinkin acknowledges personal grant, given by foundation. Dynasty under the program for young scientists support.

References

1. F. Krausz, M. Ivanov, *Rev. Mod. Phys.* **81**, 163 (2009)
2. E. Gustafsson, T. Ruchon, M. Swoboda, T. Remetter, E. Pourtal, R. López-Martens, Ph. Balcou, A. L'Huillier, *Opt. Lett.* **32**, 1353 (2007)
3. Y.V. Radeonychev, M.D. Tokman, A.G. Litvak, O. Kocharovskaya, *Phys. Rev. Lett.* **96**, 093602 (2006)
4. Y.V. Radeonychev, V.A. Polovinkin, O. Kocharovskaya, *Laser Phys.* **19**, 769 (2009)
5. Y.V. Radeonychev, V.A. Polovinkin, O. Kocharovskaya, *Phys. Rev. Lett.* **105**, 183902 (2010)
6. Y.V. Radeonychev, V.A. Polovinkin, O. Kocharovskaya, *Laser Phys.* **21**, 1243 (2011)

7. V.A. Polovinkin, Y.V. Radeonychev, O. Kocharovskaya, *Opt. Lett.* **36**, 2296 (2011)
8. Y.V. Radeonychev, V.A. Polovinkin, O. Kocharovskaya, *Laser Phys.* issue 10, accepted (2012)
9. G. Newton, D.A. Andrews, P.J. Unsworth, *Phil. Trans. R. Soc. London* **290**, 373 (1979)
10. R.F. Stebbings, F.B. Dunning, *Rydberg States of Atoms and Molecules* (Cambridge University Press, Cambridge, 1983)
11. E.V. Vanin, A.V. Kim, A.M. Sergeev, M.C. Downer, *JEPT Lett.* **58**, 900 (1993)
12. C. Rajyaguru, T. Higashiguchi, M. Koga, K. Kawasaki, M. Hamada, N. Dojyo, W. Sasaki, S. Kubodera, *Appl. Phys. B* **80**, 409 (2005)
13. M.A. Klosner, W.T. Silfvast, *Appl. Opt.* **39**, 3678 (2000)
14. T. Harada, T. Hatano, M. Yamamoto, *Proc., 8th International Conference on X-ray Microscopy, Conf. Proc. Series IPAP 7*, 195 (2006) Tokyo, Japan: Institute of Pure and Applied Physics

Chapter 13

Exploration of Below-Threshold Harmonic Generation Mechanisms of Cesium Atoms in Intense Mid-Infrared Laser Pulses

Y.-J. Chen, C. Laughlin, and S.-I. Chu

Abstract We present a non-perturbative quantum study of high-order harmonic generation (HHG) of Cesium atoms in intense mid-infrared laser pulses. An accurate angular-momentum—dependent model potential is constructed for the high-precision description of the Cs atom electronic structure. The three-dimensional time-dependent Schrodinger equation is solved accurately and efficiently by means of the time-dependent generalized pseudospectral methods (TDGPS) [Tong and Chu, Chem Phys 217(2–3), 119–130 (1997)].

Besides the expected odd harmonics, the calculated HHG power spectra show additional structures due to the strong 6s–np couplings. The spectral and temporal characteristics of the HHG are further explored through the wavelet transformation [Tong and Chu, Phys Rev A 6102(2), 21802 (2000)]. As a result, we can investigate the prevailing mechanisms in different energy regimes, especially those contributing to the below- and near-threshold harmonics [Power et al., Nat Photon 4(6), 352–356 (2010); Soifer et al., Phys. Rev. Lett. 105(14), 143904 (2010); Yost et al., Nat Phys 5(11), 815–820 (2009)].

Y.-J. Chen (✉)

Department of Physics, Center for Quantum Science and Engineering, National Taiwan University, Taipei 106, Taiwan
e-mail: r98222033@ntu.edu.tw

C. Laughlin

School of Mathematical Sciences, University of Nottingham, Nottingham NG7 2RD, UK
e-mail: Cecil.Laughlin@nottingham.ac.uk

S.-I. Chu

Department of Chemistry, University of Kansas, Lawrence, KS 66045, USA
e-mail: sichu@ku.edu

13.1 Introduction

High-order harmonic generation (HHG) resulting from the non-linear interaction of intense lasers with atoms or molecules is of much current interest due to its fundamental importance and practical applications. The mechanism of HHG is well understood in two energy extremes: the formation of the first few harmonics with energy well below the ionization threshold I_P can be described perturbatively by the multiphoton mechanism [1], while the production of the harmonics with energy well above I_P can be explained non-perturbatively by the semi-classical three-step model [2]. For the harmonics lying between the two extremes, i.e. the harmonics below or near I_P , the generating mechanism is a relatively unexplored area of forefront research.

Recently, some experimental studies have shown that both the perturbative multiphoton mechanism and the semi-classical long-trajectory pathway participate in the generation of harmonics in this intermediate energy regime [3–5]. Power et al. [3] performed the experiments with Cesium gas and mid-infrared laser pulses. In this work, we present an ab initio calculation under similar conditions, aiming to examine the mechanisms of below- and near-threshold harmonics from a theoretical, single-atom, and pure quantum point of view. Comparisons with experimental data [3] are made.

13.2 Theoretical Methods

An accurate one-electron model potential is constructed for the high-precision description of the Cs atom electronic structure. The model potential is angular-momentum—dependent, that is, its parameters have distinct numerical values for different angular-momentum symmetries [6]. Table 13.1 presents a comparison of the bound-state energies predicted by the model potential with the experimental values from [7].

The three-dimensional time-dependent Schrodinger equation is then solved non-perturbatively by means of the time-dependent generalized pseudospectral method (TDGPS) [8], which allows non-uniform and optimal grid distribution through a non-linear mapping as well as accurate and efficient propagation of the wave function by the second-order split-operator method in the energy representation.

13.3 Results and Discussion

For the present study, we use a linearly polarized laser pulse with parameters similar to the experimental ones in [3]: central wavelength $\lambda = 3,600$ nm, peak intensity $I = 2 \cdot 1$ TW/cm², and a Gaussian envelope with full-width-at-half-maximum $\tau_{\text{FWHM}} = 110$ fs. In this case, I_P is about $11.3\omega_0$. Figure 13.1 shows the HHG power spectrum by Fourier transforming the dipole acceleration. Note

Table 13.1 Comparison of the calculated Cs energies with the experimental values (in a.u.). For each angular momentum l , two rows of energies $E(n, l)$ are listed: the upper row refers to the calculated model-potential energies, and the lower row refers to the experimental values from [7]

$l \backslash n$	$E(n, l)$						
	4	5	6	7	8	9	10
0			-0.1430990	-0.0586446	-0.0323015	-0.0204845	-0.0141531
			-0.1430990	-0.0586446	-0.0323014	-0.0204845	-0.0141531
1			-0.0904543	-0.0434199	-0.0257368	-0.0170564	-0.0121389
			-0.0904839	-0.0433784	-0.0257093	-0.0170393	-0.0121279
2		-0.0767537	-0.0401010	-0.0243947	-0.0163741	-0.0117426	-0.0088300
		-0.0767685	-0.0400591	-0.0243586	-0.0163493	-0.0117259	-0.0088183
3	-0.0316125	-0.0202221	-0.0140293	-0.0102970	-0.0078767	-0.0062189	-0.0050341
	-0.0315953	-0.0202086	-0.0140200	-0.0102907	-0.0078723	-0.0062157	-0.0050317
4		-0.0200405	-0.0139152	-0.0102218	-0.0078248	-0.0061817	-0.0050066
		-0.0200407	-0.0139152	-0.0102217	-0.0078248	-0.0061817	-0.0050066

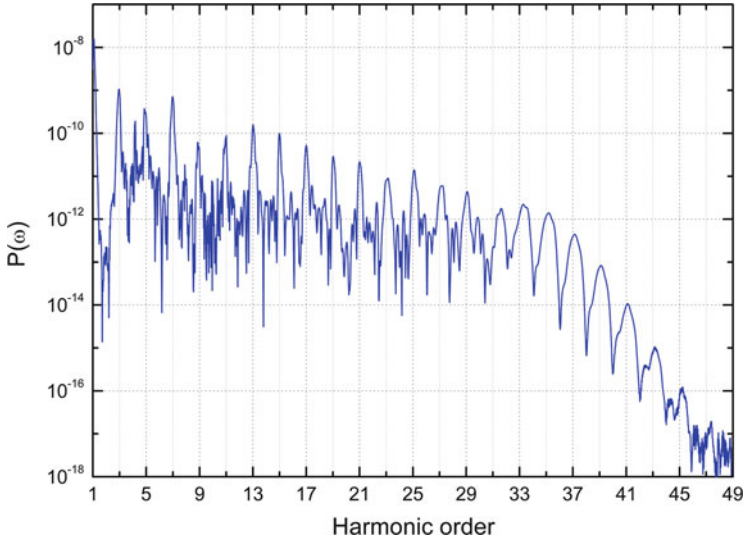


Fig. 13.1 Calculated HHG power spectrum of Cs in a linear-polarized laser pulse with $\lambda = 3,600$ nm, $I = 2 \cdot 1$ TW/cm², and a Gaussian envelope with $\tau_{\text{FWHM}} = 110$ fs

that there is an additional peak around $4.13\omega_0$, which may be attributed to the multiphoton resonance between the strongly coupled $6s$ – $6p$ states. The field-free energy difference between the two energy levels predicted by the model potential is $4.16\omega_0$.

To explore the HHG mechanisms in different energy regimes, we perform the time-frequency analysis by wavelet transformation [9]:

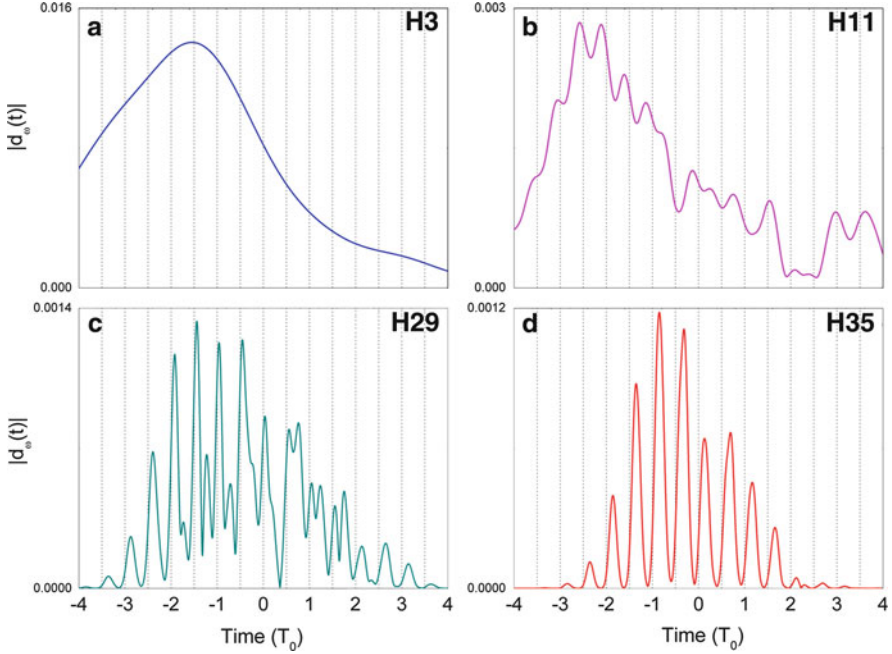


Fig. 13.2 Typical time profiles of harmonics in various energy regimes. Panel (a) is the 3rd harmonic, panel (b) the 11th, (c) the 29th, and (d) the 35th. The interval between two vertical dotted lines represents half an O.C.

$$d_{\omega}(t) = \int_{t_i}^{t_f} d(t') W_{\omega,t}(t') dt', \text{ where } W_{\omega,t}(t') = e^{-\frac{\omega^2(t-t')^2}{2\tau^2}} e^{-i\omega(t-t')}.$$

Figure 13.2 shows the typical time profiles $|d_{\omega}(t)|$ in various energy regimes:

- First few harmonics [Fig. 13.2, panel (a)]: the time profile is a smooth function of time, mimicking the pulse envelope. This indicates that the perturbative multiphoton mechanism dominates the generation of harmonics here. The peak of the time profile shifts to an earlier time owing to the ground state depletion.
- Plateau [Fig. 13.2, panel (c)] and cut-off [Fig. 13.2, panel (d)] harmonics: the time profile contains fast bursts in time. This points out that the tunneling ionization [10] works here, which is the first step in the semi-classical model. Therefore, the harmonic emission is sensitive to the instantaneous laser field strength. For the plateau harmonics, there are two bursts per half optical cycle (O.C.), corresponding to contributions from the short and long trajectory. For the cut-off harmonics, there is only one burst per half O.C. These findings are qualitatively in agreement with that predicted by the semi-classical three-step model.
- Below- and near-threshold harmonics [Fig. 13.2, panel (b)]: the time profile may be seen as a superposition of a smooth function and fast bursts occurring once per

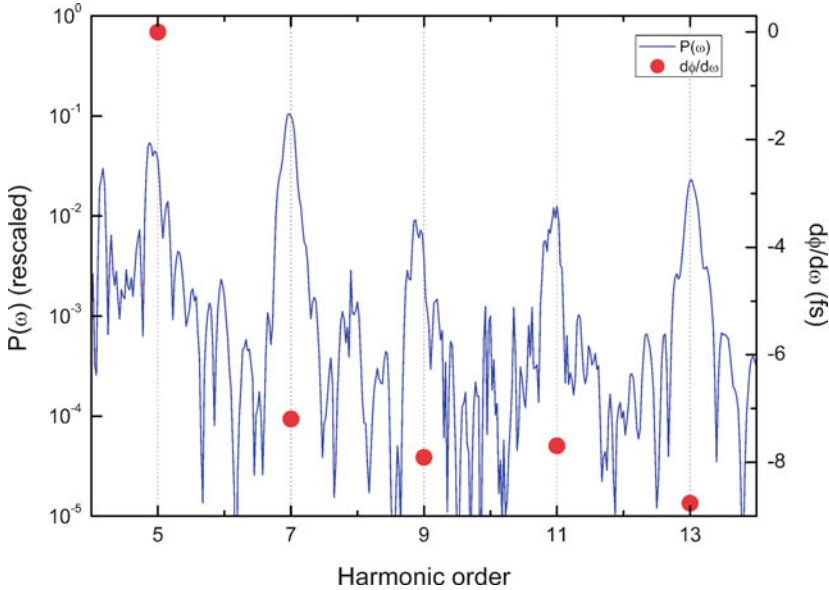


Fig. 13.3 Calculated group delay (*dots*) and power spectrum (*line*) for below- and near-threshold harmonics

half O.C. Accordingly, below- and near-threshold harmonics can be generated by two channels: the perturbative multiphoton mechanism as well as one type of the trajectories from the semi-classical process.

To dig out which trajectory is responsible for the fast bursts in the time profiles of the harmonics close to I_p , we calculate the group delay defined as the derivative of the Fourier spectral phase with respect to frequency. The result is shown in Fig. 13.3. The group delay exhibits an overall decreasing tendency, which means that the harmonics are subjected to negative chirp. Hence, these bursts are supposed to originate from the contribution of the long trajectory. This conclusion is consistent to the experimental results reported in [3–5]. Note that the calculated group delay between the 5th and 13th harmonic lies in a range of approximate 10 fs, in good agreement with that observed by Power et al. [3].

13.4 Conclusions

In summary, we have presented an accurate 3D quantum simulation of Cs atoms in intense mid-infrared laser pulses. The mechanisms of the below- and near-threshold harmonics are investigated by the wavelet transformation and the calculated group delay. Our findings are in accordance with the experimental ones [3–5]: along with

the perturbative multiphoton pathway, the semi-classical long trajectory can also lead to the harmonic generation with energy lower than or near I_p .

Acknowledgements This work was partially supported by the U.S. Department of Energy and by the U.S. National Science Foundation. We also would like to acknowledge the partial support of National Science Council of Taiwan (Grant No. 100-2119-M-002-013-MY3) and National Taiwan University (Grant No. 10R80700).

References

1. A. Lhuillier, K.J. Schafer, K.C. Kulander, Theoretical aspects of intense field harmonic-generation. *J. Phys. B Atom. Mol. Opt. Phys.* **24**(15), 3315–3341 (1991)
2. P.B. Corkum, Plasma perspective on strong field multiphoton ionization. *Phys. Rev. Lett.* **71**(13), 1994 (1993)
3. E.P. Power et al., XFROG phase measurement of threshold harmonics in a Keldysh-scaled system. *Nat. Photon.* **4**(6), 352–356 (2010)
4. H. Soifer et al., Near-threshold high-order harmonic spectroscopy with aligned molecules. *Phys. Rev. Lett.* **105**(14), 143904 (2010)
5. D.C. Yost et al., Vacuum-ultraviolet frequency combs from below-threshold harmonics. *Nat. Phys.* **5**(11), 815–820 (2009)
6. Y.J. Chen, S.I. Chu, C. Laughlin, in preparation
7. J.E. Sansonetti, Wavelengths, transition probabilities, and energy levels for the spectra of cesium (Cs I–Cs LV). *J. Phys. Chem. Ref. Data* **38**(4), 761–923 (2009)
8. X.M. Tong, S.I. Chu, Theoretical study of multiple high-order harmonic generation by intense ultrashort pulsed laser fields: a new generalized pseudospectral time-dependent method. *Chem. Phys.* **217**(2–3), 119–130 (1997)
9. X.M. Tong, S.I. Chu, Probing the spectral and temporal structures of high-order harmonic generation in intense laser pulses. *Phys. Rev. A* **61**(2), 21802 (2000)
10. L.V. Keldysh, Ionization in field of a strong electromagnetic wave. *Sov. Phys. JETP USSR* **20**(5), 1307 (1965)

Chapter 14

XUV Supercontinuum Generated by Incommensurate Two-Color Mid-IR Optical Parametric Amplifier

M. Negro, C. Vozzi, K. Kovacs, C. Altucci, R. Velotta, F. Frassetto, L. Poletto,
P. Villorresi, S. De Silvestri, V. Tosa, and S. Stagira

Abstract High-order harmonic generation is nowadays a topic of crucial interest since it allows the production of isolated attosecond pulses. Several efforts have been made so far for extending the generation of attosecond bursts beyond the 100 eV spectral region, in order to access to deeper electronic states in atoms and molecules. Recently, mid-infrared laser sources have demonstrated to be ideal candidates for pushing the high harmonic emission up to the soft X-rays. Here we show that it is possible to obtain continuous harmonic spectra, that are the signature of single attosecond pulse generation, by properly mixing two laser pulses, coming from optical parametric amplifiers, with wavelengths of 1.35 and 1.75 μm respectively, with either parallel or perpendicular polarizations. Our results demonstrate the generation of isolated attosecond burst driven by mid-infrared laser pulses of a duration larger than 30 fs.

M. Negro (✉) · S. De Silvestri · S. Stagira
Dipartimento di Fisica, Politecnico di Milano, Milan, Italy
e-mail: matteo.negro@mail.polimi.it

C. Vozzi
Istituto di Fotonica e Nanotecnologie, CNR, Milan, Italy
e-mail: caterina.vozzi@polimi.it

K. Kovacs · V. Tosa
National Institute R&D Isotopic and Molecular Technologies, Cluj-Napoca, Romania
e-mail: tosa@itim-cj.ro

C. Altucci · R. Velotta
CNISM & Dipartimento di Fisica, Università di Napoli Federico II, Naples, Italy
e-mail: velotta@na.infn.it

F. Frassetto · L. Poletto · P. Villorresi
CNR-IFN & DEI, Università di Padova, Padova, Italy
e-mail: poletto@dei.unipd.it

14.1 Introduction

High-order harmonic generation (HHG) is a strong field process, where the interaction of an intense laser pulse with a gaseous medium produces the emission of coherent XUV light in the form of a train of attosecond bursts. The gating of the harmonic emission over a single half-cycle of the driving field allows the generation of an isolated attosecond pulse. Several techniques have been proposed so far for the generation of attosecond bursts, like polarization gating, spectral filtering and two color-gating [1]. In this field, the possibility of extending the generation of attosecond pulses to the 100-eV spectral region has encouraged lot of efforts in the development of mid-IR parametric sources [2]. Indeed, due to the scaling of the cutoff frequency in HHG (proportional to λ^2), such sources allow to obtain XUV spectra which can extend up to the water window spectral region [3]. Up to now, mid-IR parametric sources have been employed in the gating of HHG in a standard two color scheme, mixed with commonly available Ti:Sapphire laser sources [4]. In this work we report on the experimental realization of a novel approach based on the exploitation of two mid-IR laser pulses with incommensurate wavelengths (1.35 and 1.75 μm) combined together, either with parallel and perpendicular polarizations, for obtaining, respectively, a two color gating and a polarization gating on the HHG process. The validity of this approach has been theoretically demonstrated by the authors, in both the two polarizations' configurations [5]. Our results show the generation of coherent continuous XUV spectra, which are the fingerprint of attosecond pulse production, starting from driving pulses longer than 30 fs.

14.2 Experimental Results

In order to obtain the two-color field, we developed two optical parametric amplifiers (OPAs) pumped by a Ti:sapphire laser system (800 nm, 60 fs, 10 Hz, 120 mJ). A portion of the pump beam was compressed down to 10 fs, by means of optical filamentation and subsequent chirped mirrors compression. This broadband pulse was sent through a 300 μm -thick type-I BBO crystal for difference frequency generation (DFG), serving as an IR seed extending from 1.1 up to 2.3 μm . Since DFG was performed between the spectral components of the same broadband pulse, the CEP of the IR seed was passively stabilized [6]. The seed was then amplified up to 50 μJ in a 3 mm-thick type-I BBO crystal, pumped by a fraction of the Ti:sapphire beam. A dichroic beamsplitter (with high transmission between 1.1 and 1.6 μm and high reflectivity between 1.6 and 1.9 μm) was positioned after the first OPA. The two resulting pulses were finally amplified by means of two high-energy OPAs, based on a 4 mm and a 5 mm-thick type-II BBO crystals, that provided at the output 1.35 μm , 35 fs, 700 μJ and 1.75 μm , 32 fs, 240 μJ pulses, respectively. For adjusting the delay between the two pulses, we exploited a 0.28-fs resolution translation stage.

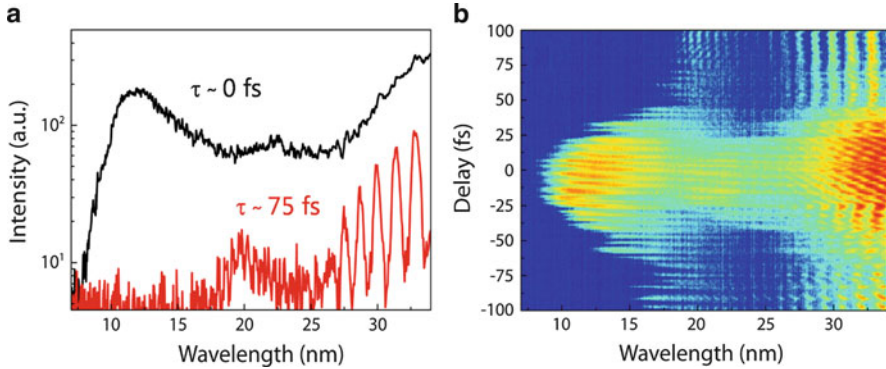


Fig. 14.1 (a) harmonic spectra generated in argon for $\tau = 0$ fs and $\tau = 75$ fs for parallel polarizations of the two fields; (b) harmonic spectra generated in argon as a function of τ for parallel polarizations (see text)

A broadband half-waveplate was used for changing the polarization direction of the first pulse. A second dichroic mirror, identical to the first one, was used for recombining the two pulses. The two-color pulse was then focused by a spherical mirror ($f = 125$ mm) on a pulsed gas jet inside a vacuum chamber for generating high-harmonics which were analyzed by a soft X-ray spectrometer equipped with a microchannel plate coupled to a phosphor screen and a CCD camera.

Figure 14.1b shows the harmonic spectra acquired in argon as a function of the delay between the two IR pulses (τ), for parallel polarizations. For $|\tau| > 50$ fs only the $1.35 \mu\text{m}$ pulse contributed to harmonic generation. Two harmonic spectra, obtained for $\tau = 0$ fs and $\tau = 75$ fs are reported in Fig. 14.1a. A noticeable extension of the spectral cutoff is observed, up to 8 nm (160 eV), for $\tau = 0$ fs, together with the periodic appearance of continuous spectra every about 5 fs (like the one shown in Fig. 14.1a for $\tau = 0$ fs). The continuous XUV emission is the signature of the single half-cycle gating occurring due to the shape of the two-color electric field, while the temporal modulation is originating from the rephasing of the two fields. The stability of both the experimental setup and the CEP of the parametric source allows to observe such a well defined modulation of the spectra with respect to the delay. We extended our investigation to the case of perpendicular polarizations, by rotating the half waveplate to an angle of 45° . Figure 14.2b shows the harmonic spectra acquired in argon as a function τ , for perpendicular polarizations while Fig. 14.2a shows two harmonic spectra, taken respectively at $\tau = 0$ fs and $\tau = 75$ fs. For perpendicular polarizations, a continuous spectrum is also observed at temporal overlap, together with a cutoff extension, even if more limited with respect to the first configuration, and a modulation of the harmonic spectra as a function of τ . In this latter scheme, the isolation of the XUV emission to a single half-cycle is due to a polarization shaping of the driving field, that opens an ellipticity gate along the two-color pulse [5]. One can notice that the efficiency of the HHG process is lower

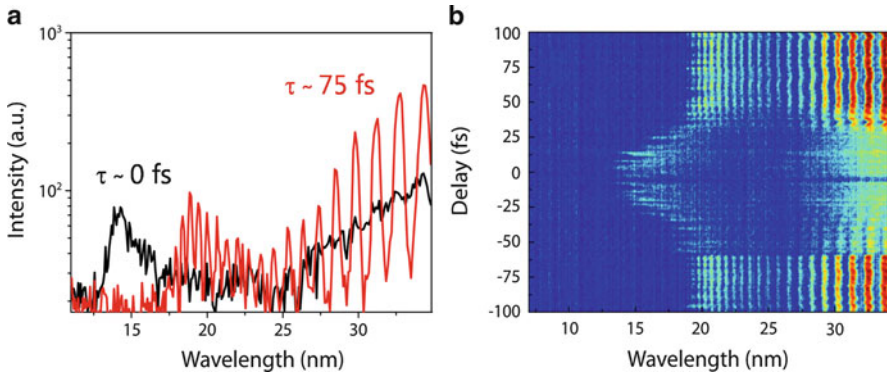


Fig. 14.2 (a) harmonic spectra generated in argon for $\tau = 0$ fs and $\tau = 75$ fs for perpendicular polarizations of the two fields; (b) harmonic spectra generated in argon as a function of τ for perpendicular polarizations (see text)

compared to the parallel polarizations scheme, where the interference between the two IR fields leads to an enhancement of the instantaneous intensity of the two-color pulse.

14.3 Conclusions

In conclusion, we demonstrated a novel approach for the temporal gating of high-order harmonic generation, by exploiting two mid-IR laser pulses with incommensurate wavelengths, generated by means of a high-energy parametric source. The results obtained for the two implemented schemes (parallel and perpendicular polarizations) show the possibility of generating robust XUV supercontinua extending beyond 100 eV. The versatility of our approach relies in the possibility of exploiting two different gating mechanisms by simply rotating the polarization direction of one of the two driving fields. Moreover, we demonstrated for the first time the generation of XUV supercontinua starting from driving pulses longer than 30 fs.

References

1. F. Krausz, M. Ivanov, Attosecond physics. *Rev. Mod. Phys.* **81**, 163 (2009)
2. G. Cerullo, A. Baltuska, O.D. Mücke, C. Vozzi, Few-optical-cycle light pulses with passive carrier-envelope phase stabilization. *Laser Photon. Rev.* **5**, 323 (2011)
3. E.J. Takahashi, T. Kanai, K.L. Ishikawa, Y. Nabekawa, K. Midorikawa, Coherent water window X ray by phase-matched high-order harmonic generation in neutral media. *Phys. Rev. Lett.* **101**, 253901 (2008)

4. F. Calegari, C. Vozzi, M. Negro, G. Sansone, F. Frassetto, L. Poletto et al., Efficient continuum generation exceeding 200 eV by intense ultrashort two-color driver. *Opt. Lett.* **34**, 3125 (2009)
5. V. Tosa, C. Altucci, K. Kovacs, M. Negro, S. Stagira, C. Vozzi et al., Isolated attosecond pulse generation by two-mid-IR laser fields. *IEEE J. Sel. Top. Quant. Electron.* (2011). Published Online (doi:10.1109/JSTQE.2011.2118193)
6. C. Vozzi, F. Calegari, E. Benedetti, S. Gasilov, G. Sansone, G. Cerullo et al., Millijoule-level phase-stabilized few-optical-cycle infrared parametric source. *Opt. Lett.* **32**, 2957 (2007)

Chapter 15

Ionization Gating for the Generation of Tunable XUV Radiation and Isolated Attosecond Pulses

F. Calegari, M. Lucchini, K.S. Kim, C. Vozzi, S. Stagira,
G. Sansone, and M. Nisoli

Abstract Few-optical-cycle pulses with high-peak intensity and controlled electric field can be used for the generation of isolated attosecond pulses, employing the ionization gating technique. The temporal reshaping of the electric field of the driving pulses, induced by propagation in a highly ionized gas cell, can be used to control the electron quantum paths, which contribute to the process of high-order harmonic generation. The peculiar effects produced on the generation process by temporal reshaping of the driving field, are investigated by using the nonadiabatic saddle-point method. In particular, a complete spectral tunability of the harmonic emission is understood upon considering the effects of driving pulse distortions on the phase of the relevant electron quantum paths.

15.1 Introduction

Since the first experimental demonstration of the generation of isolated attosecond pulses, the attosecond technology has become an important branch of ultrafast science [1,2]. Isolated attosecond pulses have been generated by using two different approaches, based on the production of XUV radiation by high-order harmonic generation (HHG) in gases. A real breakthrough in attosecond science would be the possibility to probe with isolated attosecond pulses the electron dynamics initiated by an attosecond pump pulse. In this case the temporal evolution of the electronic rearrangement could be measured, with attosecond time resolution, by ionizing the excited atomic or molecular system with a second attosecond pulse and measuring the velocity and angular characteristics of the generated charged particles, electrons

F. Calegari · M. Lucchini · K.S. Kim · C. Vozzi · S. Stagira · G. Sansone · M. Nisoli (✉)
Department of Physics, Politecnico di Milano, National Research Council of Italy,
Institute of Photonics and Nanotechnologies (CNR-IFN), Piazza L. da Vinci 32, 20133
Milano, Italy
e-mail: mauro.nisoli@fisi.polimi.it

and ions, as a function of the time delay between the pump and probe attosecond pulses. So far, the reported applications of isolated attosecond pulses have been limited by the low photon flux of the available sources.

We have recently demonstrated a technique for the generation of isolated attosecond pulses with energy in the nanojoule range [3]. The key elements are: (a) the use of few-optical-cycle driving pulses with stable carrier-envelope phase (CEP), linear polarization and peak intensity beyond the saturation intensity of the gas used for HHG; and (b) the optimization of the interaction geometry in terms of gas pressure, position and thickness of the gas cell. Such a method is based on the combined action of complete depletion of the neutral atom population on the leading edge of the few-cycle excitation pulse and efficient spatial filtering in the XUV beam-line. The same technique can be also used for the generation of tunable XUV radiation in a broad spectral range, by changing the CEP of the driving pulses. This is particularly important for various applications, ranging from seeding of Free Electron Lasers, to XUV spectroscopy and novel attosecond measurement techniques.

15.2 Experimental Results

We used 5-fs driving pulses with stable CEP, generated by the hollow-fiber compression technique [4]. 25-fs infrared (IR) laser pulses generated by a Ti:sapphire laser system (1.2-mJ energy, 1 kHz repetition rate) are injected into a 60-cm-long hollow fiber (input diameter 0.5 mm, output diameter 0.3 mm) filled with neon at a pressure of 2.1 bar. Sub-6-fs pulses were obtained by broadband dispersion compensation by five reflections onto chirped mirrors. Output pulse energy was 0.65 mJ, at a central wavelength of 750 nm. The IR beam was divided into two parts by using a drilled mirror with a 5-mm-diameter central hole. High-order harmonic generation was produced by focusing the inner part of the beam into a 2.5-mm-thick cell filled with xenon or argon at static pressure (2.5–3 torr). The gas cell was placed after the laser focus in order to select the short electron trajectories [5]. The XUV radiation was spectrally dispersed by using a flat-field grazing incidence spectrometer and detected by a microchannel plate coupled to a phosphor screen and a CCD camera [6]. The XUV spectra generated in xenon at a peak intensity of $2.5 \times 10^{15} \text{ W/cm}^2$ and in argon at a peak intensity of $4 \times 10^{15} \text{ W/cm}^2$ display an evolution from a continuous behavior to a modulated one by changing the CEP value, as shown in Fig. 15.1a in the case of xenon. The energy of the XUV pulses in the case of continuous spectra was 2.1 nJ in xenon and 1.4 nJ in argon. Continuous spectra can be generated within a broad range of CEP values, much larger than the residual CEP fluctuations after stabilization. We have measured the temporal characteristics of the attosecond pulses by using the Frequency Resolved Optical Gating for Complete Reconstruction of Attosecond Bursts (FROG CRAB) method [7]. The retrieved temporal intensity profile, reported in Fig. 15.1b, corresponds to a pulse duration of 155 as. The temporal structure

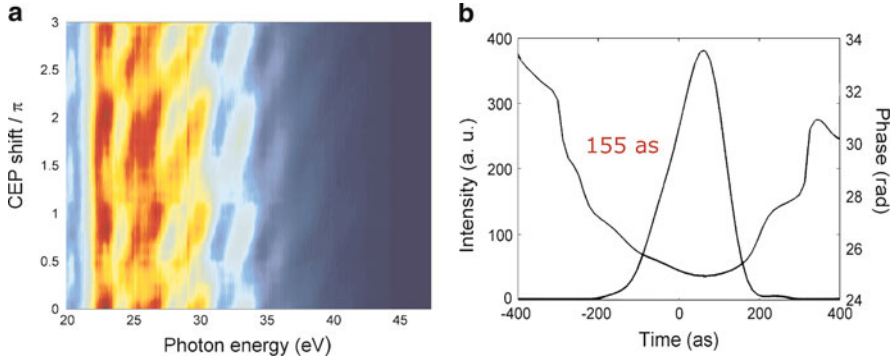


Fig. 15.1 (a) XUV spectra generated in xenon by 5-fs pulses at a peak intensity of $2.5 \times 10^{15} \text{ W/cm}^2$, as a function of the CEP. (b) Temporal evolution of the intensity profile and phase of isolated attosecond pulses, retrieved from the measured FROG CRAB trace

of the attosecond pulses was retrieved using the principal-component generalized projection algorithm (PCGPA) [8].

We have then investigated the harmonic generation process in argon, upon decreasing the driving peak intensity. Figure 15.2a shows the measured harmonic spectra generated in argon in the case of a driving peak intensity of $3.5 \times 10^{15} \text{ W/cm}^2$, upon changing the CEP value. A complete tunability of the harmonic peak position as a function of the CEP has been obtained. Such tunability is not limited to the cutoff region of the XUV spectra.

15.3 Physical Model

The physical mechanisms at the basis of the generation of isolated attosecond pulses and of tunable XUV radiation are related to the ionization dynamics in the generating medium. The role of ionization in the generation of isolated attosecond pulses has been already investigated in the case of longer driving pulses [9, 10]. In both cases a spectral selection of the XUV emission was required to isolate single attosecond pulses, and the physical process was explained in terms of the very rapid loss of phase matching occurring on the leading edge of the excitation pulses.

We used a nonadiabatic three-dimensional (3D) numerical model [11], which takes into account both temporal plasma-induced phase modulation and spatial plasma lensing effect on the driving beam. The ionization rates have been calculated by using the Ammosov, Delone and Krainov (ADK) model [12]. In agreement with experimental results, the XUV spectra calculated in xenon at a peak intensity $I = 2.5 \times 10^{15} \text{ W/cm}^2$ and in argon at $I = 4 \times 10^{15} \text{ W/cm}^2$ display an evolution from a continuous behavior to a modulated one by changing the CEP value. We have then calculated the propagation of the XUV beam from the gas cell to the target position. With a proper choice of the CEP, isolated attosecond pulses are generated,

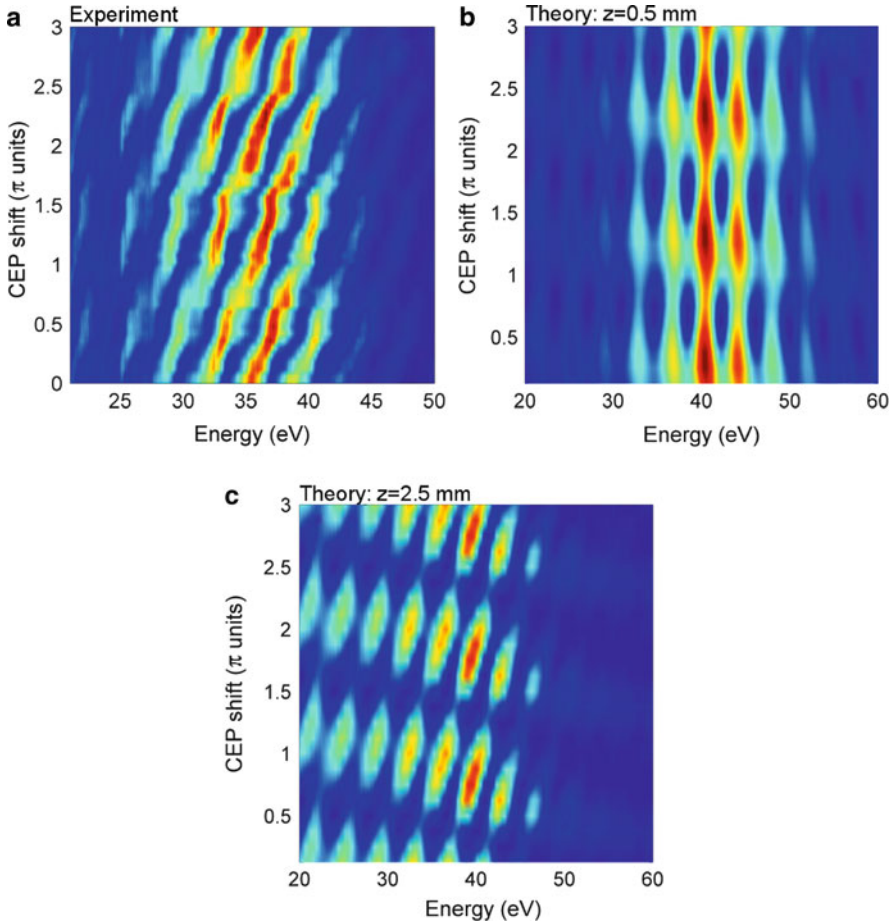


Fig. 15.2 (a) Experimental XUV spectra generated in argon and acquired as a function of the CEP of the driving field. XUV spectra calculated after a propagation of 0.5 mm (b) and 2.5 mm (c) inside the gas cell assuming the experimental conditions of (a)

with a constant pulse duration across the transverse profile of the beam, thus demonstrating the excellent spatial characteristics of the generated attosecond pulses.

Figure 15.2b, c show the evolution of the XUV spectra calculated in argon assuming a laser peak intensity $I = 3.5 \times 10^{15} \text{ W/cm}^2$, as a function of the CEP, after a propagation of $z = 0.5 \text{ mm}$ and $z = 2.5 \text{ mm}$ in the gas cell. At $z = 0.5 \text{ mm}$ the harmonic peak-position is almost insensitive to the CEP values, contrary to what experimentally observed. Complete tunability of the XUV peaks is perfectly reproduced by the numerical simulation upon considering the correct propagation length, as shown in Fig. 15.2c. The Gabor analysis [13] indicates that the tunability of the XUV peaks can be completely assigned to the reshaping of the two short quantum trajectories, which contribute to the XUV emission, as a result of the propagation in

the ionizing medium. A more direct physical interpretation can be obtained by using nonadiabatic saddle-point simulations [14, 15]. We have used a generalized model, which uses an arbitrary non-analytical driving field [16]. In agreement with the results of the 3D model, the saddle-point simulations demonstrate that a complete tunability of the XUV emission can be achieved as a result of the reshaping of the driving electric field induced by the propagation in the ionizing medium.

Acknowledgements The research leading to the results presented in this paper has received funding from the European Research Council under the European Community's Seventh Framework Programme (FP7/2007-2013)/ERC grant agreement n. 227355-ELYCHE. We acknowledge financial support from the Italian Ministry of Research (FIRB-IDEAS RBID08CRXX), support from European Union within contract n. 228334 JRA-ALADIN (Laserlab Europe II) and from MC-RTN ATTOFEL (FP7-238362).

References

1. F. Krausz, M. Ivanov, Attosecond physics. *Rev. Mod. Phys.* **81**, 163–234 (2009)
2. M. Nisoli, G. Sansone, New frontiers in attosecond science. *Prog. Quant. Electron.* **33**, 17–59 (2009)
3. F. Ferrari et al., High-energy isolated attosecond pulses generated by above-saturation few-cycle fields. *Nat. Photon.* **4**, 875–879 (2010)
4. M. Nisoli, S. De Silvestri, O. Svelto, Generation of high energy 10 fs pulses by a new pulse compression technique. *Appl. Phys. Lett.* **68**, 2793–2795 (1996)
5. Y. Mairesse et al., Attosecond synchronization of high-harmonic soft X-rays. *Science* **302**, 1540–1543 (2003)
6. L. Poletto, S. Bonora, M. Pascolini, P. Villoresi, Instrumentation for analysis and utilization of extreme-ultraviolet and soft x-ray high-order harmonics. *Rev. Scient. Instrum.* **75**, 4413–4418 (2004)
7. Y. Mairesse, F. Quéré, Frequency-resolved optical gating for complete reconstruction of attosecond bursts. *Phys. Rev. A* **71**, 011401(R) (2005)
8. K.W. Delong, D.N. Fittinghoff, R. Trebino, Practical issues in ultrashort-laser-pulse measurement using frequency-resolved optical gating. *IEEE J. Quantum Electron.* **32**, 1253–1264 (1996)
9. M.J. Abel et al., Isolated attosecond pulses from ionization gating of high-harmonic emission. *Chem. Phys.* **366**, 9–14 (2009)
10. I. Thomann et al., Characterizing isolated attosecond pulses from hollow-core waveguides using multi-cycle driving pulses. *Opt. Express* **17**, 4611–4633 (2009)
11. E. Priori et al., Nonadiabatic three-dimensional model of high-order harmonic generation in the few-optical-cycle regime. *Phys. Rev. A* **61**, 063801 (2000)
12. M.V. Ammosov, N.B. Delone, V.P. Krainov, Tunnel ionization of complex atoms and atomic ions in a varying electromagnetic-field. *Zh. Eksp. Teor. Fiz.* **91**, 2008–2013 (1986) [*Sov. Phys. JETP* **64**, 1191 (1986)]
13. V.S. Yakovlev, A. Scrinzi, High harmonic imaging of few-cycle laser pulses. *Phys. Rev. Lett.* **91**, 153901 (2003)
14. M. Lewenstein, Ph. Balcou, M.Y. Ivanov, A. L’Huillier, P.B. Corkum, Theory of high-harmonic generation by low-frequency laser pulses. *Phys. Rev. A* **49**, 2117–2132 (1994)
15. G. Sansone, C. Vozzi, S. Stagira, M. Nisoli, Nonadiabatic quantum path analysis of high-order harmonic generation: role of the carrier-envelope phase on short and long paths. *Phys. Rev. A* **70**, 013411 (2004)
16. K. Kovács, V. Toşa, *J. Mod. Opt.* **57**, 977–983 (2010)

Chapter 16

Efficient Generation of Isolated Attosecond Pulse with CEP-Unstabilized Multicycle Infrared Double Optical Gating

Pengfei Lan, Eiji J. Takahashi, and Kastumi Midorikawa

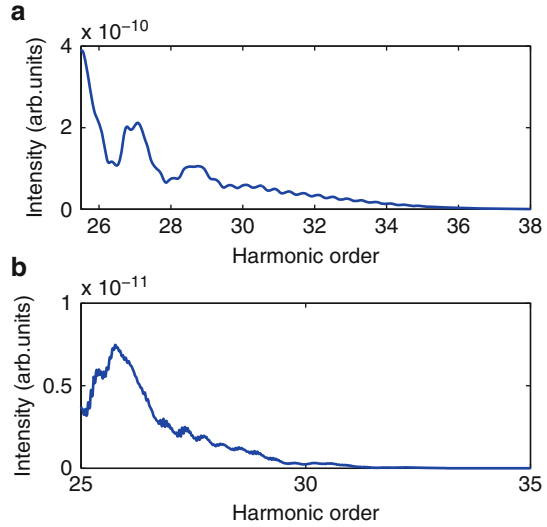
Abstract We proposed and theoretically demonstrated an optimized gating scheme, which we called infrared double optical gating (IRDOG), to create isolated attosecond pulses (IAPs) with a multicycle laser pulse. Our simulation shows that IAP can be generated by using a pulse up to 60 fs and carrier-envelope phase stabilization is not required.

16.1 Introduction

During the past decade, the advent of attosecond pulses has made a breakthrough of ultrafast optics. A number of impressive applications, such as probing the electron motions inside atoms, molecules and solids, have been realized with the infrared (IR) femtosecond pump/attosecond probe (or vice versa) technique. To produce isolated attosecond pulse (IAP), several methods, such as few-cycle pumping [1], polarization gating (PG) [2] and two-color gating [3, 4], have been experimentally demonstrated. Some other methods have also been proposed with the motivation to reduce the attosecond pulse duration [5] or to relax the requirement of the driving pulse duration [6]. Recently, the shortest pulse duration attained for an IAP has been reduced to 80 as. However, most of these methods for IAP generation require a CEP-stabilized driving pulse, which is a big challenge for the high-power (>100-TW) lasers. Therefore, the driving laser pulse energy is usually less than millijoule and the output energy of IAP is still quite limit. Double optical gating (DOG) [7] and generalized double optical gating (GDOG) [8] schemes have been proposed to relax the requirements of the pulse duration and CEP stabilization of the driving pulse, however, the target medium gas would be fully ionized and the

P. Lan (✉) · E.J. Takahashi · K. Midorikawa
Extreme Photonics Research Group, RIKEN Advanced Science Institute, 2-1 Hirosawa, Wako,
Saitama 351-0198, Japan
e-mail: pengfeilan@riken.jp; ejtak@riken.jp; kmidori@riken.jp

Fig. 16.1 Harmonic spectra generated with the (a) IRDOG and (b) GIRDOG. The driving pulse durations are 25 fs and 45 fs, respectively. The laser intensities are 1×10^{14} (fundamental) and 1×10^{13} W/cm² (IR), respectively



ionized medium makes it difficult to achieve the phase-matching and enhance the HHG efficiency.

16.2 Results and Conclusions

In this work, we proposed an infrared double optical gating (IRDOG)[9] method that combines the conventional polarization gating and the optimized two-color infrared synthesis gating [4, 10] methods for generating IAP. In our scheme, two counter-rotating, elliptically polarized fundamental Ti:sapphire laser pulses (800 nm) with a proper delay are utilized as the main driving pulse. In addition, a weak IR control pulse at 1,300 nm, which can be produced by OPA system pumped by Ti:sapphire laser, is synthesized with the main driving pulse. In such an IR synthesis, attosecond pulses are generated in every 6.7 fs as compared to 1.3 fs in the fundamental field alone. Consequently, it enables to easily isolate an attosecond pulse with a broader gating of 6.5 fs, which is 5 or 2.5 times longer compared with the conventional PG or DOG methods, respectively. Moreover, IRDOG can be generalized to the elliptically polarized laser case (e.g., ellipticity is 0.5), called GIRDOG, which allows us to increase the driving pulse duration more.

Our concept was theoretically demonstrated with the Lewenstein model by including the propagation effects [11]. Figure 16.1a shows the harmonic spectrum generated with the IRDOG scheme using two 25-fs counter rotating circularly polarized laser pulses. Supercontinuum high harmonics can be obtained from 29-th harmonics, from which IAP can be generated. A longer driving pulse can be used in GIRDOG case. As shown in Fig. 16.1b, supercontinuum harmonics are generated using a 42-fs elliptically polarized pulses. One great advantage of our IRDOG and GIRDOG is that the requirement of carrier-envelope phase (CEP)

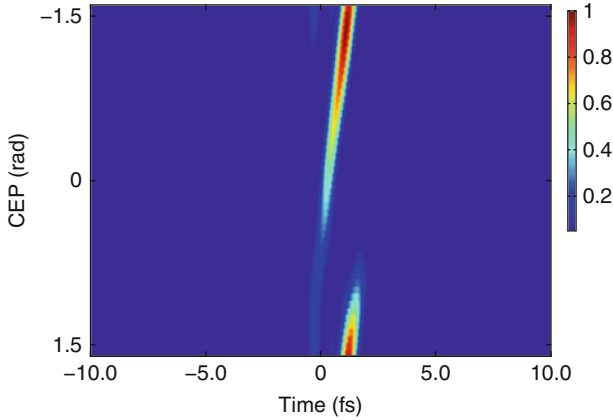


Fig. 16.2 CEP dependence of IAP generated by GIRDOG method

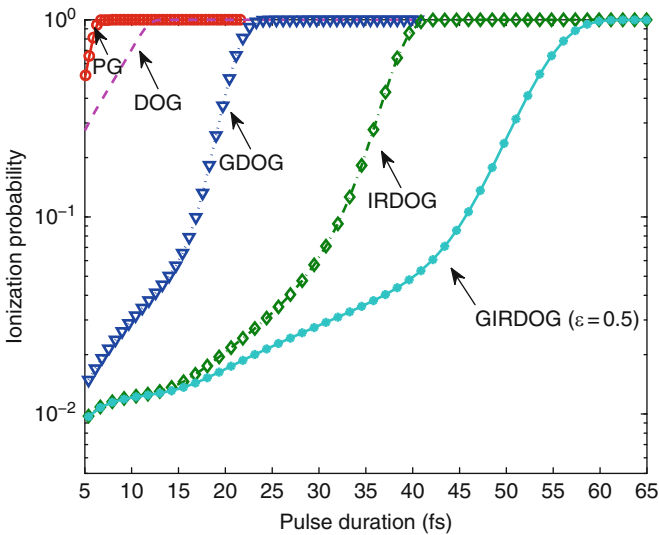


Fig. 16.3 Ionization probability as a function of driving pulse duration for PG [2, 7], DOG [7], GDOG [8], IRDOG and GIRDOG, respectively. The target is Ar and ADK model [13] was used in this calculation

stabilization can be significantly relaxed. Figure 16.2 shows the CEP dependence of the temporal profile of IAP generated by the GIRDOG scheme. We can see that IAPs are generated for most CEPs although its intensity changes with the CEP shift. Note that the weak attosecond pulse does not play an important role in many application, therefore, CEP-unstabilized laser pulses can be used to create the IAP.

Another great advantage of IRDOG and GIRDOG is that the low ionization enables us to realize the phase-matching of HHG. In comparison with the PG, DOG, GDOG schemes, the ionization is significantly reduced in our IRDOG and GIRDOG schemes. As shown in Fig. 16.3, the ionization probability of GIRDOG is only 4%

if the driving pulse is 40 fs and has not been completely depleted even for a 60-fs driving pulse. Such a low ionization allows us to realize the phase-matching and to enhance the efficiency. By using the energy-scaling technique [12], it is possible to produce the microjoule level IAP with a high-power driving laser.

In conclusion, we have theoretically demonstrated the IRDOG and GIRDOG schemes for generating an intense IAP. This optimized gating scheme significantly relaxes the requirements both of pulse duration and CEP stabilization of the driving laser and it is possible to create high-power IAPs using a multicycle conventional driving laser pulse that is easy access for most laser laboratories.

References

1. E. Goulielmakis, M. Schultze, M. Hofstetter, V.S. Yakovlev, J. Gagnon, M. Uiberacker, A.L. Aquila, E.M. Gullikson, D.T. Attwood, R. Kienberger, F. Krausz, U. Kleineberg, *Science* **320**, 1614 (2008)
2. G. Sansone, E. Benedetti, F. Calegari, C. Vozzi, L. Avaldi, R. Flammini, L. Poletto, P. Villoresi, C. Altucci, R. Velotta, S. Stagira, S. De Silvestri, M. Nisoli, *Science* **314**, 443 (2006)
3. Y. Oishi, M. Kaku, A. Suda, F. Kannari, K. Midorikawa, *Opt. Express* **14**, 7230 (2006)
4. E.J. Takahashi, P.F. Lan, O.D. Muecke, Y. Nabekawa, K. Midorikawa, *Phys. Rev. Lett.* **104**, 233901 (2010)
5. P.F. Lan, P.X. Lu, W. Cao, Y.H. Li, X.L. Wang, *Phys. Rev. A* **76**, 011402 (R) (2007)
6. P.F. Lan, P.X. Lu, W. Cao, X.L. Wang, W. Hong, *Opt. Lett.* **32**, 1186–1188 (2007)
7. H. Mashiko, S. Gilbertson, C. Li, S.D. Khan, M.M. Shakya, E. Moon, Z. Chang, *Phys. Rev. Lett.* **100** 103906 (2008)
8. S. Gilbertson, S.D. Khan, Y. Wu, M. CHini, Z.H. Chang, *Phys. Rev. Lett.* **105**, 093902 (2010)
9. P.F. Lan, E.J. Takahashi, K. Midorikawa, *Phys. Rev. A* **83**, 063839 (2011)
10. P.F. Lan, E.J. Takahashi, K. Midorikawa, *Phys. Rev. A* **82**, 053413 (2010)
11. P.F. Lan, P.X. Lu, Q.G. Li, F. Li, W.Y. Hong, *Phys. Rev. A* **79**, 043413 (2009)
12. E. Takahashi, Y. Nabekawa, T. Otsuka, M. Obara, K. Midorikawa, *Phys. Rev. A* **66**, 021802 (R) (2002)
13. M.V. Ammesov, N.B. Delone, V.P. Krainov, *Sov. Phys. JETP* **64**, 1191 (1986)

Chapter 17

Frequency-Controlled Isolated Attosecond Pulses Characterized by Both 750 and 400 nm Wavelength Streak Fields

H. Mashiko, M.J. Bell, A.R. Beck, M.J. Abel, K.R. Siefertmann, P.M. Nagel, J. Robinson, D.M. Neumark, and S.R. Leone

Frequency tunability of isolated attosecond pulses provides options for the study of temporal dynamics and phases of electronic processes [1]. Techniques to generate frequency-controlled attosecond pulses (XUV and VUV) and wavelength selective streak pulses (NIR and UV) are discussed here. A novel Mach-Zehnder (MZ) interferometer is used to combine all optical fields before the high-harmonic generation region.

Figure 17.1a shows the optical layout. The novel feature of this setup is the compact MZ interferometer, shaded in Fig. 17.1a and shown in the photograph in Fig. 17.1b. A carrier-envelope (CE) phase stabilized Ti:Sapphire laser pulse (7 fs, 1 mJ, 750 nm) is sent to the MZ interferometer, which has <40 as RMS delay jitter as shown in Fig. 17.1c. The double optical gating (DOG) [2] and streaking fields are generated in the two arms of the interferometer. The optical fields are collinearly combined, pass through a BBO crystal and a cell filled with Ar gas in which the DOG field generates an isolated attosecond pulse. Figure 17.2 shows a typical harmonic spectrum (upper figure) with a linearly polarized pulse and DOG

H. Mashiko (✉)

Ultrafast X-ray Science Laboratory, Chemical Sciences Division, Lawrence Berkeley National Laboratory, Berkeley, CA 94720, USA

Present address: NTT Basic Research Lab, 3-1 Morinosato Wakamiya, Atsugi-shi, Kanagawa, 243-0198, Japan

e-mail: mashiko.hiroki@lab.ntt.co.jp

M.J. Bell, A.R. Beck, M.J. Abel, K.R. Siefertmann, P.M. Nagel, D.M. Neumark, S.R. Leone
Ultrafast X-ray Science Laboratory, Chemical Sciences Division, Lawrence Berkeley National Laboratory, Berkeley, CA 94720, USA

Departments of Chemistry and Physics, University of California, Berkeley, CA 94720, USA

J. Robinson

Material Sciences Division, Lawrence Berkeley National Laboratory, Berkeley, CA 94720, USA

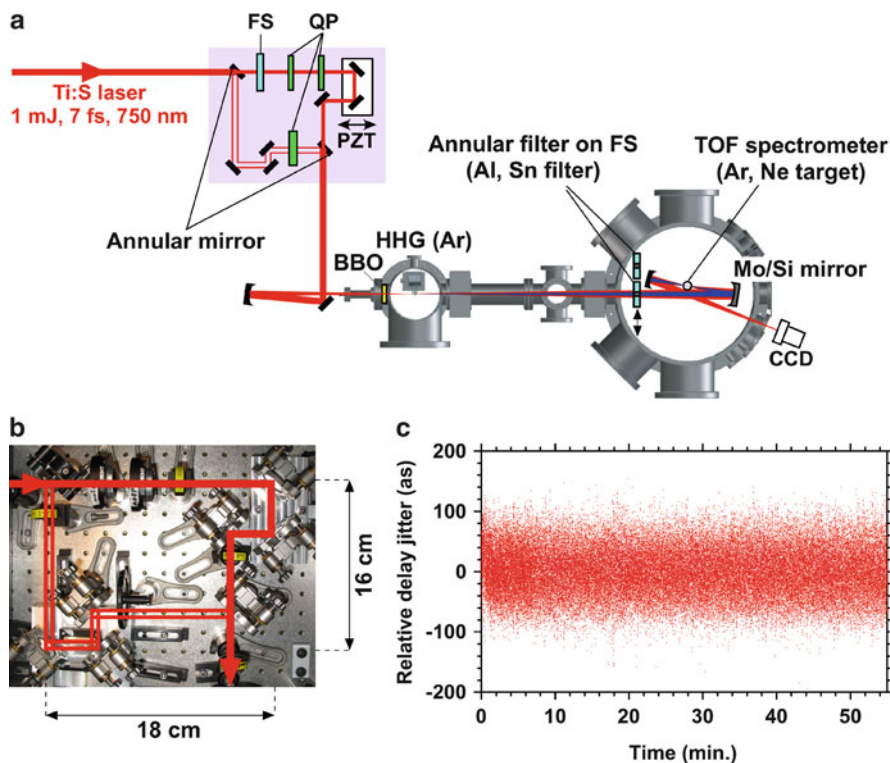


Fig. 17.1 Experimental setup and the stability with MZ interferometer. (a) Schematic of the entire setup. *FS* fused silica plates with 1 mm thickness, *QP* quartz plates with 250 μm and 480 μm thickness in HHG arm and 730 μm thickness in streak arm. (b) Schematic of the interferometer. (c) The relative delay jitter between HHG arm and streak arm in the interferometer

and the CE phase dependence with DOG (lower figure). The harmonic and streak beams are then focused into the interaction region of a photoelectron spectrometer. The BBO can also be used to produce the 400 nm streak field.

Figure 17.3 shows the (a) measured and (b) reconstructed (with the Principal Component Generalized Projections Algorithm method [3]) streak traces with a 750 nm streak field using an Al filter and Ne as the target gas in the spectrometer. The temporal profile and phase indicate a 114 as pulse (Fig. 17.3c). The satellite pulses are suppressed with less than a 1% contribution at 750 nm half (± 1.25 fs) and full (± 2.5 fs) cycles in the reconstructed temporal profile, indicating a well isolated pulse. In addition, the measured and the reconstructed harmonic spectra agree well as shown in Fig. 17.3d. Figure 17.3 shows the (e) measured and (f) reconstructed streak trace with a 750 nm field using a Sn filter and Ar as the target. The reconstructed temporal profile and phase indicate a 395 as pulse (Fig. 17.3g). The pre- and post-pulses were suppressed to less than a 1% contribution

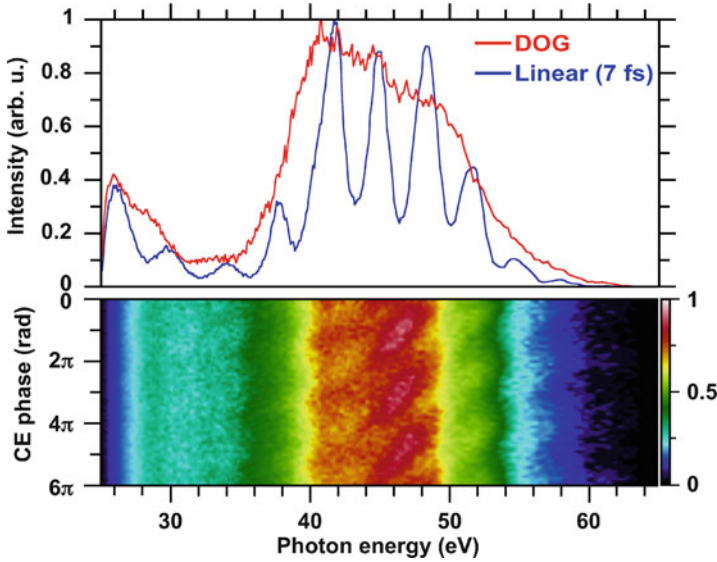


Fig. 17.2 Typical high-harmonic spectrum with linearly polarized pulse and DOG (*upper figure*) and CE phase dependence with DOG (*lower figure*)

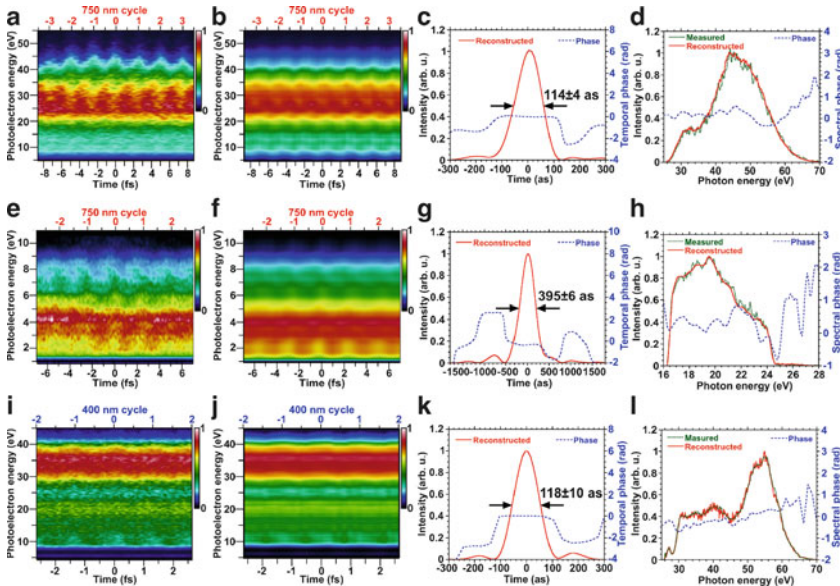


Fig. 17.3 Streak traces and pulse characterization. (a) Measured and (b) reconstructed streak traces with Al filter using 750 nm field. (c) The reconstructed pulse (*solid line*) and phase (*dotted line*). (d) The reconstructed spectrum (*solid line*) and phase (*dotted line*) and the measured spectrum (*dashed line*) without the streak field. (e) Measured and (f) reconstructed streak traces with Sn filter using 750 nm field. (g) Pulse reconstruction, as in (c). (h) Spectrum reconstruction, as in (d). (i) Measured and (j) reconstructed streak traces with Al filter using 400 nm field. (k) Pulse reconstruction, as in (c). (l) Spectrum reconstruction, as in (d)

at the 750 nm half and full cycle regions. In addition, the measured and the reconstructed harmonic spectra agree well as shown in Fig. 17.3h. These results indicate the flexibility of selecting the XUV or VUV frequency of the isolated attosecond pulses. Of course, future experiments are not limited to the frequencies selected in this study. Finally, a streak trace is obtained for the first time with a 400 nm streak field using an Al filter and Ne as the target (Fig. 17.3i). The reconstructed streak trace is shown in Fig. 17.3j. The reconstructed temporal profile and phase indicate a 118 as pulse (Fig. 17.3k). The measured and the reconstructed spectra agree well as shown in Fig. 17.3l. The compact interferometer design allows the streak field to be modified independently of the driving HHG field, while keeping mechanical stability high enough for attosecond experiments.

We have demonstrated an important step for future attosecond dynamics studies by generating XUV/VUV isolated attosecond pulses and NIR/UV streak fields with variable center frequency. The tunability of isolated attosecond pulses will allow a greater variety of dynamics in atoms and molecules to be studied. The increased flexibility of both the isolated attosecond field and the probe field will pave the way for chemical applications of attosecond science.

References

1. T. Pfeifer et al., *Chem. Phys. Lett.* **463**, 11 (2008)
2. H. Mashiko et al., *Phys. Rev. Lett.* **100**, 103906 (2008)
3. D.J. Kane, *J. Opt. Soc. Am. B* **25**, A120 (2008)

Chapter 18

Generation of Highly Phase-Matched Isolated Attosecond Pulses Using Multi-mJ, Carrier-Envelope Phase Stabilized, Few-Cycle Laser Pulses

Tsuneto Kanai, Yuxi Fu, Yasuhiro Kamba, Samuel Bohman, Hiroshi Yoshida, Takuya Kanai, Shigeru Yamaguchi, Eiji J. Takahashi, Yasuo Nabekawa, Akira Suda, and Katsumi Midorikawa

Abstract We generated highly phase-matched isolated attosecond pulses using multi-mJ, carrier-envelope phase stabilized, few-cycle laser pulses. Through the parametric amplification process of isolated attosecond pulses, only supercontinuum component was spectrally selected and by using a heterodyne interferometry using mixed gas, we found that the attochirp of the pulse is small.

T. Kanai (✉)

Extreme Photonics Research Group, RIKEN ASI, 2-1 Hirosawa, Wako-shi, Saitama 351-0198, Japan

Department of Physics, Blackett laboratory, Imperial College London, London SW7 2BW, United Kingdom

e-mail: tkanai@riken.jp

Y. Fu · Y. Nabekawa · E.J. Takahashi · K. Midorikawa

Extreme Photonics Research Group, RIKEN ASI, 2-1 Hirosawa, Wako-shi, Saitama 351-0198, Japan

Y. Kamba · S. Bohman · T. Kanai

Department of Physics, School of Science and Technology, Tokai University, 1117 Kita-kaname, Hiratsuka, Kanagawa 259-1292, Japan

H. Yoshida

Coherent Japan, Inc., Toyo MK Building 7-2-14 Toyo, Koto-ku, Tokyo, 135-0016, Japan

S. Yamaguchi

Extreme Photonics Research Group, RIKEN ASI, 2-1 Hirosawa, Wako-shi, Saitama 351-0198, Japan

Department of Physics, School of Science and Technology, Tokai University, 1117 Kita-kaname, Hiratsuka, Kanagawa 259-1292, Japan

A. Suda

Extreme Photonics Research Group, RIKEN ASI, 2-1 Hirosawa, Wako-shi, Saitama 351-0198, Japan

Department of Physics, Faculty of Science and Technology, Tokyo University of Science, 2641 Yamazaki, Noda, Chiba 278-8510, Japan

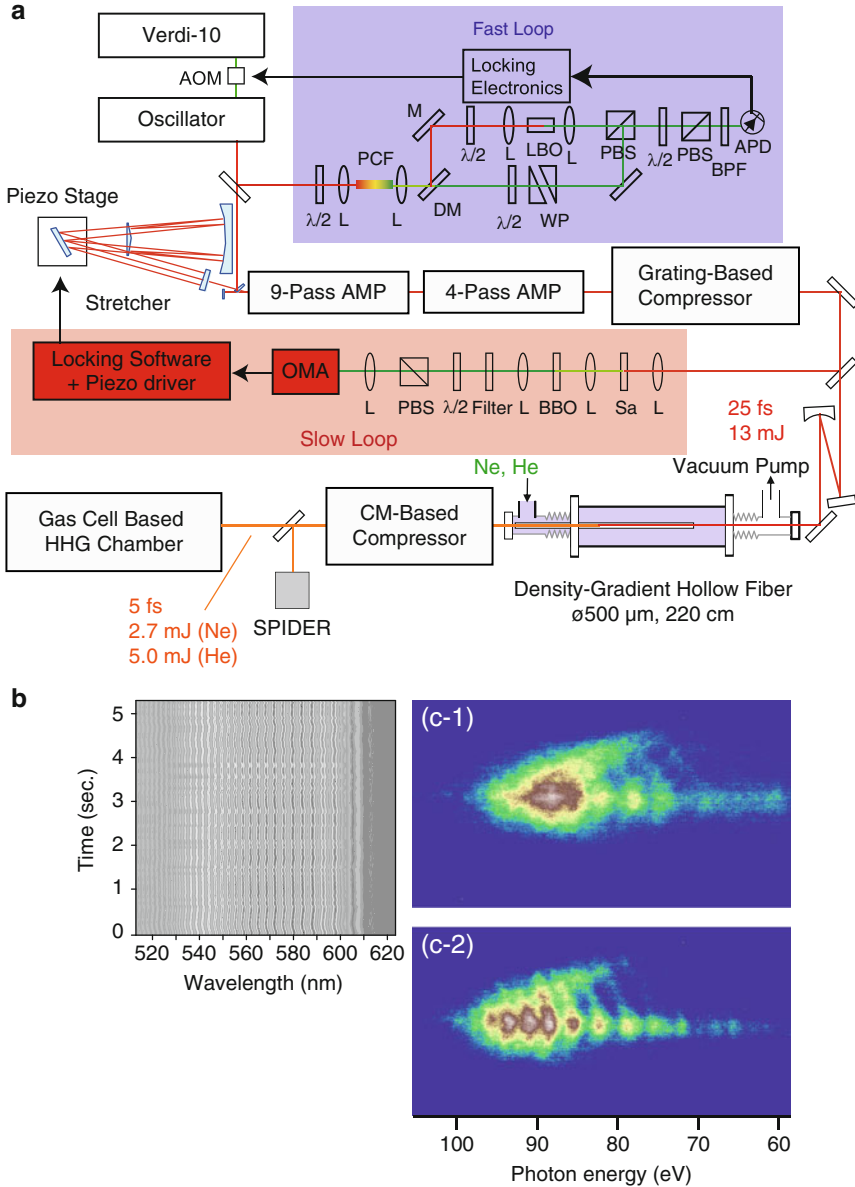


Fig. 18.1 (a) Experimental setup. (b) Time evolution of the $f-2f$ fringe of the amplified pulses. (c) Spectra of the IAP's directly generated in a Ne gas cell for $\phi_{cc} = \phi_0$ (c-1) and $\phi_{cc} = \phi_0 + \pi/2$ (c-2)

One of the most crucial issues for the present attoscience is to increase the energy of isolated attosecond pulses (IAP's). Typical pulse energy of IAP's reported before is order of pJ, which is enough for streaking-type experiments [1], but not for fundamental pump-and-probe-type experiments using IAP's only. For this purpose, there are two crucial experimental challenges to demonstrate; one is to develop a multi-mJ few cycle laser with a stabilized carrier-envelope phase (CEP) and the other is the phase-matching between the few cycle pulses and high harmonics of them.

In this paper, we realized both. This became possible by stabilizing CEP actively with two feedback loops and by blocking mechanical vibrations on the laser system thoroughly. To realize the phase-matching between the few cycle pulses and high harmonics of them we used a gas cell, with which one can control the condition of the nonlinear medium freely and precisely. Through the phase matching process, we could select the supercontinuum component of the harmonics without any use of bandpass filters such as Mo/Si mirrors. By using a heterodyne interferometry using high harmonic generation in mixed gases [2-4], we verified that the attochirp of the supercontinuum is small ($2 \times 10^3 \text{ as}^2$) as predicted, and in the time domain, this means that we could select IAP directly.

Figure 18.1c shows a typical harmonic spectra generated in Ne gas (9.0×10^1 Torr) using our TW-class 2-cycle laser system, which consists of a giant hollow fiber with graded medium density [5,6] and a high power Ti:sapphire based chirped pulse amplification system (pulse duration 5 fs, centre wavelength 800 nm, pulse energy >5 mJ, repetition rate 1 kHz). This IAP, whose estimated energy is order of 10 nJ and duration is 150 as, can allow us to explore attosecond science with the fundamental pump-and-probe-type scheme.

References

1. E. Goulielmakis et al., *Science* **320**, 1614 (2008)
2. T. Kanai et al., *Phys. Rev. Lett.* **98**, 153904 (2007)
3. T. Kanai et al., *New J. Phys.* **10**, 025036 (2008)
4. T. Kanai et al., *Phys. Rev. A* **77**, 041402(R) (2008)
5. A. Suda et al., *Appl. Phys. Lett.* **86**, 111116 (2005)
6. S. Bohman et al., *Opt. Lett.* **35**, 1887 (2010)

Chapter 19

Route to One Atomic Unit of Time: Development of a Broadband Attosecond Streak Camera

Kun Zhao, Qi Zhang, Michael Chini, and Zenghu Chang

19.1 Introduction

Generation of isolated extreme ultraviolet (XUV) pulses with durations of less than 200 as [12, 15, 17, 26, 32] has been reported. As the duration of XUV pulses approaches one atomic unit of time (about 25 as), the characteristic time scale of the electron dynamics in atoms, molecules and solid-state materials, direct measurement and control of the electron wave packets [16, 21, 22, 29, 33] with pump-probe techniques would profoundly impact our understanding of light-matter interaction.

The shortest pulses that have been characterized to date [17] were generated by selecting only the continuous spectrum near the high harmonic cutoff, yielding an XUV spectrum with a full-width-at-half-maximum (FWHM) bandwidth of 28 eV centered at 80 eV (55 eV photoelectron energy). Continuous spectra covering both the plateau and cutoff harmonics can support even shorter pulses [2, 3]. Recently a supercontinuum spanning 30–620 eV which is able to support pulses as short as 16 as was demonstrated [26] with the double optical gating (DOG) technique [14, 27]. Using both the plateau and cutoff spectrum to compose an isolated attosecond pulse is also advantageous for studying autoionization processes [13, 36] and for generating pulses with higher flux. Such a broadband XUV attosecond source could therefore become an extremely flexible and versatile tool to study ultrafast electron dynamics.

Attosecond XUV pulses are typically characterized using an attosecond streak camera, whereby an electron replica of the XUV pulse produced through photoionization of atoms is accelerated in a delayed dressing near-infrared (NIR) laser field [20, 23]. The amplitude and phase of the XUV pulse can be retrieved from the

K. Zhao · Q. Zhang · M. Chini · Z. Chang (✉)

Department of Physics and CREOL, University of Central Florida, Orlando, FL 32816, USA
e-mail: Zenghu.Chang@ucf.edu

delay-dependent streaked spectrogram [6, 25, 37]. Though the previous attosecond streak camera built by our group is very successful [12, 15, 26] to measure pulse durations >100 as, its accessible spectrum and energy resolution are both limited [11]. A 25-as pulse corresponds to a spectrum of 75 eV FWHM, which requires the spectrometer to cover at least a 150-eV range. To resolve pre- and/or post-pulses one laser cycle away from the main attosecond pulse, the spectrometer is required to have an energy resolution of 0.5 eV within the detection range [8]. To this end, a new attosecond streak camera based on a magnetic-bottle time-of-flight electron spectrometer (MBES) is designed and constructed [39, 40] to produce and measure shorter attosecond pulses with broader XUV spectra.

Using a technique known as FROG-CRAB (frequency-resolved optical gating for complete reconstruction of attosecond bursts) [25, 37], the amplitude and phase of attosecond XUV pulses have been retrieved from the delay-dependent streaked spectrogram obtained in attosecond streak cameras. The FROG-CRAB technique approximates the momentum of the photoelectrons with the central momentum of the spectrum, which is only valid when the bandwidth is much smaller than the central energy of the spectrum [25]. However, photoelectron spectra produced by continuous XUV spectra covering both the plateau and cutoff harmonics are centered at relatively low energies, thereby violating the central momentum approximation (CMA) of FROG-CRAB. For this reason, the PROOF (phase retrieval by omega oscillation filtering) technique has been developed [6], which extracts the XUV spectral phase from interference oscillations in the laser-dressed photoelectron spectrogram and does not rely upon the CMA.

In the following sections, we describe the experimental setup of the new attosecond streak camera. Then, we discuss the calculations of the magnetic fields and electron trajectories in MBES, as well as the measurement of the temporal resolution of the electron detection system. Finally, we present preliminary streaking results and conclude the chapter.

19.2 Experimental Setup

Figure 19.1 shows the experimental setup of the new broadband attosecond streak camera for measuring isolated attosecond pulses generated with DOG. The driving laser for the XUV pulse generation is a home-built 14-pass Ti:Sapphire chirped-pulse amplifier [15, 34] followed by a hollow-core fiber filled with Ne gas and a chirped-mirror compressor [28]. The NIR laser pulses of 8 fs and 1.2 mJ with a central wavelength at 790 nm are produced at 2 kHz repetition rate.

The NIR beam is split into two arms, which compose a Mach-Zehnder interferometer configuration similar to previous ones [7, 12]. The XUV generation arm, containing 80% of the total energy, is sent through the DOG optics, which consists of two quartz plates (QP1 and QP2) and a beta-barium-borate (BBO) crystal [14, 27]. A Brewster window can be inserted between the two quartz plates for generalized

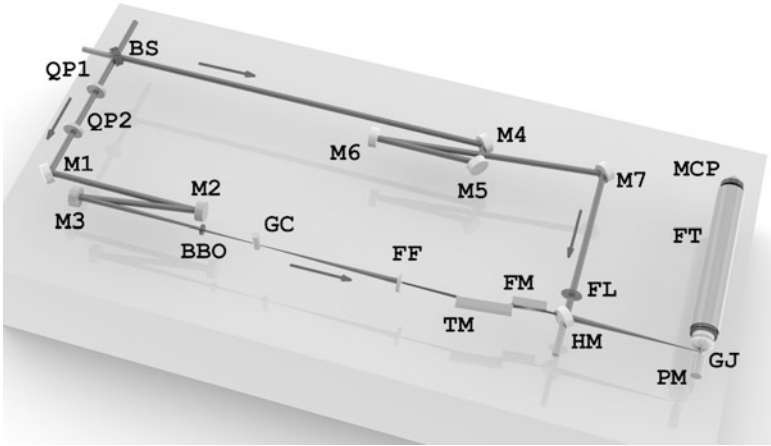


Fig. 19.1 Experimental setup of the new broadband attosecond streak camera. The components are BS: broadband beam splitter; QP1 and QP2: quartz plates; M1–M7: silver mirrors; BBO: second harmonic crystal; GC: gas cell; FF: metal foil as an XUV filter; TM: toroidal mirror; FM: flat mirror; FL: focusing lens for the streaking beam; HM: hole-drilled mirror; GJ: gas jet; PM: permanent magnet; FT: electron flight tube; and MCP: microchannel plate electron detector. The arrows indicate the laser propagation directions in the two arms of Mach-Zehnder interferometer

double optical gating (GDOG) experiments [12, 15]. The beam is focused by two spherical mirrors (M2 and M3) to a Ne gas cell. The generated XUV beam passes through a metal foil to filter out the residual NIR light and to compensate the intrinsic XUV chirp. After focused by a grazing-incidence gold-coated toroidal mirror which reflects more than 30% of XUV photons at energies as high as 200 eV, the XUV beam passes through the hole of a drilled broadband dielectric mirror to a Ne gas jet in the MBES. A gold-coated flat mirror between the toroidal and hole-drilled mirrors reduces the difficulty of the optical alignment. The streaking arm (20% of the total energy), focused by a lens, is recombined with the XUV pulses by the hole-drilled mirror to the same gas jet. The delay between the two arms is controlled by a PZT attached to one of the flat mirrors (M6) in the streaking arm. A 532-nm green laser co-propagates through both arms. The two green beams also recombine at the drilled mirror and propagate in a direction orthogonal to the recombined XUV and streaking NIR beams. The interference fringes of the recombined green beams are used to stabilize the Mach-Zehnder interferometer and to control the delay as well [7].

The second Ne gas target for photoelectron production is located between the entrance of the flight tube and the tip of the strong permanent magnet in the MBES. The photoelectrons produced at the gas target are focused by the non-uniform magnetic field of the MBES and fly through a 3-m-long flight tube. The non-uniform field ensures the detector has a large acceptance angle [24]. It is critical to detect as many electrons as possible in high-energy photo-electron measurements because of the low XUV photon flux and low photon-to-electron conversion efficiency. A pair

of retarding potential plates are placed at the entrance of the flight tube. The flight tube is wrapped with a solenoid coil to produce the weak confining magnetic field. The tube and the coil are further enclosed by a 3-m-long μ -metal tube to shield off the earth magnetic field. A 40-mm-diameter chevron microchannel plate (MCP) is attached at the end of the flight tube to detect photoelectrons. A uniform accelerating potential is applied between the input grid and the MCP front surface to adjust the electron impact energy on the MCP. The signal from the MCP is collected by a data acquisition system (DAQ), which consists of two constant-fraction discriminators (CFD), and a time-to-digital converter (TDC). A computer communicates to the TDC and processes data. A schematic diagram of DAQ is shown in Fig. 19.4. The temporal resolution of the detection system was found to be better than 250 ps [39], which is sufficient for the MBES to achieve an energy resolution of 0.5 eV at 150 eV photoelectron energy to retrieve XUV pulses as short as 25 as. Details of MBES will be discussed in the next section.

19.3 Magnetic-Bottle Time-of-Flight Electron Spectrometer

The conventional device of an electron energy spectrometer is a TOF detector to measure the flight time of the electron from the interaction region where it is produced to a detector placed a distance away. There are three common designs, field free TOF, TOF with uniform magnetic field, and magnetic-bottle TOF. Among them, only the magnetic-bottle TOF can achieve high energy resolution and high collection efficiency simultaneously due to its non-uniform magnetic field. More discussion regarding the different types of electron energy spectrometers can be found elsewhere [4, 18]. Since it is critical to detect as many photoelectrons as possible and we require energy resolution better than 0.5 eV for our broadband attosecond streak camera, as detailed above, we choose the magnetic bottle TOF as our electron energy spectrometer.

19.3.1 Operating Principle

The basic operating principle of MBES is that the non-uniform magnetic field collimates the trajectories of the electrons produced at the interaction region so that the electrons, initially emitted into all directions, form a nearly parallel beam as they fly through the flight tube [10, 18, 19, 24, 30, 31, 35, 38]. The non-uniform field, as the key for the MBES to achieve high energy resolution [5] and collection efficiency [1, 9], consists of a strong field (close to 1 Tesla) near the interaction region produced by a conical-shaped pole piece of an electromagnet or a permanent magnet and a weak field (0.001–0.01 Tesla) produced by a solenoid coil. The Lorentz force of such a field causes each electron to spiral closely around a magnetic field line which goes from the tip of the pole piece to the flight tube (Fig. 19.2). In our spectrometer, a permanent magnet is used to produce the strong field to reduce the complexity of the system.

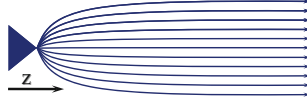


Fig. 19.2 Schematic diagram showing the field lines of the non-uniform magnetic field in MBES. The z-axis is along the flight tube

Let's consider an electron emitted at an angle θ_i , relative to the direction of the flight tube (z-axis), with an energy $E = m_e v^2/2$, where m_e is the electron mass and v is the velocity. The electron then undergoes spiral motion in the field B_i near the interaction region, with an angular momentum $l_i = (m_e^2/e) \cdot (v^2 \sin^2 \theta_i/B_i)$ [24], where e is the electron charge. As the electron enters the region of the weak uniform magnetic field, B_f , in the flight tube, the angular momentum could be conserved if the variation of the field along z-axis is adiabatic. The adiabaticity here means that the change of the field experienced by an electron is negligible in one revolution of the spiral motion. An adiabaticity parameter χ_1 has been introduced to give a quantitative measure, $\chi_1 = (2\pi m_e/e) \cdot (v/B_z^2) |dB_z/dz|$ [24]. It should be less than one to assure that the electron motion is adiabatic. By setting $l_i = l_f$, where l_f is the angular momentum in the flight tube, the longitudinal component of the velocity can be derived as $v_{z,f} = v\sqrt{1 - \sin^2 \theta_i B_f/B_i}$. If the flight distance is L , the electron flight time is then $t = (L/v) \cdot [1 + (\sin^2 \theta_i/2) \cdot (B_f/B_i)]$, which is almost independent of the initial emission direction. The maximum difference of the flight time caused by the emission angle is $\Delta t/t = B_f/(2B_i)$. Since the energy of the electron in such a TOF detector is measured as $E = m_e \cdot (L/t)^2/2$, the spread of the measured energy caused by the difference of the emission angle is $\Delta E/E = 2\Delta t/t = B_f/B_i$ [24]. Therefore, the energy resolution can be improved by increasing B_i or decreasing B_f .

In the region between the pole piece and the flight tube, the magnetic field and its gradient are both strong, and the flight time is significantly different for electrons with different emission angles. It has been found [24] that the flight time spread in this transition region is larger than that in the flight tube and may be decreased if the length of transition region is decreased. However, if this region is reduced while B_i remains unchanged, the gradient $|dB_z/dz|$ and thus χ_1 will increase. These two requirements are contradictive and a compromise must be found.

19.3.2 Calculations of the Magnetic Field and Electron Trajectory

With a given permanent magnet, the quality of the magnetic field is largely determined by the shape of the conical pole piece, i.e., the diameter of the tip and the length (or cone angle). To determine the optimal parameters, we calculate the magnetic field produced by different magnets and pole pieces with SATE software

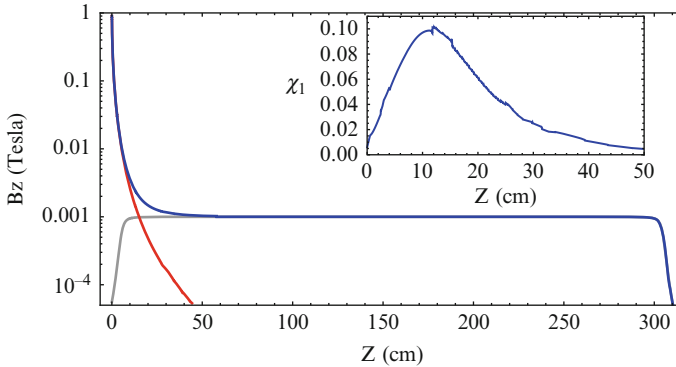


Fig. 19.3 Calculated magnetic field along z -axis (B_z) and the adiabaticity parameter (χ_1) calculated with electron energy of 1 eV (inset). *Red*: field of the permanent magnet and the pole piece; *gray*: the solenoid coil; *blue*: total field

(Field Precision LLC), which is able to calculate the field based on hard and soft ferromagnetic materials with finite element methods.

Based on the considerations of the field strength near the tip, the ease of fabrication and handling of the tip, the adiabaticity parameter of the field, and the experimental constraints on the distance between the tip and the entrance of the flight tube, we choose a permanent magnet (neodymium-iron-boron, NdFeB) 50 mm long and 25 mm in diameter, and a pole piece (soft iron) 12 mm long with a tip of 2 mm diameter. In the final design, $B_i > 0.8$ T while $B_f = 1$ mT. This gives an intrinsic energy resolution of $\Delta E/E = B_f/B_i \approx 0.13\%$. For 1 eV electrons, $\chi_1 < 0.11$ for a transition region of about 5 cm. The total field of the magnetic bottle and its adiabaticity parameter are plotted in Fig. 19.3.

With the non-uniform magnetic field calculated by SATE, we use Simion software (Scientific Instrument Services, Inc.) to simulate the electron trajectories in the MBES. The trajectories of an ensemble of electrons emitted from the interaction point with an isotropic distribution are simulated. The distribution of the trajectories as a function of flight time is extracted, and the temporal and energy spreads at FWHM of the distributions are determined to be 600 ns and 0.44 eV, respectively, for 150 eV electrons. For electrons with lower energies, the energy resolution would be better. This result can be regarded as the intrinsic temporal and energy resolution of the magnetic-bottle TOF. To further improve the energy resolution, a retarding potential is placed at the entrance of the flight tube, to reduce the electron kinetic energies uniformly.

19.3.3 Temporal Resolution of the Detection System

In order to practically realize an energy resolution of 0.5 eV for 150 eV electrons in the MBES, a temporal resolution of 250 ps is required for the MCP and DAQ.

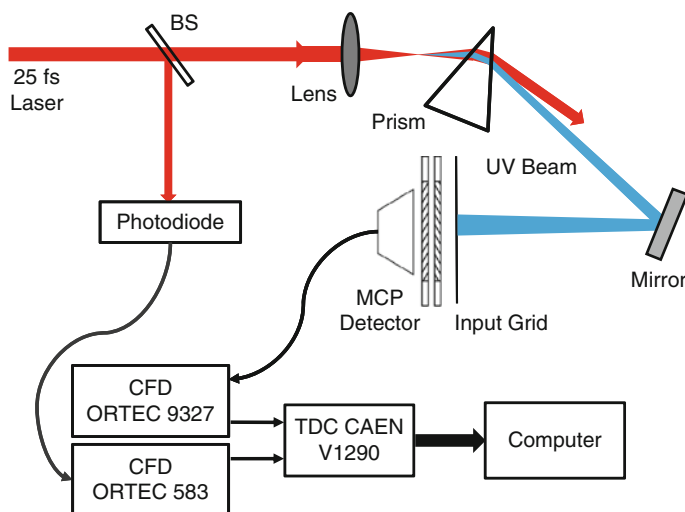


Fig. 19.4 Experimental setup to measure the temporal resolution of the electron detection system. Laser pulses of 25 fs at 800 nm are focused in air to generate UV photons at 267 nm, which is sent to the MCP detector. Part of the laser beam is reflected by a beam splitter (BS) to a photodiode. Signals from the photodiode and the MCP are processed by two CFDs and sent to the TDC. A computer takes the TDC data for analysis

Experimentally, we used UV photons at the 3rd order harmonic wavelength (267 nm) produced by our 25-fs NIR laser as the signal to measure the detector resolution [39].

A schematic diagram of the experimental setup including the detection system is shown in Fig. 19.4 [39]. Laser pulses of 25 fs at 800 nm directly from the multi-pass amplifier [15] are focused in air to produce third harmonic UV light, which is sent to the MCP detector. Part of the laser beam is sent to a fast photodiode. The MCP and photodiode signals are processed by the DAQ system, as described earlier. This DAQ system is identical to that of the electron TOF measurement. The FWHM of the photon “TOF” peak was measured as a function of the MCP voltage, and the best temporal resolution of the detection system including the MCP and DAQ was found to be about 200 ps at an MCP voltage of 1,800 V [39]. This resolution satisfies the requirement for the MBES setup to correctly retrieve the duration of 25-as XUV pulses [8].

19.4 Preliminary Experimental Result

To demonstrate the applicability of the MBES to attosecond science, an attosecond streaking experiment [12, 20, 23] was performed. Isolated attosecond XUV pulses are generated in Ne gas with DOG, filtered by a 150-nm Titanium (Ti) foil, and

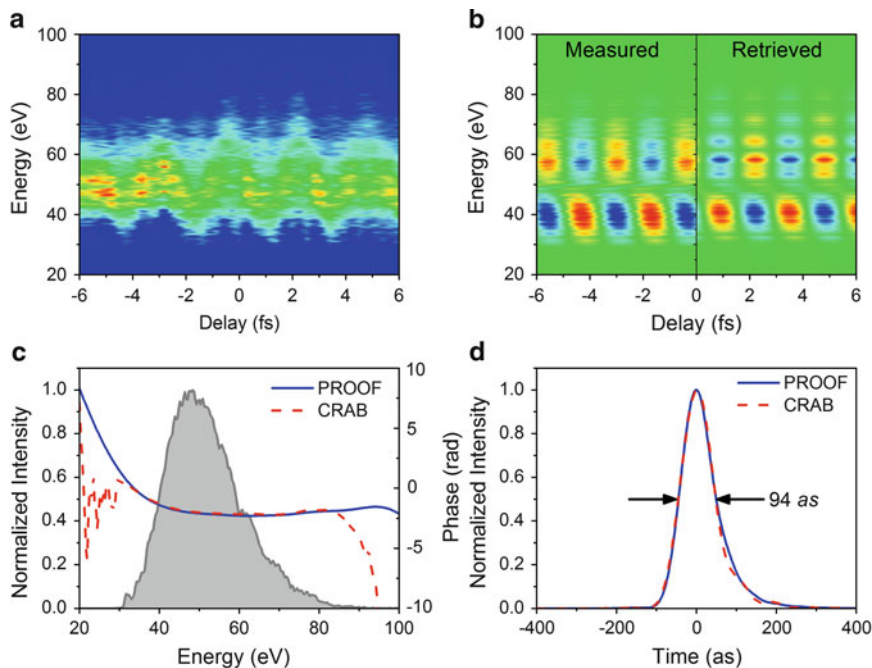


Fig. 19.5 Characterization of a chirped 94-as XUV pulse. (a) Streaked photoelectron spectrogram with 150 nm Ti foil obtained experimentally. (b) laser-frequency oscillation (LFO) trace from the spectrogram in (a) (on the left), along with the retrieved LFO trace (on the right). (c) Photoelectron spectrum (shaded) and retrieved spectral phase from PROOF (blue solid) and FROG-CRAB (red dashed). (d) Retrieved 94-as pulses from PROOF (blue solid) and FROG-CRAB (red dashed)

detected by a second Ne target. The experimental streaking spectrogram is shown in Fig. 19.5a, along with measured and PROOF-retrieved filtered traces showing the amplitude and phase angle of the laser-frequency oscillation in Fig. 19.5b [6]. The PROOF method yields a positively-chirped parabolic phase profile and a pulse duration of 94 as, shown in Fig. 19.5c, d. The FROG-CRAB retrieves similar phase and pulse duration. The transform-limited pulse duration of the spectrum is 83 as. Since the bandwidth is smaller than the central energy of the photoelectrons ($E_0 \approx 50$ and $\text{FWHM} \approx 20$ eV), the Central Momentum Approximation for FROG-CRAB is valid. Therefore, this result shows that, for a spectrum where the CMA is valid, the retrieved attosecond XUV pulses of PROOF and FROG-CRAB have consistent phase profiles and pulse durations. This is the first experimental comparison of these two retrieval methods for a sub-100-as pulse. The consistency of the attosecond XUV pulses retrieved by both PROOF and FROG-CRAB is strong evidence showing that our newly developed attosecond streak camera is able to produce and characterize isolated attosecond pulses.

19.5 Summary

In summary, a new attosecond streak camera based on an MBES is developed. The XUV beam in the new setup is focused by a grazing-incidence gold-coated toroidal mirror, which ensures that the accessible XUV spectrum covers a range of more than 200 eV. The calculations of the non-uniform magnetic field and the electron trajectory show that the MBES has an intrinsic energy resolution of 0.44 eV for 150 eV electrons. The temporal resolution of the detection system including the MCP and DAQ is measured to be better than 250 ps [39] which is sufficient to achieve an energy resolution of 0.5 eV at 150 eV photonelectron energy for the MBES to retrieve XUV pulses as short as 25 as. The preliminary experimental results show that the new attosecond streak camera is able to produce and characterize isolated sub-100-as pulses. The results also show that the also newly developed method, PROOF [6], is able to retrieve an attosecond pulse consistent with the result given by the well-accepted traditional method, FROG-CRAB.

With broader XUV spectrum and better chirp-compensation mechanisms, the new attosecond streak camera, along with the new PROOF retrieval algorithm, will be able to produce and characterize much shorter isolated attosecond pulses, and has the potential to realize an optical pulse as short as one atomic unit of time (25 as). With simple modifications, the new attosecond streak camera can be upgraded to a versatile broadband attosecond XUV apparatus for ultrafast electron dynamics studies with XUV-NIR pump-probe, XUV-XUV pump-probe and transient absorption experiments.

Acknowledgements We acknowledge the technical assistance of A. Rankin, Prof. K. D. Carnes, and Dr. B. Zhao. This material is supported by the U.S. Army Research Office, U.S. Department of Defense, by the Chemical Sciences, Geosciences, and Biosciences Division, U.S. Department of Energy, and by the National Science Foundation.

References

1. C.Y. Cha, G. Ganteför, W. Eberhardt, New experimental setup for photoelectron spectroscopy on cluster anions. *Rev. Sci. Instrum.* **63**, 5661 (1992)
2. Z. Chang, Single attosecond pulse and xuv supercontinuum in the high-order harmonic plateau. *Phys. Rev. A* **70**, 043802 (2004)
3. Z. Chang, Controlling attosecond pulse generation with a double optical gating. *Phys. Rev. A* **76**, 051403(R) (2007)
4. Z. Chang, *Fundamentals of Attosecond Optics* (CRC Press, Boca Raton, 2011)
5. O. Cheshnovsky, S.H. Yang, C.L. Pettiette, M.J. Craycraft, R.E. Smalley, Magnetic time-of-flight photoelectron spectrometer for mass-selected negative cluster ions. *Rev. Sci. Instrum.* **58**, 2131 (1987)
6. M. Chini, S. Gilbertson, S.D. Khan, Z. Chang, Characterizing ultrabroadband attosecond lasers. *Opt. Express* **18**, 13006 (2010)
7. M. Chini, H. Mashiko, H. Wang, S. Chen, C. Yun, S. Scott, S. Gilbertson, Z. Chang, Delay control in attosecond pump-probe experiments. *Opt. Express* **17**, 21459 (2009)

8. M. Chini, H. Wang, S.D. Khan, S. Chen, Z. Chang, Retrieval of satellite pulses of single isolated attosecond pulses. *Appl. Phys. Lett.* **94**, 161112 (2009)
9. J.H.D. Eland, S.S.W. Ho, H.L. Worthington, Complete double photoionisation spectrum of NO. *Chem. Phys.* **290**, 27 (2003)
10. J.H.D. Eland, O. Vieuxmaire, T. Kinugawa, P. Lablanquie, R.I. Hall, F. Penent, Complete two-electron spectra in double photoionization: the rare gases Ar, Kr, and Xe. *Phys. Rev. Lett.* **90**, 053003 (2003)
11. X. Feng, S. Gilbertson, S.D. Khan, M. Chini, Y. Wu, K. Carnes, Z. Chang, Calibration of electron spectrometer resolution in attosecond streak camera. *Opt. Express* **18**, 1316 (2010)
12. X. Feng, S. Gilbertson, H. Mashiko, H. Wang, S.D. Khan, M. Chini, Y. Wu, K. Zhao, Z. Chang, Generation of isolated attosecond pulses with 20 to 28 femtosecond lasers. *Phys. Rev. Lett.* **103**, 183901 (2009)
13. S. Gilbertson, M. Chini, X. Feng, S. Khan, Y. Wu, Z. Chang, Monitoring and controlling the electron dynamics in helium with isolated attosecond pulses. *Phys. Rev. Lett.* **105**, 263003 (2010)
14. S. Gilbertson, H. Mashiko, C. Li, S.D. Khan, M.M. Shakya, E. Moon, Z. Chang, A low-loss, robust setup for double optical gating of high harmonic generation. *Appl. Phys. Lett.* **92**, 071109 (2008)
15. S. Gilbertson, Y. Wu, S.D. Khan, M. Chini, K. Zhao, X. Feng, Z. Chang, Isolated attosecond pulse generation using multicycle pulses directly from a laser amplifier. *Phys. Rev. A* **81**, 043810 (2010)
16. E. Goulielmakis, Z.H. Loh, A. Wirth, R. Santra, N. Rohringer, V.S. Yakovlev, S. Zherebtsov, T. Pfeifer, A.M. Azzeer, M.F. Kling, S.R. Leone, F. Krausz, Real-time observation of valence electron motion. *Nature* **466**, 739 (2010)
17. E. Goulielmakis, M. Schultze, M. Hofstetter, V.S. Yakovlev, J. Gagnon, M. Uiberacker, A.L. Aquila, E.M. Gullikson, D.T. Attwood, R. Kienberger, F. Krausz, U. Kleineberg, Single-cycle nonlinear optics. *Science* **320**, 1614 (2008)
18. H. Handschuh, G. Ganteför, W. Eberhardt, Vibrational spectroscopy of clusters using a “magnetic bottle” electron spectrometer. *Rev. Sci. Instrum.* **66**, 3838 (1995)
19. Y. Hikosaka, T. Aoto, P. Lablanquie, F. Penent, E. Shigemasa, K. Ito, Auger decay of Ne 1s photoionization satellites studied by a multi-electron coincidence method. *J. Phys. B* **39**, 3457 (2006)
20. J. Itatani, F. Quéré, G.L. Yudin, M.Y. Ivanov, F. Krausz, P.B. Corkum, Attosecond streak camera. *Phys. Rev. Lett.* **88**, 173903 (2002)
21. P. Johnsson, R. López-Martens, S. Kazamias, J. Mauritsson, C. Valentin, T. Remetter, K. Varjú, M.B. Gaarde, Y. Mairesse, H. Wabnitz, P. Salières, P. Balcou, K.J. Schafer, A. L’Huillier, Attosecond electron wave packet dynamics in strong laser fields. *Phys. Rev. Lett.* **95**, 013001 (2005)
22. F. Kelkensberg, C. Lefebvre, W. Siu, O. Ghafur, T.T. Nguyen-Dang, O. Atabek, A. Keller, V. Serov, P. Johnsson, M. Swoboda, T. Remetter, A. L’Huillier, S. Zherebtsov, G. Sansone, E. Benedetti, F. Ferrari, M. Nisoli, F. Lépine, M.F. Kling, M.J.J. Vrakking, Molecular dissociative ionization and wave-packet dynamics studied using two-color XUV and IR pump-probe spectroscopy. *Phys. Rev. Lett.* **103**, 123005 (2009)
23. R. Kienberger, E. Goulielmakis, M. Uiberacker, A. Baltuska, V. Yakovlev, F. Bammer, A. Scrinzi, T. Westerwalbesloh, U. Kleineberg, U. Heinzmann, M. Drescher, F. Krausz, Atomic transient recorder. *Nature* **427**, 817 (2004)
24. P. Kruit, F.H. Read, Magnetic field paralleliser for 2π electron-spectrometer and electron-image magnifier. *J. Phys. E* **16**, 313 (1983)
25. Y. Mairesse, F. Quéré, Frequency-resolved optical gating for complete reconstruction of attosecond bursts. *Phys. Rev. A* **71**, 011401(R) (2005)
26. H. Mashiko, S. Gilbertson, M. Chini, X. Feng, C. Yun, H. Wang, S.D. Khan, S. Chen, Z. Chang, Extreme ultraviolet supercontinua supporting pulse durations of less than one atomic unit of time. *Opt. Lett.* **34**, 3337 (2009)

27. H. Mashiko, S. Gilbertson, C. Li, E. Moon, Z. Chang, Optimizing the photon flux of double optical gated high-order harmonic spectra. *Phys. Rev. A* **77**, 063423 (2008)
28. H. Mashiko, C.M. Nakamura, C. Li, E. Moon, H. Wang, J. Tackett, Z. Chang, Carrier-envelope phase stabilized 5.6 fs, 1.2 mJ pulses. *Appl. Phys. Lett.* **90**, 161114 (2007)
29. J. Mauritsson, T. Remetter, M. Swoboda, K. Klünder, A. L'Huillier, K.J. Schafer, O. Ghafur, F. Kelkensberg, W. Siu, P. Johnsson, M.J.J. Vrakking, I. Znakovskaya, T. Uphues, S. Zherebtsov, M.F. Kling, F. Lépine, E. Benedetti, F. Ferrari, G. Sansone, M. Nisoli, Attosecond electron spectroscopy using a novel interferometric pump-probe technique. *Phys. Rev. Lett.* **105**, 053001 (2010)
30. L. Nugent-Glandorf, M. Scheer, D.A. Samuels, V. Bierbaum, S.R. Leone, A laser-based instrument for the study of ultrafast chemical dynamics by soft x-ray-probe photoelectron spectroscopy. *Rev. Sci. Instrum.* **73**, 1875 (2002)
31. A.M. Rijs, E.H.G. Backus, C.A. de Lange, N.P.C. Westwood, M.H.M. Janssen, 'magnetic bottle' spectrometer as a versatile tool for laser photoelectron spectroscopy. *J. Electron. Spectrosc.* **112**, 151 (2000)
32. G. Sansone, E. Benedetti, F. Calegari, C. Vozzi, L. Avaldi, R. Flammini, L. Poletto, P. Villoresi, C. Altucci, R. Velotta, S. Stagira, S.D. Silvestri, M. Nisoli, Isolated single-cycle attosecond pulses. *Science* **314**, 443 (2006)
33. G. Sansone, F. Kelkensberg, J.F. Pérez-Torres, F. Morales, M.F. Kling, W. Siu, O. Ghafur, P. Johnsson, M. Swoboda, E. Benedetti, F. Ferrari, F. Lépine, J.L. Sanz-Vicario, S. Zherebtsov, I. Znakovskaya, A. L'Huillier, M.Y. Ivanov, M. Nisoli, F. Martín, M.J.J. Vrakking, Electron localization following attosecond molecular photoionization. *Nature* **465**, 763 (2010)
34. B. Shan, C. Wang, Z. Chang, High peak-power kilohertz laser system employing single-stage multi-pass amplification. U.S. Patent 7050474, 2006
35. T. Tsuboi, E.Y. Xu, Y.K. Bae, K.T. Gillen, Magnetic bottle electron spectrometer using permanent magnets. *Rev. Sci. Instrum.* **59**, 1357 (1988)
36. H. Wang, M. Chini, S. Chen, C.H. Zhang, F. He, Y. Cheng, Y. Wu, U. Thumm, Z. Chang, Attosecond time-resolved autoionization of argon. *Phys. Rev. Lett.* **105**, 143002 (2010)
37. H. Wang, M. Chini, S.D. Khan, S. Chen, S. Gilbertson, X. Feng, H. Mashiko, Z. Chang, Practical issues of retrieving isolated attosecond pulses. *J. Phys. B* **42**, 134007 (2009)
38. L.S. Wang, C.F. Ding, X.B. Wang, S.E. Barlow, Photodetachment photoelectron spectroscopy of multiply charged anions using electrospray ionization. *Rev. Sci. Instrum.* **70**, 1957 (1999)
39. Q. Zhang, K. Zhao, Z. Chang, Determining time resolution of microchannel plate detectors for electron time-of-flight spectrometers. *Rev. Sci. Instrum.* **81**, 073112 (2010)
40. K. Zhao, C. Wang, X. Feng, S. Gilbertson, S.D. Khan, Z. Chang, Magnetic-bottle electron energy spectrometer for measuring 25 as pulses, in *Second International Conference on Attosecond Physics*. Manhattan, Kansas, 2009. <http://jrm.phys.ksu.edu/Atto-09/>

Chapter 20

Quantum Path Interference in HHG: Impact on Harmonic Polarization and Molecular Imaging

M.Yu. Ryabikin, A.A. Gonoskov, I.A. Gonoskov, and V.V. Strelkov

Abstract In high-order harmonic generation (HHG) from gases, two electronic quantum paths, the so-called “short” and “long” ones, are known to make the dominant contribution to the harmonics in the plateau. While the properties of the contributions from the individual quantum paths usually depend smoothly on the laser field parameters, the dependence of the total microscopic harmonic signal on them is complicated due to the interference of the different quantum paths. Our study shows that the above also holds for the polarization state of high-order harmonics, as well as for the multi-center interference patterns in the harmonic spectra from molecules. It is therefore important to take care of an accurate selection of the contributions from the individual quantum paths in order to produce the XUV radiation with controllable polarization state or correctly extract an information about the molecular structure from the HHG spectra.

20.1 Signatures of Quantum-Path Interference in the Polarization Properties of High-Harmonic Field

Very recently, much attention is paid, both experimentally and theoretically, to the polarization properties of high-order harmonics generated from gases in intense laser field. These studies show that the harmonics generated in elliptically-polarized laser field are elliptically polarized, and the polarization ellipse is rotated by some angle with respect to the polarization ellipse of the fundamental (so called rotation

M.Yu. Ryabikin (✉) · A.A. Gonoskov · I.A. Gonoskov
Institute of Applied Physics of RAS, 46 Ulyanov Street, 603950 Nizhny Novgorod, Russia
e-mail: mike@ufp.appl.sci-nnov.ru; arkady.gonoskov@gmail.com; ivan.gonoskov@gmail.com

V.V. Strelkov
A.M. Prokhorov General Physics Institute of RAS, 38 Vavilova Street, 119991 Moscow, Russia
e-mail: v-strelkov@fpl.gpi.ru

angle). The origin of this rotation is clear already in the framework of the “simple-man” approach [1, 2], which describes HHG as a result of tunneling ionization of the atom by the laser field, free electron motion in this field, and recombination accompanied by the XUV emission upon the return to the parent ion. Thus, according to this approach, the direction of the high harmonic field can be well described as the direction of the momentum of the electron coming back to the origin and generating XUV, as confirmed by the numerical simulation [3]. However, the “simple-man” consideration can hardly predict correctly the harmonic ellipticity.

Recently, we offered an explanation for the origin of the ellipticity of the harmonics generated in atomic gases [3]. The harmonic ellipticity was shown to result from the limited size of the electronic wave packet coming back to the parent ion and generating harmonics: the ellipticity naturally appears when the center of the wave packet misses the parent ion. We have also proposed the generalization of this approach to the molecular case.

In our theoretical approach [3, 4] and 3D numerical simulations [3, 5] we accomplished the separation of short and long quantum paths in the problem of HHG. It allowed us to derive and test very simple analytical equations describing harmonic polarization properties, which turned out to agree well with the numerical results. These equations allow, in particular, clear description of the sub-laser-cycle evolution of the XUV polarization state. The polarization properties of the contributions to the total harmonic field from the short and long electronic quantum paths prove to be very different. The rotation angles of the polarization ellipse given by the short and long paths are of opposite sign; the harmonic ellipticity for the short-path contribution is significantly higher than for the long-path one. It is therefore natural to expect that the interference of these contributions can greatly influence the polarization state of high harmonics. The signatures of quantum-path interference in the polarization properties of high-harmonic field is the focus of the present study.

Our study shows that the quantum-path interference does indeed lead to very irregular behavior of both the rotation angle and the ellipticity of high harmonics with their order and can result in the harmonics with quite counter-intuitive polarization properties.

As an example, Fig. 20.1 plots the numerical results for the ellipticity and rotation angle of high harmonics produced by Ar atoms irradiated by 1300 nm, 2.2×10^{14} W/cm², elliptically polarized laser field. It can be seen that, when the short-path contribution is selected, both the ellipticity and rotation angle vary rather smoothly with the harmonic order; we have checked that their behavior agrees very well with the predictions of the theory [3]. On the contrary, although for the total harmonic signal the general trend of changes in both of these quantities is their absolute values decrease with increasing harmonic order, the deviations from the average of these values are often very significant. For example, whereas the ellipticities of the both dominant quantum paths contributions have the same sign as the fundamental has, in the total response some harmonics have the ellipticity of the opposite sign (i.e., the instantaneous harmonic field and the fundamental field vectors rotate in opposite directions). Our study shows that this anomalous ellipticity originates from the contributions of the quantum paths with the excursion

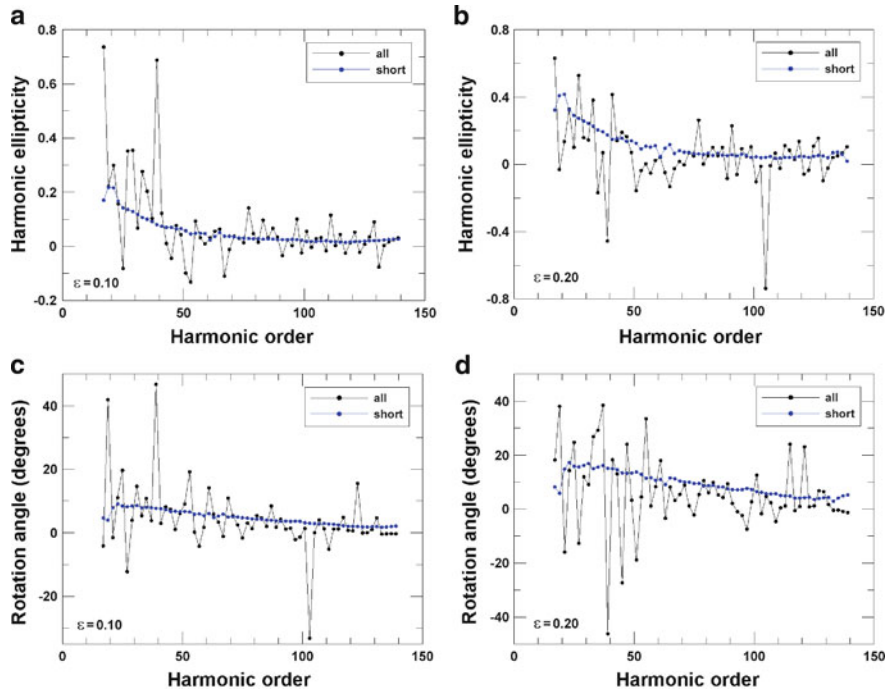


Fig. 20.1 (a, b) Ellipticity and (c, d) rotation angle of high harmonics produced by Ar atoms irradiated by 1,300 nm, 2.2×10^{14} W/cm², elliptically polarized laser field with ellipticity (a, c) 0.1 and (b, d) 0.2. Numerical results for the total signal (*irregular curves*) and short-path contribution (*smooth curves*) are shown

time exceeding optical cycle. To generate high harmonics and attosecond pulses with controllable polarization state, one therefore should take care of an accurate selection of the contributions from the individual quantum paths.

20.2 Modification of Multi-Center Patterns in the Harmonic Spectra from Molecules Due to the Quantum-Path Interference

As the other application of our approach to the electronic quantum-path selection, we studied numerically the impact of the short and long quantum path interference on the two-center interference patterns [6] in the harmonic spectra from H₂⁺ molecular ion. The interference patterns of this kind are known to be highly sensitive to the molecular orientation and structure. Due to this property, multicenter interference in molecular HHG is of interest as a promising means of molecular ultrafast dynamic imaging. The focus of our study is on the laser intensity dependence of

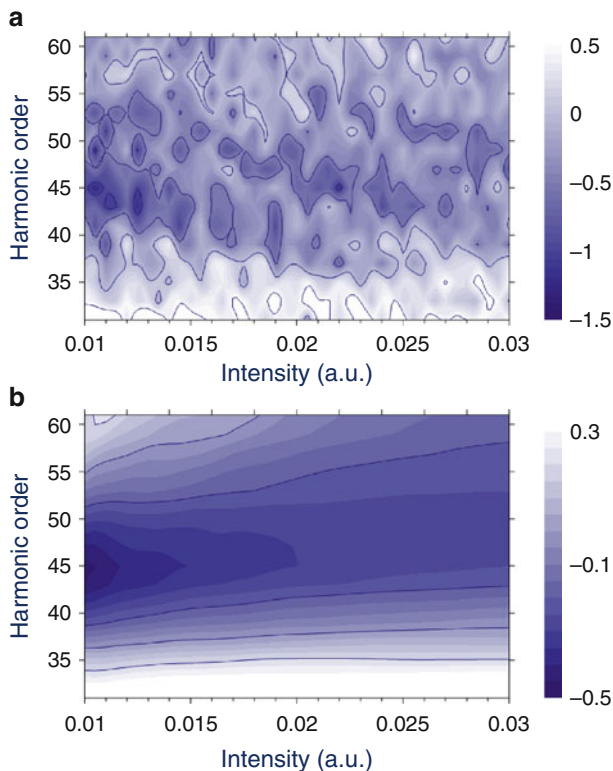


Fig. 20.2 Contour plot of harmonic spectra versus laser intensity for aligned H_2^+ ions (orientation angle 45° , internuclear distance 2 a.u.) irradiated by linearly polarized laser field (wavelength 800 nm). Numerical results for (a) the total signal and (b) the short-path contribution are shown. Harmonic power is plotted on a logarithmic scale

the two-center minimum in the harmonic spectrum, which is the subject of recent controversy [7, 8].

Figure 20.2 shows the results for harmonic spectra from aligned H_2^+ ions in a wide range of laser intensities. One can see that, if no quantum path selection is made, the interplay of the two above-mentioned kinds of interference leads to interference fringes on the plot of the harmonic yield versus laser intensity and thereby to the seeming significant downshifting of the two-center minimum with the laser intensity [9]. On the contrary, when the individual short-path contribution is selected, the position of the two-center interference minimum remains almost unchanged in a full range of laser intensities under study. This emphasizes the importance of selection of the electronic quantum paths for accurate extraction of the information about the molecular structure from the HHG spectra. On the

other hand, this result strengthens the arguments in favor of the many-electron nature of the experimentally observed laser-intensity dependence of the multi-center interference minima.

References

1. P.B. Corkum, Phys. Rev. Lett. **71**, 1994 (1993)
2. K.J. Schafer, B. Yang, L.F. DiMauro, K.C. Kulander, Phys. Rev. Lett. **70**, 1599 (1993)
3. V.V. Strelkov, A.A. Gonoskov, I.A. Gonoskov, M.Yu. Ryabikin, Phys. Rev. Lett. **107**, 043902 (2011)
4. V.V. Strelkov, Phys. Rev. A **74**, 013405 (2006)
5. A.A. Gonoskov, I.A. Gonoskov, arXiv:physics/0607120
6. M. Lein, N. Hay, R. Velotta, J.P. Marangos, P.L. Knight, Phys. Rev. Lett. **88**, 183903 (2002)
7. T. Kanai, S. Minemoto, H. Sakai, Nature **435**, 470 (2005)
8. C. Vozzi, F. Calegari, E. Benedetti, J.-P. Caumes, G. Sansone, S. Stagira, M. Nisoli, R. Torres, E. Heesel, N. Kajumba, J.P. Marangos, C. Altucci, R. Velotta, Phys. Rev. Lett. **95**, 153902 (2005)
9. I.A. Gonoskov, M.Yu. Ryabikin, J. Mod. Opt. **55**, 2685 (2008)

Chapter 21

XUV Interferometry of Attosecond Pulses

Yasuo Nabekawa, Eiji J. Takahashi, Yusuke Furukawa, Tomoya Okino,
Kaoru Yamanouchi, and Katsumi Midorikawa

Abstract We demonstrate the interferometry and Fourier analysis of the attosecond pulse train (APT), which is formed with the Fourier synthesis of multiple high-order harmonic fields in the XUV wavelength region. The ion yield originating from nonlinear interaction of the APT with the nitrogen molecule exhibits the interference fringes of the XUV harmonic fields on the pulse envelope of the APT in the interferometric autocorrelation (IAC) measurement. We have resolved the kinetic energy spectrum in three distinct regions in accordance with the characteristic of the fringe frequency, although the detailed ionization/dissociation process is not clear. Another example of the IAC trace obtained from the deuterium ion dose not show the pulse envelope of the APT, while we can clearly observe the interference fringes of low order harmonic field, instead. We have determined the distinct sequential processes of ionization followed by dissociation with Fourier analysis of these fringes. The available wavelength resolution of the measurement device for the IAC, which we call “attocorrelator,” has been also demonstrated with the linear interferometry.

21.1 Introduction

The recent development of attosecond light sources of coherent XUV/soft X-ray has enabled us to reveal the ultrafast dynamics of electron wavepackets in a range of sub-fs time scale. The researchers in this science field typically utilize the

Y. Nabekawa (✉) · E.J. Takahashi · Y. Furukawa · K. Midorikawa
RIKEN, 2-1 Hirosawa Wako-shi, Saitama 351-0198, Japan
e-mail: nabekawa@riken.jp

T. Okino · K. Yamanouchi
Department of Chemistry, School of Science, the University of Tokyo, 7-3-1 Hongo,
Bunkyo, Tokyo 113-0033, Japan
e-mail: kaoru@chem.s.u-tokyo.ac.jp

attosecond pulse to initiate quantum mechanical motions of matter, then, afterwards, they investigate the temporal evolution of the quantum states by irradiating the laser field synchronized with the attosecond pulses, or vice versa. Sub-fs resolution of this pump-probe experimental scheme is ensured with the stabilized shape of electro-magnetic field in the envelope of the laser pulse [1]. In contrast to this main stream of attosecond science, we have concentrated on exploring the nonlinear interactions of XUV attosecond pulses (attosecond pulse train, APT) [2] because we expect these nonlinear interactions can be utilized for probing attosecond dynamics of matters without the aid of a visible laser field. The lowest order nonlinear interaction, namely, two-photon interaction of XUV light field itself is also an interesting phenomenon in atomic and molecular physics, even though the pulse duration of the field is much longer than 1 fs. In this sense, our autocorrelation (AC) technique of the APT is very important for exhibiting the feature of two-photon double ionization [3], above threshold ionization [4, 5], and Coulomb explosion [6, 7]. We owe our successful observations of the AC traces to our invention of an autocorrelator composed of XUV beam splitter mirrors. Now, we aim to extract the information of matter or XUV light field from the interferometric fringes appearing on the pulse envelope of the AC trace.

In this paper, we demonstrate the interferometry of the APT in the XUV wavelength region utilized for revealing the molecular dissociation processes or the performance of the autocorrelator itself. This idea is based on a simple fact that the linear interaction cannot give the interference fringes in the AC trace because our autocorrelator, which we call “attocorrelator,” makes two replicas of the input APT by spatial division. The interference term with the linear interaction should be disappear in the correlated signal of ions or electrons after the volume integration around the focal point of the two replicas of the APT. Therefore, the interference fringes themselves are the evidence of nonlinear interactions [8].

21.2 Experimental Setup

Our experimental scheme is based on the spatial split of the harmonic beam in order to make two replicas of the APT field needed for IAC measurement. The harmonic beam is reflected near the boundaries of harmonic beam splitter (BS) mirror pair [9] set closely as possible, as shown in Fig. 21.1. Thus, the delay of the lower part of the split harmonic beam can be controlled by adjusting the position of the lower BS mirror with a translation stage. The BS mirror pair significantly reduces the energy of the fundamental laser field owing to the fact that the incident angle to the BS mirror pair is set to the Brewster angle. The pulse energy of the remaining fundamental laser field is estimated to be lower than $1 \mu\text{J}$ after passing through an aperture set behind the BS mirror pair, while the pulse energy of the high-order harmonic fields generated from Xe gas, with a loosely focused geometry of the fundamental laser field, is totally more than $1 \mu\text{J}$. The high-order and remaining fundamental and low order harmonic fields are focused into the molecular beam

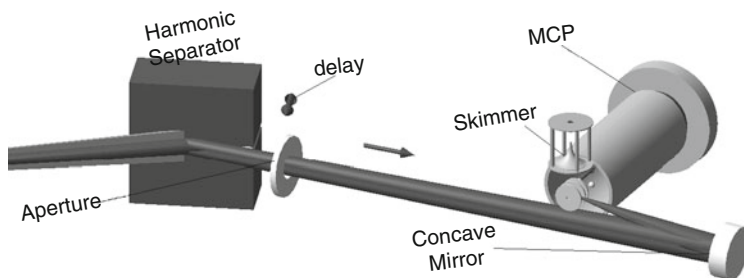


Fig. 21.1 Schematic figure of the experimental setup for the interferometry of the APT

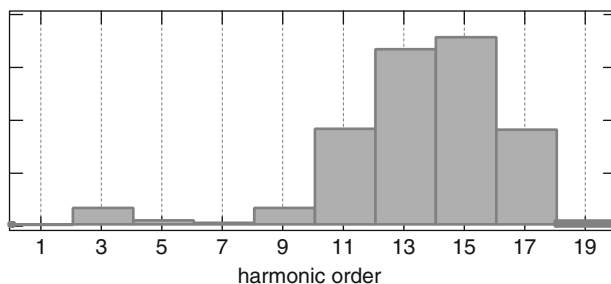


Fig. 21.2 Relative intensity distribution of the harmonic fields at the focal position of the SiC concave mirror

with a concave mirror made of SiC. The intensity distribution of all the light fields components is shown in Fig. 21.2. We assume in this estimation that the beam waist at focal position should be proportional to the wavelength.

The mass spectrum from the nitrogen molecule is obtained from the time-of-flight (TOF) measurement of the accelerated ion with three electrodes under the Wiley–McLaren condition as shown in Fig. 21.1. In contrast, the deuterium ion is angularly resolved with the velocity map imaging (VMI) technique [10]. The chamber for the ion measurement is replaced by an XUV spectrograph in the linear interferometry experiment to find the spatial interference fringes [11].

21.3 IAC Measurement Using Nitrogen Molecule

We show a typical ion TOF mass spectrum at $m/z = 14$ in Fig. 21.3a originating from nitrogen molecule under the irradiation of the APT field. Clear peaks appearing both sides of the central peak in this spectrum are the results from the finite kinetic energy release of N^+ ion yields, while the central peak may contain N_2^{2+} ion and N^+ ion with low kinetic energy that cannot be resolved in our experimental setup.

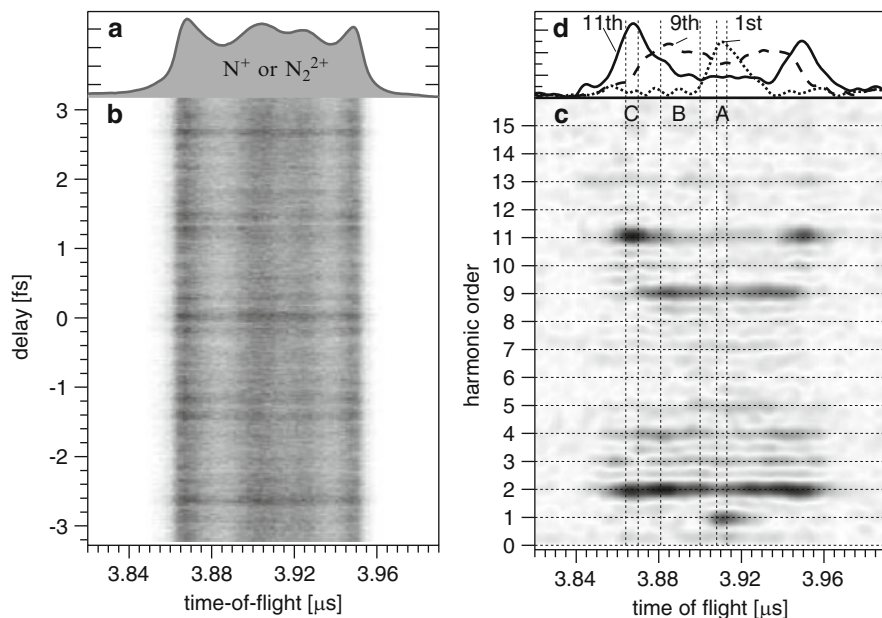


Fig. 21.3 (a): TOF mass spectrum of N^+ or N_2^{2+} ion with two-photon absorption of the APT field. (b): IAC image of the TOF mass spectrum. (c): Fourier transform amplitude of IAC image. (d): Line profiles at the 11th (solid curve), 9th (dashed curve), and 1st (dotted curve) order frequency components in the TOF mass spectrum

This TOF mass spectrum is modulated by scanning delay between the two replicas of the APT field as shown in Fig. 21.3b. Major period of the modulation is the same as the half optical period of the fundamental laser field (1.33 fs) reflecting the autocorrelation of the pulse envelope in the APT. Other fine fringes come from the optical field interferences of the XUV harmonic fields that forms the APT. Thus, we can recognize that this is the IAC of the APT and the ions are certainly generated with nonlinear interaction (two- or more photon absorption) of the APT thanks to the appearance of the interference fringes.

In the previous report [7] on this measurement, we concentrated on revealing the characteristic of the APT from the IAC trace. We now focus on the frequency spectrum of the IAC that should change according to the ionization/dissociation pathways of nitrogen molecule accompanying the nonlinear response against the APT. We have executed Fourier transform of the IAC trace of ion yield at each TOF to find such discrimination of ionization/dissociation pathways, resulting in Fig. 21.3c. We can clearly see that the 11th order harmonic field contained in the APT contributes the yield of the spectral component in region C with large kinetic energy release, while the 9th order harmonic field is relevant to the region A and B. The fundamental laser field affects only the central region A. These features enable us to decompose the TOF mass spectrum at each frequency component as shown in Fig. 21.3d. We can qualitatively identify from this result that there are, at least,

three distinct ionization/dissociation pathways, to which the harmonic components contribute by different ways. Nevertheless, the detailed interaction of the nitrogen molecule with the APT is still not clear because there are too many electronic states of singly and doubly charged ions to be considered for broad spectral range of the APT field. Thus, we have moved on the experiment using one of the simplest molecule, deuterium.

21.4 IAC Measurement Using Deuterium Molecule

Although the title of this section contains the word “IAC,” the D^+ ion yield from deuterium molecule dose not exhibit the pulse envelope of the APT. The correlation trace exhibits only the interference fringes of the fundamental and low order harmonic fields separately depending on the kinetic energy, as depicted in Fig. 21.4a [10]. In order to find Fig. 21.4a, we have integrated the VMI of D^+ ion along the angular coordinate at each delay point, resulting in the kinetic energy spectrum. Then, we have arranged the energy spectrum with ascending order of delay. The traces in Fig. 21.4b are the line profiles of this delay-energy spectrum by averaging in areas around the three pronounced peaks, notated as A, B, and C, in the kinetic energy spectrum of Fig. 21.4a.

Why does the pulse envelope disappear from the correlation? One of the candidates of the reason is that the D^+ ion is created via one photon absorption. This cannot, however, resolve the reason for the appearance of the interference fringes of the low order harmonic fields. In order to address the issue, we should note that the time response of the nonlinear interaction to be utilized for an autocorrelation measurement should be shorter than the pulse duration of the measured pulse, or equivalently, the transition amplitude to all the intermediate states should be similar at the frequency range of the measured optical pulse. Hence, it is natural to consider that there are some kinds of resonance effects smearing out the rapid time response against the APT field in the D_2 molecule. In fact, we know that from literatures that the D_2 molecule can be strongly ionized and situated at the ground bound electronic state ($1s\sigma_g$) with one photon absorption of the 11th order harmonic field contained in the APT field. The transition to the real bound states of the D_2^+ consequently induces the sequential process to the dissociation via transition to the repulsive electronic state ($2p\sigma_u$) by absorbing another photon of the low order harmonic or fundamental laser field. The three peaks in the kinetic energy spectrum of the released D^+ ion is considered to be the map of the particular nuclear distances where the energy gap between the $1s\sigma_g$ and $2p\sigma_u$ states are similar to the photon energies of the fundamental, third, and fifth harmonic fields, respectively. We convinced ourselves that this is the most probable story that can explain the experimental results. The detailed discussion concerning the ionization/dissociation process and the reason why the interference fringes appear in this experiment are presented in [10].

As we have known that the interference fringes can be utilized for resolving the kinetic energy spectrum of nitrogen ion, we have carried out the Fourier analysis of the interference fringes of the D^+ ion with the similar manner. Note that we

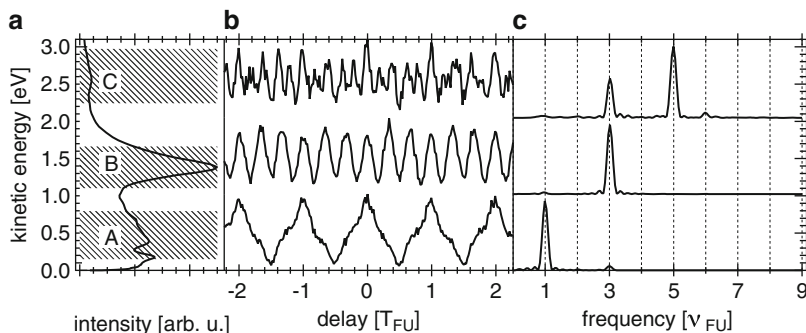


Fig. 21.4 (a): Kinetic energy spectrum of D^+ . (b): Autocorrelation trace obtained by integrating each hatched area located aside in (a). (c): Fourier transform intensity of each autocorrelation trace in (b)

have clearly determined the relevant electronic states of the ion in this experimental scheme in contrast to the experiment for the nitrogen molecule. Another difference from the experiment mentioned in Sect. 21.3 is that the ion spectrum is two-dimensional thanks to the VMI technique (Fig. 21.5a). Hence, we derive the IAC traces from each pixel in the two-dimensional images of the velocity map arranged in accordance with delay, and then we implement the Fourier transform to each IAC trace. After passing through the band-pass filter at the range of the fundamental, third, and fifth harmonic frequencies, the integrated Fourier spectrum at each pixel is placed at the position of the original image, resulting in the three VMI's for each filtering frequency as shown in Fig. 21.5b–d.

Thus, we have clearly decomposed the original VMI depicted in Fig. 21.5a into the three separate VMI's corresponding to the three dissociation pathways at three different nuclear distances by utilizing the Fourier component of the interference fringes. We call this method for identifying and decomposing the ionization/dissociation process of a molecule, nonlinear Fourier transform spectroscopy (NFTS).

21.5 Linear Interferometry of APT: Instrumental Test of “Autocorrelator”

We have been aware of the importance of the interference fringes in the IAC measurement by the experiments mentioned in the previous two sections. Nevertheless, we do not have the technical knowledge about the key instrument in the experiment, that is the “attocorrelator.” Particularly, the resolving power against the wavelength is the most important issue whenever we extend the experimental scheme into the shorter wavelength region. Therefore, we have executed the instrumental test to find the available wavelength-resolving power of the autocorrelator by linear interferometry [11].

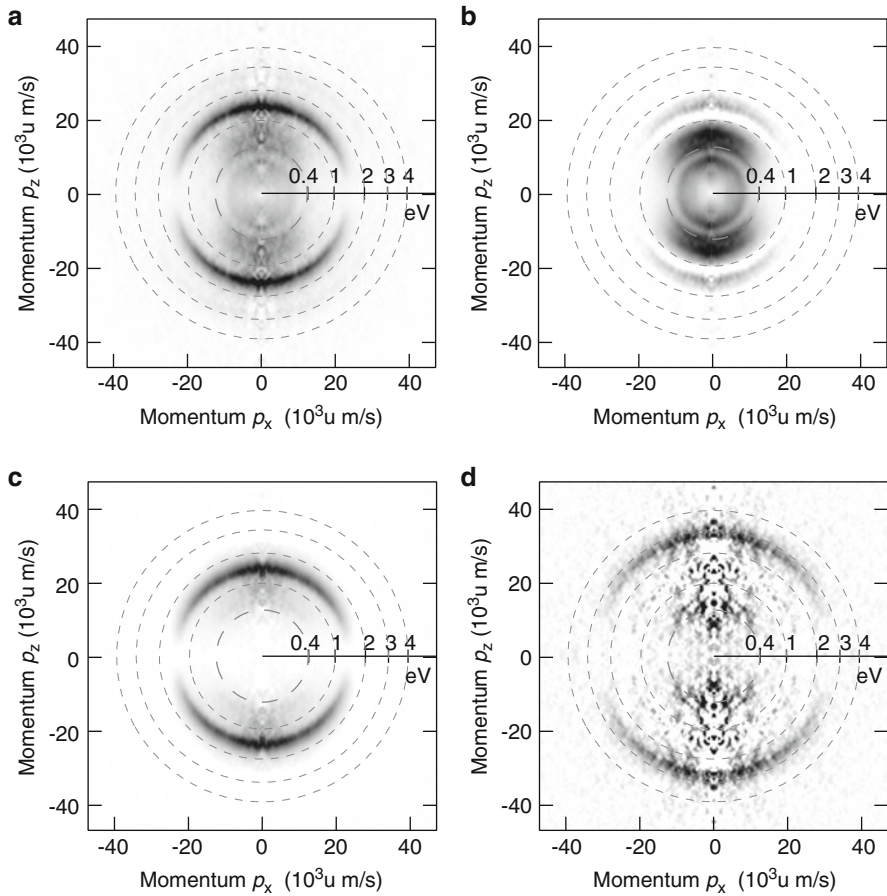


Fig. 21.5 (a): Typical sliced velocity map image of D^+ . (b): Fundamental frequency components in Fig. 21.4a. (c): Third harmonic frequency components in Fig. 21.4a. (d): Fifth harmonic frequency components in Fig. 21.4a

In the experiment, we have just placed an XUV spectrograph instead of the ion spectrometer behind the “attocorrelator” with an appropriate distance, as mentioned in the Sect. 21.2. We can observe the spatial interference fringes near the boundaries of the two replicas of the harmonic beam due to the spatial overlap of the two beams with Fresnel diffraction at some long propagated distance. The spectral-spatial fringes move by altering the delay between the two harmonic beams. Thus, we have acquired the spectrally resolved image of the spatial interference with an X-ray CCD camera attached to the XUV spectrograph at every delay point. An image at each delay is converted to a point in the interference trace at each delay by extracting and integrating the central part of the image along the wavelength coordinate. The scanning step of the piezo actuator mounted on the translation stage is set to 10 nm, so that the given optical path difference for each step should be

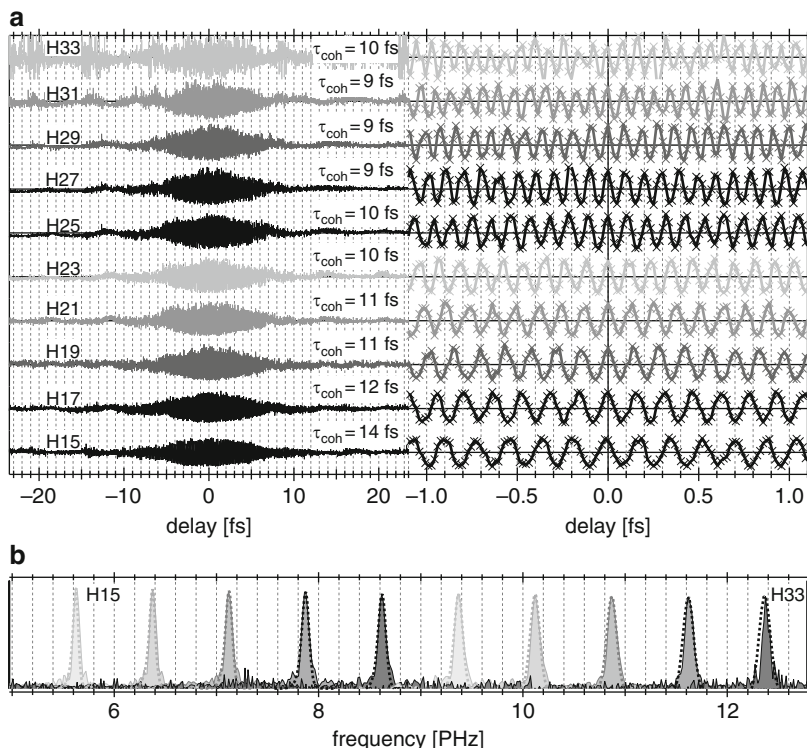


Fig. 21.6 (a): Linear interference traces of HOH fields ranging from the 15th to 33rd orders (*left panel*) and the magnified view of the traces near 0 delay (*right panel*). Coherence time (full width at half maximum of the fitted Gaussian envelope) for each trace is annotated in the figure. (b): Fourier transform amplitude of each interference traces (*hatched area*) and the measured spectrum of each harmonic field (*dotted curve*)

approximately ~ 5 nm due to the large incident angle (75°) to the BS mirror pair. We use Ar, instead of Xe, as nonlinear medium for the high-order harmonic generation in order to shorten the cutoff wavelength of the high-order harmonic fields until the reflectivity of the Si BS mirror is notably decreased.

The resultant interference traces are depicted in Fig. 21.6. We can clearly observe the interference fringes of the ten harmonic fields ranging from the 15th to 33rd orders in the magnified view of the figure. Thus, we conclude the resolving power of the autocorrelator consisting of the Si BS mirror pair is strong enough for all the harmonic wavelength range, which can be efficiently reflected from the Si surface at an incident angle of 75° , namely the range from 60 to 24 nm. In addition to the proof for the resolving power, the resultant interference trace give us one of the most basic features of the interference. As the scanning range of the delay is sufficiently wider than the coherence time of each harmonic field, we can find the spectrum by Fourier transforms of these traces as shown in Fig. 21.6. This is, to the best of my knowledge, the first demonstration of the full scanning Fourier spectroscopy of the

XUV harmonic field the wavelength of which is shorter than 30 nm. Even though the experimental result may be classified into just a consequence of the classical optics, we should notice the importance of the Fourier spectroscopy of vacuum ultraviolet (VUV) or XUV light field as Nelson de Oliveira and coworkers point out in [12], which is a report on the VUV Fourier spectroscopy using a synchrotron radiation.

21.6 Summary and Prospects

We have demonstrated nonlinear and linear interferometric experiments using the APT. In particular, we have successfully found the ionization/dissociation pathways of D^+ by using the NFTS technique. The NFTS, however, gives us only the stationary information of the interaction concerned with the ion yield because it is intrinsically an analysis in frequency domain. Actually, we cannot specify the temporal delay of the excitation to the $2p\sigma_u$ after the preparation of the $1s\sigma_g$ state with one-photon ionization of deuterium molecule, nor any other time evolutions of the quantum states for electrons and nuclei. Hence, the NFTS should be more effective tool if we combined it with another information in time domain which may be provided by extending the scanning range of delay or shortening the pulse durations of the fundamental laser and APT fields [13].

References

1. F. Krausz, M. Ivanov, *Rev. Mod. Phys.* **81**, 163 (2009)
2. P. Antoine, A. L'Huillier, M. Lewenstein, *Phys. Rev. Lett.* **77**, 1234 (1996)
3. Y. Nabekawa, H. Hasegawa, E.J. Takahashi, K. Midorikawa, *Phys. Rev. Lett.* **94**, 043001 (2005)
4. N. Miyamoto, M. Kamei, D. Yoshitomi, T. Kanai, T. Sekikawa, T. Nakajima, S. Watanabe, *Phys. Rev. Lett.* **93**, 083903 (2004)
5. Y. Nabekawa, T. Shimizu, T. Okino, K. Furusawa, H. Hasegawa, K. Yamanouchi, K. Midorikawa, *Phys. Rev. Lett.* **96**, 083901 (2006)
6. T. Okino, K. Yamanouchi, T. Shimizu, K. Furusawa, H. Hasegawa, Y. Nabekawa, K. Midorikawa, *Chem. Phys. Lett.* **432**, 68 (2006)
7. Y. Nabekawa, T. Shimizu, T. Okino, K. Furusawa, H. Hasegawa, K. Yamanouchi, K. Midorikawa, *Phys. Rev. Lett.* **97**, 153904 (2006)
8. Y. Nabekawa, K. Midorikawa, *New J. Phys.* **10**, 025034 (2008)
9. E.J. Takahashi, H. Hasegawa, Y. Nabekawa, K. Midorikawa, *Opt. Lett.* **29**, 507 (2004)
10. Y. Furukawa, Y. Nabekawa, T. Okino, S. Saugout, K. Yamanouchi, K. Midorikawa, *Phys. Rev. A* **82**, 013421 (2010)
11. Y. Nabekawa, T. Shimizu, Y. Furukawa, E.J. Takahashi, K. Midorikawa, *Phys. Rev. Lett.* **102**, 213904 (2009)
12. N. de Oliveira, M. Roudjane, D. Joyeux, D. Phalippou, J.C. Rodier, L. Nahon, *Nat. Phys.* **5**, 149 (2011)
13. Y. Nabekawa, A. Amani-Eilanlou, Y. Furukawa, K. Ishikawa, H. Takahashi, K. Midorikawa, *Appl. Phys. B* **101**, 523 (2010)

Chapter 22

Exploiting Energetic XUV Super-Continua

P. Tzallas, E. Skantzakis, L.A.A. Nikolopoulos, and D. Charalambidis

Abstract We report (a) the observation of two-XUV-photon direct double ionization, while the two-XUV-photon sequential channel is open, (b) a second order autocorrelation of an ultra-broadband XUV continuum and (c) an XUV-pump–XUV-probe study of an induced atomic coherence with 1fs scale temporal resolution.

22.1 Introduction

During the last decade we have been systematically developing elements, including methods and instrumentation, towards coherent XUV sources, emitting intense pulses of ultra-short pulse duration. As a practical measure of the high intensity of the pulses we consider the feasibility of inducing and observing non-linear XUV processes. At the same time the term ultra-short addresses sub-fs pulse durations. The choice of this research target relays on the appropriateness and necessity of non-linear XUV processes in (a) attosecond (as) pulse metrology, (b) XUV-pump–XUV-probe studies of ultrafast dynamics, (c) reaching highest 4D (spatiotemporal)

P. Tzallas

Foundation for Research and Technology – Hellas, Institute of Electronic Structure and Laser,
P.O. Box 1527, GR-71110 Heraklion (Crete), Greece
e-mail: ptzallas@iesl.forth.gr

E. Skantzakis · D. Charalambidis (✉)

Foundation for Research and Technology – Hellas, Institute of Electronic Structure and Laser,
P.O. Box 1527, GR-71110 Heraklion (Crete), Greece

Department of Physics, University of Crete, P.O. Box 2208, GR71003 Heraklion (Crete), Greece
e-mail: chara@iesl.forth.gr

L.A.A. Nikolopoulos

School of Physical Science, Dublin City University, Glasnevin, Dublin 9, Ireland

resolution and (d) exploring new physics in inner-shell non-linear or even strong field processes. We consider the above as an important development route of attoscience that will soon strongly represented in the field. In particular such goals are recently targeted by new large scale research infrastructures on European or even global level.

Our 10 years long developments are based on frequency upconversion of many cycle high peak power fs laser fields through the process of harmonic generation in gas or laser surface plasma media. Within this framework energetic attosecond pulse trains have been produced [1, 2] through which two-XUV-photon single and double ionization of atoms became observable [3, 4]. The processes have been soon exploited in the first direct and unambiguous quantitative measurement of an asec pulse train [1, 5], utilizing the successfully developed intensity volume second order autocorrelation (second order IVAC) technique. Some evidence of the necessity and importance of this technique was recently provided in a comparative study between asec pulse metrology techniques [6]. The highest ever attosecond train energy at the source of 40 μJ has been obtained by surface plasma harmonics [2], an approach with great perspectives for even relativistic XUV intensities [7].

For time domain applications isolated asec pulses are highly advantageous compared to asec pulse trains. Towards overcoming the lack of energetic isolated sub-fs pulses the interferometric polarization gating technique (IPG) has been developed [8, 9], demonstrating emission of sub-100 nJ coherent ultra-broadband XUV continua, supporting asec confinement, from a gas target interacting with many cycle high peak power laser pulses. These energy levels are sufficient to induce observable two-XUV-photon ionization. In this contribution we present the main intricacies of the very recently observed two-XUV-photon direct double ionization of Xe and its exploitation in the measurement of the temporal width of the XUV continuum. We further elaborate on the first XUV-pump–XUV-probe experiment in the temporal scale of 1 fs, tracking the evolution of an induced atomic coherence i.e. of a coherent superposition of a dense manifold of autoionizing states that are single photon resonant with part of the broad XUV spectrum.

22.2 Results and Discussion

For the experiment, continuum XUV radiation spanning the range 15–24 eV was used and was generated through IPG and harmonic generation in xenon. The experimental apparatus can be found elsewhere [10]. The XUV beam was focused into a xenon gas jet at intensities between 10^{13} and 10^{14} W/cm². Ions produced have been detected through mass spectroscopy. The set up allowed the formation of two XUV pulses delayed to each other with a variable delay [1] and thus time resolved measurements could be implemented. Figure 22.1 shows an ion mass spectrum. The spectrum is dominated by a strong Xe⁺ mass peak, while a small Xe²⁺ peak is clearly observable. For the given XUV spectrum singly ionized Xenon species are produced through single photon absorption, while doubly ionized species require absorption of two-photons.

Fig. 22.1 Xe ion mass spectrum

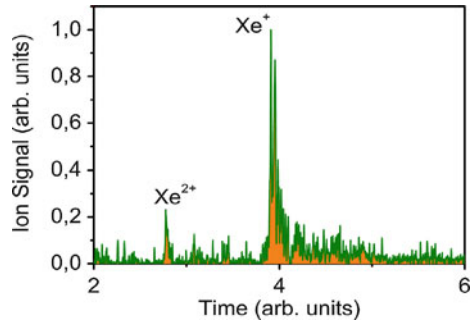
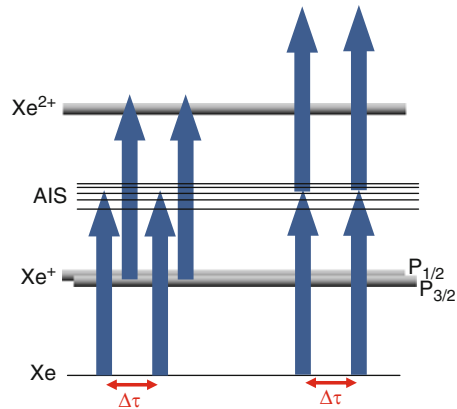
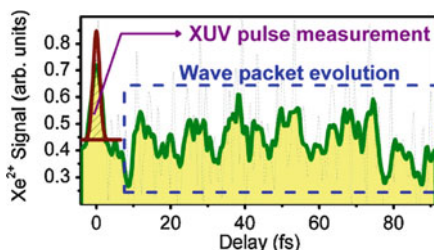


Fig. 22.2 Ionization scheme of Xe



The ionization scheme under investigation is shown in Fig. 22.2. Two conceptually different paths may lead to double ionization. In the first one single photon absorption singly ionizes xenon populating the two fine structure levels $P_{3/2}$ and $P_{1/2}$ of the ionic ground state. Because of the large bandwidth and thus the short pulse duration (see below) Xe^{+} is formed before the spin-orbit coupling occurs (precession period of 3.2 fs larger than the pulse duration) a coherent superposition of the two states is formed. Population of the lowest excited states of the ion may also occur by the very far high energy wing of the spectrum. The populated ionic states may then absorb a second photon from the high energy part of the spectrum doubly ionizing Xe. The process is known as sequential two-photon double ionization (SDI) as electrons are ejected one by one, without requiring any correlation between them for the process to happen. Each of the two steps is proportional to the corresponding cross-section σ_1 and σ_2 and the interaction time i.e. the pulse duration τ . Thus the Xe^{2+} yield produced by the sequential process is $\propto \sigma_1 \cdot \sigma_2 \cdot \tau^2$. The second process is the direct double ionization process (DDI) in which no intermediate Xe^{+} ions are formed. One or two electrons are excited by single photon absorption to a virtual state bringing the atom above the single ionization threshold, while subsequent absorption of a second photon brings the

Fig. 22.3 Measured temporal trace



atom above the second ionization threshold. In this process electron–electron correlation may play a major role. Furthermore absorption of the second photon has to occur before the system decays to $\text{Xe}^+ + e^-$. The Xe^{2+} yield of this process is $\propto \sigma^{(2)} \cdot \tau$, $\sigma^{(2)}$ being the generalized two-photon double ionization cross section of Xe, the value of which is not accurately known. Traditionally the sequential process is considered to be the by far dominant double ionization process. This is because for the commonly available pulse durations at intensities that can two-photon ionize an atom $\sigma_1 \cdot \sigma_2 \cdot \tau > \sigma^{(2)}$. However, for pulse durations of the order of 1 fs or shorter $\sigma_1 \cdot \sigma_2 \cdot \tau$ may become smaller than $\sigma^{(2)}$ forcing two-photon double ionization to occur through the direct process.

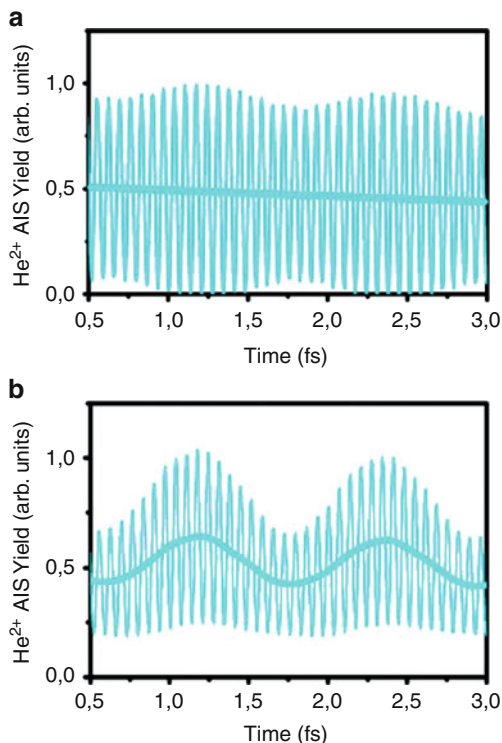
Figure 22.3 shows the measured ion yield as a function of the delay between the two XUV pulses. It consists of two parts. The first is for delays around zero, where a pronounced maximum is observed and where the two pulses are overlapping in time, i.e. it is an autocorrelation (AC) of the XUV continuum. Note that the SDI process would result in the square of the first order AC, while the DDI is a second order AC. The coherence time of the given XUV spectrum is 420 as. Thus the square of the AC should have a width of ~ 420 as. The almost five times longer measured width of the AC proves that this part of the spectrum is a second order AC and thus that we have reached the temporal regime in which DDI is becoming the dominant process. The above argument can be amended with considerations about the measured contrast of the AC trace given elsewhere [10, 11]. Due to the non stable carrier envelope phase (CEP) in our experiment the XUV pulses vary from shot to shot from single to double peak structure. Thus the duration τ_{XUV} of the isolated XUV pulses (whenever they are emitted) can be given only with a large error $\tau_{XUV} = 1.5^{+0.2}_{-0.7}$ [10, 11].

The second part of the trace depicts a beating structure of many frequencies. The origin of this part is in the single photon excitation of a manifold of doubly excited and inner-sub-shell excited autoionizing states of xenon. Single photon absorption excites a coherent superposition of these decaying states. The excited one- and two-electron wavepackets undergo a multi-frequency oscillatory evolution and “slow” autoionization decay. The second delayed XUV pulse excites a replica of the wave packet that interferes with the evolved first one and thus controls the excitation. At the same time, in one of the possible quantum pathways it brings the first wave packet above the second ionization threshold, thus probing through double ionization, its dynamics in a XUV-pump–XUV-probe sequence. Fourier

transform (FT) of the temporal trace reveals the frequency differences between the autoionizing states as at the available temporal resolution their excitation frequencies (Ramsey fringes) are too high to be resolved. The tracking of the dynamics of the atomic coherence and the ultra-broadband FT spectroscopy are discussed in detail elsewhere [10,11]. If the experiment would be a two color pump-probe experiment one would expect to see the low frequency beating because the first color excites an atomic coherence and the second one only probes its evolution (quantum beats). In the present one color experiment though both pulses excite and both ionize thus complicating the situation. The excited coherence by the first pulse evolves and thus the second pulse may enhance or decrease excitation. This affects the double ionization in turn. Suppose for simplicity that we deal with two coherently excited states and that the high excitation frequencies are resolvable. Assuming only excitation and double ionization (1 + 1 double ionization) the measured Ramsey fringes would depict beating symmetric with respect to the line corresponding to the signal at delays $\rightarrow \infty$. In an experiment that cannot resolve the high frequency the signal would average to a straight line with no signature of low frequency beating. What is missing in this consideration though are Raman couplings between that two states. Because the bandwidth of the radiation is larger than the separation of the two states, the two states are coupled through Raman processes. Since these couplings go through a continuum they cause (a) periodic redistribution of the populations of the two states with a period equal to the inverse of the frequency separation of the states and (b) periodic modification of the induced atomic coherence with the same period. Population redistribution causes the two interfering channels coupling the two states with the same final states in the double continuum to have amplitudes periodically varying at the above frequency. This together with the periodically varying atomic coherence introduces an asymmetry in the Ramsey fringes that maintains the beating structure as a signal modulation even when the high frequency fringes are not resolved. The situation is shown in Fig. 22.4 for the 2s2p and 2s2p states of He. In the left panel no Raman coupling through the double continuum is considered, while in the right one the calculation includes this Raman coupling. Periodic population redistribution allows also tracking of the evolution of the atomic coherence even looking not at interfering channels but simply through single channel absorption spectroscopy [12]. The issue of the observation of the low frequency beating was subject of discussion in IR femtosecond pump-probe experiments [13–15].

Finally the drawback of non stable CEP can be surmounted by tagging the measured spectra with the on line measured CEP value. An approach allowing this tagging has been recently demonstrated [16]. Most probably in the presented averaged spectra there are isolated asec pulses that can be tagged by the CEP value. Relevant work is in progress. In this sense the presented work is a precursor of the era of non-linear XUV process induced solely by isolates asec pulses, and their applications in asec pulse metrology and XUV-pump-XUV-probe experiments with sub-fs resolution.

Fig. 22.4 Calculated beating signals in He (2s2p and 2s3p autoionizing states) without (a) and with (b) Raman couplings



Acknowledgements This work is supported in part by the European Commission programs Laser-Lab Europe-ULF and ALADIN (Grant Agreement No. 228334), ATTOFEL (Grant Agreement No. 238362), FASTQUAST (PITN-GA-2008-214962), ELI-PP (Grant Agreement No. 212105) and FLUX (Contract No. PIAPP-GA-2008-218053) of the 7th FP. We thank G. Konstantinidis and A. Kostopoulos for their assistance in developing special optical components. L.A.A.N. acknowledges support from COST CM0702 action and ICHEC at Dublin.

References

1. P. Tzallas, D. Charalambidis, N.A. Papadogiannis, K. Witte, G.D. Tsakiris, *Nature* **426**, 267 (2003)
2. Y. Nomura, R. Hörlein, P. Tzallas, B. Dromey, S. Rykovanov, S. Major, J. Osterhoff, S. Karsch, M. Zepf, D. Charalambidis, F. Krausz, G.D. Tsakiris, *Nat. Phys.* **5**, 124 (2009)
3. N.A. Papadogiannis, L.A.A. Nikolopoulos, D. Charalambidis, P. Tzallas, G. Tsakiris, K. Witte, *Phys. Rev. Lett.* **90**, 133902 (2003)
4. E. Benis, D. Charalambidis, T.N. Kitsopoulos, G.D. Tsakiris, P. Tzallas, *Phys. Rev. A* **74**, 051402 (2006)
5. P. Tzallas, D. Charalambidis, N.A. Papadogiannis, K. Witte, G.D. Tsakiris, *J. Mod. Opt.* **52**, 321 (2005)

6. J. Kruse, P. Tzallas, E. Skantzakis, C. Kalpouzos, G.D. Tsakiris, D. Charalambidis, *Phys. Rev. A* **82**, 021402(R) (2010)
7. G.D. Tsakiris et al., *New J. Phys.* **8**, 19 (2006)
8. P. Tzallas, E. Skantzakis, C. Kalpouzos, E. Benis, G.D. Tsakiris, D. Charalambidis, *Nature Phys.* **3**, 846 (2007)
9. E. Skantzakis, P. Tzallas, C. Kalpouzos, D. Charalambidis, *Opt. Lett.* **34**, 1732 (2009)
10. P. Tzallas, E. Skantzakis, L.A.A. Nikolopoulos, G.D. Tsakiris, D. Charalambidis, *Nat. Phys.*, published on line 3 July (2011). doi:10.1038/NPHYS2033
11. P. Tzallas, E. Skantzakis, D. Charalambidis, *J. Phys. B* (submitted)
12. E. Goulielmakis et al., *Nature* **466**, 739 (2010)
13. L.D. Noordam, D.I. Duncan, T.F. Gallagher, *Phys. Rev. A* **45**, 4734 (1992)
14. R.R. Jones et al., *Phys. Rev. Lett.* **71**, 2575 (1993)
15. V. Blanchet et al., *J. Chem. Phys.* **108**, 4862 (1998)
16. P. Tzallas, E. Skantzakis, D. Charalambidis, *Phys. Rev. A* **82**, 061401(R) (2010)

Chapter 23

The Influence of Plasma Defocusing in High Harmonic Generation

Chien-Jen Lai, Kyung-Han Hong, and Franz X. Kärtner

Abstract We numerically investigate the influence of plasma defocusing in high harmonic generation (HHG) by solving the first-order wave equation in an ionized medium. To quantitatively analyze of the influence of plasma defocusing, we define an enhancement factor that considers the macroscopic propagation effects including phase-matching and reabsorption. While degrading the driver pulse intensity, plasma also has a strong impact on HHG phase-matching and efficiency. With the aid of the scaling relation between the single atom efficiency and the HHG driver wavelength, our results give an estimate of HHG efficiencies with different driver wavelengths and show a limited HHG efficiency in high density media.

23.1 Introduction

The rapid progress made in optical parametric amplification and optical parametric chirped-pulse amplification technologies has been pushing the cutoff of HHG towards higher photon energy by providing ultrashort pulses with center wavelengths in near- or mid-infrared (IR) range [2] that is longer than $0.8 \mu\text{m}$ of

C.-J. Lai (✉) · K.-H. Hong
Department of Electrical Engineering and Computer Science and Research Laboratory of Electronics, Massachusetts Institute of Technology, 77 Massachusetts Avenue, Cambridge, MA 02139, USA
e-mail: cjlai@mit.edu; kyunghan@mit.edu

F.X. Kärtner
Department of Electrical Engineering and Computer Science and Research Laboratory of Electronics, Massachusetts Institute of Technology, 77 Massachusetts Avenue, Cambridge, MA 02139, USA

Center for Free-Electron Laser Science, DESY, and Department of Physics, University of Hamburg, 22607 Hamburg, Germany
e-mail: kaertner@mit.edu

Ti:sapphire lasers. However, the longer driving wavelength also results in a worse single-atom efficiency (SAE) of HHG that is proportional to $\lambda^{-(5\sim 6)}$ [4, 9], where λ is a driving wavelength. A straightforward way of compensating the low SAE is to increase the medium density. For low atomic density the phase-matched HHG is easy to achieve, and the efficiency can be enhanced quadratically with pressure, but plasma defocusing starts to become important as the free electron density increases. This effect not only decreases the cutoff photon energy but also shortens the interaction length for HHG. Although many HHG experiments have emphasized the importance of plasma defocusing, a quantitative discussion has been missing. In this work, we numerically investigate plasma defocusing on IR pulse propagation and discuss how it affects HHG.

23.2 Numerical Model for Plasma Defocusing

Our numerical analysis first calculates how an optical pulse propagates and interacts with HHG gas media. In the slowly evolving wave approximation, a first order propagation equation adapted from [5] is employed in our model:

$$\frac{\partial E}{\partial z} = \frac{i}{2k} \nabla_{\perp}^2 E + i \frac{k}{2} n_2 \varepsilon_0 c |E|^2 E - \frac{1}{2c} \int_{-\infty}^{\tau} \omega_p^2 E d\tau' - \frac{I_p}{2c \varepsilon_0 \text{Re}(E)^2} \frac{\partial \rho}{\partial \tau} E, \quad (23.1)$$

where E is the complex representation of the electric field; z and τ are the propagation distance and the retarded time in the retarded time frame respectively; k is the wave-vector at the carrier frequency; n_2 is the nonlinear index of refraction; ω_p is the plasma frequency; I_p is the ionization potential of the atom; ρ is the number density of the ionized atoms. Dispersion and other nonlinear effects are neglected because the medium under consideration is a short gas jet. The ionization rate $\partial \rho / \partial \tau$ is given by the ADK formula [1]. Because of cylindrical symmetry, E is a function of z , τ , and the radial coordinate r .

Figure 23.1 shows the peak intensity and ionization level distribution when a 2.5 mJ, 40 fs, 2 μm laser pulse propagates from $-z$ to $+z$ through a He jet with three different pressures. The laser pulse is focused to an intensity of $7 \times 10^{14} \text{ W/cm}^2$ at the center of the jets. Figure 23.1a–c shows the peak intensity of the pulse during propagation. In Fig. 23.1a, the gas density is small, so the plasma does not have too much impact on the pulse. As the pressure becomes higher in Fig. 23.1b, c, plasma defocusing starts to play an important role. A drop of intensity near the center of the jet can be seen. Figure 23.1d–f shows the distribution of the ionization level (i.e., the fraction of atoms that are ionized). While the ionization in Fig. 23.1d occurs widely across the jet, the ionizations in Fig. 23.1e and f happen mostly before the focus. In the latter situation, the high-density center of the gas jet does not help HHG but reabsorbs the high harmonic photons instead.

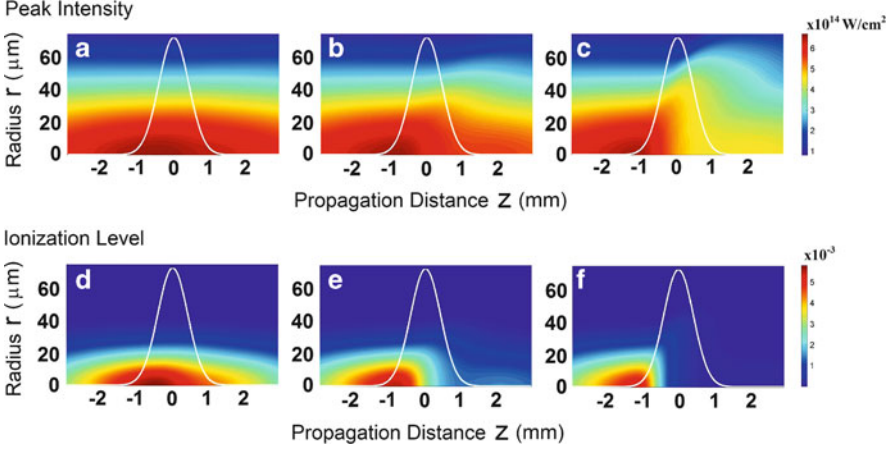


Fig. 23.1 Numerical results of the 2 μm laser pulse propagation toward the $+z$ direction through a He gas jet. The upper row shows the peak intensity when the peak pressure at the jet is (a) 0.1 bar, (b) 1 bar, and (c) 10 bar. The Gaussian curves illustrate the relative pressure profile of the jet. The lower row shows the ionization level when the pressure is (d) 0.1 bar, (e) 1 bar, and (f) 10 bar

23.3 Phase-Matching and HHG Enhancement

To quantitatively discuss the influence of plasma defocusing, we generalize the analysis of [3] to three dimensional cases and result in the following integral:

$$\xi \equiv \int 2\pi r dr \int d\tau \left| \int_{-\infty}^L \sqrt{w} P(z) \exp[iz\Delta k_q(r, z, \tau)] \exp[-\beta(L-z)] dz \right|^2, \quad (23.2)$$

where $w = w(r, z, \tau)$ is the ionization rate given by the ADK formula; $P(z)$ is the medium pressure; $\Delta k_q = qk_1 - k_q$ is the mismatch between the fundamental and the q th harmonic wave-vectors; β represents the absorption of the harmonics. The integral over z is due to the coherent addition of the high harmonic field generated over the non-uniform pressure $P(z)$. Its magnitude square would be proportional to the harmonic intensity generated from the point (r, τ) in the parameter space. Then, the integrals over r and τ consider the HHG contribution from every part of the driver pulse and result in the total amount of high-harmonic energy in a given harmonic. The calculation of Δk_q considers neutral atom dispersion, plasma dispersion, the geometric phases, and the dipole phase. The depletion of the ground states is neglected. We define the integral part of (23.2) as the enhancement factor ξ . It comprises the propagation effects of HHG and is proportional to the high-harmonic photon energy.

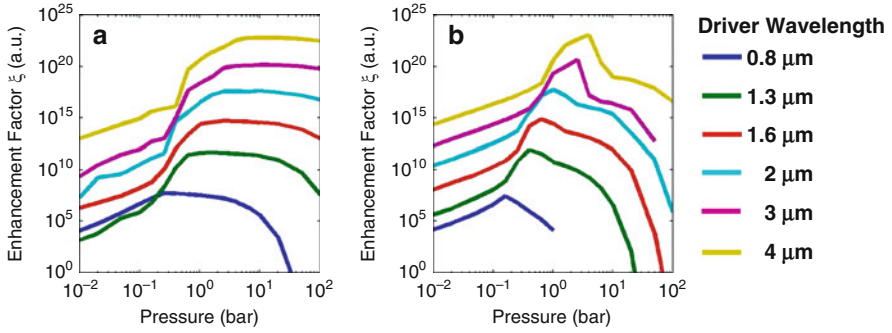


Fig. 23.2 Enhancement factor ξ for He. (a) and (b) show the enhancement of a 1 mm He jet and a 10 mm He cell respectively. For each driver wavelength, the curve is intentionally shifted for clarity. The number near each curve indicates the driver wavelength in units of $1 \mu\text{m}$

Figure 23.2 shows the calculated enhancement factors ξ for a 1 mm He jet and a 10 mm He cell for six different driver wavelengths. The driver pulses of different wavelengths have the same energy, duration, and peak intensity as in Fig. 23.1. In Fig. 23.2a, the sharp transitions at about 0.3 bar are due to a transition from phase-mismatching to phase-matching when the medium becomes dense enough to compensate the Guoy phase. With higher medium density, the strong plasma defocusing and reabsorption start to limit the HHG efficiency and result in a saturation feature. In Fig. 23.2b, the basic features of a He cell are similar to those of a He jet except that the optimal pressure is lower due to a longer interaction length. Determining the working pressure is important to the design of the vacuum system and the choice of appropriate gas geometry. The numerical analysis on plasma defocusing provided here gives the necessary information as well as the maximum enhancement due to the macroscopic propagation effects of the medium, and is therefore of great practical importance.

23.4 HHG Efficiency

Although the HHG efficiency is closely related to the microscopic dynamics of atoms which we did not directly calculate here, our model can still estimate the efficiency for different driving wavelengths. Since the SAE has been shown to scale with $\lambda^{-(5\sim 6)}$, the efficiencies at different driving wavelengths can be estimated by comparing ξ with known experimental results, for instance, using a $0.8 \mu\text{m}$ driver. This method is then able to give an estimate for the HHG efficiency with a different driver wavelength.

Figure 23.3a and b show the calculated HHG efficiency of He and Ne respectively. The reference efficiencies for He and Ne $0.8 \mu\text{m}$ HHG are 1×10^{-8} [7] and 2×10^{-7} [6] respectively, as indicated by the arrows in Fig. 23.3. Since the main

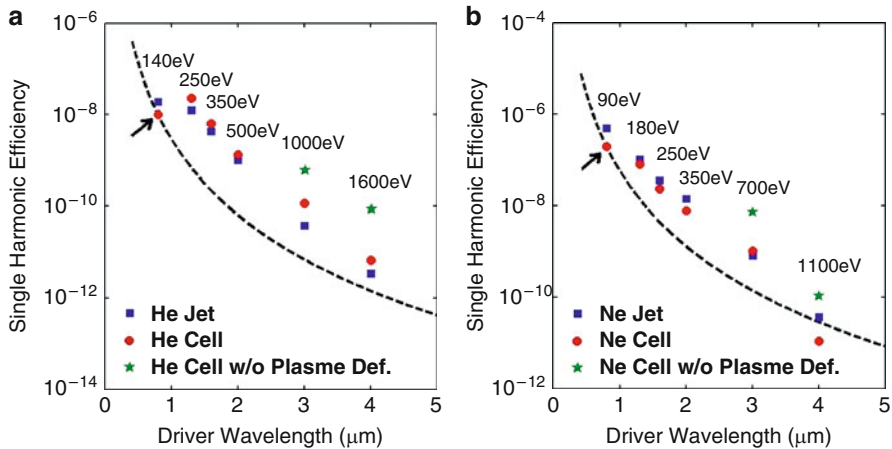


Fig. 23.3 Calculated HHG efficiency for optimal pressures in (a) He and (b) Ne. The *black dotted* curves also show a $\lambda_1^{-5.5}$ dependence starting from the efficiency reference point. For different driver wavelengths, different photon energies that are near the corresponding cutoffs are considered, as labeled

advantage of using a long-wavelength driver is to extend the cutoff of HHG spectra, the efficiencies are calculated at the photon energies near the cutoff. Our calculation shows similar results as the 1.6 and 2 μm experiments [2, 8]. The dashed curves show a $\lambda^{-5.5}$ -scaling starting from the 0.8 μm reference points. For comparison, we also calculate the cases without any plasma defocusing, represented by the green stars. Most points are 0–2 orders higher than the dashed curves, meaning that they have up to hundreds times enhancements than the 0.8 μm case, but this only partially compensates the efficiency loss due to reduced SAE.

23.5 Summary

We quantitatively analyzed the influence of plasma defocusing on HHG for different driving wavelengths by defining and comparing the enhancement factor ξ that considers macroscopic characteristics including plasma defocusing, reabsorption, and phase-matching. Our numerical results show good agreement with experiments and provide an easy way to calculate and explain HHG performance without referring to the complex microscopic behavior of strong-field dynamics and the atomic parameters. Although increasing the medium pressure can partially make up the severe loss of SAE with a long-wavelength driver, the compensation is still limited due to the plasma defocusing.

References

1. M.V. Ammosov, N.B. Delone, V.P. Krainov, Tunnel ionization of complex atoms and of atomic ions in an alternating electromagnetic field. *Sov. Phys. JETP* **64**, 1191–1194 (1986)
2. M.C. Chen, P. Arpin, T. Popmintchev et al., Bright, coherent, ultrafast soft x-ray harmonics spanning the water window from a tabletop light source. *Phys. Rev. Lett.* **105**, 173901 (2010)
3. E. Constant, D. Garzella, P. Breger et al., Optimizing high harmonic generation in absorbing gases: model and experiment. *Phys. Rev. Lett.* **82**, 1668–1671 (1999)
4. E.L. Falcao-Filho, V.M. Gkortsas, A. Gordon et al., Analytic scaling of high harmonic generation conversion efficiency. *Opt. Express* **17**, 11217–11229 (2009)
5. M. Geissler, G. Tempea, A. Scrinzi et al., Light propagation in field-ionizing media: extreme nonlinear optics. *Phys. Rev. Lett.* **83**, 2930–2933 (1999)
6. E.J. Takahashi, Y. Nabekawa, K. Midorikawa, Low-divergence coherent soft x-ray source at 13 nm by high-order harmonics. *Appl. Phys. Lett.* **84**, 4–6 (2004)
7. E.J. Takahashi, Y. Nabekawa, H. Mashiko et al., Generation of strong optical field in soft x-ray region by using high-order harmonics. *IEEE J. Sel. Top Quantum. Electron.* **10**, 1315–1328 (2004)
8. E.J. Takahashi, T. Kanai, K.L. Ishikawa et al., Coherent water window X ray by phase-matched high-order harmonic generation in neutral media. *Phys. Rev. Lett.* **101**, 253901 (2008)
9. J. Tate, T. Augustine, H.G. Muller et al., Scaling of wave-packet dynamics in an intense midinfrared field. *Phys. Rev. Lett.* **98**, 013901 (2007)

Chapter 24

Beam Splitters for High-Order Harmonics Using Transparent Materials to Visible Light

Yosuke Kojima, Yuske Furukawa, Yasuo Nabekawa, Eiji J. Takahashi, Fumihiko Kannari, and Katsumi Midorikawa

Abstract High-order harmonic (HOH) beam generated from the intense femtosecond laser pulse always propagates coaxially with the fundamental laser field. Thus, we need to separate the fundamental laser field from the HOH beam whenever we apply the HOH to spectroscopies. Conventional thin foil metal filters can completely eliminate visible or infrared fundamental laser light, while the thin foils are very fragile and easily damaged with the intense fundamental laser pulse. We have already demonstrated that a silicon or silicon carbide plate is useful for splitting the fundamental and HOH beams thanks to the Brewster incident angle to the fundamental laser beam. Nevertheless, the silicon or silicon carbide (amorphous) beam splitter (BS) is not fully satisfactory for the application because the BS is opaque for visible light. Hence, we cannot reuse the transmitted light. Thermally induced effects such as deformation of the surface may not be negligible under the high-power irradiation of the laser field. Thus, we have searched for transparent materials for visible light which should be suitable for the BS of the HOH beam.

24.1 Introduction

It is a crucial issue to separate high-order harmonic (HOH) beams from the intense fundamental (FU) laser beam when we apply the HOH beams to spectroscopic measurements. The beam splitter (BS) mirror made of silicon (Si) or amorphous

Y. Kojima · Y. Furukawa · Y. Nabekawa (✉) · E.J. Takahashi · K. Midorikawa
Yasuo Nabekawa, Advanced Science Institute, RIKEN, 2-1 Hirosawa, Wako-shi, Saitama,
351-0198, Japan
e-mail: nabekawa@riken.jp

Y. Kojima · F. Kannari
Yosuke Kojima, Faculty of Science and Technology, Keio University, 3-4-1 Hiyoshi Kouhoku-ku,
Yokohama 233-8522, Japan
e-mail: kannari@elec.keio.ac.jp

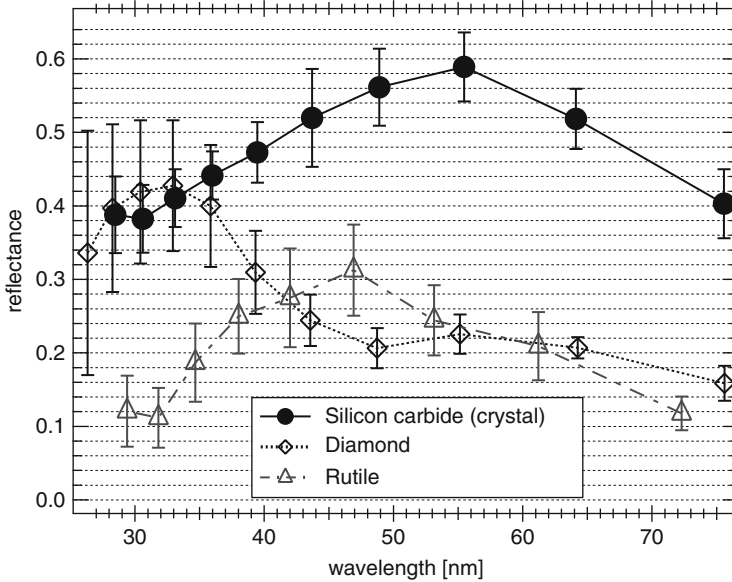


Fig. 24.1 Measured reflectance of sample materials

silicon carbide (SiC) has been conventionally used for the attenuation of the FU beam since the first demonstration of the high-reflectivity to the HOH beams at the Brewster incident angle for the visible light [1, 2]. Nevertheless, we have to notice a drawback of the Si BS, because the thick Si BS completely absorbs the FU beam. Thus, we cannot reuse the FU beam behind the Si BS nor put the BS in an enhanced cavity for XUV comb, either. Additionally, we may not neglect the degradation of beam quality of the HOH beams due to the thermal effect with increase of an average power of the FU beam. In fact, the average power of the FU beam from our laser system is now tenfold magnitude [3] compared with that from the previous laser system.

In this paper, we report on preliminary studies for the reflectivities of some optical materials against the HOH and FU beams in order to fabricate the novel BS mirror transmitting the near infrared or visible light.

24.2 Results

High refractive index to the visible light is advantageous to the HOH reflectivity because it requires large incident angle to satisfy the Brewster condition. Hence, we have chosen three kinds of optical materials, the refractive indices of which are all more than two; crystalline SiC, diamond (C), and rutile (TiO_2). In the measurement, we used a sub 15-fs 100-Hz laser system as the pumping FU beam [3]. The HOH

beams are generated from Xe (11th–19th) and Kr (15th–27th) filled in a static gas cell. We put a pair of BS materials in parallel in front of an XUV spectrometer such that the input and output beams to the BS pair should be parallel. Thus, we can easily measure the HOH intensities with and without the BS pair by parallel sliding the XUV spectrometer. Figure 24.1 shows the measured reflectivity of each BS material. We have found that the SiC BS shows the best efficiency in the measured wavelength region, while we expect from the calculation that the rutile BS may be suitable for the wavelength region shorter than 25 nm. The extinction ratio of the SiC BS against the pump beam was measured to be $\sim 10^{-5}$. Thus, we conclude the crystalline SiC is the most appropriate material for the BS mirror if the surface quality is sufficient to focus the XUV HOH beam.

References

1. E.J. Takahashi, H. Hasegawa, Y. Nabekawa, K. Midorikawa, *Opt. Lett.* **29**, 507 (2004)
2. E.J. Takahashi, Y. Nabekawa, H. Mashiko, H. Hasegawa, A. Suda, K. Midorikawa, *IEEE Selct. Top. Quant. Electron.* **10**, 1315 (2004)
3. Y. Nabekawa, A. Amani-Eilanlou, Y. Furukawa, K. Ishikawa, H. Takahashi, K. Midorikawa, *Appl. Phys. B* **101**, 523 (2010)

Chapter 25

Enormous Amplification of Full-Coherent Radiation in the Extreme Ultraviolet Region with a Free-Electron Laser

Eiji J. Takahashi, Tadashi Togashi, Makoto Aoyama, Koichi Yamakawa, Takahiro Sato, Atsushi Iwasaki, Shigeki Owada, Kaoru Yamanouchi, Toru Hara, Shinichi Matsubara, Takashi Ohshima, Yuji Otake, Hitoshi Tanaka, Takashi Tanaka, Hiromitsu Tomizawa, Takahiro Watanabe, Makina Yabashi, Katsumi Midorikawa, and Tetsuya Ishikawa

Abstract High-order harmonic beam was injected as a seeding source to a 250-MeV free-electron-laser amplifier. When the amplification conditions were satisfied, strong enhancement of the radiation intensity by a factor of 650 was observed at a wavelength of 61.5 nm. The random and uncontrollable spikes, which appeared in the spectra of the Self-Amplified Spontaneous Emission based FEL radiation without the seeding pulse, were found to be suppressed drastically to form to a narrow-band, single peak profile at the seeding wavelength. The properties of the seeded FEL radiation were well reproduced by numerical simulations.

E.J. Takahashi (✉) · K. Midorikawa
RIKEN-ASI, Hirosawa 2-1, Wako, Saitama 351-0198, Japan
e-mail: ejtak@riken.jp

T. Togashi · S. Matsubara · H. Tomizawa
JASRI, Kouto 1-1-1, Sayo, Hyogo 679-5198, Japan

M. Aoyama · K. Yamakawa
JAEA, Umemidai 8-1, Kizugawa, Kyoto 619-0215 Japan

T. Hara · T. Ohshima · Y. Otake · T. Tanaka · M. Yabashi · H. Tanaka · T. Ishikawa ·
Takahiro Watanabe
RIKEN SPring-8 Center, Kouto 1-1-1, Sayo, Hyogo 679-5148, Japan

T. Sato
RIKEN SPring-8 Center, Kouto 1-1-1, Sayo, Hyogo 679-5148, Japan
University of Tokyo, Hongo 7-3-1, Bunkyo-ku, Tokyo 113-0033, Japan

A. Iwasaki · S. Owada · K. Yamanouchi
University of Tokyo, Hongo 7-3-1, Bunkyo-ku, Tokyo 113-0033, Japan

25.1 Introduction

Since the advent of laser technology, scientists have endeavored to shorten the wavelength of lasers. Recently, single-pass free-electron lasers (FELs) based on self-amplified spontaneous emission (SASE) have successfully produced intense light from extreme ultraviolet (EUV) regions to X-ray regions [1–3]. Since the amplification of SASE-FEL starts up from stochastic density modulations in the electron bunch, however, radiation spectra in the temporal and frequency domains are composed of random spikes varying from shot-to-shot [4].

Another key method for generating coherent radiation in short wavelengths is high-order harmonic generation (HHG) [5]. A significant advantage of the high-order harmonic (HH) radiation is to keep both transverse and longitudinal coherence from the pump laser. The conversion efficiency of HHG is, however, limited by the dephasing of the atomic dipole oscillators and the plasma defocusing of the laser pulse. At present, the shortest wavelength with a large amount of photon flux ($>1 \times 10^{10}$ photons/shot) has been restricted to the EUV region [6].

The “HH-seeded FEL” technique is the most straightforward and promising method for creating full-coherent, short-wavelength radiation with a high photon flux. An injection of HH radiation as a seed source into an FEL amplifier enables enhancement of the final output power by orders of magnitude, while preserving both the transverse and longitudinal coherence properties of HH radiation. In this report, we first observed a seeding effect of an FEL amplifier working at an extreme ultraviolet (EUV) region [7] with wavelength of 61.5 and 53.3 nm. The 13th and 15th harmonic of a Ti:sapphire laser was generated with a loosely-focusing geometry[8], which is a key technique for generating intense HH radiation, and selected as the seed pulse. The final output exceeded 1 μ J per pulse with a significant enhancement ratio of 650 at a wavelength of 61.5 nm. This achievement directly paves the way for generating single-mode intense radiation in the X-ray region.

25.2 Experimental Setup of the Seeded FEL

The experiment was performed at the SPring-8 Compact SASE source (SCSS) test accelerator operating with a beam energy of 250 MeV [2]. SCSS can achieve continuous SASE FEL power saturation over wavelengths ranging from 50 to 62 nm. Figure 25.1 shows the configuration for an seeding experiment. The HH source used as the seed light was designed by our energy scaling strategy of HHG [9]. The pumping laser system, used for generating the HH light, is based on a chirped pulsed amplification of a Ti:sapphire laser (800 nm, 100 mJ, 160 fs, 30-Hz), and is mainly composed of a mode-locked oscillator (TSUNAMI Spectra Physic), which is synchronized to a 238-MHz master clock of SCSS by feedback locking the cavity length (Lok-to-Clock system, Spectra Physics), a regenerative amplifier (SPITFIRE, Spectra physics) and a 4-pass amplifier. The HH radiation was gener-

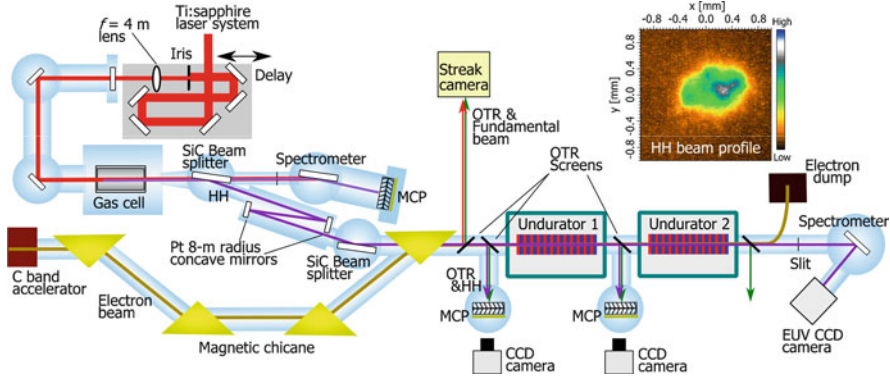


Fig. 25.1 Experimental setup of the seeded-FEL

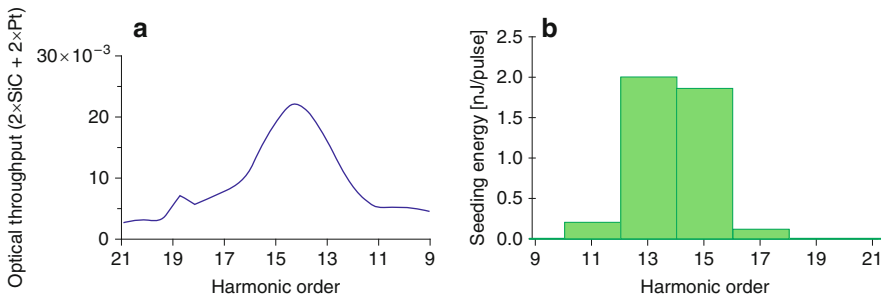


Fig. 25.2 (a) Calculated optical throughput with two Pt mirrors and two SiC separator mirrors. (b) Harmonic energy distribution in front of the first Undulator section. Other harmonic energies were less than 10 pJ/pulse

ated in a Xe gas cell by focusing (focal length $f = 4,000$ mm) the Ti:S laser and reflected with a SiC harmonic separator mirror [10] set at a Brewster angle (69°) for the pump laser. To collimate and focus the HH radiation, we arranged two Pt-coated, nearly-normal-incidence mirrors with a radius of curvature of 8,000 mm. By taking advantage of the magnetic chicane part of the SCSS, the HH radiation is transported into the undulator section after passing through a second SiC separator mirror. Figure 25.2a shows the calculated throughput with four optical devices. The inset of Fig. 25.1 shows the beam profile of HH radiation at the undulator entrance. The spatial profile were measured by a phosphor screen coupled with a multichannel plate (MCP) and CCD camera. The beam size of HH at the entrance of the first undulator is 0.80 and 0.53 mm in the horizontal and vertical directions, respectively. Figure 25.2b shows the measured harmonic energy at the first undulator. The effective seeding energy of 61.5 nm (13th HH) and 53.3 nm (15th HH) were measured to be approximately 2 nJ/pulse. The resulting peak power of the seed pulse was estimated to be 40 kW, assuming a 50 fs pulse duration [11].

Producing efficient seeding interaction requires spatial and temporal overlaps between the electron bunch and the HH radiation. Moreover, the HH wavelength should be tuned with that of the SASE-FEL radiation. First, profile monitoring systems, which simultaneously visualize the spatial profiles of HH radiation and those of the optical transition radiation (OTR) from the electron beam, are installed to ensure the spatial overlap in the first undulator. The spatial and angular deviations between the HH radiation and the electron beam are suppressed below $100\ \mu\text{m}$ and $100\ \mu\text{rad}$, respectively, by precise steering of the HH radiation trajectory by aligning the Pt-coated mirrors. Second, a temporal overlap between the electron bunch and the HH radiation is monitored with a streak camera (FESCA-200, Hamamatsu Photonics K.K.) through OTR and the fundamental radiation of the Ti:S laser. The timing deviation is adjusted using the delay system of the Ti:S laser with a step of 50 fs, although a temporal jitter (typically ~ 1 ps) of the modelocked oscillator to the rf signal reduced the possibility of temporal overlapping. Third, a spectral overlap of SASE-FEL with the seed source was achieved by monitoring the spectra with a spectrometer located at the end of the beamline and by adjusting an undulator gap. The seeded FEL is observed by the spectrometer at the end of the beamline.

25.3 SCSS Seeded by High-Order Harmonic Beam

One of crucial requirement for observing the seeding effect is to control the SASE-FEL intensity that is regarded as a background. Figure 25.3 shows an optimized condition obtained using a 3D FEL simulator, SIMPLEX[12]. Here the SASE FEL power is lowered to $0.7\ \mu\text{J}$ per pulse by controlling the amplification parameters. This condition has been achieved by reducing the acceleration charge down to $0.1\ \text{nC}$, which is approximately one-third of that in the normal operations, at the entrance of the first undulator.

Figure 25.4 shows the measured spectra of the FEL radiation in successive 50 shots without (a)/with (b) HH injection. We observe sharp increases in the spectral intensity for several shots shown as red lines in Fig. 25.4b. A threshold level for selecting these curves is set to be three times of the average intensity of the SASE-FEL radiation in Fig. 25.4a. It is natural to conclude that the enhancements, which are appeared only with the presence of HH radiation, result from the seeding effect. Note that the small appearance ratio of the enhancement, which is typically ~ 10 shots per 1,000 shots, is due to the timing jitter between the seeding laser pulse and the electron bunch. Furthermore, we investigated the resonant effect by changing the undulator gap and shifting the SASE-FEL wavelength. The high-intensity pulses are observable only in the vicinity of the conditions with a SASE-FEL wavelength of $61.5\ \text{nm}$, as shown in the inset of Fig. 25.4a. This resonant behavior provides conclusive proof of the successful operations of the seeded FEL at the EUV regime. Figure 25.5a shows typical spectra for seeded and unseeded conditions, as well as that for HH radiation. Improvement of spectral shapes to a single mode has

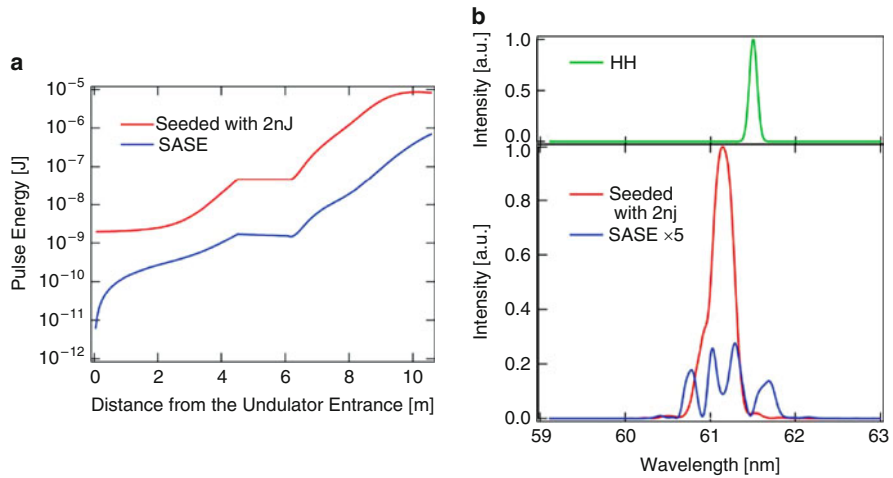


Fig. 25.3 Comparison of radiation power growth (a) and spectra (b) for seeded and unseeded conditions in the SCSS. Both were simulated using SIMPLEX

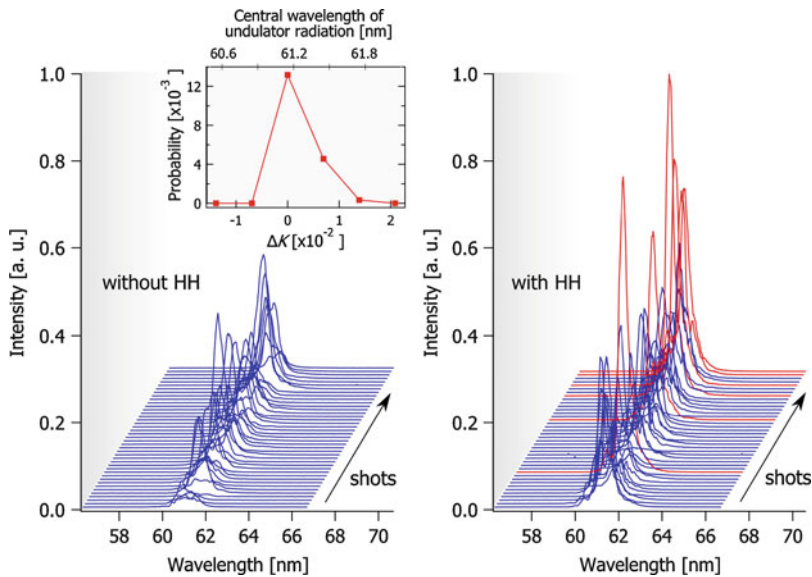


Fig. 25.4 Spectra of FEL radiation in successive 50 shots without (a)/with (b) HH injection. The red lines in (b) show profiles that have higher intensities than the threshold level. The inset shows an appearance probability of the high-intensity condition as a function of the central wavelength of the SASE-FEL

been observed for the seeded condition at a central wavelength of 61.5 nm. The spectral intensity for the seeded condition is three times higher than the SASE-FEL background. The pulse energy of the seeded FEL is estimated to be 1.3 μ J, compared with 0.7 μ J for unseeded SASE-FEL. This value corresponds to a significant

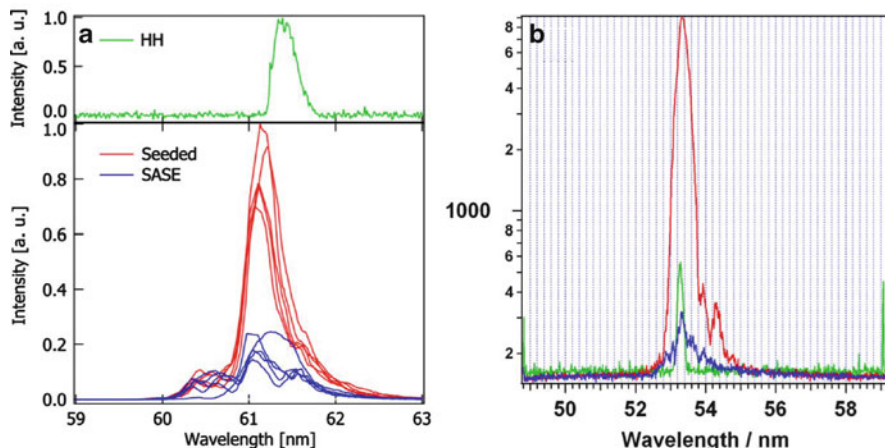


Fig. 25.5 Spectra of typical shots of seeded (*red lines*) and unseeded pulses (*blue lines*), compared with HH radiation (*green line*). Seeding harmonic order: (a) 13th, (b) 15th

amplifying ratio of 650 from the original HH source with the pulse energy of ~ 2 nJ. It should be noted that the central wavelength of the seeded radiation is shifted towards the shorter direction compared with that of the HH radiation. This deviation, which is also seen for the simulation results in Fig. 25.3b, is explained by a slight compression of the chirped electron bunch traveling through the undulator. For the intensity level of the seeded FEL, we still have a discrepancy between the measurements and the simulation results. We consider the primary cause to be a difference of the envelopes of the HH radiation in the undulator for experimental and simulation conditions. Moreover, we successfully demonstrated the seeded FEL at a wavelength of 53.3 nm (see Fig. 25.5b), which is the shortest wavelength in the direct seeded FEL scheme.

25.4 Summary

The HH radiation was significantly amplified with the SCSS test accelerator employed as an FEL amplifier. The temporal and spatial overlap of the electron beam and the HH radiation, as well as the adjustment of the wavelength of the undulator radiation to that of the HH radiation, were precisely tuned for achieving the seeded FEL operation. The spectral narrowing and the wavelength shift observed in the seeded conditions agreed with the results obtained by the numerical simulations. Moreover, we successfully demonstrated the seeded FEL at a wavelength of 53.3 nm, which is the shortest wavelength in the direct seeded FEL scheme.

References

1. W. Ackermann et al., *Nat. Photon.* **1**, 336 (2007)
2. T. Shintake et al., *Nat. Photon.* **2**, 555 (2008)
3. P. Emma et al., *Nat. Photon.* **4**, 641 (2010)
4. R. Bonifacio, L. De Salvo, P. Pierini, N. Piovela, C. Pellegrini, *Phys. Rev. Lett.* **73**, 70 (1994)
5. F. Krausz, M. Ivanov, *Rev. Mod. Phys.* **81**, 163 (2009)
6. E.J. Takahashi, Y. Nabekawa, K. Midorikawa, *Appl. Phys. Lett.* **84**, 4 (2004)
7. T. Togashi et al., *Opt. Express* **19**, 317 (2011)
8. E. Takahashi, Y. Nabekawa, T. Otsuka, M. Obara, K. Midorikawa, *Phys. Rev. A* **66**, 021802 (2002)
9. E. Takahashi, Y. Nabekawa, K. Midorikawa, *Opt. Lett.* **27**, 1920 (2002)
10. E.J. Takahashi, H. Hasegawa, Y. Nabekawa, K. Midorikawa, *Opt. Lett.* **29**, 507 (2004)
11. J.L. Krause, K.J. Schafer, K.C. Kulander, *Phys. Rev. A* **45**, 4998 (1992)
12. T. Tanaka, in *Proceedings of the FEL 2004*, 1994, p. 70

Part III

Ionization of Atoms

Chapter 26

Breakdown of the Independent Electron Approximation in Sequential Double Ionization

C. Cirelli, A.N. Pfeiffer, M. Smolarski, X. Wang, J.H. Eberly, R. Dörner, and U. Keller

Abstract Correlated electron emission in strong field double ionization is dominated by recollision of the first ionized electron with its parent ion. With laser pulses that are close to circularly polarized, recollision may be greatly modified or avoided and the electrons are usually assumed to be field ionized without mutual interaction. Here we present coincidence momentum measurements of the doubly charged ion and the two electrons that are in contradiction with the independent electron assumption for close to circularly polarized fields. These experiments demonstrate that recollision is not the only mechanism that can lead to correlated electron emission in strong field double ionization.

26.1 Introduction

In strong field double ionization it is typically distinguished between sequential double ionization (SDI), where the electrons are assumed to interact independently with the laser field, and non-sequential double ionization (NSDI), where the electrons cannot be treated separately [1]. During the last few years the research focus has been on double ionization by linearly polarized laser pulses with the result that over a wide intensity range the dominating NSDI mechanism is electron impact ionization, whereas at higher intensities SDI becomes dominant: ion momentum and electron correlation measurements [2] revealed a more direct evidence for the existence of recollision induced ionization.

Still an open question remains whether other mechanisms rather than recollision can occur in strong field double ionization. Elliptically (close to circularly) polarized pulses are ideally suited to answer this question, since recollision of the first emitted electron with the parent ion is prevented.

C. Cirelli (✉) · A.N. Pfeiffer · M. Smolarski · X. Wang · J.H. Eberly · R. Dörner · U. Keller
Physics Department, ETH Zurich, 8093 Zurich, Switzerland
e-mail: cirelli@phys.ethz.ch

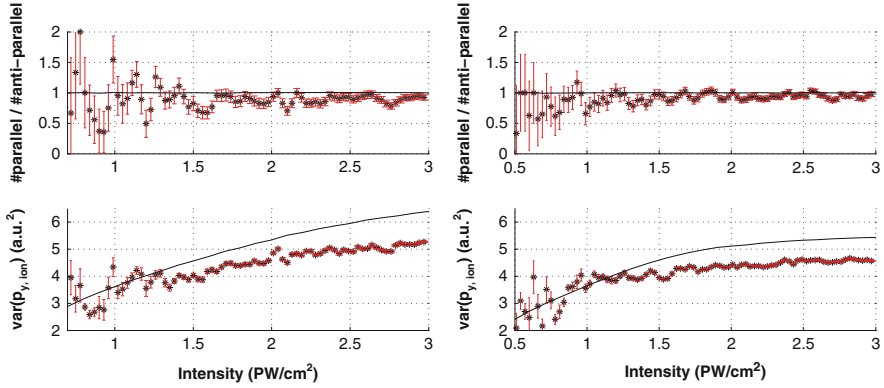


Fig. 26.1 Ratio of parallel to anti-parallel electron emission (*left*) and variance of the ion momentum distribution along the small polarization axis (*right*) for 33-fs laser pulses as a function of intensity; the *curve* predicted by the independent electron model is shown as a *solid line*

26.2 Results

Here we present experimental evidence that the standard picture of SDI is limited in describing double ionization by close to circularly polarized laser pulses [3]. Two different observables are extracted from coincidence momentum measurements revealing an intensity dependence that is qualitatively different from the prediction of the standard SDI model [4].

The first observable is the ratio of the numbers of electrons that are emitted into opposite or the same directions, a ratio expected to be unity on the basis of the standard independent-tunneling SDI scenario. In contrast we observe substantial oscillations around unity, see Fig. 26.1. The second observable is the variance of the ion momentum distribution along the small polarization axis. This quantity is closely related to the first observable and shows the same oscillations (Fig. 26.1).

For the first test of an independent electron model we ask the following question: does the emission direction of the first ionized electron influence the direction of the second electron? In the case of recollision induced double ionization there is a strong tendency that both electrons are emitted into the same direction. For our intensity range the semi-classical model based on SDI, predicts a ratio of 1:1 for electrons that fly into the same hemisphere (parallel emission) and electrons that fly into opposite directions (anti-parallel emission).

Figure 26.2 shows the electron correlation spectrum, integrated over the scanned intensity range. The counts in the 1st and 3rd quadrant represent parallel electron emission; the counts in the 2nd and 4th quadrant represent anti-parallel electron emission. The shape of distribution in the quadrants for parallel emission deviates slightly from the distribution in the quadrants for anti-parallel emission for the coincidence data shown in Fig. 26.2a. This is in contrast to the prediction of the standard SDI model, which predicts equally shaped islands in each quadrant.

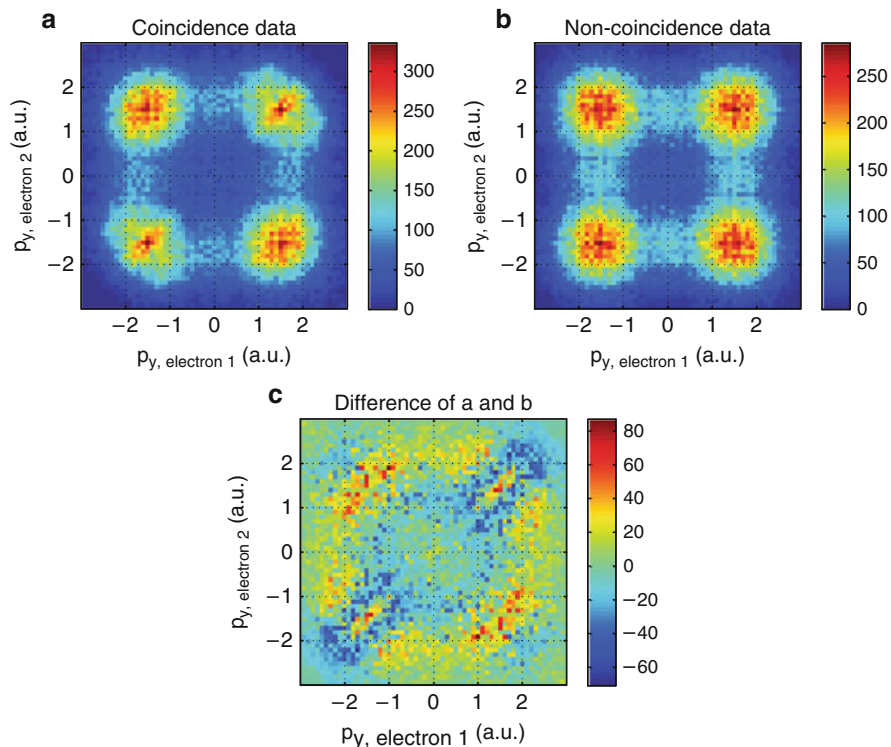


Fig. 26.2 Momentum correlation between both electrons for double ionization of argon by a 7-fs close to circular polarized laser pulse. The spectrum is integrated over the intensity range of the experiment (0–3 PW/cm²). *Horizontal axis*: momentum component of one electron along the minor axis of the polarization ellipse, *vertical axis*: same momentum component of the second electron. **(a)** Coincidence data: for each laser shot where the detected particles consist of one Ar⁺⁺ ion and one electron, the momentum of the other electron is calculated according to momentum conservation. Since there is no information whether the detected electron is the first or the second electron, both possibilities are considered and the spectrum is symmetric. **(b)** Non-coincidence data: the same as **(a)**, but the momentum of the Ar⁺⁺ ion is paired with the electron momentum from the successive laser shot where the detected particles consist of one Ar⁺⁺ ion and one electron. **(c)** For each pixel, the number of counts in **(b)** is subtracted from the number of counts in **(a)** to highlight the subtle differences in the quadrants

To verify that these subtle differences are not caused by calibration errors of our spectrometer, we generated non-coincidence data by pairing ions and electrons from different laser shots (Fig. 26.2b). The non-coincidence data does indeed not exhibit the slight deviations in the different quadrants, but it shows instead equally shaped islands just like the SDI model predicts.

A fully classical calculation [5], based on large-ensemble solutions of time-dependent Newton equations (TDNE), reproduces the observed oscillations qualitatively, suggesting that the measured electron correlations can be explained by

considering mutual electron interaction at all times, both before as well as after the times of ionization of the two electrons.

26.3 Conclusion

In conclusion we have found unexpected deviations from the independent electron assumption in strong field double ionization by close-to-circularly polarized laser pulses. Two different observables of coincidence momentum data exhibit an intensity dependence that is not captured by the standard independent-electron SDI model.

By carefully analyzing the emission direction of the electrons it was found that the ratio of parallel to anti-parallel electron emission exhibits an oscillatory behaviour around one at certain intensities. Similar oscillations are found by analyzing the variance of the doubly charged Argon ions in the direction of the minor polarization axis avoiding any potential systematic errors in electron detection. This behaviour can be qualitatively reproduced by a classical ensemble calculation.

Acknowledgements This work was supported by the NCCR Quantum Photonics (NCCR QP), a research instrument of the Swiss National Science Foundation (SNSF), by ETH Research Grant ETH-03 09-2, the SNSF REquip grant 206021-128551/1, and by US DOE Grant ER-FG02-05ER15713. R.D. acknowledges support by a Koselleck Project of the Deutsche Forschungsgemeinschaft.

References

1. A. Becker, R. Dörner, R. Moshhammer, Multiple fragmentation of atoms in femtosecond laser pulses. *J. Phys. B At. Mol. Opt. Phys.* **38**, S753–S773 (2005)
2. Th. Weber, H. Giessen, M. Weckenbrock, G. Urbasch, A. Staudte, L. Spielberger, O. Jagutzki, V. Mergel, M. Vollmer, R. Dörner, Correlated electron emission in multiphoton double ionization. *Nature* **405**, 658–661 (2000)
3. A. N. Pfeiffer, C. Cirelli, M. Smolarski, X. Wang, J. H. Eberly, R. Dörner, U. Keller, Breakdown of the independent electron approximation in sequential double ionization, *New J. Phys.* **13**, 093008 (2011)
4. C.M. Maharjan, A.S. Alnaser, X.M. Tong, B. Ulrich, P. Ranitovic, S. Ghimire, Z. Chang, I.V. Litvinyuk, C.L. Cocke, Momentum imaging of doubly charged ions of Ne and Ar in the sequential ionization region. *Phys. Rev. A* **72**, 041403(R) (2005)
5. W. Wang, J.H. Eberly, Multielectron Effects in Sequential Double Ionization with Elliptical Polarization, (2011) [arXiv:1102.0221v1]

Chapter 27

Sequential Double Ionization: The Timing of Release

A.N. Pfeiffer, C. Cirelli, M. Smolarski, R. Dörner, and U. Keller

Abstract The timing of electron release in strong field double ionization poses great challenges both for conceptual definition and for conducting experimental measurement. Here we present coincidence momentum measurements of the doubly charged ion and of the two electrons arising from double ionization of Argon using elliptically polarized laser pulses. Based on a semi-classical model, the ionization times are calculated from the measured electron momenta across a large intensity range. This paper discusses how this method provides timings on a coarse and on a fine scale, similar to the hour and the minute hand of a clock. We found that the ionization time of the first electron is in good agreement with the simulation, whereas the ionization of the second electron occurs significantly earlier than predicted.

27.1 Introduction

Among all methods used to measure time, one of the most fundamental approach is to measure the angle of a rotating hand, such as it is done on an analogue watch face. This is the principle used in strong field ionization by the attoclock technique [1]. The rotating electric field vector of a close-to-circularly polarized laser pulse is used to deflect photo-ionized electrons, such that the instant of ionization is mapped to the final angle of the momentum, similar to the minute hand of a clock. The attoclock technique is based on the definition of time by counting cycles [2]. During one period the watch hand completes one cycle, such that measuring the emission angle of the electron enables us to measure time at a precision well below one optical period. Thus the measurement provides attosecond timing without using an attosecond pulse.

A.N. Pfeiffer · C. Cirelli (✉) · M. Smolarski · R. Dörner · U. Keller
Physics Department, ETH Zurich, 8093 Zurich, Switzerland
e-mail: cirelli@phys.ethz.ch

27.2 Results

We used the attoclock to measure the ionization times of the two electrons in double ionization of argon [3]. Due to depletion the averaged ionization time of the electrons is shifted towards the beginning of the pulse with increasing intensity, confirming the results of Maharjan et al. [4]. As a consequence, a multi-cycle measurement is required. Nevertheless, the attoclock technique gives access to two different time scales. First, the magnitude of the electron momenta follows the envelope of the laser pulse and gives a coarse timing for the electron releases (i.e. the hour hand of the clock). Second, the emission angle of the electrons subsequently gives the fine timing (i.e. the minute hand of the clock).

The result of the attoclock measurements addresses a fundamental question in double ionization: are there electron correlation mechanisms, which are not induced by recollision?

Typically people distinguish between sequential double ionization (SDI), where the electrons are assumed to interact independently with the laser field, and non-sequential double ionization (NSDI), where the electrons cannot be treated separately [5]. During the last few years the research focus has been on double ionization by linearly polarized laser pulses with the result that over a wide intensity range the dominating NSDI mechanism is electron impact ionization or excitation at recollision of the first ionized electron with the parent ion, whereas at higher intensities SDI becomes dominant [6, 7].

Still an open question remains whether other mechanisms rather than recollision can occur in strong field double ionization. Elliptically (close to circularly) polarized pulses are ideally suited to answer this question, since recollision of the first emitted electron with the parent ion is prevented. Approaches to high-field ionization problems via classical ensembles recently have predicted NSDI behavior for elliptically polarized laser pulses [8, 9]. Experimental investigations for circular polarization in contrast are rare. An exception is [4], where the structure of the momentum distribution of the double charged ions can be explained both analytically and intuitively as arising from SDI.

We performed experiments on double ionization of Argon with two different laser pulses: a 33-fs laser pulse at a center wavelength of 788 nm and a 7-fs laser pulse from a two-stage filament compressor at a center wavelength of 740 nm and measured the momentum of ions and electrons in coincidence with a COLTRIMS.

The intensity of the 33-fs pulse was adjusted by a rotating half-wave plate followed by a polarizer; the intensity of the 7-fs pulse was tuned by a motorized iris. The measured ratio of Ar^{++} to Ar^+ ions was used for intensity calibration. The ellipticity was 0.78 for the 7-fs pulse and 0.77 for the 33-fs pulse.

We detect one ion and two electrons in three-particle-coincidence, which means that for each laser shot we select groups consisting of one ion and two electrons out of all detected particles according to the condition $p_{\text{ion}} + p_{\text{electron1}} + p_{\text{electron2}} < 0.3$ a.u., see Fig. 27.1. This ensures that false coincidences are kept low.

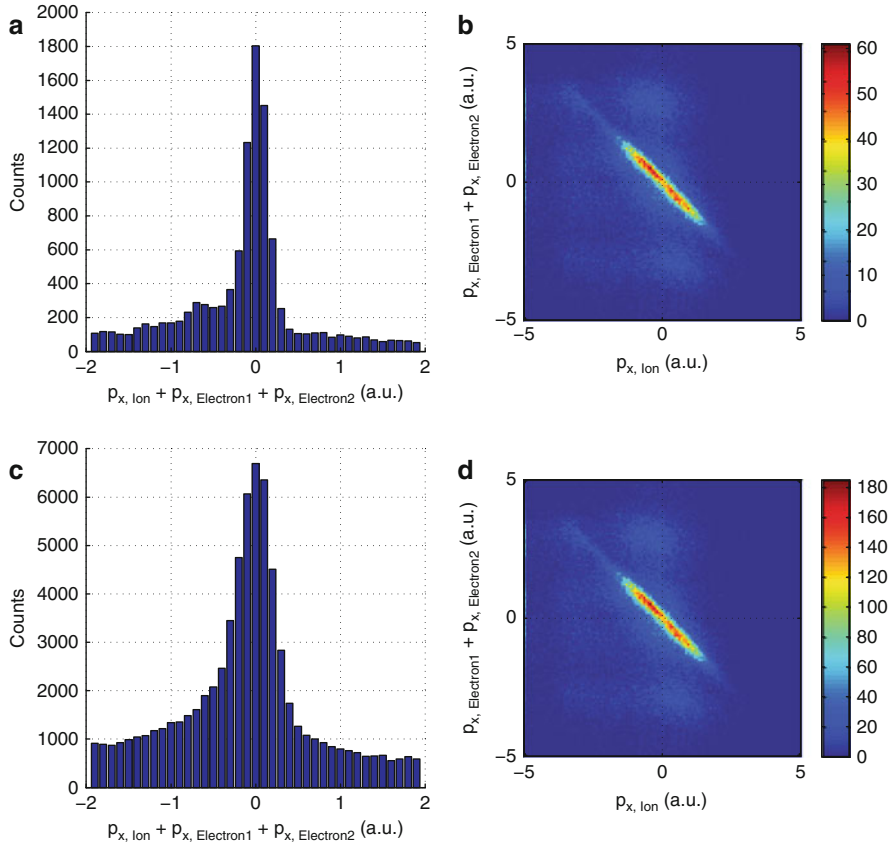


Fig. 27.1 Coincidence spectra for the 7-fs laser pulse (**a** and **b**) and the 33-fs pulse (**c** and **d**). Due to momentum conservation, the sum of the ion momentum and the two electron momenta must equal zero if the detected particles stem from the breakup of a single atom

27.3 Conclusion

The ionization time measurement performed with the attoclock (Fig. 27.2) shows that the release time of the first electron is in good agreement with the semi-classical simulation performed on the basis of Sequential Double Ionization (SDI), whereas the ionization of the second electron occurs significantly earlier than predicted. This observation suggests that electron correlation and other Non-Sequential Double Ionization (NSDI) mechanisms may play an important role also in the case of strong field double ionization by close-to-circularly polarized laser pulses.

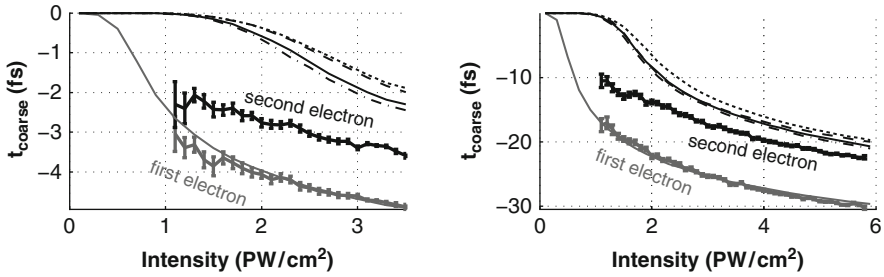


Fig. 27.2 The coarse estimate for the first (*grey*) and the second (*black*) release time for 7-fs (*left*) and 33-fs (*right*) laser pulses. The SDI simulation for the first (second) ionization time is shown in *grey* (*black*) *solid line*; for the second ionization different model *curves* are shown considering different distribution of the five valence electrons over the m quantum states in Ar⁺. *Solid line*: equal distribution over the possible m states; *dotted line*: one electron with $|m| = 0$ and four electrons with $|m| = 1$, *dash-dotted line*: 2 electrons with $|m| = 0$ and three electrons with $|m| = 1$, *dashed line*: a beating of the two previous configurations with a period of 23.3 fs

Acknowledgements This work was supported by the NCCR Quantum Photonics (NCCR QP), a research instrument of the Swiss National Science Foundation (SNSF), by ETH Research Grant ETH-03 09-2 and by an SNF equipment grant. R.D. acknowledges support by a Koselleck Project of the Deutsche Forschungsgemeinschaft.

References

1. P. Eckle, M. Smolarski, P. Schlup, J. Biegert, A. Staudte, Schöffler, H.G. Muller, R. Dörner, U. Keller, Attosecond angular streaking. *Nat. Phys.* **4**, 565–570 (2008)
2. P. Eckle, A.N. Pfeiffer, C. Cirelli, A. Staudte, R. Dörner, H.G. Muller, M. Büttiker, U. Keller, Attosecond ionization and tunneling delay time measurements in Helium. *Science* **322**, 1525–1529 (2008)
3. A.N. Pfeiffer, C. Cirelli, M. Smolarski, R. Dörner, U. Keller, Timing the release in sequential double ionization. *Nat. Phys.* **7**, 428–433 (2011)
4. C.M. Maharjan, A.S. Alnaser, X.M. Tong, B. Ulrich, P. Ranitovic, S. Ghimire, Z. Chang, I.V. Litvinyuk, C.L. Cocke, Momentum imaging of doubly charged ions of Ne and Ar in the sequential ionization region. *Phys. Rev. A* **72**, 041403(R) (2005)
5. A. Becker, R. Dörner, R. Moshhammer, Multiple fragmentation of atoms in femtosecond laser pulses. *J. Phys. B At. Mol. Opt. Phys.* **38**, S753–S773 (2005)
6. Th. Weber, H. Giessen, M. Weckenbrock, G. Urbasch, A. Staudte, L. Spielberger, O. Jagutzki, V. Mergel, M. Vollmer, R. Dörner, Correlated electron emission in multiphoton double ionization. *Nature* **405**, 658–661 (2000)
7. A. Rudenko, K. Zrost, B. Feuerstein, V.L.B. de Jesus, C.D. Schröter, R. Moshhammer, J. Ullrich, Correlated multielectron dynamics in ultrafast laser pulse interactions with atoms. *Phys. Rev. Lett.* **93**, 253001 (2004)
8. W. Wang, J.H. Eberly, Effects of elliptical polarization on strong-field short-pulse double ionization. *Phys. Rev. Lett.* **103**, 103007 (2009)
9. F. Mauger, C. Chandre, T. Uzer, Recollisions and correlated double ionization with circularly polarized light. *Phys. Rev. Lett.* **105**, 083002 (2010)

Chapter 28

Study of Asymmetric Electron Emission in Two-Color Ionization of Helium (XUV–IR)

G. Laurent, W. Cao, I. Ben-Itzhak, and C.L. Cocke

Abstract In this work, we focused on the angular photoelectron emission from helium generated by an Attosecond Pulse Train (APT) in the presence of a weak Infrared (IR) field. The APT creates both an excited and a continuum electron wave packets. By ionizing the excited state with the IR pulse, a delayed new continuum electron wave packet is created. Consequently, a mix of energy-degenerate even and odd parity states is fed in the continuum by one- and two-photon transitions. These interfere, leading to an asymmetric electron emission along the polarization vector. The interference can be controlled by varying the time delay between the APT and IR pulses.

28.1 Introduction

The recent development of light pulses on an attosecond timescale has opened up the possibility to probe temporal aspects of electron transitions in atoms, molecules and condensed matter [1–3]. For that purpose, attosecond pulse trains are particularly attractive for initiating a dynamical process which evolves nontrivially in time, as they inherently possess high time and energy resolution [4, 5]. In this work, we focused on the dynamics of the electron emission induced by an APT (formed by even and odd harmonics) on helium, in the presence of a weak IR field (intensity lower than $10^{12} \text{ W cm}^{-2}$). The principle of our experiment is depicted in Fig. 28.1a. The APT creates both an excited and a continuum electron wave packets, through absorption by the He of the 15th and 16th harmonics, respectively. By ionizing the excited state with the IR pulse, a delayed new continuum electron wave packet is created. Consequently, energy-degenerate even and odd parity states in

G. Laurent (✉) · W. Cao · I. Ben-Itzhak · C.L. Cocke
James R. Macdonald Laboratory, Department of physics, Kansas State University, Manhattan,
KS 66506, USA
e-mail: gl Laurent@phys.ksu.edu; caowei@phys.ksu.edu; ibi@phys.ksu.edu; cocke@phys.ksu.edu

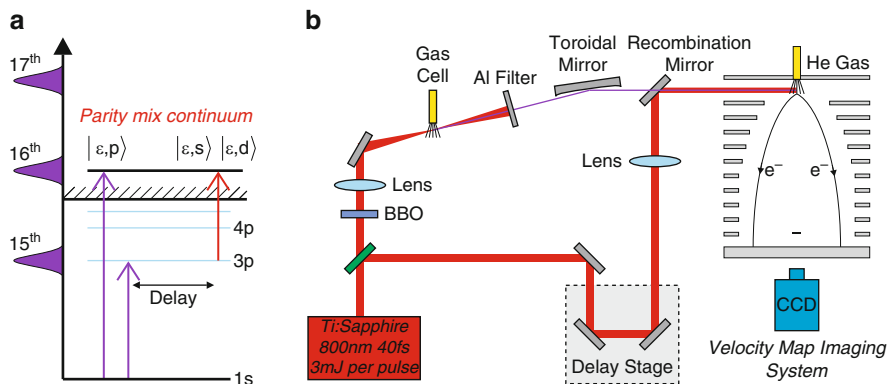


Fig. 28.1 (a) Principle of the measurement. The APT creates both an excited and a continuum electron wave packets, through the absorption by He of the 15th and 16th harmonics, respectively. By ionizing the excited state with the IR pulse, a delayed new continuum electron wave packet is created. Consequently, energy-degenerate even and odd parity states in the continuum are fed. (b) Schematic view of the experimental setup combining an XUV-IR interferometer and a Velocity Map Imaging (VMI) system

the continuum are fed, and thus interfere. We show that the interference pattern leads to large asymmetry in the angular distribution of the photoelectron along the polarization of the light, which can be controlled by varying the time delay between the APT and the IR pulses.

28.2 Experimental Setup

A schematic view of our apparatus is shown in Fig. 28.1b. It combines an XUV-IR interferometer and a Velocity Map Imaging (VMI) system. Part of the incoming linearly polarized IR beam is first frequency doubled in a 140 μm thick BBO (Beta barium borate, $\beta\text{-BaB}_2\text{O}_4$), type I crystal. The fundamental and its second harmonic beams are then focused into a windowless cell filled with 10 Torr of argon. By combining both 800 and 400 nm for the high-order harmonics generation, odd and even harmonic orders are produced [6]. The APT is then filtered by using a spatial aperture and a 200-nm thick Al thin film to remove harmonics below the 11th order. A replica of the IR beam used to generate the APT is sent into the second arm of the interferometer, whose total length can be changed in order to vary the time delay τ between the APT and IR pulses. Both beams are focused, collinearly recombined, and finally sent into a vacuum chamber containing an effusive helium gas jet. At the focal point, the IR intensity is estimated to be below $10^{12} \text{ W cm}^{-2}$. A VMI coupled to a CCD camera is used to measure the photoelectrons momenta [7]. Electrons detected in the upper (lower) part of the detector are associated with the emission in the Up (Down) direction along the polarization of the light.

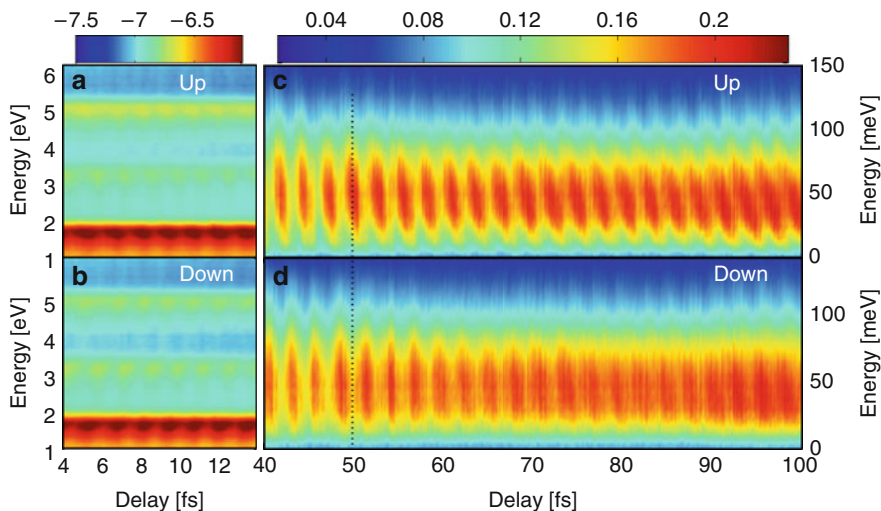


Fig. 28.2 *Up* and *Down* photoelectron energy spectra as a function of the time delay between the APT and the IR pulses. (a),(b) APT formed by odd order harmonics only. (c, d) APT formed by both odd and even order harmonics

28.3 Results and Discussion

Our experiment presents some analogies with the RABBITT technique (Reconstruction of Attosecond Beating By Interference of Two-photon Transitions) used to determine the duration of attosecond pulses [8, 9]. In that case, a comb of odd order harmonics only is used to ionize helium in the presence of a weak fundamental laser field. Figure 28.2a,b present the *Up* and *Down* photoelectron energy spectra as a function of the time delay τ between the XUV and the IR pulses. Electrons are observed at energies corresponding to one photon absorption of the odd-order harmonics, and, located in between, sidebands peaks due to two-photon transitions (absorption of one XUV photon plus absorption or emission of one IR photon). The intensity of each sideband peak strongly oscillates with the time delay τ at twice the fundamental field frequency (ω_0), as predicted by second-order perturbation theory [10]. Moreover, by comparing Fig. 28.2a, b, we observe that oscillations for the electrons emitted in both *Up* and *Down* directions are in phase, which means that the electron emission is symmetric along the polarization vector of the light, at any time delay between APT and IR.

We now turn our attention toward the case where both odd and even harmonics are used to ionize helium in presence of a weak IR field. Figure 28.2c, d present the *Up* and *Down* energy spectra as a function of the time delay τ . The strong band is centered at an energy corresponding to absorption of 16th harmonic. We can observe two main differences from the RABBITT technique described above. First, the 16th energy peak oscillates with τ at the IR frequency ω_0 . Then, electrons

emitted in the Up and Down direction are totally out-of-phase. To better understand these features, we have modeled the angular-resolved photoelectron distribution $\frac{d\sigma}{d\Omega}$, in the framework of second-order perturbation theory. It can be shown that:

$$\begin{aligned} \frac{d\sigma}{d\Omega} &= |Y_{10}a_{16} + (Y_{00} + Y_{20})a_{15}|^2 \\ &= (|a_{16}|^2 + |a_{15}|^2) \sum_{J_{\text{even}}} P_J[\cos(\theta)] \\ &\quad + |a_{16}a_{15}| \cos(\omega_0\tau + \Delta_{15}^{16}\varphi + \Delta_{15}^{16}\Phi) \sum_{J_{\text{odd}}} P_J[\cos(\theta)], \end{aligned} \quad (28.1)$$

where a_{16} and a_{15} are, respectively, the one- and two-photon probability amplitudes associated with the 16th and 15th harmonics, P_J is the Legendre polynomial of J th order, and $\Delta_{15}^{16}\varphi$, $\Delta_{15}^{16}\Phi$ are, respectively, the phase difference between 16th and 15th harmonics and the atomic phase difference. Equation (28.1) shows that the angular distribution is the sum of two terms. The first term is the sum of the angular distributions for the one-photon and two-photon processes individually. This term does not depend on the time delay τ , and is proportional to even order Legendre polynomials, which are symmetric along the light polarization. The second term is an interference term coming from the cross product of the one- and two-photon transition amplitudes. This interference term varies sinusoidally with τ at the IR frequency ω_0 . Moreover, the interference term is proportional to odd order Legendre polynomials, which are antisymmetric along the light polarization.

Equation (28.1) clearly reproduces our experimental observations. The up/down asymmetry observed in the experiment is the consequence of the interference between one- and two-photon transitions. Finally, it is important to note that the total cross section is not modulated, since the continuum states populated by one- and two-photon absorption are orthogonal to each other.

28.4 Conclusion

In conclusion, we have studied the angular photoelectron emission from helium generated by an attosecond pulse train in the presence of a weak infrared field. A mix of energy-degenerate even and odd parity states is fed in the continuum by absorption of one, or two photons, and thus interferes. We show that the interference between the two electron wave-packets leads to an asymmetric electron emission along the polarization vector of the light, which can be controlled by varying the time delay between the APT and the IR pulses. We have observed the same effect (not shown here) for various different atomic targets (Ar, Ne, Kr).

Acknowledgements We are very grateful to C. D. Lin for bringing this study to our attention and for the illuminating discussions. This work was supported by the U.S. Army Research Office under Grant No. W911NF-071-0475, by Chemical Sciences, Geosciences and Biosciences Division, Office of Basic Energy Sciences, Office of Science, U.S. Department of Energy, and by the National Science Foundation under Grant No. CHE-0822646.

References

1. M. Schultze et al., *Science* **328**, 1658–1662 (2010)
2. G. Sansone et al., *Nature* **465**, 763–767 (2010)
3. A.L. Cavalieri et al., *Nature* **449**, 1029–1032 (2007)
4. J. Mauritsson et al., *Phys. Rev. Lett.* **105**, 053001 (2010)
5. N.N. Choi et al., *Phys. Rev. A* **82**, 013409 (2010)
6. J. Mauritsson et al., *Phys. Rev. Lett.* **97**, 013001–013004 (2006)
7. A.T.J.B. Eppink et al., *Rev. Sci. Instrum.* **68**, 3477–3484 (1997)
8. P.M. Paul et al., *Science* **292**, 1689–1692 (2001)
9. Y. Mairesse et al., *Science* **302**, 1540–1543 (2003)
10. V. Vénierard et al., *Phys. Rev. A* **54**, 721–728 (1996)

Chapter 29

Control the Electron Dynamics in Nonsequential Double Ionization with the Orthogonal Two-Color Field

Yueming Zhou and Peixiang Lu

Abstract We numerically demonstrate the control of the recollision process in nonsequential double ionization (NSDI) of helium with the orthogonally polarized two-color field. By changing the relative phase of the fields, the revisit time of the recolliding electron wave packet can be precisely controlled. As a result, the two-electron momentum distributions from NSDI are manipulated to reveal strong correlated or anticorrelated behaviors. We also demonstrate the application of the orthogonal two-color scheme in the molecular clock experiment.

29.1 Introduction

Nonsequential double ionization (NSDI) has been a hot topic in strong field laser-matter interactions ever since the observation of the surprisingly high double ionization (DI) yield [1]. In NSDI the two ionized electrons exhibit strong correlated behaviors [2]. Nowadays, it is widely accepted that the recollision mechanism is responsible for NSDI [3]. According to this mechanism, the first electron that tunnels out of the atom is accelerated by the electric field, and returns to the parent ion when the electric field reverses its direction, kicking out the second electron with an inelastic recollision. The recollision between the first electron and the parent ion is the centra of the studies on the electron dynamics of NSDI. In this paper, with a classical ensemble model, we demonstrated the control of the recollision process with the orthogonally polarized two-color field. As an efficient tool to control the electron dynamics, the orthogonal two-color field has been widely studied [4]. Here, we show that the revisit time of the recolliding electron wave packet (REWP) can be controlled with attosecond resolution by changing the

Y. Zhou · P. Lu (✉)

Wuhan National Laboratory for Optoelectronics, Huazhong University of Science and Technology, Wuhan 430074, People's Republic of China
e-mail: lupeixiang@mail.hust.edu.cn

relative phase of the orthogonal two-color field. Because of the control of the revisit time, the two-electron momentum distributions are manipulated to exhibit correlated or anticorrelated patterns, which implies that the orthogonal two-color field can serve as a powerful tool to control the electron dynamics in NSDI. We also demonstrate the application of this orthogonal two-color field in improving the time resolution of the well-known molecular clock. This offers a promising method for real-time observation of the ultrafast molecular dynamics with attosecond resolution.

29.2 Results and Discussion

We employ the classical ensemble model proposed by Haan and Eberly et al. [5]. We have investigated the physical process of NSDI with this classical model before [6–9]. The details of the calculation are given in [10, 11]. The electric field is expressed as $\mathbf{E}(t) = f(t)[E_{x0}\cos(\omega t)\hat{\mathbf{x}} + E_{y0}\cos(2\omega t + \phi)\hat{\mathbf{y}}]$. $\hat{\mathbf{x}}$ and $\hat{\mathbf{y}}$ are the polarization vectors. $f(t)$ is the laser envelope which turns on and turns off linearly during $2T_1$ and keeps full strength for $6T_1$ (T_1 is the period of the laser field along x axis). E_{x0} , E_{y0} are amplitudes of the electric fields, ω is the laser frequency and ϕ is the relative phase.

We first show the DI yield of helium as a function of the relative laser phase of the orthogonal two-color field which is consisted by an 800nm field (along x axis) and a 400nm field (along y axis). It is clearly shown in Fig. 29.1 that the yield depends sensitively on the relative phase. This phenomenon results from the fact that only at a certain range of relative phase the electron wave packet fulfills the recollision conditions in two dimensions. In the relative phase ranges where the recollision conditions in two dimensions are not fulfilled, DI yields are strongly suppressed. In Fig. 29.2 we show the two-electron momentum distributions along the polarization direction of the 800nm field. It is clearly seen that for the two-color field the electron correlation behaviors depend sensitively on the relative phase. When $\phi = 0.5\pi$, the correlated electron momentum reveals a surprising anticorrelated behavior. When ϕ changes to 0.6π , the distribution extends to the first and third quadrants and the anticorrelation is not as strong as that for $\phi = 0.5\pi$. When $\phi = 0.7\pi$, $\phi = 0.8\pi$ and $\phi = 0.9\pi$, the electron momentum spectra are dominated by correlated emission. The detailed explanation for the phase-dependence electron correlation is given in [10]. These results mean that the orthogonal two-color field is a powerful tool to control the electron dynamics in NSDI.

We also investigated the control of the REWP in molecular NSDI by the orthogonal two-color field [11]. In the molecular clock experiment proposed in a previous paper [12], by changing the wavelength of the driving field, the revisit time of REWP is controlled. As a result, the molecular dynamics is observed with a time resolution of about 1 fs. In the following we demonstrate that the revisit time of REWP can be controlled with a much higher accuracy, thus the time resolution of the molecular clock can be improved significantly.

Fig. 29.1 DI yield of He as a function of the relative phase. The intensities of both laser fields are 0.4 PW/cm^2

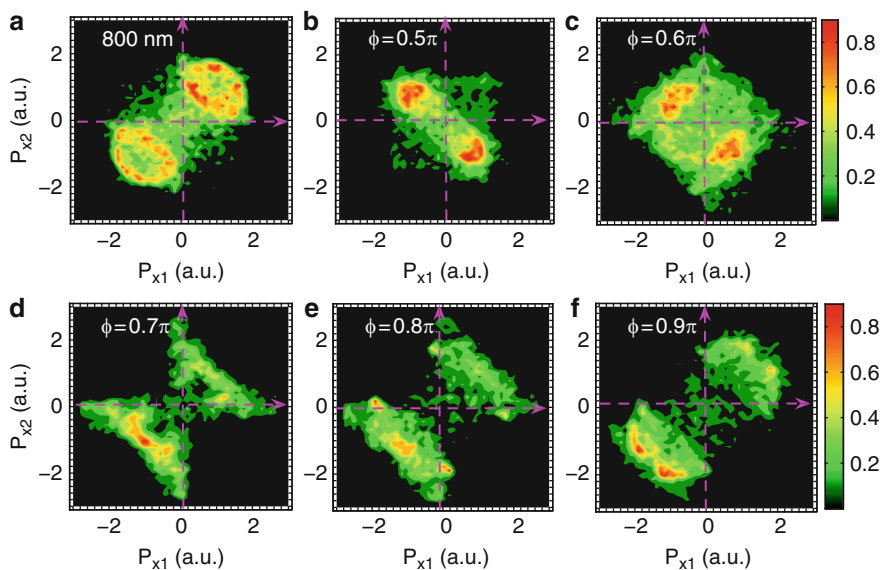
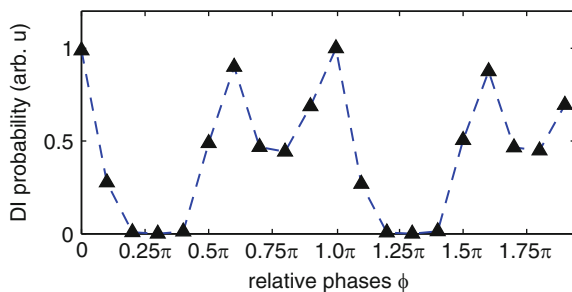


Fig. 29.2 Two-electron momentum distributions along the polarization direction of the 800-nm field for NSDI of helium (a) by the 800-nm field, and (b)–(f) by the orthogonally polarized *two-color* fields with relative phase $\phi = 0.5\pi, 0.6\pi, 0.7\pi, 0.8\pi, 0.9\pi$, respectively. The intensities of both fields are 0.4 PW/cm^2

For small molecules, the electron-ion recollision can either induce double ionization (DI) or dissociation [13]. Here we concern with the recollision-induced DI channel. Thus we only analyze the REWP of the DI trajectories of H_2 . In Fig. 29.3 we display the travel time of REWP, i.e., the time delay between recollision and first ionization for the DI trajectories of H_2 , as a function of the relative phase. The travel time varies gradually with the changing relative phase for both the $800 + 400 \text{ nm}$ and $1,600 + 800 \text{ nm}$ two-color fields. For the $800 + 400 \text{ nm}$ field, a variation of ϕ as much as 0.1π induces a change of delay time less than 200 as, and for the $1,600 + 800 \text{ nm}$ field a resolution of about 400 as is achieved. It can be expected that a smaller variation of the relative phase will result in a higher time resolution.

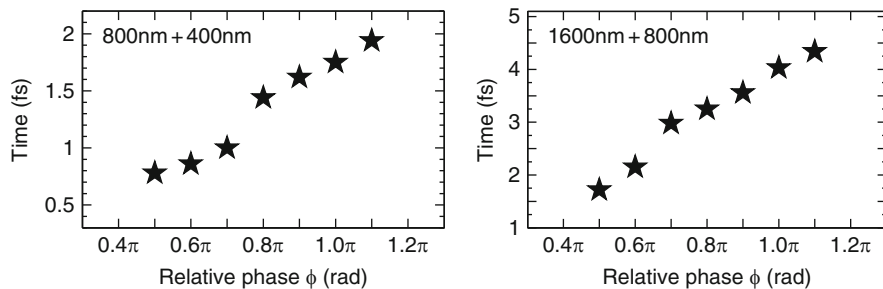


Fig. 29.3 The time delay as a function of the relative phase ϕ . Here only the DI ionization trajectories of H_2 are included in the statistics. The intensities of both fields are 0.1 PW/cm^2

This characteristic makes the orthogonal two-color field a promising method for the real-time observation of the attosecond molecular dynamics.

29.3 Conclusion

In conclusion, we demonstrated the control of revisit time of REWP by the orthogonal two-color field. By changing the relative phase of the fields, the revisit time of REWP is controlled with attosecond resolution. Thus the two-electron momentum distributions is manipulated to exhibit correlated or anticorrelated patterns. The precise control of the revisit time of REWP implies significant applications in observing the ultrafast molecular dynamics with attosecond resolution.

Acknowledgements This work was supported by the National Natural Science Foundation of China (NSFC) (No. 60925021 and No. 11004070) and the 973 Program of China (No. 2011CB808103).

References

1. A. IHuillier, L.A. Lompre, G. Mainfray, C. Maus, Phys. Rev. A **27**, 2503 (1983)
2. Th. Weber et al., Nature (London) **405**, 658 (2000)
3. P.B. Corkum, Phys. Rev. Lett. **71**, 1994 (1993)
4. M. Kitzler, M. Lezius, Phys. Rev. Lett. **95**, 253001 (2005)
5. S.L. Haan, L. Breen, A. Karim, J.H. Eberly, Phys. Rev. Lett. **97**, 103008 (2006)
6. Y. Zhou, Q. Liao, P. Lu, Phys. Rev. A **80**, 023412 (2009)
7. Y. Zhou, Q. Liao, P. Lu, Phys. Rev. A **82**, 053402 (2010)
8. Y. Zhou, C. Huang, P. Lu, Phys. Rev. A **84**, 023405 (2011)
9. Y. Zhou et al., Opt. Express **18**, 16025 (2010)
10. Y. Zhou et al., Opt. Express **19**, 2301 (2011)
11. Y. Zhou et al., Opt. Lett. **36**, 2758 (2011)
12. H. Niikura et al., Nature **421**, 826 (2003)
13. X.M. Tong, Z.X. Zhao, C.D. Lin, Phys. Rev. Lett. **91**, 233203 (2003)

Chapter 30

Sideband and Angular Distribution Oscillation of Photoelectrons Observed with XUV/IR 3D Momentum Imaging Spectroscopy

A. Sperl, H. Rietz, M. Schoenwald, A. Fischer, K. Simeonidis, and J. Ullrich

Abstract Noble gas atoms can be ionized by irradiation with an extreme-ultraviolet (XUV) attosecond pulse train emitting electron wave packets. The attosecond pulse trains can be characterized by superimposing the XUV and its generating, fundamental IR field and considering the energy transfer to the electron wave packets as a function of time delay between both fields, resulting in oscillating energy-sidebands. The three-dimensional dynamics of the photoelectrons however can now be studied in more detail by combining the XUV light source with a Reaction Microscope. In this context we changed the polarisation of the XUV and the IR fields with respect to each other by 90° , detecting a remarkable change of the angular distribution of the sideband-photoelectrons.

30.1 Introduction

Thirty years after A. Zewails pioneering experiments (Nobel Prize 1999), fast quantum-dynamical processes are intensively studied and analyzed by pump-probe experiments with short-pulse lasers. The recent crossover from femto- to attosecond light sources expands the measurable dynamical range of fast processes from nuclear to ultra-fast electron wave packet dynamics. Moreover, new spectroscopic

A. Sperl (✉) · H. Rietz · M. Schoenwald · A. Fischer · K. Simeonidis
MPI für Kernphysik, Saupfercheckweg 1, 69117 Heidelberg, Germany
e-mail: alexander.sperl@mpi-hd.mpg.de; helga.rietz@mpi-hd.mpg.de;
michael.schoenwald@mpi-hd.mpg.de; andreas.fischer@mpi-hd.mpg.de;
k.simeonidis@mpi-hd.mpg.de

J. Ullrich
MPI für Kernphysik, Saupfercheckweg 1, 69117 Heidelberg, Germany

Physikalisch-Technische Bundesanstalt, Bundesallee 100, D-38116 Braunschweig
e-mail: joachim.ullrich@mpi-hd.mpg.de

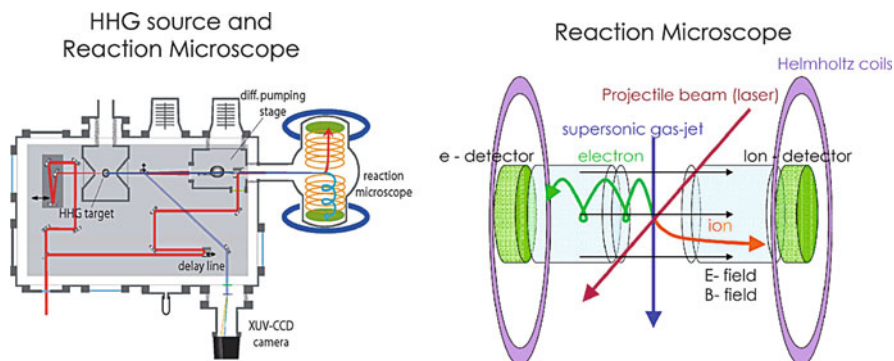


Fig. 30.1 *Left:* Setup for the High Harmonic Generation together with the Reaction Microscope. *Right:* Reaction Microscope with the dedicated detection geometry. By combining homogeneous electric and magnetic fields, the full three dimensional momentum components as well as the kinetic energy of all charged particles can be reconstructed. Furthermore electrons and ions can be measured in coincidence, allowing a kinematically full understanding of the underlying processes. Particularly with regard to molecular systems, the separation of different dissociation and ionization channels becomes possible

techniques have become available, thus offering unique possibilities for studying ultra-fast electron dynamics.

30.2 Experimental Setup

The experimental setup for the generation of the High Harmonics together with the Reaction Microscope is schematized in Fig. 30.1. The corresponding laser system delivers infrared (IR) pulses of 30 fs duration at single pulse energies of 1 mJ, a central wavelength of 785 nm and a repetition rate of 8 kHz. A part of the fundamental IR beam is focused into an argon gas tube at a pressure of 50–100 mbar, so that according to the well known “Three-Step-Model” [1], Higher Harmonics of the fundamental wave are generated. The High Harmonics consist of $2\hbar\omega$ -spaced high harmonic photons with a large plateau region, so that by an appropriate spectral selection a remarkable intensity with photon energies from 15 to 25 eV can be achieved. In the time domain these Harmonics are confined in a train of very short attosecond pulses where the single pulse duration is in the range of a few 100 as. The remaining IR-probe-beam can be varied in intensity up to values of 10^{15} W/cm² and delayed with respect to the XUV pulses, thus allowing phase-locked pump-probe experiments.

Many photoionization processes in atomic and molecular systems can be studied using the technique of momentum spectroscopy of charged particles (Reaction Microscope). The basic scheme behind this setup can be described in brief as follows: A photon beam is crossed with a supersonic atomic or molecular gasjet, with the interaction volume lying in the center of the Reaction Microscope. The generated charged particles can then be guided and detected by combining a cold

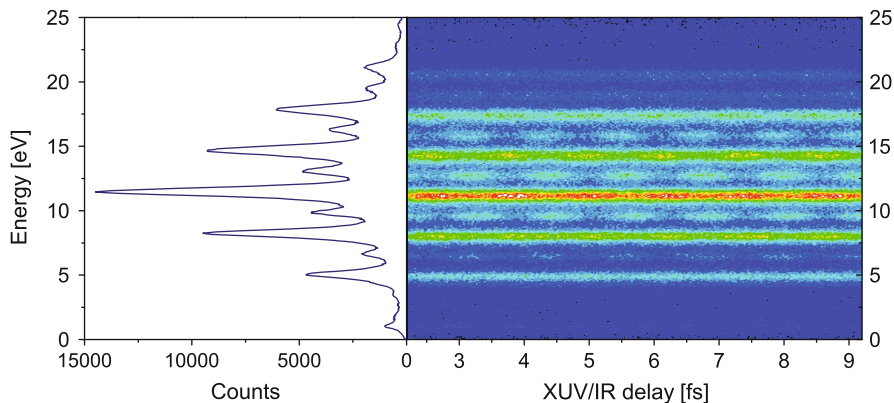


Fig. 30.2 Delay-dependent energy distribution of the photoelectrons together with the corresponding projection onto the energy axis. Since only odd Harmonics of the fundamental IR photons are generated, the energy of the sideband photoelectrons are exactly between two neighbouring High Harmonic photoelectron peaks. The plotted temporal delay covers a range of 3.5 optical cycles, which corresponds to 9.5 fs. The sideband peaks as well as the main XUV energy peaks oscillate once at every half IR cycle

target recoil-ion momentum spectrometer (COLTRIMS) with a large solid angle electron momentum spectrometer [2].

30.3 Sideband Oscillations

Here we report on photoionization of noble gas atoms as a result of simultaneous irradiation with extreme-ultraviolet (XUV) attosecond pulse trains and a moderately intense infrared (IR) laser field. As shown in Fig. 30.2 (left) under exact time and space overlap condition, harmonic as well as sideband peaks (all spaced by $\hbar\omega$) will appear in the photoelectron energy spectrum.

For each sideband there are two indistinguishable contributions, where one comes from the absorption of an IR-photon together with a primary XUV harmonic transition (q), and the other corresponds to the emission of an IR-photon from the consecutive primary XUV harmonic transition ($q+2$). Provided that the individual pulses within the attosecond pulse train are short, i.e. the intra-harmonic dispersion is small enough, the observed sideband intensity as well as the high-harmonic ionization lines show a periodic modulation with a period equal to the half-cycle period of the fundamental laser pulse, when the XUV-IR delay is varied (Fig. 30.2, right) [3]. However, as the width and especially the relative temporal position of a sideband maximum is determined by the phase difference between two neighbouring fundamental harmonic peaks, only the oscillation of the high-harmonic ionization signal in the delay dependent electron-energy spectrum contains the exact spectral

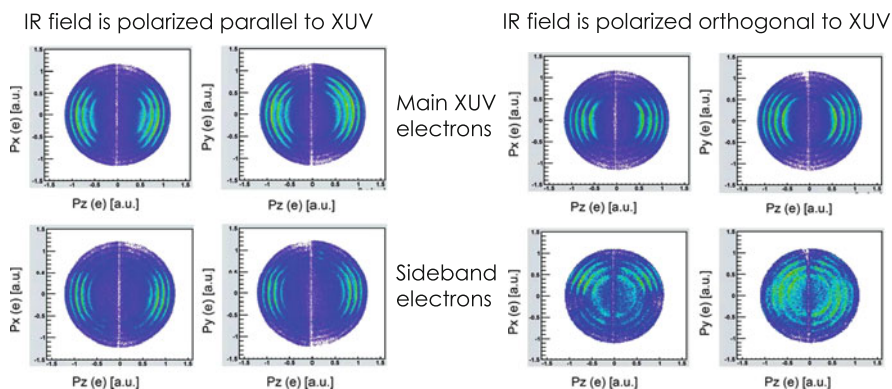


Fig. 30.3 Momentum distributions in the px – pz plane, as well as the py – pz plane of the sideband photoelectrons for two different polarisation settings. In the four spectra on the *left* side, both the XUV and the IR field are polarized along the spectrometer axis (*plong*), while in the *right* spectra the IR-polarization is changed by 90° (*y*-axis). The *upper row* represents only the momentum distribution of the XUV photoelectrons, while the *lower row* shows merely sideband electrons

phase information of the XUV pulses, allowing a precise characterization of the attosecond pulse trains. This technique is usually referred to as RABBIT (reconstruction of attosecond beating by interference of two-photon transitions) [4].

30.4 Angular Distributions

With the conducted experiments we study the three-dimensional (3D) photoelectron dynamics in the sideband-oscillations [5]. Changing the polarisation of the IR field by 90° with respect to the XUV, leads to significant modifications in the angular distribution of the detected sideband-photoelectrons, (Fig. 30.3).

Preliminary comparison with theoretical calculations show reasonable agreement (X.M. Tong, 2010, private communication), suggesting a main contribution of $3s$ -electrons in Argon. A detailed analysis of the time-resolved 3D-momentum spectra, particularly fully exploiting the angular distributions, promises new insight into ultra-fast electron dynamics.

References

1. P. Corkum, Phys. Rev. Lett. **71**, 1994, (1993) 81
2. J. Ullrich et al., Rep. Prog. Phys. **66**, 1463, (2003) 82
3. P. Johnsson et al., J. Mod. Opt. **53**, 233–245, (2006) 83
4. H.G. Muller, Appl. Phys. B **74**, 17–21, (2002) 84
5. T. Remetter et al., Nat. Phys. **2**, 323–326, (2006) 85

Chapter 31

Attosecond Pump-Probe of Doubly Excited States of Helium through Two-Photon Interferometry

Johannes Feist, Stefan Nagele, Christopher Ticknor, Barry I. Schneider, Lee A. Collins, and Joachim Burgdörfer

Abstract We show that correlated dynamics in wave packets of doubly excited helium can be followed in real time by a pump-probe setup based on two-photon interferometry. This approach promises to map the evolution of the two-electron wave packet onto experimentally easily accessible non-coincident single electron spectra.

Recent advances in laser sources have allowed the production of extreme ultraviolet (XUV) light pulses as short as 80 as [1]. This initiated the field of *attosecond physics*, dedicated to exploring electronic dynamics in atoms, molecules and solids in the time domain (see [2] and references therein). Most measurement protocols realized or proposed up to now rely on the interplay of a few-cycle IR pulse with a duration of a few femtoseconds and the synchronized attosecond XUV pulses produced by it. To achieve sub-fs time resolution, nonlinear effects depending on the instantaneous IR field strength (such as tunneling or streaking) are exploited. However, the presence of the non-perturbative IR field can strongly influence the dynamics under scrutiny. Therefore, excitation of an electronic wavepacket by an attosecond pump pulse, followed by an attosecond probe pulse to take snapshots of the ensuing electronic motion, has been dubbed the “holy grail” of attosecond

J. Feist (✉)

ITAMP, Harvard-Smithsonian Center for Astrophysics, Cambridge, MA 02138, USA
e-mail: jfeist@cfa.harvard.edu

S. Nagele · J. Burgdörfer

Institute for Theoretical Physics, Vienna University of Technology, 1040 Vienna, Austria, EU
e-mail: stefan.nagele@tuwien.ac.at

C. Ticknor · L.A. Collins

Theoretical Division, Los Alamos National Laboratory, Los Alamos, NM 87545, USA

B.I. Schneider

Office of Cyberinfrastructure, National Science Foundation, Arlington, VA 22230, USA

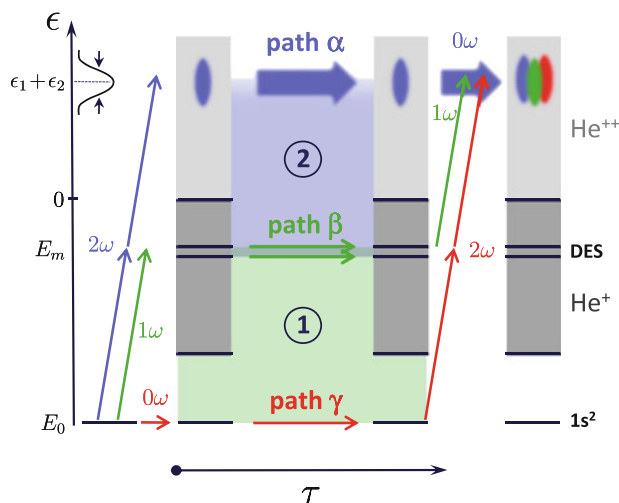


Fig. 31.1 Three-path interferometer for attosecond two-photon double ionization probing the coherent dynamics in DES. The three paths α , β , and γ are represented by *blue*, *green*, and *red arrows*, respectively (see text). Interference areas $\Delta E\tau$: area 1 (*light-green*) is delineated by (quasi-) bound states and is stable under average over ϵ_1, ϵ_2 ; area 2 (*in light-blue*) is delineated by the energy $E = \epsilon_1 + \epsilon_2$ of the two-electron continuum state and varies rapidly under variation of ϵ_1 or ϵ_2

physics. One obvious difficulty is the limited intensity of most current attosecond pulse sources, although rapid progress in increasing their efficiency is being made [3,4]. Accordingly, a first pump-probe experiment for autoionizing resonances in Xe on the one-femtosecond timescale has very recently been reported [5].

This experimental perspective challenges theory to identify possibilities for monitoring non-trivial correlated electronic motion in an XUV-XUV pump-probe setup. Hu and Collins [6] proposed to map out the wavepacket dynamics in *singly excited* helium. This requires a two-color pump-probe sequence and dominantly probes single-electron dynamics. Morishita *et al.*[7] showed that the correlated motion in a wavepacket among the *doubly excited* states (DES) of helium can be resolved by an XUV-XUV pump-probe scheme provided that the full six-dimensional momentum distribution is available. We here summarize our recently proposed single-color XUV-XUV *interferometric* pump-probe protocol [8], which allows to follow the correlated two-electron motion in DES by observing only (relatively) easily accessible non-coincident observables. We exploit the interference between three two-photon double ionization pathways (see Figure 31.1) in a fashion which greatly enhances the observable signal. To provide quantitatively accurate results, we solve the time-dependent Schrödinger equation (TDSE) in its full dimensionality (see [9] for more details).

The attosecond two-photon pump-probe sequence (Figure 31.1) can be viewed as a three-path interferometer, with the time delay τ between the pulses corresponding

to the ‘‘arm length.’’ Path α corresponds to two-photon double ionization by the pump pulse alone (see e.g. [9]), path γ is its replica induced by the probe pulse. The intermediate path β represents a proper pump-probe sequence where the first one-photon transition coherently excites a wavepacket of DES whose time evolution is then probed by double ionization by the second photon after the delay time τ . Two specific features of this three-path interferometer are key: first, path α represents a ‘‘fuzzy’’ slit, such that the interference phase $\Delta E \tau$ (represented by Area 2 in Figure 31.1) between path α and any other path rapidly varies over the Fourier width of the final energy $E = \epsilon_1 + \epsilon_2$ in the continuum, where ϵ_i is the energy of electron i . Any partial trace over unobserved variables, e.g. ϵ_1 , will wipe out the interference fringes associated with path α and will result in an incoherent and τ -independent background contribution to the observed electron spectra. Second, the contribution from path γ can be seen as a delay-independent *reference wave* that the signal of interest from path β interferes with, enhancing the observable signal.

By choosing an appropriate spectral window between the two ‘‘sequential peaks’’ at $\omega - I_1$ and $\omega - I_2$ (where I_n is the n th ionization potential) in the single-electron spectrum, contributions from unwanted paths¹ can be eliminated. We analyze the results using a simple semianalytical model (similar to those used in [10, 11] for XUV-IR setups). This exploits the fact that only the initial state $|\gamma\rangle \equiv |1s^2\rangle$ and DES $|\beta^m\rangle \equiv |2snp^\pm\rangle$ within the pump pulse bandwidth² contribute to double ionization within the spectral window. Up to a global phase, the double ionization amplitude is $\langle \mathbf{K} | \psi_f \rangle = \gamma_{\mathbf{K}} + \sum_m e^{-i\Delta E_m \tau} \beta_{\mathbf{K}}^m$, where $\mathbf{K} \equiv (\mathbf{k}_1 \mathbf{k}_2)$, $\Delta E_m = E_m^\beta - E_0^\gamma$, τ is the time between the pulses, and $g_{\mathbf{K}} = \langle \mathbf{K} | \hat{U}^{(2)} | g \rangle \langle g | \hat{U}^{(1)} | \gamma \rangle$ (for $g = \beta, \gamma$). E_m^β (E_0^γ) is the complex energy of the doubly excited state $|\beta^m\rangle$ (initial state $|\gamma\rangle$), while $\hat{U}^{(i)}$ is the time evolution operator associated with the i th pulse (1=pump, 2=probe).

Each of the mixed terms $\gamma_{\mathbf{K}}^* \beta_{\mathbf{K}}^m$ in the probability $P_{\mathbf{K}} = |\langle \mathbf{K} | \psi_f \rangle|^2$ oscillates with frequencies $\text{Re}(\Delta E_m)$ corresponding to periods of ≈ 70 as. The superposition of several terms, $\widehat{\beta}_{\mathbf{K}}(\tau) = \sum_m e^{-i\Delta E_m \tau} \beta_{\mathbf{K}}^m$, leads to a modulation with frequencies $\text{Re}(E_m - E_{m'})$ corresponding to periods on the (multi-)femtosecond scale (Figure 31.2). Since $|\widehat{\beta}_{\mathbf{K}}|^2$ is proportional to the product of two one-photon two-electron transition probabilities, it is three to four orders of magnitude smaller than $|\gamma_{\mathbf{K}}|^2$. Consequently, $\text{Re}(\gamma_{\mathbf{K}}^* \widehat{\beta}_{\mathbf{K}})$ is enhanced by orders of magnitude compared to the true pump-probe signal $|\widehat{\beta}_{\mathbf{K}}|^2$. The modulation amplitude is $A_M(\tau) = 4 \left| \int_M \gamma_{\mathbf{K}}^* \widehat{\beta}_{\mathbf{K}} d\mathbf{K} \right|$, where M is the region of final-state electron momenta integrated over. $A_M(\tau)$ is the experimentally accessible signal and agrees remarkably well with the (inaccessible) direct contribution from the DES pump-probe path, $P_M^\beta = \int_M |\widehat{\beta}_{\mathbf{K}}|^2 d\mathbf{K}$ (Figure 31.3).

It is now of crucial importance to identify the observables which the signal $A_M \propto P_M^\beta$ can give access to. Single-photon double ionization of DES is mediated by final

¹Such as single ionization or ejection of one electron by each pulse.

²We obtain the autoionizing DES as isolated states by *exterior complex scaling*, cf. [12].

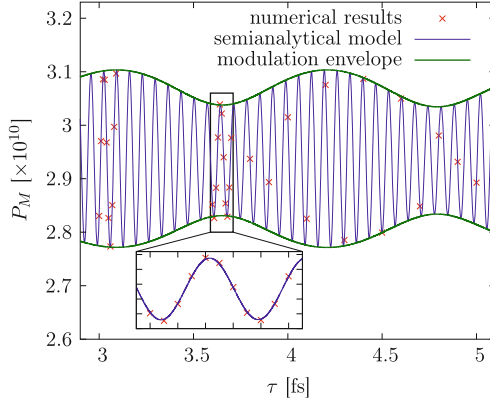


Fig. 3.12 Yield of the restricted one-electron spectrum ($16.3 \text{ eV} < \epsilon < 28.6 \text{ eV}$) resulting from double ionization of He by a 1 fs 20 nm pump-1 fs 20 nm probe sequence from the ground state as a function of delay time τ . *Crosses*: full numerical solution of the TDSE; *thin blue line*: semianalytical model including doubly excited resonances $|2snp^+\rangle$, $n = 2-5$, and $|2s3p^-\rangle$; *thick green line*: envelope of the modulation of the fast oscillation $A_M(\tau)$. *Inset*: magnification for detailed quantitative comparison

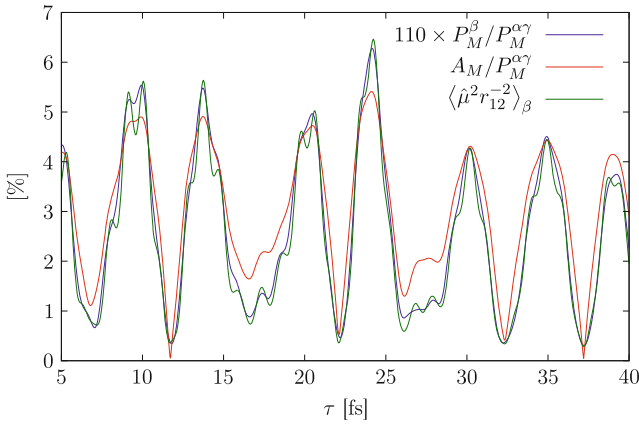


Fig. 3.13 Yield P_M^β from DES and modulation A_M , shown as ratios to the background yield $P_M^{\alpha\gamma} = 2 \int_M |\gamma \mathbf{k}|^2 d\mathbf{K}$ from paths α and γ , for the restricted one-electron spectrum ($17.7 \text{ eV} < \epsilon < 30.0 \text{ eV}$), compared with the DES expectation value $\langle \hat{\mu}^2 r_{12}^{-2} \rangle_\beta$. The pulses (\sin^2 shape with 2 fs total duration, central wavelength 19 nm) coherently excite $|2snp^+\rangle$ ($n = 3-8$) with appreciable probability

state correlation, i.e., to lowest order perturbation theory by the well-known two-step-one (TS1) process where one electron absorbs the photon and ejects the second electron by a collisional interaction [13]. The probability for this process is

$$P_M^\beta(\tau) \propto \int_M d\mathbf{K} \langle \psi_\beta | \hat{\mu} r_{12}^{-1} | \mathbf{K}_{(0)} \rangle \langle \mathbf{K}_{(0)} | r_{12}^{-1} \hat{\mu} | \psi_\beta \rangle \approx \langle \psi_\beta | \hat{\mu}^2 r_{12}^{-2} | \psi_\beta \rangle, \quad (31.1)$$

where $\mathbf{K}_{(0)}$ represents the uncorrelated double continuum state, $\hat{\mu} = \hat{p}_{z,1} + \hat{p}_{z,2}$ is the dipole transition operator and $|\psi_{\beta}\rangle$ is the DES part of the intermediate wave packet. In the second step in Eq. (31.1), the closure approximation $\int_M |\mathbf{K}_0\rangle \langle \mathbf{K}_0| d\mathbf{K} \approx 1$ has been used. Given the poor *a priori* justification for this approximation, Eq. (31.1) agrees surprisingly well with A_M (Figure 31.3).

In summary, we have shown that time-resolved correlated dynamics in doubly excited states of helium can be followed in real time through two-photon interferometry in the non-coincident single-electron spectrum [8]. Absorption of two photons from the probe pulse provides a *reference wave* that the signal of interest interferes with and that greatly enhances the observable signal.

Acknowledgements We acknowledge support by the FWF-Austria, grants No. SFB041 and P21141-N16 (S.N. and J.B.) and by the NSF through a grant to ITAMP (J.F.). C.T. and L.A.C. acknowledge support from LANL, which is operated by LANS, LLC for the NNSA of the U.S. DOE under Contract No. DE-AC52-06NA25396. The computations used the Vienna Scientific Cluster, Institutional Computing resources at Los Alamos National Laboratory, and NSF TeraGrid resources provided by NICS and TACC under grant TG-PHY090031.

References

1. E. Goulielmakis *et al.*, Science **320**, 1614 (2008). <http://dx.doi.org/10.1126/science.1157846>
2. F. Krausz, M. Ivanov, Rev. Mod. Phys. **81**, 163 (2009). <http://dx.doi.org/10.1103/RevModPhys.81.163>
3. E.J. Takahashi *et al.*, Phys. Rev. Lett. **104**, 233901 (2010). <http://dx.doi.org/10.1103/PhysRevLett.104.233901>
4. S. Gilbertson *et al.*, Phys. Rev. A **81**, 043810 (2010). <http://dx.doi.org/10.1103/PhysRevA.81.043810>
5. P. Tzallas *et al.*, Nature Physics **7**, 781 (2011). <http://dx.doi.org/10.1038/nphys2033>
6. S.X. Hu, L.A. Collins, Phys. Rev. Lett. **96**, 073004 (2006). <http://dx.doi.org/10.1103/PhysRevLett.96.073004>
7. T. Morishita, S. Watanabe, C.D. Lin, Phys. Rev. Lett. **98**, 083003 (2007). <http://dx.doi.org/10.1103/PhysRevLett.98.083003>
8. J. Feist *et al.*, Phys. Rev. Lett. **107**, 093005 (2011). <http://dx.doi.org/10.1103/PhysRevLett.107.093005>
9. R. Pazourek *et al.*, Phys. Rev. A **83**, 053418 (2011). <http://dx.doi.org/10.1103/PhysRevA.83.053418>
10. J. Mauritsson *et al.*, Phys. Rev. Lett. **105**, 053001 (2010). <http://dx.doi.org/10.1103/PhysRevLett.105.053001>
11. N.N. Choi *et al.*, Phys. Rev. A **82**, 013409 (2010). <http://dx.doi.org/10.1103/PhysRevA.82.013409>
12. C.W. McCurdy, M. Baertschy, T.N. Rescigno, J. Phys. B **37**, R137 (2004). <http://dx.doi.org/10.1088/0953-4075/37/17/R01>
13. S.L. Carter, H.P. Kelly, Phys. Rev. A **24**, 170 (1981). <http://dx.doi.org/10.1103/PhysRevA.24.170>

Chapter 32

Controlling and Reading Interference Structures Created by Strong Field Ionizing Attosecond Electron Wave Packets

X. Xie, S. Roither, D. Kartashov, L. Zhang, E. Persson, S. Gräfe, M. Schöffler, J. Burgdörfer, A. Baltuška, and M. Kitzler

Abstract We use cycle-sculpted two-color waveforms to drive electronic wavepackets generated by strong-field ionization from helium gas atoms and analyse their momentum spectra measured by electron-ion coincidence momentum spectroscopy. Varying the relative phase of the two colors allows to sculpt the ionizing field and hence to control the emission times and motion of the wavepackets on an attosecond timescale. We show that the measured electron momentum spectra contain interference patterns created by pairs of electron wavepackets that are released within a single laser-field-cycle. We experimentally distinguish these sub-cycle interference structures from above-threshold ionization (ATI) peaks and argue that they can be used to extract the sub-cycle phase-evolution of the laser-driven complex bound-state wavefunction.

Recording the momentum spectra of coherently generated electron wavepackets allows for interferometric measurements: When the spectra overlap at their time of detection one observes interference structures [1, 2] very similar to the interference fringes of coherent optical pulses imprinted onto optical intensity spectra. A well-known type of interference structures created by electron wavepackets are the above-threshold ionization (ATI) peaks in photoelectron energy spectra [3]. These are generated by wavepackets released by strong-field ionization during different cycles of period T of an intense laser field [4] and are spaced by the laser photon energy $\hbar\omega$ with $\omega = 2\pi/T$ the laser frequency. These type of interferences have also been called the intercycle structures [4]. Interfering pairs of wavepackets, however, can also be created within the same laser cycle [4, 5] released with delays

X. Xie · S. Roither · D. Kartashov · L. Zhang · M. Schöffler · A. Baltuška · M. Kitzler (✉)
Photonics Institute, Vienna University of Technology, A-1040 Vienna, Austria

E. Persson · S. Gräfe · J. Burgdörfer
Institute for Theoretical Physics, Vienna University of Technology, A-1040 Vienna, Austria
e-mail: markus.kitzler@tuwien.ac.at

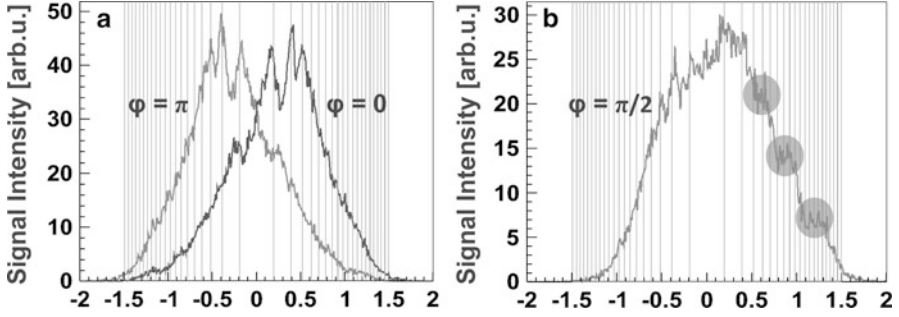


Fig. 32.1 (a) Measured momentum spectra of He^+ along the laser polarization direction, z , for $|p_y| < 0.2$ au with p_x integrated over for $\varphi = 0$ and $\varphi = \pi$. Due to momentum conservation the ion momentum distribution is the mirrored electron momentum distribution. The vertical lines mark the position of the ATI peak of order n , $p_{n,ATI} = \pm\sqrt{2(n\omega - I_p - U_p)}$, where I_p is the ionization potential and U_p the ponderomotive potential. (b) Same as (a) but for $\varphi = \pi/2$. The dots mark the sub-cycle interference patterns

smaller than T . They lead to interference fringes of sub-cycle origin which are visible as a modulation of the ATI-peak structures. Their relative sub-cycle release time Δt is encoded in momentum with smaller Δt interfering at higher momenta.

When pairs of wavepackets are launched at different instants of time, their differences in quantum phases are accumulated during ionization and propagated in the presence of both the ionic and laser field. It is thus possible to actively control and modify the interference fringes with cycle-sculpted laserfields. We describe experiments that exploit this opportunity for helium atoms using a two-color incarnation of such laser fields.

In our experiments we generated cycle-sculpted field-cycles by coherently superimposing a strong ~ 30 fs (FWHM) 790 nm laser pulse, frequency ω , and its roughly twice as long second harmonic pulse, frequency 2ω , with parallel polarization directions in a collinear geometry and with equal peak intensities at the focus of a spherical mirror, such that the total electric field of the two-color pulse can be written as $E(t) = \hat{E}[f_1(t) \cos(\omega t) + f_2(t) \cos(2\omega t + \varphi)]$, with $f_i(t)$, $i = 1, 2$, Gaussian pulse envelopes with maximum values of 1, φ the two colors' relative phase and \hat{E} the peak electric field (here and throughout the paper atomic units are used unless otherwise stated). The repetition rate of the pulses was 5 kHz. Varying the relative phase φ of the two colors allows to sculpt the ionizing field and hence to control the emission times and motion of the interfering wavepackets on an attosecond timescale. We use Cold Target Recoil Ion Momentum Spectroscopy (COLTRIMS) [6] to measure the three-dimensional vector of electrons and ions emerging from the interaction of a single atom with the sculpted laserfields.

Interference structures of intercycle (ATI peaks) and sub-cycle origin are contained in the measured momentum spectra along p_z as a function of φ shown in Fig. 32.1. The electron momentum in the orthogonal direction, y , has been restricted to $|p_y| < 0.2$. The third dimension p_x has been integrated over. The spectra display

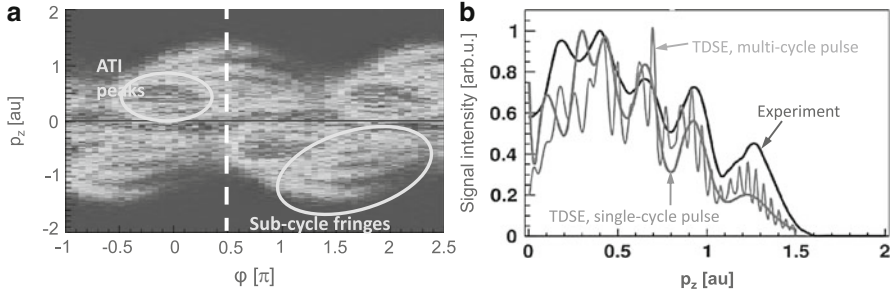


Fig. 32.2 (a) Measured momentum spectra of He^+ along p_z , for $|p_y| < 0.2$ au with p_x integrated over as a function of φ . From the raw spectra [as shown in Fig. 32.1a, b] an overall Gaussian shape has been subtracted to enhance the visibility of the sub-cycle interference patterns that sensitively depend on the laserfield shape and therewith on φ , visible as the indicated bow-like structures. The ATI-peaks do not depend on the field's shape and are therewith independent of φ . (b) Comparison of the measured spectrum for $\varphi = \pi/2$, normalized to 1, with spectra calculated using the TDSE for a multi-cycle pulse and single-cycle pulse

interference peaks of different origin and whose position and shape strongly depend on φ . While at small $|p_z|$, i.e., small energies, they coincide with the position of interference peaks equispaced in $\hbar\omega$, commonly known as ATI peaks [3, 4], for larger momenta $|p_z| \gtrsim 1$ au the experimental resolution is insufficient to resolve them. Instead, the spectrum for $\varphi = \pi/2$ features a modulation of the spectrum unrelated to ATI. These kinks are the sub-cycle interference fringes which can be described as an interferogram of the form $P(p_z) \propto \cos^2(\Delta\alpha(p_z)/2)$ created by the phase-difference $\Delta\alpha(p_z)$ of two electron wavepackets released within a single laser cycle.

The position and shape of the sub-cycle interference peaks sensitively depend on the shape of the laser field cycle which we control by varying φ . By contrast, the ATI peaks are created by interference of wavepackets released during different laser cycles and their positions thus reflect the periodicity T of the field giving equispaced peaks in $\hbar\omega$ independent of φ . Sub-cycle and ATI fringes can be clearly separated from each other by studying the variation of the longitudinal spectrum with φ , see Fig. 32.2a. The sub-cycle fringes appear as bow-like structures whose positions vary strongly with φ . The strong asymmetry of the spectra about $p_z = 0$, which is a further consequence of the two-color field, allows to detect them well apart from low-energy resonances [7]. Maximum fringe spacing and highest momenta are reached for $\varphi = (0.5 + n)\pi$, $n \in \mathbb{Z}$. In contrast, the position of the ATI peaks is independent of φ only determined by T (or, equivalently, ω).

A detailed comparison between experiment and simulation using the time-dependent Schrödinger equation (TDSE) can be found in Fig. 32.2b for $\varphi = \pi/2$, for which the sub-cycle fringes reach the highest momenta and largest fringe spacing. In the figure the experimental spectrum is compared to simulated spectra for a multi-cycle and single-cycle pulse. The spectrum for the multi-cycle pulse consists of a series of ATI peaks equidistant in energy, i.e. with decreasing spacing

towards higher momenta. The ATI peak structure is clearly modulated with minima and maxima following those of the spectrum for a single-cycle pulse, for which the periodicity of the laser field cycle is broken and thus the creation of ATI peaks is suppressed. Comparison of the experimental spectrum with that created by the single-cycle pulse clearly confirms the appearance of the sub-cycle peaks in the experiment while the more densely spaced ATI peaks are not resolved.

From the measured interferogram at fixed φ , $P(p_z, \varphi) \propto \cos^2(\Delta\alpha(p_z)/2)$, it is possible to extract the phase-difference $\Delta\alpha(p_z)$ accumulated by two wavepackets that are released within one optical cycle of the two-color pulse. By using the semi-classical connection [8] between the momentum p_z and the time of birth of the wavepacket, the phase difference $\Delta\alpha(p_z)$ can be expressed as a function of the time delay between the emission of the two wavepackets within the same cycle. Using the relation $\mathbf{p} = -\mathbf{A}(t_b)$, with $\mathbf{A}(t)$ the laser vector potential, for the final momentum of an electron released at time t_b , allows t_b to be determined by inversion. However, this approximation neglects the force of the Coulomb binding potential on released wavepackets and only considers the force of the laser electric field. Time scales below ≈ 50 as are effectively inaccessible in our experiment since ionization is suppressed at small fields. Moreover, the useful time window is limited to reasonably high momenta $\gtrsim 0.3$ au or $\Delta t \lesssim 0.8$ fs due to the failure of the SFA for small momenta, for which the influence of the Coulomb potential and low-energy resonances becomes increasingly important. For the present two-color sculpted pulse, delay times between 50 as $\lesssim \Delta t \lesssim 800$ as can be probed with an estimated precision of less than 10 as at the largest delay times.

The such obtained phase-difference $\Delta\alpha(\Delta t)$ contains contributions due to the interaction with the laser field and with the Coulomb potential. The contribution of the laser field is the well-known Volkov phase and that due to the Coulomb field is the Coulomb eikonal phase [9]. If both of them are subtracted from the measured phase $\Delta\alpha(\Delta t)$, we are left with the sub-cycle phase-evolution of the bound state $\Delta\alpha_B(\Delta t)$. Thus, our work shows that measurement of sub-cycle electron wavepacket interference patterns can serve as a tool to measure the dynamics of the valence electron cloud in atoms and molecules, complementary to high-harmonic spectroscopy [10] and single attosecond pulse spectroscopy [11].

Acknowledgements We acknowledge funding by the Austrian Science Fund (FWF), Grant Numbers P21463-N22, P21141-N16, P23359-N16, SFB-016, V193-N16.

References

1. T. Remetter, P. Johnsson, J. Mauritsson, K. Varjú, Y. Ni, F. Lépine, E. Gustafsson, M. Kling, J. Khan, R. López-Martens, K.J. Schafer, M.J.J. Vrakking, A. LHuillier, *Nat. Phys.* **2**(5), 323 (2006)
2. F. Quéré, J. Itatani, G. Yudin, P. Corkum, *Phys. Rev. Lett.* **90**(7), 1 (2003)
3. P. Agostini, F. Fabre, G. Mainfray, G. Petite, N. Rahman, *Phys. Rev. Lett.* **42**(17), 1127 (1979)
4. D.G. Arbó, K.L. Ishikawa, K. Schiessl, E. Persson, J. Burgdörfer, *Phys. Rev. A* **81**(2), 021403 (2010)

5. R. Gopal, K. Simeonidis, R. Moshhammer, T. Ergler, M. Dürr, M. Kurka, K.U. Kühnel, S. Tschuch, C.D. Schröter, D. Bauer, J. Ullrich, A. Rudenko, O. Herrwerth, T. Uphues, M. Schultze, E. Goulielmakis, M. Uiberacker, M. Lezius, M. Kling, *Phys. Rev. Lett.* **103**(5), 053001 (2009)
6. R. Dörner, V. Mergel, O. Jagutzki, L. Spielberger, J. Ullrich, R. Moshhammer, H. Schmidt-Böcking, *Phys. Rep.* **330**(2–3), 95 (2000)
7. R. Freeman, P. Bucksbaum, H. Milchberg, S. Darack, D. Schumacher, M. Geusic, *Phys. Rev. Lett.* **59**(10), 1092 (1987)
8. M. Lewenstein, K. Kulander, K. Schafer, P. Bucksbaum, *Phys. Rev. A* **51**(2), 1495 (1995)
9. D. Arbó, K. Ishikawa, K. Schiessl, E. Persson, J. Burgdörfer, *Phys. Rev. A* **82**(4), 043426 (2010)
10. O. Smirnova, Y. Mairesse, S. Patchkovskii, N. Dudovich, D. Villeneuve, P. Corkum, M.Y. Ivanov, *Nature* **460**(7258), 972 (2009)
11. E. Goulielmakis, Z.H. Loh, A. Wirth, R. Santra, N. Rohringer, V.S. Yakovlev, S. Zherebtsov, T. Pfeifer, A.M. Azzeer, M.F. Kling, S.R. Leone, F. Krausz, *Nature* **466**(7307), 739 (2010)

Chapter 33

Electron Wavepacket Interference Observed by Attosecond Transient Absorption Spectroscopy

L. Gallmann, M. Holler, F. Schapper, and U. Keller

Abstract Attosecond time-resolved transient absorption spectroscopy is performed in a dense helium target by superimposing an attosecond pulse train (APT) with a moderately strong infrared field. We observe rapid oscillations of the absorption of the individual harmonics as a function of time-delay between the APT and IR field even for harmonic energies well below the ionization threshold. The phase dependence of these modulations on atto-chirp and IR intensity yields direct evidence for the interference of transiently bound electronic wavepackets as the underlying mechanism.

33.1 Introduction

In a recent experiment, the He^+ ion yield after the absorption of high-harmonics generated in xenon and superimposed with an IR field was investigated [1]. It was found that the ion yield is modulated with twice the IR driving laser frequency. The result was explained by the interference of transiently bound electron wavepackets. We investigated this physical system with the all-optical approach of attosecond time-resolved transient absorption spectroscopy [2–4]. With our method, we spectrally resolve the harmonic photons transmitted through the target as a function of delay and thereby also gain direct access to bound–bound transitions inaccessible through techniques detecting the ionization fragments only. The different aspects probed by our optical technique enable us to verify the plausibility of the previously introduced intuitive theoretical model by Johnsson et al. [1] and to demonstrate attosecond control of the relative absorption of the individual spectral constituents of an APT. The rapid absorption modulation represents the fastest dynamics resolved by all-optical methods so far.

L. Gallmann (✉) · M. Holler · F. Schapper · U. Keller
Physics Department, ETH Zurich, 8093 Zurich, Switzerland
e-mail: gallmann@phys.ethz.ch

33.2 Results

We generate the APT in xenon with 30-fs pulses from a Ti:sapphire amplifier system. The average pulse duration in the APT was determined to 380 as with the RABBITT technique [5]. The energetic location of the harmonics forming the APT is shown in Fig. 33.1a. The infrared intensity in the helium target is chosen on the order of 10^{13} W/cm², which alone is not sufficient to induce strong-field processes in ground-state helium.

Figure 33.1b shows the transmitted photons of harmonic 13 as a function of delay. It can be clearly seen that the transmission (or absorption) of the harmonic is modulated at twice the infrared frequency. We find that the relative phases between the modulations at harmonics 13, 15, and 17 sensitively depend on the infrared intensity but remain unchanged within experimental uncertainty for

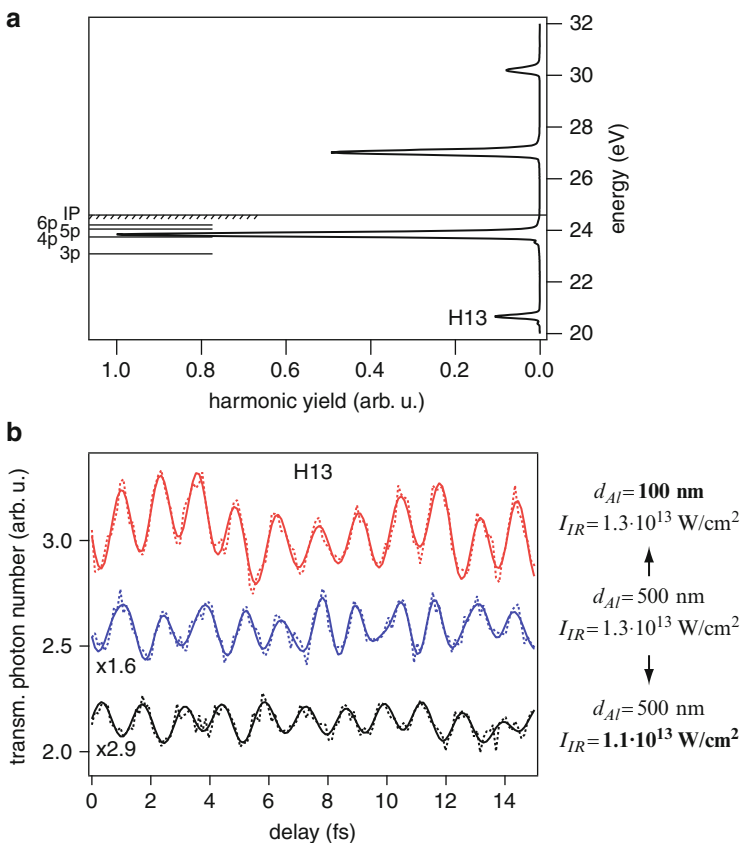


Fig. 33.1 (a) Energetic configuration of this experiment. Harmonic 13 is located well below the ionization threshold of helium. (b) Harmonic yield modulations as a function of APT-IR delay. The phase of the modulations is insensitive to the atto-chirp, but sensitively depends on the IR intensity

changing atto-chirp of the APT. This is due to the fact that the interference occurs between an EWP having accumulated phase during acceleration in the IR field and an EWP having just been excited from the ground state by the following attosecond pulse [4]. The relative phase is thus always being governed by the contribution from the IR driven EWP excursion. The atto-chirp phase contribution, on the other hand, is identical for each EWP and thus cancels upon interference. A more detailed discussion is given in [4].

33.3 Conclusion

These observations confirm the theoretical model by Johnsson et al. [1] and are consistent with two alternative theoretical pictures based on strong-field approximation [6] and Floquet theory [7], respectively.

The rapid absorption modulation observed in our experiment represents the fastest dynamics resolved by all-optical methods so far. By changing the IR-APT delay and the IR intensity, the relative absorption of the individual harmonics can be controlled with high precision. This can be considered a form of absorptive pulse shaping of the original APT.

Acknowledgements This research was supported by the NCCR Quantum Photonics (NCCR QP), a research instrument of the Swiss National Science Foundation (SNSF).

References

1. P. Johnsson, J. Mauritsson, T. Remetter, A. L'Huillier, K.J. Schafer, Attosecond control of ionization by wave-packet interference. *Phys. Rev. Lett.* **99**, 233001 (2007)
2. E. Goulielmakis, Z.-H. Loh, A. Wirth, R. Santra, N. Rohringer, V.S. Yakovlev, S. Zherebtsov, T. Pfeifer, A.M. Azzeer, M.F. Kling, S.R. Leone, F. Krausz, Real-time observation of valence electron motion. *Nature* **466**, 739–743 (2010)
3. H. Wang, M. Chini, S. Chen, C.-H. Zhang, F. He, Y. Cheng, Y. Wu, U. Thumm, Z. Chang, Attosecond time-resolved autoionization of argon. *Phys. Rev. Lett.* **105**, 143002 (2010)
4. M. Holler, F. Schapper, L. Gallmann, U. Keller, Attosecond electron wave-packet interference observed by transient absorption. *Phys. Rev. Lett.* **106**, 123601 (2011)
5. P.M. Paul, E.S. Toma, P. Breger, G. Mullot, F. Augé, P. Balcou, H.G. Muller, P. Agostini, Observation of a train of attosecond pulses from high harmonic generation. *Science* **292**, 1689–1692 (2001)
6. P. Rivière, O. Uhden, U. Saalmann, J.M. Rost, Strong field dynamics with ultrashort electron wave packet replicas. *New. J. Phys.* **11**, 053011 (2011)
7. X.M. Tong, P. Ranitovic, C.L. Cocke, N. Tushima, Mechanisms of infrared-laser-assisted atomic ionization by attosecond pulses. *Phys. Rev. A* **81**, 021404 (2010)

Chapter 34

Observing the Real-Time Evolution of Helium Atoms in a Strong Laser Field

Niranjan Shivaram, Henry Timmers, Xiao-Min Tong,
and Arvinder Sandhu

Abstract The interaction of a strong laser field with an atom significantly modifies its atomic structure. Such an atom can be modeled using the Floquet theory in which the atomic states are described by Floquet states composed of several Fourier components. We use high-order harmonics present in extreme-ultraviolet (XUV) attosecond pulse trains (APTs) to create excited states in infra-red(IR) laser dressed He atoms which are ionized by the dressing laser field itself. The quantum interference between different components of the Floquet states leads to oscillation in the ion yield as a function of XUV-IR time delay. We measure the phase of this quantum interference process through the phase of the ion yield signal which allows us to follow the evolution of the dressed atom, in real-time, as the intensity of the IR field is varied. We observe a transition from a 5p Floquet state dominated ionization to a 2p Floquet state dominated ionization with increasing IR intensity.

34.1 Introduction

Strong laser fields are routinely used to probe atomic and molecular dynamics in attosecond resolved pump-probe experiments. The effect of the strong field itself on the system that is being probed is often assumed to be quite small. But even laser fields with intensities on the order of 10^{12} W/cm² can significantly modify atomic and molecular structure. In the case of the Helium atom, which is the subject of investigation here, at intensities of $\sim 5 \times 10^{12}$ W/cm² the atomic structure bears no resemblance to the unperturbed atom. Hence, the study of strong field modification

N. Shivaram (✉) · H. Timmers · A. Sandhu
Department of Physics, University of Arizona, Tucson, AZ 85721, USA
e-mail: niranjan@physics.arizona.edu

X.-M. Tong
University of Tsukuba, Ibaraki 305-8573, Japan

of atomic and molecular systems is essential in understanding photoabsorption and photoionization processes in the presence of such strong fields.

In this work, we use high harmonics generated in Xe to excite He atoms from their ground state. An IR field created by the superposition of two IR pulses simultaneously dresses the atoms while they are being excited. One of the IR pulses (IR_d) is the high harmonic driving pulse and hence is phase locked to the APT. The other pulse (IR_p) is the probe pulse which is time delayed with respect to the $\text{APT} + \text{IR}_d$ and is about two orders of magnitude stronger in intensity compared to IR_d . We measure the ion yield as a function of this time-delay and observe oscillations in the ion yield. An intensity dependent phase change is observed in the 2ω (ω is the angular frequency of the IR fields) component of the signal which we interpret using a Floquet model. Through this phase variation, we observe the real-time evolution of the He atom in the IR field as the dominant ionization channel changes from being 5p Floquet state dominant to 2p Floquet state dominant with increasing IR intensity.

34.2 Floquet Model

According to the Floquet theory, an atom placed in an oscillating electric field is composed of Floquet states with many Fourier components [1]. When the atom is excited to more than one Fourier component with more than one high harmonic, the Fourier components corresponding to a given Floquet state interfere. This quantum interference leads to oscillations in ion yield signal as seen in this experiment.

The electric fields for the net IR field created by the superposition of IR_p and IR_d can be written as $E_{net} = A(\tau) \cos(\omega t + \delta(\tau))$. IR_d is delayed by τ with respect to IR_p . Here $A(\tau) = \sqrt{A_p^2 + A_d^2 + 2A_p A_d \cos(\omega\tau)}$ and $\delta(\tau) = \arcsin\left(\frac{A_d \sin(\omega\tau)}{A(\tau)}\right)$. A_p and A_d are the amplitudes of IR_p and IR_d respectively. Similar to the discussion in [2], for the case of APT and two IR fields used here, the probability of ionization can be written as

$$P(\tau) \propto \left| M_0[A(\tau)]f_0 + M_2[A(\tau)]f_2 e^{i(2\omega\tau + 2\delta_0 - 2\delta(\tau) + \phi)} \right|^2 \quad (34.1)$$

$M_0[A(\tau)]$ and $M_2[A(\tau)]$ are the intensity dependent matrix elements for transitions to two components of a given Floquet state, f_0 and f_2 are the strengths of the harmonics resonant with the two components and ϕ is the phase difference between these matrix elements. ϕ can have values of either 0 (2π) or π since the matrix elements of transitions to Floquet components are real numbers. δ_0 is the phase at which the APT is locked to IR_d .

In the approximation that $A_d \ll A_p$, the probability of ionization becomes

$$P(\tau) = P_1(\tau) \cos(\omega\tau) + P_2(\tau) \cos(2\omega\tau + 2\delta_0 + \phi) \quad (34.2)$$

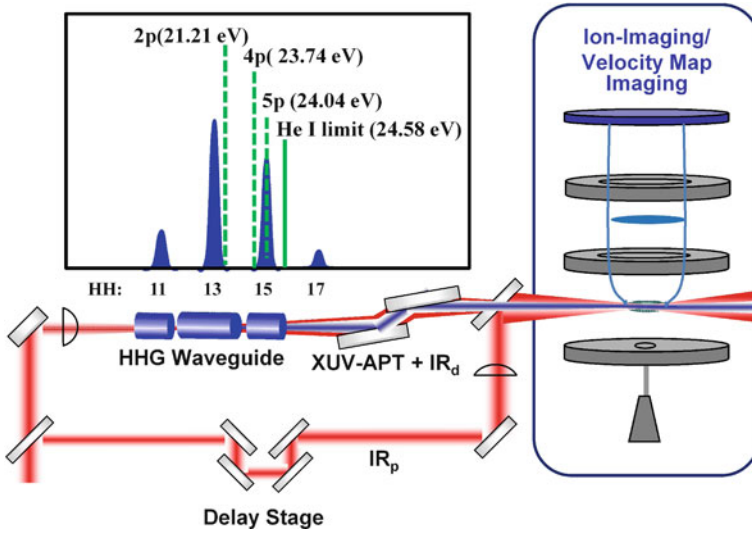


Fig. 34.1 Experimental setup. The *inset* shows the high harmonic spectrum used in the experiment and the relevant He atomic states

$P_1(\tau)$ and $P_2(\tau)$ are the time-delay dependent amplitudes of the ω and 2ω frequencies in the ion yield signal. When the ionization is mediated by a single dominant Floquet state, ϕ can be extracted from the phase of the ion yield signal by using time-dependent Schrodinger equation (TDSE) simulations to fix its absolute value.

34.3 Experimental Setup

The experimental setup is shown in Fig. 34.1. Amplified 65 fs, 785 nm IR pulse of 1.5 mJ energy is split into two pulses. One of the pulses is focused onto a Xe gas filled glass capillary to generate APTs. The APT along with its driving IR beam (IR_d) is focused onto an effusive He gas jet using a toroidal mirror. The other pulse (IR_p) goes on to a delay stage and is then focused with a 50 cm lens onto the He gas jet. He⁺ ions are imaged using a spatial imaging technique which allows us to eliminate signal washout due to Gouy phase averaging and obtain a high quality signal [3].

34.4 Results and Discussion

Figure 34.2a shows the normalized ion yield as a function of time-delay τ . At long time delay (lowest instantaneous intensity), the oscillations are dominated by the ω signal. As the intensity increases, the oscillations develop an asymmetric

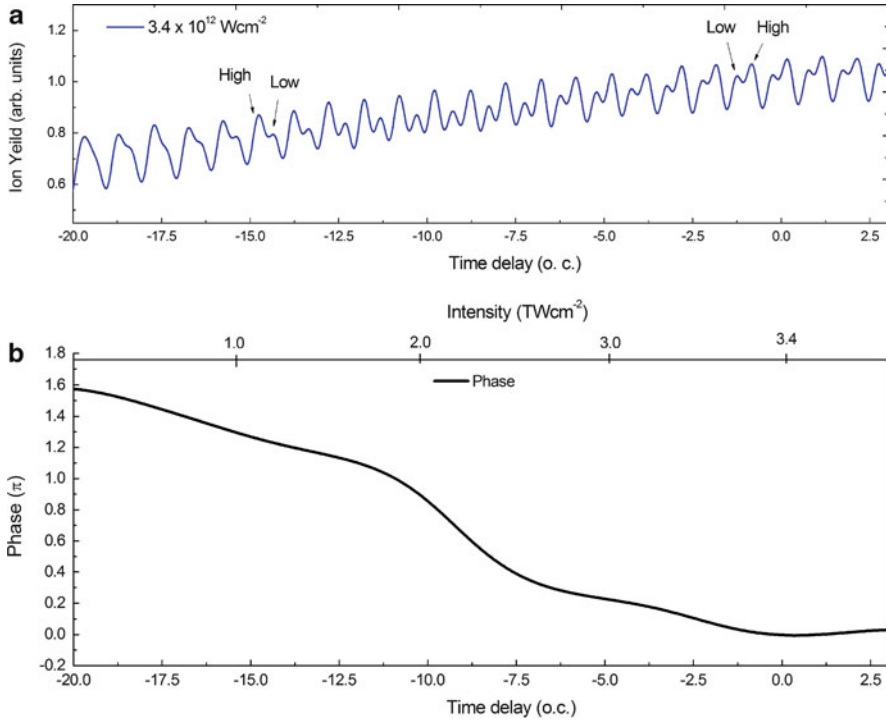


Fig. 34.2 (a) Normalized ion yield as a function of time delay τ in optical cycles (o.c.) between $\text{APT} + \text{IR}_d$ and IR_p for a peak IR_p intensity of 3.4 TW/cm^2 . (b) The phase of 2ω component of the scan. The *top axis* indicates the instantaneous intensity

double peak structure which is an indication of the presence of a 2ω signal. More importantly, the asymmetry of the double peak structure reverses with increasing intensity. This is a clear signature of the change of the 2ω phase with respect to the ω phase. The ω signal mainly appears due to an interference between the two IR pulses and we use this as a reference against which we measure the 2ω phase variation.

We use a Fourier transform based phase extraction technique to extract the phase variation of the 2ω signal as a function of time-delay. Figure 34.2b shows the extracted 2ω phase. From photo-electron angular distributions obtained in this same experiment, we deduce that at the peak intensity of 3.4 TW/cm^2 (near $\tau = 0$), the dominant ionization channel is a three IR-photon ionization of the XUV excited $2p$ Floquet state and at the lowest intensity of 0.7 TW/cm^2 the ionization is dominated by the $5p$ Floquet state. Ionization probability numbers based on XUV absorption cross section calculations corroborate this conclusion. TDSE simulations as in [2], for the parameters used in this experiment suggest that when the ionization is dominated by the $2p$ Floquet state, the phase ϕ is equal to zero. At an intensity of about 1.8 TW/cm^2 , the $4p$ Floquet state becomes dominant and has ϕ equal to π .

As the intensity is lowered further, the 5p Floquet state starts to become dominant with ϕ equal to 2π . The experimentally extracted phase in Fig. 34.2b clearly shows this variation as a function of time-delay (instantaneous intensity).

In conclusion, we have measured the variation of the quantum phase difference between transition matrix elements to Floquet state components as the dominant Floquet state mediating the ionization changes with intensity. This represents a real-time observation of the evolution of a laser dressed atom with the intensity of the laser field. This measurement can provide us with valuable insight into understanding photo-absorption and photo-ionization processes in the presence of strong laser fields.

Acknowledgements This work was supported by NSF grant PHY-0955274.

References

1. S.I. Chu, D.A. Telnov, Phys. Rep. Rev. Section Phys. Lett. **390**(1–2), 1 (2004)
2. X.M. Tong, N. Toshima, Phys. Rev. A **81**(4), 043429 (2010)
3. N. Shivaram, A. Roberts, L. Xu, A. Sandhu, Opt. Lett. **35**(20), 3312 (2010)

Chapter 35

Electron Correlation and Interference Effects in Strong-Field Processes

Markus C. Kohler, Carsten Müller, Christian Buth, Alexander B. Voitkiv, Karen Z. Hatsagortsyan, Joachim Ullrich, Thomas Pfeifer, and Christoph H. Keitel

Abstract Several correlation and interference effects in strong-field physics are investigated. We show that the interference of continuum wave packets can be the dominant mechanism of high-harmonic generation (HHG) in the over-the-barrier regime. Next, we combine HHG with resonant X-ray excitation to force the recolliding continuum electron to recombine with a core hole rather than the valence hole from that it was previously tunnel ionized. The scheme opens up perspectives for nonlinear xuv physics, attosecond X-ray pulses, and spectroscopy of core orbitals. Then, a method is proposed to generate attochirp-free harmonic pulses by engineering the appropriate electron wave packet. Finally, resonant photoionization mechanisms involving two atoms are discussed which can dominate over the direct single-atom ionization channel at interatomic distances in the nanometer range.

M.C. Kohler (✉) · C. Müller · A.B. Voitkiv · K.Z. Hatsagortsyan · T. Pfeifer · C.H. Keitel
Max-Planck-Institut für Kernphysik, Saupfercheckweg 1, 69117 Heidelberg, Germany
e-mail: markus.kohler@gmx.de; carsten.mueller@mpi-hd.mpg.de;
alexander.voitkiv@mpi-hd.mpg.de; k.hatsagortsyan@mpi-hd.mpg.de; tpfeifer@mpi-hd.mpg.de;
keitel@mpi-hd.mpg.de

C. Buth
Max-Planck-Institut für Kernphysik, Saupfercheckweg 1, 69117 Heidelberg, Germany
Argonne National Laboratory, Argonne, Illinois 60439, USA
e-mail: christian.buth@web.de

J. Ullrich
Max-Planck-Institut für Kernphysik, Saupfercheckweg 1, 69117 Heidelberg, Germany
Physikalisch-Technische Bundesanstalt, Bundesallee 100, 38116 Braunschweig, Germany
e-mail: joachim.ullrich@mpi-hd.mpg.de

35.1 High-Harmonic Generation by Continuum Wave Packets

High-order harmonic generation (HHG) is a key process in ultrafast science and well-understood within the three-step model [1]: the bound wave function of an atom is partially freed by a strong laser field, accelerated in it, and driven back to its parent ion. At that point, the ionized and bound portions of the electronic wave packet interfere, giving rise to a strong, coherent high-frequency dipole response that can lead to the emission of a HHG photon along with the recombination of the electron into the bound state.

In our work [2], we advance the interference model of HHG [3, 4] to provide a comprehensive physical picture including continuum–continuum (CC) transitions: any two wave packets of the same electronic wave function that have been split and have acquired different energies lead to coherent HHG emission when they simultaneously reencounter the core region. The emitted photon energy is exactly the energy difference of the two wave packets. Starting from this point of view, we found that a new CC transition plays a significant role in the over-the-barrier (OBI) ionization regime. This transition occurs when two wave packets ionized in different half cycles of a laser pulse recollide at the same time. Note that this transition is different to the CC harmonics described in [5].

As a realistic model, we study the hydrogen atom in a laser field in the OBI regime and solve the three-dimensional time-dependent Schrödinger equation numerically [6]. The laser pulse is shown in Fig. 35.1a and chosen such that almost complete depletion of the ground state occurs on the leading edge of the pulse.

To analyze the time-resolved frequency response of HHG, we calculate the windowed Fourier transform of the dipole acceleration obtained from the TDSE calculation and display it in Fig. 35.1b. For comparison, the two dashed black lines in the figure are the classical recollision energies for trajectories starting from two different laser half cycles, respectively, which are in agreement with the traditional continuum–bound (CB) signal whereas the red line denotes their difference. The CC transition is evidenced by the excellent agreement of the quantum-mechanical response with the red line. Interestingly, the CC component of the dipole response is the dominant contribution for several half cycles after $t = 150$ a.u. (atomic units are employed throughout). This can be understood from the fact that depletion of the ground state occurs around that time. Then, coherent HHG can only occur by the presence of the various parts of the wave function in the continuum.

Moreover, we developed a strong-field approximation model for CC HHG suitable for the OBI regime and based on the evaluation of the dipole acceleration $\mathbf{a}(t) = -\langle \Psi, t | \nabla V | \Psi, t \rangle$ [7] rather than the dipole moment to include the distortion of the recolliding waves by the Coulomb potential required for momentum conservation. The saddle-point approximation is applied to the expression making a computationally fast evaluation of the process possible.

This analytical model also allows to extract the HHG emission phase $\phi = S(\mathbf{p}'', t'') - S(\mathbf{p}', t') + I_p(t' - t'') - \omega_H t$ with the classical action S [8], canonical

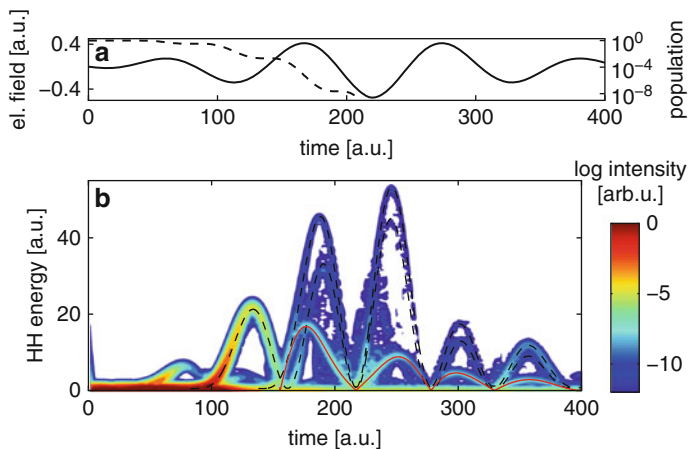


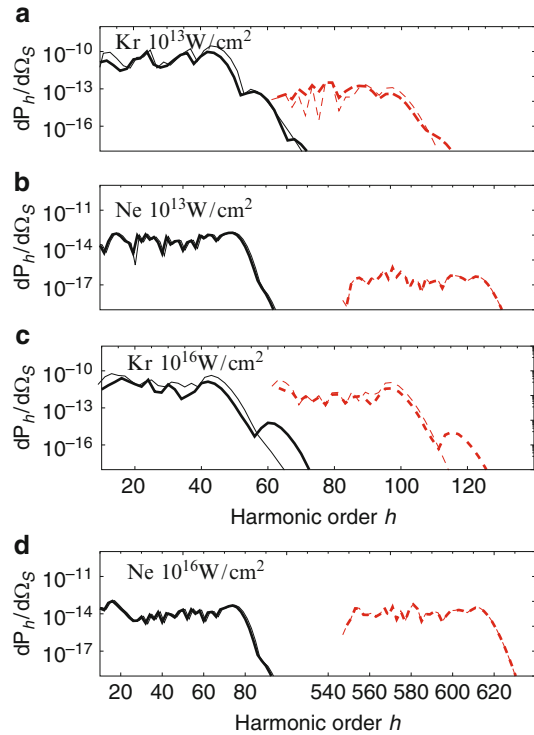
Fig. 35.1 Time-frequency analysis of HHG showing the signature of CC wave-packet interference. (a) Laser pulse used for the calculation (solid line, left axis) and ground-state population (dashed line, right axis). (b) Windowed Fourier transform of the HHG emission. The dashed black lines are the classically calculated kinetic energies of electrons returning to the ion and the solid red line their difference energy. Reproduced from [2]. Copyright (2010) by the American Physical Society

momentum \mathbf{p} , HHG emission time t , ionization times t' and t'' , HHG frequency ω_H and ionization energy I_p . The expression can be converted to $\phi(I) = \alpha_{cc} I$ being a function of the laser pulse peak intensity I , which reveals a striking difference for CB as compared to CC transitions: the sign of α_{CC} and α_{CB} differs for both types of transitions allowing to separate the CC from the CB harmonics via phase-matching. This way, the measurement of CC spectra could be employed for qualitatively advancing tomographic molecular imaging [4]: instead of probing the orbital shape of the active electron, the effective atomic or molecular potential mediating the transition between the two wave packets could be assessed.

35.2 Emergence of a High-Energy Plateau in HHG from Resonantly Excited Atoms

In the last two decades, HHG in the non-relativistic regime has been developed to a reliable source of coherent extreme ultraviolet (XUV) radiation. Its advancement into the hard X-ray domain would allow for a much wider range of applications. The straightforward approach to employ larger laser intensities is demanding due to the relativistic electron drift [9] and the large electron background that is generated by the strong laser field causing phase-mismatch [10]. On the other hand, the large scale X-ray free electron lasers (XFEL) routinely generate several keVs of photon energy but are limited in coherence and, thus, sub-femtosecond pulses with this

Fig. 35.2 HHG photon numbers of the h th harmonic for different X-ray intensities from (a), (c) krypton and (b), (d) neon. The *solid black line* stands for the recombination to the valence state whereas the more energetic plateau arising from core hole recombination is the *red dashed line*. The *thin lines* in the spectrum are obtained by neglecting ground-state depletion due to direct X-ray ionization. The xuv and laser pulse durations are three optical laser cycles in all cases



technique are not in reach at the moment. We show [12] that by combining both, the HHG process and radiation from an XFEL, coherent light pulses can be obtained having the extremely short time structure of the HHG and photon energies larger than the XFEL. In addition to the increase of the HHG photon energy, the scheme can be employed for ultrafast time-dependent imaging [11] involving inner shells and for the characterization of the X-ray pulse of the XFEL.

The proposed scheme works as follows: atoms are irradiated by both an intense optical laser field and an X-ray field from a FEL. The X-ray energy is chosen to be resonant with the transition between the valence and a core level in the cation. As soon as the valence electron is tunnel ionized by the optical laser field, the core electron can be excited to the valence vacancy. Then the continuum electron, returning after a typical time of 1 fs, can recombine with a core hole rather than with the valence hole from that it was previously tunnel ionized and thus emit a much higher energy.

We developed an analytical formalism to cope with the two-electron two-color problem [12, 13]. A two-electron Hamiltonian is constructed mostly from tensorial products of one-electron Hamiltonians that describe the losses due to tunnel ionization and direct X-ray ionization via phenomenological decay constants in conjunction with Auger decay of the intermediate hole. The system is described by equations of motions based on the Schrödinger equation and the solutions can

be found in the dressed state basis. We apply our theory to the $3d \rightarrow 4p$ resonance in a krypton cation as well as to the $1s \rightarrow 2p$ resonance in a neon cation. The results for a resonant sinusoidal X-ray field for two different intensities are shown in Fig. 35.2. The chosen optical laser field intensity is $3 \times 10^{14} \text{ W/cm}^2$ for krypton and $5 \times 10^{14} \text{ W/cm}^2$ for neon both at 800 nm wavelength.

The most striking feature in the obtained spectra is the appearance of a second plateau. It is upshifted in energy with respect to the first plateau by the energy difference between the two involved core and valence states. The two plateaus have comparable harmonic yields for X-ray intensities above 10^{16} W/cm^2 . Quite importantly, the losses due to X-ray ionization do not lead to a significant drop of the HHG rate as can be seen by comparing the thick and thin lines. Both lines almost coincide for neon due to the negligible depletion induced by ionization. The second plateau bears signatures of the core state and may offer a route for ultrafast time-dependent chemical imaging of inner shells [4, 11]. Moreover, by exploiting the upshift in energy, attosecond X-ray pulses come into reach.

35.3 High-Harmonic Generation Without Attochirp

A particularly fascinating property of HHG is its time structure enabling for the generation of extremely short pulses [14, 15]. Nowadays pulses down to a duration of 63 as [16] have been generated and the bandwidth to generate pulses of only 11 as is available [17]. The emitted pulses have an intrinsic chirp, the so-called attochirp [18, 19] and, thus, are much longer than their bandwidth limit. To compensate the attochirp, dispersive optical media [16, 20] are employed.

An alternative way to circumvent this problem would be to modify the HHG process such that the light is emitted without attochirp. It is shown [21] that by means of laser pulse shaping, employing soft x rays for ionization [22] and using an ionic gas medium, attosecond pulses with arbitrary chirp can be formed including the possibility of attochirp-free HHG and bandwidth-limited attosecond pulses.

The principles are illustrated in the trajectory picture of HHG [1, 8] in Fig. 35.3. Since the recollision time of a certain harmonic can be identified with its group delay [18, 19] in the emitted pulse, a simultaneous recollision of all trajectories would lead to a bandwidth-limited attosecond pulse. The demand of simultaneous recollision can be fulfilled if the electron is freed by single-photon ionization when the X-ray frequency ω_X is much larger than the binding energy. In this case the electron has a large initial kinetic energy directly after ionization. Let us focus on the two example trajectories marked by α and β in Fig. 35.3b. Both are ionized at instants separated by a small time difference δt_i . The chosen starting direction of the trajectories along the laser polarization direction is such that they are subsequently decelerated by the laser field and eventually recollide. Note that the velocity difference between α and β is conserved in time for a homogeneous laser field. With a convenient choice of the parameters, the velocity difference between both acquired during δt_i can be such that both recollide simultaneously.

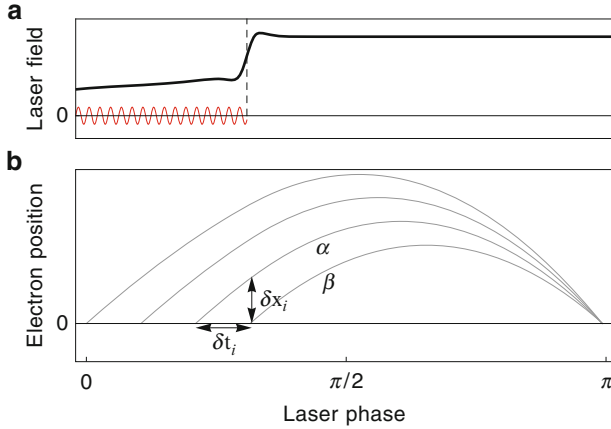


Fig. 35.3 Schematic of the recollision scenario: (a) A half cycle of the tailored laser field (black). The red line is the assisting X-ray pulse. (b) Different one-dimensional classical trajectories in the field of (a) which start into the continuum at different times but revisit the ionic core at the same time. Reproduced from [21]. Copyright (2011) by the Optical Society of America

Table 35.1 Parameters for the two examples in Fig. 35.4: N_F represents the number of Fourier components contained in the tailored driving pulse, I_L its peak intensity, ω_X the X-ray frequency employed for ionization, I_X its intensity and the ionization energy I_p

N_F	I_L [W/cm ²]	ω_X [eV]	I_X [W/cm ²]	Ion	I_p [a.u.]
8	10^{16}	218	3.5×10^{14}	Li ²⁺	4.5
20	10^{17}	996	1.4×10^{15}	Be ³⁺	8

In the following, we exemplify our method in two cases producing bandwidth-limited pulses below 10 and 1 as. The optimized optical laser pulses (frequency $\omega = 0.06$ a.u.) are shown in Fig. 35.4a and c and the parameters are indicated in Table 35.1.

The attosecond pulses are bandwidth limited as can be seen from the spectral phases (red lines in Fig. 35.4b and d).

However, the method still has several drawbacks. It is experimentally demanding to create a pure ionic gas and to achieve phase-matching in a macroscopic medium due to the free electron dispersion. Moreover, the required large initial momentum and the dipole angular distribution of the ionization process lead to an increased spread of the ionized wave packet as compared to tunnel ionization. Further, the ionization rate is small due to $\omega_X \gg I_p$. Precise shaping of intense driver fields with intense harmonics as well as the synchronization of the X-ray and IR pulses is also demanding. A potential route to overcome the former difficulties could be to derive the X-rays, the IR light and its Fourier components from the same FEL electron bunch.

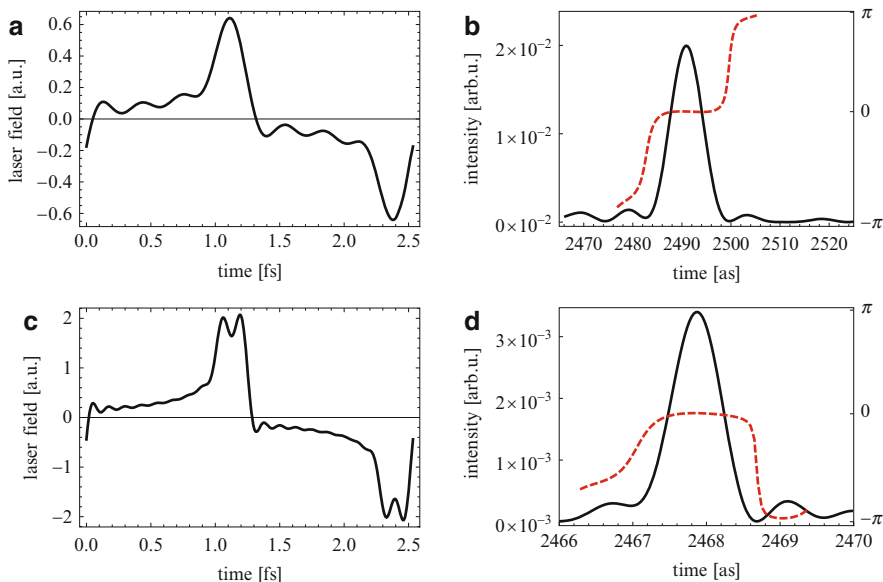


Fig. 35.4 (a) the laser field composed of eight Fourier components that illuminates an Li^{2+} ion with $I_p = 4.5$ a.u. The parameters of the additional X-ray field are indicated in the first row of Table 35.1. The resulting 8 as pulse is shown in (b). (c) displays the laser field needed to create a pulse of 800 zs duration from Be^{3+} ions with $I_p = 8$ a.u. The parameters are indicated in the second row of Table 35.1. The respective pulse is shown in (d). The dashed red lines are the temporal phases of the pulses. Reproduced from [21]. Copyright (2011) by the Optical Society of America

35.4 Resonant Photoionization Involving Two Atoms

Interatomic electron–electron correlations are responsible for a variety of interesting phenomena, ranging from dipole–dipole interactions in cold quantum gases to Förster resonances between biomolecules. They may also lead to very characteristic effects in the photoionization of atoms.

As an illustrative example, let us consider resonant two-photon ionization in a system consisting of two hydrogen atoms [23]. The atoms are assumed to be separated by a sufficiently large distance R so that one may indeed speak about individual atoms. The system interacts with a monochromatic laser field whose frequency is resonant with the $1s$ – $2p$ transition in hydrogen. In this situation there are two quantum pathways for ionization: (a) the direct channel where a single atom is ionized by absorbing two photons from the field, without any participation of the neighboring atom; and (b) an interatomic channel where both atoms are first excited to the $2p$ level by absorbing one photon each and afterwards the doubly excited two-atom state decays via so-called interatomic Coulombic decay (see [24]

for recent reviews). In other words, one of the atoms deexcites and transfers its energy radiationlessly to the second atom, this way causing its ionization.

Leading to the same final state, the direct and two-center ionization pathways show quantum mechanical interference. It becomes manifest in the photoelectron spectra which consist of four lines due to the Autler–Townes splitting of the atomic levels in the external field [23]. Moreover, the two-center channel can be remarkably strong and even dominate over the direct channel by orders of magnitude. In fact, the ratio $[d/(R^3 E)]^2$ determines the strength of the former with respect to the latter, where d is the $1s$ – $2p$ transition dipole moment and E denotes the laser field strength. For example, at $R = 1$ nm and $E = 10^4$ V/cm this ratio is of the order of 10^4 .

Interatomic resonant photoionization may also occur in hetero-atomic systems [25, 26]. In this case, one of the centers is first excited by single-photon absorption and subsequently, upon deexcitation, the partner atom is ionized. Evidently, this mechanism requires a hetero-atomic system with an excitation energy of the one center exceeding the ionization potential of the other.

The interplay between resonant laser fields and interatomic electron–electron correlations can thus give rise to interesting and rather unexpected effects.

Acknowledgements C.B. and M.C.K. were supported by a Marie Curie International Reintegration Grant within the 7th European Community Framework Program (call identifier: FP7-PEOPLE-2010-RG, proposal No. 266551). C.B.’s work was funded by the Office of Basic Energy Sciences, Office of Science, U.S. Department of Energy, under Contract No. DE-AC02-06CH11357. T.P. acknowledges support by an MPRG grant of the Max-Planck Gesellschaft. This work was supported in part by the Extreme Matter Institute EMMI.

References

1. P.B. Corkum, Phys. Rev. Lett. **71**, 1994 (1993); K.J. Schafer et al., Phys. Rev. Lett. **70**, 1599 (1993)
2. M.C. Kohler et al., Phys. Rev. Lett **105**, 203902 (2010)
3. A. Pukhov, S. Gordienko, T. Baeva, Phys. Rev. Lett. **91**, 173002 (2003)
4. J. Itatani et al., Nature **432**, 867 (2004)
5. M. Protopapas et al., Phys. Rev. A **53**, R2933 (1996); M. Yu. Emelin et al., JETP **106**, 203 (2008); D.B. Milošević, in *NATO Science Series II: Mathematics, Physics and Chemistry*, vol. 12, ed. by B. Piraux, K. Rzazewski (Kluwer, Dordrecht, 2001), pp. 229–238; D.B. Milošević, F. Ehloltzky, Adv. At. Mol. Opt. Phys. **49**, 373 (2003)
6. D. Bauer, P. Koval, Comput. Phys. Commun. **174**, 396 (2006)
7. A. Gordon, F.X. Kärtner, Phys. Rev. Lett. **95**, 223901 (2005)
8. M. Lewenstein et al., Phys. Rev. A **49**, 2117 (1994)
9. O. Latinne et al., Euro. Phys. Lett. **26**, 333 (1994)
10. T. Popmintchev et al., Proc. Nat. Acad. Sci. USA **106**, 10516 (2009)
11. T. Morishita et al., Phys. Rev. Lett. **100**, 013903 (2008)
12. C. Buth et al., Opt. Lett **36**, 3530 (2011)
13. C. Buth et al., (manuscript in preparation)
14. E. Goulielmakis et al., Science **320**, 1614–1617 (2008)
15. F. Ferrari et al., Nat. Photon. **4**, 875–879 (2010)

16. D.H. Ko et al., *New J. Phys.* **12**, 063008 (2010)
17. M.-C. Chen et al., *Phys. Rev. Lett.* **105**, 173901 (2010)
18. Y. Mairesse et al., *Science* **302**, 1540–1543 (2003) and supplementary material
19. S. Kazamias, Ph. Balcou, *Phys. Rev. A* **69**, 063416 (2004)
20. K.T. Kim et al., *Phys. Rev. A* **69**, 051805(R) (2004); R. López-Martens et al., *Phys. Rev. Lett.* **94**, 033001 (2005); K.T. Kim et al., *Phys. Rev. Lett.* **99**, 223904 (2007)
21. M.C. Kohler, C.H. Keitel, K.Z. Hatsagortsyan, *Opt. Express* **19**, 4411 (2011)
22. K. Ishikawa, *Phys. Rev. Lett.* **91**, 043002 (2003); K. J. Schafer et al., *Phys. Rev. Lett.* **92**, 023003 (2004); M.B. Gaarde et al., *Phys. Rev. A* **72**, 013411 (2005); M. Klaiber et al., *Opt. Lett.* **33**, 411–413 (2008)
23. C. Müller, A.B. Voitkiv, *Phys. Rev. Lett.* **107**, 013001 (2011)
24. V. Averbukh et al., *J. Electron Spectrosc. Relat. Phenom.* **183**, 36–47 (2011); U. Hergenhahn, *J. Electron Spectrosc. Relat. Phenom.* **184**, 78–90 (2011)
25. A. Kay et al., *Science* **281**, 679 (1998)
26. B. Najjari, A.B. Voitkiv, C. Müller, *Phys. Rev. Lett.* **105**, 153002 (2010); A.B. Voitkiv, B. Najjari, *Phys. Rev. A* **84**, 013415 (2011)

Chapter 36

Adiabatic Theory of Ionization of Atoms by Intense Laser Pulses

Toru Morishita and Oleg I. Tolstikhin

Abstract We present the adiabatic theory of ionization of atoms by intense ultrashort laser pulses. We discuss a *trilobite-like structure* in a photoelectron spectrum generated by a pulse of overbarrier intensity.

The Keldysh theory [1] and its extensions [2, 3], commonly called the strong field approximation, in contradiction to the latter name are known [4] to apply only to weak in atomic scale laser fields whose amplitude satisfies $F_0 \ll \alpha^3$, $\alpha = (2I_p)^{1/2}$. Considering ionization from the ground state of neutral atoms by near-IR pulses with $\lambda \sim 800$ nm, this approximation is only qualitatively correct for $F_0 \sim 0.1$ a.u. ($I \sim 10^{14}$ W/cm²) and completely fails in the overbarrier regime $F_0 \sim 1$ a.u. ($I \sim 10^{16}$ W/cm²). Thus a reliable theory capable of treating the interaction of atoms with truly intense laser pulses of current interest is needed.

Such a theory can be developed on the basis of adiabatic approximation. The problem is characterized by two dimensionless parameters, the ratios of the atomic and laser time $\epsilon = \omega/\alpha^2$ and energy $\xi = F_0/\alpha^3$ scales, respectively; their ratio gives the Keldysh parameter γ . The adiabatic theory is a uniform with respect to ξ asymptotics for $\epsilon \rightarrow 0$, i.e., it becomes exact in the low-frequency limit for arbitrary intensity of the pulse. Recently, we have developed the adiabatic theory for a model one-dimensional problem [5]. A key object in this theory is the atomic Siegert state in a static electric field equal to the momentary value of the laser field. The advent of a powerful method to calculate such states for realistic atomic potentials [6] has made the extension of the adiabatic theory [5] to the three-dimensional (3D)

T. Morishita (✉)

Department of Engineering Science, The University of Electro-communications, 1-5-1
Chofu-ga-oka, Chofu-shi, Tokyo 182-8585, Japan
e-mail: toru@pc.uec.ac.jp

O.I. Tolstikhin

National Research Center “Kurchatov Institute,” Kurchatov Square 1, Moscow 123182, Russia

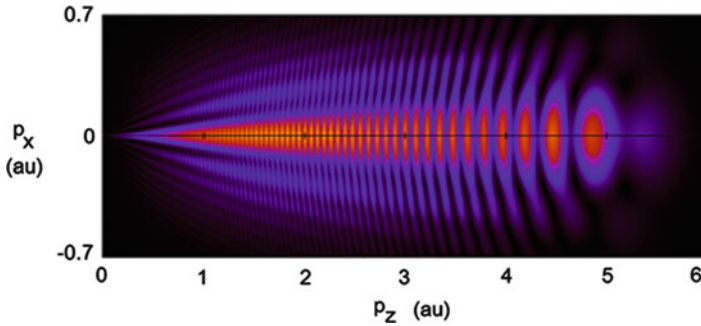


Fig. 36.1 Photoelectron spectrum generated by a one-cycle laser pulse with $\lambda = 800$ nm and $F_0 = 0.5$ a.u.

case possible. A comparison of adiabatic results with exact numerical solution of the time dependent Schrödinger equation (TDSE) shows that the adiabatic theory works well already in the mid-UV range ($\lambda \sim 200$ nm) and becomes progressively more accurate as one moves to the mid-IR range ($\lambda \sim 7 \mu\text{m}$), where solving the TDSE becomes prohibitively difficult, thus providing a reliable quantitative theory suitable for treating the variety of current applications of intense laser pulses.

Figure 36.1 shows a trilobite-like structure in a photoelectron spectrum generated by a pulse of overbarrier intensity. Similar spectra were recently observed experimentally [7]. The adiabatic theory explains the origin of the horizontal (low-contrast) interference fringes and shows that they bear structural target information on the scattering amplitude of the ionized electron by the parent ion.

Acknowledgements This work was partially supported by a Grant-in-Aid for scientific research (C) from the Japan Society for the Promotion of Science (JSPS) and the Russian Foundation for Basic Research for the support through grant No. 11-02-00390-a.

References

1. L.V. Keldysh, *Sov. Phys. JETP* **20**, 1307 (1965)
2. F.H.M. Faisal, *J. Phys. B* **6**, L89 (1973)
3. H.R. Reiss, *Phys. Rev. A* **22**, 1786 (1980)
4. V.S. Popov, *Phys. Usp.* **47**, 855 (2004)
5. O.I. Tolstikhin, T. Morishita, S. Watanabe, *Phys. Rev. A* **81**, 033415 (2010)
6. P.A. Batishchev, O.I. Tolstikhin, T. Morishita, *Phys. Rev. A* **82**, 023416 (2010)
7. Y. Huismans et al., *Science* **331**, 61 (2011)

Chapter 37

Trajectory-Based Coulomb-Corrected Strong Field Approximation

T.-M. Yan, S.V. Popruzhenko, M.J.J. Vrakking, and D. Bauer

Abstract The strong field approximation (SFA) is one of the most successful theoretical approaches in strong field physics. In the semiclassical limit, the SFA possesses an appealing interpretation in terms of interfering quantum trajectories. In this work, trajectory-based Coulomb-corrected SFA (TCSFA), a conceptually simple extension towards the inclusion of Coulomb interaction, is presented.

37.1 Theoretical Description of Atomic Strong Field Ionization

The development of ultrafast intense laser technology has offered the unprecedented opportunity to explore electronic dynamics of atomic and molecular system. With the strength of the external light field comparable to the atomic binding force, and the temporal resolution of ultrafast laser high enough to resolve the motion of an electron on the sub-femto or even attosecond time scale, nowadays, researchers are able to image electronic dynamics and study material structures with diverse strong

T.-M. Yan

Institut für Physik, Universität Rostock, 18051 Rostock, Germany

Max-Planck-Institut für Kernphysik, Postfach 103980, 69029 Heidelberg, Germany

S.V. Popruzhenko

National Research Nuclear University “Moscow Engineering Physics Institute”, Kashirskoe Shosse 31, 115409, Moscow, Russia

M.J.J. Vrakking

FOM-Institute AMOLF, Science Park 113, 1098 XG Amsterdam, The Netherlands

Max-Born-Institut, Max-Born-Strasse 2A, 12489 Berlin, Germany

D. Bauer (✉)

Institut für Physik, Universität Rostock, 18051 Rostock, Germany

e-mail: dieter.bauer@uni-rostock.de

field processes. Among these strong field phenomena, atomic single-ionization is undoubtedly the fundamental key process and the prerequisite for further understanding of strong field physics [1]. In this work, a systematical method based on the strong field approximation (SFA), the trajectory-based Coulomb-corrected SFA (TCSFA), is introduced, intending to provide an improved theoretical tool for the study of strong field physics.

37.1.1 Strong Field Approximation

The SFA is one of the most widely used theoretical approaches to describe strong field processes. The idea behind the SFA is the assumption that after the electron enters the continuum at time $t = t_0$, only the interaction between electron and the external field needs to be considered, while the influence of the binding potential is neglected. In its simplest form the SFA accounts only for the so-called “direct” ionization. The final state of the electron characterized by the asymptotic momentum \mathbf{p} in the Keldysh–Faisal–Reiss amplitude [2–4] is a Gordon–Volkov state $|\psi_p^{(\text{GV})}(t)\rangle = e^{-iS_p(t)}|\mathbf{p} + \mathbf{A}(t)\rangle$, leading to the transition matrix element [5,6]

$$M_p^{(0)} = -i \int_0^\infty \langle \mathbf{p} + \mathbf{A}(t') | \mathbf{r} \cdot \mathbf{E}(t) | \psi_0 \rangle e^{iS_{I_p, \mathbf{p}}(t)} dt, \quad (37.1)$$

with $|\psi_0\rangle$ the initial bound state of the electron, I_p the ionization potential of the atom, $\mathbf{A}(t)$ the vector potential of the light pulse, $\mathbf{E}(t) = -\partial_t \mathbf{A}(t)$ the electric field vector in dipole approximation, and the action

$$S_{I_p, \mathbf{p}}(t) = \int^t \left[\frac{1}{2} (\mathbf{p} + \mathbf{A}(\tau))^2 + I_p \right] d\tau$$

(atomic units are used unless noted otherwise).

The SFA has achieved gratifying agreement with *ab initio* results for atomic systems with a short-range potential (as is the case for electron detachment from negative ions [7]). However, in the case of neutral atoms or positive ions, the neglect of the interaction between released electrons and the long-range binding potential is shown to result in large deviations from experimental or *ab initio* results, which implies the necessity of Coulomb corrections to the SFA model.

37.1.2 Steepest Descent Method Applied to the SFA

Though the time integration in (37.1) can be carried out numerically with ease, the transition amplitude can be further simplified using the steepest descent method [8], which is also the crucial step to implement the TCSFA. If the number of

photons N of energy $\hbar\omega$ required to overcome the ionization potential I_p is large, $N = I_p/\hbar\omega \gg 1$, the time integral in the SFA matrix element may be approximated by a sum over all saddle points $\{t_s^{(\alpha)}\}$,

$$M_p^{(0)} = -\frac{\kappa}{\sqrt{2}} \sum_{\alpha} \frac{e^{iS_{I_p,p}(t_s^{(\alpha)})}}{S''_{I_p,p}(t_s^{(\alpha)})}, \quad (37.2)$$

where $\kappa = \sqrt{2I_p}$ is the characteristic momentum for the bound electron, and S'' denotes the second-order time derivative of S . The α th saddle point $t_s^{(\alpha)}$ satisfies the stationary phase equation (SPE)

$$\frac{1}{2} (\mathbf{p} + \mathbf{A}(t_s^{(\alpha)}))^2 = -I_p. \quad (37.3)$$

It is evident that, as $I_p > 0$, the solution $t_s^{(\alpha)}$ is complex. There are two restrictions imposed on the selection of valid saddle points. Firstly, $t_s^{(\alpha)}$ is required to have its real part, $t_0 = \text{Re}t_s$, within the pulse duration, i.e., $0 < t_0 < T_p$. In the picture of tunneling ionization, t_0 indicates the time when an electron reaches the outer turning point of the potential barrier and enters the continuum. Moreover, t_s is chosen to satisfy $\text{Im}t_s > 0$, which guarantees a sensible tunneling ionization probability. Generally, smaller $\text{Im}t_s$ assign larger weights to the corresponding terms in (37.2). Usually, the terms with smallest $\text{Im}t_s$ have t_0 near the time when the amplitude of the electric field is close to a local maximum.

The summation (37.2), approximating the integral (37.1), not only alleviates the computational demand, but also offers clearer physical insight into the ionization process by virtue of “quantum orbits” [9], equivalent to the semiclassical limit of the path integral [10]. At $t_s^{(\alpha)}$ a trajectory is launched (by “trajectory” we mean the classical path), with $S_{I_p,p}(t_s^{(\alpha)})$ the action integral. The summation over different trajectories which end up with the same asymptotic momentum provides a qualitative description of the quantum interference. In addition, since $t_s^{(\alpha)}$ is complex, the calculation of trajectories has been naturally extended into the complex plane, known as the imaginary time method (ITM) [11], thereby including tunneling effects. Although the SFA starts with an assumption neglecting the Coulomb interaction, the intuitive concept of trajectories allows us to incorporate Coulomb effects by modifying the action integral and the trajectories accordingly.

37.1.3 Trajectory-Based Coulomb Correction

In this section, a method to “patch” the plain SFA quantum orbits is introduced. Henceforth, the subscript “0” is used to indicate unperturbed variables, i.e., variables

in the absence of the binding potential. The action as a function of the saddle point $t_s^{(\alpha)}$ can be recast into

$$S_{I_p, \mathbf{p}}(t_{s0}^{(\alpha)}) = C(\mathbf{p}) - \int_{t_{s0}^{(\alpha)}}^{\infty} \left[\frac{1}{2} \mathbf{v}_0^2(t) + I_p \right] dt, \quad (37.4)$$

where $\mathbf{v}_0(t) = \mathbf{p} + \mathbf{A}(t)$ is the velocity of an electron in a light field and $C(\mathbf{p}) = \int_{t_{s0}^{(\alpha)}}^{\infty} \left[\frac{1}{2} \mathbf{v}_0^2(t) + I_p \right] dt$ varies with different asymptotic momenta \mathbf{p} , independent of individual saddle points $t_{s0}^{(\alpha)}$.

The first term in (37.4), $C(\mathbf{p})$, does not contribute to the final ionization probability, since it can be factored out of the summation and eventually cancels as an overall phase factor. The integrand in the second term corresponds to the Hamiltonian $H_0(t) = \frac{1}{2} \mathbf{v}_0^2(t)$ for a free electron in the electromagnetic field, and (37.4) becomes

$$S_{I_p, \mathbf{p}}(t_{s0}^{(\alpha)}) = C(\mathbf{p}) - \int_{t_{s0}^{(\alpha)}}^{\infty} [H_0(t) + I_p] dt. \quad (37.5)$$

When the Coulomb field is switched on, firstly, the motion of the electron is expected to be altered and the trajectory will be distorted, i.e., $\mathbf{r}_0 \rightarrow \mathbf{r}$ and $\mathbf{v}_0 \rightarrow \mathbf{v}$. Moreover, the Hamiltonian in (37.5) is modified to include the Coulomb potential [12],

$$H_0 \rightarrow H = H_0 + U_{\text{Coulomb}} = H_0 - \frac{Z}{|\mathbf{r}(t)|}.$$

With these modifications, we have the Coulomb-corrected transition amplitude

$$M_{\mathbf{p}}^{(0)} \sim e^{iC(\mathbf{p})} \sum_{\alpha} \frac{\exp \left[-i \int_{t_s^{(\alpha)}}^{\infty} \left(\frac{1}{2} \mathbf{v}^2(t) - \frac{Z}{|\mathbf{r}(t)|} + I_p \right) dt \right]}{S''(t_s^{(\alpha)})} \equiv e^{iC(\mathbf{p})} \sum_{\alpha} M_{\mathbf{p}}(t_s^{(\alpha)}). \quad (37.6)$$

In practice, the integration in (37.6) from $t_s^{(\alpha)}$ to infinity is splitted into two parts: the sub-barrier part $W_{\text{sub}} = \int_{t_s^{(\alpha)}}^{t_0^{(\alpha)}}$ and the real-time propagation part $W_{\text{re}} = \int_{t_0^{(\alpha)}}^{\infty}$.

37.1.4 Applications and Numerical Implementation

The implementation of the trajectory-based calculation is conceptually simple. We work in a 2D momentum plane $\mathbf{p} = (p_z, p_x)$ ($p_z = p_{\parallel}$ in the polarization direction of the laser field, $p_x = p_{\perp}$ in the perpendicular direction). For one trajectory, the steps to evaluate the transition matrix element of atomic ionization are:

- (i) Given \mathbf{p}_0 and $t_{\text{guess}}^{(\alpha)}$, which is an estimated time when the electron emerges at the tunnel exit, solve the SPE (37.3) with a complex root-finder to obtain the

exact saddle point $t_s^{(\alpha)}$ around $t_{\text{guess}}^{(\alpha)}$. The value of $t_{\text{guess}}^{(\alpha)}$ is empirically set as the time when the absolute value of electric field reaches a local maximum.

- (ii) Calculate the sub-barrier integral W_{sub} with the ITM. In our current work we neglect the Coulomb correction for W_{sub} so that this step is fully analytical.
- (iii) Given the calculated initial conditions in step (ii), solve the ordinary differential equations of motion and find the real trajectory \mathbf{r} of the electron in the combined fields of the laser and the ion.
- (iv) Calculate W_{re} along the trajectory \mathbf{r} for the real time propagation. After the laser is switched off at T_p , the asymptotic momentum \mathbf{p} can be found by solving the standard central field problem [13].
- (v) Calculate the individual transition amplitude $M_p(t_s^{(\alpha)})$ in (37.6) for this trajectory.

One should note that, for a multi-cycle light field, each sample \mathbf{p}_0 generally corresponds to several trajectories. However, since only saddle points with the lowest imaginary parts possess the largest weights, it is not necessary to include all trajectories.

Thanks to the independence of all these trajectories, the parallelization of the method is straightforward. In practice, we launch trajectories with uniformly sampled, random \mathbf{p}_0 in the initial momentum plane. Following the above recipe (i)–(v), one obtains the asymptotic momentum \mathbf{p} and individual transition matrix elements $M_p(t_s^{(\alpha)})$ for each trajectory. All information related to this trajectory can be stored for further analysis.

With all trajectories available, one can calculate the momentum distribution of the ionization probability on a grid representing the final momentum $\tilde{\mathbf{p}}$. All trajectories are binned according to their asymptotic momentum \mathbf{p} , and the total transition amplitude for momentum $M_{\tilde{\mathbf{p}}}$ is the sum of the contributions from trajectories whose asymptotic momenta \mathbf{p} fall into the bin centered at $\tilde{\mathbf{p}}$, $M_{\tilde{\mathbf{p}}} = \sum_i M_p^{(i)}$, with i the index of these trajectories.

37.2 Results and Discussion

In order to demonstrate the TCSFA method, we consider atomic hydrogen ($I_p = 0.5$) subjected to a linearly polarized (along the z -axis) light field described by the vector potential with a \sin^2 -envelope,

$$A(t) = -\frac{E_0}{\omega} \sin^2\left(\frac{\omega t}{2N_c}\right) \sin \omega t.$$

Here, ω is the laser frequency, E_0 is the peak field strength, and N_c is the number of optical cycles. The actual values are listed in the caption of Fig. 37.1.

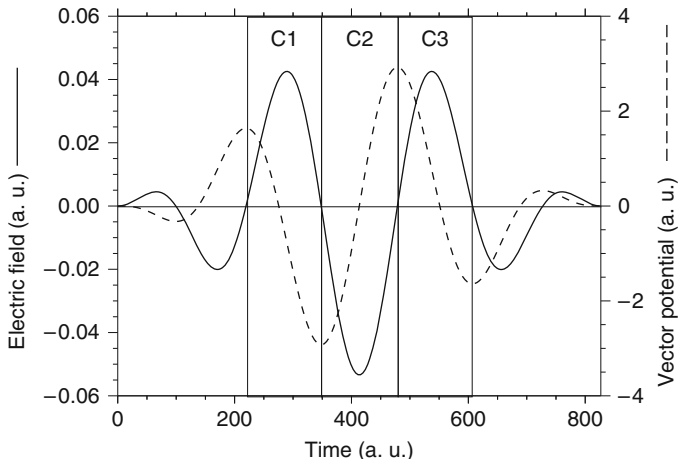


Fig. 37.1 The vector potential and the electric field amplitude of the light field with \sin^2 -envelope, $\omega = 0.0228$ (wavelength $2 \mu\text{m}$), $E_0 = 0.0534$ (intensity $1 \times 10^{14} \text{ W/cm}^2$) and $N_c = 3$. To facilitate the analysis of the tunnel time, we partition the dominating optical cycles into three time-intervals C1–C3

Figure 37.2 shows the calculated photoelectron momentum distributions with different methods: the time-dependent Schrödinger equation (TDSE), the TCSFA and the plain SFA. The TDSE result obtained numerically with Qprop [17] serves as a benchmark for other methods. Several important spectral features are observed. Firstly, the momentum spectrum exhibits a global asymmetrical distribution in z -direction due to the few cycles [14, 15]. In addition, the distribution reveals a near-threshold ($p \simeq 0$) radial structure, with a spoke-like pattern, which has been explained classically using Kepler’s hyperbola [13]. At higher energies side lobes are visible, which are shown to originate from the intra-cycle interference and play the essential role for applications like the holography of atoms [16]. All these interesting features are well reproduced by the TCSFA calculation, while being absent in the plain SFA result.

One advantageous feature of the TCSFA method is that important information can be easily retrieved in terms of quantum orbits. Based upon the fact that the plain SFA possesses two types of trajectories, known as “short” and “long” (labeled as T1 and T2), respectively, we introduce two new types of trajectories for classification, T3 and T4, when long-range Coulomb interaction is included [18]. Details for this categorization are listed in Table 37.1.

Momentum spectra constructed from individual types of trajectories are shown in Fig. 37.3. For T1, there exists a ring-like distribution with significant interference in the negative-half momentum plane, and a structureless distribution in the positive-half plane. The interference in the negative-half plane originates from the coherent superposition of trajectories whose t_0 fall into the time interval C1 and C3 (as indicated in Fig. 37.1). Since the sub-peak intensities of $\mathbf{E}(t)$ in C1 and C3 are

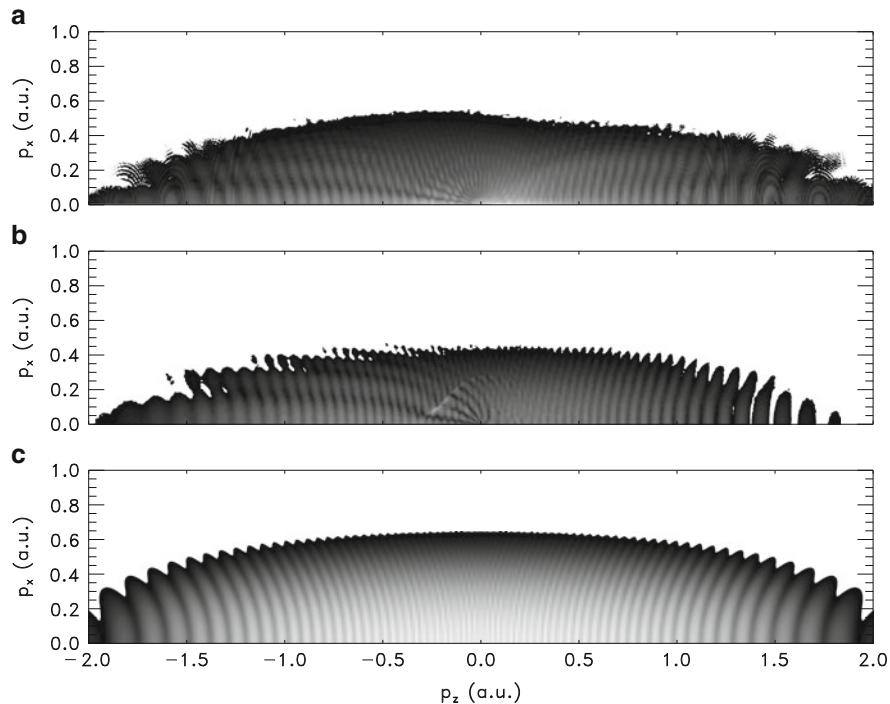


Fig. 37.2 Logarithmically scaled photoelectron momentum distributions in the $p_z p_x$ plane ($p_{\parallel} = p_z$) calculated using (a) TDSE, (b) TCSFA, and (c) SFA. The spectra have been normalized to their maximum value and cover 4, 4.4, and 2 orders of magnitude, respectively

Table 37.1 Categorization of trajectories for the TCSFA

Types	Longitudinal condition	Transversal condition
T1	$p_z(\infty)z(t_0) > 0$	$p_x(t_0)p_x(\infty) > 0$
T2	$p_z(\infty)z(t_0) < 0$	$p_x(t_0)p_x(\infty) > 0$
T3	$p_z(\infty)z(t_0) < 0$	$p_x(t_0)p_x(\infty) < 0$
T4	$p_z(\infty)z(t_0) > 0$	$p_x(t_0)p_x(\infty) < 0$

the same, the weights for trajectories born in these intervals are similar, leading to significant inter-cycle interferences. In fact, these are the well-known ATI peaks with only inter-cycle components, which become equidistant if they are mapped to the energy domain. But in the positive-half plane, the distribution mainly originates from trajectories within the time interval of C2 around the main peak of $E(t)$. The weights of these trajectories are typically much larger than those from other sub-peaks. Thus, hardly can any clear interference develop. Similarly, the explanation also applies to the partial spectra of T2. However, since T2 represents the “long” trajectories with the initial “tunnel exit” opposite to that of T1, the spectrum is reversed.

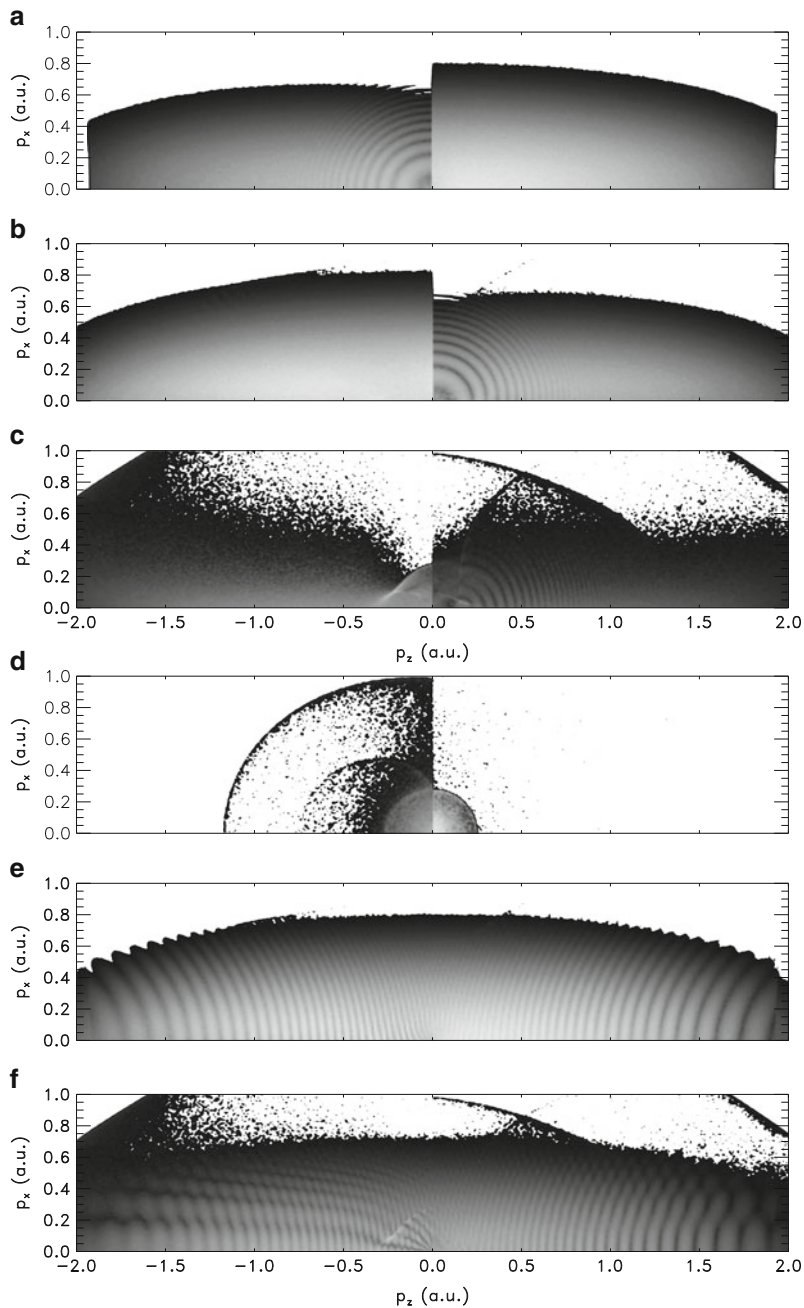


Fig. 37.3 Partial distribution constructed from four types of trajectories: (a) T1, (b) T2, (c) T3, (d) T4, (e) T1 + T2 and (f) T1 + T2 + T3. The grayscaleing is logarithmic and covers 7 orders of magnitude

For trajectories T1 and T2 during the propagation, the signs of the transversal momenta do not change and corrections are small, as can be seen by comparison between the SFA result in Fig. 37.2c and the spectra for T1 + T2 in Fig. 37.3e. The distribution in the low-energy domain is apt to be influenced by the Coulomb potential, as slow electrons spend more time close the core. However, this perturbative correction to T1 and T2 is far from a correct description of the low-energy regime. The good agreement is achieved only when trajectories T3 are included, as is shown in Fig. 37.3f. Trajectories T3 have their signs of transversal momenta altered because of the rather strong interaction with the Coulomb field. It results in some striking features, as is shown in Fig. 37.3c: (a) The weights of trajectories T3 are sufficiently large, comparable to those of T1 or T2, to form the side lobes. (b) Exaggerated local maxima, known as caustics, are also visible. In Fig. 37.3c, a caustics is located at $\mathbf{p} = (-0.2, 0.1)$, related to the recently discovered low energy structure (LES) [19, 20], as discussed in [18].

In conclusion, the TCSFA method is developed, starting with the widely used SFA and including Coulomb effects using trajectories. The method shows good agreement with results from recent experiments and ab initio calculations, especially for problems with light fields at long-wavelengths, for which the solution of the TDSE becomes extremely cumbersome. New types of quantum trajectories due to Coulomb interaction have been found to play a crucial role for the complex interference patterns in momentum spectra, particularly in the low energy regime. The TCSFA allows to analyze any spectral feature in terms of its contributing trajectories. More insight into quantum dynamics is hardly possible.

Acknowledgements The work was partially supported by the Deutsche Forschungsgemeinschaft (SFB 652) and the Russian Foundation for Basic Research. T.-M. Y. acknowledges support from the International Max Planck Research School for Quantum Dynamics (IMPRS-QD) in Heidelberg. The work of M. J. J. V. is part of the research program of the “Stichting voor Fundamenteel Onderzoek der Materie (FOM)”, which is financially supported by the “Nederlandse organisatie voor Wetenschappelijk Onderzoek (NWO)”.

References

1. D.B. Milošević et al., *J. Phys. B* **39**, R203 (2006)
2. L.V. Keldysh, *Zh. Éksp. Teor. Fiz.* **47**, 1945 (1964)
3. F.H.M. Faisal, *J. Phys. B At. Mol. Phys.* **6**, L89 (1973)
4. H.R. Reiss, *Phys. Rev. A* **22**, 1786 (1980)
5. W. Gordon, *Z. Phys.* **40**, 117 (1926)
6. D.V. Volkov, *Z. Phys.* **94**, 250 (1935)
7. M.V. Frolov et al., *Phys. Rev. A* **79**, 033406 (2009)
8. D.B. Milošević et al., *Rev. Lett.* **89**, 153001 (2002)
9. W. Becker et al., *Adv. At. Mol. Opt. Phys.* **48**, 35 (2002)
10. P. Salières et al., *Science* **292**, 902 (2001)
11. V.S. Popov, *Phys. At. Nucl.* **68**, 686 (2005)
12. S.V. Popruzhenko, D. Bauer, *J. Mod. Opt.* **55**, 2573 (2008)
13. D.G. Arbó et al., *Phys. Rev. Lett.* **96**, 143003 (2006)

14. R. Gopal et al., Phys. Rev. Lett. **103**, 053001 (2009)
15. S. Chelkowski, A.D. Bandrauk, Phys. Rev. A **71**, 053815 (2005)
16. Y. Huismans et al., Science **331**, 61 (2010)
17. D. Bauer, P. Koval, Comput. Phys. Commun. **174**, 396 (2006)
18. T.-M. Yan et al., Phys. Rev. Lett. **105**, 253002 (2010)
19. C.I. Blaga et al., Nat. Phys. **5**, 335 (2009)
20. W. Quan et al., Phys. Rev. Lett. **103**, 093001 (2009)

Part IV
Molecules in Intense Laser Fields

Chapter 38

Classical Models of H_3^+ Interacting with Intense Laser Fields

E. Lötstedt, T. Kato, and K. Yamanouchi

Abstract Two different classical models are proposed for describing the interaction of H_3^+ with an intense laser field. In the first model, called the auxiliary potential method (APM), certain auxiliary, momentum-dependent potentials are added to the classical Hamiltonian. In the second model, called the soft-core potential model (SPM), the Coulomb potential is truncated at short distances and connected smoothly to a finite core potential by introducing a softening parameter. In both cases, the electrons are prevented from collapsing into the Coulomb singularity, which is a necessary condition to make the lowest-energy configuration of the molecule stable.

38.1 Introduction

When a molecule is exposed to an intense laser pulse, it is in most cases both ionized as well as dissociated. This means that if one aims to simulate the complete motion of the molecule in the pulsed laser field, the motion of both electrons and nuclei needs to be treated simultaneously.

A numerically exact solution of the time-dependent Schrödinger equation (TDSE), with both the electronic and nuclear degrees of freedom included, is currently available only for H_2^+ [1], the simplest molecular system. For larger

E. Lötstedt (✉)

Department of Chemistry, School of Science, The University of Tokyo, 7-3-1 Hongo, Bunkyo-ku, Tokyo 113-0033, Japan

Present address: Laser Technology Laboratory, RIKEN Advanced Science Institute, 2-1 Hirosawa, Wako, Saitama 351-0198, Japan

e-mail: loetstedte@riken.jp

T. Kato · K. Yamanouchi

Department of Chemistry, School of Science, The University of Tokyo, 7-3-1 Hongo, Bunkyo-ku, Tokyo 113-0033, Japan

molecular systems, alternative methods such as the Monte-Carlo surface hopping method [2] and the multi-configuration time-dependent Hartree–Fock method [3] have been adopted.

In this contribution, we propose an alternative theoretical model, in which both electrons and nuclei are treated as classical point particles. The time evolution of the system is obtained by solving the classical Hamiltonian equations of motion, which is a much easier task compared to the numerical integration of the TDSE. The fundamental problem of a purely classical model of a molecule is the realization of a stable equilibrium configuration for the classical ground state having the lowest energy. In general, a collection of electrons and nuclei interacting with the Coulomb potential cannot form a stable molecule. Two kinds of methods for solving this problem are presented in Sect. 38.2. These two methods are fully self-consistent, in the sense that the molecule does not autodissociate, autoionize, or collapse in the absence of the laser field.

We apply our methods to describe the triatomic molecule H_3^+ interacting with an intense, long-wavelength (790 nm), few-cycle laser pulse. We compare with experimental data presented in [4], and show that the experimental kinetic energy release spectra are well described by the APM, while the relative yields of the dissociation channels without ionization are better reproduced by the SPM.

38.2 Theoretical Models

In the APM, we keep the classical Hamiltonian of H_3^+ , but add certain quasiclassical potentials [5, 6]. The Hamiltonian reads in atomic units (a.u.),

$$\begin{aligned}
 H_{\text{H}_3^+}^{(1)} = & \sum_{j=1}^3 \frac{\mathbf{p}_j^2}{2M} + \sum_{k=1}^2 \frac{\mathbf{p}_k^2}{2} + \frac{1}{|\mathbf{r}_{12}|} + \sum_{j<k} \frac{1}{|\mathbf{R}_{jk}|} + \sum_{j=1}^3 \sum_{k=1}^2 \left[-\frac{1}{|\mathbf{s}_{jk}|} \right. \\
 & \left. + \frac{f(\mathbf{q}_{jk}, \mathbf{s}_{jk}, \xi)}{\mu s_{jk}^2} \right] \\
 & + \sum_{j<k} \left[\sum_{l=1}^2 \frac{f(\mathbf{Q}_{jkl}, \mathbf{S}_{jkl}, \chi_1)}{\nu \mathbf{R}_{jk}^2} + 2 \frac{f(\frac{\mathbf{p}_{12}}{2}, \mathbf{r}_{12}, \chi_2)}{\mathbf{R}_{jk}^2} \right] \\
 & - 2 \frac{f(\frac{\mathbf{p}_{12}}{2}, \mathbf{r}_{12}, \eta)}{(\sum_{j<k} |\mathbf{R}_{jk}| + \beta)^2}, \tag{38.1}
 \end{aligned}$$

where the two electrons have coordinates \mathbf{r}_k , momenta \mathbf{p}_k ($k = 1, 2$), and the three protons have mass M , coordinates \mathbf{R}_j , and momenta \mathbf{P}_j , ($j = 1, 2, 3$). For the numerical value of the proton mass M , we use $M = 1836.2$. In (38.1), we have adopted the following notation, $\mathbf{r}_{12} = \mathbf{r}_1 - \mathbf{r}_2$, $\mathbf{p}_{jk} = \mathbf{p}_j - \mathbf{p}_k$, $\mathbf{R}_{jk} = \mathbf{R}_j - \mathbf{R}_k$, $\mathbf{q}_{jk} = (\mathbf{P}_j - M\mathbf{p}_k)/(M + 1)$, $\mathbf{s}_{jk} = \mathbf{R}_j - \mathbf{r}_k$, $\mathbf{Q}_{jkl} = (\mathbf{P}_j/2 + \mathbf{P}_k/2 - 2M\mathbf{p}_l)/(2M + 1)$,

$\mathbf{S}_{jkl} = (\mathbf{R}_j + \mathbf{R}_k)/2 - \mathbf{r}_l$, $\mu = M/(M+1)$, and $\nu = 2M/(2M+1)$. The parameters in (38.1) take the values of $\xi = 0.9428$, $\chi_1 = 0.90$, $\chi_2 = 1.73$, $\eta = 1.85$ and $\beta = 0.1$.

In the above Hamiltonian, the function $f(\mathbf{q}, \mathbf{s}, \xi)$, which has the form $f(\mathbf{q}, \mathbf{s}, \xi) = (\xi^2/16) \exp\{4[1 - (|\mathbf{q}||\mathbf{s}|/\xi)^4]\}$, plays a key role. This type of potential was first introduced in [5] and [6]. This quasiclassical potential prevents an electron with a small momentum from falling into the Coulomb singularity at the nucleus. We have shown [7] that the Hamiltonian (38.1) leads to a stable H_3^+ molecule, and its ground state potential energy surface is reasonably close to the quantum mechanical one.

The second model of H_3^+ , the SPM, where the Coulomb interaction among the particles is modified by three softening parameters α_{ee} , α_{ep} , and α_{pp} , reads

$$H_{\text{H}_3^+}^{(2)} = \sum_{j=1}^3 \frac{\mathbf{P}_j^2}{2M} + \sum_{k=1}^2 \frac{\mathbf{p}_k^2}{2} + \frac{1}{\sqrt{\mathbf{r}_{12}^2 + \alpha_{ee}^2}} + \sum_{j < k} \frac{1}{\sqrt{\mathbf{R}_{jk}^2 + \alpha_{pp}^2}} - \sum_{j=1}^3 \sum_{k=1}^2 \frac{1}{\sqrt{\mathbf{s}_{jk}^2 + \alpha_{ep}^2}}. \quad (38.2)$$

It is possible to show [8] that if the parameters α_{ee} , α_{ep} , and α_{pp} are chosen appropriately, the Hamiltonian (38.2) yields stable structures for H , H_2^+ , H_2 , and H_3^+ , but unstable H_3^{2+} . In the following calculation, we choose $\alpha_{ee} = 1.5$, $\alpha_{ep} = 1.2$, and $\alpha_{pp} = 0.87$.

38.3 Results

We have simulated the response of the H_3^+ molecule to a three cycle, 790 nm laser pulse in the wide range of the laser intensity, using both APM and SPM. The simulation procedure can be described as follows. First, initial values for the momenta and coordinates of all the particles were sampled from a distribution in the phase space where the molecule is randomly oriented and vibrationally excited by 0.08 a.u. (APM), and 0.03 a.u. (SPM). Vibrational excitation in the initial state enhances the probability of dissociation and/or ionization. Then, the equations of motion,

$$\begin{aligned} \frac{d\mathbf{p}_k}{dt} &= -\frac{\partial H_{\text{H}_3^+}^{(N)}}{\partial \mathbf{r}_k} - \mathbf{E}(t), \quad \frac{d\mathbf{P}_j}{dt} = -\frac{\partial H_{\text{H}_3^+}^{(N)}}{\partial \mathbf{R}_j} + \mathbf{E}(t), \quad \frac{d\mathbf{r}_k}{dt} \\ &= \frac{\partial H_{\text{H}_3^+}^{(N)}}{\partial \mathbf{p}_k}, \quad \frac{d\mathbf{R}_j}{dt} = \frac{\partial H_{\text{H}_3^+}^{(N)}}{\partial \mathbf{P}_j}, \end{aligned} \quad (38.3)$$

are integrated in time until the point where we can judge the final state of the system, where $1 \leq j \leq 3$, $1 \leq k \leq 2$, $\mathbf{E}(t)$ is the laser field, and $N = 1$ or 2 depending

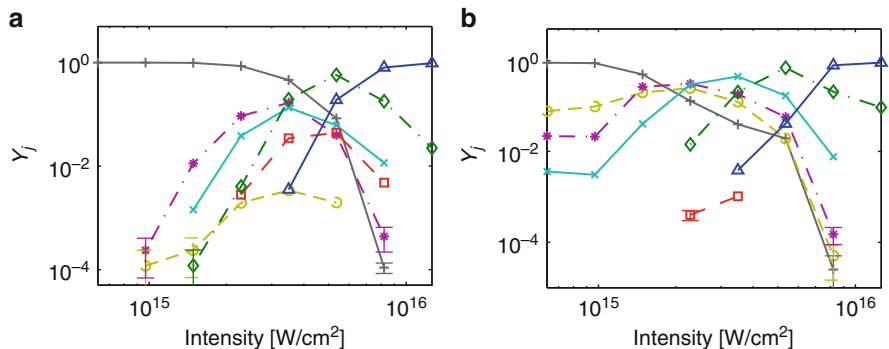


Fig. 38.1 Relative yields of the seven pathways H_3^+ (+), $\text{H}_2^+ + \text{H}$ (asterisk), $\text{H}^+ + 2\text{H}$ (cross), $\text{H}^+ + \text{H}_2$ (open circle), $\text{H}^+ + \text{H}_2^+$ (open square), $2\text{H}^+ + \text{H}$ (diamond), and 3H^+ (triangle), as a function of laser field intensity. Statistical errorbars $\pm\sigma$ are shown when they are larger than the size of the symbols. (a) APM. (b) SPM

on the model used. As a result of the interaction with the laser pulse, there are the following seven possible pathways to form (a) H_3^+ , (b) $\text{H}^+ + \text{H}_2$, (c) $\text{H}_2^+ + \text{H}$, (d) $\text{H}^+ + \text{H} + \text{H}$, (e) $\text{H}^+ + \text{H}_2^+ + \text{e}^-$, (f) $\text{H}^+ + \text{H}^+ + \text{H} + \text{e}^-$, and (g) $\text{H}^+ + \text{H}^+ + \text{H}^+ + \text{e}^- + \text{e}^-$. The relative yield Y_j of pathway j is defined as $Y_j = n_j/n_{\text{tot}}$, where n_j is the number of trajectories categorized into pathway j , and $n_{\text{tot}} \approx 10^4$ is the total number of trajectories simulated. The statistical error is defined as $\sigma = \sqrt{n_j/n_{\text{tot}}}$.

The results of the simulations are displayed in Fig. 38.1, where the relative yields of the respective pathways are shown as a function of the laser field intensity for both models. At intermediate intensities below $5 \times 10^{15} \text{ W/cm}^2$, the pathways without ionization have larger yields than the ionization pathways, while the yield of the double ionization pathway becomes close to unity for the largest intensity.

As shown in Fig. 38.1a, APM gives a very small yield for the $\text{H}^+ + \text{H}_2$ pathway as compared to the $\text{H}_2^+ + \text{H}$ pathway. This is in disagreement with the experimental results [4], where the $\text{H}^+ + \text{H}_2$ and $\text{H}_2^+ + \text{H}$ pathways were found to have comparable yields over the whole range of the laser intensity. To the contrary, as shown in Fig. 38.1b, SPM gives comparable yields for the $\text{H}^+ + \text{H}_2$ and $\text{H}_2^+ + \text{H}$ pathways.

In addition to the total yields, we have also compared the kinetic energy release (KER) distributions and the angular distributions of the yields obtained by the two models [7, 8] with the experimental data. We found that the observed KER spectra as well as the observed distributions of the alignment angle between the laser field vector and the molecular plane are well reproduced by APM, but not so well by SPM.

In conclusion, we have constructed the two new classical model Hamiltonians to describe laser-driven H_3^+ , and found that some features of the observed spectra could be qualitatively reproduced. The APM is able to reproduce both the experimental KER spectra and some parts of the distributions of the angular yields, but fails when it comes to the total yields of the dissociative pathways without ionization. On the

other hand, SPM was able to reproduce the observed intensity dependence of the yields of the $\text{H}^+ + \text{H}_2$ and $\text{H}_2^+ + \text{H}$ pathways. Concerning the overall performance of the two models, we judge that APM is superior.

Acknowledgements We acknowledge support from the Ministry of Education, Culture, Sports, Science and Technology (MEXT), Japan (Grant-in-Aid for Specially Promoted Research on Ultrafast Hydrogen Migration No. 19002006, and Grant-in-Aid for Global COE Program for Chemistry Innovation). E. Lötstedt is grateful for the support from a Grant-in-Aid for Scientific Research (No. 21-09238, JSPS).

References

1. A. Kästner, F. Grossmann, R. Schmidt, J.M. Rost, *Phys. Rev. A* **81**(2), 023414 (2010)
2. H.A. Leth, L.B. Madsen, K. Mølmer, *Phys. Rev. Lett.* **103**(18), 183601 (2009)
3. T. Kato, K. Yamanouchi, *J. Chem. Phys.* **131**(16), 164118 (2009)
4. J. McKenna, A.M. Saylor, B. Gaire, N.G. Johnson, K.D. Carnes, B.D. Esry, I. Ben-Itzhak, *Phys. Rev. Lett.* **103**(10), 103004 (2009)
5. C.L. Kirschbaum, L. Willets, *Phys. Rev. A* **21**(3), 834 (1980)
6. J.S. Cohen, *Phys. Rev. A* **56**(5), 3583 (1997)
7. E. Lötstedt, T. Kato, K. Yamanouchi, *Phys. Rev. Lett.* **106**(20), 203001 (2011)
8. E. Lötstedt, T. Kato, K. Yamanouchi, *Phys. Rev. A* **85**(5), 053410 (2012)

Chapter 39

Electron-Scattering and Photoionization of H_2^+ and HeH^{2+}

H. Miyagi, T. Morishita, and S. Watanabe

Abstract We have developed an efficient numerical method for calculating the electron-scattering differential cross sections (ESDCSs) and the photoionization differential cross sections (PIDCSs) of one-electron diatomic molecules based on the R -matrix propagation method in the prolate spheroidal coordinates. Analysis based on the Coulomb corrected independent atom model identifies a local minimum in the ESDCSs of HeH^{2+} that stems from the two-center interference, while attributing others to multiple-scattering.

39.1 Introduction

When an atom or molecule is exposed to a short intense laser pulse, ejected photoelectrons may be driven back by the oscillating electric field of the laser to recollide with the parent ion. These recollisions play an important role in various nonlinear phenomena, such as high-order harmonic generation, high-energy above-threshold ionization, nonsequential double ionization. To elucidate such nonlinear dynamics, it is important to study the interaction between an electron and a parent ion from the scattering theoretical point of view. Recent studies have shown that the recollision mechanism indeed permits us to retrieve accurate elastic cross sections and photorecombination cross sections from above-threshold ionization and high order-harmonic spectra, respectively [1, 2]. Thus, the study of cross sections of a simple molecule based on *accurate calculations* is desired for complementing investigations of recollision processes. Investigating one-electron diatomic molecules in the fixed-nuclei approximation, we have established an accurate method to calculate electron-scattering differential cross sections (ESDCSs)

H. Miyagi (✉) · T. Morishita · S. Watanabe
University of Electro-Communications, 1-5-1 Chofu-ga-oka, Chofu-shi, Tokyo 182-8585, Japan
e-mail: miyagi@power1.pc.uec.ac.jp

as well as the photoionization differential cross sections (PIDCSs) based on the R -matrix propagation method in the prolate spheroidal coordinates. We also analyze the structure of the ESDCSs by using the Coulomb corrected independent atom model (CCIAM).

39.2 Formulation and Numerical Procedure

In the scattering problem of the one-electron diatomic molecules, the time-independent Schrödinger equation in the molecular frame reads

$$\left(-\frac{1}{2}\nabla^2 - \frac{Z_1}{r_1} - \frac{Z_2}{r_2}\right)\Psi(\mathbf{r}; R) = E\Psi(\mathbf{r}; R), \quad (39.1)$$

where the two positive charges Z_1 and Z_2 are located at $z = -R/2$ and $R/2$, respectively. In the above equation, r_1 and r_2 are the distances of the electron from the charges Z_1 and Z_2 , respectively. Unless otherwise stated, atomic units are used throughout this article.

The Coulomb singularities are fully taken into account by using the prolate spheroidal coordinates $\xi = (r_1 + r_2)/R$, $\eta = (r_1 - r_2)/R$, and ϕ . By expressing the solution in the form of $\Psi(\mathbf{r}; R) = \Pi_{|m|q}(\xi; k, R)\mathcal{E}_{|m|q}(\eta; k, R)e^{im\phi}/\sqrt{2\pi}$, (39.1) is decomposed into two separable equations in ξ and η ,

$$\left[\frac{d}{d\eta}(1-\eta^2)\frac{d}{d\eta} - \frac{m^2}{1-\eta^2} + c^2(1-\eta^2) + b\eta + \lambda_{mq}\right]\mathcal{E}_{|m|q}(\eta; k, R) = 0, \quad (39.2)$$

$$\left[\frac{d}{d\xi}(\xi^2-1)\frac{d}{d\xi} - \frac{m^2}{\xi^2-1} + c^2(\xi^2-1) + a\xi - \lambda_{mq}\right]\Pi_{|m|q}(\xi; k, R) = 0, \quad (39.3)$$

where λ_{mq} is the separation constant, $m = 0, \pm 1, \dots$, $q = 0, 1, \dots$ (q represents the number of zeros in η), and other symbols are $a = R(Z_2 + Z_1)$, $b = R(Z_2 - Z_1)$, and $c = \sqrt{2E}R/2$. We solve the spheroidal angular equation (39.2) by the discrete-variable-representation (DVR) method using the Gauss–Legendre quadrature, obtaining λ_{mq} and $\mathcal{E}_{|m|q}(\eta; k, R)$. Substituting λ_{mq} into the spheroidal radial equation (39.3), we solve the equation with the R -matrix propagation method and obtain the spheroidal phase-shift Δ_{mq} by matching to the asymptotic boundary condition at sufficiently large $\xi = \xi_m \gg 1$.

Having Δ_{mq} , we obtain the S -matrix elements as well as the scattering wave function with the outgoing wave boundary condition. The ESDCS is calculated by using the S -matrix, and the PIDCS is evaluated within the framework of the perturbation theory by using the scattering wave functions.

39.3 Results and Discussion

We checked the convergence of the calculations of the ESDCS and the PIDCSs for the fixed-in-space H_2^+ and HeH^{2+} for several electron energies. As an example, Fig. 39.1 shows the ESDCSs of HeH^{2+} ($R = 2.0$) for the collision energy at 50 eV as a function of the scattering angle $\theta_{\text{si}} = \cos^{-1}(\mathbf{k}_s \cdot \mathbf{k}_i / (|\mathbf{k}_s||\mathbf{k}_i|))$, where \mathbf{k}_i and \mathbf{k}_s are the wave vectors of the incident and scattering electron, respectively. Several local minima due to the two-center nature of the problem can be seen, and are also expected to appear in the photoelectron momentum distributions for the laser ionization as an imprint of the molecule. For collisions between an electron and a neutral molecule, minima in the ESDCSs are often explained by the two-center interference using the so called *independent atom model* (IAM) [3]. In the IAM, the scattering amplitude is approximated by the sum of the scattering amplitudes of each atom in the molecule. For electron-molecular ion collisions, the Coulomb interaction in the asymptotic region is important. In this work, we introduce the *Coulomb corrected independent atom model* (CCIAM). In this model, the approximated scattering amplitude is

$$f_{\text{CCIAM}}(\mathbf{k}_s, \mathbf{k}_i) = \frac{Z_1}{Z_1 + Z_2} f_{-R/2}(\mathbf{k}_s, \mathbf{k}_i) + \frac{Z_2}{Z_1 + Z_2} f_{R/2}(\mathbf{k}_s, \mathbf{k}_i), \quad (39.4)$$

where $f_{\pm R/2}(\mathbf{k}_s, \mathbf{k}_i)$ is the amplitude of an electron scattered by a single charge of $Z_1 + Z_2$ located at $z = \pm R/2$ on the z axis. The CCIAM amplitude in (39.4) is derivable from a proper decomposition of the Lippmann–Schwinger equation, satisfying the correct asymptotic boundary condition at $r \rightarrow \infty$. Note that the (CC)IAM only takes into account the two-center quantum interference but neglects other multiple-scattering processes.

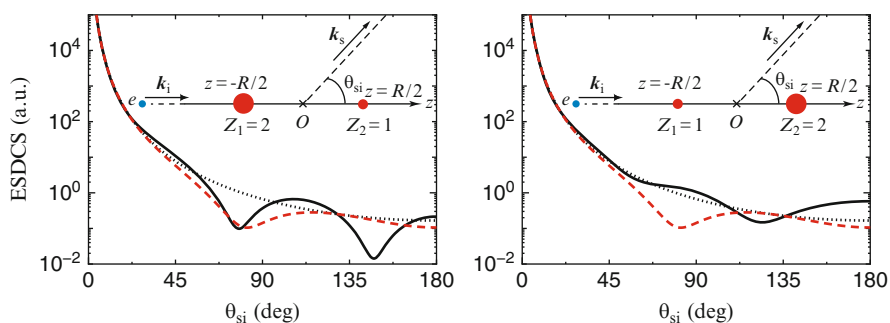


Fig. 39.1 The ESDCSs for the fixed-in-space HeH^{2+} ($R = 2.0$) for the electron energy 50 eV. In each panel, the *inset* indicates the geometry of the collision system. *Solid black curves*: accurate ESDCSs, *dotted black curves*: results of the one-center Coulomb scattering by total charge $Z_1 + Z_2 = 3$, i.e., the result for $R = 0.0$, and *dashed red curves*: results of the CCIAM $|f_{\text{CCIAM}}(\mathbf{k}_s, \mathbf{k}_i)|^2$

The left panel of Fig. 39.1 shows the result where the incident electron collides the target from the He^{2+} side. Two local minima can be seen at $\theta_{\text{si}} = 70^\circ$ and 140° . The CCIAM reproduces only one at $\theta_{\text{si}} = 70^\circ$. The origin of the local minimum at $\theta_{\text{si}} = 70^\circ$ is thus ascribable to the two-center quantum interference, while the other at $\theta_{\text{si}} = 140^\circ$ is due to the multiple-scattering neglected in the CCIAM. In the case of H_2^+ , we obtained results and identifications almost similar to those of HeH^{2+} discussed above.

The ESDCS changes drastically when the incident electron collides from the other side as shown in the right panel of Fig. 39.1. In this case, the CCIAM does not agree well and the multiple-scattering is extremely important. Note that in the CCIAM the cross sections for the two cases remain the same under the exchange of Z_1 and Z_2 as can be seen in (39.4). Further analyses will be needed to explain what mechanism induces the multiple-scattering strongly in this collision geometry.

39.4 Conclusion

We have calculated the accurate ESDCSs and PIDCSs for the one-electron diatomic molecules H_2^+ and HeH^{2+} by using the method based on the R -matrix propagation in the prolate spheroidal coordinates. Analysis based on the CCIAM classifies the origin of each local minimum in the ESDCS of HeH^{2+} into two categories: the two-center quantum interference and the multiple-scattering. It was found that the importance of the multiple-scattering largely depends on the incident angle.

References

1. T. Morishita, A.T. Le, Z. Chen, C.D. Lin, Accurate retrieval of structural information from laser-induced photoelectron and high-harmonic spectra by few-cycle laser pulses. *Phys. Rev. Lett.* **100**, 013903-1-4 (2008)
2. Z. Chen, A.T. Le, T. Morishita, Quantitative rescattering theory for laser-induced high-energy plateau photoelectron spectra. *Phys. Rev. A* **79**, 033409-1-18 (2009)
3. P.D. McCaffrey, J.K. Dewhurst, D.W.H. Rankin, R.J. Mawhorter, S. Sharma, Interatomic contributions to high-energy electron-molecule scattering. *J. Chem. Phys.* **128**, 204304-1-7 (2008)

Chapter 40

Molecular Orientation by Intense Visible and THz Optical Pulses

K. Kitano, N. Ishii, and J. Itatani

Abstract We propose an all-optical method for achieving molecular orientation by two-step excitation with visible femtosecond laser (fs) and terahertz (THz) pulses. First, the femtosecond laser pulse induces off-resonant impulsive Raman excitation to create rotational wavepackets. Next, a delayed intense THz pulse effectively induces resonant dipole transition between neighboring rotational states. By controlling the intensities of both the pulses and the time delay, we can create rotational wavepackets consisting of states with different parities in order to achieve a high degree of molecular orientation under a field-free condition. We numerically demonstrate that the highest degree of orientation of $\langle \cos \theta \rangle > 0.8$ in HBr molecules is feasible under experimentally available conditions.

40.1 Introduction

Manipulation of the rotational freedom in gas-phase molecules has long been an important subject in the study of reaction dynamics. It is roughly classified into two types: alignment and orientation. Alignment refers to the rotational states in which the symmetry axis of a molecule is localized along a laboratory-fixed axis, whereas orientation refers to the states in which the upward and downward directions of the axis are additionally controlled. Techniques for molecular alignment have been well developed by applying non-resonant laser pulses with nanosecond to femtosecond durations and applied in various strong-field experiments [1]. On the other hand, molecular orientation still remains a significant challenge. Until now, the methods that have been proposed and demonstrated include the use of a strong DC field [2],

K. Kitano (✉) · N. Ishii · J. Itatani
Institute for Solid-State Physics, University of Tokyo, Kashiwanoha 5-1-5, Kashiwa, Chiba
277-8581, Japan
e-mail: kitano@issp.u-tokyo.ac.jp; ishii@issp.u-tokyo.ac.jp; JItatani@issp.u-tokyo.ac.jp

preparing state-selected molecules with hexapole focusing [3], DC and intense non-resonant laser fields [4, 5], and phase-locked two-color laser fields [6]. The highest degree of orientation was achieved by a combination of the hexapole focusing with DC and intense non-resonant laser fields [7]. The orientation degree, which is given by the ensemble average of $\cos \theta$, where θ is the angle between the laboratory-fixed and the molecular axes, reached up to $\langle \cos \theta \rangle \sim 0.74$. However, the number density of molecules was significantly reduced through the state-selection process. Furthermore, the orientation was achieved in the presence of a DC field, which may perturb the quantum states of target molecules.

In addition to these approaches, optical fields in the THz region have been considered to be a promising tool for realizing orientation with a reasonable number density of molecules under field-free conditions. There have been many proposals for molecular orientation using a half-cycle pulse (HCP) [8, 9]. However, none of these proposals has been experimentally realized, probably because of the technical difficulty in generating intense HCPs. The recent breakthrough in THz technology has opened a new possibility. Intense THz pulses become easily obtainable via the pulse-front-matching technique in optical rectification of amplified femtosecond laser pulses [10]. The maximum field intensity of the THz pulses has recently reached the order of 1 MV/cm [11]. However, these intense THz pulses are nearly single-cycle pulses, and not half-cycle pulses, which is difficult to be applied to the proposed methods.

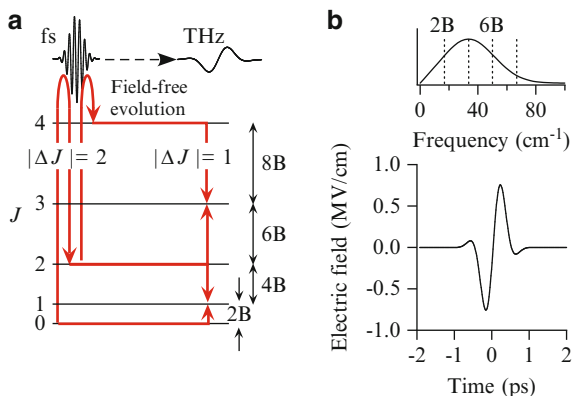
Based on these recent technological advances, we propose a new method to achieve a high degree of molecular orientation using a single-cycle intense THz pulse in combination with a visible femtosecond laser pulse.

40.2 Basic Strategy

The schematic of our method is shown in Fig. 40.1a. First, a linearly polarized intense non-resonant femtosecond laser pulse creates rotational wavepackets through impulsive Raman excitation according to the selection rule of $\Delta J = 0, \pm 2$, and $\Delta M = 0$, where J is the total angular momentum and M is its projection on a laboratory-fixed Z -axis (defined parallel to the laser electric field). At this stage, the molecules are aligned but not oriented because of the lack of coherence between the even and odd J states. After a variable time delay, a nearly single-cycle THz pulse (Fig. 40.1b) whose polarization is set parallel to the femtosecond laser field is applied to induce resonant dipole transition between the even and odd states according to the selection rule of $\Delta J = \pm 1$ and $\Delta M = 0$. This fs-THz scheme can be understood as a sort of double pulse scheme. By optimizing the time delay between them, a high degree of molecular orientation can be realized under a field-free condition during the evolution of the wavepackets.

Fig. 40.1 (a) Schematic representation of rotational transitions by non-resonant femtosecond laser and resonant THz pulses.

(b) Temporal shape of the THz pulse. The upper part shows its spectrum and the energy spacings between neighboring rotational states of HBr

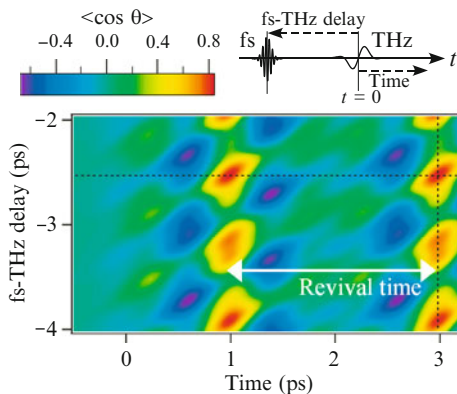


40.3 Simulation Results

Based on the method described in the previous section, we performed simulations by solving a time-dependent Schrödinger equation numerically within the rigid-rotor approximation. We used HBr as the target molecule, which is a polar molecule with a moderate permanent dipole moment of $\mu_0 = 0.828$ Debye [12] and a polarizability anisotropy of $\Delta\alpha = 0.91 \text{ \AA}^3$ [13]. The rotational constant in its vibronic ground state and the rotational period are $B_e = 8.3482 \text{ cm}^{-1}$ [12] and $\tau_{\text{rot}} = 2.0$ ps, respectively. We set the peak electric field amplitude of the femtosecond laser pulse as 0.116 GV/cm , which corresponds to the intensity of 18 TW/cm^2 , and the pulse duration as 100 fs FWHM in intensity. The temporal shape and power spectrum of the THz pulse is shown in Fig. 40.1b. The peak electric field amplitude, the pulse duration, and the central frequency of the THz pulse are 0.76 MV/cm , 500 fs FWHM in intensity, and 1.0 THz , respectively. These values are taken from a recent experiment on the generation of intense THz pulse reported by Watanabe et al. [11].

Figure 40.2 shows the calculated results of the orientation parameter $\langle \cos \theta \rangle$ obtained by assuming that the HBr molecule is initially in its ground rotational state $|J, M\rangle = |0, 0\rangle$. The horizontal axis in Fig. 40.2 represents a time, where we define the envelope peak of the THz pulse as the origin of the coordinate. The vertical axis represents a time delay of the femtosecond laser pulse with respect to the THz pulse. The time ranges of both axes in Fig. 40.2 are set longer than the full revival time to show all the information for understanding the orientation dynamics. The maximal orientation value under field-free conditions reaches $|\langle \cos \theta \rangle|_{\text{max}} = 0.84$ at the time delay of -2.53 ps and the time of 2.98 ps . In our simulations, $\langle \cos \theta \rangle > 0$ corresponds to the case where H atoms are directed in the positive direction of the laboratory-fixed Z -axis. We performed another simulation with the same parameters but without the femtosecond laser pulse. In this case, the maximum orientation parameter was $|\langle \cos \theta \rangle|_{\text{max}} = 0.38$. Thus we conclude that the pre-excitation with the femtosecond laser pulse enhances the degree of molecular orientation.

Fig. 40.2 2-D plot of orientation dynamics with respect to the time delay between the femtosecond and THz pulses (y-axis), and the time after the irradiation of the THz pulse (x-axis). The timings for the maximal orientation is indicated by dashed lines



40.4 Conclusion

We proposed a new method to realize a high degree of molecular orientation using a single-cycle intense THz pulse combined with an intense femtosecond laser pulse. The method is based on non-resonant pre-excitations of molecules with femtosecond laser pulses to create rotational wavepackets, followed by resonant excitations with THz pulses to establish coherence between neighboring rotational states. Because of this simple and clear strategy, this method can be applicable to wide ranges of polar molecules.

Acknowledgements This research was partially supported by the Photon Frontier Network Program of the Ministry of Education, Culture, Sports, Science and Technology, Japan.

References

1. H. Stapelfeldt, T. Seideman, *Rev. Mod. Phys.* **75**, 543 (2003)
2. H.J. Loesch, A. Remscheid, *J. Chem. Phys.* **93**, 4779 (1990)
3. D.H. Parker, P.B. Bernstein, *Annu. Rev. Phys. Chem.* **40**, 561 (1989)
4. B. Friedrich, D. Herschbach, *J. Chem. Phys.* **111**, 6157 (1999)
5. H. Sakai et al., *Phys. Rev. Lett.* **90**, 083001 (2003); L. Holmegaard et al., *Phys. Rev. Lett.* **102**, 023001 (2009)
6. S. De et al., *Phys. Rev. Lett.* **103**, 153002 (2009); K. Oda et al., *Phys. Rev. Lett.* **104**, 213901 (2010)
7. O. Ghafur et al., *Nat. Phys.* **5**, 289 (2009)
8. M. Machholm, N.E. Henriksen, *Phys. Rev. Lett.* **87**, 193001 (2001); C.M. Dion et al., *Eur. Phys. J. D* **14**, 249 (2001); D. Sugny et al., *Phys. Rev. A* **69**, 033402 (2004); E. Gershonabel, I.S. Averbukh, R.J. Gordon, *Phys. Rev. A* **74**, 053414 (2006)
9. D. Daems et al., *Phys. Rev. Lett.* **94**, 153003 (2005)
10. K.-L. Yeh et al., *Appl. Phys. Lett.* **90**, 171121 (2007)
11. S. Watanabe et al., *Opt. Express* **19**, 1528 (2011)
12. NIST Database <http://webbook.nist.gov/chemistry/>
13. J.O. Hirschfelder et al., *Molecular Theory of Gases and Liquids* (Wiley, New York, 1954)

Chapter 41

Below-Threshold High-Harmonic Spectroscopy with Aligned Hydrogen Molecular Ions

Fu-Yuan Jeng, Dmitry A. Telnov, and Shih-I Chu

Abstract We present fully ab initio three-dimensional (3D) calculations of high-order harmonic generations (HHG) of aligned hydrogen molecular ions, H_2^+ , subject to intense linearly-polarized laser pulses. The numerical method is based on the high-precision time-dependent generalized pseudospectral method and the wavelet transform as the tool for time-frequency analysis. We show that the orientation of the molecular axis with respect to the polarization of the laser field strongly affect the electron returning times and below-threshold HHG dynamics. In this study, we find that the short (long) trajectories dominate the emission of below-threshold harmonics when the molecular axis is parallel (perpendicular) to the polarization vector of the laser field.

HHG has been experimentally and theoretically investigated more than twenty years. In the past the major attention has been focused on the regime well above the threshold. However, more recently, considerable attention has been devoted to the below- and near- threshold regimes [1–4]. Particularly, Soifer et al. [4] has demonstrated a study of harmonic generations in aligned N_2 and O_2 close to the ionization threshold using an intense laser field of controllable ellipticity. In order to reveal the underlying dynamic features of below-threshold harmonics, we present

F.-Y. Jeng (✉)

Department of Physics, National Taiwan University, Taipei 10617, Taiwan (ROC)

e-mail: fuyuanjeng@google.com

D.A. Telnov

Department of Physics, St. Petersburg State University, St. Petersburg 198504, Russia

e-mail: telnov@pcqnt1.phys.spbu.ru

S.-I. Chu

Department of Chemistry, University of Kansas, Lawrence, Kansas 66045, USA

e-mail: sichu@ku.edu

fully ab initio and high-precision calculations by means of the time-dependent generalized pseudo-spectral method and wavelet transform as time-frequency analysis of harmonic generations from aligned H_2^+ .

We solve the time-dependent Schrödinger equation of the aligned H_2^+ in linearly-polarized pulsed laser fields, in atomic units:

$$i \frac{\partial}{\partial t} \Psi(t) = [H_0 + V(t)] \Psi(t), \quad (41.1)$$

where H_0 is the unperturbed Hamiltonian, and $V(t)$ is the electron-laser interaction. To properly describe the laser-free Hamiltonian of a two-center problem, we make use of the prolate spheroidal coordinates ξ , η and φ , which are related to the Cartesian coordinates x , y and z as

$$\begin{aligned} x &= a \sqrt{(\xi^2 - 1)(1 - \eta^2)} \cos \varphi, \\ y &= a \sqrt{(\xi^2 - 1)(1 - \eta^2)} \sin \varphi, \\ z &= a \xi \eta \end{aligned} \quad (41.2)$$

The molecular axis is directed along the z axis, and the nuclei are located on this axis at the position -1 and 1 . Because of the rotational symmetry with respect to the molecular axis, the time-independent wave function can be represented as

$$\Psi(\xi, \eta, \varphi) = \psi_m(\xi, \eta) e^{im\varphi}. \quad (41.3)$$

We then discretized the coordinates ξ and η using the generalized pseudospectral method, and the time propagation of the wave function is achieved by the second-order split-operator method in the energy representation [5, 6]

$$\Psi(\mathbf{r}, t + \Delta t) = e^{-i\widehat{H}_0 \frac{\Delta t}{2}} e^{-i\widehat{V}(\xi, \eta, t + \frac{\Delta t}{2}) \Delta t} e^{-i\widehat{H}_0 \frac{\Delta t}{2}} \Psi(\mathbf{r}, t) + O(\Delta t^3). \quad (41.4)$$

Without loss of generality, we assume that the polarization vector of the field lies in the $x - z$ plane. Then, we can write the coupling $V(t)$ in the following form:

$$V(t) = aF(t)(\xi\eta \cos \beta + \sqrt{(\xi^2 - 1)(1 - \eta^2)} \cos \varphi \sin \beta). \quad (41.5)$$

Here β is the angle between the polarization vector of the laser field and the molecular axis. In our calculation, we used the following time-dependent function $F(t)$:

$$F(t) = F_0 \sin^2 \frac{\pi t}{T} \sin \omega_0 t, \quad (41.6)$$

where F_0 is the peak field strength, T is the pulse duration, and ω_0 is the carrier frequency. The laser parameters used are 3×10^{14} W/cm², 20 optical cycles (O.C.) and 800 nm.

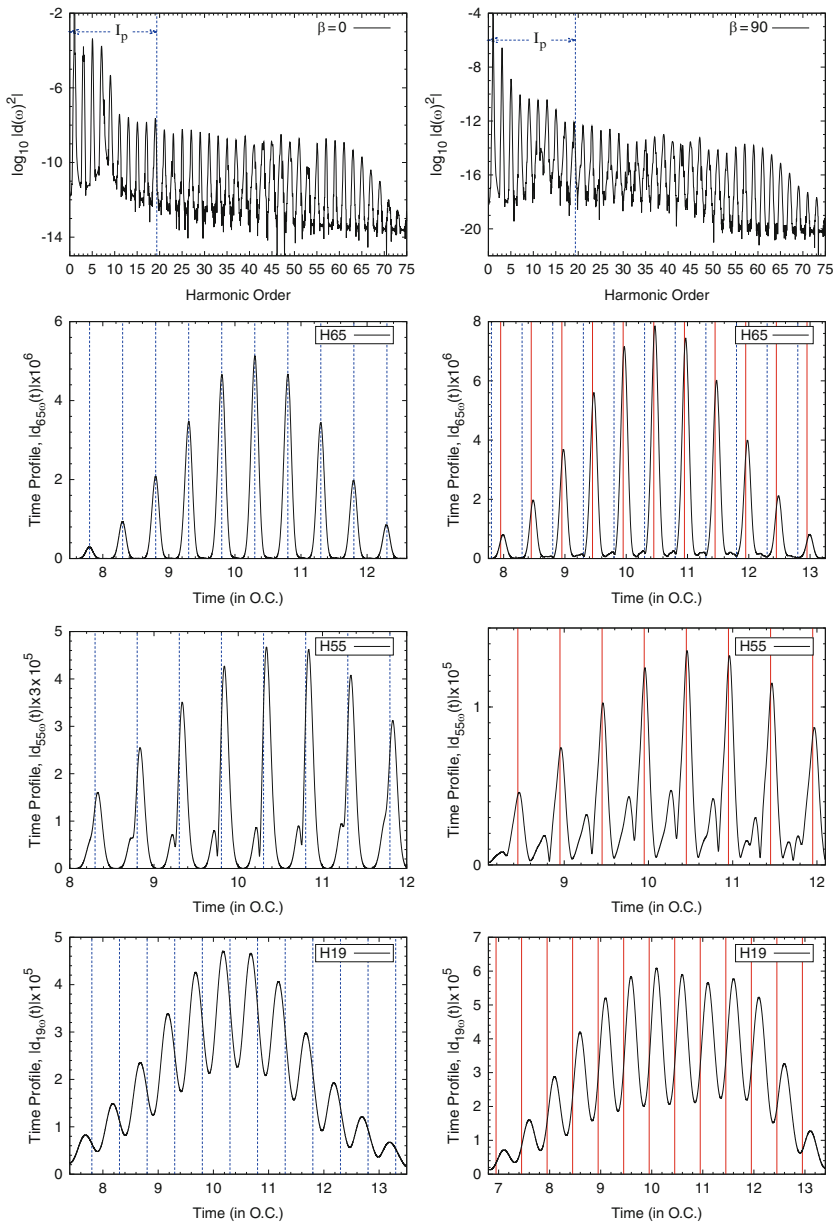


Fig. 41.1 The power spectra and time profiles of the 65th (near the cut-off), the 53rd (the plateau) and the 19th (below the threshold) harmonics for aligned H_2^+ in linearly-polarized laser pulses. Shown in the *left (right) column* is the case of the polarization vector being parallel (perpendicular) to the molecular axis. The *blue vertical dashed lines* are the electron returning times (with phase $\omega_0 t = 108^\circ$ or 288°) predicted by the quasi-classical model of H_2^+ [8]. The *red vertical solid lines* are the electron returning times (with phase $\omega_0 t = 162^\circ$ or 342°) predicted by the quasi-classical model of atomic H [9]. See text for more details

To probe the spectral and temporal structures of HHG, we perform the wavelet transform of the induced dipole moment [7],

$$d_{\omega}(t) = \int d(t') \sqrt{\omega} W(\omega(t' - t)) dt'. \quad (41.7)$$

The usual choice of $W(t)$, a windowed oscillating function, is Morlet wavelet:

$$W(x) = \frac{1}{\sqrt{\tau}} e^{ix} e^{-x^2/2\tau^2}, \quad (41.8)$$

where τ , a parameter, can vary its value from 5 to 30. Since the general pattern does not change while varying the value of τ , we choose $\tau = 15$ to perform this wavelet transform.

Based upon the above theoretical method, we present two extreme cases below. We first demonstrate the results of the polarization vector being parallel to the molecular axis in the left column of Fig. 41.1. The time profile of the 65th (near the cut-off) harmonic exhibits two bursts within each optical cycle. Each burst is due to the re-collision of the electronic wave packet with the molecular ionic core. The agreement of the full quantum calculation and quasi-classical prediction is quite striking. We then examine the 55th (the plateau) harmonic and notice that its time profile shows that there exists two returning trajectories: The short trajectory returns at a phase ($\omega_0 t$) less than 108° (or 288°), and the long trajectory at a phase larger than 108° (or 288°). However, the time profile of the 19th (below the threshold) harmonic indicates that the short trajectory is more important than the long one.

Shown in the right column of Fig. 41.1 is the other case which the polarization vector is perpendicular to the molecular axis. As expected, the time profile of the 65th (near the cut-off) harmonic shows that H_2^+ in this set-up acts as an atom with its ground state energy being -1.102634 a.u. In this case, the time profile of the 19th harmonic, a harmonic just below threshold, indicates that the long trajectory at a phase larger than 162° (or 342°) dominates the emission of below-threshold harmonics.

In sum, we have presented ab initio 3D non-perturbative calculations of HHG from the ground state of H_2^+ . We identify the dominant trajectories according to the phase accumulated by the electron wave function along a returning trajectory. The results provide us insights regarding HHG mechanism in different energy regimes. We will address more somewhere else.

References

1. D.C. Yost, T.R. Schibli, J. Ye, J.L. Tate, J. Hostetter, M.B. Gaarde, K.J. Schafer, Nat. Phys. **5**, 815 (2009)
2. E.P. Power, A.M. March, F. Catoire, E. Sistrunk, K. Krushelnich, P. Agostini, L.F. Dimauro, Nat. Photon. **4**, 352 (2010)

3. J.A. Hostetter, J.L. Tate, K.J. Schafer, M.B. Gaarde, Phys. Rev. A **82**, 023401 (2010)
4. H. Soifer, P. Botheron, D. Shafir, A. Diner, O. Raz, B.D. Bruner, Y. Mairesse, B. Pons, N. Dudovich, Phys. Rev. Lett. **105**, 143904 (2010)
5. D.A. Telnov, S.I. Chu, Phys. Rev. A **76**, 043412 (2007)
6. X.M. Tong, S.I. Chu, Chem. Phys. **217**, 119 (1997)
7. X.M. Tong, S.I. Chu, Phys. Rev. A **61**, 021802 (R) (2000)
8. R. Kopold, W. Becker, M. Kleber, Phys. Rev. A **58**, 4022 (1998)
9. P.B. Corkum, Phys. Rev. Lett. **71**, 1994 (1993)

Chapter 42

Two-Center Interference of Heteronuclear Diatomic Molecules in High-Order Harmonic Generation

Xiaosong Zhu and Peixiang Lu

Abstract We have investigated the phenomenon of two-center destructive interference for heteronuclear diatomic molecules (HeDM) in the high-order harmonic generation, which results in the minimum in high-order harmonic spectrum. It is found that the minimum is shifted to lower harmonic orders compared with that in a homonuclear case, which is explained by performing phase analysis. The analysis shows that for an HeDM the harmonic spectrum contains information not only on the internuclear separation but also on the properties of the two separate centers, which implies the potential application of estimating the asymmetry of molecules and judging the linear combination of atomic orbitals (LCAO) for the highest occupied molecular orbital (HOMO). In addition to that, the possibility to monitor the evolution of HOMO itself in molecular dynamics is also promised.

42.1 Introduction

When atoms and molecules are exposed to intense laser irradiation, high-order harmonics are generated [1]. A very important phenomenon for molecular high-order harmonic generation (HHG) is the “minimum” in the harmonic spectrum [2, 3]. The predicted minimum by Lein et al. from a diatomic molecule results from the two center interference between the two atomic centers, which is called “structural minimum.” A structural minimum contains very important information, from which structure of objective molecule can be probed and symmetry of the bond can be judged. The two-center interference also plays an important role in the study of the attosecond nuclear motion and the imaging of molecular orbital.

X. Zhu · P. Lu (✉)

Wuhan National Laboratory for Optoelectronics, Huazhong University of Science and Technology, Wuhan 430074, People’s Republic of China
e-mail: zxs.201@gmail.com; lupeixiang@mail.hust.edu.cn

In this paper, two-center interference for heteronuclear diatomic molecule (HeDM) is investigated. We focus on the structural minimum and find that the minimum takes on new characteristics. The results show that the harmonic spectrum encodes information not only on the internuclear separation but also on the properties of the two separate centers, which indicates that the two-center interference still offers opportunities to estimate the asymmetry of the objective HeDM and to judge the linear combination of diatomic orbital (LCAO) for molecular orbitals. Moreover, the possibility to monitor the evolution of the molecular orbital in molecular dynamics is promised.

42.2 Model

We focus on the molecule CO as an example, where the contributions from each atom to HOMO are comparable to ensure that effective destructive interference could be observed. The Lewenstein model [1] is employed to calculate the harmonic radiation, where the harmonic spectrum is at last obtained by Fourier transforming the time-dependent dipole acceleration. Based on the LCAO approximation, the transition dipole moment between the ground state and the continuum state $|\mathbf{p}\rangle$ is finally obtained [4]

$$\mathbf{d}_{CO}(\mathbf{p}) = \langle \Psi_{CO}(\mathbf{r}) | \mathbf{r} | e^{-i\mathbf{p}\cdot\mathbf{r}} \rangle \quad (42.1)$$

$$= |d_C(\mathbf{p})| e^{i\phi_C - i\mathbf{p}\cdot\mathbf{R}_C} + |d_O(\mathbf{p})| e^{i\phi_O - i\mathbf{p}\cdot\mathbf{R}_O}. \quad (42.2)$$

\mathbf{R}_C and \mathbf{R}_O indicate the positions of nuclei C and O respectively. The two terms in (42.2) describe the recombination process of each center respectively. $-\mathbf{p}\cdot\mathbf{R}_C$ and $-\mathbf{p}\cdot\mathbf{R}_O$ represent phases gained by the returning electrons before recombination. The phases ϕ_C and ϕ_O arise from the recombination, which are obtained by the phase angle of the transition dipole moments \mathbf{d}_C and \mathbf{d}_O respectively.

The total phase difference between the emissions from the two center is then defined as

$$\Delta\phi = [\phi_C + (-\mathbf{p}\cdot\mathbf{R}_C)] - [\phi_O + (-\mathbf{p}\cdot\mathbf{R}_O)] \quad (42.3)$$

$$= (\phi_C - \phi_O) + pR \cos\theta, \quad (42.4)$$

where θ indicates the angle between the directions of the intrinsic dipole moment of CO and the electric field. The former term in (42.4), called the recombining phase difference, represents the phase difference from the unequal recombination processes; while the latter one, called the spatial phase difference, represents the phase difference that originates when the wave packet of returning electron travels through the projection of the internuclear distance on the laser polarization axis.

42.3 Result and Discussion

We first think about the parallel orientation at $\theta = 0^\circ$. According to the two-center model for a homonuclear diatomic molecule (HoDM) with internuclear distance $R=1.13 \text{ \AA}$, the destructive interference takes place when electron recombines with energy 29.54 or 265.87 eV predicted by

$$pR \cos \theta = m\pi, m = 0, \pm 1, \dots, \quad (42.5)$$

which corresponds to about the 31st and the 279th orders for 1,300 nm laser. Nevertheless, the observed minimum in the obtained high-order harmonic spectrum shown in Fig. 42.1a locates at the 131st order, which is quite different from the prediction. Figure 42.1b presents the spatial phase difference, the recombining phase difference and the total difference. The spatial phase difference reaches π at about 29.54 and 265.87 eV, which predicts the minima for a bonding HoDM. However, owing to the additional recombining phase difference, the positions where the actual total phase difference reaches π have been shifted to lower energy 15 eV and 121.6 eV respectively, the second of which right corresponds to the observed minimum at the 131st order.

We then extend to all orientation angles. Figure 42.2a shows the spatial phase difference as a function of angle θ and the kinetic energy of the recombining

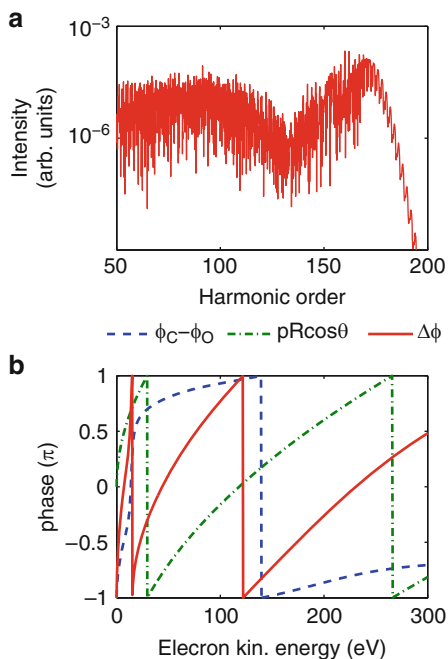
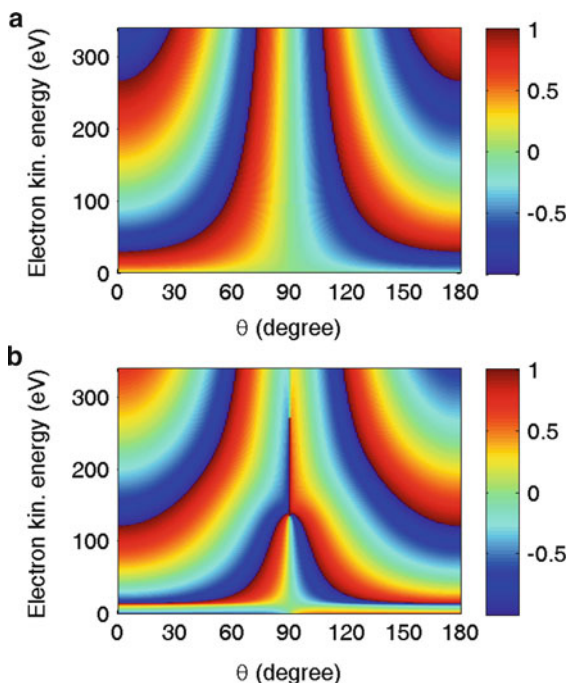


Fig. 42.1 (a) High-order harmonic spectrum of CO at 0° orientation excited by 1,300 nm laser. (b) The corresponding phase analysis

Fig. 42.2 (a) The spatial phase difference and (b) the total phase difference as a function of angle θ and the kinetic energy of the recombining electron



electron, and in Fig. 42.2b the total phase difference is considered. Comparing the two panels, boundaries of the red and blue colors, where the phase differences reach π , bend to lower energy, which means that the recombining phases difference still plays an important role and the shift of minimum occurs at all angles.

The results show that minima in HeDMs are not only dependent on the internuclear separation. Thus, shift of the position of minimum, which originates from the difference between the two recombination processes, is an important measurement for the asymmetry of the molecule. According to the molecular orbital theory, only atomic orbitals with close energy levels can efficiently combine to molecular orbitals. For an HoDM, pairs of identical atomic orbitals overlap to form molecular orbitals with equal contributions. But the case is more complex in HeDMs. Our investigation has offered an opportunity to identify the molecular orbitals, with the help of the relationship between the minimum and the orbital combination. Since the position of minimum is dependent on the orbital combination, one will be able to judge which kind of LCAO is the HOMO combined of by comparing the observation of the position of minimum with the theoretical predictions. Moreover, once the relationship between the harmonic spectra and the LCAO is known, it will be possible to monitor molecular dynamics. How the combination of the orbitals changes or how the HOMO evolves can be deduced by reading the harmonic spectra.

References

1. M. Lewenstein, Ph. Balcou, M.Yu. Ivanov, A. L'Huillier, P.B. Corkum, Theory of high-harmonic generation by low-frequency laser fields. *Phys. Rev. A* **49**, 2117–2132 (1994)
2. M. Lein, N. Hay, R. Velotta, J.P. Marangos, P.L. Knight, Role of the intramolecular phase in high-harmonic generation. *Phys. Rev. Lett.* **88**, 183903 (2002)
3. M. Lein, N. Hay, R. Velotta, J.P. Marangos, P.L. Knight, Interference effects in high-order harmonic generation with molecules. *Phys. Rev. A* **66** 023805 (2002)
4. X.S. Zhu, Q.B. Zhang, W.Y. Hong, P.F. Lan, P.X. Lu, Two-center interference in high-order harmonic generation from heteronuclear diatomic molecules. *Opt. Express* **19** 436–447 (2011)

Chapter 43

Toward the Extension of High Order Harmonic Spectroscopy to Complex Molecules: Investigation of Aligned Hydrocarbons

C. Vozzi, R. Torres, M. Negro, L. Brugnera, T. Siegel, C. Altucci, R. Velotta, F. Frassetto, P. Villoresi, L. Poletto, S. De Silvestri, J.P. Marangos, and S. Stagira

Abstract High-order harmonic generation is as a powerful tool for the study of molecular properties. Up to now this investigation tool has been confined to simple molecules, with a relatively high ionization potential, since ionization saturation hindered its exploitation to fragile molecules. In this work we show that such limitation can be overcome by using mid-IR ultrashort driving pulses; as prototypical molecules we considered hydrocarbons. Clear signatures of the highest occupied molecular orbital were found in the harmonic spectra generated in unsaturated aligned hydrocarbons like acetylene, ethylene, allene and 1,3-butadiene. Our findings demonstrate that high-order harmonic generation spectroscopy can be extended to complex molecular species.

C. Vozzi (✉)

Istituto di Fotonica e Nanotecnologie - CNR, Milan, Italy
e-mail: caterina.vozzi@polimi.it

R. Torres · L. Brugnera · T. Siegel · J.P. Marangos
Blackett Laboratory, Imperial College, London, UK
e-mail: j.marangos@imperial.ac.uk

C. Altucci · R. Velotta
CNISM and Università di Napoli Federico II, Napoli, Italy
e-mail: velotta@na.infn.it

F. Frassetto · P. Villoresi · L. Poletto
Istituto di Fotonica e Nanotecnologie - CNR & DEI, Università di Padova, Italy
e-mail: poletto@dei.unipd.it

M. Negro · S. De Silvestri · S. Stagira
Dipartimento di Fisica, Politecnico di Milano, Milan, Italy
e-mail: salvatore.stagira@fisi.polimi.it

43.1 Introduction

High-order harmonic generation is nowadays considered as a powerful tool for the investigation of dynamical properties of matter. It is exploited for the generation of attosecond pulses in the extreme ultraviolet (XUV) spectral region [1] which allow investigations in atomic [2], molecular [3] and solid-state spectroscopy [4] with unprecedented temporal resolution. The harmonic emission process is by itself extremely sensitive to the nature of the generating medium; this feature can be effectively exploited in the study of the intimate properties of the target [5–7], enabling a novel kind of investigation tool that is known as *high-order harmonic generation spectroscopy* (HHGS). In spite of its sensitivity, HHGS has been up to now limited to atomic or molecular species with relatively high ionization potential. The reason for such a limitation is related to the use of Ti:Sapphire ultrafast laser sources as drivers in the harmonic generation process: an extended harmonic plateau is required for the extraction of structural information while with standard 800-nm driving sources, the onset of ionization saturation strongly limits the extension of the XUV spectrum emitted by fragile molecules. In this work we show that these limitations can be overcome by using mid-IR ultrashort driving pulses. The use of few cycle driving pulses reduces the degree of ionization accumulated at the peak of the pulse, leading to an effective decrease of the ionization depletion. Moreover, since the harmonic cutoff scales as the square of the driving laser wavelength, the mid-IR source allows a noticeable increase of the emitted XUV spectral range with respect to standard Ti:Sapphire source.

43.2 Experimental Results

The experimental setup is described in detail elsewhere [8, 9]. A portion of the 800-nm laser was used to excite a rotational wavepacket in the rotationally cooled molecular sample. In those molecules having a large enough anisotropy of polarizability, field free alignment is observed immediately after the laser pulse and, in the case of linear and symmetric top molecules, in the subsequent rotational revivals. Figure 43.1 shows the harmonic spectra as a function of the angle θ between the polarization directions of the aligning and the driving field for acetylene; similar results have been obtained in ethylene, allene and 1,3-butadiene. Harmonics were generated by 1,450-nm, 18-fs driving pulses with an intensity of $1 \times 10^{14} \text{ W cm}^{-2}$ and were detected by a flat-field spectrometer operating between 35 and 150 eV [10]. We observed well defined HHG spectra with cut-offs from 45 to 70 eV. In all the molecules, a strong suppression at $\theta = 0^\circ$ was observed, likely due to the nodal plane in the HOMO wavefunction. Moreover, an extension of the harmonic spectral cutoff was observed at specific angles, according to the nature of the driven molecules; in particular, in acetylene such cutoff extension was observed around $\theta = 40^\circ$.

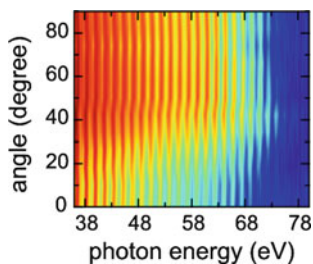


Fig. 43.1 Sequence of harmonic spectra generated in acetylene as a function of the angle between pump and probe polarizations (log color map)

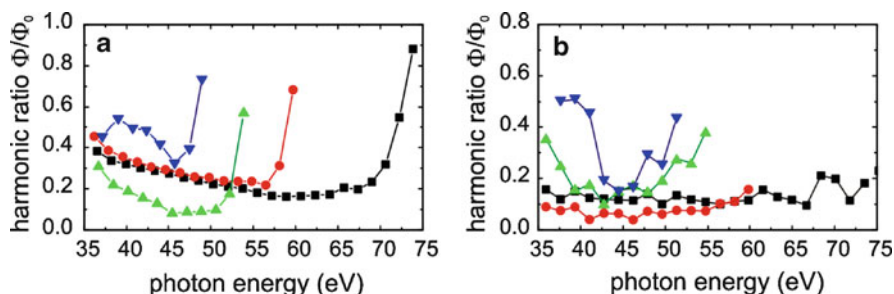


Fig. 43.2 Experimental (a) and calculated (b) ratio between harmonic spectra obtained in an aligned distribution at $\theta = 0^\circ$ and spectra without alignment for acetylene (squares), ethylene (circles), allene (up triangles), and 1,3 butadiene (down triangles)

Figure 43.2a shows the ratio Φ/Φ_0 between harmonic spectra obtained in an aligned distribution at 0° (Φ) and spectra without alignment (Φ_0) for the considered species. These ratios show a minimum as a function of photon energy ascribed to quantum interference effects that reveal the structure of the molecules. A calculation, based on the Strong-Field-Approximation (SFA) adapted to molecular systems [11], was performed in order to reproduce the experimental findings; the corresponding calculated harmonic ratios are reported in Fig. 43.2b; the position of the spectral minima as well as the modulation of the harmonic signal are well reproduced by this simple model, although the quantitative differences between experimental and calculated ratios call for a more sophisticated model, which should take into account the effects of the Coulomb potential of the molecular ion on the harmonic generation process.

43.3 Conclusions

Our findings demonstrate that the use of mid-IR radiation will allow HHGS to be applied to a wide range of molecules. For instance, typical building block biomolecules, which have ionization potentials in the range 7.5–9 eV, could be

studied by HHGS with mid-IR laser pulses thus avoiding the ionization saturation issue [9]. Moreover the large cutoff extension of the harmonic radiation driven by mid-IR laser pulses could be effectively exploited in tomographic reconstruction of complex molecules [6] allowing a retrieval of the molecular orbital on a finer level of details with respect to standard driving lasers.

Acknowledgements We acknowledge the financial support from the ECs Seventh Framework Programme (LASERLAB-EUROPE, Grant Agreement No. 228334), EPSRC Grant No. EP/E028063/1, and the partial support from Fondazione Cariplo (Project No. 2009–2562).

References

1. F. Krausz, M. Ivanov, Attosecond physics. *Rev. Mod. Phys.* **81**, 163–234 (2009)
2. E. Goulielmakis, Z.-H. Loh, A. Wirth, R. Santra, N. Rohringer, V.S. Yakovlev et al., Real-time observation of valence electron motion. *Nature* **466**, 739–744 (2010)
3. G. Sansone, F. Kellensberg, J.F. Perez-Torres, F. Morales, M.F. Kling, W. Siu et al., Electron localization following attosecond molecular photoionization. *Nature* **465**, 763–767 (2010)
4. M. Schultze, M. Fiess, N. Karpowicz, J. Gagnon, M. Korbman, M. Hofstetter et al., Delay in photoemission. *Science* **328**, 1658–1662 (2010)
5. J. Itatani, J. Levesque, D. Zeidler, H. Niikura, H. Pepin, J.C. Kieffer et al., Tomographic imaging of molecular orbitals. *Nature* **432**, 867–871 (2004)
6. C. Vozzi, M. Negro, F. Calegari, G. Sansone, M. Nisoli, S. De Silvestri, S. Stagira, Generalized molecular orbital tomography. *Nat. Phys.* (2011). doi:10.1038/nphys2029
7. A.D. Shiner, B.E. Schmidt, C. Trallero-Herrero, H.J. Wörner, S. Patchkovskii, Corkum et al., Probing collective multi-electron dynamics in xenon with high-harmonic spectroscopy. *Nat. Phys.* **7**, 464–467 (2011)
8. C. Vozzi, F. Calegari, E. Benedetti, S. Gasilov, G. Sansone, G. Cerullo et al., Millijoule-level phase-stabilized few-optical-cycle infrared parametric source. *Opt. Lett.* **32**, 2957–2959 (2007)
9. C. Vozzi, R. Torres, M. Negro, L. Brugnera, T. Siegel, C. Altucci et al., High harmonic generation spectroscopy of hydrocarbons. *Appl. Phys. Lett.* **97**, 241103 (2010)
10. L. Poletto, G. Tondello, P. Villoresi, High-order laser harmonics detection in the EUV and soft X-ray spectral regions. *Rev. Sci. Instrum.* **72**, 2868–2874 (2001)
11. R. Torres, N. Kajumba, J.G. Underwood, J.S. Robinson, S. Baker, J.W.G. Tisch et al., Probing orbital structure of polyatomic molecules by high-order harmonic generation. *Phys. Rev. Lett.* **98**, 203007 (2007)

Chapter 44

Nonlinear Fourier-Transform Spectroscopy of D₂ Using High-Order Harmonic Radiation

Yusuke Furukawa, Yasuo Nabekawa, Tomoya Okino, Kaoru Yamanouchi, and Katsumi Midorikawa

Abstract High-order harmonic radiation is available to investigate ultrafast nonlinear optical phenomena, such as two-photon absorption process, in the vacuum and extreme ultraviolet wavelength region. We have determined the sequential two-photon dissociative ionization pathways of D₂ with the simultaneous irradiation of multiple order harmonics of a Ti:sapphire laser in the visible-vacuum ultraviolet region with the aid of both an interferometric autocorrelation measurement and a Fourier-transform spectroscopy. By analyzing the interferometric autocorrelation signals appearing in the measured momentum distribution of D⁺, we were able to decompose the measured momentum distribution into three momentum distribution images representing the three distinct dissociation pathways, which are sequentially two-photon excitation processes of D₂. D₂⁺ is prepared in the electronic ground state of D₂⁺, and then excited to the first excited state, leading to the dissociation into D⁺ and D.

44.1 Introduction

Intense high-order harmonic (HH) pulses induce nonlinear optical phenomena, such as two- or more-photon absorption process in the vacuum ultraviolet (VUV) and extreme ultraviolet (EUV) wavelength region. The interferometric autocorrelation (IAC) measurements of intense HH pulses have been demonstrated owing to nonlinear response of molecules. Fragment ion yields via two-photon absorption process of N₂ and CO₂ molecules were utilized as correlated signals of the HH pulse

Y. Furukawa (✉) · Y. Nabekawa, · K. Midorikawa
Laser Technology Laboratory, RIKEN ASI, 2-1 Hirosawa, Wako, Saitama 351-0198, Japan
e-mail: furukawa-y@riken.jp

T. Okino · K. Yamanouchi
Department of Chemistry, School of Science, the University of Tokyo, 3-7-1 Hongo, Bunkyo,
Tokyo 113-0033, Japan

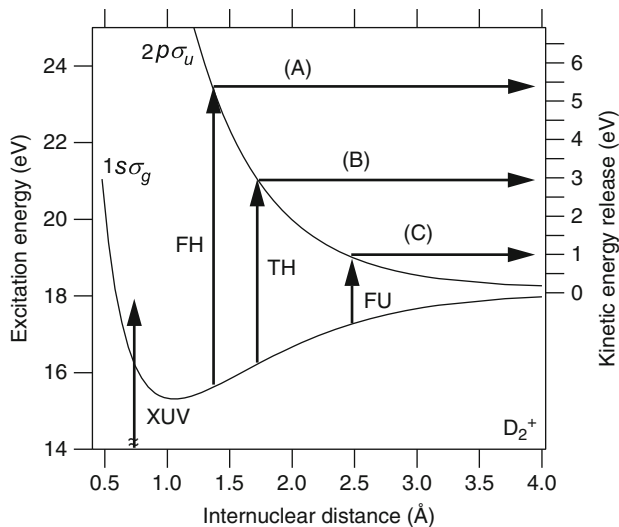


Fig. 44.1 Potential energy curves of D_2^+ . Vertical arrows schematically indicate excitation photons, XUV, FH, TH, and FU, and horizontal arrows indicate the three dissociation pathways, (A), (B), and (C). Observed kinetic energy of D^+ should be half of the kinetic energy release (KER) shown in this figure because the KER is shared with D and D^+

in the IAC measurement [1, 2]. The measured yields of the respective fragment ions, modulated in accordance with the temporal separation between two replicas of the HH pulse, exhibited an IAC signal. The interference fringes appeared on the IAC traces can be utilized for identifying the ionization and/or dissociation pathways of ion fragments. We call this method nonlinear Fourier-transform spectroscopy (NFTS), which is useful for investigating the ionization and/or dissociation processes induced by a two- or more-photon process within an HH pulse.

In this paper, we demonstrate the feasibility of NFTS by determining the three distinct dissociation pathways of deuterated hydrogen molecules (D_2) irradiated with multiple harmonic fields generated through high-order harmonic generation (HHG) scheme of Ti:sapphire laser. The three dissociation pathways are assigned to be the sequential two-photon dissociative ionization processes, whose excitation scheme is shown in Fig. 44.1. In brief, the HH pulse ionizes D_2 in the $1s\sigma_g$ electronic ground state of D_2^+ with one-photon absorption of XUV pulses. And then, the D_2^+ in the $1s\sigma_g$ is excited to the $2p\sigma_u$ by absorbing one-photon of either the fifth harmonic (FH) pulse in VUV region, the third harmonic (TH) pulse in deep ultraviolet (DUV) region, or the fundamental (FU) pulse in near infrared (NIR) region.

44.2 Experimental

The experimental setup to generate HH radiation is basically the same as that described in [3] except for the driving fundamental laser system. The chirped pulse amplification system of a Ti:sapphire laser delivered driving-laser pulses with a

pulse duration of 15 fs and a repetition rate of 100 Hz to generate high-harmonic fields in the extreme ultraviolet region [4]. High-harmonic radiation was generated by focusing of the driving laser into a 10-cm gas cell, which was filled with Xe gas as a nonlinear medium for HHG. The focal length of the driving laser was 5 m, which was appropriate for yielding intense harmonic pulses owing to the large cross section at the focal region in the static gas cell. The HH radiation was spatially divided into two replicas by a pair of Si plates, and the delay between the two replicas was controlled by moving one of the Si plates with a piezo actuator. The molecular beam of D₂ was introduced through a skimmer from a pulsed gas valve with a backing pressure of 2 atm. The ions yielded at the intersection of the focused HH radiation and the molecular beam were accelerated using two static electric fields generated with three metal acceleration plates. To measure the IAC trace of the D⁺ yield to the HH radiation, we scanned the delay of the two replicas of HH radiation every 40 nm within a range of $\pm 20 \mu\text{m}$, and the momentum distribution images of D⁺ was acquired at each delay point. The scanned range corresponded to approximately 27 cycles of the frequency of the FU pulse.

44.3 Results and Discussion

In Fig. 44.2a, the kinetic energy (KE) spectrum of D⁺, which is obtained by integrating the momentum distribution image of D⁺ over polar angle, exhibits three components: (A) a region around the peak at 2.6 eV, (B) a region around the peak at 1.4 eV, and (C) a region around the peak at 0.4 eV. By arranging the KE spectra in order of increasing the delay of the two replicas of the HH radiation, the variation of the KE distribution was constructed, as shown in Fig. 44.2b. The periods of the modulations at the three KE regions, (A), (B), and (C), are different from each other.

We obtained the IAC traces of the three regions, (A), (B), and (C) by averaging at each time delay and plotted as a function of the delay. And then, the squares of the modulus of the Fourier amplitude of the three IAC traces at the regions, (A), (B), and (C), are obtained by carrying out a Fourier-transform, as shown Fig. 44.3. The main frequencies contributing to the interference fringes in the regions, (A), (B), and (C), are match to the low-order optical frequencies of the FH, TH, and FU pulses, respectively.

We note that the observation of the optical frequencies is an evidence that the D⁺ ions are generated from nonlinear optical processes [5] in which two- or more-photons are involved. We have experimentally observed the eleventh-order harmonic pulse contributes this dissociative ionization process of D₂ [3]. The higher than the ninth-order harmonic field (14 eV) can produce D₂⁺ in the $1s\sigma_g$ state because the ionization potential of D₂ is 15.5 eV, which lies between the photon energies of the ninth-order harmonic pulse (14 eV) and the 11th-order harmonic pulse (17 eV). And more, the kinetic energies of peaks in the regions (A), (B), and (C), in Fig. 44.2a are consistent with the kinetic energy release from the dissociation at the specified internuclear distances of the $2p\sigma_u$, to which D₂⁺ in the $1s\sigma_g$ state is

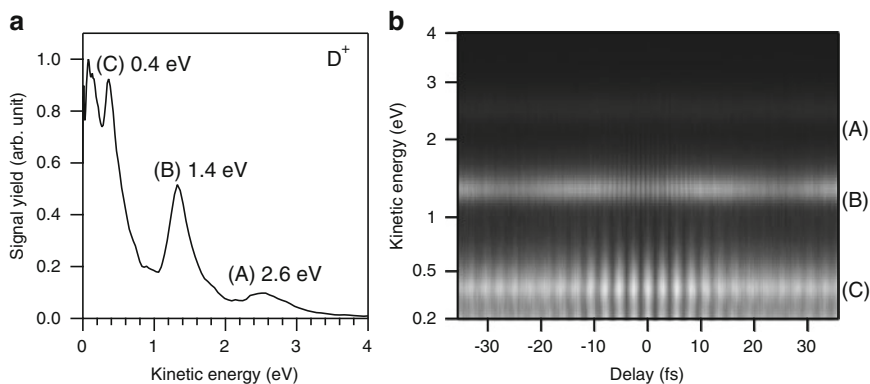


Fig. 44.2 (a) The typical kinetic energy spectrum of D^+ . The kinetic energy spectrum exhibits three components: (A) a region around the peak at 2.6 eV, (B) a region around the peak at 1.4 eV, and (C) a region around the peak at 0.4 eV. (b) Kinetic energy spectrogram of D^+ as a function of the delay between a pair of the input HH pulse

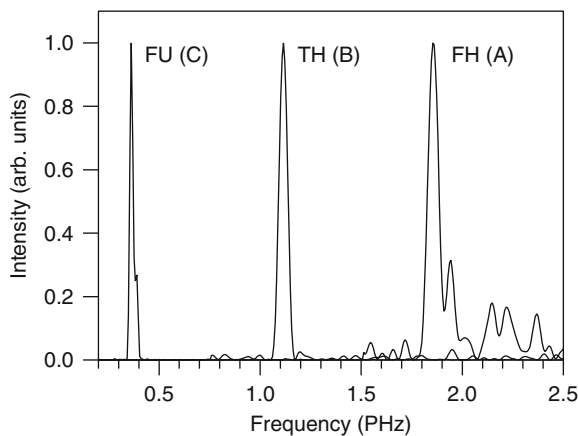


Fig. 44.3 The absolute squares of Fourier amplitude of the IAC traces of the three KE regions, (A), (B), and (C). The main contributions to the optical fringes in the regions, (A), (B), and (C), are the frequencies of the FH, the TH, and the FU pulse, respectively

excited by one-photon absorption of the FH, the TH, and FU pulses. The observation that all the three optical frequencies of the interference fringes appear in different kinetic energy regions of the D^+ reflects the fact that D_2^+ in the $1s\sigma_g$ state is excited to the $2p\sigma_u$ state at three different internuclear distance regions, where the energy differences between the $1s\sigma_g$ potential and the $2p\sigma_u$ potential match the photon energies of the FH, the TH, and FU pulses. Hence, we conclude that D_2 molecules absorbing one photon of the HH radiation ionized to the $1s\sigma_g$ state of D_2^+ , followed by excitation to the $2p\sigma_u$ state by the one-photon absorption of the three low-order harmonic radiation, resulting in the dissociation into D^+ and D.

References

1. Y. Nabekawa et al., Phys. Rev. Lett. **97**, 153904 (2006)
2. T. Okino et al., J. Chem. Phys. **129**, 161103 (2008)
3. Y. Furukawa et al., Phys. Rev. A **82**, 013421 (2010)
4. Y. Nabekawa et al., Appl. Phys. B **101**, 523 (2010)
5. Y. Nabekawa, K. Midorikawa, New. J. Phys. **10**, 025034 (2008)

Chapter 45

Steering of Molecular Multiple Dissociative Ionization with Strong Few-Cycle Laser Fields

Yunquan Liu, Xianrong Liu, Yongkai Deng, Chengyin Wu,
and Qihuang Gong

Abstract Coherent control is an implicit goal of quantum physics and quantum chemistry, which have been significantly developed in utilizing light to control over the dynamics of atomic and molecular systems. We show that the process of multiple dissociative ionization of carbon monoxide (CO) molecules is controllable using an intense phase-stabilized few-cycle laser field (4.2 fs, 740 nm, 6×10^{14} W/cm²). We demonstrate that the controllable emission direction of C²⁺ from charge asymmetrical dissociation and ionization of CO dications is out of phase in a linearly polarized laser field. The strong coupling between the dissociative channels is explained with the mechanisms of recollision excitation and recollision ionization. The competition between excitation and ionization in a recollision process leads to the opposite asymmetrical property. The results provide an insight into the controllable attosecond dynamics of multiple dissociative ionization of a complex molecule.

45.1 Introduction

The manipulation and coherent control of complex molecular systems using a strong laser field are of great fundamental research in the area of atomic, molecular, and optical physics [1–3]. Since the measurement and control of the carrier-envelope phase (CEP) of few-cycle laser pulses were demonstrated [4], the waveform of a few-cycle laser field, i.e., $E(t) = a(t) \cos(\omega t + \varphi)$ (where $a(t)$ is the envelope amplitude, ω is the frequency and φ is the CEP), can be precisely manipulated. This enable the basic laser-assisted electron recollision process in strong-field physics [5, 6], can be steered by the specified light field. Many interesting strong-field

Y. Liu (✉) · X. Liu · Y. Deng · C. Wu · Q. Gong
School of Physics and State Key Laboratory for Mesoscopic Physics, Peking University,
Beijing 100871, PR China
e-mail: yunquan.liu@pku.edu.cn; qhong@pku.edu.cn

phenomena, e.g., high-harmonic generation (HHG) [4], high-order above threshold ionization (HATI) [7] and non-sequential double ionization (NSDI) [8] in an atomic system, or electron localization in a molecular system [9–11], are closely related with the electron recollision process and are strongly dependent on the CEP of few-cycle light fields.

The dynamics of multiple ionization of atoms [12, 13] or molecules [14] in intense laser fields is great interest in the community of strong-field physics. When a diatomic molecule (or molecular ion) dissociates in a phase-stabilized few-cycle laser field, an evident result is to generate a pair of well separated atomic (ionic) fragments through dissociation or Coulomb explosion. During dissociation, the electrons could localize near a specific nucleus [11]. Even a two atoms system comprising a heteronuclear diatomic molecule exhibits different electronic structures, and hence the unevenly shared electrons can be controlled between the two nuclei. Recently, attosecond control of electron dynamics of CO in few-cycle laser fields was demonstrated [11], where the control was experimentally verified via an asymmetric distribution of C^+ or O^+ fragments after breaking of the molecular bond. A two-step (ionization and recollision excitation) mechanism was used to explain the dissociation behavior of CO and D_2 [15].

The ionization and dissociation of CO in strong laser fields were recently investigated by several groups [11, 16–20]. In this process, there is a large possibility to produce stable CO dications. Guo proposed that CO dications produced by moderate intensity fs laser pulses could be formed from NSDI process [16–18]. The CO dication represents a typical model system, in which two electrons are removed from the nonbonding orbitals, that is stable or quasi-stable with respect to dissociation. The strong-field multiple dissociative ionization of complex molecule is a strong coupling process.

45.2 Method and Results

We studied the behaviors of heteronuclear CO molecule in a phase-stabilized few-cycle laser field [21]. In the experiments, we used the linearly phase-stabilized polarized laser pulses running at the center wavelength around 740 nm and at a peak intensity of 6×10^{14} W/cm² with a repetition of 3 kHz to dissociatively ionize CO molecule. The pulse duration near the interaction region is ~ 4.2 fs (FWHM). The directional emission of ionic fragments is monitored via a “reaction microscopy” [22]. All experiments were performed at an ion rate below 0.1 per laser pulse. The momentum distribution, angular distribution and energy of the fragments are calculated with the position and the time-of-flight on the detector. The momentum resolution is about 0.02 a.u. along the time-of-flight direction and is about 0.05 a.u. in the transverse momentum direction. The laser polarization is perpendicular to the time-of-flight direction. The CEP of laser pulses is adjusted by insertion of fused silica into the light path with a pair of wedges and is calibrated with the method using photoelectron spectra of argon in the plateau [7].

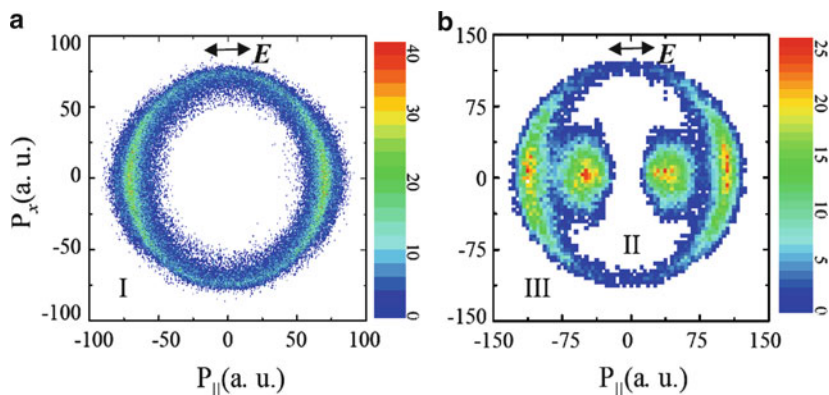


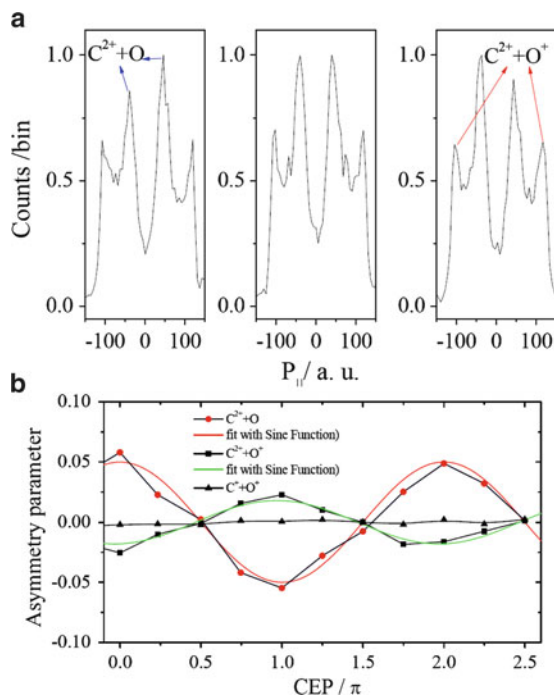
Fig. 45.1 The two-dimensional momentum distribution of C^+ fragments from channel I (a), and of C^{2+} fragments from channel II and channel III (b) in the linear laser polarization plane

The dominated breakup pathways of CO^{2+} in a strong laser field are the symmetrical Coulomb explosion channel $CO^{2+} \rightarrow C^+ + O^+$ (I) and the charge asymmetrical dissociation channel $CO^{2+} \rightarrow C^{2+} + O$ (II). There are two main channels that can introduce C^{2+} , i.e., $CO^{2+} \rightarrow C^{2+} + O$ and $CO^{3+} \rightarrow C^{2+} + O^+$ (III) at the current laser intensity. Figure 45.1 illustrates the momentum distributions of C^+ and C^{2+} from their corresponding channels in the laser polarization plane at the phase of π . The angular distribution of C^{2+} from the channel II is in the narrow cone angle ($\sim 50^\circ$) along polarization axis compared with other two channels.

In the experiment, we changed the laser parity from linear to circular and the intensity of circularly polarized light was about twice as for linearly polarized light. The ratio of yields for those channels were suppressed about 0.52(I), 0.12(II) and 0.23(III) while using circularly polarized light. Compared with the channel I, both the channel II and the channel III are more suppressed and are more sensitive to the laser polarization property.

The mechanism behind the laser polarization dependence is electron recollision. A more interesting question will arise, for example, is it possible to manipulate multiple dissociation or ionization process of CO through controlling the CEP of laser pulses? Figure 45.2a illustrates the momentum distributions of C^{2+} along the laser polarization axis at three phase positions of 0 , $\pi/2$ and π . One can clearly find that the directional emission of C^{2+} ions from the channel II is strongly dependent on the CEP. It seems that the channel III is not sensitive to the CEP from Fig. 45.2a. The directional emission is represented by the angle-integrated asymmetrical parameter, $A = \frac{P_{left} - P_{right}}{P_{left} + P_{right}}$, where P_{left} and P_{right} are the measured angle-integrated ion yields in the left and right directions along the laser polarization axis. Figure 45.2b shows the evolution of the asymmetry parameter A as function of the laser phase for all the channels in the same cone angle ($\sim 50^\circ$) along the laser polarization axis. We employed about 2×10^6 laser pulses each phase position. The directional emission of C^{2+} from both the channels

Fig. 45.2 (a) The momentum distribution of C^{2+} fragments from channel II and channel III in the laser polarization plane at the phases of 0 , $\pi/2$ and π (in the cone of 50° in the laser polarization plane). (b) The angle-integrated (in the cone of 50° in the laser polarization plane) asymmetric parameters as a function of CEP for the three channels



II and III oscillates with the CEP of laser pulses. This represents that dissociation and ionization of CO dications can be controlled with the well-defined laser fields. The peak contrasts of the oscillations are about 5% (the channel II) and about 3% (the channel III) respectively. The asymmetrical amplitude is much less than that of C^+ ($\sim 20\%$) from the channel of $(CO^+ \rightarrow C^+ + O)$ at lower laser intensity [14, 15]. More importantly, the emission direction of C^{2+} from those two channels is out of phase.

45.3 Discussion

Due to the large density of states, already for the relatively small molecules, it is extremely difficult to describe the dynamics of double or triple ionization of molecules in quantitative calculation. In order to illustrate a consistent explanation for the interesting findings, we present a qualitative picture, as shown in Fig. 45.3. Although the pulse duration is ~ 4.2 fs, the arising edge of laser pulse is still large enough to remove one electron from the out orbitals of neutral molecule. When the maximum light field is around, another electron will tunnel out. It will launch a nuclear wave-packet in the bound states of CO dication. The tunneling electron can be guided back by the laser field near the zero-crossing of light field, and then, it will

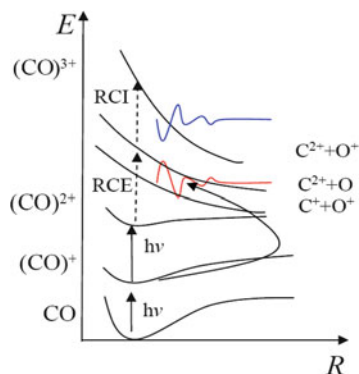


Fig. 45.3 The schematic view of multiple dissociative pathways of CO in an intense laser field (*RCE* recollision excitation, *RCI* recollision ionization, *EI* enhanced ionization). The dissociation and ionization of $(CO)^{2+}$ are II and channel III in a few-cycle laser field respectively triggered by RCE and RCI respectively. The *oscillation curves* represent the temporal evolution of the yield probability of C^{2+} fragments for channel

elastically or in-elastically scatter with doubly charged molecular ion. As a result, the CO dication will be excited to higher electronic states initiating dissociation or be ionized into trication starting explosion by the returning electron wave-packet. We should note that the excited states of the dication that are populated vertically in the Franck–Condon region are above the asymptotic limit of the channel I.

The returning electron wave-packet takes the information of the waveform of laser field. Because the electron cloud in asymmetric diatomic molecules prefers to be displaced near one nucleus, the energy level of the lower bounded states are excited by the returning CEP dependent electron wave-packet, leading to a larger dissociation through excited states of the dication. The collision of the CEP dependent electron wave-packet with parent molecular ion induces a directional movement of the fragments. The dissociation of the excited dications will introduce the channel II, which is dominated by RCE. On the other hand, if the recollision electron taking enough energy, it can kick out one more electron to produce the trications. The impacted trications are influenced by the retuning electron wave-packet. The directional emission of trications will dissociate through the channel III. Consequently, it is dominated by RCI. The strong coupling of recollision electron and nuclear motion gives the contribution to the observed controllable effect.

The directional emission of C^{2+} from those two channels is out of phase. Basically, this phenomenon can be qualitatively interpreted within above scenario. In a single event, the dication impacted by a returning electron wave-packet will either be excited dissociating into the channel II or be ionized dissociating into the channel III. The opposite asymmetry results from the competition between excitation dissociation and direct ionization at certain recollision energy. Reducing the excitation dissociation possibility leads to an increase the fraction of direct ionization possibility. On the other hand, reducing the direction ionization possibility

leads to an increase the fraction of excitation dissociation possibility. Because it needs more recollision energy to reach CO trication, the asymmetrical amplitude of the channel III is slightly smaller than that of channel II. Beside RCE and RCI mechanisms, there are other two pathways that can induce the asymmetrical dynamics of molecules, i.e., angular dependence of ionization probability and laser-induced coherent population transfer between different excite states. Before dissociation or ionization of $(\text{CO})^{2+}$, the molecular ion has the same interaction environment for those two channels, i.e., the same highest occupied molecular orbital (HOMO) and the same orientation. Thus we can expect that the cross sections of ionization and excitation of CO dication in a linear field has similar angular distribution. On the other hand, there are much more close lying excitation states of $(\text{CO})^{2+}$ compared with $(\text{CO})^+$. The electron localization and the population transfer between excitation states are largely reduced due to fast decay. Thus, the other two pathways seem unable to explain the opposite dissociation effect.

Experimentally, three observations support such an interpretation, firstly, using circularly polarized pulses, the yields of the channel II and the channel II are much suppressed. The suppression effect induced by RCE and RCI is less pronounced compared with asymmetrical charge dissociation of $(\text{CO})^+$ and this manifests the effect on the smaller asymmetry amplitude. Second, the KER distributions of those two channels are modified into the opposite direction with a linearly polarized field if we assume that a circular laser field has the same effect on both channels [21]. The competition between RCE and RCI introduces the opposite asymmetry. Third, we find that the momentum distribution of $(\text{CO})^{2+}$ looks similar with that of $(\text{CO})^+$ [21] and both of them have momentum cut-off around $2(U_p)^{1/2}$ ($\sim 2U_p$ in energy domain, $U_p = (E_0/2\omega)^2$ is the ponderomotive potential, where E_0 : field amplitude and ω : frequency) and have an evident plateau, which are the typical indications of electron elastically re-scattering process for atoms [23]. The plateau of momentum distribution of $(\text{CO})^{2+}$ is enhanced about one order than that of $(\text{CO})^+$ due to a larger cross section of scattering. The momentum distribution of $(\text{CO})^{2+}$ at the current intensity does not reveal any “double hump” structure or the minimum near the zero momentum that are typical features of NSDI. It implies that the rescattering effect just facilitates the dissociation or ionization of CO dications.

45.4 Conclusion and Outlook

In conclusion, we have shown that charge asymmetrical dissociation and ionization of the complex multi-electron and multi-core CO dications can be controlled with the CEP stabilized few-cycle pulses. Interestingly, for the first time we observe that the emission direction of C^{2+} from those channels is out of phase in strong few-cycle laser fields. Those interesting observations are partially explained as the controllable $\text{CO}^{2+} \rightarrow \text{C}^{2+} + \text{O}$ channel is resulted from electron RCE and subsequent dissociation and the controllable $\text{CO}^{3+} \rightarrow \text{C}^{2+} + \text{O}^+$ channel is resulted from RCI and subsequent Coulomb explosion. The competition between RCE and

RCI introduces the opposite asymmetrical property. Since $(\text{CO})^{2+}$ is a typical heteronuclear diatomic molecular ion with a permanent dipole, the CEP dependent enhanced ionization should be considered [24–26]. The asymmetrical property of the dissociation and ionization of $(\text{CO})^{2+}$ can be favored by the effect of CEP dependent enhanced ionization using few-cycle laser pulses with a cosine waveform. For a sine light waveform, the left–right symmetrical laser field results in no asymmetry for both parallel or antiparallel case. The experiments suggest a route to control molecular multiple dissociative ionization and to selectively manipulate the outcome of chemical reactions using intense few-cycle laser pulses.

Acknowledgements We thank for the support by the program for New Century Excellent Talents in University (NCET) and PhD program of Ministry of Education and the National Science Foundation of China (11125416 and 61078025).

References

1. H. Rabitz et al., *Science* **288**, 824 (2000)
2. M. Dantus, V.V. Lozovoy, *Chem. Rev.* **104**, 1813 (2004)
3. A.H. Zewail, *J. Phys. Chem. A* **104**, 5660 (2000)
4. A. Baltuška et al., *Nature* **421**, 611–615 (2003)
5. K. Schafer et al., *Phys. Rev. Lett.* **70**, 1599 (1993)
6. P. B. Corkum, *Phys. Rev. Lett.* **71**, 1994 (1993)
7. G.G. Paulus et al., *Phys. Rev. Lett.* **91**, 253004 (2003)
8. X. Liu et al., *Phys. Rev. Lett.* **93**, 263001 (2004)
9. M. F. Kling et al., *Science* **312**, 246 (2006)
10. M. Kremer et al., *Phys. Rev. Lett.* **103**, 213003 (2009)
11. I. Znakovshaya et al., *Phys. Rev. Lett.* **103**, 103002 (2009)
12. Y. Liu et al., *Phys. Rev. Lett.* **101**, 053001 (2008)
13. Y. Liu et al., *Phys. Rev. Lett.* **104**, 173002 (2010)
14. E. Eremina et al., *Phys. Rev. Lett.* **92**, 173001 (2004)
15. P. ven don. Hoff et al., *Chem. Phys.* **366**, 139 (2009)
16. C. Guo, *Phys. Rev. A* **73**, 041401(R) (2006)
17. A. S. Alnaser et al., *Phys. Rev. A* **71**, 031403(R) (2005)
18. Q. Liang et al., *Int. J. Mass Spectrom.* **286**, 28 (2009)
19. E. Wells et al., *J. Phys. B* **43**, 015101 (2010)
20. J. McKenna et al., *Phys. Rev. A* **81**, 061401(R) (2010)
21. Y. Liu et al., *Phys. Rev. Lett.* **106**, 073004 (2011)
22. J. Ullrich et al., *Rep. Prog. Phys.* **66**, 1463 (2003)
23. A. Rudenko et al., *J. Phys. B* **37**, L407 (2004)
24. S. Chelkowski, A. D. Bandrauk, *J. Phys.* **B28**, L723 (1995)
25. T. Zuo, A. D. Bandrauk, *Phys. Rev. A* **52**, R2511 (1995)
26. G. Lagmago Kamta, A. D. Bandrauk, *Phys. Rev. Lett.* **94**, 203003 (2005)

Chapter 46

A Generalized Approach to Molecular Orbital Tomography

C. Vozzi, M. Negro, F. Calegari, G. Sansone, M. Nisoli, S. De Silvestri,
and S. Stagira

Abstract Imaging of the outermost molecular orbital by high-order harmonic generation has been limited so far to very simple molecules like nitrogen, since several difficulties had to be overcome in order to extend it to more complex species. In this work we show that molecular imaging can be applied to a triatomic molecule like carbon dioxide, hence paving the way to the exploitation of such technique to the imaging of polyatomic species.

46.1 Introduction

High order harmonic generation (HHG) is a nonlinear process driven by ultrashort laser pulses in atoms or molecules, able to produce coherent radiation in the extreme ultraviolet (XUV) spectral region. In the framework of the so called three-step model, it is understood as follows [1]: the intense electric field of the laser pulse ionizes the target molecules and accelerates the freed electron to large kinetic energies; upon field reversal, the electron is driven back to the parent ion, where it can recombine releasing its energy in attosecond bursts of XUV radiation. In the framework of the Strong-Field Approximation (SFA) and of the Single Active Electron (SAE) description of the molecule, the spectrum of the XUV emission carries the fingerprint of the outermost molecular orbital (HOMO) [2]. In particular, according to the SFA, the recolliding electron wavepacket is described by a plane wave, since the effect of the Coulomb field of the molecular ion is considered

C. Vozzi (✉)

Istituto di Fotonica e Nanotecnologie - CNR, Milan, Italy

e-mail: caterina.vozzi@polimi.it

M. Negro · F. Calegari · G. Sansone · M. Nisoli · S. De Silvestri · S. Stagira

Dipartimento di Fisica, Politecnico di Milano, Milan, Italy

e-mail: salvatore.stagira@fisi.polimi.it

negligible; this assumption allows to express the emission spectrum in terms of the spatial Fourier transform of the HOMO. Hence a tomographic reconstruction of the target molecule can be obtained from the harmonic spectra by a suitable retrieving procedure [2]. Nevertheless such a simplified picture has been refuted by several theoretical and experimental works, which demonstrated that the Coulomb field of the molecular ion plays a role in HHG [3] and reported the observation of multielectron effects in the laser-molecule interaction [4].

In this work we will show that orbital imaging by HHG can be achieved in carbon dioxide molecules [5] exploiting a mid-IR driving source [6]; in particular, a suitable retrieval procedure allows to determine the single molecular XUV emission map (SM-XEM) in amplitude and phase as a function of photon energy and molecular orientation. The SM-XEM can then be exploited for the tomographic reconstruction of the CO₂ HOMO beyond the SFA approach. Multielectron effects are shown to be negligible in our experimental conditions, hence ensuring the validity of the reconstruction procedure.

46.2 Experimental results

HHG spectra were measured in impulsively aligned CO₂ molecules as a function of the delay between aligning and generating pulses. Harmonics were generated by tunable few-cycle mid-IR pulses (1.45–1.8 μm, 18–25 fs, energy larger than 1 mJ in all the tuning range [6]) focused in a synchronized pulsed gas jet (absolute backing pressure 4 bar, nozzle diameter 500 μm). The target molecules were impulsively aligned by a 800-nm, 100-fs pulse (with an intensity of about 4×10^{13} W/cm²) collinearly combined with the driving pulse by a dichroic mirror; the temporal delay between the two pulses was explored around the half rotational revival of carbon dioxide using a high-precision delay line; the polarization directions of the two fields were parallel. The intensity of the driving pulse was varied by a variable-density neutral filter. Aligning and driving pulses were focused by a spherical mirror (12.5 cm focal length), with the focus positioned about 1 mm upstream of the gas jet to maximize the contribution of the short electron trajectories to HHG. The emitted XUV radiation was recorded using a flat-field spectrometer operating between 35 and 150 eV [7].

Figure 46.1a shows the alignment factor simulated in our experimental conditions around the half rotational revival of carbon dioxide; molecular alignment is achieved for a pump-probe delay $\tau = 21.1$ ps, whereas anti-alignment is obtained for $\tau = 21.65$ ps. Figure 46.1b shows the harmonic spectra measured in CO₂ at alignment, anti-alignment and when the alignment pulse is absent; as can be seen, a strong modulation of the XUV spectra is observed for maximum and minimum alignment with respect to the not-aligned case. In particular, for $\tau = 21.1$ ps a deep minimum is present around 60 eV; such minimum is ascribed to the molecular orbital structure. Multielectron effects give negligible contribution to this spectral shape; indeed they should give rise to spectral features depending on the driving

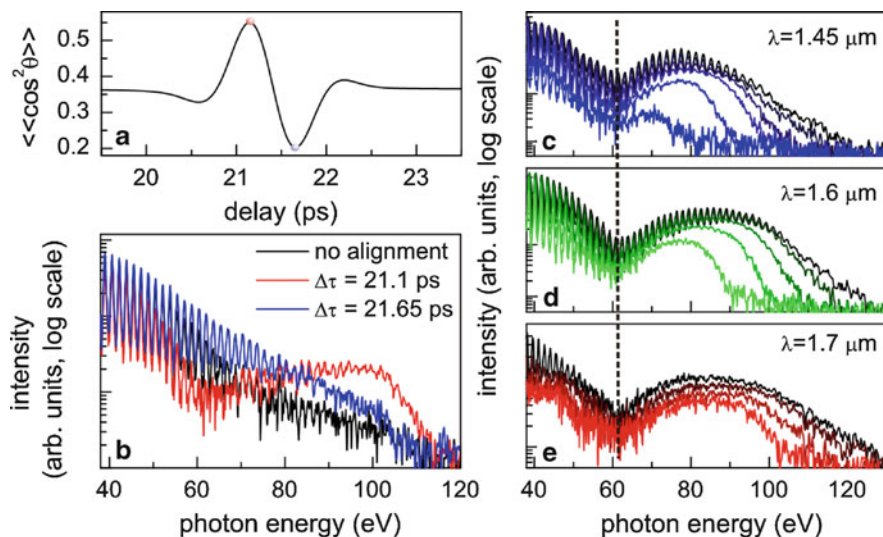


Fig. 46.1 (a) Simulated alignment factor in CO₂; (b) harmonic spectra measured at alignment (pump-probe delay $\tau = 21.1$ ps), anti-alignment ($\tau = 21.65$ ps) and without alignment pulse; (c)–(e) harmonic spectra in aligned CO₂ for different driving intensities and driving wavelengths

wavelength and intensity [4]. Since, as shown in Fig. 46.1c–e, the position of the minimum does not change with neither of the two parameters, we conclude that the harmonic spectra generated in our experimental conditions are predominantly related to the HOMO structure.

Figure 46.2a shows a scan of the harmonic spectra as a function of the pump-probe delay τ ; during this scan, the molecular angular distribution changes with the delay, hence the macroscopic harmonic emission from the driven molecules will change accordingly. In particular, the amplitude and phase of the single molecule XUV contribution will be encoded in such changes. From a suitable set of XUV spectra corresponding to different delays, one can retrieve the SM-XEM as a function of the emitted photon energy and of the angle θ between the molecular axis and the driving field polarization direction. Since the measured spectra are real-value functions, the determination of the complex-value single-molecule contribution implies the solution of a phase-retrieval problem [5].

A retrieval algorithm applied to the delay scan shown in Fig. 46.2a allowed the reconstruction of the SM-XEM field both in amplitude, Fig. 46.2b, and phase, Fig. 46.2c. It is worth noting that the phase of the single-molecule emission shows a jump of 2.2 rad around 50 eV; this jump differs from the π rad phase jump predicted by the SFA model and is attributed to the influence of the Coulomb molecular ion field on the recolliding the discrepant electron wavepacket during the harmonic emission [3].

The retrieved single-molecule response was then exploited in the reconstruction of the bidimensional projection of the molecular orbital of carbon dioxide, which is shown in Fig. 46.3. The tomographic reconstruction was performed taking into

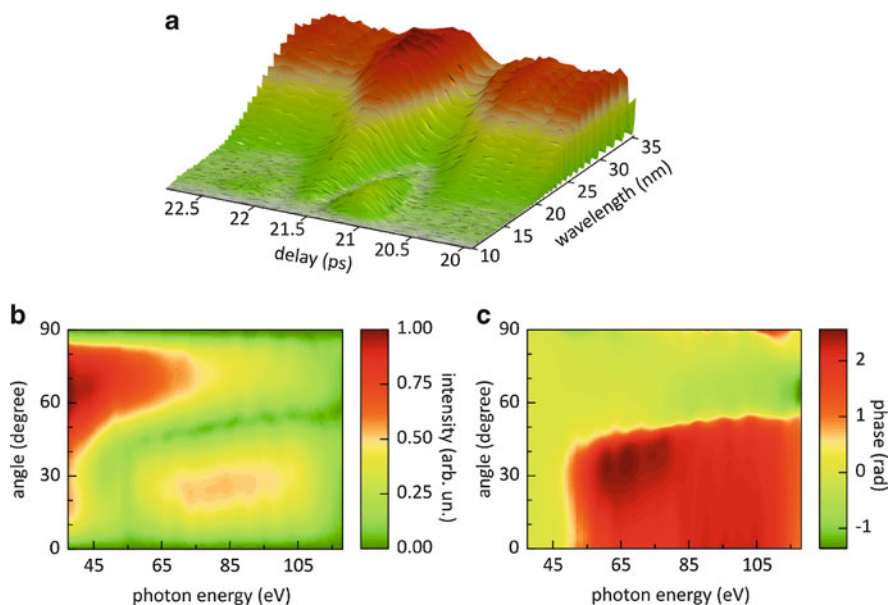


Fig. 46.2 (a) High order harmonic spectra measured in CO₂ molecules as a function of the delay between the aligning and the generating pulse. Retrieved normalized amplitude (b) and phase (c) of the single-molecule contribution to XUV emission in carbon dioxide as a function of photon energy and angular orientation

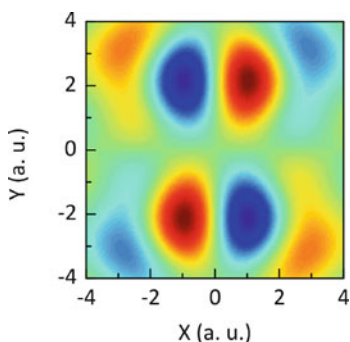


Fig. 46.3 Tomographic reconstruction of the CO₂ HOMO; the departure between the actual bidimensional projection of the wavefunction and the retrieved one is attributed to the lower limit of the XUV photon energies acquired by the spectrometer

account the effects of the molecular potential on the recolliding electron in a first order perturbative approach [5]; in the framework of such model, the SM-XEM is still interpreted as a function of the spatial Fourier transform of the HOMO, where the recolliding electron momentum has the role of spatial frequency. It is worth noting that there is an univocal relationship between photon energies of the

emitted radiation and momenta of the recolliding wavepacket; in our experimental conditions we had no access to photon energies lower than 40 eV, hence the reconstructed HOMO shows additional lobes which can be attributed to the lack of low spatial frequency components in the measurement [5].

46.3 Conclusions

Our results show that mid-IR ultrafast sources are particularly suitable for applications to HHG molecular imaging. In particular, the approach to the tomographic reconstruction presented here provide a solution to several difficulties which hindered so far its extension to complex species. These findings redeem the idea of HOMO spectroscopy by high order harmonic generation and open new perspectives on the imaging of molecular orbitals. In particular, the recent application of mid-IR laser pulses to high-order harmonic generation spectroscopy in fragile molecules [8] hold promise for extending molecular tomography to species with low ionization potential like biomolecules.

Acknowledgements We acknowledge the partial financial support from the Cariplo Foundation through the project 2009-2562 and from the European Union within the contract n. 228334 JRA-ALADIN (Laserlab Europe II). We gratefully acknowledge the contributions of F. Frassetto, L. Poletto and P. Villoresi in the development of the XUV spectrometer. We thank C. Altucci, P. Corkum, P. Hockett, M. Ivanov, J. Marangos, A. Staudte, C. Smeenk, R. Torres, R. Velotta and D. Villeneuve for the useful discussions.

References

1. P.B. Corkum, Plasma perspective on strong field multiphoton ionization. *Phys. Rev. Lett.* **71**, 1994–1997 (1993)
2. J. Itatani, J. Levesque, D. Zeidler, H. Niikura, H. Pepin, J.C. Kieffer et al., Tomographic imaging of molecular orbitals. *Nature* **432**, 867–871 (2004)
3. W. Boutu, S. Haessler, H. Merdji, P. Breger, G. Waters, M. Stankiewicz et al., Coherent control of attosecond emission from aligned molecules. *Nat. Phys.* **4**, 545–549 (2008)
4. O. Smirnova, Y. Mairesse, S. Patchkovskii, N. Dudovich, D. Villeneuve, P. Corkum, P.B. Corkum, High harmonic interferometry of multi-electron dynamics in molecules. *Nature* **460**, 972–977 (2009)
5. C. Vozzi, M. Negro, F. Calegari, G. Sansone, M. Nisoli, S. De Silvestri, S. Stagira, Generalized molecular orbital tomography. *Nat. Phys.* (2011). doi:10.1038/nphys2029
6. C. Vozzi, F. Calegari, E. Benedetti, S. Gasilov, G. Sansone, G. Cerullo et al., Millijoule-level phase-stabilized few-optical-cycle infrared parametric source. *Opt. Lett.* **32**, 2957–2959 (2007)
7. L. Poletto, G. Tondello, P. Villoresi, High-order laser harmonics detection in the EUV and soft X-ray spectral regions. *Rev. Sci. Instrum.* **72**, 2868–2874 (2001)
8. C. Vozzi, R. Torres, M. Negro, L. Brugnera, T. Siegel, C. Altucci et al., High harmonic generation spectroscopy of hydrocarbons. *Appl. Phys. Lett.* **97**, 241103 (2010)

Chapter 47

Tracing Attosecond Electron Motion Inside a Molecule

Liang-You Peng, Ming-Hui Xu, Zheng Zhang, and Qihuang Gong

Abstract By using a planar model of homonuclear molecule, we present a theoretical study of photoelectron emission of a homonuclear molecule by an attosecond xuv pulse. Through a pump-probe scheme, we show that attosecond electron motion inside the molecule can be mapped out by measuring the interference fringe visibility of the angle-resolved photoelectron momentum distributions. In addition, the visibility (V) depends on the degree of which-path information (P). The inequality, $P^2 + V^2 \leq 1$, which quantifies the wave-particle duality, is verified.

47.1 Introduction

Attosecond physics aims to trace and steer the electronic motion in the microcosm [1]. As it is known, absorption of one photon by the homonuclear molecule launches coherent electron wavepackets originating from two indistinguishable atomic sites, which should give rise to a typical two-slit interference pattern [2]. We show that the intramolecular electron motion indeed causes non-, partially-, or fully-localized electron distribution with respect to the core sites, leading to a priori which-path information (WPI). By applying a time-delayed attosecond xuv pulse, such a dynamical motion of the electron can then be captured by measuring the interference fringe visibility. We show that, not only is the wave-particle duality of the electron demonstrated in the molecular photoionization, it is also likely that applications exploiting interferometric techniques for tracing electronic wavepacket motion in molecules will become possible.

L.-Y. Peng (✉) · M.-H. Xu · Z. Zhang · Q. Gong
State Key Laboratory for Mesoscopic Physics and Department of Physics, Peking University,
Beijing 100871, China
e-mail: liangyou.peng@pku.edu.cn

47.2 The Model and the Results

In the present study, we consider a planar model molecule consisting of two protons and a single electron. Attosecond xuv pulse is used to induce a single-photon ionization. With its polarization perpendicular to the molecular axis, the scheme strongly resembles the Young's double-slit experiment. For our simulation, we numerically solve the time-dependent Schrödinger equation (TDSE),

$$i \frac{\partial}{\partial t} \Psi(x, y, t) = H \Psi(x, y, t), \quad (47.1)$$

employing the finite element discrete variable representation (FE-DVR) method to span the 2D Cartesian coordinate space. The total Hamiltonian is given by

$$H = [\mathbf{p} - \mathbf{A}(t)]^2 / 2 - 1 / \sqrt{(x - R/2)^2 + y^2 + a^2} - 1 / \sqrt{(x + R/2)^2 + y^2 + a^2}, \quad (47.2)$$

where \mathbf{p} is the canonical momentum, and $\mathbf{A}(t)$ is the vector potential of the pulse linearly polarized along the y -axis with a \sin^2 envelope. The choice of $a = 1/\sqrt{2}$ gives the ground state energy of -1.11 a.u. We employ the Arnoldi method [3] to propagate the wavefunction.

Making use of attosecond xuv pulses, the de Broglie wavelength of the ejected electrons can be engineered to be commensurate with the internuclear distances in molecules. Thus, clear interference pattern can be obtained from the angular distribution of the ejected photoelectrons in the molecular frame [4]. In Fig. 47.1, we show the ground state of the molecule and the electron momentum distributions ionized from the ground state after absorbing a photon with energy of 270 eV. One

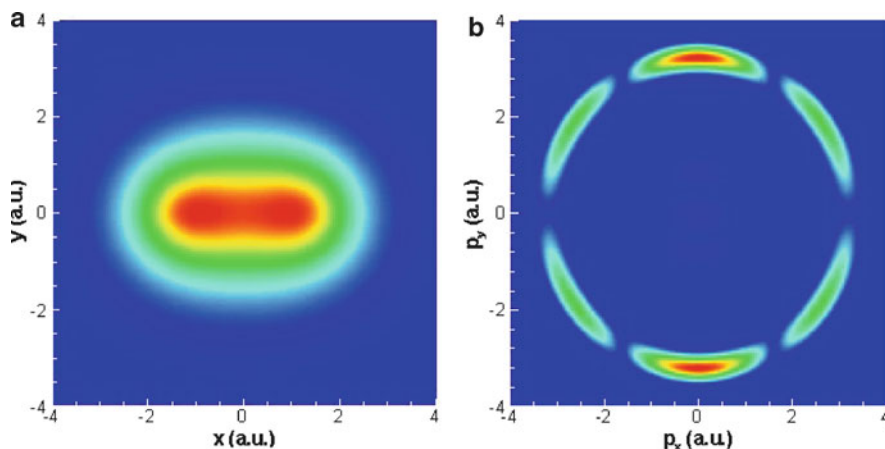


Fig. 47.1 (a) The ground state probability in coordinate space for $R = 2.0$. (b) The electron momentum distribution ionized from the ground state by absorbing one photon with energy 270 eV

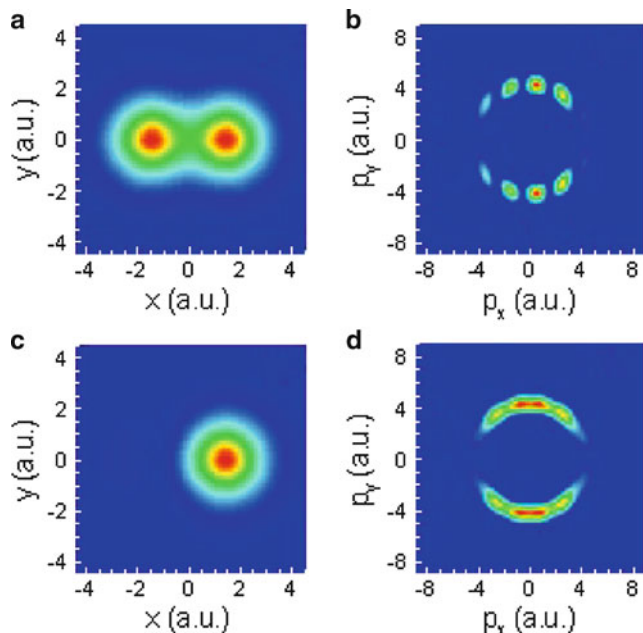


Fig. 47.2 Snapshots of the temporal evolution of probability densities of electron wavepacket prepared by a superposition of the field-free ground and the first excited state: (a) the wavepacket expands equally over the two core sites; (c) the wavepacket shrinks to the right core. The corresponding molecule-frame photoelectron momentum distributions are shown in (b) and (d), respectively. Adapted from [6]

can easily see the diffraction pattern which is similar to the traditional double-slit diffraction. Actually, we have done a series of calculations for different photon energies, the diffraction angles in all cases agree very well with the results from the realistic H_2^+ , which were carried out by Hu et al. from a 4D calculations [5, 6].

In order to carry out which-path experiment in the molecule photoionization, an initial wave packet is prepared as a coherent sum of the ground and the first excited state with an initial phase ϕ , i.e., $\Psi = c_0\psi_0 + c_1 \exp(-i\phi)\psi_1$, where $c_{0,1}^2$ are their populations ($c_0^2 + c_1^2 = 1$). The energy separation between them is ΔE . The initial phase ϕ depends on the particular excitation scheme. To attain maximized electron motion, we first take $c_0^2 = c_1^2 = 0.5$. However, it will be shown later that the same conclusions which will be drawn in the following can be reached for different populations in each state. The electron wave packet expands [cf. Fig. 47.2a] and shrinks [cf. Fig. 47.2c] with respect to the two nuclei with a period of $2\pi/\Delta E$ under free propagation. In Fig. 47.2, the internuclear separation is $R = 3$ a.u., corresponding to $\Delta E = 6.62$ eV. Thus, one can observe that the electron migrates from one nucleus to the other with an interval of about 312.6 as.

Now, we consider a single-photon ionization of the coherently coupled states by a time-delayed attosecond xuv pulse (the probe) with photon energy of 300 eV

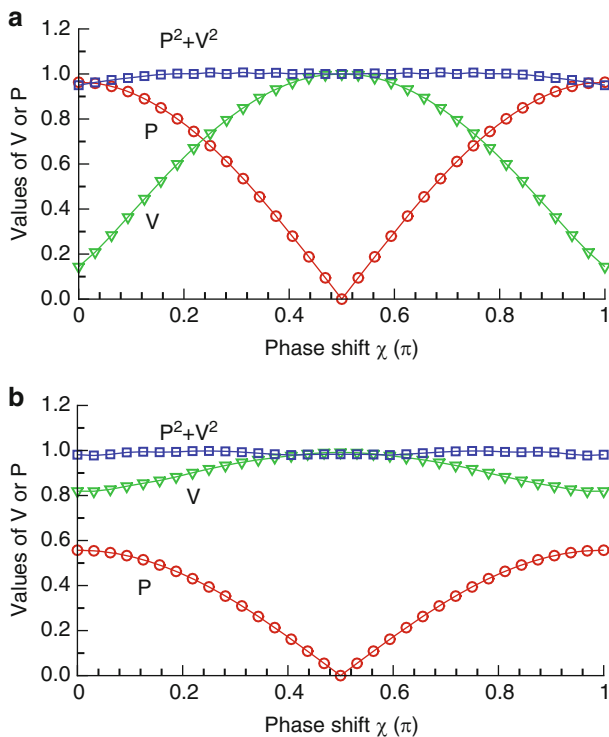


Fig. 47.3 Visibility V (triangles) and predictability P (circles) as a function of the phase shift χ for: (a) $|c_0|^2 : |c_1|^2 = 1 : 1$; (b) $|c_0|^2 : |c_1|^2 = 9 : 1$. $P^2 + V^2$ (squares) is also plotted to test the duality relation, $P^2 + V^2 = 1$ for both cases

and pulse duration of 20 as (full width at half maximum, FWHM). As shown in Fig. 47.2b, clearly visible interference fringe is exhibited if one can not tell along which nucleus the electron has traversed. In contrast, when the electron almost localizes on one of the two nuclei, it can be considered as a double-slit experiment with only one of the two slits open. Therefore, particle-like behavior is evident via the obscured interference fringe as shown in Fig. 47.2d. The photoelectron spectra originating from the two bound states overlap and interfere with a time-dependent phase shift ($\chi = \Delta Et + \phi$, determined by the evolution of the wavepacket).

The above model is a natural and simple system for observing intermediate particle-wave behavior, in which case the WPI is incomplete. The intermediate stage has been theoretically investigated in [7, 8]. A quantitative duality relation was derived to quantify how much which-path knowledge (P) can be obtained and how much fringe visibility (V) can be observed at the output of an interferometer [7, 8]:

$$P^2 + V^2 \leq 1. \quad (47.3)$$

In our case, the electronic motion leads to a priori which-path knowledge called *predictability* (P). The magnitude of the difference can be expressed as: $P = |p(|\mathbf{r} - \mathbf{R}/2| < R_0) - p(|\mathbf{r} + \mathbf{R}/2| < R_0)|$, where R_0 is the radius of the circle centered at each nucleus. The visibility V is calculated in the usual way. In the present calculations, we take $R = 3$ a.u. and $R_0 \approx 1$ a.u. The calculated values of P as a function of the phase shift χ are displayed in Fig. 47.3 (denoted by circles). Therefore P , which is in the range of $[0, 1]$, quantifies how much WPI we have in the molecular double-slit experiment. For a given P , the visibility of the interference is limited by (47.3). The equality holds for pure initial states of the electron, while the inequality applies to mixed states. In order to verify the duality relation, the value of $P^2 + V^2$ as a function of χ is also plotted in Fig. 47.3 (denoted by squares). Indeed, the equality is satisfied for both cases for different populations in the two states.

Note that the oscillation of the interference visibility as a function of χ shown in Fig. 47.3 indeed is able to reveal the dynamical evolution of the electronic density distribution. The visibility V as a function of the time delay indeed shows the modulation by the period of the electron jump between the two nuclei [6]. Hence, the interference pattern in the molecule-frame photoelectron angular distribution provides a simple signature of the electron motion.

47.3 Conclusions

In conclusion, we have demonstrated an intriguing implementation of the time-dependent double-slit experiment using photoelectrons in the molecular single-photon ionization. The wave-particle duality of the electron is well illustrated via the interference pattern in the angular distribution of the photoelectrons. One can also directly trace out the rapid electron wavepacket motion inside a molecule.

Acknowledgements This work was supported in part by the National Natural Science Foundation of China under Grant Nos. 10974007, 11174016, and 10821062.

References

1. F. Krausz, M. Ivanov, Rev. Mod. Phys. **81**, 163 (2009)
2. H.D. Cohen, U. Fano, Phys. Rev. **150**, 30 (1966)
3. L.-Y. Peng et al., J. Chem. Phys. **120**, 10046 (2004)
4. M. Walter, J. Briggs, J. Phys. B **32**, 2487 (1999)
5. S.X. Hu, L.A. Collins, B.I. Schneider, Phys. Rev. A **80**, 023426 (2009)
6. M.-H. Xu, L.-Y. Peng, Z. Zhang, Q. Gong, J. Phys. B **44**, 021001 (2011)
7. G. Jaeger, A. Shimony, L. Vaidman, Phys. Rev. A **51**, 54 (1995)
8. B.-G. Englert, Phys. Rev. Lett. **77**, 2154 (1996)

Chapter 48

Natural Orbital Analysis of Ultrafast Multielectron Dynamics of Molecules

Hirohiko Kono, Takayuki Oyamada, Tsuyoshi Kato, and Shiro Koseki

Abstract The ionization dynamics of molecules in intense laser fields is investigated by using a time-dependent multiconfiguration theory for propagating the many-electron wave function in a grid space. We use the natural orbitals obtained from the many-electron wave function, i.e., the molecular orbitals obtained by diagonalizing the one-particle electron density matrix, to analyze the ionization process. We eliminate the ionizing portions of orbitals reaching the grid boundaries set far away from the nuclei; the occupation numbers of natural orbitals decrease due to ionization. The ionization probabilities of individual natural orbitals can be obtained from the accumulated reductions in occupation numbers. We also propose a new definition of molecular orbital energy in order to investigate the energetics of natural orbitals. It is shown that when energies are assigned to natural orbitals $\{\phi_j(t)\}$ as chemical potentials $\{\bar{\epsilon}_j(t)\}$, one can quantify a correction to the total electronic energy that represents electron correlation; that is, time-dependent correlation energy is introduced. Our attempt is illustrated by numerical results on the time-dependence of the spatial density and chemical potential for a H_2 molecule interacting with an intense, near-infrared laser field. We compared the energy $\zeta_j(t)$ supplied by the applied field with the net energy gain $\Delta\bar{\epsilon}_j(t)$ in the chemical potential for $\phi_j(t)$ and found that energy accepting orbitals of $\Delta\bar{\epsilon}_j(t) > \zeta_j(t)$ exhibit high ionization efficiency.

H. Kono (✉) · T. Oyamada
Department of Chemistry, Graduate School of Science, Tohoku University, Sendai 980-8578,
Japan

T. Kato
Department of Chemistry, School of Science, The University of Tokyo, 7-3-1 Hongo, Bunkyo-ku,
Tokyo 113-0033, Japan

S. Koseki
Department of Chemistry, Graduate School of Science, Osaka Prefecture University, Osaka
599-8531, Japan
e-mail: hirohiko-kono@m.tohoku.ac.jp

48.1 Introduction

For quantitative understanding of the ultrafast electronic dynamics of molecules in intense fields, it is necessary to solve the time-dependent Schrödinger equation for the electronic degrees of freedom. The quantum chemical approach using molecular orbitals can provide precise electronic structures of many-electron systems. This approach can be extended to time-dependent problems such as electronic dynamics of molecules interacting with laser light [1–3]. The possible tractability of such methods to treat many-electron systems makes them attractive for development. Moreover, recent progresses in experimental attoscience [4–6] motivate the development of theoretical methods for quantum simulations and analysis of laser driven electron dynamics. As one of the attempts, we have developed time-dependent multiconfiguration theory for electronic dynamics, namely, the multi-configuration time-dependent Hartree–Fock method (MCTDHF) [7–10]. In this theory, an N -electron wave function is expanded as a linear combination of Slater determinants (or configuration state functions, CSFs) in which the spin-orbitals and the CI-coefficients are both treated as time-dependent quantities to fully utilize their flexibility as variational parameters to describe the wave function. The equations of motion (EOMs) for spin orbitals in the coordinate representation are derived within the framework of the time-dependent multiconfiguration theory developed for electronic dynamics of molecules in intense laser fields.

Numerical results [8] demonstrate that the time-dependent numerical multi-configuration many-electron wave function is able to describe correlated electron motions as well as the ionization processes of a molecule in intense laser fields including nonsequential double ionization [11, 12]. To analyze the ionization process, we use the natural orbitals obtained by diagonalizing the one-particle electron density matrix [13]. The occupation numbers of natural orbitals decrease due to ionization. We show that the ionization probabilities of individual natural orbitals can be obtained from the accumulated reductions in occupation numbers.

We also proposed a new definition of molecular orbital energy in order to investigate the energetics of constituent natural orbitals. It is shown that when energies are assigned to natural orbitals as chemical potentials, the total energy is given by the sum of chemical potential times occupation number. We can therefore evaluate the time-dependence of the chemical potentials $\{\bar{\epsilon}_j(t)\}$ and accompanying correlation energies for natural orbitals $\{\phi_j(t)\}$. We calculated these quantities for $\{\phi_j(t)\}$ of a H_2 molecule interacting with an intense, near-infrared laser field. We compared the energy $\zeta_j(t)$ supplied by the applied field with the net energy gain $\Delta\bar{\epsilon}_j(t)$ in the chemical potential for $\phi_j(t)$ and found that the natural orbitals with $\Delta\bar{\epsilon}_j(t) > \zeta_j(t)$, which are called “energy accepting orbitals,” exhibit high efficiency for ionization.

48.2 Quantification of Energy Exchange Among Molecular Orbitals

We briefly introduce time-dependent multiconfiguration theory for electronic (ionization) dynamics [7, 8] together with related theoretical background [14]. In this theory, a time-dependent N -electron wave function $\Phi(t)$ is expanded as a linear combination of Slater determinants $\{\Phi_I(t)\}$ representing various electron configurations. The spin-molecular orbitals in $\{\Phi_I(t)\}$ and the configuration interaction (CI)-coefficients $\{C_I(t)\}$ are both treated as time-dependent quantities to fully utilize their flexibility as variational parameters:

$$\Phi(t) = \sum_{I=1}^M C_I(t) \Phi_I(t), \quad (48.1)$$

where M is the number of Slater determinants used in the expansion. The equations of motion (EOMs) for spin orbitals in the coordinate representation (grid point representation) are derived [8]. We have tailored the EOMs for diatomic (or linear) molecules to apply the theory to the electronic dynamics of H_2 and N_2 in intense, near-infrared laser fields.

The energy for the total electronic Hamiltonian $H(t)$ including the interaction with the field is given by

$$E(t) = \sum_{I=1}^M |C_I(t)|^2 \langle \Phi_I(t) | H(t) | \Phi_I(t) \rangle + \sum_{I \neq I'}^M C_{I'}^*(t) C_I(t) \langle \Phi_{I'}(t) | H(t) | \Phi_I(t) \rangle, \quad (48.2)$$

where the first and second sums are considered “mean field energy” and “correlation energy.” These two quantities can be divided into the individual components $\bar{\epsilon}_j(t)$ for natural orbitals $\phi_j(t)$ (the molecular orbitals obtained by diagonalizing the one-particle electron density matrix) as [14]

$$E(t) = \sum_j w_j(t) \bar{\epsilon}_j(t), \quad (48.3)$$

where $w_j(t)$ is the occupation number for $\phi_j(t)$. $\bar{\epsilon}_j(t)$ is regarded as the chemical potential for $\phi_j(t)$; the chemical potentials of natural orbitals are all degenerate for a stationary state.

In the natural orbital representation of the two-electron system, the two electrons occupy the same spatial orbital with different spins α and β ; therefore, the two electrons occupy $\phi_j(t)\alpha$ and $\phi_j(t)\beta$ in the j th electron configuration. The j th natural orbital corresponds to the j th electron configuration ($w_j = |C_j|^2$). The chemical potential for the j th natural orbital in a two-electron system is thus expressed as [14]

$$\begin{aligned} \bar{\varepsilon}_j(t) = & h_{jj}(t) + \frac{1}{2}[j_\beta(t)j_\beta(t)|j_\alpha(t)j_\alpha(t)] \\ & + \frac{1}{2} \operatorname{Re} \left[\sum_{k \neq j}^{N_o} [k_\beta(t)j_\beta(t)|k_\alpha(t)j_\alpha(t)] \frac{C_k(t)}{C_j^*(t)} \right], \end{aligned} \quad (48.4)$$

where $h_{jj}(t)$ is the one-body Hamiltonian including the dipole interaction with the field and the explicit form of the integral $[\dots|\dots]$ is given by

$$[k_\beta(t)j_\beta(t)|k_\alpha(t)j_\alpha(t)] = \iint d\mathbf{r}_1 d\mathbf{r}_2 \phi_k^*(\mathbf{r}_1, t) \phi_j(\mathbf{r}_1, t) \frac{1}{|\mathbf{r}_2 - \mathbf{r}_1|} \phi_k^*(\mathbf{r}_2, t) \phi_j(\mathbf{r}_2, t). \quad (48.5)$$

The second term in (48.4) is the Coulomb integral and the third term is regarded as a correlation energy that represents the interaction between natural orbitals.

On one hand, within the dipole approximation in the length gauge, the change in the total energy is given by

$$E(t) - E(0) = - \int_0^t \boldsymbol{\mu}(t') \cdot \frac{d}{dt'} \mathcal{E}(t') dt' = - \boldsymbol{\mu}(t) \cdot \mathcal{E}(t) + \int_0^t \frac{d\boldsymbol{\mu}(t')}{dt'} \cdot \mathcal{E}(t') dt', \quad (48.6)$$

where $\boldsymbol{\mu}$ is the total dipole moment of the molecule. Inserting (48.3) into (48.6) and evaluating $\boldsymbol{\mu}$ in terms of natural orbitals, we have

$$\begin{aligned} \sum_{j=1}^{N_o} w_j(t) [\bar{\varepsilon}_j(t) - \bar{\varepsilon}_j(0) + \boldsymbol{\mu}_j(t') \cdot \mathcal{E}(t)] &= \sum_{j=1}^{N_o} \int_0^t \frac{dw_j(t') \boldsymbol{\mu}_j(t')}{dt'} \cdot \mathcal{E}(t') dt' \\ &\approx \sum_{j=1}^{N_o} w_j(t) \zeta_j(t), \end{aligned} \quad (48.7)$$

where the quantity $\zeta_j(t)$ defined below is regarded the energy supplied to the natural orbital j from the radiation field per unit time [15]

$$\zeta_j(t) = \int_0^t \frac{d\boldsymbol{\mu}_j(t')}{dt'} \cdot \mathcal{E}(t') dt', \quad (48.8)$$

We compare the rhs and lhs of (48.7), i.e., $\zeta_j(t)$ and

$$\Delta \bar{\varepsilon}_j(t) = \bar{\varepsilon}_j(t) - \bar{\varepsilon}_j(0) + \boldsymbol{\mu}_j(t) \cdot \mathcal{E}(t). \quad (48.9)$$

The difference between $\Delta \bar{\varepsilon}_j(t)$ and $\zeta_j(t)$ is attributed to energy exchange between natural orbitals reflecting the multielectron dynamics. We have calculated $\zeta_j(t)$ and

$\bar{\epsilon}_j(t)$ for H_2 interacting with an intense, near-infrared laser field, as shown in the next section.

48.3 Numerical Results: H_2

In the following, we consider the electronic dynamics of a H_2 molecule in an intense near-infrared laser field of which the polarization direction is parallel to the molecular axis. The internuclear distance R is fixed at $R = 1.6a_0$, where a_0 is the Bohr radius. The molecular orbitals are represented as the amplitudes on grid points of the cylindrical coordinates z (parallel to the molecular axis) and ρ . The dual transformation method is used to avoid the numerical divergence of the electron-nucleus attraction potential [16, 17] and the electron–electron repulsion is evaluated by the Legendre polynomial expansion. The grid points to accommodate the numerical orbital functions are set in the rectangular space of $|z| \leq 40a_0$ and $\rho \leq 40a_0$. To obtain the singlet ground state wave function, we used nine spatial orbital functions (the number of spin orbitals, $N_o = 18$); $(1\sigma_g)$, $(1\sigma_u, 1\pi_u^\pm, 2\sigma_g)$, $(1\pi_g^\pm, 3\sigma_g, 2\sigma_u)$, of which the Hartree–Fock orbital energies are roughly grouped into three. The total number of electron configurations (Slater determinants) used to expand the wave function of (48.1) is 81 (since the number of spatial orbitals is $N_o/2$).

We adopt the dipole approximation in the length gauge for the laser–molecule interaction. The electric field is assumed to have a form $\mathcal{E}(t) = \vec{e}_z f(t) \sin(\omega t)$, where the polarization vector \vec{e}_z is parallel to the molecular axis and the laser frequency is $\omega = 0.06E_h/\hbar$ (wavelength $\lambda = 760$ nm, $T_c = 2\pi/\omega = 104.7\hbar/E_h = 2.53$ fs). The envelope function $f(t)$ is linearly ramped so that $f(t)$ attains its maximum value of f_{\max} at the end of the first optical period of $t = T_c$ and then decreases linearly in the second optical period (two-cycle pulse). The envelope maximum of $f(t)$ at $t = T_c$ is set to be $f_{\max} = 0.0534 E_h/ea_0$, where e is the elementary charge (the corresponding light intensity for f_{\max} is $I_{\max} = 1.0 \times 10^{14}$ W/cm²).

The moduli of the nine natural orbitals at $t = T_c$ are plotted in Fig. 48.1 on a logarithmic scale. The assignment of time-dependent natural orbitals is correlated with the orbital symmetry in the ground electronic state. It is noticeable that ionization of π -orbitals is significantly suppressed in the case where the polarization direction is parallel to the molecular axis. In previous theoretical and experimental studies, the suppression of ionization in π -orbitals is attributed to the destructive interference between the ionizing currents from two lobes of the 2p orbitals in a π -orbital [18–23]. The present MCTDHF scheme demonstrates that ionization from π -orbitals is suppressed even if electron correlation is taken into account.

We quantify the ionization probabilities from individual natural orbitals by eliminating the ionizing components reaching the grid boundaries. The norms of the orbital functions are kept unity during the propagation by taking advantage of the redundancy between the CI-coefficients and the orbital functions; i.e., the decreases in the norms of orbital functions at every time step (say, at t_i) are converted into the

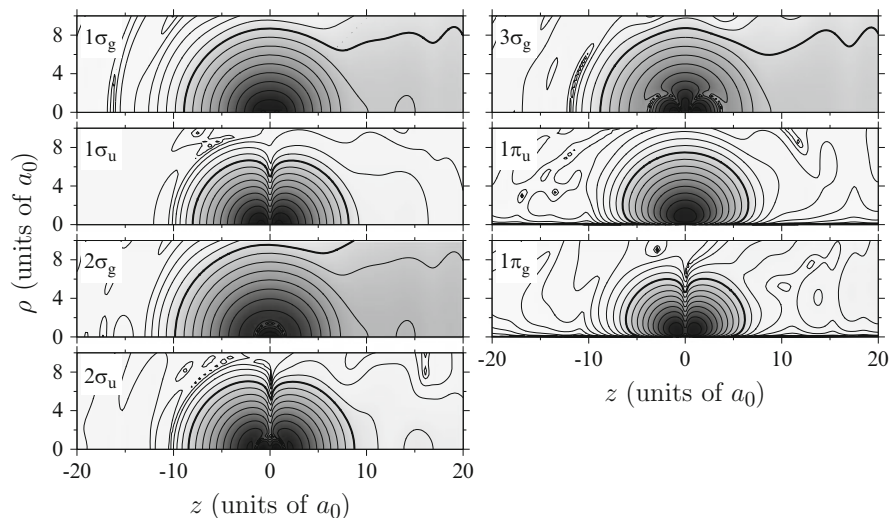


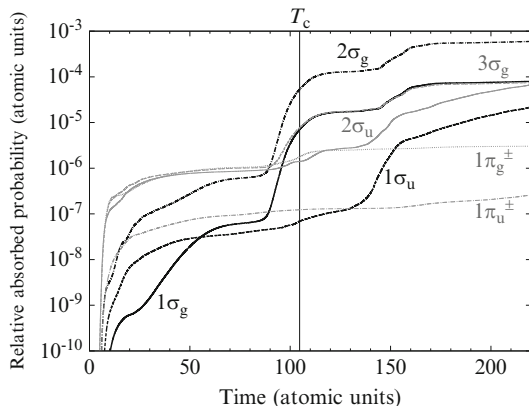
Fig. 48.1 Natural logarithmic plot of the moduli of the time-dependent natural orbitals of H_2 at $t = T_c = 2\pi/\omega = 2.53$ fs. The parameters for the two-cycle pulse are given in the text. The symmetry symbols stand for the orbital symmetry when the molecule is in the electronic ground state, i.e., the initial state. The bold contour lines designate the contour lines at $\ln|\phi_j(\rho, z)/a_0^{3/2}| = -10$ and the contour interval is set to be unity

decreases in the absolute values of CI-coefficients. The reduction in the occupation number of the natural orbital j due to ionization, $\Delta w_j(t_i)$, can be obtained from the CI-coefficients of the converted wave function. The accumulated ionization probability at time t through the natural orbital j , $\Delta w_j^{ab}(t)$, is thus defined as

$$\Delta w_j^{ab}(t) = \sum_i^{t_i < t} \Delta w_j(t_i). \quad (48.10)$$

The total ionization probability was 7.8×10^{-5} for the present applied field. We found that the $1\sigma_g$ orbital contributes most to the reduction in the total norm ($\Delta w_{1\sigma_g}^{ab}(t = \infty) = 7.6 \times 10^{-5}$); the next one is the $2\sigma_g$ ($\Delta w_{2\sigma_g}^{ab}(t = \infty) = 1.7 \times 10^{-6}$), though it spreads most widely in space. This comes from the fact that the occupation number of $1\sigma_g$ is 0.978 while that of $2\sigma_g$ is ~ 0.003 . To evaluate the efficiency in ionization of individual natural orbitals, we divide $\Delta w_j^{ab}(t)$ by the initial occupation number $w_j(t = 0)$. The quantities $\{\Delta w_j^{ab}(t)/w_j(t = 0)\}$ are plotted in Fig. 48.2 The ionization efficiency is the highest for the $2\sigma_g$ natural orbital, as expected from Fig. 48.1. For a pair of σ orbitals such as $(1\sigma_g, 1\sigma_u)$ or $(2\sigma_g, 2\sigma_u)$, σ_g is easier to ionize than σ_u . It is clearly shown that the relative ionization probabilities for π orbitals are extremely small.

Fig. 48.2 Efficiency in ionization for natural orbitals $\phi_j(t)$: common logarithmic plot of $\left\{ \Delta w_j^{ab}(t)/w_j(t=0) \right\}$

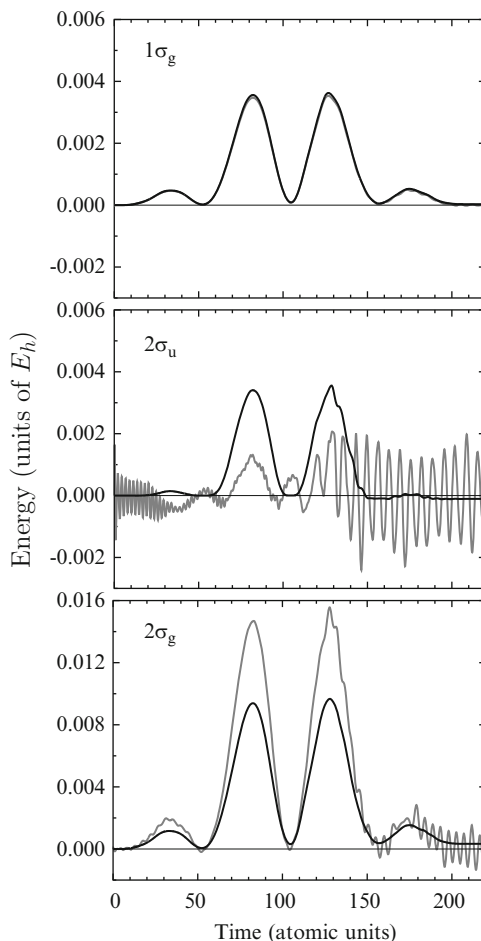


We next compare the temporal profiles of the net energy supplies $\zeta_j(t)$ and the energy gains $\Delta\bar{\epsilon}_j(t)$ for natural orbitals. The quantities $\zeta_j(t)$ and $\Delta\bar{\epsilon}_j(t)$ for $1\sigma_g$, $2\sigma_g$, and $2\sigma_u$ are shown in Fig. 48.3. As shown in Fig. 48.3, the values of $\zeta_j(t) \approx \Delta\bar{\epsilon}_j(t)$ for $1\sigma_g$ hit zero at $\mathcal{E}(t) = 0$ and reach a maximum value when $|\mathcal{E}(t)|$ takes a maximum, indicating that the $1\sigma_g$ orbital adiabatically changes according to the change in $\mathcal{E}(t)$. We note from (48.8) that $\zeta_j(t) > 0$ if the dipole moment of a natural orbital follows the field adiabatically, which is clearly demonstrated by the plots of $\{\zeta_j(t)\}$ in Fig. 48.3. The fact that the energy accepting $2\sigma_g$ orbital spreads most is consistent with the present analysis that the $2\sigma_g$ orbital has the largest induced dipole and the energy supply $\zeta_j(t)$ to the $2\sigma_g$ orbital is the largest, more than twice as large as those of the other orbitals.

From the plots, we can categorize the temporal behavior of the two energy values $\zeta_j(t)$ and $\Delta\bar{\epsilon}_j(t)$ into three groups: (a) “spectator orbital” for which $\zeta_j(t)$ and $\Delta\bar{\epsilon}_j(t)$ have almost the same time-dependence ($1\sigma_g$ and $1\pi_u$); (b) “energy donating orbitals” of $\zeta_j(t) > \Delta\bar{\epsilon}_j(t)$ ($1\sigma_u$ and $2\sigma_u$); (c) “energy accepting orbitals” of $\zeta_j(t) < \Delta\bar{\epsilon}_j(t)$ ($2\sigma_g$). The change in the correlation energy [the third term in (48.4)] is very small for $1\sigma_g$ (less than $1.2 \times 10^{-4} E_h$). It is the mean field energy [the first and second terms in (48.4)] that dominates $\Delta\bar{\epsilon}_{1\sigma_g}(t)$; for $1\sigma_g$, the change in the total two-body interaction energy comes from the Coulomb term [the second terms in (48.4)]. The $1\sigma_g$ is hence isolated from the other orbitals. As a result, $\Delta\bar{\epsilon}_{1\sigma_g}(t) \approx \zeta_{1\sigma_g}(t)$. On the other hand, the change in the total two-body interaction energy is dominated by the correlation energy for the $2\sigma_g$. The large increase in the correlation energy explains why the amount of energy gained from the other orbitals, $\Delta\bar{\epsilon}_j(t) - \zeta_j(t)$, is the largest for $2\sigma_g$. The $2\sigma_g$ orbital gains energy from the energy donating orbitals $1\sigma_u$ and $2\sigma_u$. The change in correlation energy plays a significant role in the energetics of natural orbitals.

For higher frequencies such as $\omega = 0.12 E_h/\hbar$ (wavelength $\lambda = 380$ nm), all the orbitals show nonadiabatic responses to the field. However, we observed that the $1\sigma_g$ orbital remains a spectator orbital and isolated from the other orbitals: $\zeta_j(t) \approx \Delta\bar{\epsilon}_j(t)$ and the correlation energy is negligible for $1\sigma_g$.

Fig. 48.3 Comparison of the temporal profiles of the energy supply $\zeta_j(t)$ (*solid line*) and the net energy gain $\Delta\bar{\epsilon}_j(t)$ (*gray line*) for natural orbitals



48.4 Conclusions

We investigated the ionization dynamics of H_2 in intense laser fields by using a time-dependent multiconfiguration theory, namely, the MCTDHF method for propagating the many-electron wave function. The natural orbitals are employed to analyze the ionization process. We quantified the ionization probabilities of individual natural orbitals by using the accumulated reductions in occupation numbers. We also proposed a new definition of molecular orbital energy in order to investigate the energetics of natural orbitals. The “time-dependent” chemical potentials $\{\bar{\epsilon}_j(t)\}$ and correlation energies for natural orbitals $\{\phi_j(t)\}$ are defined.

We presented numerical results on the time-dependence of the spatial density and chemical potentials for H_2 interacting with an intense, near-infrared field. We

compared the energy $\zeta_j(t)$ supplied by the applied field with the net energy gain $\Delta\bar{\epsilon}_j(t)$ for respective natural orbitals $\phi_j(t)$. The responses of natural orbitals can be classified into three: (a) $\Delta\bar{\epsilon}_j(t) = \zeta_j(t)$ (spectator orbital); (b) $\Delta\bar{\epsilon}_j(t) < \zeta_j(t)$ (energy donating orbital); and (c) $\Delta\bar{\epsilon}_j(t) > \zeta_j(t)$ (energy accepting orbital). We concluded that the $1\sigma_g$ orbital plays a key role in the ionization process because of its large occupation number and that the ionization efficiency is the highest for the time-developing $2\sigma_g$ accepting orbital. Ionization of a molecule, including multielectron dynamics [24], can be interpreted or quantified by the time-dependent molecular orbital picture, namely, in terms of the occupation numbers and chemical potentials of time-dependent natural orbitals.

References

1. M. Awasthi, A. Saenz, *J. Phys. B* **39**, S389 (2006)
2. J.F. Pérez-Torres, J.L. Sanz-Vicario, H. Bachau, F. Martín, *J. Phys. B* **43**, 015204 (2010)
3. M. Nest, T. Klamroth, *Phys. Rev. A* **72**, 012710 (2005)
4. F. Krausz, M. Ivanov, *Rev. Mod. Phys.* **81**, 163 (2009)
5. M.F. Kling, M.J.J. Vrakking, *Annu. Rev. Phys. Chem.* **59**, 463 (2008)
6. H. Niikura, H.J. Wörner, D.M. Villeneuve, P.B. Corkum, *Phys. Rev. Lett.* **107**, 093004 (2011)
7. T. Kato, H. Kono, *Chem. Phys. Lett.* **392**, 533 (2004)
8. T. Kato, H. Kono, *J. Chem. Phys.* **128**, 184102 (2008)
9. G. Jordan, J. Caillat, C. Ede, A. Scrinzi, *J. Phys. B* **39**, S341 (2006)
10. T.T. Nguyen-Dang, M. Peters, S.-M. Wang, F. Dion, *Laser Phys.* **19**, 1521 (2009)
11. Th. Weber, H. Giessen, M. Weckenbrock, G. Urbasch, A. Staudte, L. Spielberger, O. Jagutzki, V. Mergel, M. Vollmer, R. Dörner, *Nature* **405**, 658 (200)
12. R. Dörner, V. Mergel, O. Jagutzki, L. Spielberger, J. Ullrich, R. Moshhammer, H. Schmidt-Böcking, *Phys. Rep.* **330**, 95 (2000)
13. P.O. Löwdin, H. Shull, *Phys. Rev.* **101**, 1730 (1956)
14. T. Kato, H. Kono, *Chem. Phys.* **366**, 46 (2009)
15. A. Yariv, *Quantum Electronics*, 3rd ed. (Wiley, New York, 1989), p. 85
16. I. Kawata, H. Kono, *J. Chem. Phys.* **111**, 9498 (1999)
17. K. Harumiya, I. Kawata, H. Kono, Y. Fujimura, *J. Chem. Phys.* **113**, 8953 (2000)
18. D. Pavicic, K.F. Lee, D.M. Rayner, P.B. Corkum, D.M. Villeneuve, *Phys. Rev. Lett.* **98**, 243001 (2007)
19. M. Okunishi, H. Niikura, R.R. Lucchese, T. Morishita, K. Ueda, *Phys. Rev. Lett.* **106**, 063001 (2011)
20. J. Müth-Bohm, A. Becker, F.H.M. Faisal, *Phys. Rev. Lett.* **85**, 2280 (2000)
21. T. Otobe, K. Yabana, J.-I. Iwata, *Phys. Rev. A* **69**, 053404 (2004)
22. D.A. Telnov, Shih-I. Chu, *Phys. Rev. A* **80**, 043412 (2009)
23. S.-F. Zhao, C. Jin, A.-T. Le, T.F. Jiang, C.D. Lin, *Phys. Rev. A* **81**, 033423 (2010)
24. The role of multielectron dynamics in the near-IR induced ionization of C_{60} is experimentally investigated. See I.V. Hertel, I. Shchatsinin, T. Laarmann, N. Zhavoronkov, H.-H. Ritze, C.P. Schulz, *Phys. Rev. Lett.* **102**, 023003 (2009)

Chapter 49

Protonic Configuration of CH₃OH within a Diatomic-Like Molecular Picture

Tsuyoshi Kato and Kaoru Yamanouchi

Abstract The electro-protonic ground state wave function of CH₃OH is calculated by imaginary time propagation of multi-configuration wave functions for a system composed of two kinds of Fermi particles. The orbital functions for both electrons and protons are described in a laboratory fixed cylindrical coordinate system in which C and O atoms are fixed on the z -axis. The cylindrical symmetry of the electro-protonic system with respect to the z -axis allows us to treat a CH₃OH molecule as a quasi-diatom molecule. The probability density distribution of the four protons agrees with the optimized spatial configuration of the protons obtained by the standard electronic structure calculation based on the Born–Oppenheimer approximation, i.e., the C atom is surrounded by three protons and the O atom by one proton, forming functional groups.

49.1 Introduction

Recent experimental studies clarified the existence of ultrafast hydrogen and/or proton migration within a hydrocarbon molecule interacting with a strong laser field ($\geq 10^{14}$ W/cm²) [1, 2]. In order to understand the mechanism of ultrafast hydrogen migration processes, we formulated the time-dependent multi-configuration wave function description of a system composed of two kinds of Fermi particles [3], e.g., electrons and protons, by extending the theory developed to describe electronic dynamics in a strong laser field [4]. In the most general treatment of a many particle system, only the center of mass of a molecule can be fixed, i.e., the system is regarded to have a spherical symmetry. A general approach to a system having a lower symmetry was demonstrated by our previous study, in which a set of equations

T. Kato (✉) · K. Yamanouchi
Department of Chemistry, School of Science, The University of Tokyo, 7-3-1 Hongo,
Bunkyo-ku, Tokyo 113-0033, Japan
e-mail: tkato@chem.s.u-tokyo.ac.jp

of motion (EOMs) for a system having a cylindrical symmetry was formulated. The EOMs being suitable to describe the electro-protonic dynamics in so-called diatomic like molecular systems, e.g., molecules composed of electrons, protons, and other two heavier nuclei, can be applied to a variety of molecular species such as CH_3OH , C_2H_2 , C_2H_4 , and H_5O_2^+ .

In the present contribution, as a numerical demonstration of our theory, we calculate the electro-protonic ground state wave function of CH_3OH by utilizing the EOMs in imaginary time integration. Then, by calculating the proton population in the domains near O and C nuclei, respectively, using the probability density function for the protonic system, we show that the four protons are calculated to be distributed in the hydroxyl group and the methyl group with the ratio of 1:3.

49.2 Theory

In this study, the heavier nuclei, e.g., the nuclei of C and O atoms, are supposed to be fixed on the z -axis and the positions of N_e -electrons and N_p -protons are denoted as $\{\mathbf{r}_j\}$ ($1 \leq j \leq N_e = 18$) and $\{\mathbf{r}_p\}$ ($1 \leq p \leq N_p = 4$), respectively, where the origin of the position vectors is taken at the center of mass of the two heavier nuclei. The time-dependent wave function of the electro-protonic system is represented by a multi-configuration expansion using Slater determinants with respect to both the electronic and the protonic structures as

$$\begin{aligned} \Phi(\{\mathbf{x}_j\}, \{\mathbf{y}_p\}, t; R) &= \sum_{IA} C_{IA}(t) \Phi_I(\{\mathbf{x}_j\}, t; R) \Psi_A(\{\mathbf{y}_p\}, t; R) \\ &\equiv \sum_{IA} C_{IA}(t) \Phi_I(t) \Psi_A(t), \end{aligned} \quad (49.1)$$

where $\mathbf{x}_j = (\mathbf{r}_j, \sigma_j)$ and $\mathbf{y}_p = (\mathbf{r}_p, \mu_p)$ denote the spatial and spin coordinates of the j th electron and those of the p th proton, respectively. Φ_I and Ψ_A , respectively, represent an N_e -electron Slater determinant and an N_p -proton Slater determinant, and $C_{IA}(t)$ is a time-dependent CI-coefficient. These determinants are explicitly expressed by specifying constituent spin-orbitals for electrons and protons, where the respective orbital functions depend parametrically on the internuclear separation R between C and O atoms. From Dirac-Frenkel variational principle, we can derive the EOMs for the CI-coefficients and the spin-orbitals [5]. Detailed explanations of the operators and the definition of the ranges of summations can be seen in [3].

The EOMs obtained for the real time propagation of the wave functions can also be used to calculate the electro-protonic ground state by changing the argument of time as $t \rightarrow -i\tau$ in the EOMs. By this imaginary time propagation we can eliminate the excited state components in a trial wave function $|\Phi_{\text{trial}}\rangle$:

$$\exp\left[-\frac{i}{\hbar}\hat{H}_{\text{ep}}t\right]|\Phi_{\text{trial}}\rangle \rightarrow \exp\left[-\frac{1}{\hbar}\hat{H}_{\text{ep}}\tau\right]|\Phi_{\text{trial}}\rangle \equiv |\Phi_{\text{trial}}(-i\tau)\rangle, \quad (49.2)$$

where \hat{H}_{ep} stands for the Hamiltonian for the electro-protonic system with the mass-polarization operator [3]. By this imaginary time propagation, both the orbital functions and the CI-coefficients are optimized for the electro-protonic ground state.

In the numerical calculation, the C–O bond length is set to be 1.4331 Å obtained by HF geometry optimization with STO-3G basis. The HF energy including the Coulomb repulsion between the nuclei of C, O and H atoms is evaluated to be $E_{\text{HF}} = -113.549 E_h$. We employ a grid representation for describing the spatial orbital functions. The same grid points are used to represent the electronic orbital functions and the protonic ones. The 155×50 grid points are generated on the rectangular z - ρ plane of $|z| \leq 7.0 a_0$ and $\rho \leq 6.0 a_0$ in the cylindrical coordinate system, where a_0 is the Bohr radius. The rotational motion of the molecule along the x - and y -axes are not taken into account in the present study.

We treat the electronic structure of CH₃OH by a closed shell model, i.e., a single determinantal structure, and mainly focus our attention on the multi-configurational structure of the protonic system. A CH₃OH molecule has 18 electrons so that we need 9 electronic spatial orbitals to build a single Slater determinant for a singlet state. We will consider an electronic Slater determinant that is composed of σ and π orbitals having the lowest and the second lowest angular momentum projections. When only σ and π orbitals are used, there are four possible sets of orbitals to make a Slater determinant for nine electron system, e.g., $(7\sigma, \pi)$, $(5\sigma, 2\pi)$, $(3\sigma, 3\pi)$ and $(1\sigma, 4\pi)$. The last set $(1\sigma, 4\pi)$ needs to be discarded because at least two σ orbitals are required to accommodate the O1s and C1s electrons.

For the protonic system, we consider two sets of orbitals, namely, $(2\sigma, 3\pi, 2\delta)$ and $(2\sigma, 3\pi, 2\delta, 2\phi)$. Since four protons are involved, the spin multiplicity of the protonic system should be the singlet, the triplet or the quintet. In the present calculation we consider the quintet state of the protonic system, which is the highest protonic spin state, to assure the highest flexibility of the spatial protonic orbital functions within a given set of orbitals.

49.3 Results and Discussion

Since the lowest energy of the electro-protonic ground state of CH₃OH, $E_g = -112.91 E_h$, is obtained when adopting the electronic orbital set of $(5\sigma, 2\pi)$ with the protonic orbital set of $(2\sigma, 3\pi, 2\delta, 2\phi)$, we examine the wave function obtained by these electronic and protonic orbital sets, calculated to have the Σ symmetry, where the summation of angular momentum projections of the electronic and the protonic orbitals is zero. This calculated energy value is comparable to $E_{\text{HF}} = -113.55 E_h$ but is higher by $\Delta E = 0.64 E_h$, including the zero-point vibrational energy contribution $\Delta E_{\text{vib}} = 0.060 E_h$.

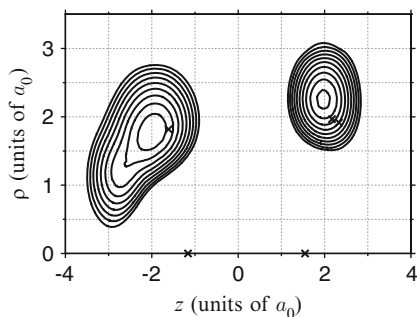


Fig. 49.1 Contour plots of the proton probability density of a CH₃OH molecule (logarithmic scale). The fixed nuclear position of C ($z > 0$) and O ($z < 0$) atoms are represented by *crosses* on the z -axis. The HF optimized positions of four protons, i.e., one proton in the hydroxyl group ($z < 0$) and three protons in the methyl group ($z > 0$) are also represented by *crosses* at $\rho > 0$. The proton in the methyl group located at the staggered position with respect to the proton in the hydroxyl group take a slightly larger ρ value compared with the other two protons

In Fig. 49.1, the probability density of protons, $\Gamma_P(\rho, z)$, in the cylindrical coordinate system is shown together with the positions of the protons obtained by the conventional HF geometry optimization calculation. In the plot we can see that the probability density function of protons has two localized distributions in the $z < 0$ and $z > 0$ domains that correspond respectively to the hydroxyl group and the methyl group. For the methyl group (in the $z > 0$ domain), we find a single peak of the probability density of protons contrary to the results obtained by the HF geometry optimization calculation in which two different C–H bond lengths are obtained.

In the HF optimization calculation, the three protons in the methyl group are grouped into two, that is, two equivalent protons and the remaining one proton, reflecting the existence of a proton in the hydroxyl group. We calculated the proton population in the domains of $z < 0$ and $z > 0$ using the populations of the natural orbitals for the protonic system, and obtained the numerical values of 1.000 and 3.000 for the O atom side and the C atom side, respectively. Note that these numbers of proton(s) are not necessarily to be integer in the present calculation in contrast to the conventional electronic structure calculation in which the number of proton(s) in the hydroxyl group and in the methyl group are assumed to be integer(s) from the beginning. The result above shows a capability of our calculation method to represent the molecular structure with the proper proton distributions in the respective functional groups [6].

Acknowledgements This research was supported by the Ministry of Education, Culture, Sports, Science and Technology (MEXT), Japan; the Grant-in-Aid for Specially Promoted Research on Ultrafast Hydrogen Migration (No.19002006), and the Global COE Program “Chemistry Innovation through Cooperation of Science and Engineering” of the University of Tokyo.

References

1. T. Okino, et al., Coincidence momentum imaging of ultrafast hydrogen migration in methanol and its isotopomers in intense laser fields. *Chem. Phys. Lett.* **423**, 220–224 (2006)
2. H. Xu, T. Okino, K. Yamanouchi, Ultrafast hydrogen migration in allene in intense laser fields: Evidence of two-body Coulomb explosion. *Chem. Phys. Lett.* **469**, 255–260 (2009)
3. T. Kato, K. Yamanouchi, Time-dependent multiconfiguration theory for describing molecular dynamics in diatomic-like molecules. *J. Chem. Phys.* **131**, 164118-1-14 (2009)
4. T. Kato, H. Kono, Time-dependent multiconfiguration theory for electronic dynamics of molecules in intense laser fields: A description in terms of numerical orbital functions. *J. Chem. Phys.* **128**, 184102-01-08 (2008)
5. T. Kato, H. Kono, Time-dependent multiconfiguration theory for electronic dynamics of molecules in an intense laser field. *Chem. Phys. Lett.* **392**, 533–540 (2004)
6. T. Kato, K. Yamanouchi, Protonic structure of CH₃OH described by electroprotonic wave functions. *Phys. Rev. A* **85**, 034504-1-5 (2012)

Chapter 50

Siegert-State Method for Strong Field Ionization of Molecules

L. Hamonou, T. Morishita, O.I. Tolstikhin, and S. Watanabe

Abstract We propose to establish a numerical method to calculate the Siegert states of molecular solution of the stationary Schrödinger equation satisfying the regularity and outgoing-wave Siegert boundary conditions. This work follows the previous one on the atomic Siegert states in an electric field. The previous method enabled the calculation of complex energy eigenvalues and eigenfunctions for one-electron atomic potential. Here we extend the method to molecular cases. We describe necessary modifications for obtaining complex energy eigenvalues and eigenfunctions in more complex molecular cases. We give preliminary results obtained for the simplest molecular ion, H_2^+ .

50.1 Introduction

Over the past few decades, ionisation processes in atoms and molecules by intense laser field have been extensively investigated both theoretically and experimentally. More precisely, in molecular cases the orientation or alignment dependence of the ionisation rates on strong electric field has been proved fundamental to understand strong interaction with molecular systems such as rescattering processes including high-order harmonic generation (HHG), high-energy photoelectron spectra [1], etc. While the MO-ADK model [2] has been widely used to estimate the ionisation rates for various systems, it is known to reach a limit in relatively weak field in the tunneling regime, therefore a new theory is needed to improve the accuracy of ionisation rates obtained and the understanding of the physical processes involved.

L. Hamonou (✉) · T. Morishita · S. Watanabe
Department of engineering Science, University of Electro-communications, Tokyo, Japan
e-mail: linda@power1.pc.uec.ac.jp

O. Tolstikhin
Russian Research Center “Kurchatov Institute”, Moscow, Russia

Siegert states of atoms placed in an electric field, defined as the solutions to the stationary Schrödinger equation satisfying the regularity and outgoing-wave boundary conditions [3], have been obtained by Batishchev et al. [4] within the restriction of the single active electron (SAE) approximation.

We present the molecular formulation of the Siegert-state method as well as the preliminary results obtained in the study of the simplest molecular ion, H_2^+ . We use atomic units if not specified otherwise.

50.2 Basic Equations

The Schrödinger equation for a molecule modeled by a potential $V(\mathbf{r})$ placed in a static uniform electric field F is given by

$$\left(-\frac{1}{2}\Delta + V(\mathbf{r}) + Fz\right)\varphi = E\varphi \quad (50.1)$$

We use the parabolic coordinates η , φ and ξ . The Schrödinger equation (50.1) in parabolic coordinates can be rewritten as

$$\left[\frac{\partial}{\partial\eta}\eta\frac{\partial}{\partial\eta} - \frac{1}{4\eta}\frac{\partial^2}{\partial\varphi^2} + \mathbf{B}(\eta) + \frac{E\eta}{2} + \frac{F\eta^2}{4}\right]\psi(\xi, \eta, \varphi) = 0, \quad (50.2)$$

where

$$\mathbf{B}(\eta) = \frac{\partial}{\partial\xi}\xi\frac{\partial}{\partial\xi} - \frac{1}{4\xi}\frac{\partial^2}{\partial\varphi^2} - \frac{\xi + \eta}{2}V(\xi, \eta, \varphi) + \frac{E\xi}{2} - \frac{F\xi^2}{4}. \quad (50.3)$$

We seek complex eigenvalue $E = \varepsilon - \frac{i}{2}\Gamma$ by iteration for given F , with ε being the energy and Γ being the ionization rate of a particular state. Shifting F slightly, we find the corresponding E .

50.3 Numerical Procedure

The Schrödinger equation is solved using the slow-variable discretization (SVD) method [5] combined with the R-matrix propagation technique [6]. Equation (50.3) is solved by expansion in terms of the direct product of the discrete variable representation (DVR) [7–9] basis sets constructed from polynomials. The solution contains integer and half-integer powers of ξ for $\xi \rightarrow 0$. To allow the representation by a DVR basis, we introduce a new variable $\xi = \zeta^2$.

In the R-matrix theory, the space is divided in two regions. In the inner region, the R-matrix basis is obtained using slow variable discretization (SVD) method. Similarly to the ξ variable, in the molecular problem in order to incorporate the regularity boundary condition $\psi(\xi, \eta)|_{\eta \rightarrow 0} \propto \eta^{|m|/2}$, the solution contains integer

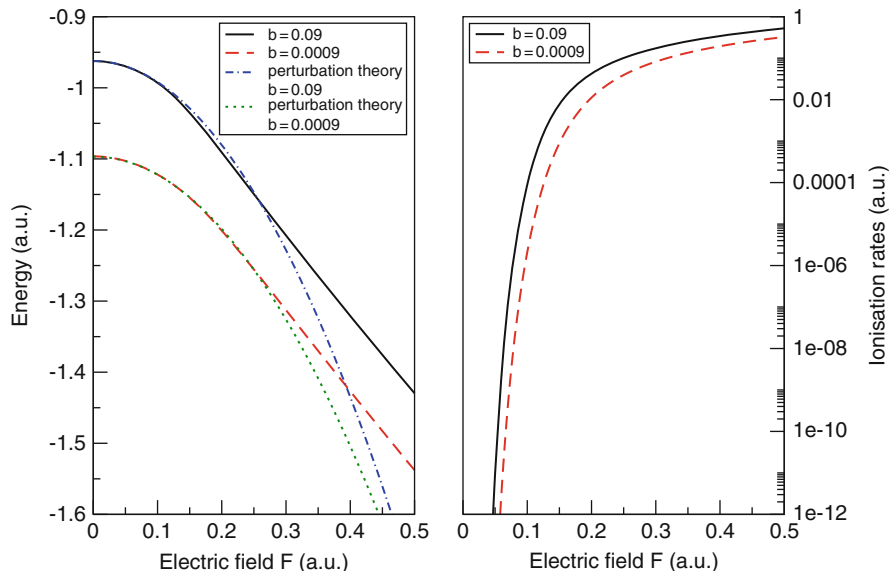


Fig. 50.1 Electric field dependent energies and ionisation rates obtained with two different potentials. The energies are compared with those obtained from perturbation theory

and half-integer powers of η . We thus introduce another change of variables in the first sector, $\eta = \chi^2$ to allow the representation of the solution by a DVR basis set which is based on polynomials. In the outer region, the molecular potential is replaced by a purely coulomb tail allowing the problem to become separable in parabolic coordinates and reducing it to find the solutions to uncoupled equations. The complex quasi energies are obtained by matching the inner-region R-matrix with the outer-region solutions.

50.4 Results

The calculations are performed for H_2^+ molecular ion in this work. We present the results for an internuclear distance fixed to $R = 2$, and the angle between the electric field direction and the molecular axis is set to $\theta = 0$. The molecular ion is modeled by a soft Coulomb potential,

$$V = \frac{1}{2}(\xi + \eta) \left(-\frac{1}{\sqrt{\xi\eta + \left(\frac{(\xi-\eta)}{2} - \frac{R}{2}\right)^2 + b^2}} - \frac{1}{\sqrt{\xi\eta + \left(\frac{(\xi-\eta)}{2} + \frac{R}{2}\right)^2 + b^2}} \right) \quad (50.4)$$

Calculations are performed with softening parameters $b = 0.09$ and $b = 0.0009$. For $b = 0.09$ giving a very rounded potential, the energies obtained are represented by the black curves and compared with energies obtained by perturbation theory in blue on the left hand side whereas the right hand side presents the corresponding ionisation rates in black. For sharper potential with $b = 0.0009$ allowing a better representation of real H_2^+ molecular ion, the energies and ionisation rates are presented by the red curves and compared with perturbation theory's energies. We obtain a good agreement with perturbation theory for electric field $F < 0.25$ which is to be expected as perturbation theory is limited to low electric field (Fig. 50.1).

50.5 Conclusion

We have presented the development necessary to calculate the molecular Siegert states in a static electric field. Starting from an atomic problem enabling the calculation of Siegert states in the single active electron approximation, we extended the problem reducing the use of the symmetries and including the coupling in the φ coordinate to solve molecular problems. This new method enables us to obtain eigenvalues and eigenfunctions for particular Siegert states as a function of a varying electric field for molecules modeled by one-electron potential. The complex eigenvalue obtained from the match of the R-matrix with the out-going wave Siegert boundary condition gives the energy and the ionization rate of a particular state.

References

1. T. Morishita, A.-T. Le, Z. Chen, C.D. Lin, Phys. Rev. Lett. **100**, 013903 (2008)
2. X.M. Tong, Z.X. Zhao, C.D. Lin, Phys. Rev. A **66**, 033402 (2002)
3. A.J.F. Siegert, Phys. Rev. **56**, 750 (1939)
4. P.A. Batishchev, O.I. Tolstikhin, T. Morishita, Phys. Rev. A **82**, 023416 (2010)
5. O.I. Tolstikhin, S. Watanabe, M. Matsuzawa, J. Phys. B **29**, L389 (1996)
6. K.L. Baluja, P.G. Burke, L.A. Morgan, Comput. Phys. Commun. **27**, 299 (1982)
7. D.O. Harris, G.G. Engerholm, W.D. Gwinn, J. Chem. Phys. **43**, 1515 (1965)
8. A.S. Dickinson, P.R. Certain, J. Chem. Phys. **49**, 4209 (1968)
9. J.C. Light, I.P. Hamilton, J.V. Lill, J. Chem. Phys. **82**, 1400 (1985)

Chapter 51

Ionisation and Fragmentation of Small Biomolecules with Femtosecond Laser Pulses

L. Belshaw, O. Kelly, M.J. Duffy, R.B. King, T.J. Kelly, J.T. Costello, I.D. Williams, C.R. Calvert, and J.B. Greenwood

Abstract We report on femtosecond laser studies of small biomolecules, produced in the gas phase via laser induced acoustic desorption. In studies of the aromatic amino acid phenylalanine, we have found that the wavelength of the femtosecond pulse can be used to manipulate molecular fragmentation. These preliminary experiments indicate that this technique provides a promising scheme for investigations of ultrafast dynamics in complex molecules. Future studies should enable temporally resolved observations, by employing ultrafast pump-probe techniques.

51.1 Introduction

The fundamental importance of elucidating and hence understanding ultrafast dynamics in molecular systems has long been recognised, with diatomic molecules the initial test bed for theory and experiment (e.g. [1]). More recently, significant applications of short pulse laser technologies to studies of biological molecules are becoming relevant, as many important biological and chemical processes occur on femtosecond (fs) or sub-femtosecond timescales. Not only do short pulse laser systems allow for time resolved studies, their versatile parameters also allow structural information to be revealed through mass spectrometry studies [2].

In the work presented here, interactions of fs laser pulses with a plume of neutral biomolecules (phenylalanine), created in the gas phase using laser induced acoustic desorption (LIAD) [3], are reported. To date, LIAD has been utilised for mass

L. Belshaw (✉) · O. Kelly · M.J. Duffy · R.B. King · I.D. Williams · C.R. Calvert · J.B. Greenwood

Queen's University Belfast, University Road, Belfast BT7 1NN, UK
e-mail: lbshaw01@qub.ac.uk; j.greenwood@qub.ac.uk

T.J. Kelly · J.T. Costello
Dublin City University, Glasnevin, Dublin 9, Ireland

spectrometry studies, with the production of neutrals coupled to chemical ionisation as a secondary ionisation step [4]. To our knowledge, we have implemented the first studies of biomolecules with an fs laser for ionisation following desorption by LIAD. Variation of the wavelength of the ionising pulse reveals possible control of fragmentation, according to the initial ionisation site. The development of understanding of dynamics and structure in these small systems provides an ideal springboard for future investigations of larger proteins and other biomolecules of interest, such as DNA base pairs and strands.

51.2 Experimental Technique

Laser induced acoustic desorption (LIAD) is a soft desorption method for the production of neutral biomolecules in the gas phase. A molecular sample is deposited on the surface of a metal foil, whose rear side is then irradiated by a ns, UV laser pulse. The laser pulse launches an acoustic shockwave through the foil, causing desorption of the sample from the front surface.

Here, the biomolecular sample was dissolved to a mM concentration in aqueous solution and deposited in steps of 2 μl onto a 10 μm thick tantalum foil and vacuum dried, until a total volume of between 10 and 20 μl had been deposited. The rear side of this foil was irradiated by a UV laser pulse of 355 nm wavelength, ~ 4 ns duration and ~ 0.3 mJ energy. The pulse was focussed onto the back of the foil producing intensities in the range 10^8 – 10^9 W cm^{-2} . The resulting neutral plume, expanding from the foil, was subsequently ionised by an fs laser pulse of 100 fs duration. The delay between the UV desorption pulse and fs ionisation pulse was of the order of 10 μs . The LIAD source was attached to an electrostatic time of flight analyser, enabling a mass spectrum of the fragments from the fs interaction to be obtained.

51.3 Results and Discussion

Figure 51.1 illustrates typical mass spectra obtained following interaction of phenylalanine with 800 nm (a) and 1,400 nm (b) radiation both at a peak intensity of $\sim 4 \times 10^{13}$ W cm^{-2} , and 267 nm (c) at $\sim 8 \times 10^8$ W cm^{-2} . Regardless of the ionising wavelength, the predominant fragments in the mass spectrum can be identified as:

1. 165 amu: the parent molecule, singly ionised
2. 120 amu: the parent molecule with the loss of the COOH group
3. 91 amu: the side chain, or functional group of the amino acid
4. 77 amu: the aromatic benzene ring
5. 74 amu: the parent molecule with the loss of the side chain

The peaks denoted 2 and 5 result from bond breakage due to the charge residing on the NH_2 group. The remaining unpaired electron forms a $\text{N} = \text{C}$ double bond

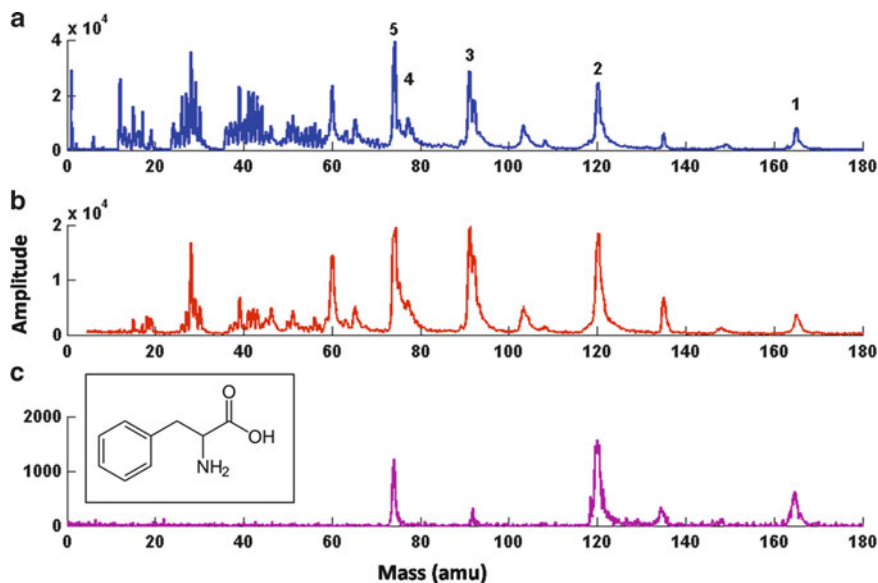


Fig. 51.1 The mass spectra produced following ionisation of phenylalanine with radiation of wavelength (a) 800 nm, (b) 1,400 nm, and (c) 267 nm. The structure of phenylalanine is depicted in the inset. The main fragments, present for all wavelengths, have been annotated 1–5. The peak present at 135 is due to a known contaminant

with an electron transferred from a C–C bond resulting in breakage of the latter. This alpha cleavage mechanism leaves either an immonium ion through loss of COOH (peak 2) or the amino acid backbone (peak 5) from loss of the C_7H_7 chromophore side chain. Peaks 3 and 4 alternatively result from the charge being resident on the chromophore site. It can be observed from Fig. 51.1 that the functional group ion of 91 amu (peak 3) is accompanied by an additional ion at 92 amu with a lower ratio. Its presence is consistent with a McLafferty rearrangement [5] whereby a hydrogen from the NH_2 group is transferred to the charged chromophore.

Besides these common features, varying the ionising wavelength induces differences in the fragmentation of the molecule. In Fig. 51.1a, b, the contribution from molecular masses below 70 at 800 nm is 76% while for 1,400 nm radiation it reduces to 47%. This confirms that for non-resonant multi-photon ionisation of complex molecules, the use of a longer wavelength at a similar intensity significantly reduces the total energy deposited in the molecule resulting in less severe fragmentation [6].

The use of the 267 nm (4.65 eV) third harmonic accesses a resonant transition in the chromophore, enabling the ionisation to be localised on the sidechain through absorption of 1 + 1 photons. Interestingly this does not enhance peaks 3 and 4 in Fig. 51.1c. In fact, peaks 2 and 5 dominate indicating the charge is quickly transferred to the NH_2 . When Fig. 51.1c is compared with the results of near threshold single photoionisation of phenylalanine molecules evaporated from

aerosols [7], the spectrum is similar to that obtained from using 9.3 eV photons at molecular temperatures of 473 K. This suggests that the molecules are desorbed not just through an acoustic shock but from heating of the foil as well.

51.4 Conclusion

The experiment detailed above demonstrates the viability of laser induced acoustic desorption as a technique with which to produce and study neutral biomolecules in the gas phase. By varying the wavelength of the ionising radiation, the fragmentation pattern produced can be controlled. These preliminary studies are encouraging towards investigations of ultrafast dynamics in complex molecules. Further studies will be focussed on experimentally studying phenomena on shorter timescales (few femtoseconds) by employing ultrafast pump-probe techniques.

Acknowledgements LB and MJD acknowledge funding from the Department of Employment and Learning (NI). OK and RBK acknowledge funding from the Leverhulme Trust. CRC acknowledges funding from the EPSRC (UK) Postdoctoral Fellowship for Physics at the Life-Science Interface. The experiments were carried out using the UFL2 laser system from the EPSRC laser loan pool.

References

1. C.R. Calvert, W.A. Bryan, W.R. Newell, I.D. Williams, *Phy. Rep.* **491**, 1 (2010)
2. C.L. Kalcic, T.C. Gunaratne, A.D. Jones, M. Dantus, G.E. Reid, *J. Am. Chem. Soc.* **131**, 940 (2009)
3. V.V. Golovlev, S.L. Allman, W.R. Garrett, N.I. Taranenko, C.H. Chen, *Int. J. Mass Spectrom. Ion Process.* **169–170**, 69 (1997)
4. J.L. Campbell, K.E. Crawford, H.I. Kenttämäa, *Anal. Chem.* **76**, 959 (2004)
5. F.W. McLafferty, *Anal. Chem.* **31**, 82 (1959)
6. D. Willingham, A. Kucher, N. Winograd, *Chem. Phys. Lett.* **468**, 264 (2009)
7. F. Gaie-Levrel, G.A. Garcia, M. Schwell, L. Nahon *Phys. Chem. Chem. Phys.* **13**, 6993 (2011)

Chapter 52

Initial Process of Proton Transfer in Salicylideneaniline Studied by Time-Resolved Photoelectron Spectroscopy

T. Sekikawa, O. Schalk, G. Wu, A.E. Boguslavskiy, and A. Stolow

Abstract Excited state intramolecular proton transfer (ESIPT) in salicylideneaniline (SA) molecules expanded in a supersonic gas jet has been investigated by femtosecond time-resolved photoelectron spectroscopy. Although ESIPT in SA was predicted to take place in a planar structure, the fattening process of a molecule from a twisted Franck–Condon state has never been resolved. Here, we identified the twisting motion of the anilino ring during the fattening process in the decay dynamics of the photoelectron yield, taking account of the energy surface of the $S1(\pi, \pi^*)$ state of the enol form and the potential surface of ESIPT calculated by a time-dependent density functional theory (TDDFT). The twisting motion was found to be slower in the bromide and methylated SAs, while that in the nitrated SA did not change significantly. These substitution effects are explained by the modification of the potential barriers by the substituents, also predicted by the TDDFT calculation, and support the assignment of the decay dynamics to the twisting motion of the anilino ring prior ESIPT.

52.1 Introduction

Proton transfer is a fundamental and important process in biological systems. To understand this process in complicated biological activities, one fruitful approach is the investigation of simpler molecular systems to gain insight into the proton transfer dynamics. Salicylideneaniline (SA), shown in Fig. 52.1, is one of the most

T. Sekikawa (✉)

Department of Applied Physics, Hokkaido University, Sapporo, 060-8628 Japan

e-mail: sekikawa@eng.hokudai.ac.jp

O. Schalk · G. Wu · A.E. Boguslavskiy · A. Stolow

Steele Institute of Molecular Sciences, National Research Council Canada, 100 Sussex Drive, Ottawa, Canada

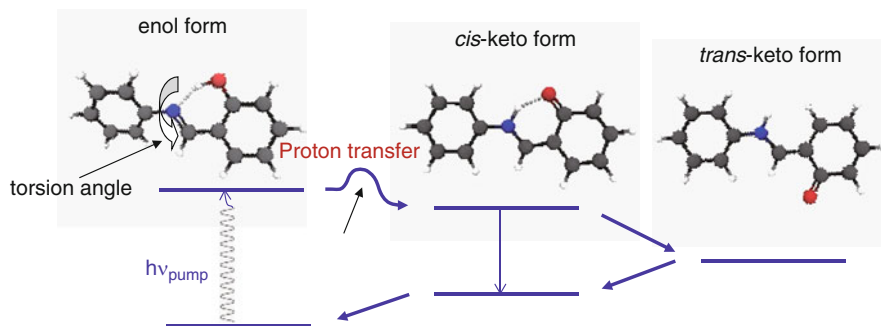


Fig. 52.1 Schematics of the relaxation processes of photo-excited salicylideneaniline

attractive molecules. The basic understanding of excited state proton transfer in SA is as follows: In the ground state, the enol form is more stable than the keto form, while in excited states, the proton-transferred keto form is preferred. Thus, the proton of the hydroxy group migrates on a fs-timescale upon photoexcitation. From there, *cis*–*trans* isomerization takes place and produces the *trans*-keto form. However, advances of experimental and theoretical investigations have revealed that the relaxation process is more complicated. To gain insight into the intrinsic nature of proton transfer dynamics, it is useful to investigate non-interacting molecules. Time-resolved photoelectron spectroscopy (TRPES) of isolated molecules from a supersonic gas jet provides a unique opportunity for such an investigation.

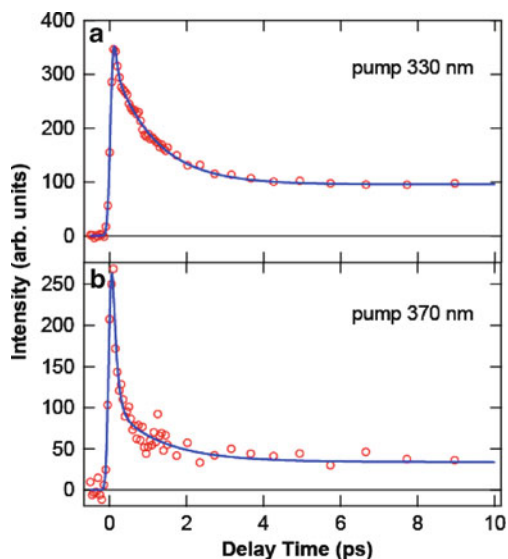
52.2 Experiment

Experimental setup for TRPES was as follows: Ti:sapphire laser pulses were converted into two-color pulses with center wavelengths of 350 and 400 nm. The former was used to pump the molecules and the latter was used to ionize via two-photon absorption. The temporal resolution of the system was 152 fs. Sample molecules were expanded into a vacuum chamber as the supersonic molecular beam with helium gas. The ejected photoelectrons were recorded by a magnetic bottle photoelectron spectrometer.

52.3 Results and Discussion

In this work, we found drastic changes in decay dynamics of photo-induced photoelectron signals depending on the excitation energy. Figure 52.2 shows the time dependent electron count for photoelectrons with kinetic energies between 1.0 and 1.2 eV. When SA was excited by 370-nm photons, a fast decay within 50 fs

Fig. 52.2 Decay dynamics of photoelectron signals pumped at (a) 330 and (b) 370 nm



was observed prominently. This decay is attributable to the proton transfer process. However, when the pump wavelength was shifted to 330 nm, the decay time was lengthened to 1.1 ps. Similar features were observed in all energy regions between 0.1 and 2 eV.

To elucidate the drastic change in the decay time, the energy levels of SA were calculated at B3LYP/aug-cc-pVDZ level of theory. These calculations predict the following points: (1) The ground state of SA is twisted about the anil group by 35° . However, the molecule can basically rotate freely about this group. (2) On the other hand, in S1 state, the planar structure is more stable. Here, the energy strongly correlates with the twist angle. (3) Proton transfer predominantly takes place in the planar structure in excited states because of an increasing barrier upon twisting the anil-group. From these predictions, the different decay dynamics can be understood as follows: 370-nm photons exclusively excite the near-planar SA, in which the proton transfer can happen just after excitation. The lifetime of proton transfer is predicted to be less than 50 fs. At 330-nm, all molecules are excited. The increased barrier reduces the rate constant and forces the molecule to planarize before the proton transfer can happen. The observed 1.1-ps relaxation should correspond to the twisting motion. Hence, planarity of is an important parameter for proton transfer in SA.

Acknowledgements TS was supported by a Grant-in-Aid for Excellent Young Researcher Overseas Visit Program and partially by a Grant-in-Aid for Scientific Research (B) (23340116) from Japan Society for the Promotion of Science. OS thanks the Humboldt foundation for a research fellowship.

Chapter 53

Visualizing Correlated Dynamics of Hydrogen Atoms in Acetylene Dication by Time-Resolved Four-Body Coulomb Explosion Imaging

Akitaka Matsuda, Mizuho Fushitani, Eiji J. Takahashi,
and Akiyoshi Hishikawa

Abstract Ultrafast hydrogen migration in deuterated acetylene dication ($C_2D_2^{2+}$) is studied by time-resolved four-body Coulomb explosion imaging, $C_2D_2^{4+} \rightarrow D^+ + C^+ + C^+ + D^+$, using a pair of few-cycle intense laser pulses (9 fs, 1.3×10^{14} W/cm²). Momentum correlation of the D^+ ions produced by the full fragmentation process shows that (1) motions of the two deuterium atoms are strongly correlated during the isomerization and (2) the molecular structure deforms to non-planar geometries.

53.1 Introduction

Recent advances in laser technology have enabled us to use a few-cycle intense laser pulse (<10 fs, $\sim 10^{15}$ W/cm²) as a new probe to visualize ultrafast chemical reaction dynamics [1]. Molecules exposed to intense laser fields, whose field intensity is comparable to the intramolecular Coulombic field, undergo multiple ionization by ejecting several electrons, and end up in rapid bond breaking called “Coulomb explosion” on the repulsive Coulombic potential energy surface of the highly charged states [2]. Since the Coulomb explosion is induced promptly before any rearrangement process in the molecule, the momenta of the resultant

A. Matsuda · M. Fushitani · A. Hishikawa (✉)
Department of Chemistry, Graduate School of Science, Nagoya University, Furo-cho, Chikusa,
Nagoya, Aichi 464-8602, Japan
e-mail: hishi@chem.nagoya-u.ac.jp

E.J. Takahashi
RIKEN, 2-1 Hirosawa, Wako, Saitama 351-0198, Japan

fragment ions reflect sensitively the geometrical structure of the target molecule just before explosion [3], thus providing direct access to the instantaneous structure of molecules at the time of laser irradiation [4–7].

Due to the large mobility of hydrogen, the ultrafast migration process often determines the main routes of chemical reactions by suppressing other competing processes [8]. Therefore, hydrogen migration is one of the most important molecular rearrangement processes in various chemical reactions [9, 10] as well as in strong laser field phenomena [11–13]. Isomerization of neutral acetylene [8, 14, 15] and its ionic species [16–22] between acetylene (HCCH) and vinylidene (H₂CC) structures has been extensively studied as a prototype of hydrogen migration. We previously reported the visualization of hydrogen migration in acetylene dication [21], by time-resolved three-body Coulomb explosion imaging.

In the present study, we extended our previous study to full fragmentation, four-body Coulomb explosion imaging, in order to clarify the correlated motion of the hydrogen atoms during the migration process in deuterated acetylene dication (C₂D₂²⁺) [23].

53.2 Experiment

The output from a Ti:Sapphire laser system (40 fs, 800 nm, 1 kHz, 1 mJ/pulse) is coupled by a lens ($f = 1, 200$ mm) to a hollow fiber (500 μ m core diameter) filled with Ar gas (0.07 MPa). The fiber output is collimated by a concave silver mirror and recompressed using dispersive mirrors to obtain a few-cycle 9 fs laser pulse with a maximum energy of 400 μ J. The obtained 9 fs laser pulse is forwarded into a broadband, high-precision Michelson-type interferometer to generate a pair of pulses, which are introduced into an ultrahigh vacuum chamber and focused onto the molecular beam by using a concave silver mirror. The laser field intensities of the pulses are 1.3×10^{14} W/cm² at the focal spot. The pump pulse is used to doubly ionize C₂D₂ to C₂D₂²⁺ and to trigger the hydrogen migration in acetylene dication, and the time-delayed probe pulse is used to induce the four-body Coulomb explosion (Fig. 53.1a).

The fragment ions produced from the target molecule in the Coulomb explosion process are guided towards a position sensitive detector (HEX80, RoentDek) by the electric field generated with four electrodes in velocity mapping configuration. All fragment ions originating from a single parent ion are detected in coincidence, and therefore, the Coulomb explosion pathway is securely assigned. The momenta of the fragment ions [labeled as p_1 , p_2 for deuterium ions, p_3 , p_4 for carbon ions, respectively (Fig. 53.1b)] are determined as three-dimensional vectors from the (x , y) position and the time-of-flight t of the arrival of the respective fragment ions at the detector.

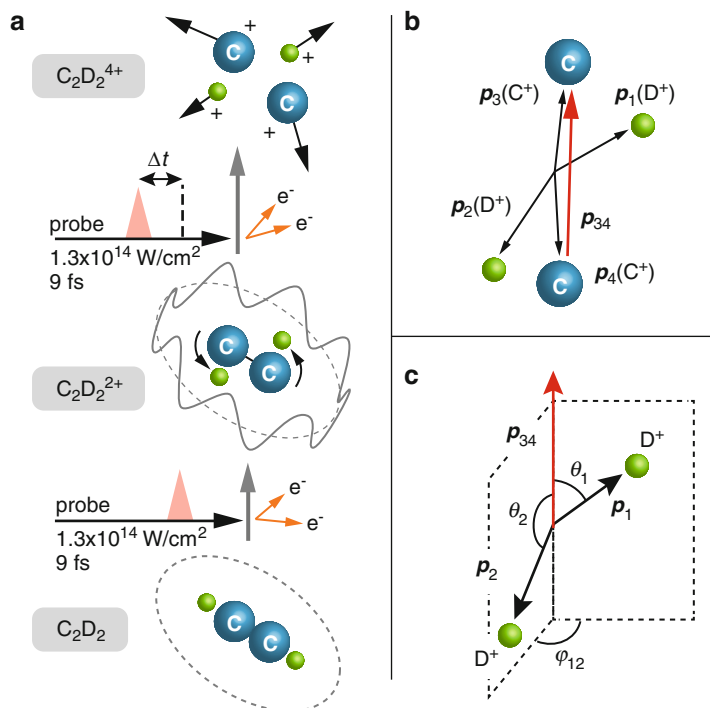


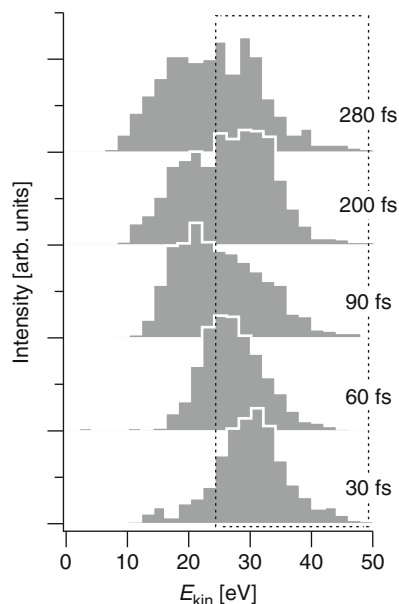
Fig. 53.1 (a) Scheme of pump-probe four-body Coulomb explosion imaging employed in the present study. (b) Definition of the momenta of the fragment ions generated in four-body Coulomb explosion. p_{34} is defined as the difference between p_3 and p_4 . (c) Definition of the polar (θ_1 , θ_2) and azimuthal (φ_{12}) angles

53.3 Results and Discussion

First we discuss the time evolution of the total kinetic energy release, $E_{\text{kin}} = \sum |\mathbf{p}_i|^2/2m_i$, shown in Fig. 53.2, where \mathbf{p}_i and m_i are the momenta and the mass of the fragment ions. At a small time delay ($\Delta t = 30$ fs), a peak centered at 30 eV is observed, however a new component with smaller kinetic energies appears at $\Delta t = 60$ fs which shifts to $E_{\text{kin}} \sim 20$ eV as Δt increases. The decrease in E_{kin} is explained by the increase in inter-fragment distances. Therefore, the new component at the lower energy side is attributed to dissociating molecules. The components with $E_{\text{kin}} \geq 24$ eV are used for further analysis to clarify the hydrogen migration dynamics in stable or undissociated $C_2D_2^{2+}$.

In order to discuss the correlated dynamics between the two deuterium atoms in the molecular frame, a momentum vector, \mathbf{p}_{34} , is defined as the difference between the two C^+ ions, $\mathbf{p}_{34} = \mathbf{p}_3 - \mathbf{p}_4$, which approximately represents the C–C bond (Fig. 53.1b). Momentum angles between \mathbf{p}_{34} and the momentum vectors of the respective D^+ ions, \mathbf{p}_1 and \mathbf{p}_2 , are defined as θ_1 and θ_2 , which reflect the

Fig. 53.2 Time evolution of the total kinetic energy release (E_{kin}). Each distribution is normalized by the peak value. The area highlighted by the dotted box with $E_{\text{kin}} \geq 24$ eV corresponds to components from stable or undissociated C_2D_2^+



positions of the deuterium atoms in the molecular frame (Fig. 53.1c). In addition, a momentum angle, φ_{12} , is defined as an angle between the two planes, one spanned by \mathbf{p}_{34} and \mathbf{p}_1 , and the other by \mathbf{p}_{34} and \mathbf{p}_2 , which represents the azimuthal correlation of the deuterium atoms (Fig. 53.1c).

The time evolution of the θ_1 – θ_2 correlation is shown in Fig. 53.3a. At a small time delay ($\Delta t = 30$ fs), distributions are observed around $(\theta_1, \theta_2) = (0^\circ, 180^\circ)$ and $(180^\circ, 0^\circ)$, which indicates that the two D^+ ions dissociate along the C–C bond with momenta to the opposite direction. Therefore, the two deuterium atoms exist around the original carbon site and the acetylene structure is preserved. As Δt increases, the distribution extends along the diagonal line, and at $\Delta t = 90$ fs, a new feature is clearly observed at $(\theta_1, \theta_2) = (90^\circ, 90^\circ)$, which shows that the D atom moved from its original carbon site to the other. At a longer time delay ($\Delta t = 280$ fs), the new feature disappears and the distributions at around $(\theta_1, \theta_2) = (0^\circ, 180^\circ)$ and $(180^\circ, 0^\circ)$ reappear. This finding shows that the isomerization occurs in 90 fs, followed by further hydrogen migration back to the original acetylene structure in 280 fs, which agrees well with our previous result obtained using three-body Coulomb explosion imaging [21].

The obtained correlation map in Fig. 53.3a shows a strong distribution along the diagonal line. This indicates that the decrease in θ_2 is always accompanied by the increase in θ_1 , showing that the motion of the two deuterium atoms are strongly correlated during hydrogen migration; when one deuterium atom starts moving, the other deuterium atom also starts moving from the other carbon site.

The correlation of the momentum angles provides a more detailed picture. The new feature observed in the θ_1 – θ_2 correlation at $(\theta_1, \theta_2) = (90^\circ, 90^\circ)$ deviates from

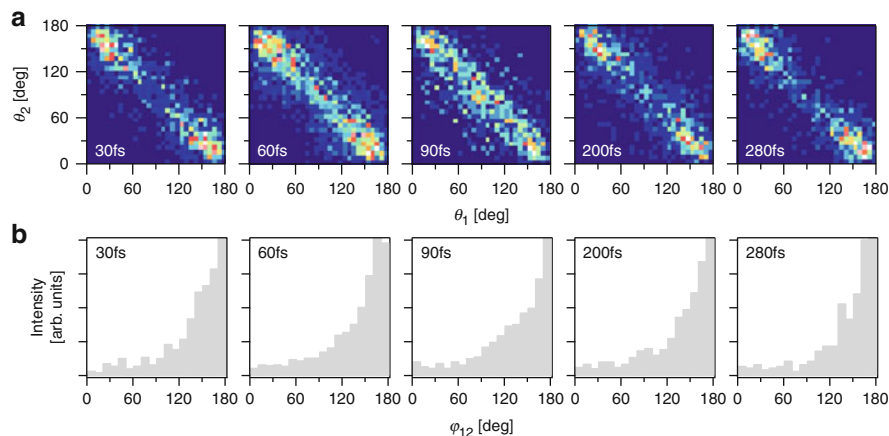


Fig. 53.3 (a) Two-dimensional correlation map between the polar angles θ_1 and θ_2 obtained for the stable or undissociated components at $\Delta t = 30, 60, 90, 200,$ and 280 fs. (b) The corresponding azimuthal momentum angle (φ_{12}) distributions. Each distribution is normalized by the peak value

the distribution expected for a typical vinylidene structure which corresponds to $(\theta_1, \theta_2) = (64^\circ, 64^\circ)$ and $(116^\circ, 116^\circ)$. As shown in the time evolution of the φ_{12} distribution (Fig. 53.3b), the tail extends more towards 0° at $\Delta t = 90$ fs than those at 30 and 280 fs. This indicates that there exists a significant contribution from non-planar structure, showing that hydrogen migration occurs in a broad structural distribution containing non-planar geometries.

53.4 Summary

We studied the ultrafast hydrogen migration in acetylene dication ($C_2D_2^{2+}$), by means of time-resolved four-body Coulomb explosion imaging with 9 fs intense laser pulses. The full fragmentation process clarified the strong correlation of the motion of the deuterium atoms during the hydrogen migration, and the structural deformation to non-planar geometries. The time-resolved Coulomb explosion imaging employed in this study is readily applicable, for instance, to neutral molecules by using a tunable ultrashort laser pulse to resonantly trigger photochemical reactions. The direct visualization of the ultrafast molecular dynamics will provide deep insights into the chemical reaction and offer a perspective on efficient coherent reaction control with tailored pulses.

Acknowledgements This work is supported by the PRESTO fund for “Evolution of Light Generation and Manipulation” from Japan Science and Technology Agency and by the Grant in Aid (#15685001) from MEXT of Japan.

References

1. C. Altucci, R. Velotta, J.P. Marangos, *J. Mod. Opt.* **57**, 916 (2010)
2. J.H. Posthumus, *Rep. Prog. Phys.* **67**, 623 (2004)
3. F. Légaré, K.F. Lee, I.V. Litvinyuk, P.W. Dooley, S.S. Wesolowski, P.R. Bunker, P. Dombi, F. Krausz, A.D. Bandrauk, D.M. Villeneuve, P.B. Corkum, *Phys. Rev. A* **71**, 013415 (2005)
4. Th. Ergler, A. Rudenko, B. Feuerstein, K. Zrost, C.D. Schröter, R. Moshhammer, J. Ullrich, *Phys. Rev. Lett.* **95**, 093001 (2005)
5. E. Skovsen, M. Machholm, T. Ejdrup, J. Thøgersen, H. Stapelfeldt, *Phys. Rev. Lett.* **89**, 133004 (2002)
6. A. Hishikawa, M. Ueyama, K. Yamanouchi, *J. Chem. Phys.* **122**, 151104 (2005)
7. F. Légaré, K.F. Lee, I.V. Litvinyuk, P.W. Dooley, A.D. Bandrauk, D.M. Villeneuve, P.B. Corkum, *Phys. Rev. A* **72**, 052717 (2005)
8. H.F. Schaefer III, *Acc. Chem. Res.* **12**, 288 (1979)
9. Y. Wakatsuki, H. Yamazaki, N. Kumegawa, T. Satoh, J.Y. Satoh, *J. Am. Chem. Soc.* **113**, 9604 (1991)
10. A.M. Mebel, E.W.G. Diau, M.C. Lin, K. Morokuma, *J. Am. Chem. Soc.* **118**, 9759 (1996)
11. A. Hishikawa, H. Hasegawa, K. Yamanouchi, *J. Electron Spectrosc. Relat. Phenom.* **141**, 195 (2004)
12. A.N. Markevitch, D.A. Romanov, S.M. Smith, R.J. Levis, *Phys. Rev. Lett.* **96**, 163002 (2006)
13. H. Xu, T. Okino, K. Yamanouchi, *J. Chem. Phys.* **131**, 151102 (2009)
14. K.M. Ervin, J. Ho, W.C. Lineberger, *J. Chem. Phys.* **91**, 5974 (1989)
15. M.P. Jacobson, R.W. Field, *J. Phys. Chem. A* **104**, 3073 (2000)
16. R. Thissen, J. Delwiche, J.M. Robbe, D. Duflot, J.P. Flament, J.H.D. Eland, *J. Chem. Phys.* **99**, 6590 (1993)
17. D. Duflot, J.M. Robbe, J.P. Flament, *J. Chem. Phys.* **102**, 355 (1995)
18. M.J. Jensen, U.V. Pedersen, L.H. Andersen, *Phys. Rev. Lett.* **84**, 1128 (2000)
19. T. Osipov, C.L. Cocke, M.H. Prior, A. Landers, Th. Weber, O. Jagutzki, L. Schmidt, H. Schmidt-Böcking, R. Dörner, *Phys. Rev. Lett.* **90**, 233002 (2003)
20. T.S. Zyubina, Y.A. Dyakov, S.H. Lin, A.D. Bandrauk, A.M. Mebel, *J. Chem. Phys.* **123**, 134320 (2005)
21. A. Hishikawa, A. Matsuda, M. Fushitani, E.J. Takahashi, *Phys. Rev. Lett.* **99**, 258302 (2007)
22. Y.H. Jiang, A. Rudenko, O. Herrwerth, L. Foucar, M. Kurka, K.U. Kühnel, M. Lezius, M.F. Kling, J. van Tilborg, A. Belkacem, K. Ueda, S. Düsterer, R. Treusch, C.D. Schröter, R. Moshhammer, J. Ullrich, *Phys. Rev. Lett.* **105**, 263002 (2010)
23. A. Matsuda, M. Fushitani, E.J. Takahashi, A. Hishikawa, *Phys. Chem. Chem. Phys.* **13**, 8697 (2011)

Chapter 54

Ultrafast Delocalization of Protons in Methanol and Allene in Intense Laser Fields

Huailiang Xu, Tomoya Okino, Katsunori Nakai, and Kaoru Yamanouchi

Abstract Ultrafast hydrogen migration in methanol and allene induced by intense laser fields was investigated by Coulomb explosion coincidence momentum imaging (CMI). For methanol, it was shown that there are two distinctively different stages in the hydrogen migration processes in singly charged methanol, i.e., ultrafast hydrogen migration occurring within the intense laser field, and slower post-laser pulse hydrogen migration, showing quantum mechanical nature of light protons. For allene, the distribution of a proton covering the wide spatial area in an allene molecule was visualized by the momentum correlation maps constructed from the observed momentum vectors of fragment ions.

54.1 Introduction

Ultrafast molecular dynamics in intense laser fields has been one of the most attractive research subjects in recent years [1, 2]. Hydrogen migration, i.e., the migration of hydrogen atoms or protons from one site to another within a molecule, is one of such chemical-bond rearrangement processes. The hydrogen migration process can induce large scale deformation of molecular skeletal structure and has so far been demonstrated in various hydrocarbon molecules (see e.g. [3]). In view of the importance of the hydrogen migration in controlling chemical bond

H. Xu

Department of Chemistry, School of Science, The University of Tokyo, Tokyo 113-0033, Japan
e-mail: kaoru@chem.s.u-tokyo.ac.jp

State Key Laboratory on Integrated Optoelectronics, College of Electronic Science and Engineering, Jilin University, Changchun 130012, China

T. Okino · K. Nakai · K. Yamanouchi (✉)

Department of Chemistry, School of Science, The University of Tokyo, Tokyo 113-0033, Japan
e-mail: kaoru@chem.s.u-tokyo.ac.jp

breaking and chemical bond formation processes, it would be worthy to investigate experimentally how such a large-scale proton migration proceeds in an intense laser field.

The proton motion within a molecule was considered to proceed very rapidly, and it was predicted that this process could occur within the light field [4, 5]. This argument was based on the assumption that those doubly or triply charged species undergo Coulomb explosion immediately after they are formed by the most intense part of the laser pulse and the hydrogen migration proceeds prior to the Coulomb explosion. The observation that the extent of anisotropy in the ejection direction of the fragment ions for the migration pathways is the same as that for the non-migration pathways was considered to be the evidence that ultrafast hydrogen migration proceeds within the laser field [5]. On the other hand, a post-pulse slower motion of a deuterium atom was shown for deuterated acetylene dication [6].

In this article, we review our recent study on the real time probing of hydrogen migration in methanol (CH_3OH) by a pump–probe coincidence momentum imaging (CMI) method [7], in which we identified two stages in the ultrafast hydrogen migration processes, that is, the instantaneous transfer of a proton from the carbon atom site to the oxygen atom site occurring within the ultrashort laser pulse, and the unimolecular isomerization processes occurring with a time scale of ~ 150 fs after the light-matter interaction.

We also introduce our recent study on the three-body Coulomb explosion processes of allene (CH_2CCH_2) by the CMI method [8], in which we found that the distribution of a proton became very broad within a molecule by the ultrafast hydrogen migration induced by an intense laser field. In the present report, we present the spread of the proton distribution in terms of the momentum correlation maps constructed from the observed momentum vectors of the fragment ions ejected from triply charged allene, $\text{C}_3\text{H}_4^{3+}$.

On the basis of these results we show an important role played by hydrogen migration in dynamical processes of hydrocarbon molecules in an intense laser field.

54.2 Experiments

The light source used in the experiments was a Ti:Sapphire femtosecond laser system (Pulsar 5000, Amplitude Technologies), in which output pulses from a Ti:Sapphire oscillator (Femtosource S20, Femtolasers) were positively chirped to ~ 100 ps in an aberration-free stretcher, and then the pulses were amplified at a high-repetition-rate (5 kHz) amplification stage, composed of a regenerative amplifier, a two-pass preamplifier and a cryogenically cooled four-pass amplifier, and finally, compressed by a two-grating compressor. In order to shorten the pulse duration, an acousto-optic programmable dispersive filter (Dazzler, Fastlite) was placed between the stretcher and the regenerative amplifier to control simultaneously the spectral phase and amplitude of the pulses, whose central wavelength was 795 nm. In the methanol case, a pair of linearly polarized laser beam were generated through a

Michelson-type interferometer with a variable time delay Δt ($= 100 \sim 800$ fs). Both of the pump and probe laser pulses were introduced into a main ultrahigh-vacuum chamber through a quartz lens ($f = 15$ cm) to achieve a light field intensity of $\sim 4 \times 10^{13}$ W/cm² at the focal spot. The minimum time delay of $\Delta t = 100$ fs was chosen to avoid the optical interference of the two laser pulses. The increment of the time delay was set to be 50 fs with the uncertainty of 0.5 fs. In the allene case, the laser field intensity was $\sim 4 \times 10^{13}$ W/cm² at the focal spot.

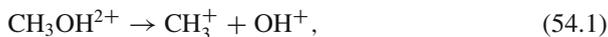
For both cases of methanol and allene, the sample gas was introduced into the sample vacuum chamber through a micro-syringe (0.51 mm ϕ), and then skimmed by a skimmer (0.48 mm ϕ) to form a molecular beam in the main ultrahigh vacuum chamber, whose base pressure was $\sim 3 \times 10^{-11}$ Torr. The molecular beam and the laser beam crossed at right angles, and the ions generated at the laser focal spot in the molecular beam were projected onto a position-sensitive detector (PSD) with delay-line anode readouts (RoentDek DLD 80) by three equally spaced parallel-plate electrodes in the velocity mapping configuration. The laser polarization direction, the surface of the electrode plates, and the surface of the detector were all set to be parallel to the plane formed by the molecular beam and laser beam axes.

The three-dimensional momentum vectors of i th fragment ions were determined by their positions (x_i, y_i) and arrival time (t_i) on the detector plane. False coincidence events originating from the fragment ions generated from two or more parent ions in the interaction region were excluded by imposing the momentum conservation condition on the sum of the momentum vectors of all the fragment ions ejected from a single parent ion. In order to secure the coincidence conditions, the number of events of the generation of ionic species per laser shot was kept to be 0.4–0.5 events/pulse. The details of the coincidence measurement were reported in [9].

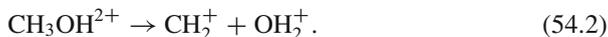
54.3 Results and Discussion

54.3.1 Methanol

Two types of two-body Coulomb explosion processes of CH₃OH²⁺ are probed in real time as a function of the time delay, Δt , between the pump and probe pulses, that is, the pathway in which the C–O bond is broken without the hydrogen migration,



and the pathway in which the C–O bond is broken after the migration of one hydrogen atom from the methyl group to the hydroxyl group,



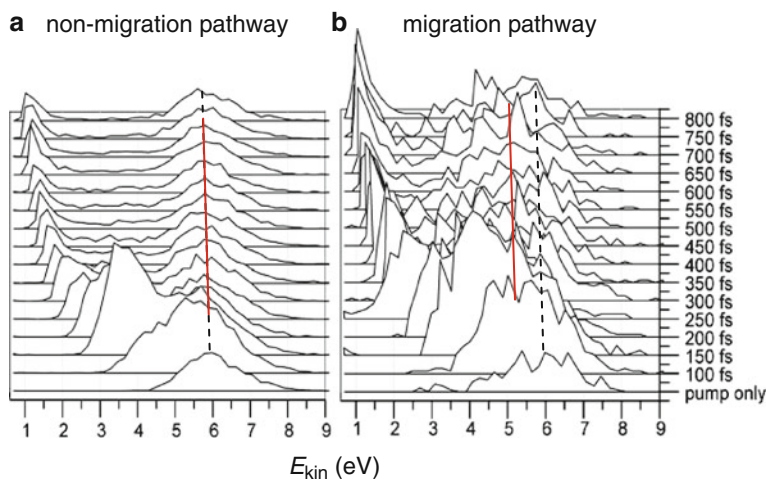


Fig. 54.1 The kinetic energy distributions of the fragment ions released from the pathways (a) $\text{CH}_3\text{OH}^{2+} \rightarrow \text{CH}_3^+ + \text{OH}^+$ and (b) $\text{CH}_3\text{OH}^{2+} \rightarrow \text{CH}_2^+ + \text{OH}_2^+$. The energy distributions of these two pathways after the irradiation with only one laser pulse excitation are both peaked at ~ 5.9 eV (dash lines). The red lines show the peak positions at 5.9 and 5.2 eV, respectively

Based on the three-dimensional momentum distributions of the fragment ions, the sum of the kinetic energy released from a pair of the fragment ions, E_{kin} , is obtained, as shown in Fig. 54.1. It can be seen in both cases of (Fig. 54.1a) and (Fig. 54.1b) that the kinetic energy can be categorized into two parts, i.e., the peaks where the kinetic energy distributions are independent of Δt , and the peaks where the kinetic energy distributions shift towards lower energies as Δt increases, exhibiting a time-dependent behavior.

The time-dependent lower peaks in Fig. 54.1a, b reflect the temporal evolution of a dissociating wave packet of the $(\text{CH}_3 \cdots \text{OH})^+$ and that of $(\text{CH}_2 \cdots \text{OH}_2)^+$, respectively. The time dependent behavior can be interpreted as follows. First the pump laser pulse prepares the singly charged $(\text{CH}_3 \cdots \text{OH})^+$ and hydrogen-migrated $(\text{CH}_2 \cdots \text{OH}_2)^+$ in the energy region higher than the dissociation barrier, and these species start dissociation. After a certain temporal delay before the complete dissociation, the probe laser pulses ionize $(\text{CH}_3 \cdots \text{OH})^+$ into $(\text{CH}_3 \cdots \text{OH})^{2+}$, and $(\text{CH}_2 \cdots \text{OH}_2)^+$ into $(\text{CH}_2 \cdots \text{OH}_2)^{2+}$. By the ionization, the respective wave packets of the singly charged dissociating ions are projected onto the mostly repulsive Coulomb potential energy surfaces (PESs) of the doubly charged manifold. Therefore, the kinetic energies released from the two-body Coulomb explosion processes through the non-migration pathway, (54.1), and the migration pathway, (54.2), decrease as the delay time increases, resulting in the increase in the distance between CH_3^+ and OH^+ and that between CH_2^+ and OH_2^+ , converted from the released kinetic energies.

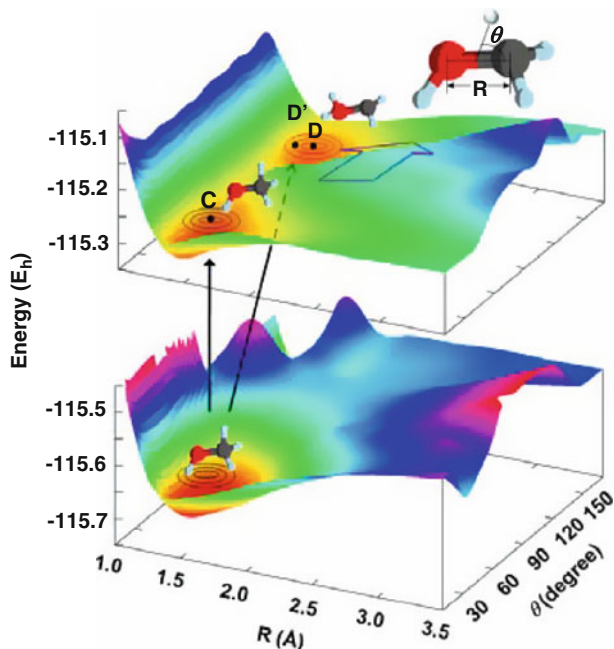


Fig. 54.2 Ground-state potential energy surfaces of CH_4O^+ and CH_4O ; the inset is the schematic molecular model for the definitions of the structural parameters: R , the C–O bond distance, and θ , the angle between the C–O bond and the position vector of the migrating hydrogen atom with respect to the center of the C–O bond. All the structural parameters other than R and θ are optimized in the calculation of the PESs

Interestingly, it can be seen in Fig. 54.1 that the time-independent peaks in Fig. 54.1a are centered at ~ 5.9 eV, while the ones in Fig. 54.1b are centered at ~ 5.2 eV. Contrary, when the non-migration pathway through (54.1) and the migration pathway through (54.2) are induced only by the pump laser, the kinetic energy distributions of the fragment ions ejected from both the non-migration and migration pathways are peaked at ~ 5.9 eV. This observation that the peak position of 5.2 eV for the migration pathway shown in Fig. 54.1b is lower by as much as 0.7 eV than the pump-only value of 5.9 eV can be interpreted in terms of the landscape of the PES of singly charged CH_4O^+ .

In Fig. 54.2, the calculated PESs of the ground states of CH_4O^+ and CH_4O obtained by the density functional theory at the UB3LYP/6–31G(d) level with the Gaussian 03 program are shown. It can be seen that there are two minima at around C (1.37 Å, 45°) and D (1.46 Å, 145°) on the PES of CH_4O^+ , representing the two geometrical structures, CH_3OH^+ and CH_2OH_2^+ , respectively.

The difference in the kinetic energy distributions shown in the time-independent peaks for CH_3OH^+ and CH_2OH_2^+ can be ascribed to the difference in their geometrical structures. When the pump laser pulse prepares a molecular wave packet

of CH_3OH^+ and that of CH_2OH_2^+ on the PES around C and D shown in Fig. 54.2, the probe laser pulse, after a certain temporal delay, ionizes CH_3OH^+ from the well C into $(\text{CH}_3\cdots\text{OH})^{2+}$, and CH_2OH_2^+ from the well D into $(\text{CH}_2\cdots\text{OH}_2)^{2+}$, which explode into the two singly charged fragment ions in each pathway through the breaking of the C–O bond. Since the C–O bond length in the well C (1.37 Å) is shorter than that in the well D (1.46 Å), the kinetic energy released from the dissociation of $(\text{CH}_3\cdots\text{OH})^{2+}$ is expected to be larger than that from the dissociation of $(\text{CH}_2\cdots\text{OH}_2)^{2+}$, which is in good agreement with the kinetic energy releases for the non-migrated (5.9 eV) and the migrated (5.2 eV) species.

The observation that the peak position of 5.2 eV for the migration pathway exhibits a large difference from the pump-only value further reveals the dynamics of the hydrogen migration within a singly charged methanol molecule. The observed peak positions at ~ 5.9 eV for both the non-migration and migration pathways indicate that the distance between the two dissociating moieties in the precursor species $\text{CH}_3^+\cdots\text{OH}^+$ and that in $\text{CH}_2^+\cdots\text{OH}_2^+$ does not change so much during the double ionization processes from neutral methanol by a 38-fs laser pulse. Since the Coulomb explosion is considered to occur immediately after the formation of doubly charged $\text{CH}_3^+\cdots\text{OH}^+$ and $\text{CH}_2^+\cdots\text{OH}_2^+$ species, the hydrogen migration should proceed during the single ionization. Therefore, the singly charged $(\text{CH}_2\cdots\text{OH}_2)^+$ can be prepared in the area D' in Fig. 54.2, where the C–O distance is close to that in the area A for $(\text{CH}_3\cdots\text{OH})^+$, rather than in the area around the bound well D. The observation that the peak position of the kinetic energy distribution in Fig. 54.1b at $\Delta t = 100$ fs decreases from 5.9 to 5.2 eV shows that the C \cdots O distance in CH_2OH_2^+ is stretched from D' to D after being irradiated with the pump pulse.

The calculated energy of the transition state located between CH_3OH^+ and CH_2OH_2^+ is 1.51 and 1.48 eV higher than the potential minimum around C and that around D, respectively. Therefore, when a methanol molecule is prepared on the PES in the wells of C and D after the pump pulse irradiation, the hydrogen migration would not proceed on the PES because of the barrier separating these two wells, and thus, the relative ion yield obtained from the yield of the non-migration pathway ($\gamma_{\text{non-mig}}$) and that of the migration pathway (γ_{mig}) with respect to the total ion yield ($\gamma_{\text{total}} = \gamma_{\text{non-mig}} + \gamma_{\text{mig}}$) defined as $\eta_{\text{non-mig}} = \gamma_{\text{non-mig}}/\gamma_{\text{total}}$ and $\eta_{\text{mig}} = \gamma_{\text{mig}}/\gamma_{\text{total}}$ are expected to be constant. This is indeed the case as observed in our experiment. In Fig. 54.3a, b, $\eta_{\text{non-mig}}$ and η_{mig} are plotted as a function of the time delay for the time-independent peaks shown in Fig. 54.1a, b with $E_{\text{kin}} > 3.8$ eV. It can be seen that the yield ratios, $\eta_{\text{non-mig}}$ and η_{mig} , are independent of the time delay between the pump and the probe pulses.

Contrary, $\eta_{\text{non-mig}}$ and η_{mig} plotted in Fig. 54.3c, d for the time-dependent peaks shown in Fig. 54.1a, b with $E_{\text{kin}} \leq 3.8$ eV exhibit clear temporal change. As the time delay increases, $\eta_{\text{non-mig}}$ in Fig. 54.3c decreases, but η_{mig} in Fig. 54.3d increases, showing that the hydrogen migration proceeds even after molecules interact with the intense laser field. The time constant for this post-laser pulse hydrogen migration is evaluated to be ~ 150 (50) fs. This is because the dissociation energies of the C–O

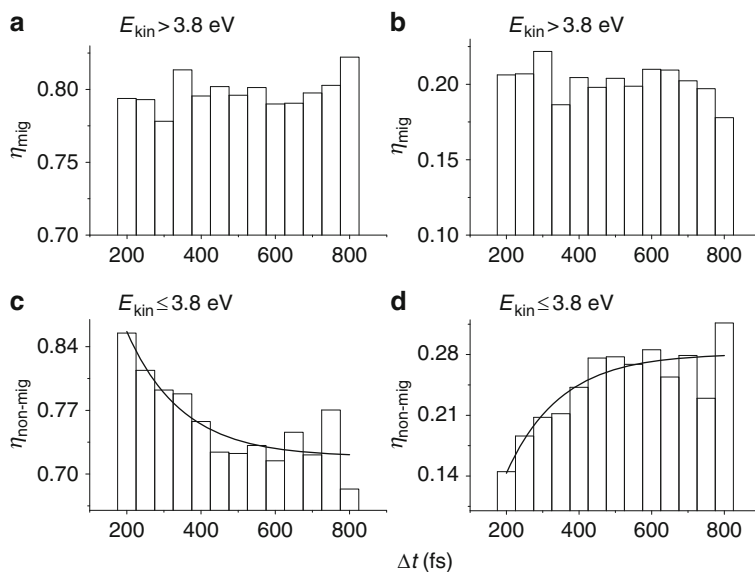


Fig. 54.3 The yield ratio of the non-migrated and migrated species $\eta_{\text{non-mig}}$ and η_{mig} as a function of Δt for the time-independent peaks ($E_{\text{kin}} > 3.8$ eV) in (a) and (b), and the time-dependent peaks ($E_{\text{kin}} \leq 3.8$ eV) in (c) and (d), shown in Fig. 54.1. The solid curves are the best-fit curves obtained by a least-squared fit

bond that are calculated to be ~ 3.2 eV for both CH_3OH^+ and CH_2OH_2^+ is much higher than the height of the barrier (~ 1.5 eV) for the migration reactions between CH_3OH^+ and CH_2OH_2^+ . Therefore, once CH_3OH^+ and CH_2OH_2^+ are prepared by the first pulse in the energy range above the threshold for the dissociation along the C–O bond, thus also above the barrier for the hydrogen migration, the post-laser pulse hydrogen migration can proceed.

54.3.2 Allene

As an example of the investigation of ultrafast hydrogen migration by the three-body Coulomb explosion of a triply charged parent hydrocarbon molecule, we introduce here our recent study on the hydrogen migration in allene. Because a triply charged allene molecule is considered to be decomposed into three fragment ions through the three-body Coulomb explosion immediately after its formation, the analysis of the momentum vectors of the three fragment ions projected onto a 3D momentum space enables us to construct the momentum correlation maps of the fragment ions and to estimate the position of the proton with respect to the other two moieties within a triply charged allene ($\text{C}_3\text{H}_4^{3+}$) just before the Coulomb explosion.

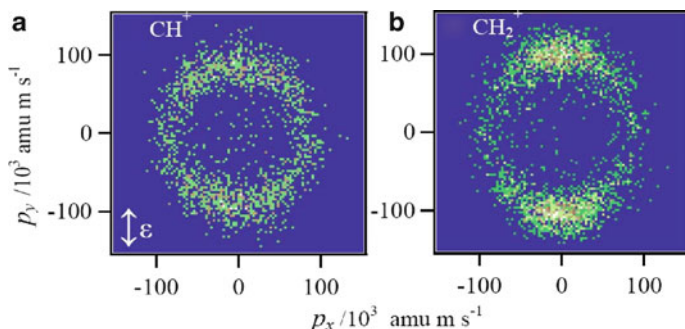


Fig. 54.4 Observed two-dimensional coincidence momentum maps of (a) CH^+ , and (b) CH_2^+ produced through the three-body Coulomb explosion processes of $\text{C}_3\text{H}_4^{3+}$. The laser polarization direction (ε) is set to be parallel with the p_y axis as indicated by the arrow

In Fig. 54.4, the momentum imaging map of CH^+ , appearing in coincidence with H^+ and C_2H_2^+ , and that of CH_2^+ , appearing in coincidence with H^+ and C_2H^+ , are shown in Fig. 54.4a and b, respectively. This shows that the following two three-body Coulomb explosion decomposition pathways of $\text{C}_3\text{H}_4^{3+}$ are unambiguously identified:



In order to extract the dynamics of these two pathways, the correlation among the three fragment ions of each pathway is plotted in terms of the two angle variables, χ_i and θ_i , defined as [10]

$$\chi_i = \cos^{-1} \left[\left(\frac{\Delta \mathbf{p}_i}{\Delta p_i} \right) \cdot \left(\frac{\mathbf{p}_{3i}}{p_{3i}} \right) \right] \quad (54.5)$$

and

$$\theta_i = \cos^{-1} \left[\left(\frac{\mathbf{p}_{1i}}{p_{1i}} \right) \cdot \left(\frac{\mathbf{p}_{2i}}{p_{2i}} \right) \right], \quad (54.6)$$

where $i = 1$, and 2 represent respectively *Pathway (54.3)* and *Pathway (54.4)*, \mathbf{p}_{1i} , \mathbf{p}_{2i} , and \mathbf{p}_{3i} are the momentum vectors of the three fragment ions in *Pathway (i)*, and the momentum difference $\Delta \mathbf{p}_i$ is defined as $\Delta \mathbf{p}_i = \mathbf{p}_{1i} - \mathbf{p}_{2i}$. The parameters p_{1i} , p_{2i} , and p_{3i} and Δp_i are the magnitudes of \mathbf{p}_{1i} , \mathbf{p}_{2i} , \mathbf{p}_{3i} , and $\Delta \mathbf{p}_i$, respectively. The parameter χ_i is the angle between $\Delta \mathbf{p}_i$ and \mathbf{p}_{3i} , and θ_i is the angle between \mathbf{p}_{1i} and \mathbf{p}_{2i} .

In Fig. 54.5a, the $\chi_1 - \theta_1$ plot of *Pathway (54.3)* is shown, where χ_1 represents the extent of hydrogen migration from the moiety C_2H^+ to CH_2^+ , and θ_1 represents the angle between the ejection directions of the two moieties C_2H^+ and CH_2^+ . When $\chi_1 \sim 0^\circ$, the proton is located at around its original position, and when $\chi_1 \sim 180^\circ$,

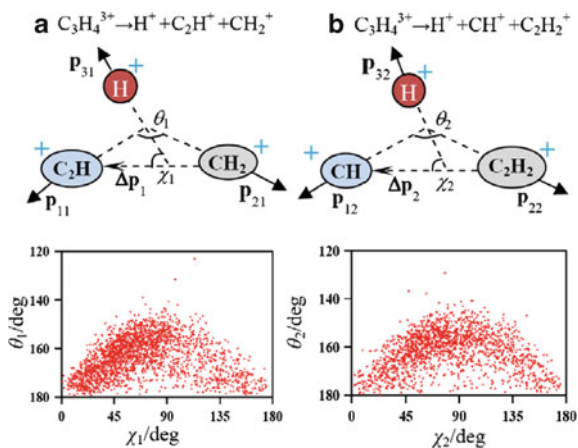


Fig. 54.5 Schematic diagrams of the two angle parameters, χ_i and θ_i , and the χ_i - θ_i correlation maps for the pathways of (a) $C_3H_4^{3+} \rightarrow H^+ + C_2H^+ + CH_2^+$ (54.3) and (b) $C_3H_4^{3+} \rightarrow H^+ + CH^+ + C_2H_2^+$ (54.4)

the proton is located at the other end of the allene molecule after the migration to form the propyne ($HC \equiv C-CH_3$) configuration. When $\theta_1 \sim 0^\circ$ or 180° the two moieties C_2H^+ and CH_2^+ are considered to be ejected along the linear C-C-C skeletal structure. When θ_1 is off from 0° or from 180° , the ejection directions of the two moieties C_2H^+ and CH_2^+ are no longer along the direction of the initially linear C-C-C molecular principal axis. Therefore, by constructing the $\chi_1 - \theta_1$ correlation map, the position of the migrating proton within the $C_3H_4^{3+}$ molecule just before the Coulomb explosion can roughly be estimated.

The resultant $\chi_1 - \theta_1$ correlation map of $C_3H_4^{3+}$ for Pathway (54.3) is plotted as shown in the lower half of Fig. 54.5a. It can be seen that the distribution spreads in the wide range of $\chi_1 = 0 - 180^\circ$, whereas the distribution along the θ_1 direction is in the range of $\theta_1 = 150 - 180^\circ$. The broad distribution of the proton in the full χ_1 angle range can be regarded as direct evidence of the ultrafast hydrogen migration process in which the proton moves from one end towards the other within an allene molecule in the intense laser field. When the proton is located in the area around its original position ($\chi_1 \sim 0^\circ$) or at the other end of the molecule ($\chi_1 \sim 180^\circ$), the distribution along θ_1 is found to be at around $\theta_1 = 180^\circ$, representing that the two moieties C_2H^+ and CH_2^+ are ejected along the C-C-C axis from the allene ($H^+ \dots HCC^+ \dots CH_2^+$) or propyne ($HCC^+ \dots CH_2^+ \dots H^+$) type geometrical configurations.

In Fig. 54.5b, a schematic diagram of the definition of two angle parameters, χ_2 and θ_2 , for Pathway (54.4) is shown, and the corresponding $\chi_2 - \theta_2$ correlation map is plotted. In this case, χ_2 denotes the extent of hydrogen migration from the moiety CH^+ to $C_2H_2^+$, and θ_2 represents the angle between the ejection directions of the two moieties CH^+ and $C_2H_2^+$. It can be found that the event distribution spreads

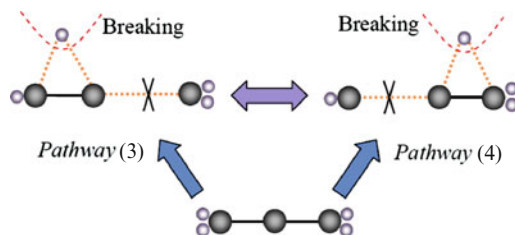


Fig. 54.6 Schematic diagram of the skeletal bond breaking schemes depending on the extent of the hydrogen migration in allene through the formation of the two different precursor species, $\text{H}^+ \cdots \text{C}_2\text{H}^+ \cdots \text{CH}_2^+$ and $\text{H}^+ \cdots \text{CH}^+ \cdots \text{C}_2\text{H}_2^+$

similarly to those in Fig. 54.1a in the entire χ_2 range of $\chi_2 = 0 - 180^\circ$, and in the θ_2 range of $\theta_2 = 150 - 180^\circ$, showing that the ultrafast hydrogen migration proceeds within an allene molecule. On the other hand, the event distribution shown in Fig. 54.5a exhibits a denser region at around $\chi_1 \leq 90^\circ$, indicating a clear tendency of the proton to be ejected on the side of the moiety C_2H^+ rather than CH_2^+ in *Pathway* (54.4).

It can also be noted that in the region of $\chi < 90^\circ$, the density of the proton distribution shown in Fig. 54.5a is higher than that in Fig. 54.5b, while in the region of $\chi > 90^\circ$, the density in Fig. 54.5b is higher than that in Fig. 54.5a. This may be interpreted as follows by referring to Fig. 54.6. When a proton is trapped in its original position in the course of the migration from one end to the other, as shown on the upper-left side of Fig. 54.6, the precursor species $\text{H}^+ \cdots \text{C}_2\text{H}^+ \cdots \text{CH}_2^+$ may preferentially be formed, that is, the C–C bond between C_2H^+ and CH_2^+ may be broken. This is *Pathway* (54.3). However, if the position of the migrating proton has moved to the other end of the molecule, as shown on the upper-right side of Fig. 54.6, the precursor species $\text{H}^+ \cdots \text{CH}^+ \cdots \text{C}_2\text{H}_2^+$ may be preferentially formed, that is, the C–C bond between CH^+ and C_2H_2^+ may be broken. This is *Pathway* (54.4). Therefore, the extent of the hydrogen migration plays a decisive role in determining which one of the two initially equivalent C–C chemical bonds, becoming inequivalent in the course of the hydrogen migration, is broken preferentially.

54.4 Summary and Challenges Ahead

We observed the intense light-field induced hydrogen migration processes in singly charged methanol, and identified the two different time scales of the migration of one hydrogen atom (or a proton) from the carbon atom site to the oxygen atom site, that is, the ultrafast migration occurring within the ultrashort laser field and the slower post-pulse migration occurring after the light-matter interaction. We also showed from the analysis of the CMI maps of the three body Coulomb explosion

processes of allene that a proton can migrate from one end to the other end of allene. These findings indicate that the hydrogen migration proceeds very rapidly within ~ 20 fs in an intense laser field so that the distribution of a proton within a hydrocarbon molecule is spread abruptly. Therefore, the extremely short laser pulse whose duration is in the attosecond time domain may be necessary to trace in real time such extremely rapid hydrogen migration processes. This should be a challenging problem in the newly emerging research field of attosecond chemistry.

We also found that the hydrogen migration plays an important role in the chemical-bond breaking and chemical-bond formation processes within a molecule. This means that once we could control hydrogen migration processes by designing an ultrashort intense laser pulse, we will also be able to control bond breaking and bond formation processes. Therefore, investigation of the dependence of the hydrogen migration on laser parameters such as its temporal pulse shape, intensity, pulse duration and polarization will be a promising approach for controlling dynamical processes of hydrocarbon molecules in an intense laser field.

It should also be noted that, as was pointed out by a recent theoretical study [11], the ultrafast hydrogen migration processes may not be described well by a conventional adiabatic picture of molecules based on the Born–Oppenheimer approximation. Therefore, new theoretical methods need to be explored in coming years for deepening our understanding of this interesting phenomenon of ultrafast hydrogen migration in an intense laser field.

Acknowledgements The present research was supported by two grants from the Ministry of Education, Culture, Sports, Science and Technology (MEXT), Japan (the Grant-in-Aid for Specially Promoted Research on Ultrafast Hydrogen Migration (#19002006), and the Grant-in-Aid for Global COE Program for Chemistry Innovation). HLX would like to acknowledge the financial support from National Natural Science Foundation (NSFC 11074098).

References

1. K. Yamanouchi et al. (eds.), *Progress in Ultrafast Intense Laser Science I–VII* (Springer, Berlin, 2006–2011)
2. K. Yamanouchi (ed.), *Lectures on Ultrafast Intense Laser Science I* (Springer, Berlin, 2010)
3. H.L. Xu, T. Okino, K. Nakai, K. Yamanouchi, Ultrafast hydrogen migration in hydrocarbon molecules driven by intense laser fields, in *Progress in Ultrafast Intense Laser Field, Vol. VII* ed. by K. Yamanouchi, D. Charalambidis, and D. Normand (Springer, Berlin, 2011), pp. 35–52
4. H.L. Xu, T. Okino, K. Yamanouchi, *Chem. Phys. Lett.* **469**, 255 (2009)
5. T. Okino, Y. Furukawa, P. Liu, T. Ichikawa, R. Itakura, K. Hoshina, K. Yamanouchi, H. Nakano, *Chem. Phys. Lett.* **423**, 220 (2006)
6. A. Hishikawa, A. Matsuda, M. Fushitani, E.J. Takahashi, *Phys. Rev. Lett.* **99**, 258, 302 (2007)
7. H.L. Xu, C. Maceau, K. Nakai, T. Okino, S.L. Chin, K. Yamanouchi, *J. Chem. Phys.* **133**, 071103 (2010)
8. H.L. Xu, T. Okino, K. Yamanouchi, *J. Chem. Phys.* **131**, 151102 (2009)
9. H. Hasegawa, A. Hishikawa, K. Yamanouchi, *Chem. Phys. Lett.* **349**, 57 (2001)
10. A. Hishikawa, H. Hasegawa, K. Yamanouchi, *Chem. Phys. Lett.* **361**, 245 (2002)
11. T. Kato, K. Yamanouchi, *J. Chem. Phys.* **131**, 164118 (2009)

Chapter 55

Double Proton Migration and Proton/Deuteron Exchange in Methylacetylene in Intense Laser Fields

T. Okino, A. Watanabe, H. Xu, and K. Yamanouchi

Abstract Two-body decomposition processes of methyl- d_3 -acetylene in intense laser fields are investigated by the coincidence momentum imaging (CMI). A total of six decomposition pathways in which one of the C–C bonds is broken and a total of six pathways in which an atomic hydrogen ion (H^+ or D^+) or a molecular hydrogen ion (H_2^+ , HD^+ , D_3^+ , or HD_2^+) is ejected are identified. It is revealed from the analysis of the CMI data that the migration of two deuterons as well as the exchange between a proton and a deuteron occur prior to the two-body decomposition of doubly charged parent molecules.

55.1 Introduction

It has been shown for a variety of hydrocarbon molecules that hydrogen atoms within a molecule can migrate very rapidly when it is irradiated with ultrashort intense laser light [1]. In our recent study on allene ($CH_2 = C = CH_2$) [2], we identified the pathway in which one of the protons migrates from one end of an allene molecule to the other end so that it takes methylacetylene ($CH_3-C\equiv C-H$) type geometrical structure in the doubly and/or triply charged states prior to the Coulomb explosion into fragment ions. We also found that distribution of the migrating proton surrounds the skeletal C–C–C structure of the three carbon atoms of allene and that the extent of the hydrogen migration plays a decisive role in determining which one of the two initially equivalent C=C chemical bonds is preferentially broken [3]. In the present study, we study two-body Coulomb explosion processes of methyl- d_3 -acetylene ($CD_3-C\equiv C-H$) in an ultrafast intense

T. Okino · A. Watanabe · H. Xu · K. Yamanouchi (✉)
Department of Chemistry, School of Science, The University of Tokyo, Bunkyo, Tokyo, Japan
e-mail: kaoru@chem.s.u-tokyo.ac.jp

laser field (790 nm, 40 fs, 5.0×10^{13} W/cm²) using the coincidence momentum imaging (CMI) method, and reveal the existence of as many as 12 different two-body decomposition pathways.

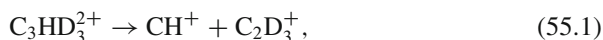
55.2 Two-Body Decomposition Processes of Methyl-*d*₃-acetylene

The decomposition pathways identified in the CMI maps in the present study are categorized into (a) C–C bond breaking pathways and (b) C–H bond breaking pathways as explained below.

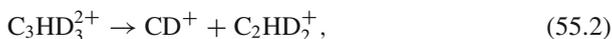
55.2.1 C–C Bond Breaking Pathways

The following six two-body decomposition pathways are identified as the C–C bond breaking pathways;

Pathway 1: No H/D migration



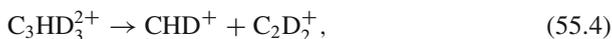
Pathway 2: 2D migration or H/D exchange



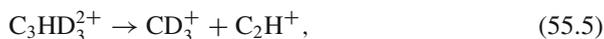
Pathway 3: D migration



Pathway 4: D migration



Pathway 5: No H/D migration



Pathway 6: 2D migration or H/D exchange



The two-dimensional CMI map of CH⁺ detected in coincidence with C₂D₃⁺ (Pathway 1) and that of CD⁺ detected in coincidence with C₂HD₂⁺ (Pathway 2)

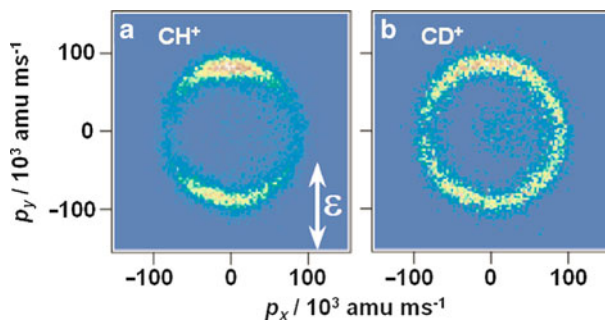


Fig. 55.1 Two-dimensional coincidence momentum images of (a) CH^+ and (b) CD^+ . The arrow ϵ shows the laser polarization direction

Table 55.1 The event numbers and the ratio of two-body dissociation pathways

Pathway	Event number	Ratio (%)	$\langle \cos^2 \theta \rangle$
(1) $\text{CH}^+ + \text{C}_2\text{D}_3^+$	15,535	1.3	0.53
(2) $\text{CD}^+ + \text{C}_2\text{HD}_2^+$	7,592	0.63	0.40
(3) $\text{CD}_2^+ + \text{C}_2\text{HD}^+$	90,987	7.5	0.42
(4) $\text{CHD}^+ + \text{C}_2\text{D}_2^+$	71,178	5.9	0.39
(5) $\text{CD}_3^+ + \text{C}_2\text{H}^+$	38,089	3.2	0.58
(6) $\text{CHD}_2^+ + \text{C}_2\text{D}^+$	2,338	0.19	0.40
(7) $\text{H}^+ + \text{C}_3\text{D}_3^+$	1,881,146	16	0.36
(8) $\text{D}^+ + \text{C}_3\text{HD}_2^+$	623,130	52	0.38
(9) $\text{D}_2^+ + \text{C}_3\text{HD}^+$	75,802	6.3	0.48
(10) $\text{HD}^+ + \text{C}_3\text{D}_2^+$	2,206	0.18	0.37
(11) $\text{D}_3^+ + \text{C}_3\text{H}^+$	26,604	2.2	0.44
(12) $\text{HD}_2^+ + \text{C}_3\text{D}^+$	64,796	5.4	0.39

are shown in Fig. 55.1. The event numbers of all the six pathways are summarized in Table 55.1. The Pathways 2, 3, 4, and 6 show clearly that the H and/or D migration processes are induced by the intense laser field prior to the Coulomb explosion processes because these fragment ions could not be generated without the transfer of a H atom or a D atom within a molecule from one carbon atom site to another.

There are two possibilities of hydrogen migration in both of Pathway 2 and Pathway 6. For Pathway 2, these two possibilities are (a) “2D migration” in which two deuterons in the CD_3 moiety migrate into the C_2H moiety (single-bond breaking) and (b) “H/D exchange” in which one deuteron in the CD_3C moiety migrates into the CH moiety simultaneously with the migration of the H atom in the CH moiety into the CD_3C moiety (triple-bond breaking). For Pathway 6, these possibilities are (a) “2D migration” in which two deuterons in the CD_3C moiety migrate into the CH moiety (triple-bond breaking) and (b) “H/D exchange” in which one deuteron in the CD_3 moiety migrates into the C_2H moiety simultaneously with the migration of the H atom in the C_2H moiety into the CD_3 moiety (single-bond breaking).

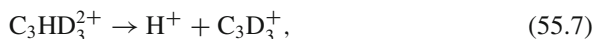
We could not judge only from our measurements which one of the “2D migration” and “H/D exchange” is a dominant process in these two pathways, but we can say that at least two light nuclei (protons and deuterons) migrate prior to the decomposition. If we consider that the originally single-bonded C–C bond should be broken more preferentially, Pathway 2 can be dominantly the 2D migration pathway and Pathway 6 can be dominantly the H/D exchange pathway. If Pathway 2 is the 2D migration pathway, the transfer of two deuterons to the neighboring central carbon atom is sufficient for the pathway to be realized. If Pathway 6 is the H/D migration pathway, the proton originally bonded to the terminal carbon atom needs to be transferred to the other end of the molecule, that is, the second next carbon atom site, in addition to the transfer of one of the three deuterons in the opposite direction at least to the neighboring carbon atom site. The shorter distance of the proton (or deuteron) transfer in Pathway 2 compared with Pathway 6 may be the reason why the event number of Pathway 2 is three times as large as that of Pathway 6.

In Pathway 3, the originally single-bonded C–C bond is broken after one of the three deuterons in the CD₃ moiety migrates into the C₂H moiety while, in Pathway 4, the originally triple-bonded C–C bond is broken after one of the three deuterons in the CD₃C moiety migrate to the CH moiety located at the other end of the molecule. The comparable event numbers for these two pathways seen in Table 55.1 suggest that an allene-type geometrical structure, [CHD=C=CD₂]²⁺, is commonly formed in the course of the proton/deuteron migration process in both Pathway 3 and Pathway 4.

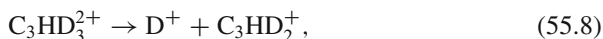
55.2.2 C–H Bond Breaking Pathways

The following six two-body decomposition pathways are identified as C–H bond breaking pathways;

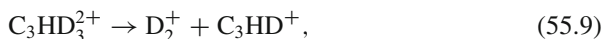
Pathway 7: No H/D migration



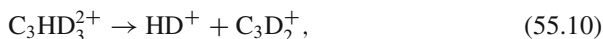
Pathway 8: No H/D migration



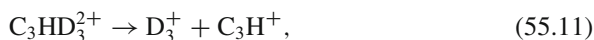
Pathway 9: No H/D migration



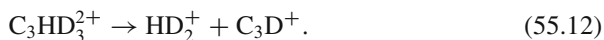
Pathway 10: H/D migration



Pathway 11: No H/D migration



Pathway 12: H/D exchange or 2D migration



The event numbers of the above six pathways are summarized in Table 55.1. It is interesting to note that the event number of Pathway 12 is almost three times as large as that of Pathway 11 even though D_3^+ can be formed from the CD_3 moiety without proton/deuteron migration in Pathway 11 while D_2H^+ can be formed only after the extensive proton/deuteron migration in Pathway 12. This may be ascribed to the fact that the precursor species prepared after the interaction with the intense laser fields has a relatively long time during which proton/deuteron could migrate in the wide area around the C–C–C skeletal structure.

55.2.3 Angular Distribution of Fragment Ions

The angular distributions, $I(\theta)$ s, of the fragment ions are obtained from the observed CMI maps, where θ is the ejection angle of the fragment ions with respect to the laser polarization direction. For evaluating the extent of the anisotropy, the expectation value of the squared cosine defined as $\langle \cos^2 \theta \rangle = \frac{\int I(\theta) \cos^2 \theta \sin \theta d\theta}{\int I(\theta) \cos^2 \theta d\theta}$ is calculated and the results are summarized in Table 55.1.

The larger $\langle \cos^2 \theta \rangle$ value suggests the fragment is ejected more anisotropic, that is, more preferentially along the laser polarization direction. The anisotropy values of the fragment ions, CH^+ in Pathway 1 ($\langle \cos^2 \theta \rangle = 0.53$) and CD_3^+ in Pathway 5 ($\langle \cos^2 \theta \rangle = 0.58$) are highest in the present measurements.

The decrease in the anisotropy may be ascribed to the long lifetime of the precursor ions and/or the offset of the ejection direction of fragment ions with respect to the molecular principle axis. There is a tendency that the $\langle \cos^2 \theta \rangle$ values of the fragment ions originated from the dissociation pathways with no H/D migration are relatively higher than those of the fragment ions ejected by the dissociation pathways accompanying the proton/deuteron migration. This tendency is clearly seen in the $\langle \cos^2 \theta \rangle$ value of CHD_2^+ in Pathway 6 ($\langle \cos^2 \theta \rangle = 0.40$), suggesting that the lifetime of a precursor state taking the geometrical structure of $[\text{CHD}_2\text{-C}\equiv\text{CD}]^{2+}$ or $[\text{CHD}_2\text{-CD}\equiv\text{C}]^{2+}$ for the formation of the CHD_2^+ is long enough for the entire molecule to rotate to make the ejection direction more isotropic.

Acknowledgements The present research was supported by the following two grants from the Ministry of Education, Culture, Sports, Science and Technology (MEXT), Japan; the Grant-in-Aid for Specially Promoted Research on Ultrafast Hydrogen Migration (# 19002006), and the Grant-in-Aid for Global COE Program for Chemistry Innovation.

References

1. T. Okino, Y. Furukawa, P. Liu, T. Ichikawa, R. Itakura, K. Hoshina, K. Yamanouchi, H. Nakano, *Chem. Phys. Lett.* **419**, 223 (2006)
2. H.L. Xu, T. Okino, K. Yamanouchi, *Chem. Phys. Lett.* **349**, 255 (2009)
3. H.L. Xu, T. Okino, K. Yamanouchi, *J. Chem. Phys.* **131**, 151102 (2009)

Chapter 56

High Energy Proton Ejection from Hydrocarbon Molecules Driven by Highly Efficient Field Ionization

S. Roither, X. Xie, D. Kartashov, L. Zhang, M. Schöffler, H. Xu, A. Iwasaki, T. Okino, K. Yamanouchi, A. Baltuška, and M. Kitzler

Abstract We report on the ejection of protons with surprisingly high kinetic energies up to 60 eV from a series of polyatomic hydrocarbon molecules exposed to Titanium-Sapphire laser pulses with moderate laser peak intensities of a few 10^{14} W/cm². Using multi-particle coincidence imaging we are able to decompose the observed proton energy spectra into the contributions of individual fragmentation channels. It is shown that the molecules can completely fragment into bare atomic ions already at relatively low peak intensities, and that the protons are ejected in a concerted Coulomb explosion from unexpectedly high charge states. We propose that a thus far undescribed process, namely that enhanced ionization (EI) taking place at all C–H bonds in parallel, is responsible for the high charge states and high proton energies. The proposition is successfully tested by using (stretched) few-cycle pulses with a bandwidth limited duration as short as 4.3 fs, for which the C–H nuclear motion is too slow to reach the critical internuclear distance for EI.

The processes that precede the Coulomb explosion of a molecular ion created by multiple ionization with a strong non-resonant laser pulse are highly complicated and involve coupled fast electronic [1–3] and slower nuclear motion. This type of molecular fragmentation has been the subject of extensive research for many years, e.g. [4–12].

We report on the observation of an ionization-fragmentation process that puts a polyatomic molecule into a very high charge state of +12 and beyond at laser intensities as low as a few 10^{14} W/cm² and subsequently leads to complete molecular decomposition. Our surprising experimental evidence shows that all of

S. Roither · X. Xie · D. Kartashov · L. Zhang · M. Schöffler · A. Baltuška · M. Kitzler (✉)
Photonics Institute, Vienna University of Technology, A-1040 Vienna, Austria
e-mail: markus.kitzler@tuwien.ac.at

H. Xu · A. Iwasaki · T. Okino · K. Yamanouchi
Department of Chemistry, School of Science, The University of Tokyo, Tokyo 113-0033, Japan

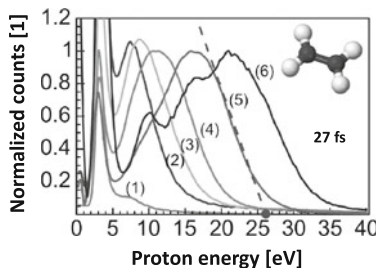


Fig. 56.1 Measured proton energy spectra for ethylene recorded with linearly polarized 27 fs laser pulses of different peak intensities. The cut-off energy is defined where a tangent on the high-energy part of the spectra cuts the abscissa, as illustrated by the *gray line*. The spectra from (1) to (6) are shown for the following intensities (in units of 10^{14} W/cm²): 1.3, 2.3, 3.3, 4.5, 8.4, 10.9

the molecule's protons are ejected with high kinetic energies, which is inconsistent with the explanation based on dynamic charge localization used in [13] to explain the proton energy observed for the laser-induced Coulomb explosion of a very large polyatomic molecule. Furthermore, the energies of all the protons are very similar, which indicates that at the instance of decomposition the protons interact with the same molecular charge state, suggesting an all-at-once (concerted) fragmentation scenario.

In our experiments we measured the energy spectra of protons ejected from methane, CH₄, ethylene, C₂H₄, 1,3-butadiene, C₄H₆, and hexane, C₆H₁₄, molecules irradiated by laser pulses from a Titanium-Sapphire chirped-pulse amplifier system, using cold target recoil ion momentum spectroscopy [14]. We use pulses with a duration of 27 fs from the output of a prism compressor and few-cycle pulses, which were obtained by spectral broadening the 27 fs pulses in a glass capillary with an inner diameter of 250 μm filled with neon gas and subsequent compression to 4.3 fs using several pairs of chirped mirrors. The laser pulses were focused by a spherical mirror with a focal length of 60 mm to peak intensities from below 10¹⁴ up to 10¹⁶ W/cm² onto a molecular jet of ≈170 μm in diameter and the created ions were guided by a weak homogeneous electric field onto a multi-hit capable detector equipped with position sensitive delay line anodes. The ion count rate was kept below 0.3–0.4 per laser shot in order to establish coincidence conditions, which ensure that all observed processes take place within a single molecule. In addition this avoids any artifacts connected with high charge density such as space charge effects. From the measured time-of-flight and position of each detected ion we calculate its three-dimensional momentum vector in the lab frame.

We obtained background-free kinetic energy spectra of the protons that are created during fragmentations of the four molecules studied by selecting all protons that are emitted towards the detector within a 90° cone. Figure 56.1 exemplarily shows the resulting proton energy spectra for ethylene measured with linear laser polarization and various peak intensities, which were calibrated with an estimated precision of ±10% by comparison to the highly intensity-sensitive proton energy

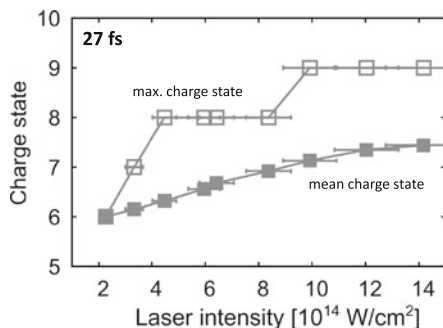


Fig. 56.2 Mean charge state as defined in the text (*full symbols*) and the maximum observed charge state from all fragmentation channels, when this channel contributes at least with 5% to the overall proton spectrum (*empty symbols*) of ethylene over laser peak intensity for linearly polarized pulses

spectra of molecular hydrogen [15]. It can be seen that the cut-offs of the proton energy spectra (as defined in the caption) increase monotonically with laser peak intensity and extend to surprisingly high energies. Similar behaviour is seen for all measured molecules.

In order to determine the fragmentation channels and therewith the charge states that are connected with the energetic protons that make up the spectra shown in Fig. 56.1, we performed a multi-coincidence selection of our data. By gating on the most energetic protons we find that they are created during fragmentations that result in decomposition of the molecular skeleton structure and the production of bare carbon ions. The carbon ions fulfill quasi-momentum conservation such that we can select certain carbon ion fragmentation channels. From this selection we can calculate the charge state that the molecules fragment from. We show an average and maximum charge state as a function of intensity for the data on ethylene in Fig. 56.2. While the latter one is defined as the maximum observed charge state from all fragmentation channels, when this channel contributes at least with 5% to the overall proton spectrum, the former one is calculated as $\sum_i Z_i N_i / \sum_i N_i$, with Z_i the charge of channel i and N_i the number of coincidence events that contribute to this channel. As we can see, the observed charge states are surprisingly high. Already for a peak intensity of few 10^{14} W/cm 2 we find that in addition to the four ejected protons the carbon ions are at least doubly ionized, such that in sum a molecular charge state of up to +9 is reached. The observed charge states increase with the molecular size [12].

The surprisingly high charge states can explain the measured proton energies, but raise other questions: Due to which mechanism can the molecules become ionized so many times? How can the molecules possibly absorb so much energy from the ionizing field?

A way to enhance ionization and to impart energy to the molecule is electron recollision. Recolliding electrons can multiply ionize the parent ion by impact

ionization, but can also impart energy to it and thus bring the ion into an excited state from which it field ionizes more easily [16]. We have repeated our experiments for 1,3-butadiene and hexane, for which the highest proton energies were observed, with circularly polarized light where no recollisions are possible. The resulting proton energy cut-offs and the reconstructed average charge states are not lower than the ones obtained for linear light. Hence, electron recollision cannot be held responsible for the high charge states.

We can also rule out that the observed high charge states shown in Fig. 56.2 are created by further ionization of the molecular fragment ions after decomposition. Then the charge state of a certain fragmentation channel would be higher than the actual one which the proton is ejected from. We can dismiss this possibility, usually dubbed post-dissociation ionization, by simply acknowledging the fact that for any two channels with different charge states we measure a higher proton energy for the higher charge state.

Instead we propose that the high charge states are caused by the following scenario: During the first field ionization stages at the leading edge of the pulse, the C–H bonds start to stretch until they reach the critical inter-nuclear distance for enhanced ionization (EI) [7, 17, 18], upon which the molecule becomes ionized several times in parallel at many different C–H bonds within a short period. Subsequently, all of the protons are removed from the highly charged ionic complex by Coulomb explosions in a concerted multi-particle fragmentation. Thereafter the remaining structure decomposes into bare atomic carbon ions.

The proposition of EI being responsible for the observed remarkably high charge states can be tested by using laser pulses with a very short duration, since for EI to take place it needs time until the C–H bonds can stretch to the critical inter-nuclear distance. If the intensity of the laser pulse has already reached its peak and the molecules at the time when the C–H bonds have stretched to the critical inter-nuclear distance only interact with the much smaller intensity of the fading pulse envelope, EI is effectively turned off and the ionization rate never reaches enhanced values [17, 18]. As a consequence the charge states are much smaller and therewith also the observed proton energies are expected to be smaller.

We show proton spectra measured for ethylene with pulses with durations ranging from 4.3 to 25 fs with the same moderate peak intensity of 5×10^{14} W/cm² in Fig. 56.3. It can be seen that the pronounced high energy proton peak is completely turned off for pulses with a duration of 4.3 fs (FWHM). If the pulses are positively stretched by introducing different amounts of glass into the beam the proton peak starts to appear. At pulse durations smaller than 10 fs it is very weak. Only at durations in excess of 10 fs it becomes discernable and for 17 fs it is well pronounced. Finally, the proton energy cut-off measured for a stretched pulse with 25 fs reaches a very similar value as the one measured for a bandwidth-limited pulse of 27 fs. The onset of the proton peak appearance at a pulse duration of ≈ 10 fs is in good agreement with the fast nuclear motion of C–H bonds on the order of 10 fs.

Here we show the mechanism of EI in parallel at many C–H bonds for the particular case of hydrocarbon molecules. But we believe that such a molecular decomposition process should occur during any interaction of laser pulses

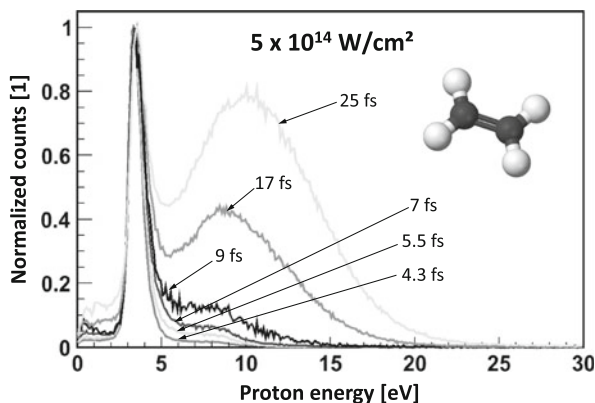


Fig. 56.3 Energy spectra of protons ejected from ethylene molecules subject to Titanium-Sapphire laser pulses with a constant peak intensity of $5 \times 10^{14} \text{ W/cm}^2$ for different pulse durations ranging from 4.3 to 25 fs. The different pulse durations have been obtained by positively stretching the 4.3 fs pulses using different amounts of fused silica

with polyatomic molecules, when the time-scale of the intra-molecular Coulomb repulsion activated nuclear motion matches the laser pulse duration. Therefore the identified mechanism has implications for any strong-field experiment on molecules, including high harmonic generation experiments [19].

Acknowledgements We acknowledge funding by the Austrian Science Fund (FWF) under grants P21463-N22 and I274-N16, and the Japanese Society for the Promotion of Science (JSPS) (#09035011-000061).

References

1. M. Lezius, V. Blanchet, M.Y. Ivanov, A. Stolow, *J. Chem. Phys.* **117**(4), 1575 (2002)
2. F. Remacle, R.D. Levine, *Proc. Natl. Acad. Sci. USA* **103**(18), 6793 (2006)
3. J. Breidbach, L. Cederbaum, *Phys. Rev. Lett.* **94**(3), 033901 (2005)
4. L. Frasniski, K. Codling, P. Hatherly, J. Barr, I. Ross, W. Toner, *Phys. Rev. Lett.* **58**(23), 2424 (1987)
5. D. Strickland, Y. Beaudoin, P. Dietrich, P. Corkum, *Phys. Rev. Lett.* **68**(18), 2755 (1992)
6. C. Cornaggia, D. Normand, J. Morellec, *J. Phys. B* **25**, L415 (1992)
7. M. Schmidt, D. Normand, C. Cornaggia, *Phys. Rev. A* **50**(6), 5037 (1994)
8. C. Cornaggia, M. Schmidt, D. Normand, *Phys. Rev. A* **51**(2), 1431 (1995)
9. P. Hering, C. Cornaggia, *Phys. Rev. A* **59**(4), 2836 (1999)
10. S. Shimizu, J. Kou, S. Kawato, K. Shimizu, S. Sakabe, N. Nakashima, *Chem. Phys. Lett.* **317**(6), 609 (2000)
11. P. Hering, C. Cornaggia, *Phys. Rev. A* **57**(6), 4572 (1998)
12. S. Roither, X. Xie, D. Kartashov, L. Zhang, M. Schöffler, H. Xu, A. Iwasaki, T. Okino, K. Yamanouchi, A. Baltuska, M. Kitzler, *Phys. Rev. Lett.* **106**(16), 163001 (2011)
13. A. Markevitch, D. Romanov, S. Smith, R. Levis, *Phys. Rev. Lett.* **92**(6), 063001 (2004)

14. R. Dörner, V. Mergel, O. Jagutzki, L. Spielberger, J. Ullrich, R. Moshhammer, H. Schmidt-Böcking, *Phys. Rep.* **330**(2–3), 95 (2000)
15. A. Alnaser, X. Tong, T. Osipov, S. Voss, C. Maharjan, B. Shan, Z. Chang, C. Cocke, *Phys. Rev. A* **70**(2), 23413 (2004)
16. A. Rudenko, K. Zrost, B. Feuerstein, V. de Jesus, C. Schröter, R. Moshhammer, J. Ullrich, *Phys. Rev. Lett.* **93**(25), 253001 (2004)
17. T. Seideman, M. Ivanov, P. Corkum, *Phys. Rev. Lett.* **75**(15), 2819 (1995)
18. T. Zuo, A.D. Bandrauk, *Phys. Rev. A* **52**(4), R2511 (1995)
19. R. Torres, N. Kajumba, J. Underwood, J. Robinson, S. Baker, J. Tisch, R. de Nalda, W. Bryan, R. Velotta, C. Altucci, I. Turcu, J. Marangos, *Phys. Rev. Lett.* **98**(20), 203007 (2007)

Chapter 57

Efficient Ionization of Acetylene in Intense Laser Fields

E. Lötstedt, T. Kato, and K. Yamanouchi

Abstract By numerically solving the time-dependent Hartree–Fock equations for a simple model of acetylene (C_2H_2) exposed to a long-wavelength, intense laser field, we show that the ionization probability is drastically enhanced when the C–H internuclear distance is stretched to twice as large as the equilibrium value.

57.1 Introduction

In the recent experiment [1], it was found that a variety of hydrocarbon molecules such as ethylene (C_2H_4) and 1,3-butadiene (C_4H_6) are ionized to extremely highly charged states when they are exposed to long-wavelength (790 nm), high-intensity (10^{14} – 10^{15} W/cm²), and ultrashort (27 fs) laser pulses. For example, at the intensity of 10^{15} W/cm², $(C_2H_4)^{9+}$ was formed after nine electrons are ejected, leading to the Coulomb explosion to form protons and carbon atom ions. Because the charge number (Z) of the parent ions is so large ($Z = 9$), the kinetic energy of the protons was found to become as high as ~ 30 eV [1]. We have performed a simple Hartree–Fock (HF) calculation of $(C_2H_4)^{8+}$ (6-311G basis set), which shows that the ionization potential to form $(C_2H_4)^{9+}$ is as much as about 90 eV as long as all the nuclei are fixed at their equilibrium positions of neutral C_2H_4 . Considering this

E. Lötstedt (✉)

Department of Chemistry, School of Science, The University of Tokyo, 7-3-1 Hongo, Bunkyo-ku, Tokyo 113-0033, Japan

Present address: Laser Technology Laboratory, RIKEN Advanced Science Institute, 2-1 Hirosawa, Wako, Saitama 351-0198, Japan

e-mail: loetstedte@riken.jp

T. Kato · K. Yamanouchi

Department of Chemistry, School of Science, The University of Tokyo, 7-3-1 Hongo, Bunkyo-ku, Tokyo 113-0033, Japan

very large vertical ionization potential, it is unlikely that the electrons are ejected one after another in a sequential manner within a very short period of time in which all the nuclei could not move so much. The kinetic energy distribution of protons ejected after the Coulomb explosion of such multiply-charged hydrocarbon molecules showed that the averaged C–H distance at the moment of the explosion was found to be approximately twice as large as the equilibrium internuclear distance in the electronic ground state of neutral molecules. Therefore, it is possible that the C–H bonds within a molecule are all stretched largely in the course of the multiple ionization process. Indeed, the enhanced ionization (EI) mechanism was proposed in [2] and [3] in order to explain the efficient ionization processes. It was also found that the averaged charge number of parent molecules is approximately twice as large as the number of the C–H bonds in a parent molecule. These findings suggest that the C–H bonds in hydrocarbon molecules play an important role in the efficient ejection of electrons in an intense laser field. In the present study, we show theoretically a possible mechanism of the efficient ionization of hydrocarbon molecules with more than one active electron, and find that electrons from the three highest occupied molecular orbitals (HOMO, HOMO – 1, and HOMO – 2) are efficiently ejected from the molecule.

57.2 Theoretical Model

In the present study, we choose acetylene (C_2H_2) as one of the simplest hydrocarbon molecules to extract an essential mechanism of the efficient multiple ionization process occurring in an intense laser field. In order to simplify the model, we assume that electrons move only along the one-dimensional H–C–C–H linear molecular axis. In addition, the laser polarization direction is set to be along the molecular axis. The time dependent Hartree–Fock (TDHF) approximation, in which the total electronic wave function is written as a single Slater determinant, is adopted for describing the electron–electron interaction among the 14 electrons, and the motion of the four nuclei is fixed during the electronic state calculation. The TDHF equations for the time-dependent spatial orbitals $\psi_n(x, t)$ ($n = 1, \dots, 7$) read in atomic units (a.u.) as

$$i \frac{\partial \psi_n(x, t)}{\partial t} = \left[-\frac{1}{2} \frac{\partial^2}{\partial x^2} - \sum_i \frac{Z_i}{\sqrt{(R_i - x)^2 + \alpha^2}} + 2 \sum_i \int \frac{|\psi_i(x', t)|^2 dx'}{\sqrt{(x - x') + \gamma^2}} \right] \psi_n(x, t) - \sum_i \int \frac{\psi_i^*(x', t) \psi_n(x', t) dx'}{\sqrt{(x - x') + \gamma^2}} \psi_i(x, t) + x E(t) \psi_n(x, t), \quad (57.1)$$

where α and γ are soft-core parameters, R_i and Z_i are the positions and the charge numbers of the nuclei, respectively, and $E(t)$ is the laser field. By adjusting

these two soft-core parameters, it becomes possible to reproduce the ground state potential energy curve of a quantum mechanical, three-dimensional C_2H_2 along the C–H distance, when the C–C distance is fixed to 2.2. This C–C distance is the equilibrium C–C distance found by a HF calculation (6-311G basis set) of a quantum mechanical, three-dimensional C_2H_2 .

57.3 Results

We solved (57.1) by the Crank–Nicholson method with a laser pulse (760 nm, 1.4×10^{15} W/cm², 10 cycles), and investigated how the ionization probability depends on the C–H internuclear distance. We define the probability P_n of the ejection of an electron from the n -th orbital as $P_n = 1 - \int_{-X}^X |\psi_n(x, \tau)|^2 dx$, where $X = 30$. The value of τ was set to be 1,500, which is larger than the laser pulse duration and is sufficiently large so that the value of $P_n(\tau)$ is in the converged domain where $P_n(\tau)$ takes a constant value. The total ionization probability is defined as $P_{\text{tot}} = \sum_{n=1}^7 P_n/7$. The ionization probabilities from the three highest lying molecular orbitals were calculated as shown in Fig. 57.1 as a function of the C–H distance, $r(\text{C–H})$. In the calculation, the C–C distance was fixed to be 2.2. It can be seen in Fig. 57.1 that when $r(\text{C–H}) = 2$, the equilibrium value, only the HOMO is ionized. Upon the ionization, two electrons are removed from the HOMO and the C–H bonds are weakened. Therefore, the protons (or hydrogen atoms) on both sides of the molecule are expected to move outwards in $(C_2H_2)^{2+}$. At $r(\text{C–H}) = 4$, the ionization probabilities from all the three highest lying molecular orbitals, HOMO, HOMO – 1, and HOMO – 2, are drastically enhanced.

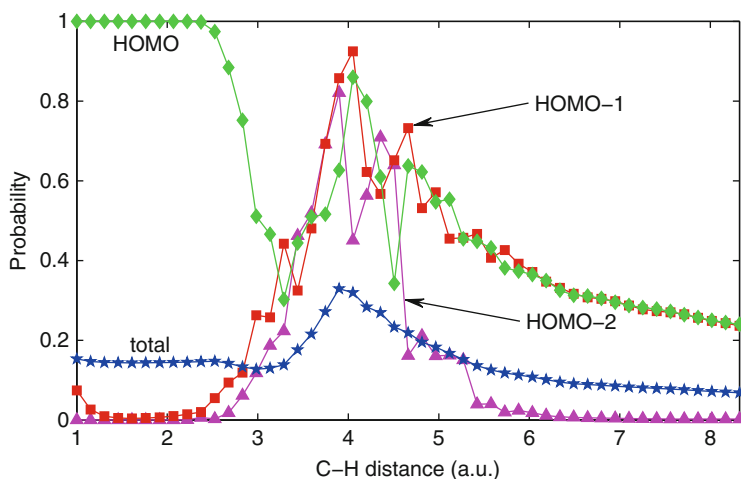


Fig. 57.1 Ejection probability for the three highest occupied molecular orbitals as a function of the C–H distance: HOMO (*diamonds*), HOMO – 1 (*squares*) and HOMO – 2 (*triangles*). The total ionization probability is shown with *stars*. The C–C distance was fixed to 2.2

The enhancement in the ionization probability shown in Fig. 57.1 at $r(\text{C-H}) = 4$, the internuclear distance twice as large as that in the electronic ground state of neutral molecules, is in good agreement with the experimental results [1]. Since each orbital is occupied by two electrons, ejection of all the electrons in these three orbitals results in the formation of $(\text{C}_2\text{H}_2)^{6+}$. The probability distributions of electrons in HOMO and HOMO - 1 are initially spatially localized at around the two H atoms, while the probability distribution of HOMO - 2 is initially localized in the region between the two carbon atoms. This means that not only the electrons forming the C-H bonds but also those forming the C-C bond are ejected.

57.4 Conclusions

We have constructed a model Hamiltonian of a one-dimensional acetylene molecule, and obtained ionization probabilities from the three highest-lying molecular orbitals in an intense ultrashort laser field by the time-dependent Hartree-Fock method. It has been revealed that the ionization probabilities from HOMO, HOMO - 1, and HOMO - 2 are enhanced largely when the C-H internuclear distance becomes approximately twice as large as that in the electronic ground state of neutral acetylene, and this enhancement leads to the ejection of as many as six electrons from these molecular orbitals to form $(\text{C}_2\text{H}_2)^{6+}$. It is true that the present theoretical results of a one-dimensional model of acetylene are consistent with the recent experimental findings [1], but further theoretical studies will be necessary for describing the efficient multiple ionization in three-dimensional acetylene as well as for clarifying the effect of electron correlations [4] in the multiple ionization process.

Acknowledgements This work was supported by the Ministry of Education, Culture, Sports, Science and Technology (MEXT), Japan (Grant-in-Aid for Specially Promoted Research on Ultrafast Hydrogen Migration No. 19002006, and Grant-in-Aid for Global COE Program for Chemistry Innovation). E. Lötstedt acknowledges a Grant-in-Aid for Scientific Research (No. 21-09238), from the Japan Society for the Promotion of Science (JSPS).

References

1. S. Roither, X. Xie, D. Kartashov, L. Zhang, M. Schöffler, H. Xu, A. Iwasaki, T. Okino, K. Yamanouchi, A. Baltuska, M. Kitzler, Phys. Rev. Lett. **106**(16), 163001 (2011). DOI 10.1103/PhysRevLett.106.163001
2. T. Seideman, M.Y. Ivanov, P.B. Corkum, Phys. Rev. Lett. **75**(15), 2819 (1995). DOI 10.1103/PhysRevLett.75.2819
3. T. Zuo, A.D. Bandrauk, Phys. Rev. A **52**(4), R2511 (1995). DOI 10.1103/PhysRevA.52.R2511
4. T. Kato, K. Yamanouchi, J. Chem. Phys. **131**(16), 164118 (2009). DOI 10.1063/1.3249967

Chapter 58

Laser-Assisted Electron Scattering and Its Application to Laser-Assisted Electron Diffraction of Molecules in Femtosecond Intense Laser Fields

Reika Kanya, Yuya Morimoto, and Kaoru Yamanouchi

Abstract The experimental results of laser-assisted electron scattering (LAES) of Xe in a femtosecond intense laser field are introduced. The intensities, angular distributions, and laser polarization dependence of the observed LAES signals for the energy gain ($+\hbar\omega$) and energy loss ($-\hbar\omega$) processes were in good agreement with numerical simulations. As an application of this femtosecond-LAES process, a new method of time-resolved gas electron diffraction for determining instantaneous geometrical structure of molecules with high precision is proposed, and its feasibility is confirmed by a numerical simulation of LAES signals for CCl_4 molecules.

58.1 Introduction

In electron-atom collision processes in a laser field, the electron can gain or lose its energy by multiples of the photon energies. This process is called laser-assisted electron scattering (LAES), which was observed first in 1976 [1]. Previously, cw-CO lasers, cw- and pulsed- CO_2 lasers, whose pulse duration were on the order of microseconds, were employed in observing the LAES process [2]. The LAES process in ultrashort laser fields had not been investigated for long years until our study [3], in which the LAES process in ultrashort laser fields was observed through scattering of a 1 keV pulsed electron beam by Xe atoms in femtosecond intense laser pulses.

As an application of the LAES phenomena with ultrashort laser pulses, we proposed a new time-resolved gas electron diffraction method for probing the change in the geometrical structure of molecules with high precision of the order of 0.01 \AA with extremely high temporal resolution of the order of femtoseconds [3], which is

R. Kanya · Y. Morimoto · K. Yamanouchi (✉)
The University of Tokyo, 7-3-1, Hongo Bunkyo-ku, Tokyo, 113-0033, Japan
e-mail: kanya@chem.s.u-tokyo.ac.jp; morimoto@chem.s.u-tokyo.ac.jp;
kaoru@chem.s.u-tokyo.ac.jp

more than two-orders of magnitude shorter than the previously achieved temporal resolution of gas electron diffraction experiments [4]. Through a model simulation of LAES by Cl_2 with different internuclear distances (2.0, 3.0 and 4.0 Å), we demonstrated a procedure for determination of molecular geometrical structures from electron diffraction patterns appearing in angular distributions of LAES signals [3].

In the present paper, we review briefly the first observation of femtosecond-LAES [3] and report the results of a new numerical simulation of an angular distribution of LAES signals of CCl_4 . From the comparison between the *S/N* ratio of the observed LAES intensity of Xe and a modulation amplitude of calculated molecular scattering intensity of CCl_4 appearing in the LAES signals, the feasibility of this ultrafast electron diffraction method to determine instantaneous geometrical structure of polyatomic molecules is confirmed.

58.2 Experimental

As shown in Fig. 58.1, the apparatus consists of an electron beam source, a sample gas nozzle, a toroidal-type electron energy analyzer [5], and an imaging detector. A monochromatic electron pulse of 1 keV kinetic energy collides with a Xe gas at a scattering point. Simultaneously, an incident laser pulse crosses both of the electron beam and the atomic beam at right angles as the scattering point. The scattered electrons are introduced into the electron energy analyzer through a slit. The kinetic energy- and angular-distributions of the scattered electrons are resolved and imaged onto a gated-microchannel plate with a phosphor screen (MCP/Phosphor) coupled with a CCD camera.

The output of a 5 kHz Ti:sapphire laser system ($\lambda = 795$ nm, 0.8 mJ/pulse, $\Delta t = 200$ fs, linearly polarized) is introduced into the scattering point through a combination of a cylindrical lens ($f = 10$ m) and a spherical lens ($f = 400$ mm), so that the laser beam profile at the scattering point takes an elliptical shape which ensures a maximum spatial overlap between three beams, that is, the atomic beam, the electron beam, and the laser beam. The peak laser field intensity is estimated to be 1.8×10^{12} W/cm² at the scattering point. The 200 fs laser pulses are obtained by chirping positively the transform-limited 50 fs pulses.

The electron pulses of 45 ps duration are created at a surface of silver-coated photocathode through the photoelectric effect by irradiating the surface with a UV laser pulse ($\lambda = 267$ nm). The UV pulses are generated as THG of the chirped fundamental pulses that are partially split from the main pulses before the pulse-compressor of the laser system. The generated electron packets are accelerated to 1 keV in the spacial gap of 0.3 mm between the cathode and the grounded anode, and are collimated by an electromagnetic lens and a series of pinholes. It is confirmed from the elastic scattering experiment of a Xe gas that the energy resolution of 0.7 eV is achieved, which is sufficiently high for observing the LAES phenomena, in which the 1.56 eV energy spacing corresponding to the one photon energy of the Ti:sapphire laser light needs to be resolved.

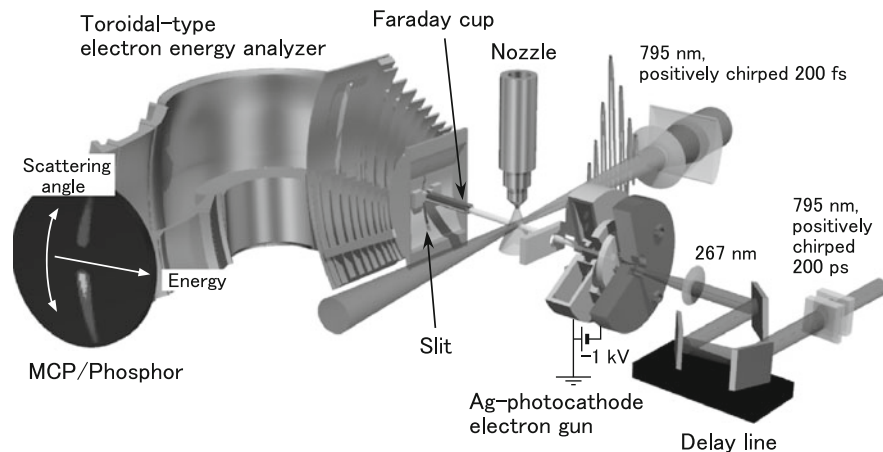


Fig. 58.1 The schematic diagram of the experimental setup of LAES

58.3 Result and Discussion

Figure 58.2a shows an energy spectrum of scattered electrons when the scattering occurred in the laser field (filled circles) and a background spectrum when the temporal delay of the electron pulse from the laser pulse was set to be +100 ps (open squares), so that the scattering occurs without the influence of the laser field. The laser polarization vector was set to be “vertical,” i.e., perpendicular to the direction of the incident electron beam (Fig. 58.1). The relative intensities are normalized by the peak intensity of the elastic scattering signal. The increases in the signal intensity are recognized at the kinetic energy shifts of $\pm\hbar\omega$, i.e. ± 1.56 eV in the spectrum of electrons scattered in the vertically polarized laser field. In Fig. 58.2b, the filled circles represent the LAES signals obtained by subtracting the background signals from the electron scattering signals in the vertically polarized laser field in Fig. 58.2a. The distinct peak structures in Fig. 58.2b show that the $\pm\hbar\omega$ -transitions in the LAES process were observed.

In order to secure our assignment, the intensities of LAES signals relative to the signal intensity of the elastic scattering were estimated by a numerical calculation based on the Bunkin–Fedorov approximation [6], which was established for LAES with high energy electrons. The result of the simulation is also plotted as a solid line in Fig. 58.2b. The calculated LAES signal intensities relative to the elastic scattering signal intensities are in good agreement with the experimental results.

According to the theoretical consideration based on the Bunkin–Fedorov approximation, the LAES signal intensities are expected to be suppressed significantly when the laser polarization vector is set to be “horizontal,” i.e., parallel to the direction of the incident electron beam (Fig. 58.1). This significant polarization dependence should provide a further verification of our assignment. In Fig. 58.2b, an energy spectrum recorded with the horizontally polarized laser fields is plotted

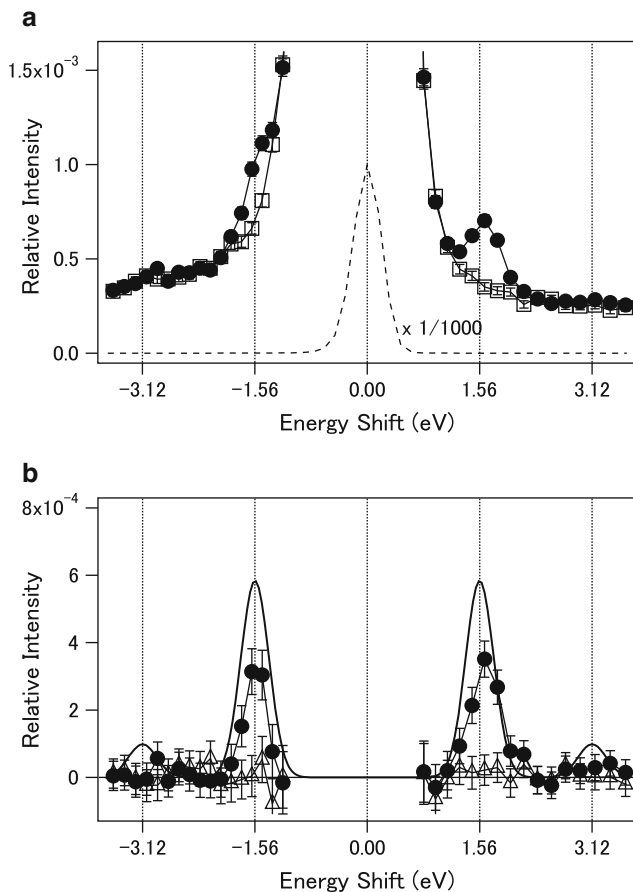


Fig. 58.2 (a) The energy spectra of scattered electrons. *Filled circles*: Electron scattering signals with vertically polarized laser fields. *Open squares*: Background electron scattering signals. *Broken line*: The elastic scattering peak reduced by a factor of 1,000. (b) The energy spectra of LAES signals. *Filled circles*: The signals with the vertically polarized laser field obtained after subtracting the background signals. *Open triangles*: The signals with the horizontally polarized laser field obtained after subtracting the background signals. *Solid line*: The simulated spectrum of LAES signals with the vertically polarized laser field

by the open triangles. In contrast to the vertically polarized case, no distinguishable signal was observed at the kinetic energy shifts of $\pm \hbar\omega$. This result is consistent with the corresponding numerical calculation, in which the relative intensity of 7×10^{-6} was estimated for the $\pm \hbar\omega$ -transitions. This clear polarization dependence also confirmed the observation of the LAES process. The filled circles in Fig. 58.3 show the observed angular distribution of the $+\hbar\omega$ -transition of LAES by Xe. The observed angular distribution is also in good agreement with a calculated angular distribution (solid line).

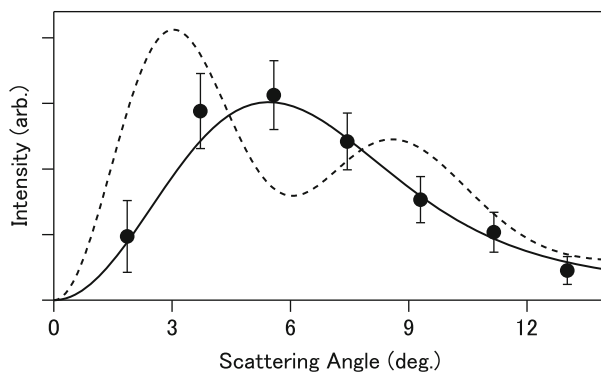


Fig. 58.3 The angular distributions of the $+\hbar\omega$ -transition of LAES. *Filled circles*: The observed LAES signals of Xe. *Solid line*: The calculated angular distribution of LAES signals of Xe. *Broken line*: The calculated angular distribution of LAES signals of CCl_4

When the femtosecond-LAES is applied to molecular samples, geometrical structure of molecules can be determined from the analysis of a diffraction pattern appearing in angular distributions of LAES signals. Considering the fact that LAES could occur only when molecules are interacting with an ultrashort laser field, the determined geometrical structure of molecules is “an instantaneous structure” during the femtosecond laser pulse duration. Therefore, if dynamical molecular processes initiated by femtosecond pump laser pulses are probed by the femtosecond LAES, the temporal resolution of a snapshot of the geometrical structure of molecules retrieved from the gas electron diffraction pattern will be of the order of femtoseconds, i.e., 10^2 – 10^3 times better than the ~ 1 ps temporal resolution achieved by previously the pulsed gas electron diffraction methods [4].

The broken line in Fig. 58.3 is a calculated angular distribution of the $+\hbar\omega$ -transition of LAES by CCl_4 , where the sample gas density and the laser field conditions are assumed to be the same as those in the experiment of Xe. The amplitude of the modulated interference pattern appearing in the calculated angular distribution of LAES signals of CCl_4 is found to be larger than the error bars associated with the experimental data of the LAES signals of Xe, showing that the instantaneous geometrical structure of CCl_4 can in principle be extracted by a femtosecond-LAES experiment using our present apparatus. Similarly, instantaneous geometrical structures of other high-symmetry molecules containing heavy atoms, such as CBr_4 , SF_6 , and CF_3I , could also be determined by the femtosecond laser-assisted electron diffraction experiment.

References

1. D. Andrick, L. Langhans, *J. Phys. B At. Mol. Opt. Phys.* **9**, L459 (1976)
2. N.J. Mason, *Rep. Prog. Phys.* **56**, 1275 (1993)

3. R. Kanya, Y. Morimoto, K. Yamanouchi, *Phys. Rev. Lett.* **105**, 123202 (2010)
4. H. Ihee, V.A. Lobastov, U.M. Gomez, B.M. Goodson, R. Srinivasan, C.-Y. Ruan, A.H. Zewail, *Science* **291**, 458 (2001)
5. F. Toffoletto, R.C.G. Leckey, J.D. Riley, *Nucl. Instrum. Meth. Phys. Res. B* **12**, 282 (1985)
6. F.V. Bunkin, N.V. Fedorov, *Sov. Phys. JETP* **22**, 844 (1966)

Part V
Laser-Induced Surface and Nanoscale
Dynamics

Chapter 59

A System for Conducting Surface Science with Attosecond Pulses

C.A. Arrell, E. Skopalova, D.Y. Lei, T. Uphues, Y. Sonnefraud, W.A. Okell, F. Frank, T. Witting, S.A. Maier, J.P. Marangos, and J.W.G. Tisch

Abstract We report the development of an apparatus to allow time resolved photoelectron spectroscopy of charge motion on solids and structured surfaces with attosecond resolution in an ultra high vacuum environment. The system, connected to the Attosecond Beamline at Imperial College, allows probing of charge dynamics on surfaces and plasmonic fields on structured surfaces with a few-cycle NIR pulse and attosecond pulse trains. The system incorporates novel methods of vibration isolation to eliminate vibrations coupling to sample and optics from mechanical vibrations. An isolated attosecond pulse can also be used with the addition of a multilayer XUV optic. A two-photon photoemission measure of a hot electron population in gold is presented.

59.1 Introduction

The unprecedented attosecond temporal resolution characteristic of high harmonic generation has been applied to solid state physics to measure electron emission from core states relative to the vacuum level in a similar fashion to the measured delay in photoemission [1, 2]. This work demonstrates that the well established atomic streaking techniques commonly used in the gas phase can be transferred to the solid state. To this end a surface science apparatus has been built to conduct atomic streaking measurements of resonant plasmonic fields on structured surfaces [3]. A brief description of the apparatus is presented followed by a discussion of measurements of hot electron thermalisation, demonstrating the capabilities of the system.

C.A. Arrell (✉) · E. Skopalova · D.Y. Lei · T. Uphues · Y. Sonnefraud · W.A. Okell · F. Frank · T. Witting · S.A. Maier · J.P. Marangos · J.W.G. Tisch
Blackett Laboratory, Imperial College, London, SW7 2AZ, UK
e-mail: christopher.arrell@imperial.ac.uk

59.2 Beamline

The apparatus in Fig. 59.1 is coupled to the Attosecond Beamline at Imperial College utilising a $300\ \mu\text{J}$ 3.5 fs carrier envelope phase (CEP) stabilised NIR pulse to produce either an isolated 250 as FWHM centred at 13.5 nm pulse or a train of attosecond pulses up to 130 eV [4]. The system allows an attosecond pulse train, or with the use of a two-part mirror arrangement, an isolated attosecond pulse to be spatially and temporally overlapped on a surface to conduct a two-photon emission or atomic streak measurement in ultra high vacuum conditions.

An electron time of flight spectrometer is used to measure the energy of the photo emitted electrons [5]. The instrument can be mounted both perpendicular and parallel to the surface, collecting electrons in a solid angle of 2×10^{-2} str with a energy resolution of $\Delta E/E$ of 0.4% at 80 eV. The larger cross section for solids compared to gases removes problems of low photoelectron detection rates for a moderate harmonic flux of 2×10^4 photons per shot.

An important consideration for interferometric measurements on a large beamline is mechanical stability. To decouple mechanical vibrations from pumps etc from the optics, a series of double balanced bellows are used to directly mount the internal breadboards onto an optical table while supporting the chambers with external frames standing on the lab floor. In this way external vibrations of the chamber wall were not detectable using a laser interferometric vibrometer (SIOS GmbH).

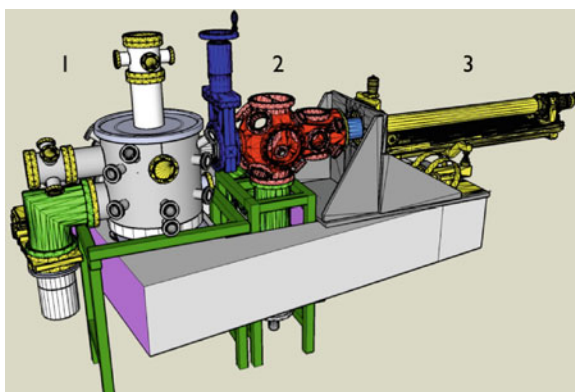


Fig. 59.1 The surface science apparatus at Imperial College. Chamber 1 is the experimental chamber housing electron time of flight spectrometers. A re-imaging system is used to ensure beams spacial and temporal overlap at the surface. Chamber 2 is a preparation chamber allowing six samples to be stored at 10^{-11} mbar conditions, further sample preparation methods can be installed in this chamber as required. The manipulator arm is item 3, this vibration isolated arm has 5° of freedom and can hold upto six samples

59.3 Two-Photon Emission from a Gold Surface

An electron occupying a state below the Fermi level absorbing a photon of energy $\hbar\omega_0$ will be either emitted from the surface (if $\hbar\omega_0 > \phi$) or promoted to a state above the Fermi level, but below the vacuum level if $\hbar\omega_0 < \phi$, where ϕ is the work function of the metal. The electron occupying this new state will not be in equilibrium and hot electrons above the Fermi level will redistribute or thermalise via scattering processes. Electrons redistribute predominately via electron–electron (e–e) scattering or electron–phonon (e–p) scattering on a characteristic timescale. Using a two-photon emission process with an IR pump and delayed XUV probe this time scale can be measured. Figure 59.3 is a representation of the process showing the XUV probe photoemitting an electron from either a state below or above the Fermi level.

The pump and probe beams were focused with a toroidal mirror ($f = 700$ mm) onto a 100 nm evaporation of Au on sapphire substrate. An interferometer with cored mirrors to produce an annular beam for generation of the XUV and an ‘inner’ beam used as the pump. The divergence of the annular IR beam was such that an iris can be used to block the unwanted IR used for XUV generation without the requirement of metallic filters. A schematic to the beam arrangement is shown in Fig. 59.2.

In the measured photoelectron spectrum an increasing population of electrons is observed with an energy slightly higher (<5 eV) than the Fermi level at delays approaching zero delay (XUV arriving after IR). While for temporal delays after the zero crossing (when the XUV pulse arrives before the IR) the population is not seen. Figure 59.3 is the integrated yield of electrons emitted from states above the Fermi level, where the thermalisation time of the hot electrons can be seen.

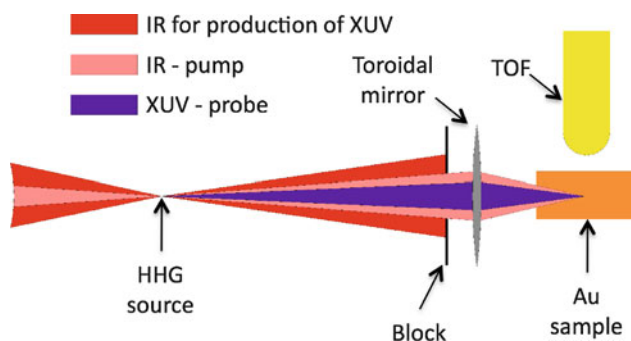


Fig. 59.2 Schematic of IR pump and XUV probe beams. Collinear beams from the interferometer are focused into a gas jet. Only the intensity of the annular outer beam (*dark red*) is sufficient to produce high harmonics. After the HHG source the two IR beams and the XUV beams diverge. An iris is used to block the more divergent XUV producing IR beam—passing the inner IR pump and XUV probe beams. Both beams are focused onto the Au target in front of an electron time of flight

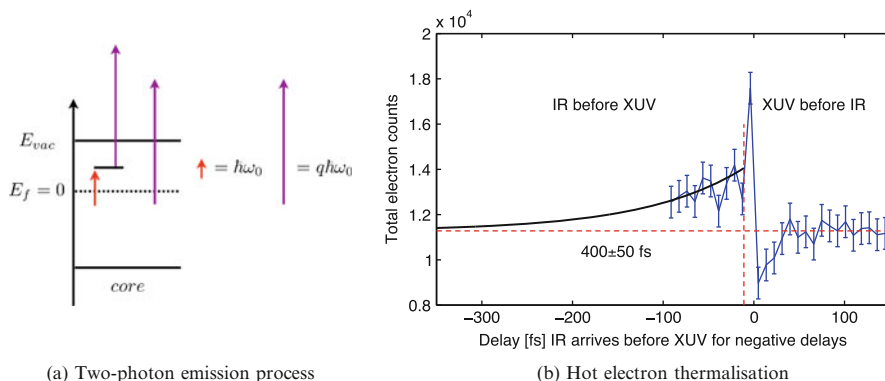


Fig. 59.3 (a) Representation of the two-photon ionisation process. An IR photon, $\hbar\omega_0$, is absorbed by an electron occupying a state below the Fermi level and is promoted to a state above the Fermi level but below the vacuum level. This electron can then absorb an XUV photon, $q\hbar\omega_0$, and be emitted from the metal. Emission of electrons from below the Fermi level can also occur with a single XUV photon. (b) The integrated yield of electron emitted from states above the Fermi level. The *black curve* is a fit of an exponential decay of the feature seen before zero delay

The pump–probe measurement was scanned 260 fs in 8.7 fs steps with an IR pump intensity of $9 \times 10^9 \text{ Wcm}^{-2}$ and probing with harmonics at 95 eV (near the cut off of the harmonics spectrum). An extrapolation of the hot electron decay time reveals a thermalisation time of 400 ± 50 fs for electrons populating states up to 5 eV above the Fermi level. This thermalisation time is consistent with Fermi-liquid theory modelling of e–e scattering indicating e–e scattering is the dominant process in hot electron thermalisation [6, 7].

In conclusion a versatile surface science system has been described facilitating the use of attosecond pulses in probing electron motion in condensed matter. It is envisaged this system will directly measure enhanced plasmonic fields on structured surfaces, an area of great importance and promise for future high harmonic sources and optoelectronics.

Acknowledgements The authors would like to acknowledge the mechanical assistance provided by Andy Gregory and Peter Ruthven, and electronic assistance provided by Bandu Ratnasekara. Financial support from the Engineering and Physical Sciences Research Council (grant EP/F034601/1) is also acknowledged.

References

1. A.L. Cavalieri et al., Attosecond spectroscopy in condensed matter. *Nature* **449**, 7165 (2007)
2. M. Schultze et al., Delay in photoemission. *Science* **328**, 5986 (2010)
3. E. Skopalova et al., Numerical simulation of attosecond nanoplasmonic streaking. *New J. Phys.* **13**, (2011)

4. T. Witting et al., Characterization of high-intensity sub-4-fs laser pulses using spatially encoded spectral shearing interferometry. *Opt. Lett.* **36**, 9 (2011)
5. O. Hemmers et al., High-resolution electron time-of-flight apparatus for the soft x-ray region. *Rev. Sci. Instrum.* **69**, 11 (1998)
6. D. Pines et al., Starting with Landau's Fermi liquid. *Phys. Today* **20**, 9 (1967)
7. V. Gasparov et al., Electron-phonon, electron-electron and electron-surface scattering in metals from ballistic effects. *Adv. Phys.* **42**, 4 (1993)

Chapter 60

Attosecond Transversal Streaking to Probe Electron Dynamics at Surfaces

Luca Castiglioni, D. Leuenberger, M. Greif, and M. Hengsberger

Abstract The feasibility of attosecond transversal streaking to probe electron transfer dynamics at surfaces and interfaces has been studied. Our simulations suggest that the temporal resolution compares well to existing methods whereas the use of an *s*-polarized streaking field significantly reduces above-threshold photoemission (ATP) and thus also enables the detection of low-energy electrons.

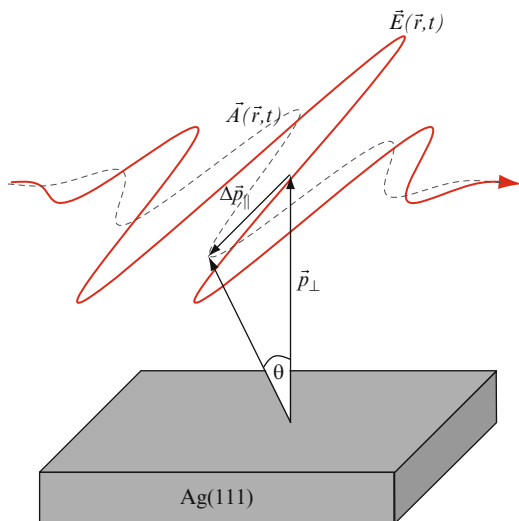
60.1 Introduction

Electron dynamics at surfaces and interfaces such as photoemission and charge transfer are of fundamental importance in chemical reactions, photovoltaic devices and photocathodes. Recent investigations of the photoemission of diamondoid (e.g. tetramantane) coated metals revealed a nearly monochromatic photoelectron spectrum and ultra-short electron transit times [1, 2]. Highly excited electrons from the metal are efficiently transferred to the molecule LUMO, from which they are supposed to be instantly emitted due to the negative electron affinity (NEA).

In a first attosecond condensed matter experiment [3] the relative delay between photoemission of $4f$ and conduction band electrons in W(110) has been determined using the atomic transient recorder (ATR) [4], which is based on longitudinal streaking. Here we propose an experiment to directly determine the electron transit time in diamondoid materials based on transversal streaking. Both the *s*-polarization of the streaking field and the lower intensities that are required lead to a significant reduction of the above-threshold photoemission (ATP) background since ATP electrons are predominantly emitted along the polarization axis [5, 6].

L. Castiglioni (✉) · D. Leuenberger · M. Greif · M. Hengsberger
Institute of Physics, University of Zürich, Winterthurerstrasse 190, 8057 Zürich, Switzerland
e-mail: luca.castiglioni@physik.uzh.ch

Fig. 60.1 Principle of transversal streaking. An electron emitted normal to the Ag(111) surface with initial momentum, \vec{p}_\perp , experiences transversal acceleration in the s -polarized NIR field, $\mathbf{E}(\mathbf{r}, t)$, leading to a change of the parallel momentum, \vec{p}_\parallel proportional to the vector potential, $\mathbf{A}(\mathbf{r}, t)$, and thus to a net-change in emission angle, θ



60.2 Simulation

We use classical equations of motion to study the feasibility of transversal streaking for our systems of interest. The parameters used in the simulation correspond to those of the planned experiments. Electrons excited by an XUV pump pulse centered around 40 eV with a pulse duration of 300 as propagate in the NIR field of the probe pulse, which is given by

$$\mathbf{E}_{\text{NIR}}(t) = A_0 \exp\left(\frac{-4 \ln 2 t^2}{\text{FWHM}^2}\right) \cos(\omega t + \phi), \quad (60.1)$$

with a FWHM of 5.5 fs being the pulse duration of the CEP-stabilized driving laser, and ω corresponding to the frequency at 800 nm. Figure 60.1 shows how the electron experiences transversal acceleration in the NIR field from the moment of its release, τ , until the pulse passes. The imparted momentum gain is given by

$$\Delta \mathbf{p}(\mathbf{r}, t) = e \int_{\tau}^{\infty} \mathbf{E}_{\text{NIR}}(\mathbf{r}, t) dt = e \mathbf{A}_{\text{NIR}}(\mathbf{r}, t), \quad (60.2)$$

where $\mathbf{A}_{\text{NIR}}(t)$ is the vector potential in the Coulomb gauge. The change of the parallel momentum, \vec{p}_\parallel , leads to a change of the emission angle, θ , which can be detected as a function of time-delay between XUV and NIR pulses by an angle-resolved electron analyzer. Initial momentum distributions were taken from experimental data, which was obtained by angle-resolved photoemission spectroscopy (ARPES) using He II_α (40.8 eV) radiation.

60.3 Discussion

The initial momentum distribution of the NEA electrons that was used in the streaking simulations is shown in Fig. 60.2a. The spectrograms that were obtained for this distribution at different streaking field intensities are presented in Fig. 60.2b–d. The slow NEA electrons ($E_{\text{kin}} = 0.5 \text{ eV}$) still experience a deflection that is large enough to be detected in an angle-resolved experiment at field intensities as low as $5 \times 10^9 \text{ W/cm}^2$. In a case where electrons are not emitted instantaneously from the tetramantane LUMO we simulated the spectrograms taking an exponential decay into account. The spectrograms we obtained for time constants of 0.5 and 5 fs are given in Fig. 60.2e and f, respectively. Interestingly, even for a lifetime nearly twice

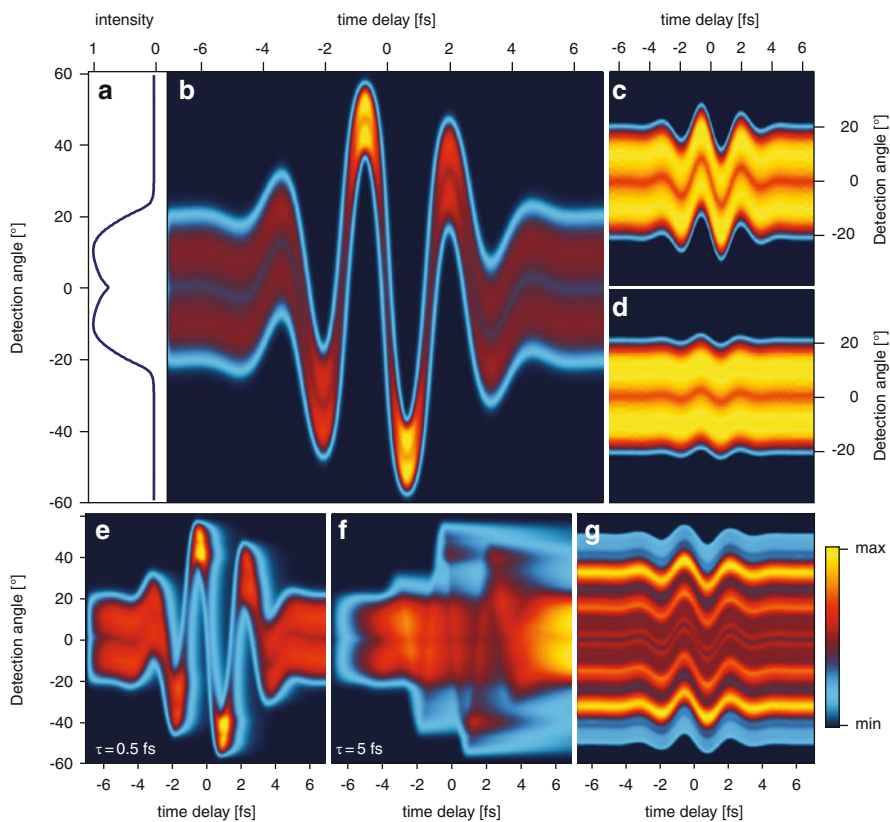


Fig. 60.2 (a) Initial momentum distribution of NEA electrons in the laboratory frame. (b–d) Simulated streaking spectrograms for given initial momentum at field intensities of $I_{\text{NIR}} = 5 \times 10^{12}$, 1×10^{11} and $5 \times 10^9 \text{ W/cm}^2$, respectively. (e, f) Spectrograms for non-instantaneous emission described by exponential decay functions with indicated time constants. (g) Spectrogram of Ag(111) 4d valence band electrons at $I_{\text{NIR}} = 5 \times 10^{12} \text{ W/cm}^2$

as long as one optical cycle of the streaking field, the shape of the vector potential, $\mathbf{A}_{\text{NIR}}(\mathbf{r}, t)$, and therefore temporal information can still be retrieved. Finally, the spectrogram of an initial momentum distribution that was obtained by a constant-energy-cut through the Ag(111) 4*d* band is shown in Fig. 60.2g. Those electrons serve as reference to clock the LUMO transit time since they were directly emitted from the Ag(111) valence band. The same field that is used to streak the slow NEA electrons is strong enough to deflect the much faster 4*d* electrons ($E_{\text{kin}} = 36 \text{ eV}$).

Preliminary experiments concerning the polarization-dependence of ATP that we performed at low field intensities on the order of 10^9 W/cm^2 on pristine and tetramantane-covered Ag(111) indicate that in particular the high-energy tail of the ATP spectrum is significantly suppressed for *s*-polarized light.

60.4 Conclusion

Our simulations suggest that transversal streaking is a valuable alternative over longitudinal streaking using the atomic transient recorder (ATR) technique, which offers two distinctive advantages. (1) The *s*-polarized streaking field leads to a significant reduction of ATP background. (2) Data acquisition time can be reduced using 2D detectors, which simultaneously use the energy and angular resolution of a hemispherical electron analyzer. This is important for surface experiments since many well-prepared systems have a limited longterm stability.

Acknowledgements We thank Reto Locher and Lukas Gallmann (ETH Zurich) for useful discussions and making their latest laser parameters available to us. Financial support from the University of Zurich and the Swiss National Science Foundation through NCCR MUST is gratefully acknowledged.

References

1. W.L. Yang, J.D. Fabbri, T.M. Willey, J.R.I. Lee, J.E. Dahl, R.M.K. Carlson, P.R. Schreiner, A.A. Fokin, B.A. Tkachenko, N.A. Fokina, W. Meevasana, N. Mannella, K. Tanaka, X.J. Zhou, T. van Buuren, M.A. Kelly, Z. Hussain, N.A. Melosh, Z.X. Shen, *Science* **316**(5830), 1460 (2007)
2. S. Roth, D. Leuenberger, J. Osterwalder, J.E. Dahl, R.M.K. Carlson, B.A. Tkachenko, A.A. Fokin, P.R. Schreiner, M. Hengsberger, *Chem. Phys. Lett.* **495**(1–3), 102 (2010)
3. A.L. Cavalieri, N. Mueller, T. Uphues, V.S. Yakovlev, A. Baltuska, B. Horvath, B. Schmidt, L. Bluemel, R. Holzwarth, S. Hendel, M. Drescher, U. Kleineberg, P.M. Echenique, R. Kienberger, F. Krausz, U. Heinzmann, *Nature* **449**(7165), 1029 (2007)
4. R. Kienberger, E. Goulielmakis, M. Uiberacker, A. Baltuska, V. Yakovlev, F. Bammer, A. Scrinzi, T. Westerwalbesloh, U. Kleineberg, U. Heinzmann, M. Drescher, F. Krausz, *Nature* **427**(6977), 817 (2004)
5. F. Bisio, M. Nyvlt, J. Franta, H. Petek, J. Kirschner, *Phys. Rev. Lett.* **96**(8), 087601 (2006)
6. M. Drescher, M. Hentschel, R. Kienberger, G. Tempea, C. Spielmann, G. Reider, P. Corkum, F. Krausz, *Science* **291**(5510), 1923 (2001)

Chapter 61

Dynamics of Coherent Optical Phonons in PbTiO₃ Excited by Impulsive Stimulated Raman Scattering

K.G. Nakamura, H. Koguchi, J. Hu, H. Takahashi, M. Nakajima, S. Utsugi, and H. Funakubo

Abstract Dynamics of coherent phonons in a ferroelectric film of PbTiO₃ is investigated using femtosecond time-resolved transient reflection measurements with a pump and probe technique. Coherent optical phonons are generated by irradiation of a femtosecond laser pulse via impulsive stimulated Raman scattering. Four coherent oscillations with frequencies of 3.2, 4.7, 6.2 and 8.6 THz are observed and assigned to optical phonons of A₁(1TO), A₁(1LO), E(2TO), and B₁ + E modes, respectively. A positive frequency chirp is observed in the soft mode (A₁(1TO)) within 2 ps, and explained by relaxation of vibrational states and anharmonicity of the potential curve in the soft mode coordinate.

K.G. Nakamura (✉) · J. Hu

Materials and Structure Laboratory, Tokyo Institute of Technology, 4259 Nagatsuta, Yokohama 226-8503, Japan

Department of Innovative Engineered Materials, Tokyo Institute of Technology, 4259 Nagatsuta, Yokohama 226-8503, Japan

CREST, Japan Science and Technology Agency, Kawaguchi 332-0012, Japan

e-mail: nakamura@msl.titech.ac.jp

H. Koguchi · H. Takahashi

Materials and Structure Laboratory, Tokyo Institute of Technology, 4259 Nagatsuta, Yokohama 226-8503, Japan

Department of Innovative Engineered Materials, Tokyo Institute of Technology, 4259 Nagatsuta, Yokohama 226-8503, Japan

M. Nakajima · S. Utsugi · H. Funakubo

Department of Innovative Engineered Materials, Tokyo Institute of Technology, 4259 Nagatsuta, Yokohama 226-8503, Japan

61.1 Introduction

Coherent phonons are represented with a wave packets superimposed of state of several vibrational wave functions of phonons, generated by irradiation of ultrashort laser pulses with the duration much shorter than a vibrational period [1]. The motion of the wave packet corresponds to time evolution of a mean value of position and can be detected as modulation in transient reflectivity or transmissivity change via a change in an electric susceptibility. There are two possible generation mechanisms for coherent phonons as the impulsive stimulated Raman scattering (ISRS) for transparent materials and displacive enhanced coherent phonons (DECP) for opaque materials [2]. The coherent phonons move in the electronic ground state via the ISRS and move in the electronic excited state via the DECP. Using this transient reflectivity or transmissivity measurement, the dynamics of coherent phonons such as time evolution of the atomic displacement, an initial phase, and the lifetime, have been studied for various materials such as semiconductors, semimetals and superconductors [2, 3]. In addition, the effect of potential anharmonicity and the electronic softening can be directly observed via time evolution of the frequency. In this paper, we studied the dynamics of coherent optical phonons in the ferroelectric PbTiO_3 film through femtosecond time-resolved reflection measurement in order to understand details of the soft-mode phonons.

61.2 Experimental

The transient reflectivity was measured using a pump and probe technique. The laser used was a mode-locked Ti:sapphire laser providing a 40-fs pulse and a wavelength centered at ~ 800 nm (~ 1.55 eV) with a bandwidth of ~ 40 nm (~ 800 meV). The output of the oscillator was split with a partial beam splitter into two beams with 9:1 ratio, and the smaller portion was used as the probe pulse. Details of the experimental setup are described elsewhere [4]. The sample used was the (1 0 0)/(0 0 1)-oriented PbTiO_3 film thicker than $1 \mu\text{m}$ grown on a (1 0 0) cSrRuO_3 //(1 0 0) LaNiO_3 //(1 0 0) CaF_2 substrate at 600°C by pulsed metal organic chemical vapor deposition (pulsed-MOCVD) [5]. The band gap (~ 3 eV) of the sample is much higher than the laser energy, therefore in general the coherent phonons are generated by ISRS.

61.3 Results and Discussion

An intense electric response and a weak successive modulation due to coherent optical phonons were found in the transient reflection signal as shown in Fig. 61.1.

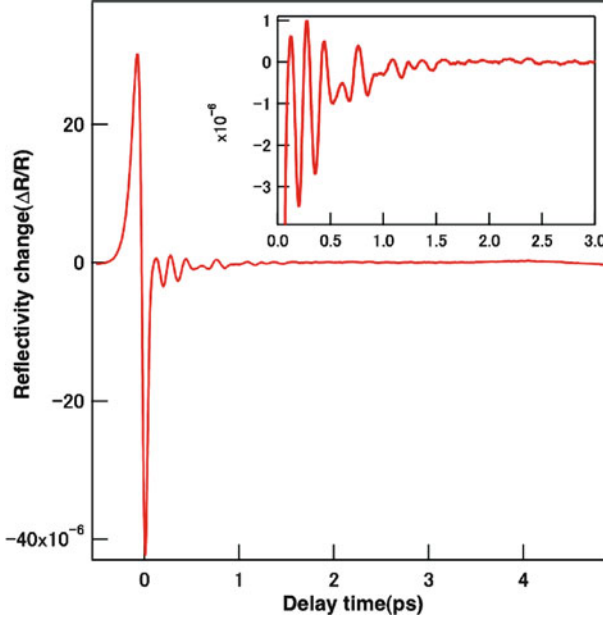


Fig. 61.1 Transient reflectivity change in PbTiO₃

The oscillatory signal was analyzed using continuous wavelet transformation, which provides the time evolution of the coherent phonons. The continuous wavelet transformation chronogram (Fig. 61.2) shows four frequency components with frequencies of 3.2, 4.7, 6.2 and 8.6 THz at delay = 0 ps, which are assigned to A₁(1TO), A₁(1LO), E(2TO), and B₁ + E modes. The frequency of the A₁(1TO) phonon was 3.2 THz at the delay of 0.4 ps, and increased to 3.5 THz at the delay of 2.4 ps. This positive chirp of the frequency is explained due to time evolution of phonon populations in an anharmonic lattice potential. The A₁(1TO) phonon, soft-mode in the ferroelectric state of PbTiO₃, is characterized by a double-well potential along the [0 0 1] direction. The microscopic potential energy $\phi(Q)$ is expressed by

$$\phi(Q) = -\frac{k}{2}Q^2 - \frac{\xi}{4}Q^4 + \frac{\zeta}{6}Q^6, \quad (61.1)$$

where Q is the normal coordinate, and k , ξ , and ζ are the potential parameters [6]. Energy differences between vibrational levels are well described by

$$\Delta E_n = E_{n+1} - E_n = \hbar\omega_0 - f(k, \xi, \zeta, n), \quad (61.2)$$

where $\hbar\omega_0$ is the solution of the harmonic term of the (61.1). The correction term f in (61.2) is linear in n for low n . The energy difference decreases as n increases. The calculated energy difference between E_0 and E_4 is 645 meV. Therefore, the

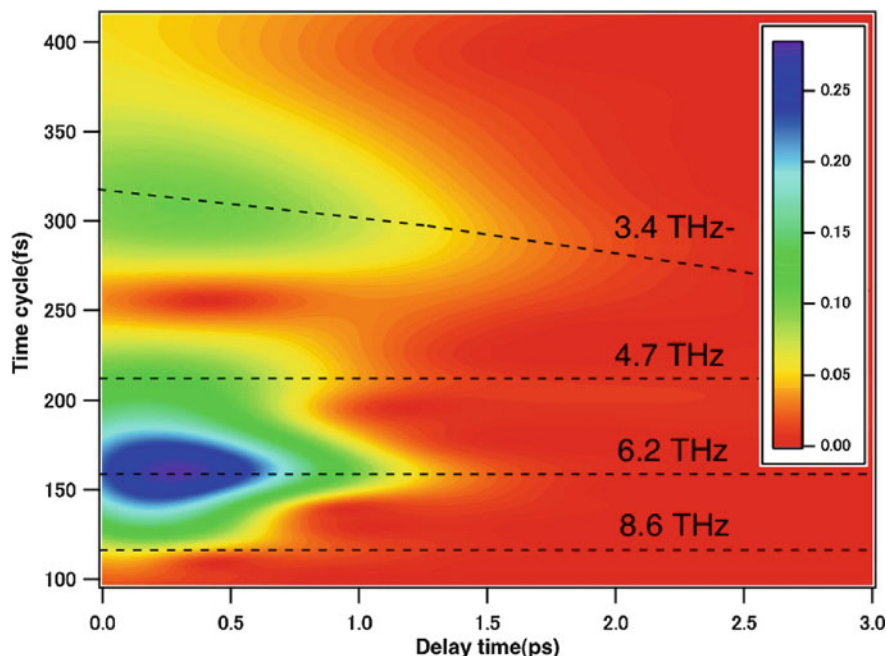


Fig. 61.2 Continuous wavelet transformation chronogram of transient reflection signals

positive frequency chirp is explained as follows: The $A_1(1TO)$ phonons were excited up to $n > 4$ having the frequency higher than 110 cm^{-1} ($\sim 3.3 \text{ THz}$) via the ISRS excitation. After delays, the phonons relaxed to lower vibrational levels and its frequency increased within 2 ps.

References

1. A.V. Kuznetsov, C.J. Stanton, *Phys. Rev. Lett.* **73**, 3243 (1994)
2. M. Först, T. Dekorsy, *Coherent Vibrational Dynamics* (CRC Press, Boca Raton, 2008), pp. 129–172
3. H. Takahashi, Y. Kamihara, H. Koguchi, T. Atou, H. Hosono, I. Katayama, J. Takeda, M. Kitajima, K.G. Nakamura, *J. Phys. Soc. Jpn.* **80**, 013707 (2011)
4. Y. Okano, H. Katsuki, Y. Nakagawa, H. Takahashi, K. G. Nakamura, K. Ohmori, *Frad. Discuss* (2011). doi:10.1039/c1fd00070e, published online
5. S. Utsugi, T. Fujiwara, R. Ikariyama, S. yasui, H. Nakai, T. Yamada, M. Ishikawa, M. Matsushima, H. Morioka, H. Funakubo, *Appl. Phys. Lett.* **94**, 052906 (2009)
6. T. Hidaka, *J. Phys. Soc. Jpn.* **61**, 1054 (1992)

Chapter 62

High-Order Harmonic Photoelectron Spectroscopy System towards Measuring Attosecond Electron Dynamics on Solid Surfaces

Katsuya Oguri, Hidetoshi Nakano, Keiko Kato, Tadashi Nishikawa, Atsushi Ishizawa, Hideki Gotoh, Kouta Tateno, and Tetsuomi Sogawa

Abstract With the aim of tracking the motion of electrons on semiconductor surfaces on an attosecond timescale, we have developed a femtosecond time-resolved surface photoelectron spectroscopy (PES) system based on a 59th harmonic pulse source, and a 90-eV high-order harmonic pulse source using a few-cycle carrier-envelope phase (CEP) stabilized laser pulse. We used this surface PES system to measure the time evolution of the surface photovoltage effect on GaAs(0 0 1). We observed an energy shift of about 200 meV of a 3d-core level photoelectron peak towards a higher binding energy. This suggests that the surface potential changed owing to the spatial separation of the electron–hole pair that was generated by laser irradiation. Our observation of the CEP dependence of the harmonic spectrum generated by the CEP-stabilized few-cycle pulse indicates that this source has the potential to produce an attosecond EUV pulse.

62.1 Introduction

Electronic processes in a condensed matter system and on its surface in an optical sub-cycle regime, which are induced by the interaction between valence electrons and an optical field, constitute phenomena that have remained elusive in spite of their fundamental and technological importance. It has been stimulated to explore

K. Oguri (✉) · K. Kato · T. Nishikawa · A. Ishizawa · H. Gotoh · K. Tateno · T. Sogawa
NTT Basic Research Laboratories, Nippon Telegraph and Telephone Corporation,
3-1 Morinosato Wakamiya, Atsugi, Kanagawa 243-0198, Japan
e-mail: oguri.katsuya@lab.ntt.co.jp

H. Nakano
Department of Electrical, Electronic and Computer Engineering, Faculty of Science
and Engineering, 2100 Kujirai, Kawagoe, Saitama 350-8585, Japan

and control electronic processes in the time domain by recent studies of sub-cycle electronic transitions and collective motions induced by an optical field in metals, semiconductors and dielectrics with theoretical approaches [1–4] and the indirect experimental measurement of attosecond electron transfer times on surfaces with the core–hole–clock technique [5, 6]. However, the direct real-time measurement of such electron dynamics is still challenging. From this point of view, the combination of a time-resolved surface PES using a high-order harmonic source in the extreme ultraviolet (EUV) region [7, 8] and an attosecond high-order harmonic generation (HHG) technique [9, 10] is expected to open the door to a direct approach for measuring electronic processes on solid surfaces [11]. In this study, we have developed a femtosecond laser-pump and EUV-probe surface PES system based on an HHG source as a prototype of attosecond time-resolved surface PES. We used this system to measure the temporal evolution of photoexcited electron–hole dynamics on a semiconductor surface, thus demonstrating the feasibility of our surface PES system. In addition, we observed the CEP dependence of a 90-eV high-order harmonic pulse source generated by a CEP-stabilized laser pulse with a duration of 6 fs. The results indicate that combining the surface PES system with the 90-eV harmonic source enables us to track attosecond electron motions on solid surfaces.

62.2 Experimental

Figure 62.1 shows a schematic illustration of a femtosecond time-resolved surface PES system based on a high-order-harmonics-probe and laser-pump scheme [12]. The system is based on a 100-fs Ti:sapphire laser system with a central wavelength of 790 nm operating at a 10 Hz repetition rate. We selected the 59th (92.5 eV) single harmonic pulse as the EUV probe by using a pair of Mo/Si multilayer mirrors from the many different orders of high-order harmonics. We assumed the pulse duration of the 59th harmonic to be roughly 100–200 fs from our previous 51st harmonic pulse duration measurements [13]. To analyze the photoelectron energy, we used a 500-mm-long time-of-flight (TOF) electron spectrometer with an electron lens system and a μ -metal shield. The sample was an undoped GaAs(0 0 1) substrate, which was chemically etched to remove a native oxidation layer from the GaAs surface.

For the attosecond HHG, we used a 25-fs Ti:sapphire laser system with a CEP fluctuation less than 300 mrad and a repetition rate of 1 kHz. The output pulse was propagated through a 1-m long capillary tube with an inner diameter of 250 μ m and filled with Ne gas, and a compressor that consisted of several pairs of chirped mirrors. The result was a 6-fs pulse with an energy of 250 μ J and a center wavelength of 735 nm. We generated high-order harmonics by using a Ne gas jet, and measured the spectrum with a grazing incidence flat-field spectrograph [14].

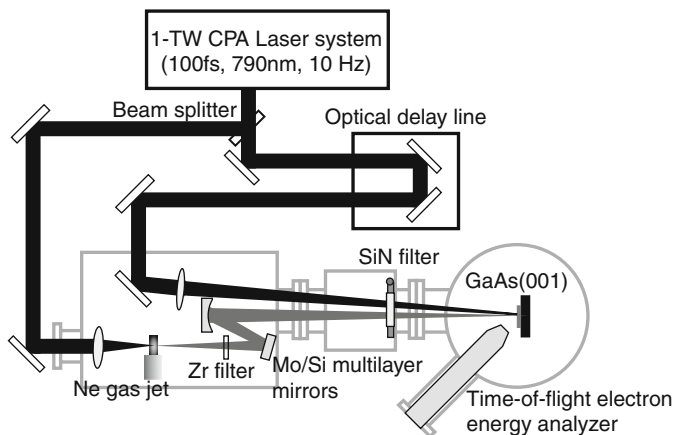


Fig. 62.1 A schematic illustration of the femtosecond time-resolved surface PES system

62.3 Results and Discussion

Figure 62.2a shows a typical photoelectron spectrum of a GaAs(0 0 1) sample measured with our PES system. This figure clearly shows three characteristic photoelectron peaks near binding energies of 0, 20, and 40 eV, which correspond to the valence bands of GaAs, and the core levels of Ga-3d, and As-3d, respectively. When the sample is excited with a 100-fs laser pulse, the 3d-core level photoelectron peak clearly shifts about 200 meV towards a higher binding energy (Fig. 62.2b). Since the binding energy of a core level photoelectron peak reflects the band bending of a semiconductor surface, the peak shift indicates that the surface potential changed the bending of the surface band due to the electric field induced by the spatial separation of the electron–hole pair that was generated by the laser excitation [15, 16]. The clear temporal change of the shift within 2 ps shown in this figure indicates that the electron–hole pair generation and the subsequent separation into electrons and holes occurs on a femtosecond time scale.

Figure 62.3a shows the high-order harmonic spectra obtained with a few-cycle laser pulse at various time delays. To match the cut-off energy to the reflection band of the multilayer mirrors in our surface PES system, we adjusted the excitation intensity of the laser pulse using a combination consisting of an ultra-broadband half-wave plate and a polarizer. This figure shows that a cut-off energy of 92 eV is achieved at an intensity of $2 \times 10^{14} \text{ W/cm}^2$. We also measured the CEP dependence of the high-order harmonic spectra generated at this intensity (Fig. 62.3b). The clear dependence of the harmonic spectrum in the cut-off region on CEP confirms that an isolated attosecond pulse can be generated at the CEP of the cosine phase [17]. Therefore, combining the time-resolved surface PES system with the potential attosecond high-order harmonic pulse will provide us with a powerful tool for tracking electron dynamics on a solid surface in the optical sub-cycle regime.

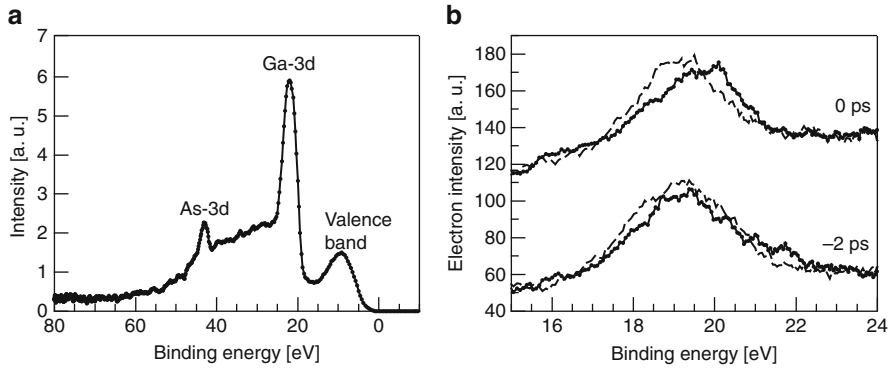


Fig. 62.2 Photoemission spectrum from a GaAs(0 0 1) surface measured with the 59th harmonic pulse source (a) and the Ga-3d photoelectron peak with (solid) and without (dashed) 100-fs laser irradiation (b)

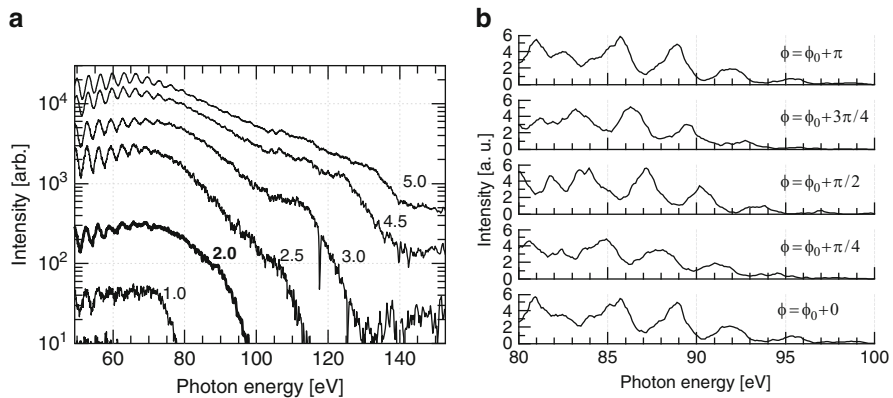


Fig. 62.3 HHG spectra obtained with the 6-fs laser pulse at various excitation intensities (a) and CEP dependence of the cut-off region (b). The unit of the number in (a) is 10^{14} W/cm²

References

1. S. Hughes, Phys. Rev. Lett. **81**, 3363 (1998)
2. O.D. Mücke, T. Tritschler, M. Wegener, U. Morgner, F.X. Kärtner, Phys. Rev. Lett. **89**, 127401 (2001)
3. M. Stockman, M. Kling, U. Kleineberg, F. Krausz, Nat. Photon. **1**, 539 (2007)
4. T. Otobe, M. Yamagiwa, J.-I. Iwata, K. Yabana, T. Nakatsukasa, G.F. Bertsch, Phys. Rev. B **77**, 165104 (2008)
5. J. Schnadt, P.A. Brühwiler, L. Patthey, J.N. O'Shea, S. Södergren, M. Odellus, R. Ahuja, O. Karis, M. Bässler, P. Persson, H. Siegbahn, S. Lunell, N. Martensson, Nature **418**, 620 (2002)
6. A. Föhlisch, P. Feulner, F. Hennies, A. Fink, D. Menzel, D. Sanchez-Portal, P.M. Echenique, W. Wurth, Nature **436**, 373 (2005)

7. P. Siffalovic, M. Drescher, M. Spieweck, T. Wiesenhal, Y.C. Lim, R. Weidner, A. Elizarov, U. Heinzmann, *Rev. Sci. Instrum.* **72**, 30 (2001)
8. M. Bauer, C. Lei, K. Read, R. Tobey, J. Claud, M.M. Murnane, H.C. Kapteyn, *Phys. Rev. Lett.* **87**, 025501 (2001)
9. G. Sansone, E. Benedetti, F. Calegari, C. Vozzi, L. Avaldi, R. Flammini, L. Poletto, P. Villoresi, C. Altucci, R. Velotta, S. Stagira, S. De Silvestri, M. Sisoli, *Science* **314**, 443 (2006)
10. E. Goulielmakis, M. Schultze, M. Hofstetter, V.S. Yakovlev, J. Gagnon, M. Uiberacker, A.L. Aquila, E.M. Gullikson, D.T. Attwood, R. Kienberger, F. Krausz, U. Kleineberg, *Science* **320**, 1614 (2008)
11. A.L. Cavalieri, N. Müller, Th. Uphues, V.S. Yakovlev, A. Baltuška, B. Horvath, B. Schmidt, L. Blümel, R. Holzwarth, S. Hendel, M. Drescher, U. Kleineberg, P.M. Echenique, R. Kienberger, F. Krausz, U. Heinzmann, *Nature* **449**, 1029 (2007)
12. K. Oguri, K. Kato, T. Nishikawa, A. Ishizawa, H. Gotoh, K. Tateno, T. Sogawa, H. Nakano, in preparation
13. K. Oguri, T. Nishikawa, T. Ozaki, H. Nakano, *Opt. Lett.* **29**, 1279 (2004)
14. H. Nakano, A. Ishizawa, K. Oguri, *Proc. Soc. Photo Opt. Instrum. Eng.* **7276**, 72760D (2009)
15. S. Tanaka, S.D. More, J. Murakami, M. Itoh, Y. Fujii, M. Kamada, *Phys. Rev. B* **64**, 155308, (2001)
16. P. Siffalovic, M. Drescher, U. Heinzmann, *Europhys. Lett.* **60**, 924 (2002)
17. A. Baltuška, T. Udem, M. Uiberacker, M. Hentschel, E. Goulielmakis, C. Gohle, R. Holzwarth, V.S. Yakovlev, A. Scrinzi, T.W. Hänsch, F. Krausz, *Nature* **421**, 611 (2003)

Chapter 63

Effect of Light Polarization on Plasma Distribution and Filament Formation

L. Arissian, D. Mirell, J. Yeak, S. Rostami, and J.-C. Diels

Abstract We show that filament formation has a strong dependence on the laser light polarization for 200 fs light at 790 nm. Filamentation does not exist for a pure circularly polarized light, propagating in vacuum before focusing in air, while there is no difference for focusing the light in air or vacuum for linearly polarized light.

63.1 Introduction

Laser polarization and its effect on strong field ionization had been studied extensively when dealing with single atoms or molecules. In laser filamentation, however, the effect of the light polarization is not clearly studied because of difficulty in (1) polarization preparation at the point of filamentation and (2) polarization measurement of a high intensity filament. This is mainly because the filamentation study is not a chamber study like most of strong field light matter interactions. Although there had been evidence of polarization deformation in focusing in air, filaments are still prepared in gases because no optical window withstands the light intensity. In order to have a clear starting point for the filament we use an

L. Arissian (✉)

Joint Laboratory for Attosecond Science, University of Ottawa and National Research Council,
100 Sussex Drive, Ottawa K1A 0R6, Canada

Electrical and Computer Engineering, University of New Mexico, Albuquerque, NM, USA

Department of Physics, Texas A & M University, College Station, TX 77843, USA
e-mail: ladan@unm.edu

D. Mirell · J. Yeak · S. Rostami

Physics and Astronomy, University of New Mexico, Albuquerque, NM, USA

J.-C. Diels

Electrical and Computer Engineering, University of New Mexico, Albuquerque, NM, USA

Physics and Astronomy, University of New Mexico, Albuquerque, NM, USA

aerodynamic window to prepare the filament in vacuum before launching it in air. By focusing the beam in vacuum to the filament size, all pre-filament nonlinear effects are eliminated. Given such initial condition, filaments are observed only with linear polarization. No filament is observed with circularly polarized light.

Since the first realization of laser filamentation in IR [3] and UV [13], there has been a considerable number of models and numerical simulations on filaments. While each of these simulations attempts to explain a particular observation, a physical picture fails to emerge. The existing formalism lacks for instance details on the effects of plasma on the wavefront and light polarization at the microscopic level. In the experiment also, there is not a direct method to image (single shot) the light propagation, or control pre-filament light environment. Optical elements that could withstand the light intensity of the order of TW/cm^2 would at best distort the filament through nonlinear effects. The controversy in filament studies can be monitored in the optics literature with complete opposite statements such as “*a filament results from balance between Kerr self-focusing and plasma defocusing*” or “*a filament is the manifestation of a moving focus,*” or “*a filament is a Bessel beam,*” to the extent that there is no more a clear definition for filamentation. At times, even a breakdown in air is referred to as a light filament. One reason is the sheer number of physical phenomena associated with the filaments, such as conical emission, THz emission, harmonic generation, spatial replenishment [9] self-healing [8], etc. Another reason is that there is an obscure curtain of the order of a meter that separates the prepared initial condition from the observed filament. Substantial temporal [1,2] and spatial [6] reshaping of the initial pulse profile takes place in amplitude and phase, such that the pulse ultimately reaching a self-focus of the size of the filament is very different from the macroscopic beam launched in the atmosphere.

Filaments have traditionally been created by letting a high power laser self-focus in air. Besides losing a lot of energy during that process, the starting point of the filament is undefined. Furthermore, it becomes difficult, sometimes impossible, to distinguish the phenomena associated with the “preparation phase” from the true “filamentation phase.” We focus instead the beam in a vacuum cell with a 3 m focal distance lens, to a beam waist at the location close to a transition of vacuum to air. The intensity at the focal spot in vacuum exceeds $100 \text{ TW}/\text{cm}^2$. At those intensities any window material is either damaged or shows significant nonlinear effects. The aerodynamic window provides a pressure gradient across a supersonic air stream, with an expansion chamber profiled in such a way that the pressure on one side is atmospheric, and on the other side less than 10 torr. The contours of the window are such that a pressure gradient is formed in the supersonic flow by Prandtl–Meyer expansion waves across which the beam propagates into the vacuum chamber. The supersonic gas flow enters the diffuser, recovers the flow pressure back to atmospheric conditions, and ejects into the atmosphere. The supply pressure upstream of the supersonic nozzle can be varied to achieve optimum performance. The compressor associated with this window supplies a continuous flow of $10 \text{ m}^3/\text{min}$ ($150 \text{ dm}^3/\text{s}$) at a pressure of $8 \text{ kg}/\text{cm}^2$.

We tackle for the first time one of the major obstacles of the filamentation studies; controlling the pre-filamentation light propagation. By focusing the beam

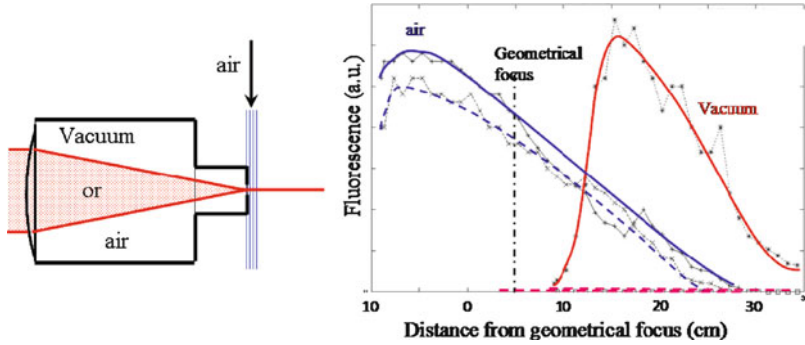


Fig. 63.1 *Left:* a 15 mm diameter beam is focused in a 3 m long vacuum tube, terminated by an aerodynamic window. *Right:* The fluorescence at 337 nm is measured as a function of distance from the geometrical focus, for linearly polarized light (*solid lines*) and circularly polarized light (*dashed lines*)

in vacuum (through aerodynamic window) to the filament size before launching in the atmosphere, all pre-filament nonlinear effects are eliminated. With such a propagation in vacuum up to the focus, filaments are observed only with linear polarization. No filament is observed with circularly polarized light, in direct contradiction with the theoretical simulation of Panov et al. [10] where it is claimed that filaments would be more uniform and intense with circularly polarized light.

To study the effect of polarization on filament formation, the output of a home-build amplified Ti:Sapphire laser with 10 mJ pulse energy and 200 fs pulse duration is focused with a 3 m focal length lens. The conductivity due to the generated free electrons and the fluorescence of nitrogen are measured as a function of distance from the geometrical focus for linearly and circularly polarized light prepared either in vacuum or air. In linear polarization, measurements of the beam profile versus distance from the aerodynamic window have indicated that filaments are produced in both vacuum and air pre-filament cases. The $1/e^2$ half-width is $w_0 = 200 \mu\text{m}$ at the focus for preparation in vacuum, and $w_0 = 250 \mu\text{m}$ when the macroscopic beam is let to self-focus in air, for the same initial input beam. The filament for both cases of a linearly polarized light is the same size of $250 \mu\text{m}$, which is not measured to be different from circularly polarized light focused in air.

To these filaments is associated a plasma, which manifests itself through fluorescence of positive ions, and an increased conductivity of air. Our measurement traces the fluorescence of nitrogen at 337 nm (Fig. 63.1), as a function of distance from the geometrical focus. In the case of linearly polarized light, the fluorescence rises and decays over approximately 30 cm. Measurements of the beam profile versus distance however shows the filament to conserve a constant diameter for more than 75 cm [5, 7]. When the linearly polarized beam is filamented in air, the plot of fluorescence versus distance is receded by about 20 cm, which represents the difference between the linear and nonlinear focus. There is very little difference in fluorescence for the initially circularly polarized beam self-focusing in air

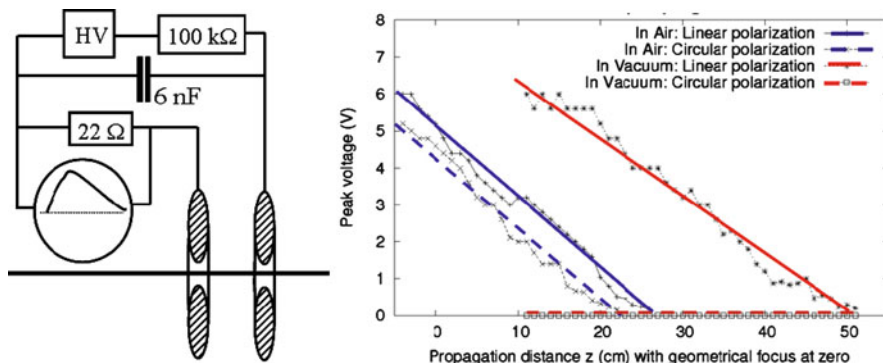


Fig. 63.2 *Left*: circuit to measure the conductivity. The filament is sent through two profiled holes in electrodes 2 cm apart. Air becomes conductive under passage of the filament, and a voltage is measured across a $22\ \Omega$ m resistor. *Right*: measured voltage (hence conductivity) as a function of distance from the geometrical focus of a 3 m focal distance lens. The *solid lines* correspond to linear polarization; the *dashed lines* to circular polarization

(dashed line). In contrast, there is no fluorescence observed in the case of circularly polarized beam started from vacuum. The absence of plasma in circular polarization is confirmed by conductivity measurements presented in Fig. 63.2, where the conductivity of plasma induced by the filaments is plotted as a function of distance from the geometric focus.

There have been several reports of observation of polarization dependence on filament properties. For instance, an experimental investigation of “polarization dependent filamentation in atoms and molecules” was reported by Varela et al. [12]. The objective of that study was to control pulse compression (to less than 3 fs), multi-filamentation, as well as supercontinuum generation, by acting only on the input state polarization (linear to elliptical to circular). The report showed that a filament is present for all degrees of ellipticity while there is no control or measurement of the polarization at the point of filamentation. A significant difference with our experimental condition is that the initial pulse launched in air had a duration of 40 fs. The shorter pulse implies (a) higher intensity, hence a shorter self-focusing distance, and (b) the reorientation contribution to the Kerr effect is smaller. These two effects may imply that, in the case of the experiment of Varela et al., the elliptical polarized beam may have been conserved during propagation and self-focusing.

Existing light propagation equation for filamentation [4] do not include the microscopic effects of the ionization process and radiation of moving charges. Recent reports on the measurement of electron momentum distribution after tunnel ionization with short pulses [11] and THz radiation associated to that [14] show that there is a major difference in the partitioning of energy for circular and linear polarization. The conservation of energy implies that the total energy absorbed during the ionization process $Nh\nu$ needs to be divided between ions (as recoil energy),

electrons (drift energy) and light (Ponderomotive energy). In both recent papers the focus was on the electrons energy and momentum, showing considerably more kinetic energy for circularly polarized light. That could explain the absence of the filamentation in circularly polarized light, owing to the difference in light modification by moving charged particles for the two polarizations. The details of the mutual interaction of radiation and moving charges has to be investigated for various light wavelengths and pulse duration, for a well defined light polarization at the focus.

References

1. A. Bernstein, T.S. Luk, T.R. Nelson, J.-C. Diels, S. Cameron, Observation of multiple pulse-splitting of ultrashort pulses in air. in *QELS 2001, QFC6* (Optical Society of America, Baltimore, 2001), pp. 262–263
2. A.C. Bernstein, T.S. Luk, T.R. Nelson, A. McPherson, J.-C. Diels, S.M. Cameron, Asymmetric ultra-short pulse splitting measured in air using frog. *Appl. Phys. B (Lasers and Optics)*, **B75**(1), 119–122 (2002)
3. A. Braun, G. Korn, X. Liu, D. Du, J. Squier, G. Mourou, Self-channeling of high-peak-power femtosecond laser pulses in air. *Opt. Lett.* **20**, 73–75 (1995)
4. A. Couairon, A. Mysyrowicz. Femtosecond filamentation in transparent media. *Phys. Rep.* **441**, 49–189 (2007)
5. J.-C. Diels, J. Yeak, D. Mirell, R. Fuentes, S. Rostami, D. Faccio, P. di Trapani, Air filaments and vacuum. *Laser Phys.* **20**, 1101–1106 (2010)
6. T.D. Grow, A.A. Ishaaya, L.T. Vuong, A.L. Gaeta, R. Gavish, G. Fibich, Collapse dynamics of super-Gaussian beams. *Opt. Express* **14**, 5468–5475 (2006)
7. M. Kolesik, D. Mirell, J.C. Diels, J.V. Moloney, On the higher-order kerr effect in femtosecond filaments. *Opt. Lett.* **35**, 3685–3687 (2010)
8. M. Kolesik, J.V. Moloney, Self-healing fs light filaments. *Opt. Lett.* **29**, 590–592 (2004)
9. M. Mlejnek, E.M. Wright, J.V. Moloney, Dynamic spatial replenishment of femtosecond pulse propagating in air. *Opt. Lett.* **23**, 382–384 (1998)
10. N.A. Panov, O.G. Kosyreva, D.S. Uryupina, A.B. Savelev-Trofimov, I.A. Perezhogin, V.A. Makarov, Filamentation of femtosecond gaussian pulses with close-to-linear or -circular elliptical polarisation. *Quantum. Electron.* **41**, 160 (2011)
11. C. Smeenk, L. Arissian, B. Zhou, A. Mysyrowicz, D.M. Villeneuve, A. Staudte, P.B. Corkum, Partitioning of the linear photon momentum in multiphoton ionization. *Phys. Rev. Lett.* **106**, 193002 (2011)
12. O. Varela, A. Zaïr, J.S. Roman, B. Alonso, N.J. Sola, C. Prieto, L. Roso, Above-millijoule super-continuum generation using polarisation dependent filamentation in atoms and molecules. *Opt. Express* **17**, 3630–3639 (2009)
13. X.M. Zhao, P. Rambo, J.-C. Diels, Filamentation of femtosecond uv pulses in air. in *QELS, 1995*, vol 16 (Optical Society of America, Baltimore, 1995), p. 178 (QThD2)
14. B. Zhou, A. Houard, Y. Liu, B. Prade, A. Mysyrowicz, A. Couairon, P. Mora, C. Smeenk, L. Arissian, P. Corkum, Measurement and control of plasma oscillations in femtosecond filaments. *Phys. Rev. Lett.* **106**(15), 255002 (2011)

Chapter 64

Ignition of Doped Helium Nanodroplets in Intense Few-Cycle Laser Pulses

S.R. Krishnan, L. Fechner, M. Kremer, V. Sharma, B. Fischer, N. Camus, J. Jha, M. Krishnamurthy, T. Pfeifer, R. Moshhammer, J. Ullrich, F. Stienkemeier, and M. Mudrich

Abstract The ultra-fast dynamics of He nanodroplets (10^3 – 10^5 atoms) in intense ($1 \dots 7 \times 10^{14}$ W/cm²), few-cycle (~ 10 fs), infrared (~ 790 nm) laser pulses has been investigated as a function of the number of dopant rare-gas atoms, the laser intensity and the rare-gas species. We find the “ignition” behaviour predicted by theory for 20 fs resulting in the complete ionisation and disintegration of the droplet, otherwise entirely transparent, initiated by just a few, less than 5 dopant atoms.

64.1 Introduction

The ionization dynamics of atomic clusters in intense ultrashort laser pulses have been an active area of research in recent years at near-infrared (NIR), vacuum-ultraviolet (VUV) and soft X-ray wavelengths [1, 2]. One of the most interesting properties of rare-gas clusters in the NIR domain result from the excellent coupling of laser light with the electronic nanoplasma, leading to energy absorption which far exceeds that possible in atomic jets or planar solid targets when irradiated with similar laser pulses. The underlying mechanism is a resonant absorption by the nanoplasma [3–5]. Resonance conditions are reached due to a fast cluster expansion on sub- or few-picosecond timescales as seen in pump-probe experiments [6] or measurements where the pulse duration is varied [7]. A recent theoretical study [8]

S.R. Krishnan (✉) · L. Fechner · M. Kremer · V. Sharma · B. Fischer · N. Camus · T. Pfeifer · R. Moshhammer · J. Ullrich
Max-Planck-Institut für Kernphysik, 69117 Heidelberg, Germany
e-mail: siva@mpi-hd.mpg.de

J. Jha · M. Krishnamurthy
Tata Institute of Fundamental Research, 1 Homi Bhabha road, Mumbai 400005, India

F. Stienkemeier · M. Mudrich
Physikalisches Institut, Universität Freiburg, 79104 Freiburg, Germany
e-mail: Marcel.Mudrich@physik.uni-freiburg.de

has predicted resonant absorption on a much shorter time scale of a few femtoseconds, where ionic motion cannot occur. The trick here is to use two-component systems like doped helium nanodroplets instead of pristine clusters. Such two-component systems open new ways to control the interaction of intense laser pulses with matter. They show remarkably different behavior when compared to pristine clusters demonstrating phenomena such as enhancements in the temperature of emitted and yield of emitted electrons under IR pulse illumination [9] and effects of local field-ionization in the VUV regime [10]. In this context, He droplets doped with other rare-gas atoms are particularly interesting systems, since conditions can be chosen such that the laser couples almost exclusively to the dopants whereas the helium droplet is transparent. Fortuitously, this applies to NIR [8, 11] as well as to X-ray [12] frequencies. Despite its transparency, the droplet becomes highly active once the core of dopant atoms is ionized.

Here we will report on experiments with doped helium droplets in strong NIR few-cycle pulses. We have used pulses as short as 10 fs in order to rule out any kind of ionic motion. Thus, the observed (singly- and double-charged) helium ions are exclusively due to electronic processes like strong-field ionization of the dopants, and resonant absorption by electrons in the nanoplasma on sub-10 fs timescales [8].

64.2 Experiment

In general, ^4He droplets ($\sim 10^3$ – 10^6 atoms per droplet) are an ideal host medium offering excellent control in designing doped systems [13]. Owing to their low internal temperature ~ 370 mK, they are in a superfluid state [13, 14] and are appropriately referred to as helium nanodroplets. Spectroscopic studies reveal that rare-gas dopants always reside at the center of spherical helium nanodroplets [14]. We performed careful experimental studies on the ionization dynamics of helium nanodroplets doped with other rare gas dopants: Xe, Kr or Ar. Pure helium nanodroplets were produced by expanding pressurized ^4He gas (70–90 bar) through a nozzle 5 μm in diameter maintained at a temperature 15–25 K. Varying the nozzle temperature allowed us to adjust the mean number of helium atoms per droplet in the range 10^3 – 10^5 . We will refer to the size of the droplets in terms of the mean number of ^4He atoms per nanodroplet. The details of the well-characterized source used by us have been reported elsewhere [14]. Doping is achieved by passing the skimmed beam of nanodroplets through a doping cell placed ~ 10 cm downstream from the skimmer. The doping cell consisted of a 3 cm long cylindrical cell with two collinear apertures ($\text{Ø} = 3$ mm) and the desired dopant gas was leaked into the doping cell with a dosing valve (leak rate $< 10^{-10}$ mbar l/s) while the pressure was monitored with a directly attached vacuum gauge. The statistical pick-up of the dopant atoms by the pure nanodroplets led to doping. The pick-up process is Poissonian as has been reported in several studies [15]. The mean number of dopants in the nanodroplets K was ascertained using the semi-empirical formulation of [15]. Recently, the pick-up process of alkali atoms that form high-spin clusters

was simulated using a Monte-Carlo model [16]. We used the same model to validate the estimate of doping levels using Kuma's formula [15] and also to estimate the loss of helium due to evaporation induced by the doping process. It is worthwhile to note here that the control of doping levels at 0.001% achieved in our experiment is unprecedented. This is an order of magnitude finer than previous studies that investigated the effect of doping on the ionization of rare-gas clusters by intense laser pulses in the IR domain [9]. Intense few-cycle laser pulses (~ 10 fs) at a central wavelength of 790 nm with peak intensities in the range 10^{14} – 10^{15} W/cm² were generated from a Ti-Sapphire based mode-locked laser system. Photoions are detected by a time-of-flight (TOF) spectrometer in the Wiley–McLaren geometry.

64.3 Results and Discussion

Time-of-flight (TOF) mass spectra for different doping numbers K of Xe in a droplet containing 1.5×10^4 He atoms are shown as insets in Fig. 64.1. The ion yields of He⁺ and He²⁺ ions are extracted from these spectra by integrating over the corresponding mass peaks. The He²⁺ peak, which is characteristic for ionizing doped He droplets and is absent in the mass spectra of atomic He gas, is split due to high momentum components directed towards and away from the detector. We measured the relative yield of a particular ionic species by integrating the area under the corresponding peak in the TOF mass spectrum. Figure 64.1 presents the doping dependence of the yields of He²⁺ and He⁺ at a peak intensity of 7×10^{14} W/cm² of the laser pulse. A gradual increase of doping number $K = 1$ up to 10 leads to a dramatic step-like increase in the yields of He⁺ and He²⁺ ions. We refer to this feature as *ignition*. The saturation of ion yields and equivalently the build-up of charge occurs for a critical doping number K_{cr} of just 7. Beyond this doping level the ionization of the helium droplet is not enhanced any further. This critical doping number K_{cr} is remarkably independent of the mean droplet size as it is varied from $N_{He} = 5,000$ to 15,000 as it remains in the range 7 ± 2 . Consequently, the mechanism underlying the charging process should be largely independent of droplet size.

Next, we address the issue of nanodroplet evaporation which occurs as a consequence collisional as well as binding energy released into the droplets upon the sequential pick up of dopant atoms that aggregate inside the He droplets. This leads to an increasing fraction of He droplets that completely evaporate at high doping pressure. The corresponding estimate from the Monte-Carlo simulation is indicated by the grey curve in Fig. 64.1. Clearly, the onset of significant nanodroplet destruction in this case of Xe doping occurs well beyond the critical doping numbers (~ 10) observed in the experiment. Thus, the step-like ignition behavior is disentangled from evaporation effects.

In contrast to the insensitivity with respect to different droplet sizes, K_{cr} markedly depends on laser intensity, as illustrated in Fig. 64.2. K_{cr} increases with decreasing laser intensity. Considering that we do not ionize He atoms in the droplet

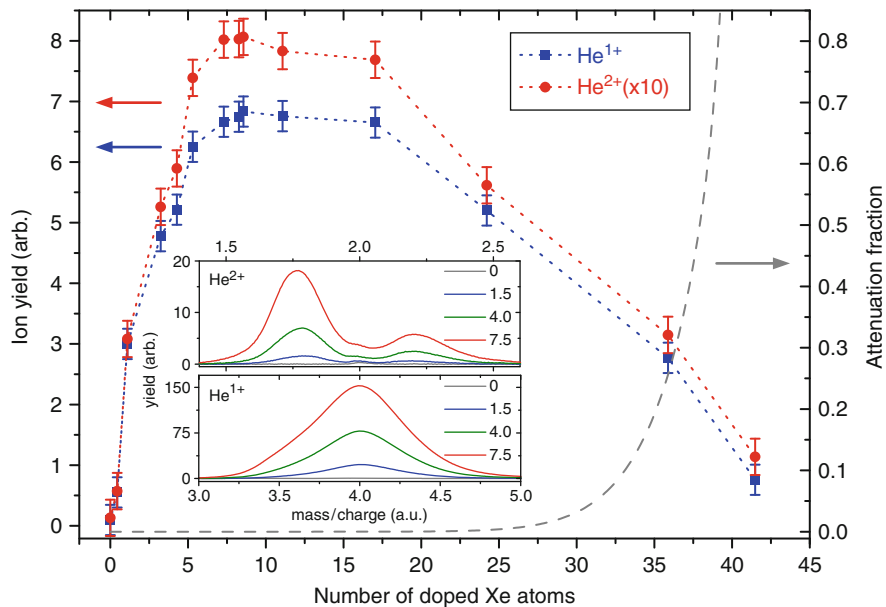


Fig. 64.1 Yields of He^+ and He^{2+} ions as a function of the number of Xe dopants in a nanodroplet containing 1.5×10^4 He atoms (*lines* to guide the eye). *Inset*: Mass spectra of He^{2+} (*top*) and He^+ (*bottom*). The fraction of droplets (*grey curve*) lost during the pick up of Xe atoms due to complete evaporation is presented as the attenuation fraction (cf. discussion in text). The loss of droplets is significant only for doping numbers $K > 20$

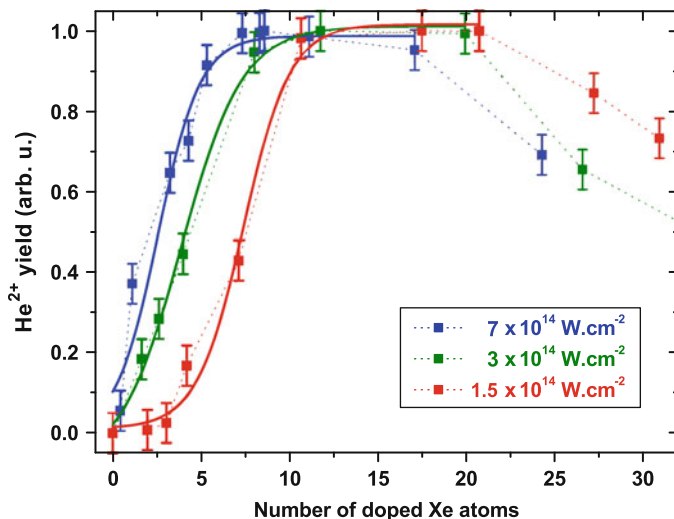


Fig. 64.2 Yield of He^{2+} ions as a function of the mean number of dopants (Xe) for three different intensities with *lines* to guide the eye

directly by photoionization, these results (Fig. 64.2) point to the fact that dopant atoms seed the ignition of the droplet. A smaller number of dopants is required to facilitate ignition under conditions where a greater number of seed electrons is released from each dopant atom within the droplet.

The numerical studies of Mikaberidze et al. [8], were performed on conditions similar to those in our experiment. The mechanism of charging revealed by these simulations relies on the formation of an ellipsoidal nanoplasma within the droplet. The efficient absorption or coupling of laser field is due to electronic resonance in an ellipsoidal nanoplasma. This occurs in the following way: The intense laser pulse creates a nanoplasma in the doped droplet with a charge density ϱ by ionizing the dopant atoms at the center. This spherical plasma has an eigenfrequency $\Omega_{sph} = (4\pi\varrho/3)^{1/2}$ much higher than the laser frequency at 800 nm. Unlike in the long pulse the electron density does not change significantly within the duration of the 10 fs pulse due to ionic motion, i.e. cluster expansion. However, the electrons released from the dopants ionize the surrounding He, the nanoplasma within the droplet grows into an ellipsoidal or cigar-shaped object with its major axis along the polarization of the laser electric field. This is due to preferential ionization of atoms the direction of laser polarization. The eigenfrequency of this ellipsoidal nanoplasma along laser polarization direction (Ω_{\parallel}) can be written in terms of the eigenfrequency for a spherical plasma of the same density: $\Omega_{\parallel} = \Omega_{sph}/g(\alpha)$, where $g(\alpha)$ is an increasing function of α [8]. The nature of this eigenmode of a spheroidal plasma has also been investigated in the context of Penning traps [17]. This anisotropic plasma maintains a favorable aspect-ratio so that the eigenfrequency Ω_{\parallel} matches the driving laser frequency thereafter during the pulse. The resonant driving of these electrons by the laser field is responsible for the complete ionization of the He atoms in an avalanche-like manner. A minimum number of seed electrons and consequently a critical number of dopant is necessary for the ignition to be triggered. Numerical studies predicted a total ionization of the entire droplet for a critical doping number of just three [8] while in our experiment the corresponding value is about seven for similar nanodroplet sizes ($\sim 10^4$ atoms). The numerical studies were performed on single doped nanodroplets at one peak pulse intensity, whereas in the experiment averaging over the distributions of intensity, nanodroplet sizes and (Poissonian) doping levels is inevitable. However, the most important feature of the numerical study—the step-like increase or ignition—survives the test of these experimental conditions. This also points to a robust underlying mechanism for nanodroplet ignition triggered by just a few dopant atoms.

64.4 Conclusion

In conclusion, we have studied threshold behavior of the ionization of helium nanodroplets containing 10^4 atoms when doped with few atoms in intense few cycle IR pulses. Our studies reveal a hitherto unobserved ignition effect due to few-atom doping.

It is pleasure to acknowledge stimulating discussions with A. Mikaberidze, U. Saalman, J.-M. Rost, Th. Fennel and J. Tiggesbäumker. We are grateful to O. Bünermann for valuable assistance in the Monte-Carlo calculations.

References

1. U. Saalman, C. Siedschlag, J.M. Rost, *J. Phys. B* **39**, R39 (2006)
2. Th. Fennel, K. -H. Meiwes Broer, J. Tiggesbäumker, P.-G. Reinhard, P. Dinh, E. Suraud, *Rev. Mod. Phys.* **82**, 1793 (2010)
3. T. Ditmire, T. Donnelly, A.M. Rubenchik, R.W. Falcone, M.D. Perry, *Phys. Rev. A* **53**(5), 3379 (1996). DOI 10.1103/PhysRevA.53.3379
4. U. Saalman, J.M. Rost, *Phys. Rev. Lett.* **91**(22), 223401 (2003). DOI 10.1103/PhysRevLett.91.223401
5. U. Saalman, *J. Mod. Opt.* **53**, 173 (2006)
6. J. Zweiback, T. Ditmire, M.D. Perry, *Phys. Rev. A* **59**, R3166 (1999)
7. L. Köller, M. Schumacher, J. Köhn, S. Teuber, J. Tiggesbäumker, K.H. Meiwes-Broer, *Phys. Rev. Lett.* **82**(19), 3783 (1999). DOI 10.1103/PhysRevLett.82.3783
8. A. Mikaberidze, U. Saalman, J.M. Rost, *Phys. Rev. Lett.* **102**, 128102 (2009)
9. J. Jha, M. Krishnamurthy, *J. Phys. B* **41**, 041002 (2008)
10. M. Hoener, C. Bostedt, H. Thomas, L. Landt, E. Eremina, H. Wabnitz, T. Laarmann, R. Treusch, A. Castro, T. Möller, *J. Phys. B Atom. Mol. Opt. Phys.* **41**, 181001 (2008)
11. A. Mikaberidze, U. Saalman, J.M. Rost, *Phys. Rev. A* **77**(4), 041201 (2008). DOI 10.1103/PhysRevA.77.041201
12. C. Gnodtke, U. Saalman, J.M. Rost, *Phys. Rev. A* **79**, 041201 (2009)
13. J.P. Toennies, A.F. Vilesov, *Angew. Chem. Int. Ed.* **43**, 2622 (2004)
14. F. Stienkemeier, K. Lehmann, *J. Phys. B* **39**, R127 (2006)
15. S. Kuma, H. Goto, M.N. Slipchenko, A.F. Vilesov, A. Khramov, T. Momose, *J. Chem. Phys.* **127**, 214301 (2007)
16. O. Bünermann, F. Stienkemeier, *Eur. Phys. J. D* **61**, 645 (2011)
17. J.J. Bollinger, D.J. Heinzen, F.L. Moore, W.M. Itano, D.J. Wineland, D.H.E. Dubin, *Phys. Rev. A* **48**(1), 525 (1993). DOI 10.1103/PhysRevA.48.525

Chapter 65

Ultrafast Nanoscale Imaging Using High Order Harmonic Generation

Willem Boutu, David Gauthier, Xunyou Ge, Fan Wang, Aura Ines Gonzalez, Benjamin Barbrel, Ana Borta, Mathieu Ducouso, Bertrand Carré, and Hamed Merdji

Abstract Coherent diffractive imaging using soft and hard X-rays ultrashort pulses is a promising technique to study ultrafast dynamics in non crystalline objects. However, up to now, it was limited to large scale facilities such as free electron lasers. We developed an optimized table-top soft X-ray source, based on high order harmonic generation. It produces a high intensity femtosecond coherent beam, with up to 1×10^{11} photons per shot at the source at $\lambda = 32$ nm. We recently demonstrated nanoscale imaging in single laser shot mode, with femtosecond time resolution. This opens fascinating perspectives in imaging dynamical phenomena to be spread over a large scientific community. First preliminary results in the investigation of femtosecond spin-reversals of magnetic nano-domains and ultrafast molecular rearrangements are presented.

65.1 Introduction

Ultrafast coherent diffraction using soft and hard X-rays is currently revolutionizing imaging science thanks to new sources recently available. This powerful technique extends standard X-ray diffraction towards imaging of non-crystalline objects. It is based on the fact that the far field diffracted by an object is its Fourier transform. Sayre and coworkers suggested that when the diffraction pattern is sufficiently oversampled, the spatial phase, lost during the recording, can be recovered, allowing the inversion of the pattern [1, 2]. Thanks to the absence of imaging lens, which are difficult to manufacture for short wavelengths, the spatial resolution of coherent diffractive imaging (CDI) is in principle limited only by the wavelength. Since its first experimental demonstration in 1999 by Miao and coworkers [3], new

W. Boutu (✉) · D. Gauthier · X. Ge · F. Wang · A.I. Gonzalez · B. Barbrel · A. Borta · M. Ducouso · B. Carré · H. Merdji
CEA Saclay, IRAMIS/SPAM, 91191 Gif sur Yvette, France
e-mail: willem.boutu@cea.fr

ultrashort pulses recently available hold the promise of watching matter evolves with unprecedented space and time resolution. Already, impressive results in biology (see e.g. [4, 5]) and physics (e.g. [6, 7]) have been reported. The first time resolved experiment have been published a few years ago [8]. They measured the ablation dynamics of a patterned sample with 50 nm spatial resolution and 10 ps temporal resolution. However, because of the large photon flux they require, those applications are mostly limited to large scale facilities like synchrotrons or free electron lasers.

High order laser harmonic sources present several interesting properties related to coherent diffractive imaging. Their degree of spatial coherence is very large over the whole beam section. The pulses are of ultrashort duration, and are naturally synchronized with the generating infrared laser, allowing easy pump-probe experiments for time resolved imaging. Moreover, a very large range of wavelengths is available, from a few eV to the keV range [9]. However, due to the low generation efficiency, the first CDI experiments were limited to large acquisition times [10, 11]. Microjoule level high order harmonic emission has been obtained using a loose focusing geometry to optimize phase matching [12, 13]. Using the same geometry, Schwenke et al. performed single shot in line holography imaging at $\lambda = 38 \text{ nm}$ [14], with a spatial resolution above $1 \mu\text{m}$.

In Sect. 65.2, we present the optimized high order harmonic setup we developed in Saclay. Section 65.3 explains briefly the two imaging techniques we demonstrated, namely phase reconstruction by iterative algorithm and holography with extended references, and presents some single shot results obtained on our beamline. Section 65.4 shows some preliminary results, paving the way towards time resolved experiments.

65.2 Optimized High Order Harmonic Beamline

High order harmonic generation suffers from a low efficiency, usually below 10^{-6} . To increase the number of generated photons, one can increase the laser intensity, up to a saturation value, due to ionization, of the order of 10^{14} W/cm^2 . To go beyond this limitation, two ways are possible: either increasing the size of the medium or improving the macroscopic construction of the field through phase-matching. The loose focusing geometry allows for both paths at the same time, thanks to gently varying spatial properties of the laser field around focus and an enlarged beam waist [12]. Here we used the LUCA laser from CEA Saclay. This Ti:Sa laser delivers 50 mJ, 50 fs pulses at $\lambda = 800 \text{ nm}$, at a repetition rate of 20 Hz. Figure 65.1 represents our experimental setup. After the last amplification stage, the laser spatial profile is flat-top, with a triangular shape and presents some hot spot. Filtering by a iris before focusing can improve the beam profile at focus, but up to a certain point only and side lobes are still present. This leads to a reduced harmonic generation efficiency and a large shot to shot variation of the harmonic beam profile, detrimental for experiments. Therefore we implemented a modal filtering of the

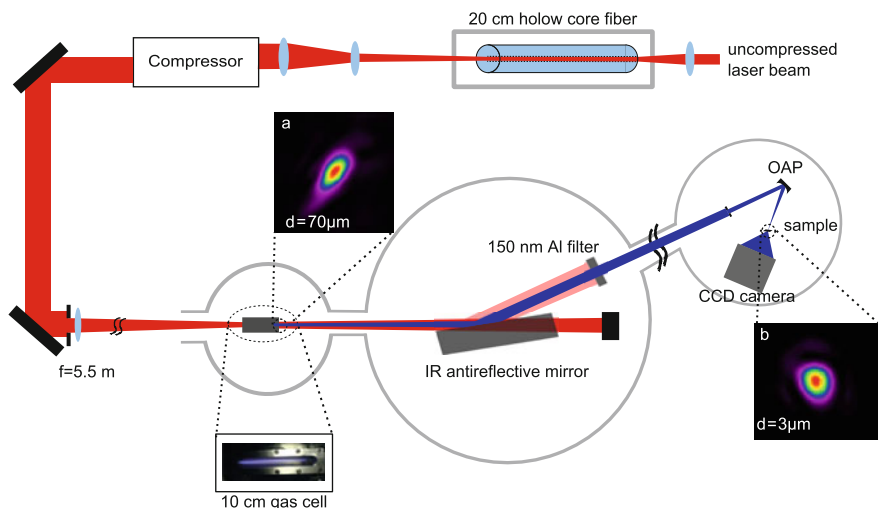


Fig. 65.1 Experimental CDI setup. (a) Spatial harmonic profile reconstructed at the harmonic source. (b) Spatial harmonic profile reconstructed at focus. See text for details

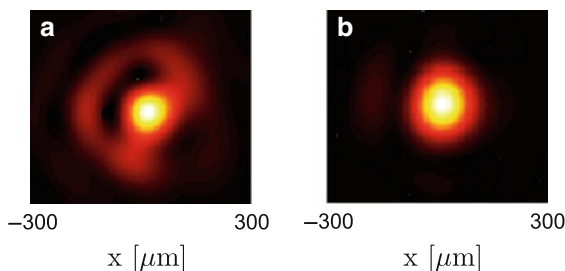


Fig. 65.2 Beam spatial characterization at the gas cell position without (a) and with (b) modal filtering

laser. As can be seen in Fig. 65.1, the picosecond uncompressed laser beam (200 ps, 180 mJ) is sent into a 20 cm long hollow core fiber, installed under vacuum. The transmission of the fiber is around 60%, with 70% of the input energy coupled to the fiber fundamental mode EH_{11} , very closed to Gaussian [15]. The filtered beam is sent into the compressor, with a transmission of around 40%. The beam spatial quality at focus, measured by a Shack–Hartmann wavefront sensor, is strongly improved, both in intensity distribution and phase, after filtering (Fig. 65.2).

The laser beam is afterwards focused using a 5.5 m focal length lens at the exit of a variable length cell. The optimal length, depending on the gas and the harmonic order, varies between 5 and 8 cm. A silicon plate at grazing incidence (for better UV reflectivity) with an antireflective coating for the infrared is used to remove most of the fundamental radiation. A high transmissivity aluminium filter ($T = 60\%$) is used to block the low order harmonics and the remaining infrared. The

optimized harmonic generation conditions (laser energy, iris diameter, cell length and gas pressure) were chosen to maximize both the number of photons and the beam profile quality at a selected wavelength (32 nm for instance). To that goal, the harmonic wavefront was measured before the iris in the last chamber using a UV Hartmann sensor [16]. The optimized beam profile has a quasi-circular shape and is almost diffraction limited. The beam profile, back propagated at the harmonic source, is presented in insert (a) in Fig 65.1.

The harmonic beam is then spatially filtered by a iris, and focused on the sample by an off-axis parabola (OAP) with a 200 mm focal length. Harmonic order 25 ($\lambda = 32$ nm) or 39 ($\lambda = 20$ nm) is selected by a multilayer coating on the parabola. We used the Hartmann sensor to optimize the off-axis parabola alignment. The beam diameter on sample is then equal to $3 \mu\text{m}$, with 5×10^8 photons per laser shot at $\lambda = 32$ nm and 10^6 at $\lambda = 20$ nm. A XUV-CCD camera (PI-MTE from Princeton Instruments, with $2,048 \times 2,048$ pixels of $13.5 \times 13.5 \mu\text{m}$ size) is put 3 cm away from the sample to measure the diffraction patterns.

65.3 Imaging Experiments

As we already mentioned in Sect. 65.1, the far field diffraction pattern created by an object is its Fourier transform. As detectors in the VUV region are only sensitive to intensity, the spatial phase information is lost and the direct inverse Fourier transform of the recorded data is not possible. However, if the sampling of the diffraction pattern is fine enough, it is possible to use iterative algorithms to recover the phase information, allowing the object image reconstruction [2]. Such algorithms use what is known from the measurements only, and do not necessarily need any other a priori knowledge on the sample properties (see e.g. [17,18]). Usually only a few thousands iterations, starting from an initial guess build with a random phase and the measured intensity, are enough for the algorithm to converge. Several such reconstructions are used, with different initial steps. The spatial resolution is usually evaluated using the Phase Retrieval Transfer Function (PRTF) [4], which is a function defined over the averaging of those different reconstructions, giving a degree of confidence that the phases were retrieved consistently.

We demonstrated single shot CDI on our soft X-ray beamline using samples made of SiC or Si₃N₄ membranes, coated with a thin gold layer and patterned with a focused ion beam with sub-100 nm details. Before any of the optimization steps presented in Sect. 65.2, we achieved a spatial resolution of 120 nm and a temporal resolution of around 20 fs, thanks to the single shot acquisition time (Fig. 65.3a–c) [19]. The sample, diffraction pattern and reconstruction are presented in Fig. 65.3. Increasing the acquisition time up to 40 laser pulses, the resolution was improved to 62 nm, twice the wavelength. After optimization of the harmonic beamline using the Hartmann sensor (the modal filtering was not yet installed at that time), and using a similar sample, the spatial resolution was improved by almost a factor of two (Fig. 65.3d–f) [16].

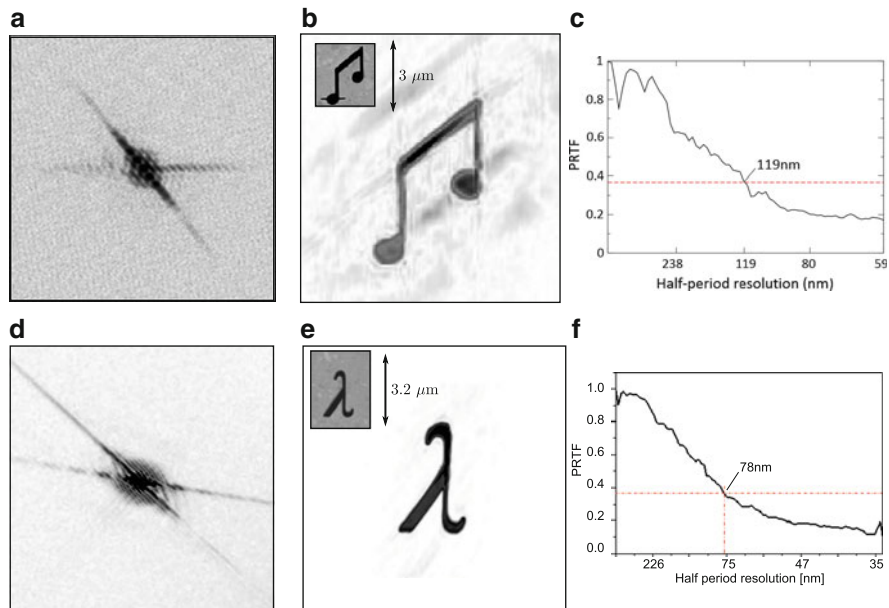


Fig. 65.3 Single shot results on CDI experiments. *Top row:* before beamline optimization. *Bottom row:* after optimization by the wavefront measurements. (a) and (d): diffraction patterns. (b) and (e) reconstruction, with a MEB image of the sample in inset. (c) and (f) PRTF, giving a spatial resolution of 119 nm for the first experiment and 78 nm for the second

Another possibility to solve the phase problem is to directly encode the spatial phase in the diffraction pattern. In Fourier Transform Holography (FTH), the field scattered by a small pinhole close to the sample interferes in the far field with the field diffracted by the object itself. The inversion of the hologram is then simply done by an inverse Fourier transform. In spite of its simplicity, FTH has some drawback related to the size of the reference, which has to be as small as possible to achieve a good spatial resolution. Guizar-Sicairos and Fienup proposed a new holography scheme using the edges of extended objects as references, named HERALDO [20, 21]. Combining a differential operator designed after the reference shape, it leads to a direct reconstruction of the sample image.

Using our beamline, we demonstrated experimentally the HERALDO technique, achieving 110 nm spatial resolution at $\lambda = 32$ nm in the single shot regime—i.e. with a 20 fs temporal resolution (Fig. 65.4) [22].

65.4 Preliminary Results

High order harmonic sources are ideal to perform time resolved studies. As a first experiment, we propose to study the ultrafast demagnetization dynamics of magnetic sample induced by an infrared ultrashort pulse [23]. We use cobalt/palladium

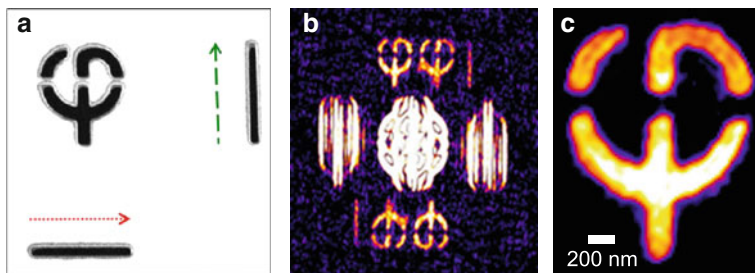


Fig. 65.4 HERALDO demonstration on our beamline. (a) Sample, with two slit references. (b) Reconstruction obtained by derivation along the *horizontal direction*. (c) Final reconstruction, which is the coherent sum of the four different reconstructions obtained from the hologram

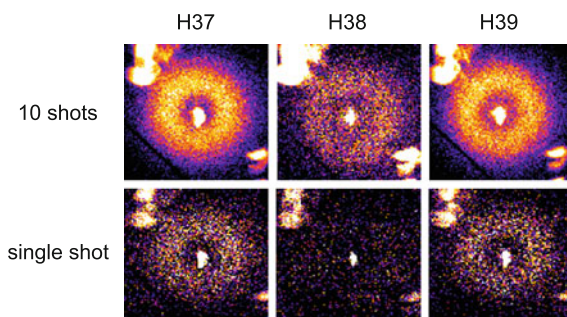


Fig. 65.5 Comparison of the magnetic diffusion ring obtained from [Co/Pd] multilayer samples, for different harmonic orders around the cobalt $M_{2,3}$ edge, in accumulative and single shot regimes. The images are not normalized, which explains the intensity variation between the different orders

multilayer samples, which present wormlike magnetic domains of typically 200 nm in transverse size. To make sure that single shot imaging of such a material is possible, we started by studying resonant magnetic scattering as a function of the wavelength around the cobalt $M_{2,3}$ edge (around 20 nm) [24]. To improve the wavelength resolution, we inserted a BBO crystal in the laser path to generate odd and even harmonic orders by mixing the fundamental field with its weak second harmonic. The evolution of the magnetic diffusion efficiency with the harmonic order reproduces the theoretical curves, even for measurements performed in the single shot regime (Fig. 65.5). Therefore we can conclude that dynamical imaging with 20 fs temporal resolution is possible, even at wavelength around 20 nm.

Another interesting topic is the study in real time of nanoscale actuators. We synthesized polymers films based on AZObenzene molecules. AZObenzene has two isomer forms (Fig. 65.6, top), and the switching from one to the other induces a change in the molecule overall size. Moreover, the isomerization process can be photo-induced using UV light and is fully reversible. All those properties makes AZO-polymers suitable tools to power and actuate molecular devices. Yu and coworkers demonstrated the bending of such films at the macroscopic level [25].

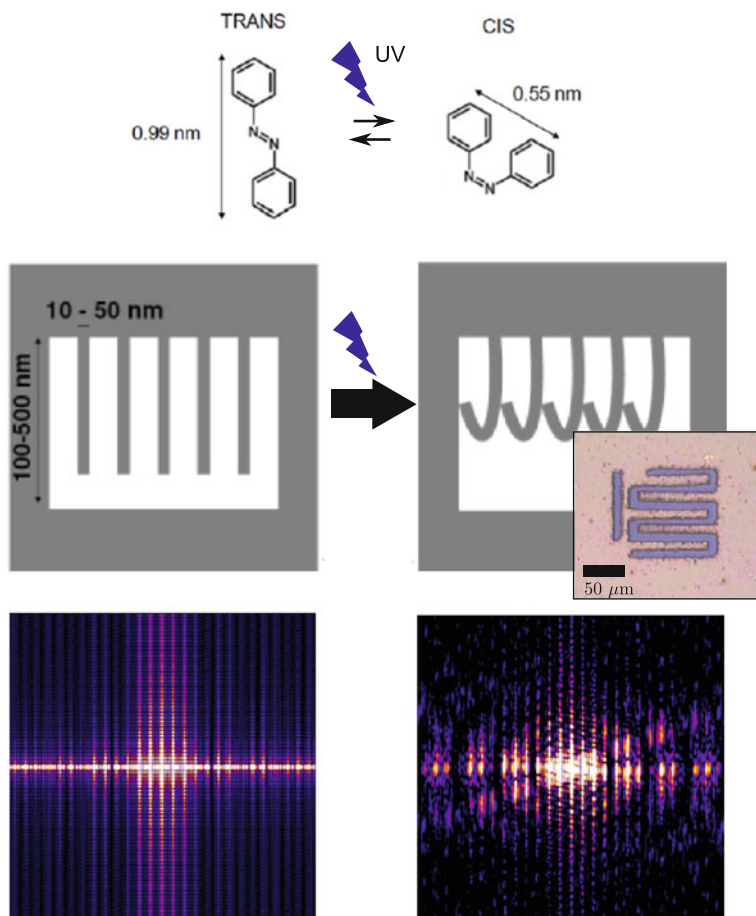


Fig. 65.6 *Top:* *trans* and *cis* AZObenzene isomers. *Bottom:* Simplified nanostructure of AZO polymers, before and after isomerization, and corresponding calculated diffraction patterns. The small inset is a picture of a microscopic test sample

We already synthesized some sample and patterned them by laser at the microscopic level (see the inset in Fig. 65.6). The actual nanoscale patterning will be done using a focus ion beam. According to first simulations, the diffraction pattern observed at the end of the isomerization step will differ quite noticeably from the initial one. Even so the isomerization takes place at the femtosecond level for an isolated molecule, it will be much slower for the polymer bending. However, observing this motion with a small temporal resolution may provide us with additional information.

65.5 Conclusion

We presented a table-top soft X-ray beamline, optimized for coherent diffractive imaging. It provides 5×10^8 at $\lambda = 32$ nm and 10^6 at $\lambda = 20$ nm photons per laser shot on the sample, in a high spatial quality spot with a $3 \mu\text{m}$ diameter. This high photon flux is sufficient to enable single shot diffractive imaging measurements with 100 nm or less spatial resolution. This opens the way towards time resolved studies of nanoscopic physical dynamics, with 20 fs time resolution.

Acknowledgements We acknowledge Marc Billon, Jan Luning, Henry Perez, Benoit Mahieu and the Saclay SLIC laser team. We acknowledge financial support from the European Union through the EU-LASERLAB and the EU-FP7 ATTOFEL programs, from the French ministry of research through the 2009 ANR grants "I-NanoX" and "Femto-X-Mag", from the "Triangle de la Physique" through the COX grant and the C'NANO research program through the X-NANO grant.

References

1. D. Sayre, Prospects for long-wavelength x-ray microscopy and diffraction. In *Imaging Processes and Coherence in Physics* (Springer, Berlin, 1980), pp. 229–235
2. D. Sayre, H.N. Chapman, J. Miao, On the extendibility of X-ray crystallography to noncrystals. *Acta Crystallogr. A* **54**, 232–239 (1998)
3. J. Miao, P. Charalambous, J. Kirz, D. Sayre D, Extending the methodology of X-ray crystallography to allow imaging of micrometre-sized non-crystalline specimens. *Nature* **400**, 342–344 (1999)
4. D. Shapiro et al., Biological imaging by soft x-ray diffraction microscopy. *Proc. Natl. Acad. Sci. USA* **102**, 15343–15346 (2005)
5. N.H. Chapman et al., Femtosecond X-ray protein nanocrystallography. *Nature* **470**, 73–77 (2011)
6. M.A. Pfeifer et al., Three-dimensional mapping of a deformation field inside a nanocrystal. *Nature* **442**, 63 (2006)
7. S. Eisebitt et al., Lensless imaging of magnetic nanostructures by X-ray spectro-holography. *Nature* **432**, 885–888 (2004)
8. A. Barty et al., Ultrafast single-shot diffraction imaging of nanoscale dynamics. *Nat. Photon.* **2**, 415–419 (2008)
9. J. Seres, E. Seres, A.J. Verhoef, G. Tempea, C. Strelt, P. Wobrauschek, V. Yakovlev, A. Scrinzi, C. Spielmann, F. Krausz, Source of coherent kiloelectronvolt X-rays. *Nature* **433**, 596–596 (2005)
10. A.-S. Morlens et al., Submicrometer digital in-line holographic microscopy at 32 nm with high-order harmonics. *Opt. Lett.* **31**, 3095–3097 (2006)
11. R.L. Sandberg et al., Lensless diffractive imaging using tabletop coherent high-harmonic soft-X-ray beams. *Phys. Rev. Lett.* **99**, 098103 (2007)
12. E. Takahashi, Y. Nabekawa, K. Midorikawa, Generation of 10- μJ coherent extreme-ultraviolet light by use of high-order harmonics. *Opt. Lett.* **27**, 1920–1922 (2002)
13. J.-F. Hergott et al., Extreme-ultraviolet high-order harmonic pulses in the microjoule range. *Phys. Rev. A* **66**, 021801 (2002)
14. J. Schwenke et al., Single-shot holography using high-order harmonics. *J. Mod. Opt.* **55**, 2723–2730 (2008)

15. B. Mahieu et al., Spatial quality improvement of Ti:Sa laser beam by modal filtering (in preparation)
16. X. Ge et al., Impact of wave front and coherence optimization in coherent diffractive imaging. Submitted to Opt. Express
17. J.R. Fienup, Reconstruction of an object from the modulus of its Fourier transform. Opt. Lett. **3**, 27 (1978)
18. S. Marchesini, A unified evaluation of iterative projection algorithms for phase retrieval. Rev. Sci. Instrum. **78**, 011301 (2007)
19. A. Ravasio et al., Single-shot diffractive imaging with a table-top femtosecond soft X-ray laser-harmonics source. Phys. Rev. Lett. **103**, 028104 (2009)
20. M. Guizar-Sicairos, J.R. Fienup, Holography with extended reference by autocorrelation linear differential operation. Opt. Express **15**, 17592–17612 (2007)
21. M. Guizar-Sicairos, J.R. Fienup, Direct image reconstruction from a Fourier intensity pattern using HERALDO. Opt. Lett. **33**, 2668–2670 (2008)
22. D. Gauthier et al., Single-shot femtosecond X-ray holography using extended references. Phys. Rev. Lett. **105**, 093901 (2010)
23. E. Beaurepaire, J.-C. Merle, A. Daunois, J.-Y. Bigot, Ultrafast spin dynamics in ferromagnetic nickel. Phys. Rev. Lett. **76**, 4250–4253 (1996)
24. M. Ducoussou et al., Ultrafast lensless resonant magnetic scattering study from 50 to 70 eV of [Co/Pd] sample. Submitted to PRL
25. Y. Yu, M. Nakano, T. Ikeda, Photomechanics: Directed bending of a polymer film by light. Nature **425**, 145 (2003)

Chapter 66

Strong-Field Effects and Attosecond Control of Electrons in Photoemission from a Nanoscale Metal Tip

M. Krüger, M. Schenk, and P. Hommelhoff

Abstract We focus few-cycle Titanium:sapphire oscillator pulses on a sharp tungsten tip and measure spectra of the emitted electrons. We observe above-threshold photoemission with a photon order of up to nine, peak shifting and peak suppression, and carrier-envelope phase sensitive photoemission. In a first attempt to understand the underlying physics we model the behavior with theory models borrowed from atomic physics, namely the Three-Step Model and an integration of the one-dimensional time-dependent Schrödinger equation. The models match the high-energy part of the spectra surprisingly well, and we infer that re-scattering and much of the well-known underlying physics of the Three-Step Model takes also place here, even though the parameters are such that this is almost surprising; for instance, the classical excursion of the electrons is only slightly larger than one atomic diameter.

66.1 Introduction

Sharp tips are employed as field emission electron sources in many high-resolution electron microscopes for their unsurpassed brightness [1]. The brightness builds on the fact that the electrons are emitted from nanometric areas if tips with a radius of curvature of around 10–100 nm are used, which can be easily fabricated using electro-chemical etching (the virtual source size is even smaller, but this is not at the center of this contribution). As the electrons follow the electric field the small emission area is projected on larger areas, easily with a magnification factor of 10^6 . Hence, a tiny source area can be imaged on a macroscopic detector, both in dc but also in laser-triggered operation [2, 3]. Here we take advantage of this fact to

M. Krüger · M. Schenk · P. Hommelhoff (✉)
Ultrafast Quantum Optics Group, Max-Planck-Institut für Quantenoptik,
Hans-Kopfermann-Str. 1, D-85748 Garching, Germany
e-mail: peter.hommelhoff@mpq.mpg.de

show that once a metal is well-controlled almost on the atomic level, and once the source area is so small that even in a tight laser focus the laser intensity can be well approximated as constant over the emission site, many if not all of the rich phenomena of multiphoton and strong-field physics can also be observed with metals [4, 5]. In addition, the smallness of the tip leads to an enhancement of the laser field at the tips apex so that these experiments can be done with a simple laser oscillator only (see [6] for related work with gold nanostructures).

66.2 Experimental Setup

An electro-chemically etched tungsten tip is mounted in an ultra-high vacuum chamber with a base pressure of a few 10^{-8} Pa. We focus ~ 6 fs oscillator pulses on the tip with the help of a 90° off-axis parabolic mirror; the spot radius is $\sim 2.4 \mu\text{m}$. In order to position the tip in the center of the focus it is mounted on a three-axis vacuum compatible translation stage. Electrons are detected with a retarding field spectrometer with a resolution of ~ 80 meV. We make sure that on average less than one electron per pulse is being emitted.

66.3 Above-Threshold Photoemission

With intensities of $\sim 2 \times 10^{11}$ W/cm² we observe above-threshold photoemission [4], see Fig. 66.1 (note that the experimental intensity values given in [4] are a factor of 2 too small; here they are correct). The spectra show that up to nine photon orders can be observed at intensities of around 3.7×10^{11} W/cm², where the electron yield monotonically drops with order. Clear strong field effects set in at 4×10^{11} W/cm², as evidenced by the suppression of the third-order peak. The peak distance is around 1.47 eV and matches the photon energy.

66.4 Strong-Field Effects and Field Enhancement

If we increase the laser intensity from 1.9×10^{11} to 4.6×10^{11} W/cm², not only is the third order peak becoming suppressed, but also do all spectral features shift with intensity to smaller energies. We interpret this as lightshifts (AC-Stark shift) of the continuum states, equalling the ponderomotive energy of an electron in a laser field of the respective frequency [7]. The lightshift of the initial state is likely negligible, as tungsten is a d-band metal where electrons near the Fermi level are quite localized and hence respond to the optical driving field to a much lesser extent [8].

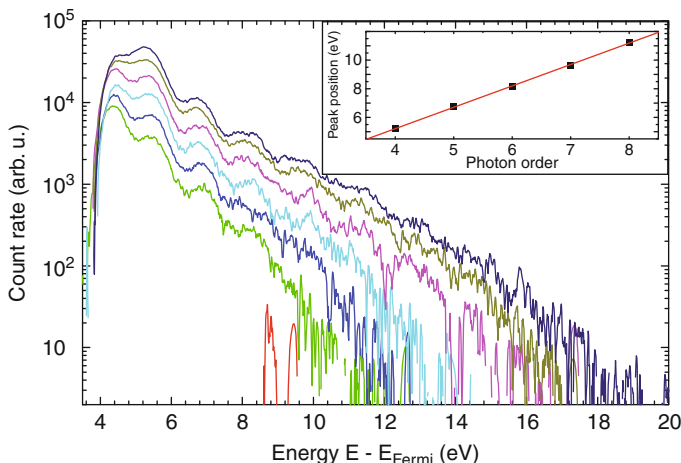


Fig. 66.1 Photo-electron spectra for various energies. From *bottom to top*, the laser intensity is $\{1.9, 2.3, 2.8, 3.2, 3.7, 4.2, 4.6\} \times 10^{11} \text{ W/cm}^2$. The *inset* shows the peak positions of the $4.6 \times 10^{11} \text{ W/cm}^2$ curve

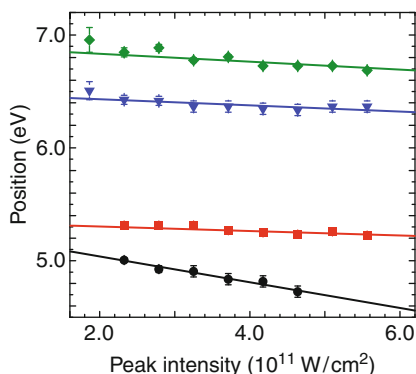


Fig. 66.2 Spectral shift of features of Fig. 66.1 as function of laser intensity. Clearly, all features exhibit decreasing energies with increasing laser intensities

In Fig. 66.2 we show the shifts for a few spectral features. The average slope directly yields the ponderomotive energy, which we compare to what we would expect in the absence of the tip. The former yields $(0.5 \pm 0.3) \text{ eV} \times I / (10^{12} \text{ W/cm}^2)$, the latter $0.055 \text{ eV} \times I / (10^{12} \text{ W/cm}^2)$, where I is the peak intensity. From the square-rooted ratio of these two numbers we obtain directly the field enhancement right at the tip's surface. It amounts to 3.0 ± 0.8 .

66.5 Carrier-Envelope Phase Effects

66.5.1 Experimental Data

With carrier-envelope phase (CEP) stabilized pulses we observe spectra as shown in Fig. 66.3. It is evident that the maximum kinetic energy of the electrons changes notably (on the 10% level). In order to make fainter effects more clearly discernable, we divide the data by an exponential curve, the result of which is shown in Fig. 66.4. Clearly, the spectra strongly depend on the CEP. For certain phase settings, the photon orders of the spectra as shown in Fig. 66.1 are clearly visible, for other settings the photon “bumps” are almost fully gone. Note that the visibility of the photon orders is exactly out of phase with the cut-off energy: For the highest visibility, the cut-off energy is smallest, and vice-versa. Furthermore, the electron current at cut-off energies can be almost fully switched on and off only by changing the CEP. This is why one might call this work a first step towards a transistor that is switched by the electric field of the laser pulse, an optical (attosecond) field effect transistor.

66.5.2 Three-Step Model

In order to try to understand this behavior, we first employ the probably most simple, but also most insightful model, the Three-Step model [9]. We extend the model

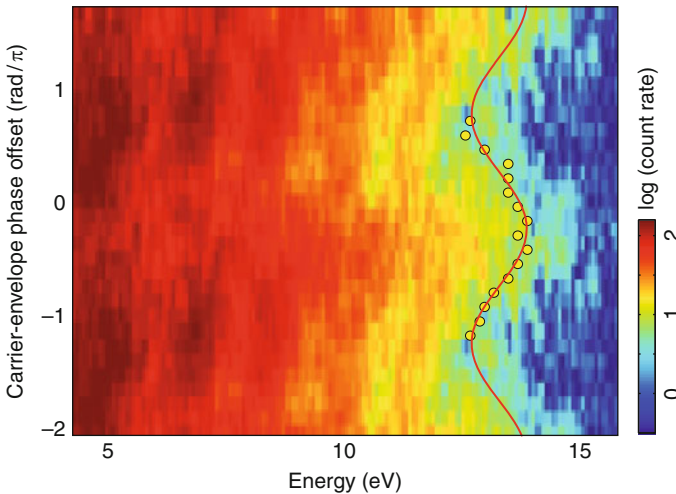


Fig. 66.3 Carrier-envelope phase effects. The data points and the *line* show the cut-off energy, defined by a fixed count rate. Here only the high-energy region is shown, starting with a kinetic energy 4.2 eV

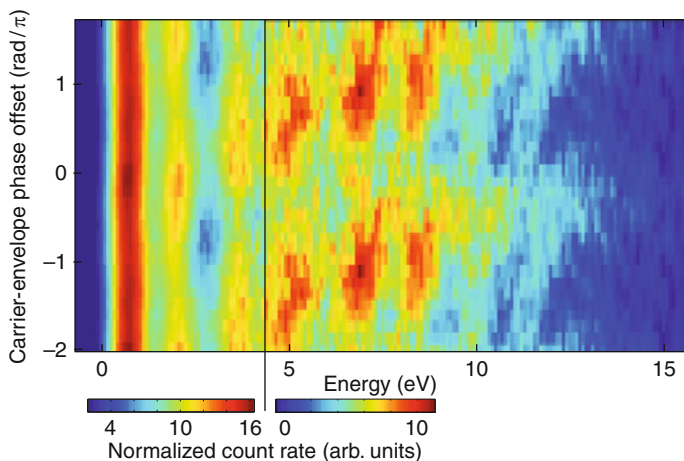


Fig. 66.4 Carrier-envelope phase effects, with only the differences of the data with respect to two exponentials shown. Clearly, regions of strong and weak photon order visibility exist

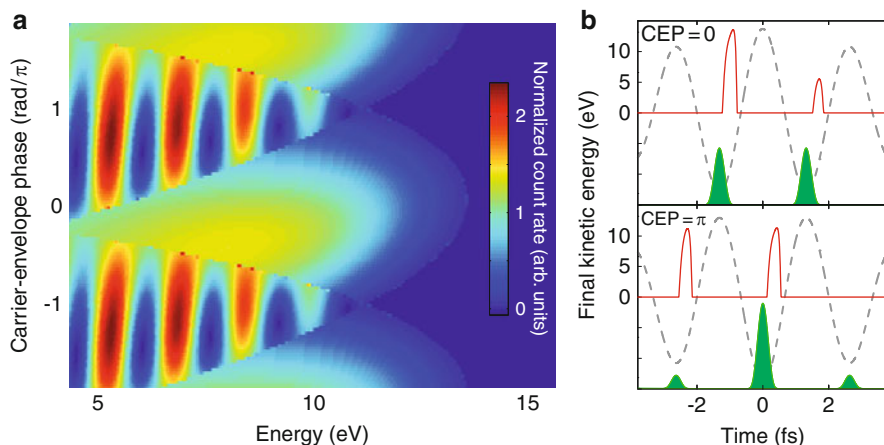


Fig. 66.5 Results of the Three-Step model. (a) Spectra that are analyzed and displayed like the experimental ones in Fig. 66.4. The sharp boundaries reflect the classical nature of the model. (b) Final electron energy (solid curve) as function of emission time for two different CEP settings (dashed curve: laser electric field; green: emission rate according to ADK theory). Note that we only consider electrons that re-scatter. Direct electrons can not reach the high energies shown

slightly by including the quantum mechanical action, in order to allow interference effects to arise; for details, see [5]. The result is shown in Fig. 66.5a. As in the experimental spectra, regions exist with a strongly modulated spectrum (around $CEP \approx \pi$), and regions where no modulation is visible at all. Figure 66.5b yields the explanation: only one emission window contributes to the unmodulated spectral regions, whereas two contribute to the highly modulated regions. Hence, in the

latter case interference arises in the conjugate variable, which is the energy. No interference arises if only one emission window in time exists, hence the spectral regions around $\text{CEP} \approx 0$ are flat.

66.6 Summary

We have shown that electrons undergo strong-field processes in photo-emission from a sharp metal tip well-known from atoms and molecules in the gas phase. Most notably, matter wave interference arises for a particular carrier-envelope phase setting. It will be interesting to work out the details of this supposedly complex metal system in much greater detail. Once this is done, one might be able to use this system as a novel tool for surface imaging with electrons emitted from the material under scrutiny, on the attosecond time scale. Furthermore, in this nanoscale solid-state system the high energy part of the electron current can be switched on and off with the help of the carrier-envelope phase only. Hence, with a nearby detector this system would resemble a first attosecond field effect transistor.

References

1. J.C.H. Spence, *High-Resolution Electron Microscopy* (Oxford University Press, New York, 2003)
2. P. Hommelhoff, Y. Sortais, A. Aghajani-Talesh, M.A. Kasevich, *Phys. Rev. Lett.* **96**(7), 077401 (2006)
3. P. Hommelhoff, C. Kealhofer, M.A. Kasevich, *Phys. Rev. Lett.* **97**(24), 247402 (2006)
4. M. Schenk, M. Krüger, P. Hommelhoff, *Phys. Rev. Lett.* **105**(25), 257601 (2010)
5. M. Krüger, M. Schenk, P. Hommelhoff, *Nature* **475**(7354), 78 (2011)
6. S. Kim, J. Jin, Y. Kim, I. Park, Y. Kim, S. Kim, *Nature* **453**(7196), 757 (2008)
7. P. Mulser, S. Uryupin, R. Sauerbrey, B. Wellegehausen, *Phys. Rev. A* **48**(6), 4547 (1993)
8. G. Saathoff, L. Miaja-Avila, M. Aeschlimann, M.M. Murnane, H.C. Kapteyn, *Phys. Rev. A* **77**(2), 022903 (2008)
9. P. B. Corkum, *Phys. Rev. Lett.* **71**(13), 1994 (1993)

Chapter 67

Femtosecond Laser-Induced X-Ray Emission from Gold Nano-Colloidal Solutions

K. Hatanaka, K. Yoshida, A. Iwasaki, and K. Yamanouchi

Abstract By irradiating droplets of chloroauric acid aqueous solution ($\sim 10^{-3}$ mol/l) and those of gold nano-colloidal solution with near-IR (~ 800 nm) femtosecond (35 fs) laser light, the X-ray intensity and the X-ray emission spectra were recorded. The laser pulses were focused onto the surface of droplets (~ 90 μ m in diameter) ejected from an ink-jet nozzle by an off-axis parabolic mirror. The X-ray intensity was about 660 times higher with the gold nano-colloidal solution than with the chloroauric acid aqueous solution. Electron temperatures calculated from the X-ray emission spectra on the basis of the assumption of the Boltzmann distribution were 0.074 keV for the chloroauric acid aqueous solution and 2.9 keV for the gold nano-colloidal solution. The significantly high X-ray intensity and electron temperature obtained with the gold nano-colloidal solution can be ascribed to the enhancement of the laser field intensity by surface plasmon resonance at the gold nano-particles.

K. Hatanaka (✉)

Center for Ultrafast Intense Laser Science, School of Science, The University of Tokyo, Tokyo 113-0033, Japan

Precursory Research for Embryonic Science and Technology, Japan Science and Technology Agency, Saitama 332-0012, Japan

e-mail: hatanaka@chem.s.u-tokyo.ac.jp

K. Yoshida

Department of Chemistry, School of Science, The University of Tokyo, Tokyo 113-0033, Japan

A. Iwasaki

Center for Ultrafast Intense Laser Science, School of Science, The University of Tokyo, Tokyo 113-0033, Japan

K. Yamanouchi

Center for Ultrafast Intense Laser Science, School of Science, The University of Tokyo, Tokyo 113-0033, Japan

Department of Chemistry, School of Science, The University of Tokyo, Tokyo 113-0033, Japan

67.1 Introduction

It has been known in these years that X-ray pulses can be generated by irradiating aqueous solutions with intense near-IR femtosecond laser pulses [1]. In this type of highly nonlinear optical processes, in which the photon energy is converted to be 10^3 – 10^4 times as high as the original photons, a variety of processes are considered to contribute such as acceleration of electrons ejected through ionization and the inelastic scattering of the accelerated electrons by atoms inducing their inner-shell excitation. It has also been reported recently that surface plasmon generated at solid substrates by ultrashort pulsed intense laser fields enhances nonlinear optical processes such as multi-photon absorption and high-order harmonics generation [2]. A numerical simulation showed that the enhancement of the high-order harmonics generation by silver-coated nano-cones [2] as well as by bowtie antennas [3] can lower the threshold laser field intensity required for the high-order harmonics generation to as much as three orders of magnitude. In the present study, in order to investigate whether the X-ray pulse generation through the interaction of condensed matter and intense laser fields could also be enhanced by surface plasmon, we measured the X-ray intensity and recorded the X-ray emission spectra by irradiating droplets of chloroauric acid aqueous solution ($\sim 10^{-3}$ mol/l) and those of gold nano-colloidal solution with near-IR (~ 800 nm) femtosecond (35 fs) laser light.

67.2 Experiment

Near-IR femtosecond laser pulses (35 fs, 800 nm, 1 kHz, Legend Elite HE USP, Coherent, Inc.) were focused in air onto sample droplets using an off-axis parabolic mirror ($f = 5$ cm). Sample droplets were generated by the ejection of the sample through an ink-jet nozzle (Microjet Inc.). The diameter of the droplets was measured under a microscope to be about $90 \mu\text{m}$. The laser pulse irradiation and the sample droplet ejection were precisely synchronized each other using a delay pulse generator (DG645, Stanford Research Systems, Inc.). X-ray intensity was measured by a Geiger counter (model 5000, Health Physics Instruments, Inc.) and the X-ray emission spectra were recorded by a Si solid-state detector (XR100, Amptek, Inc.). Chloroauric acid aqueous solution (2.5×10^{-3} mol/l) was chemically processed to form gold nano-colloidal solution by the addition of citric acid in a reflux system. The synthesis of gold nano-particles was confirmed by a scanning electron microscope and their diameter was confirmed to be in the range of 30–40 nm. Absorption spectra of the gold nano-colloidal solution showed a peak at the wavelength of 520 nm with a tail extending towards the longer wavelength region. This peak profile is ascribable to the enhancement of the absorption by the surface plasmon resonance.

67.3 Results and Discussion

Figure 67.1 shows the intensities of X-ray emission as a function of incident laser intensity obtained when distilled water, the chloroauric acid aqueous solution, and the gold nano-colloidal solution were irradiated with the near-IR femtosecond laser pulses. The X-ray intensities for distilled water and the chloroauric acid aqueous solution are almost the same, while the X-ray intensity when using the gold nano-colloidal solution becomes much higher than the other two samples. When the laser pulse energy is 0.2 mJ/pulse, the X-ray intensity obtained with the gold nano-colloidal solution is about 660 times higher than that obtained with the chloroauric acid aqueous solution. The X-ray emission spectra obtained with the chloroauric acid aqueous solution and the gold nano-colloidal solution were also recorded using the Si solid-state detector. After the intensity correction of the recorded X-ray emission spectra by the transmittance curve of the X ray in air, the normalized X-ray emission spectra were obtained. From the slope of the tail of the normalized X-ray emission spectra extending towards the high photon energy side obtained with the laser intensity of 0.6 mJ/pulse, the electron temperatures of the laser induced plasma through which the X-ray was generated were calculated to be 0.074 keV

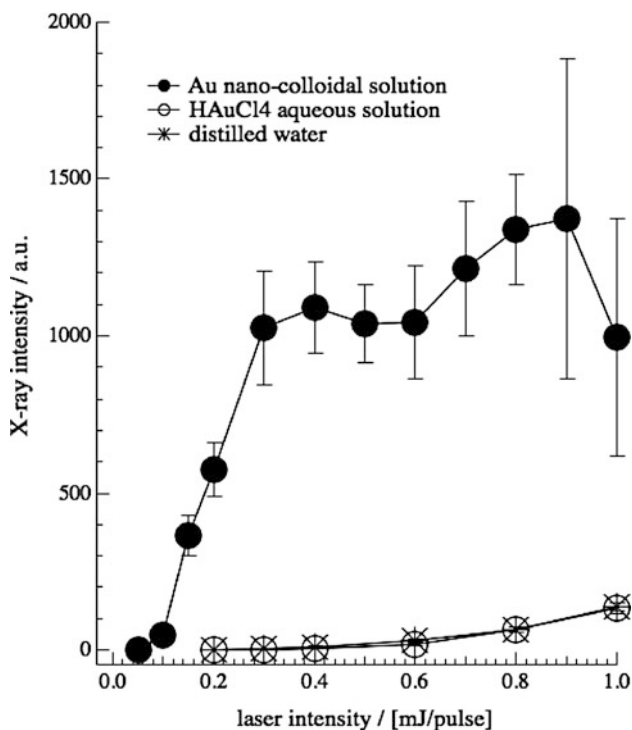


Fig. 67.1 X-ray intensity as a function of the incident laser intensity

for the chloroauric acid aqueous solution and 2.9 keV for the gold nano-colloidal solution by assuming the Boltzmann distribution for the electron energy distribution.

The increase in the X-ray intensity and the electron temperature for the gold nano-colloidal solution described above can be ascribed to the surface plasmon resonance of the gold nano-particles. It is well known that the absorption peak of the surface plasmon resonance of gold nano-particles is located at around 520 nm and that the long tail of the absorption band extends to the longer wavelength side, reflecting the aggregation of nano-particles [4]. On the other hand, the self-phase modulation induced by the propagation of the intense ($\sim 10^{14}$ W/cm²) laser pulse in air results in the wavelength shift towards the shorter wavelength side from the original wavelength at 800 nm [5]. Therefore, the tail part of the absorption band of the gold nano-colloidal solution could be efficiently excited by the wavelength-shifted laser light, resulting in the enhancement of the X-ray generation through the surface plasmon resonance.

References

1. K. Hatanaka, H. Fukumura, *X-Ray Spectrometry* (2012), in press.
2. A. Husakou, S.-J. Im, J. Herrmann, *Phys. Rev. A* **83**, 043839 (2011)
3. S. Kim, J. Jin, Y.-J. Kim, I.-Y. Park, Y. Kim, S.-W. Kim, *Nature* **453**, 757 (2008)
4. S.A. Maier, *Plasmonics: Fundamentals and Applications* (Springer, New York, 2007)
5. K. Hatanaka, T. Miura, H. Fukumura, *Appl. Phys. Lett.* **80**, 3925 (2002)

Index

- Above-threshold ionization (ATI), 193
Above-threshold photoemission (ATP), 365, 402
Acetylene, 260, 316–321, 348
AC-stark shift, 402
Adiabatic theory, 218–220
Angle-integrated, 271
Angle-resolved photoemission spectroscopy (ARPES), 366
Anticorrelated behavior, 180
Argon, 65–66
Asymmetrical, 271
 charge dissociation, 274
Asymptotics, 219
Atomic coherence, 141
Attochirp, 213
Attoclock, 169–171
Attoscience, 290
Attosecond, 187–191
 pulses, 123
 bandwidth-limit, 213
 conversion efficiency, 76
 discrete atomic energy level structure, 74
 generation, 86
 optical shutter/switcher, 75
 train, 128, 173
 X-ray, 213
 XUV radiation pulses, 76
 science, 32–40
 streak camera, 109, 110, 112, 116
Autocorrelation (AC), 62–63, 128

Band structure, 367, 368
Beamline, 360
Beam splitter (BS), 151

Below-threshold harmonics, 247
BIBO, 28
Biomolecules, 309, 310
 alpha cleavage mechanism, 311
 amino acid, 310, 311
 gas phase, 310
 McLafferty rearrangement, 311
 neutral, 310, 312
 phenylalanine, 310, 311
Bunkin–Fedorov approximation, 353
1,3-Butadiene, 260

Carrier-envelope phase (CEP), 3–7, 9, 11, 15, 16, 21, 24, 32–40, 46, 107, 269, 404
 dependent enhanced ionization, 275
 every-single-shot, 9, 10, 13
 high-field transient, 40
 regenerative amplifier (RGA), 10
 stabilization, 7
 synthesized pulses, 38
CBr₄, 355
CCl₄, 351–352, 355
Cesium, 80
CF₃I, 355
Charge asymmetrical dissociation and ionization, 274
Charge state, 343
Chemical potentials, 289–291, 296
Chirped pulse amplifier (CPA), 9
 regenerative amplifier (RGA), 9
Cl₂, 352
Classical models, 233–237
Clusters, 385
Coherence
 partial, 63–64
Coherent

- control, 269
- diffractive imaging
 - AZObenzene, 396
 - holography, 395
 - isomerization, 397
 - magnetic domains, 396
 - phase retrieval, 394
- phonons, 370, 371
- XUV sources, 137
- Coincidence
 - data, 166–167
 - momentum
 - data, 168
 - measurements, 166
- Coincidence momentum imaging (CMI), 336
- Cold target recoil ion momentum spectroscopy (COLTRIMS), 170, 194, 342
- Complex scaling
 - exterior, 189
- Correlated emission, 180
- Coulomb explosion, 341
 - imaging, 62, 318, 320, 321

- Deuterium, 131–132
- Diatomic molecule, 253, 300
 - heteronuclear diatomic molecule (HeDM), 254, 256
 - homonuclear diatomic molecule (HoDM), 255, 256
- Dipole approximation, 292, 293
- Dirac–Frenkel variational principle, 300
- Direct double ionization (DDI), 139
- Discrete variable representation (DVR), 306
 - DVR basis, 306, 307
- Dissociation, 132
- Doping, 386
- Double ionization, 188
- Double optical gating (DOG), 109, 110, 115
 - generalized (GDOG), 111
- Doubly excited states (DES), 188
- Driven by mid-IR sources, 260
- Droplets, 408
- Dual-chirped OPA (DC-OPA), 41, 42, 44
- Dual transformation method, 293

- Electron
 - correlation, 165–167, 170, 171
 - dynamics on solid surfaces, 373–376
 - recollision, 271
 - time of flight, 360
 - transit time, 365
- Electronic (ionization) dynamics, 290, 291, 293
 - laser driven electron dynamics, 290
 - multielectron dynamics, 292, 297
 - ultrafast electronic dynamics, 290
- Electronic wavepacket, 199
- Electron-scattering differential cross sections (ESDCSs), 239–240
- Electro-protonic wave function, 300
- Energy, 305–308
- Enhanced ionization (EI), 344, 348
- Ethylene, 260
- Evolution, 207
- Extinction ratio, 153
- Extreme ultraviolet (EUV), 156

- Femtosecond laser, 309
 - 267 nm, 311
 - 800 nm, 311
 - 1,400 nm, 311
- Few-cycle, 15, 20, 21, 318, 386
 - laser pulses, 107
- Field emission electron sources, 401
- Filamentation, 379
- Floquet states, 203
- Fourier
 - components, 204
 - spectroscopy, 134
 - transform, 130
- Fragmentation, 343
- Free-electron lasers (FELs), 62, 65, 156, 211
- Frequency-resolved optical gating (FROG), 49
- Frequency-resolved optical gating for complete reconstruction of attosecond bursts (FROG-CRAB), 110, 116

- Gas electron diffraction experiments, 351–352
- Gold nano-colloidal solutions, 407–410
- Gordon–Volkov state, 222
- Gouy phase, 205
- Group delay dispersion (GDD), 42–44

- H_2^+ , 305–307
- H_3^+ , 232–237
- Hard X-ray, 211
- Harmonic
 - generation, 138
 - spectrum, 253–256
- H/D exchange, 337
- Helium, 187–191
- Heterodyne interferometry, 105

- High-harmonic generation (HHG), 27, 33, 34, 36, 37, 40, 145, 148, 149
 - continuum–continuum (CC), 210
 - efficiency, 145, 148
 - interference model, 210
 - isolated attosecond pulse generation, 40
 - macroscopic, 149
 - propagation, 148
 - optimal pressure, 148
 - phase-matching, 145, 147–149
 - reabsorption, 145, 149
 - synthesized
 - electric field, 39
 - pulse, 39
 - waveform, 40
 - two-electron model, 212
- High-harmonics, 46, 107, 204
- High-order harmonic (HH), 156, 174, 373–376
- High-order harmonic generation (HHG), 80, 81, 86, 121, 156, 260, 277–281, 392
 - below- and near-threshold harmonics, 80, 82, 83
 - experimental setup, 393
 - gases, 121
 - harmonics close to I_p , 83
 - laser spatial filtering, 392
 - loose focusing, 392
 - lower than or near I_p , 84
 - optimization, 394
 - polarization state, 122
- Hollow core fiber (HCF), 49
- Hollow-fiber compression, 92
- Hot electrons, 361
- Hydrogen
 - migration, 299, 316–321, 335
 - molecular ions, 247
- Hydrogen-like atoms, 71–77
 - three-level system, 73
- Ignition, 384–390
- Imaginary time method (ITM), 223
- Imaging, 123
 - ultrafast, 123
- Independent atom model, 240
- Infrared double optical gating (IRDOG), 98
- Inner shell orbitals, 212
- Instantaneous
 - energies, 73
 - geometrical structure, 352, 355
 - ionization rates, 73
- Intense few cycle, 384–390
- Interatomic
 - Coulombic decay, 215
 - photoionization, 216
- Interference, 122, 123
 - center, 123
 - fringes, 124
 - quantum-path, 122
- Interferometric polarization gating, 138
- Interferometry, 128, 187–191
- Ionization, 385
 - above threshold ionization (ATI), 227
 - atomic single-ionization, 222
 - channel, 204
 - dynamics, 296
 - gating, 90–95
 - holography, 226
 - multiple, 65–66
 - probability, 206
 - processes, 290, 296, 305
 - energy accepting orbitals, 289
 - ionization efficiency, 294, 297
 - ionization probabilities, 290, 293, 294, 296
 - nonsequential double ionization, 290
 - suppression of ionization, 293
 - rates, 305–308
 - times, 170–172
- Ions, 76
 - Li^{2+} -plasma source, 76
 - molecular, 123
 - XUV lithography, 76
- Isolated attosecond pulses (IAPs), 96–104, 107
- Isomerization, 318, 320
- Keldysh
 - parameter, 219
 - theory, 219
- Kinetic energy spectrum, 132
- Laser-assisted electron scattering (LAES), 351–355
- Laser field
 - electric field, 306, 307
 - intense laser field, 305
 - strong electric field, 305
 - weak field, 305
- Laser induced acoustic desorption (LIAD), 309, 310, 312
 - acoustic shockwave, 310, 312
- Laser pulse shaping, 213
- Lightshifts, 402
- Long trajectory, 226
- Low energy structure (LES), 229

- Magnetic-bottle, 110, 112, 114
- Matter wave interference, 406
- Mid-infrared laser, 80, 83
- Mid-IR source, 278, 281
- Minimum, 253–256
 - structural minimum, 253, 254
- Molecular
 - clock, 180
 - dissociation, 235
 - fragmentation, 341
 - ionization, 235
 - orbital imaging, 281
- Molecule
 - molecular, 305–307
- Momentum
 - distribution, 225
 - spectra, 226
- Morlet wavelet, 250
- Multi-configuration wave function, 299
- Multiphoton process in atoms, 173
- Multiple ionization, 270
- Multiple-scattering, 241

- Nanodroplets, 384–390
- Natural orbitals, 290, 302
 - correlation energies for natural orbitals, 290, 296
 - energetics of natural orbitals, 296
 - energy
 - accepting orbitals, 290, 295, 297
 - donating orbitals, 295
 - ionization efficiency, 289
 - spectator orbital, 295, 297
- Nonadiabatic
 - responses, 295
 - saddle-point, 95
- Nonlinear interaction, 130
- Non-linear XUV processes, 137
- Nonsequential double ionization (NSDI), 179

- Octave, 28
- Optical parametric amplifiers (OPAs), 15–18, 21, 24, 28, 45–47, 86
- Optical parametric chirped-pulse amplifiers (OPCPAs), 32–40
 - coherent wavelength multiplexing, 37
 - synthesized
 - pulses, 38
 - waveform, 37
- Orientation, 243–246
- Orthogonal two-color field, 179
- Oscillation, 183–186

- Out of phase, 273, 274
- Over-the-barrier ionization (OBI) regime, 210

- Parameter, 271
- PbTiO₃, 370
- Phase
 - matching, 53–55
 - variation, 206
- Phase retrieval by omega oscillation filtering (PROOF), 110, 116
- Photoelectron momentum, 226
- Photoelectron spectroscopy (PES), 373
- Photoemission, 365
- Photoionization
 - of atoms, 215
 - differential cross section, 239
 - processes, 204
- Plasma, 381
 - defocusing, 146, 148, 149
- Polarization, 378–383
 - ellipse, 121
 - ellipticity, 122
 - rotation angle, 121–122
- Ponderomotive energy, 403
- Probability density of protons, 302
- Prolate spheroidal coordinates, 240, 248
- Propagation, 75
- Proton transfer, 313
- Pump-probe, 187–191, 361

- Quantum
 - beats, 141
 - interference, 203
 - orbits (or quantum trajectory), 223
- Quantum-path, 122
 - long, 122
 - selection, 123, 124
 - short, 122

- Reaction
 - microscope, 63, 184
 - COLTRIMS, 185
 - microscopy, 270
- Recollision, 165, 166, 239
- Reflectivity, 153
- Refractive index, 152
- Relative phase, 180–181
- Resolving power, 134
- Resonant interaction, 71, 72
 - ionization from the excited states, 71, 73
 - optically dense medium, 72

- Stark splitting, 71, 74
- Revisit time, 180
- R-matrix, 307, 308
 - basis, 306
 - inner region, 306, 307
 - outer region, 307
 - propagation
 - method, 240
 - technique, 306
 - theory, 306
- Saddle point approximation, 223
- SASE FEL, 156
- Schrödinger equation, 306
 - stationary Schrödinger equation, 306
- SEA-F-SPIDER, 50
- SEA-SPIDER, 50
- Second order autocorrelation (second order IVAC), 138
- Seeded FEL, 158
- Self-amplified spontaneous emission (SASE), 62, 63, 156
- Self-difference frequency generation (DFG), 45–47
- Sequential two-photon double ionization (SDI), 139
- SF₆, 355
- Short trajectory, 226
- Sideband, 183–186
 - oscillation of energy sidebands, 183
 - RABBIT, 186
 - sideband oscillation, 185–186
- Siegert
 - outgoing-wave boundary conditions, 306
 - regularity boundary conditions, 306
 - Siegert boundary conditions, 308
 - Siegert-state method, 306
 - Siegert states, 219, 306, 308
- Silicon, 151
 - carbide, 151
- Slow variable discretization, 306
- S-matrix, 240
- Soft-mode, 371
- Soft X-ray, 127
- Space-time couplings, 52
- Spatial imaging, 205
- Spatially-encoded arrangement (SEA), 50
- Spectral phase interferometry for direct electric field reconstruction (SPIDER), 49
- Spectral shearing interferometry, 50
- Spectrogram, 110, 116
- Spectroscopy, 260
- SPring-8 Compact SASE source (SCSS), 156
- Stationary phase equation (SPE), 223
- Steepest descent approximation, 222
- Streaking
 - transversal, 366
- Strong-field
 - ionization, 193
 - processes, 406
- Strong-field approximation (SFA), 196, 222
 - trajectory-based Coulomb-corrected SFA (TCSFA), 222
- Sub-cycle interference, 195
- Sub-fs, 141
- Supercontinuum, 47, 107
- Surface
 - photovoltage, 373
 - plasmon, 408, 410
- Terahertz (THz), 243–246
- Three-step model, 404–406
- Time-compensated monochromator, 53–55
- Time-delay-compensated monochromator, 56–59
- Time-dependent generalized pseudospectral method (TDGPS), 80
- Time dependent Hartree–Fock (TDHF), 348
- Time-dependent multiconfiguration theory, 290, 291, 296
 - multi-configuration time-dependent Hartree–Fock method (MCTDHF), 290
- Time-dependent Schrödinger equation (TDSE), 195
- Time-of-flight (TOF), 129
- Time-resolved photoelectron spectroscopy, 313
- Trajectories, 250
- Trajectory-based Coulomb-corrected strong field approximation (TCSFA), 222
- Transient absorption, 198–201
- Tungsten tip, 402
- Tunnel ionization, 223
- Two-center interference, 241
- Two-color pulse, 194
- Two photon emission, 361–362
- Ultrafast dynamics, 309, 312
- Ultra-violet
 - extreme, 62
- Velocity map imaging (VMI), 129
- Vibration isolation, 360
- Vinylidene, 318, 321
- Volkov state, 222

Waveform synthesis, [37–40](#)
Wavelength selective streak pulses,
[101](#)
Wavelet transform, [250](#)
Wavepacket interference, [198–201](#)

Xe, [351–352](#), [354–355](#)
X-Ray, [407–410](#)
XUV, [127](#)
 spectrograph, [133](#)
XUV-pump–XUV-probe, [140](#), [187](#)